Fluorescence and ZEKE spectroscopy of small, jet-cooled aromatic molecules

Alexander R. Davies

Thesis submitted to the University of Nottingham for the degree of
Doctor of Philosophy

June 2022

ABSTRACT

A detailed spectroscopic analysis is presented for the $S_1 \leftrightarrow S_0$ and $D_0^+ \leftarrow S_1$ transitions of *meta*-fluorotoluene (*m*FT) and *N*-methylpyrrole (NMP) through resonance-enhanced multiphoton ionisation (REMPI), laser-induced fluorescence (LIF), dispersed fluorescence (DF), two-dimensional laser-induced fluorescence (2D-LIF) and zero-electron-kinetic-energy (ZEKE) spectroscopy. Assignments have been made for various vibrations, torsions and vibration-torsion bands in these spectra, detailing the energy levels in the three electronic states. These studies comprise the most comprehensive spectroscopic studies of these two molecules to date.

For *m*FT, discussion has been made regarding how vibration-vibration and vibration-torsion eigenstates couple together and how this evolves from a purely localised, restricted coupling mechanism at low internal energies to widespread, dissipative intramolecular vibrational energy redistribution (IVR) at only modest internal energy. Furthermore, an extreme case of Duschinsky mixing has been examined, which manifests itself in the spectra in a similar way to anharmonic coupling; this has been elucidated through a combination of emission and excitation spectroscopy, quantum chemical calculations and a comparison to *meta*-chlorotoluene (*m*ClT), in which this mixing is also present, yet not so extreme. In the D_0^+ cationic state, the activity observed is discussed largely in terms of significant changes in torsional potential compared to the S_1 state, leading to off-diagonal torsional transitions having considerable, and often dominant, intensities. Additionally, the ZEKE spectra appear less enlightening in ascertaining the assignment of the activity in S_1 than do the 2D-LIF spectra, although they are useful as a confirmatory/diagnostic tool.

The $S_1 \leftarrow S_0$ transition of NMP is electric dipole forbidden and, as such, the activity observed in the REMPI and LIF spectra is largely due to vibronic coupling with nearby, higher-lying electronic states. Routes for the observed vibronic coupling have been proposed and discussed, alongside commentary regarding the results of previous photodynamical studies. The ZEKE spectra of NMP have been investigated, which exhibit highly diagonal Franck-Condon factors, except for those *via* the b_1

symmetry, ring-localised modes. Nevertheless, it was possible to derive a precise adiabatic ionisation energy (AIE) of 64250 ± 5 cm^{-1}. The 2D-LIF spectra are significantly more complicated than one might expect.

Furthermore, a new labelling scheme for *N*-substituted pyrroles is proposed, which allows for the comparison of vibrations of different molecules of the same symmetry class, which are expected to be valid for almost all (reasonable) substituents. This scheme is similar to those proposed for mono- and disubstituted benzene molecules, and the corresponding scheme for *meta*-disubstituted benzenes is used in the analysis of *m*FT.

Finally, REMPI and ZEKE spectra have been recorded for the first time, of the NMP-RG (RG = Ar, Kr) complexes, noting that the presence of the rare gas is sufficient to perturb the electronic structure to allow the observance of the NMP-RG origin in the REMPI spectra. Furthermore, we deduce AIEs of 64077 ± 5 cm^{-1} and 64029 ± 5 cm^{-1} for NMP-Ar and NMP-Kr, respectively.

Table of Contents

ABSTRACT ii

I. Publications included as a part of this thesis vii

II. Other publications by the author ix

III. Acknowledgements x

IV. Glossary of terms xii

1. Introduction 1

2. Theoretical background 10

  2.1. Born-Oppenheimer approximation 10

  2.2. Allowed electronic transitions 12

  2.3. Franck-Condon principle 14

  2.4. Herzberg-Teller (vibronic) coupling 19

  2.5. Vibrations of diatomic molecules 24

    2.5.1. Hooke’s law and the harmonic oscillator 24

    2.5.2. The anharmonic oscillator and the Morse potential 27

    2.5.3. Extension to polyatomic molecules 29

  2.6. Anharmonic coupling 31

    2.6.1. Fermi resonance 36

    2.6.2. Restricted IVR 39

    2.6.3. Statistical (dissipative) IVR 40

  2.7. Duschinsky mixing 41

3. The effect of the methyl rotor in molecular spectroscopy 45

  3.1. The free rotor 46

  3.2. The hindered rotor 48

  3.3. The splitting of the free-rotor torsional levels upon the application of a hindering potential 53

3.4. Molecular symmetry groups 59
3.4.1. The G_6 molecular symmetry group 60
3.4.2. The G_{12} molecular symmetry group 62
3.4.3. The symmetries of vibrational and vibrational-torsional levels using MSGs 65
4. Labelling schemes and notations 67
4.1. Vibrational labelling 67
4.1.1. The Wilson/Varsányi labelling scheme 67
4.1.2. The Mulliken/Herzberg labelling scheme 68
4.1.3. The ${}^{m}D_i$ and P_i labelling schemes 69
4.2. The labelling of vibrational, vibtor and torsional transitions 70
5. Experimental methods 73
5.1. Supersonic jet expansions 73
5.2. Resonance-enhanced multiphoton ionisation (REMPI) spectroscopy 76
5.3. Laser-induced fluorescence (LIF) spectroscopy 80
5.4. Dispersed fluorescence (DF) and two-dimensional laser-induced fluorescence (2D-LIF) spectroscopy 82
5.5. Zero-electron-kinetic-energy (ZEKE) spectroscopy 85
5.6. Quantum chemical calculations 88
5.7. Experimental apparatus: REMPI/ZEKE 89
5.8. Experimental apparatus: 2D-LIF 94
5.9. A note on gratings and grating anomalies 95
6. Introduction to the published papers 99
7. Variations in Duschinsky rotations in *m*-fluorotoluene and *m*-chlorotoluene during excitation and ionization 102
8. Methyl-torsion-facilitated internal energy delocalization following electronic excitation in *m*-fluorotoluene: can *meta* and *para* substitution be directly compared? 104

9. Unpicking vibration-vibration and vibration-torsion interactions in *m*-fluorotoluene 106

10. Torsions of *N*-methylpyrrole and its cation 108

11. Vibrations of pyrrole, *N*-substituted pyrroles, and their cations 110

12. Electronic, vibrational and torsional couplings in *N*-methylpyrrole: ground, first excited and cation states 112

  12.1. Comment on "Electronic, vibrational and torsional coupling in *N*-methylpyrrole: ground, first excited and cation states" [J. Chem. Phys. 154, 224305 (2021)] 116

13. Spectroscopy of *N*-methylpyrrole-RG (RG = Ar, Kr) complexes: first excited neutral and cationic states 118

14. Final remarks and outlook 120

15. References 126

Appendix 1. Mode diagrams for *N*-fluoropyrrole and *meta*-difluorobenzene 137

Appendix 2. Pertinent character tables 139

Appendix 3. The $^{m}D_i$ labels and vibrations for *meta*-disubstituted benzenes and the P_i labels and vibrations for *N*-substituted pyrroles 141

Appendix 4. Supplementary material 144

I. Publications included as a part of this thesis

1. “Variations in Duschinsky rotations in *m*-fluorotoluene and *m*-chlorotoluene during excitation and ionization”, A. R. Davies, D. J. Kemp, L. G. Warner, E. F. Fryer, A. Rees and T. G. Wright, *J. Chem. Phys.*, 2020, **152**, 214303.

2. “Methyl-torsion-facilitated internal energy delocalization following electronic excitation in *m*-fluorotoluene: can *meta* and *para* substitution be directly compared?”, A. R. Davies, D. J. Kemp and T. G. Wright, *AIP Adv.*, 2020, **10**, 125206.

3. “Unpicking vibration-vibration and vibration-torsion interactions in *m*-fluorotoluene”, A. R. Davies, D. J. Kemp and T. G. Wright, *J. Molec. Spectrosc.*, 2021, **381**, 111522.

4. “Torsions of *N*-methylpyrrole and its cation”, A. R. Davies, D. J. Kemp and T. G. Wright, *Chem. Phys. Lett.*, 2021, **763**, 138227.

5. “Vibrations of pyrrole, *N*-substituted pyrroles and their cations”, A. R. Davies, D. J. Kemp and T. G. Wright, *J. Molec. Spectrosc.*, 2021, **376**, 111410.

6. “Electronic, vibrational and torsional couplings in *N*-methylpyrrole: ground, first excited and cation states”, A. R. Davies, D. J. Kemp and T. G. Wright, *J. Chem. Phys.*, 2021, **154**, 224305.

7. “Comment on: “Electronic, vibrational and torsional couplings in *N*-methylpyrrole: ground, first excited and cation states” [*J. Chem. Phys.* 154, 224305 (2021)]”, A. R. Davies, D. J. Kemp and T. G. Wright, *J. Chem. Phys.*, 2021, **155**, 117101.

8. “Spectroscopy of *N*-methylpyrrole-RG (RG = Ar, Kr) complexes: first excited neutral and cationic states”, A. R. Davies, J. T. L. Haynes and T. G. Wright, *Chem. Phys. Lett.*, 2022, **803**, 139800.

II. Other publications by the author

1. "Vibration-modified torsional potentials and vibration-torsion ("vibtor") levels in the *m*-fluorotoluene cation", D. J. Kemp, E. F. Fryer, A. R. Davies and T. G. Wright, *J. Chem. Phys*, 2019, **151**, 084311.

   This paper, while not included in this thesis, as the work was conducted and written up during an MSci project, lays the foundation for the work on *meta*-fluorotoluene that *is* presented as a part of this thesis. As well as discussion of the pure torsional levels in S_0, S_1 but mostly D_0^+, several low-energy vibrational modes are also considered. The reader may find it useful to consult this paper for the background to the torsional levels in *meta*-fluorotoluene.

2. "Interactions of Si^+ (^2P_J) and Ge^+ (^2P_J) with rare gas atoms (He – Rn): interaction potentials, spectroscopy and ion transport coefficients", A. R. Davies, A. Cranney, L. A. Viehland and T. G. Wright, *Phys. Chem. Chem. Phys.*, 2022, **24**, 7144.

3. "Interactions of coinage-metal/ligand complexes, CM-L, and their cations (CM = Cu, Ag, Au; L = CO, N_2 and H_2)", A. R. Davies, H. Azim and T. G. Wright, *Mol. Phys.*, 2022, *in press*. DOI: 10.1080/00268976.2022.2101956.

III. Acknowledgements

First and foremost, I have to extend my sincerest gratitude to my supervisor, Prof. Tim Wright, whose guidance, support and insight has been invaluable over the course of the last three years. His unwaning optimism, humour (?) and patience has made him a pleasure to work with. I also have to thank him for putting up with my excessive sarcasm, pessimism, whining and just generally being a bit of hard work. Cheers, Tim, it has been a good, and productive, few years! Enjoy your retirement, you deserve it – I hope you find many good books to read, and I hope the dog doesn't become too expectant of walks.

I also have to thank Dr. David Kemp, a former member of the group, but also a good friend, for teaching me how to run the experiments efficiently and single-handedly. I also thank him for his patience, and his willingness to explore the gastronomical pleasures (and horrors) of Nottingham with me. I wish him all the best with his career. He has also been an excellent vent for my frustrations with various things, both listening and offering practical solutions – so thanks for putting up with that!

Thank you to Dr. James Thompson, a postdoctoral research fellow in the Reid group, who has been available to help me out with various practical and laser issues over the last three years, as well as lending me optics and electronics while I've been waiting for replacements/repairs. The spontaneous scientific lunchtime conversations have also been both entertaining and stimulating.

I must also extend my thanks to the technical staff in the School of Chemistry who have made my life over the last three years so much easier. Firstly, Dave Litchfield and James Warren, from the electronics workshop, have helped me out when I inevitably broke every single laser power supply we own at some point. Secondly, to everyone in the mechanical workshop, who have been on hand (sometimes begrudgingly) to help whenever I needed 'just a quick job' done. Also, thank you to Neil Barnes, who has always been around to sort me out with gas regulators, deal with my turbopump issues (notably when I was silly enough to drop a screw inside one…) and for also being constantly available confirm that what I was about to do was a silly idea. Jim and Eric from the chemical stores also deserve a mention for delivering any packages and chemicals I ordered to me, as well arranging the disposal of waste solvent for me. Last, but not least, to everyone else in the School of Chemistry who has helped me out in some way at some point throughout this PhD.

A special mention must go to the University of Nottingham Archery Club – an absolute institution that has kept me sane (remarkable feat) for seven years, and has given me an avenue to destress and make some invaluable friends. Thanks a bunch to everyone I've had the pleasure to shoot with over the years and I wish you all the best.

Finally, I have to thank my parents, for their unwavering support and confidence in me over the last few years, especially my mother, who (bravely) offered to check this mighty tome to ensure my eyes had not glanced over any potentially lewd typos.

IV. Glossary of terms

2D-LIF	two-dimensional laser-induced fluorescence
AIE	adiabatic ionisation energy
aug-cc-pVTZ	augmented, correlation-consistent, polarised, valence triple-zeta (basis set)
B3LYP	A hybrid exchange-correlation functional, for use in DFT calculations, comprising Becke's three-parameter exchange functional and the correlation functional of Lee, Yang and Parr
BBO	(β-) barium borate
CAM-B3LYP	Coulomb attenuating method B3LYP
CCD	charge-coupled device
D_0^+	ground doublet electronic state of the cation
DF	dispersed fluorescence (also known in the literature as 'single vibronic level fluorescence', SVLF)
DFT	density functional theory
DM	Duschinsky matrix
DNA	deoxyribonucleic acid
FC	Franck-Condon
FCF	Franck-Condon factor
FWHM	full width at half maximum
HOMO	highest occupied molecular orbital
HT	Herzberg-Teller
IR	infrared
IVR	intramolecular vibrational (energy) redistribution – the 'E' from 'energy' is often omitted from the initialism, although some authors do use the initialism 'IVER' instead.
KDP	potassium dihydrogen phosphate
MATI	mass-analysed threshold ionisation
*m*ClFB	*meta*-chlorofluorobenzene
*m*ClT	*meta*-chlorotoluene
MCP	microchannel plate
*m*DFB	*meta*-difluorobenzene

*m*FT	*meta*-fluorotoluene
MSG	molecular symmetry group
Nd:YAG	neodymium-doped yttrium aluminium garnet
NFP	*N*-fluoropyrrole
NMP	*N*-methylpyrrole
PC	personal computer
*p*DFB	*para*-difluorobenzene
PFI	pulsed-field ionisation
*p*FT	*para*-fluorotoluene
PIE	photoionisation efficiency
PMT	photomultiplier tube
*p*Xyl	*para*-xylene
(R)CCSD(T)	(restricted open shell) coupled cluster theory with single and double excitations and perturbative inclusion of triple excitations
REMPI	resonance-enhanced multiphoton ionisation
RG	rare gas (also known as ‘noble gas’)
S_0	ground singlet electronic state
S_1	first excited singlet electronic state
TD	time-dependent
ToF	time-of-flight
UV	ultraviolet
vdW	van der Waals
vibtor	vibration-torsion
vibtoronic	vibration-torsion-electronic
VUV	vacuum ultraviolet
XUV	extreme ultraviolet
ZEKE	zero-electron-kinetic-energy
ZOB	zero-order bright (state)
ZOD	zero-order dark (state)
ZOS	zero-order state

1. Introduction

The work presented in this thesis focuses on the electronic spectroscopy of small, aromatic compounds, namely *meta*-fluorotoluene (*m*FT) and *N*-methylpyrrole (NMP); schematics of these are shown in Figure 1.1. However, numerous references and comparisons will be drawn to closely related molecules, such as *para*-fluorotoluene (*p*FT), *meta*-chlorotoluene (*m*ClT) and pyrrole. In this thesis, NMP and *m*FT will be investigated in their neutral ground state, S$_0$, first excited neutral state, S$_1$, and the cationic ground state, D$_0^+$. The electronic structures of these molecules will be studied in these three electronic states, by employing several spectroscopic techniques, including resonance-enhanced multiphoton ionisation (REMPI), laser-induced fluorescence (LIF), zero-electron-kinetic-energy (ZEKE) spectroscopy, dispersed fluorescence (DF) and two-dimensional laser-induced fluorescence (2D-LIF) spectroscopies; these techniques will be discussed in greater detail in Section 5. In this section, some of the motivations behind this work will be discussed, alongside a brief description of the field to date.

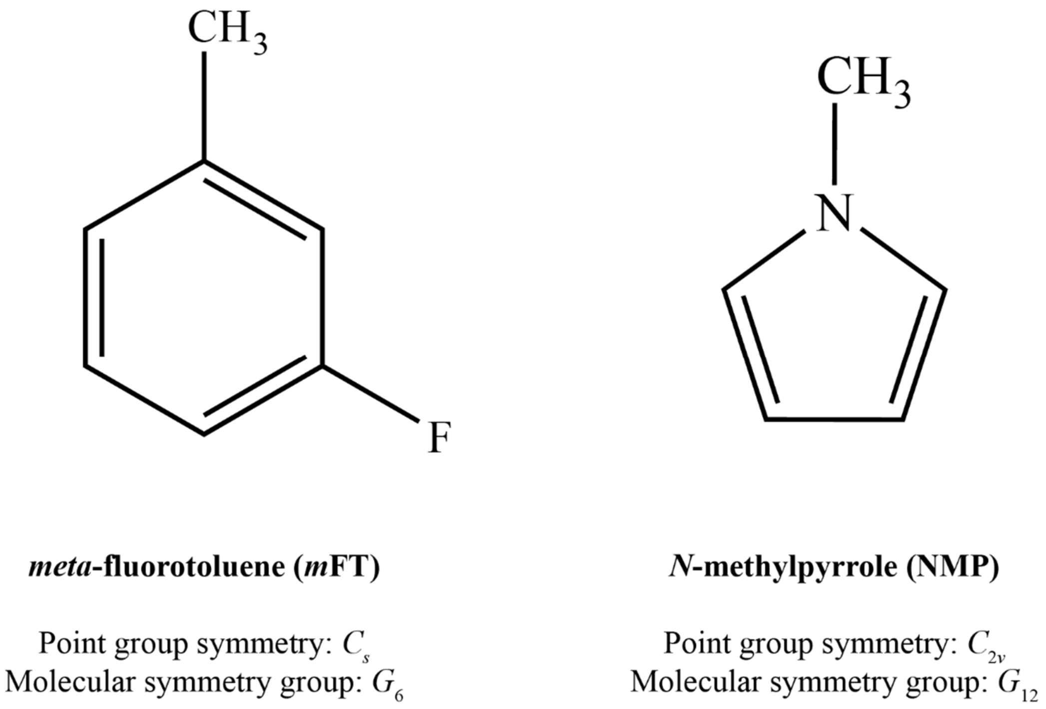

***meta*-fluorotoluene (*m*FT)**

Point group symmetry: C_s
Molecular symmetry group: G_6

***N*-methylpyrrole (NMP)**

Point group symmetry: C_{2v}
Molecular symmetry group: G_{12}

Figure 1.1. Simple schematics showing the molecules under investigation in this thesis, *m*FT and NMP. Effective point group symmetries and the molecular symmetry group (see Section 3.4) are given. Hydrogen atoms on the aromatic rings have been omitted for clarity.

Simple aromatic molecules, such as *m*FT and NMP, can be viewed as simple analogues to larger, more complex systems such as amino acids and proteins. For example, the amino acids tyrosine[1] and phenylalanine[2] both contain a benzene ring, and tryptophan[3] contains an indole system, which, in itself, is a fusion of a benzene and pyrrole ring. Furthermore, the bases of DNA are made up of various heterocycles or fused heterocycles. One can envisage that, by learning about these simple systems, one can begin to apply this knowledge to more complex systems, which provides underpinning knowledge for biochemistry and materials chemistry.

Ultraviolet (UV) light has long been associated with the generation of free radicals, reactive species with an unpaired electron, within living systems, such as the human body[4,5]. These radicals can go on to damage DNA, causing mutations, which can potentially lead to cancer, potentially endangering the life of the affected organism.

The major source of UV radiation that poses a risk to life on Earth comes from the Sun. While oxygen and ozone in the atmosphere filter out the majority of the shorter wavelength, higher energy UV light, a significant portion of the lower energy UV-A radiation still makes it to the surface and UV-A radiation from the Sun has been shown to cause certain types of malignant melanoma[5].

In order to develop preventatives for such cancers, one would need to understand how this damage arises. This ultimately requires an understanding of the photostability of these molecules, and the fates of their electronically excited states. This should allow conclusions to be drawn on how biomolecules rapidly dissipate excess, localised energy to prevent damage to both the molecule and therefore the organism.

These ideas can also be extended to the development of preventatives, such as sunscreens[6–9]. These need to be both photostable *i.e.*, the molecules redistribute the absorbed energy efficiently without causing damage to the molecule (whether acute damage or as a slow degradation of efficiency), with the excess energy often given off as heat, and non-toxic. There are two main types of sunscreens: physical blockers, such as TiO_2 and ZnO, which scatter sunlight and prevent it reaching the skin, and absorbing sunscreens such as *para*-aminobenzoate derivatives which will absorb and filter out UV light[6]. There has been some debate surrounding the toxicity of nanoparticle-based physical blockers, as they are known to be a photocatalyst in the formation of some reactive species upon exposure to UV light[10,11], which may be counterproductive. Nonetheless, Newman *et al*.[11] stress that it is unlikely that these types of sunscreens have toxic effects as the nanoparticles cannot penetrate deep into the skin, although more data is required to ensure this is not the case on already damaged skin. Therefore, it may be wise to pursue UV absorbing sunscreens instead. However, a disadvantage of these is that they have a limited lifetime after application, leading to diminishing protection over time; their effectiveness relies on the user to reapply sunscreen regularly.

Aromatic rings, with their conjugated π-systems, effectively absorb UV radiation since their electronic transitions are often within the UV region of the electromagnetic spectrum. This absorbed energy can then be redistributed around the conjugated ring system *via* interactions with the vibrational levels, including those of the methyl rotor. The ultimate theme of this thesis is to understand how the methyl rotor in *m*FT and NMP can interact with the ring-localised vibrations in excited electronic states, and how this assists in dissipating the energy absorbed during the electronic transition.

In terms of spectroscopy, there are several physical and practical reasons why one cannot easily study the spectra of these biological molecules directly, driving spectroscopic study towards smaller analogues:

i. Large, complex molecules tend to be solids with low vapour pressures, meaning it is difficult to get them into the gas phase without excessive heating. Even with heating, it can be difficult to prevent the vapour from condensing and solidifying inside the spectroscopic apparatus, leading to blockages and an inconsistent gas flow. In contrast, *m*FT and NMP are liquids at room-temperature and do not require heating to get an adequate number density seeded in the free-jet expansion.

ii. As the number of atoms increases, the number of vibrational degrees of freedom increase. Therefore, complex molecules such as large amino acids will have highly congested spectra arising from overlapping structure, meaning it will be difficult to discern any individual routes for energy dispersal, and any normal modes of vibration that facilitate this.

iii. These smaller molecules tend to be spectroscopically 'bright' meaning that it is possible to use the techniques mentioned above to achieve high levels of signal, allowing their energy levels to be probed with relative ease.

iv. The energy levels of interest in *m*FT and NMP are easily accessible with common spectroscopic tools, such as dye lasers.

v. The ring-localised vibrations of these systems remain similar between molecules of the same class (*e.g.*, for *meta*-substituted benzenes and for *N*-substituted pyrroles) so the identification of vibrational structure may become more straightforward, allowing for some comparisons to be drawn between related systems.

Substituted benzenes have been studied spectroscopically for many years. A number of gas-phase studies initially focused on monosubstituted benzenes such as fluorobenzene[12–20], chlorobenzene[15,20–26] and toluene[27–39]. This has later been extended to disubstituted benzene molecules, with *para*-difluorobenzene[40–47] (*p*DFB) and *p*FT[48–54] being amongst the most widely studied molecules of their class. Additionally, *para*-xylene[48,55–61] (*p*Xyl) has also been considered, with it being a natural extension to the study of energy dispersal as it has two methyl rotors which can modify the routes for energy dispersal.

In spite of this, the *meta*-substituted molecules are relatively under studied, with one of the most well-known being *meta*-difluorobenzene[62–66] (*m*DFB). The earliest found study on *m*FT is a microwave study by Rudolph and Trinkaus[67], from 1968, in which they determine rotational constants and values of the torsional parameters, V_3 and V_6 (see Section 3), in the S_0 state. Additionally, Green reported and analysed IR and Raman spectra for *m*FT, alongside numerous other *meta*-disubstituted benzene systems[62]. Weisshaar and co-workers employed some low-level *ab initio* methods to rationalise torsional energy barriers in various substituted benzene molecules[68].

Later, Ito and co-workers reported pioneering work on these systems in which they presented LIF and DF spectra, as well as ZEKE spectra, on jet-cooled *ortho*-, *meta*- and *para*-fluorotoluene, assigning a number of bands in the S_0, S_1 and D_0^+ states[69–73] – all three electronic states of interest in this work (however some of the assignments will be questioned in this work). Furthermore, they derive a number of parameters to describe the methyl internal rotation, or torsion, in all of these states which corroborate the values determined in the microwave study[67]. However, these studies focus on a very low internal energy region, covering only the torsional activity.

Parmenter and co-workers employed chemical timing experiments to explore how the methyl rotor accelerates the rate of intramolecular vibrational energy redistribution (IVR) between *p*DFB, *p*FT and *m*FT[74]. The main conclusion was that, by exchanging a fluorine atom in *p*DFB with a methyl rotor, the rate of IVR increased by a factor of ~40 owing to the presence of new pathways for coupling: mainly through the methyl torsion interacting with the ring-localised vibrations. They also noted that lowering the (effective) point group symmetry from C_{2v}, in the case of *p*FT, to C_s in *m*FT increased the rate of IVR further, by an additional factor ~12, arising from the increase the density of same-symmetry states that can couple together, further increasing the dispersal of energy.

Much later, in 2019, Stewart *et al.*[75] revisited the low-energy region of *m*FT in the S_1 state with a modern technique, 2D-LIF. There, they discussed the activity of the first ~350 cm^{-1} of the $S_1 \leftarrow S_0$ spectrum, commenting on the rather strong vibration-torsion interaction occurring in *m*FT. Additionally, in light of the new 2D-LIF data, they made a number of reassignments of various bands, in both S_0 and S_1, from Ito's early work[69] and presented the most accurate and precise torsional parameters to date, largely in agreement with previous work[67–69]. Shortly after, Kemp and co-workers analysed the same region in S_1 using ZEKE spectroscopy[76], deducing a precise adiabatic ionisation energy (AIE) for *m*FT of 71997 ± 5 cm^{-1} and assigning a number of vibrations and torsions in the D_0^+ state, using this new knowledge to confirm the reassignments made by Stewart, *et al.* in the S_1 state. Furthermore, the possibility of the distortion of the methyl rotor during vibrations was discussed, with these perturbations modifying the geometry of *m*FT away from the G_6 molecular symmetry group. Despite this, the focus of these studies continued to be towards the low-wavenumber region of the $S_1 \leftrightarrow S_0$ electronic transition.

The work presented in this thesis rectifies this by presenting REMPI and LIF spectra covering the first ~1350 cm^{-1} of the $S_1 \leftarrow S_0$ electronic transition, assigning the majority of the features observed in the corresponding ZEKE and 2D-LIF spectra. Further discussed is the build-up of energy redistribution pathways from localised couplings through to wide-spread IVR, often owing to vibration-torsion interactions and the increased density of same-symmetry states. The present work constitutes the most comprehensive study of the vibrational and torsional activity of *m*FT in the S_0, S_1 and D_0^+ states to date. This is presented in Sections 7-9.

Related to *m*FT, *m*ClT has also been neglected in the literature; only a couple of studies were conducted in the 1990s[77,78], and later by this research group[79,80]. In spite of this, the study of *m*ClT is a useful extension to that of *m*FT as one can begin to understand the effects of changing the mass of the substituent and also the electronic structure, without changing the symmetry (the latter, as noted by Parmenter, is an important factor in the redistribution of internal energy). Furthermore, the two common isotopes of chlorine (^{35}Cl and ^{37}Cl) allow the elucidation of mass effects on the ring-localised vibrations of *m*ClT.

Unlike *m*FT, whose $S_1 \leftarrow S_0$ transition is symmetry-allowed, the $\tilde{A}\,^1A_2$ (S_1) $\leftarrow$ $\tilde{X}\,^1A_1$ (S_0) transition in NMP is symmetry-forbidden which means the activity observed in the one-photon excitation spectra to the $\tilde{A}\,^1A_2$ electronic state is due to vibronic interactions (although a two-photon excitation REMPI spectrum allows the selection rules to be altered such that Franck-Condon allowed activity is observable, see Refs. 81 and 82, also Sections 2, 10 and 12). Interestingly, the highest-occupied molecular orbital (HOMO) for the S_1 state of NMP is a mixture of valence and Rydberg character, being a 3s Rydberg state in the Franck-Condon region, evolving into a σ* state when extending along the N-CH_3 coordinate. The combination of a symmetry-forbidden electronic transition, alongside the mixed-character HOMO of the S_1 state makes this a rather interesting molecule to explore. Notably, this is reminiscent of benzene, whose $\tilde{A}^1B_{2u}$ (S_1) ← $\tilde{X}^1A_{1g}$ (S_0) transition is also symmetry-forbidden and therefore work on benzene has generally investigated the vibronically allowed states[83–86].

Despite the general lack of literature surrounding the *meta*-disubstituted benzenes, NMP has attracted interest for many years. Some early microwave studies on NMP initially determined the geometry of the ground state[87–89], accompanied by some gas-phase electron diffraction studies[90,91], which largely corroborate the results. Other early work included IR and Raman studies on various substituted pyrroles[92,93], with a more detailed and targeted study by Béc and co-workers[94] coming later. Ambient absorption spectra have been reported, as far back as 1944, by Milazzo[95] but there are also later studies by Compton[81] and McDiarmid and Xing[96].

The first jet-cooled studies of NMP were conducted by Compton and co-workers[81] (who report an AIE which concurs with an earlier photoelectron study by Kirby *et al.*[97]), McDiarmid and Xing[96], Philis[98,99] and Biswas *et al.*[100]. The latter additionally reported assignments for the torsional levels and low-energy vibrations based on dispersed fluorescence spectra presented therein. [A paper reinterpreting the assignments of the torsional levels of the (1+1)-REMPI spectrum using theoretical techniques was published by Kanamaru[101], although a number of assignments therein are symmetry-forbidden and thus the work presented as part of this thesis (Sections 10-13) agrees more with the conclusions of Philis[98,99] and Biswas[100].] Later, along with the continued development of ultrafast laser systems, a number of photodynamical studies[102–109] have been conducted on NMP to provide insight into the photophysical properties, such as the nature of the electronic states as well as routes for photodissociation.

A photodynamic study by Woo and Kim[110] also provides a number of hypothesised assignments for almost all S_1 levels below ~1850 cm^{-1} and reports lifetimes for many of these levels. However, they find that the dynamics is complicated and, often, multiple nanosecond-scale time constants are required to fit the experimental data.

The frequency-resolved spectra of the present work (Section 12) provide concrete evidence for the assignments of the bands in the S_1 state, and also of the coherent excitation of multiple eigenstates in a number of cases in the study by Woo and Kim, something they briefly propose. This further highlights the complementarity of time-resolved and frequency-resolved experiments. Additionally, Gascooke and Lawrance have very recently published a far-infrared study regarding the P_{16} vibration in the S_0 state of NMP, which is an out-of-plane wagging vibration (see Appendix 1 for relevant mode diagrams). Here, they discussed the magnitude of the vibration-torsion interaction of the methyl rotor and this vibration. They deduced a very large vibration-torsion coupling matrix element and also the zero-order (unperturbed) V_6 barrier height.

Interestingly, the possibility for rapid energy delocalisation in pyrroles, including *N*-methylpyrrole, have made substituted pyrroles candidates for use in molecular wires[111] and also in medicines[112,113]. Furthermore, poly(*N*-methylpyrrole) deposited on a surface has been proposed to have applications in biosensors[114–117].

Similar to the work presented herein for *m*FT, the results presented for NMP constitute a comprehensive study, comparing the new data collected as part of this work with all the available information from past studies. Numerous assignments in the S_0, S_1 and D_0^+ electronic states are proposed, and vibrational wavenumbers are extracted for many fundamental vibrations in each state. Also given is a description of the role of the methyl rotor and vibrations in the spectroscopy of the S_0, S_1 and D_0^+ electronic states.

This work is divided into four distinct sections, the first of which reinvestigates the torsional region of the $S_1 \leftarrow S_0$ transition, this time with the advantages of 2D-LIF and ZEKE spectroscopy, allowing for the determination of the torsional parameters[118]. Secondly, a vibrational labelling scheme is proposed, expected to bring consistency to the vibrational labelling of *N*-substituted pyrroles[119]. The third, and largest, section details the spectroscopy of essentially all levels below ~1100 cm^{-1} relative to the S_1 origin, including a region of highly-localised and extensive coupling[120,121]. Finally, ZEKE and REMPI spectra are presented for NMP-RG (RG = Ar, Kr).

The following sections will provide a basic description of the spectroscopic quantum chemistry required for the understanding of the work presented. This will include a discussion of a number of approximations pertinent to the work (such as the Born-Oppenheimer approximation and the Franck-Condon principle), as well as what occurs when these approximations break down. Additionally, the effects of anharmonicity will be discussed, followed by a brief picture of how anharmonicity can cause coupling between multiple zero-order states and how this manifests itself in vibrationally- and torsionally-resolved spectra. This will then be followed by a consideration of the effect of the methyl rotor on the spectra: there will be a discussion of the free rotor, evolution to the hindered rotor and how a hindering potential can affect the torsional levels. Furthermore, there will be discussion on the permutation-inversion molecular symmetry group treatment of *m*FT and NMP; a general overview of the vibrational labelling schemes and notation is then given. A summary of the experimental techniques, and apparatus used to collect the data that make up the results and discussion, follows.

The background theory presented over the next few sections is not intended to be comprehensive, merely to be adequate for the understanding of the work presented herein. Texts by Herzberg[122,123], Bunker and Jensen[124,125], Atkins[126] and Hollas[127,128] provide a far more comprehensive and wide-ranging discussion of the theoretical background.

The main results and discussion part of this thesis will comprise an introduction to each published piece, followed by the published papers themselves. Finally, the main conclusions of these papers are drawn together, with some suggestions for extending the present work.

2. Theoretical background

2.1. Born-Oppenheimer approximation

A fundamental idea that underpins a large part of spectroscopy is that the wavefunctions that describe electronic, vibrational, rotational and, indeed, torsional components of the overall molecular wavefunction can be separated, based on the idea that the nuclear and electronic motions can be decoupled. In 1927, Born and Oppenheimer proposed that, due to the nuclei of atoms being significantly heavier than electrons, their corresponding motions occur on vastly different timescales[129]: the electronic motion is orders of magnitude faster than the motion of the nuclei.

The molecular Hamiltonian comprises the following components:

$$\hat{H} = T_{\mathrm{e}} + T_{\mathrm{n}} + V_{\mathrm{nn}} + V_{\mathrm{ee}} + V_{\mathrm{ne}}$$

Equation 2.1

Where T_{e} and T_{n} are the kinetic energy terms of the electrons and nuclei, respectively; the V_{nn} term is the Coulombic repulsion term for the interactions between nuclei; V_{ee}, similarly, is the two-electron interaction energy term and V_{ne} describes the attractive forces experienced between an electron and a nucleus.

If one assumes that the electronic motion is so rapid relative to the nuclear motion, as Born and Oppenheimer did[129], and that the nuclei remain effectively stationary on the timescale of electronic motions, then T_{n} can be treated as zero and the V_{nn} term simply becomes a constant, given a fixed geometry. One can, therefore, decompose the Hamiltonian given in Equation 2.1 to identify an electronic Hamiltonian:

$$\hat{H}_{\mathrm{elec}} = T_{\mathrm{e}} + V_{\mathrm{ne}} + V_{\mathrm{ee}}$$

Equation 2.2

Where V_{ne} is now only dependent on the electrons interacting with the stationary nuclei. The most difficult term to evaluate in the electronic Hamiltonian (and indeed the overall Hamiltonian) is the V_{ee} term and is the reason the Schrödinger equation cannot be solved exactly for systems with more than one electron. Under these conditions, one would want to calculate a set of electronic wavefunctions, ψ_{elec}, that satisfy the Schrödinger equation:

$$\widehat{H}_{\mathrm{elec}}\psi_{\mathrm{elec}} = E_{\mathrm{elec}}\psi_{\mathrm{elec}}$$

Equation 2.3

Here, E_{elec} is the electronic energy of the system obtained by solving the Schrödinger equation in Equation 2.3. One can see from Equation 2.2 that, as $\widehat{H}_{\mathrm{elec}}$ is dependent on the nuclear coordinates (albeit only as a parameter through V_{ne}), then ψ_{elec} and E_{elec} must also be dependent on the nuclear coordinates. If one applies the Born-Oppenheimer approximation at this point, one can assume that the electrons move with the nuclei as the system vibrates, rotates, or translates. The remaining terms from Equation 2.1 comprise the nuclear Hamiltonian, $\widehat{H}_{\mathrm{nuc}}$:

$$\widehat{H}_{\mathrm{nuc}} = T_{\mathrm{n}} + V_{\mathrm{nn}}$$

Equation 2.4

One can also consider calculating a set of nuclear wavefunctions, ψ_{nuc}, that satisfy an analogous Schrödinger equation as that in Equation 2.3. As the electronic and nuclear Hamiltonians can be separated, therefore, so can the wavefunctions, meaning the total wavefunction (ψ_{tot}) can be factorised into its nuclear (ψ_{nuc}) and the electronic (ψ_{elec}) component wavefunctions:

$$\psi_{\mathrm{tot}} = \psi_{\mathrm{nuc}}(Q)\psi_{\mathrm{elec}}(Q, q)$$

Equation 2.5

Where Q are the nuclear, and q the electronic, coordinates, respectively, and the overall energy of the system can be described as the sum of the electronic (E_{elec}) and nuclear (E_{nuc}) energies:

$$E_{\mathrm{tot}} = E_{\mathrm{nuc}} + E_{\mathrm{elec}}$$

Equation 2.6

For the most part, the separation of the nuclear and electronic components is a very good approximation. Despite this, a number of the ideas discussed in this thesis describe scenarios in which the separation of the nuclear and electronic wavefunctions is no longer a good approximation, and hence are termed a 'breakdown' of the Born-Oppenheimer approximation.

Additionally, it is possible to separate the nuclear wavefunction into its constituent vibrational (ψ_{vib}), rotational (ψ_{rot}), torsional (ψ_{tor}) and nuclear spin (ψ_{ns}) wavefunctions such that the total wavefunction is the product of its constituent wavefunctions:

$$\psi_{\mathrm{tot}} = \psi_{\mathrm{elec}}\psi_{\mathrm{vib}}\psi_{\mathrm{rot}}\psi_{\mathrm{tor}}\psi_{\mathrm{ns}}$$

Equation 2.7

Although the separation of the nuclear wavefunction into vibrational, rotational, torsional and nuclear spin components is generally less good an approximation than the separation of the electronic and nuclear wavefunctions, it holds up well in the majority of situations.

2.2. Allowed electronic transitions

For now, consideration shall only be given to a pure electronic transition *i.e.*, there is no concomitant vibrational or rotational excitation, and the Born-Oppenheimer approximation is assumed. In the context of the experimental techniques described in Section 5, first a system shall be considered in which a single photon is absorbed leading to the promotion of an electron from a lower electronic state, ψ_{e}'', to an upper electronic state, ψ_{e}'. The electronic transition moment, $\boldsymbol{R}_{\mathrm{e}}$, for such a transition may be expressed as:

$$\boldsymbol{R}_{\mathrm{e}} = \langle \psi_{\mathrm{e}}'' | \boldsymbol{\mu}_{\mathrm{e}} | \psi_{\mathrm{e}}' \rangle$$

Equation 2.8

Where $\boldsymbol{\mu}_e$ is the electric dipole moment operator, which has components along all three Cartesian axes (therefore $\boldsymbol{\mu}_e = \boldsymbol{\mu}_x + \boldsymbol{\mu}_y + \boldsymbol{\mu}_z$). In order for such a transition to be allowed, $\boldsymbol{R}_e$ must be non-zero. The intensity of the transition is proportional to the square of the transition moment, $\langle \boldsymbol{R}_\mathrm{e} \rangle^2$. A quantity proportional to the transition intensity, and therefore $\langle \boldsymbol{R}_\mathrm{e} \rangle^2$, is often attributed to an electronic state and is used in certain contexts in this thesis. This is known as the oscillator strength of an electronic state.

For $\boldsymbol{R}_e \neq 0$, the direct product of the irreducible representations of ψ_e', ψ_e'' and $\boldsymbol{\mu}_e$ must transform as the totally-symmetric irreducible representation of the point group (or molecular symmetry group, see Section 3.4) of the molecule; the character tables of pertinent symmetry groups for the systems in this thesis have been given in Appendix 2. As an example, we shall discuss the $\tilde{B}^1B_2 \leftarrow \tilde{X}^1A_1$ electronic transition of NMP as the $\tilde{A}^1A_2 \leftarrow \tilde{X}^1A_1$ electronic transition is symmetry-forbidden. As discussed above, for $\boldsymbol{R}_e \neq 0$, and, therefore, for the transition to be electric dipole allowed, the following must be true:

$$\Gamma(\psi_\mathrm{e}'') \times \Gamma(\boldsymbol{\mu}_\mathrm{e}) \times \Gamma(\psi_\mathrm{e}') \supseteq A_1$$

Equation 2.9

Where Γ represents the irreducible representation of the wavefunction (or electric dipole moment operator), × represents taking the direct product, and A_1 is the totally-symmetric symmetry class of the C_{2v} point group (to which NMP belongs, assuming the methyl rotor to be a point mass, which is a reasonable approximation when the electronic transition in question is ring-localised). In this example, and indeed the work in this thesis, the pyrrolyl ring of NMP is located in the *yz*-plane, with the C-CH_3 bond pointing along the *z*-axis.

Because the symmetries of the upper and lower electronic states have already been specified (B_2 and A_1, respectively) as the subject of this example, one can look towards identifying which, if any, of the irreducible representations of $\boldsymbol{\mu}_e$ satisfy Equation 2.9 and therefore facilitate this electronic transition. Looking at the C_{2v}

character table in Appendix 2, one can identify that $\Gamma(T_x) = B_1$, $\Gamma(T_y) = B_2$ and $\Gamma(T_z) = A_1$, such that $\Gamma(\boldsymbol{\mu}_\mathrm{e}) \supseteq A_1, B_1$ and B_2. In order for Equation 2.9 to be satisfied, the irreducible representation of one of the components of $\boldsymbol{\mu}_\mathrm{e}$ must match the direct product of the symmetries of the ground and excited state electronic wavefunctions, $\Gamma(\psi_\mathrm{e}'') \times \Gamma(\psi_\mathrm{e}')$, which can be evaluated as $A_1 \times B_2 = B_2$. Hence, the *only* component of $\boldsymbol{\mu}_\mathrm{e}$ that facilitates this electronic transition is $\boldsymbol{\mu}_y$, as $\Gamma(\boldsymbol{\mu}_y) = B_2$. As such, we say that this transition is electric dipole allowed and polarised along the *y*-axis.

Conversely, the $\tilde{A}^1A_2 \leftarrow \tilde{X}^1A_1$ transition of NMP is electric dipole forbidden as there is no component of $\boldsymbol{\mu}_\mathrm{e}$ that satisfies Equation 2.9. The direct product of the irreducible representations of ψ_e'' and ψ_e' in this scenario is A_2 and therefore would require $\boldsymbol{\mu}_\mathrm{e}$ to have a component of A_2 symmetry; however, no such component exists and, therefore, this transition is electric dipole forbidden.

2.3. Franck-Condon principle

In molecular spectroscopy, it is possible for vibrational and electronic transitions to occur simultaneously, thus one must also consider the nuclear coordinates at the time of the transition. The discussion of the Franck-Condon (FC) principle in this section relies on the Born-Oppenheimer approximation being applicable, although, in Section 2.4, we will discuss what may happen when this approximation breaks down. Despite the breakdown of the Born-Oppenheimer being discussed as a part of this thesis, the FC principle, within the Born-Oppenheimer approximation, is largely a good basis for describing vibrational transitions built upon an allowed electronic transition, as is the case in *m*FT.

Recalling that the Born-Oppenheimer approximation states that the electronic motion is so rapid in comparison to nuclear motion, then, when a photon is absorbed, one observes a ‘vertical transition’ between two electronic states. This is where the transition involves a change in the electronic structure, but with no corresponding change in nuclear coordinates *i.e.*, no displacement from the ground state equilibrium geometry *during* the transition. As a result, this is said to occur directly upwards on the potential energy surface (see Figure 2.1) and is a direct consequence of the nuclei remaining stationary on the timeframe of the electronic transition. Notably, after the transition, the nuclei will rearrange themselves to minimise the forces within the molecule to accommodate the new electronic structure.

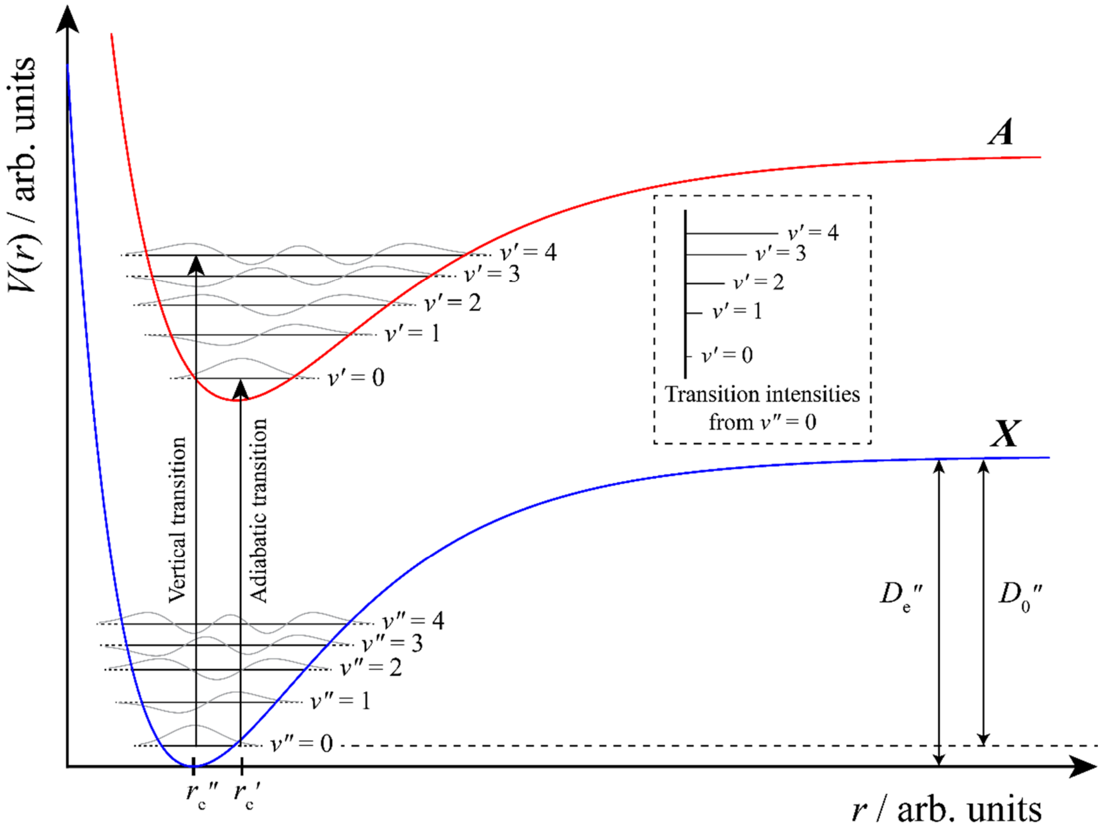

Figure 2.1. Schematic representation of a vertical transition (as given by the FC principle) and the adiabatic transition for a diatomic molecule. Vibrational wavefunctions (harmonic) are shown in grey. The $v' = 4 \leftarrow v'' = 0$ vertical transition is shown, and one can see that there is good vibrational wavefunction overlap between $\psi_{v''=0}(r)$ and $\psi_{v'=4}(r)$. Furthermore, the expected transition intensities from $v'' = 0$ to various levels in the A state are shown, which can be seen as a crude approximation of the Franck-Condon factors (see text). The ground and excited state equilibrium bond lengths, r_e'' and r_e' respectively, are indicated, and the lowest energy transition between the two electronic states at their equilibrium geometries is shown as the adiabatic transition. The dissociation energies, D_e'' and D_0'', are shown for the X state, noting the excited state, A, will have equivalent parameters (not shown). The axis units are arbitrary.

If two electronic states of a diatomic molecule have different equilibrium geometries (as in Figure 2.1), the minima of the two states may not coincide in terms of internuclear separation. Given the way the vertical excitation is drawn, one may think that a band corresponding to the adiabatic $v' = 0 \leftarrow v'' = 0$ transition would not be expected in an experimental spectrum; the observance of this, however, depends on whether there is reasonable overlap between the initial and final state vibrational wavefunctions – see below. It may be, simply, that the origin transition (the $v' = 0 \leftarrow v'' = 0$ transition) will not be the most intense.

As an example, consider the starting level $v'' = 0$ (such as because the molecule is in a free-jet expansion, see Section 5.1). This level will have a wavefunction with a probability of finding population between the classical turning points of the potential energy curve (with there being some probability of finding it outside of the potential well too), and this has favourable overlap with the wavefunction of the $v' = 4$ level, and so a vertical transition may occur. In addition, as there may be vibrational wavefunction overlap with multiple vibrational levels in the upper electronic state, so that one can observe a series of vibrational bands with varying intensities dependent on the magnitude of this overlap – this is known as a vibrational progression and is depicted in Figure 2.1 as an inset.

Assuming the accompanying electronic transition is allowed, one can explain the intensities of the observed vibrational bands by the degree of overlap between the vibrational wavefunctions of the upper and lower states. If this overlap is poor, for example, because the wavefunctions are out-of-phase, the transition intensity will be low. If the wavefunction overlap is perfect (*i.e.*, the upper and lower state vibrational wavefunctions are *identical* and as is the electronic structure), the transition intensity will be determined, purely, by that of the electronic transition, which, recalling, is simply $\langle \boldsymbol{R}_{\mathrm{e}} \rangle^2$. The square of the degree of overlap in vibrational wavefunctions can be generalised and is called the Franck-Condon factor (or FCF). In short, if the electronic component of a vibronic transition is symmetry-allowed, then the intensity of this transition will be greatest when the FCF, or upper and lower state vibrational wavefunction overlap, is largest. Indeed, the stick spectrum in Figure 2.1 is also approximately representative of the FCFs between $v'' = 0$ and multiple levels (indicated) in the upper state.

This can be formalised mathematically by the separation of the vibrational and electronic wavefunctions from the vibronic wavefunction, which will be considered below.

Recalling the transition dipole moment for an electronic transition in Section 2.2, one can similarly write the transition dipole moment for a vibronic transition, $\boldsymbol{R}_{\mathrm{ev}}$, as:

$$\boldsymbol{R}_{\mathrm{ev}} = \langle \psi''_{\mathrm{ev}} | \boldsymbol{\mu}_{\mathrm{ev}} | \psi'_{\mathrm{ev}} \rangle$$

Equation 2.10

Where ψ_{ev}'' and ψ_{ev}' are the vibronic wavefunctions in the lower and upper states, respectively, and the vibronic dipole moment operator, $\boldsymbol{\mu}_{\mathrm{ev}}$, comprises both electronic ($\boldsymbol{\mu}_{\mathrm{e}}$) and nuclear ($\boldsymbol{\mu}_{\mathrm{n}}$) parts, such that:

$$\boldsymbol{\mu}_{\mathrm{ev}} = \boldsymbol{\mu}_{\mathrm{e}} + \boldsymbol{\mu}_{\mathrm{n}}$$

Equation 2.11

Combining Equations 2.10 and 2.11, and separating the vibronic wavefunctions into their constituent vibrational and electronic components by assuming the Born-Oppenheimer approximation:

$$\boldsymbol{R}_{\mathrm{ev}} = \langle \psi''_{\mathrm{e}} \psi''_{\mathrm{v}} | \boldsymbol{\mu}_{\mathrm{e}} + \boldsymbol{\mu}_{\mathrm{n}} | \psi'_{\mathrm{e}} \psi'_{\mathrm{v}} \rangle$$

Equation 2.12

This can be (simply) manipulated into the sum of two integrals:

$$\boldsymbol{R}_{\mathrm{ev}} = \langle \psi''_{\mathrm{e}} \psi''_{\mathrm{v}} | \boldsymbol{\mu}_{\mathrm{e}} | \psi'_{\mathrm{e}} \psi'_{\mathrm{v}} \rangle + \langle \psi''_{\mathrm{e}} \psi''_{\mathrm{v}} | \boldsymbol{\mu}_{\mathrm{n}} | \psi'_{\mathrm{e}} \psi'_{\mathrm{v}} \rangle$$

Equation 2.13

Which can be expanded, taking note that only the electronic component of the vibronic dipole moment operator can act on the electronic wavefunctions and, similarly, the nuclear part of the vibronic dipole moment operator can only act on the vibrational wavefunctions, to yield:

$$\boldsymbol{R}_{\mathrm{ev}} = \langle \psi''_{\mathrm{e}} | \boldsymbol{\mu}_{\mathrm{e}} | \psi'_{\mathrm{e}} \rangle \langle \psi''_{\mathrm{v}} | \psi'_{\mathrm{v}} \rangle + \langle \psi''_{\mathrm{e}} | \psi'_{\mathrm{e}} \rangle \langle \psi''_{\mathrm{v}} | \boldsymbol{\mu}_{\mathrm{n}} | \psi'_{\mathrm{v}} \rangle$$

Equation 2.14

For any given, static, nuclear arrangement, the two electronic wavefunctions are orthogonal. This means that $\langle\psi_{\mathrm{e}}''|\psi_{\mathrm{e}}'\rangle = 0$, and the entire second term in Equation 2.14 becomes zero, leaving us with the more familiar formulation of the vibronic transition moment:

$$\boldsymbol{R}_{\mathrm{ev}} = \langle\psi_{\mathrm{e}}''|\boldsymbol{\mu}_{\mathrm{e}}|\psi_{\mathrm{e}}'\rangle\langle\psi_{\mathrm{v}}''|\psi_{\mathrm{v}}'\rangle$$

Equation 2.15

Recalling that $\boldsymbol{R}_{\mathrm{e}}$ is the electronic transition moment from Equation 2.8:

$$\boldsymbol{R}_{\mathrm{ev}} = \boldsymbol{R}_{\mathrm{e}}\langle\psi_{\mathrm{v}}''|\psi_{\mathrm{v}}'\rangle$$

Equation 2.16

In Equations 2.15 and 2.16, the vibronic transition moment is shown with two distinct components: the first is simply the electronic transition moment, $\boldsymbol{R}_{\mathrm{e}}$, which was presented in Equation 2.8, and the second is a quantification of the overlap between the vibrational wavefunctions of the two electronic states being considered. As noted above, it is the *square* of this latter component that is the FCF:

$$\mathrm{FCF} = \langle\psi_{\mathrm{v}}''|\psi_{\mathrm{v}}'\rangle^{2}$$

Equation 2.17

The FCF, therefore, describes the probability of the vibrational transition occurring during the electronic transition.

In order for the transition to be considered Franck-Condon allowed, both integrals in Equations 2.15 and 2.16 must be non-zero, *i.e.*, the pure electronic transition itself must be allowed, but there must also be some degree of vibrational wavefunction overlap for the FCF to be non-zero, and therefore making $\boldsymbol{R}_{\mathrm{ev}}$ non-zero. The expected intensity of such a transition is now dependent on both components of Equations 2.15 and 2.16, such that, even for a strongly electric dipole allowed electronic transition to a state with a high oscillator strength, one may observe little intensity in a spectrum should the vibrational wavefunctions have poor overlap.

2.4. Herzberg-Teller (vibronic) coupling

The previous section has discussed vibrational transitions when the accompanying electronic transition was electric dipole allowed. By assuming the electronic and vibrational wavefunctions were separable, the intensities of the transition could be determined both in terms of the overlap between the vibrational wavefunctions and the overall nature of the corresponding electronic transition. However, this separability is only true to a degree, and the breakdown of this becomes more pertinent if the electronic component of the transition is electric dipole forbidden.

Here, it is acknowledged that the electronic wavefunction depends on the nuclear coordinates as well as the electronic coordinates (*i.e.*, a breakdown of the Born-Oppenheimer approximation). Qualitatively, it is logical to think that, as a molecule vibrates, the geometry of the molecule changes and therefore the electronic structure will also change to account for this vibrational motion. Therefore, the vibrational and electronic wavefunctions must have some degree of interdependence.

If one expresses the electronic transition moment in terms of both electronic coordinates, q, as well as the nuclear coordinates at equilibrium, Q_0:

$$\boldsymbol{R}_{\mathrm{e}} = \langle \psi''_{\mathrm{e}}(q, Q''_0) | \boldsymbol{\mu}_{\mathrm{e}} | \psi'_{\mathrm{e}}(q, Q'_a) \rangle$$

Equation 2.18

Here, Q'_a are the nuclear coordinates of the upper electronic state. For a forbidden electronic transition within the Born-Oppenheimer approximation, $\boldsymbol{R}_{\mathrm{e}}$ is equal to zero. If a vibrational excitation causes deviation away from the equilibrium geometry in the upper electronic state to some alternate nuclear coordinate, Q'_a, one can see that $\boldsymbol{R}_{\mathrm{e}}$ may not necessarily be zero anymore, especially if Q'_a perturbs $\psi'_{\mathrm{e}}(q, Q'_a)$ in a direction that gives rise to a distorted geometry at which a transition from $\psi''_{\mathrm{e}}(q, Q''_0)$ is allowed. This essentially means the vibronic transition moment is not zero:

$$\boldsymbol{R}_{\mathrm{ev}} = \langle \psi''_{\mathrm{ev}}(q, Q''_0) | \boldsymbol{\mu}_{\mathrm{ev}} | \psi'_{\mathrm{ev}}(q, Q'_a) \rangle \neq 0$$

Equation 2.19

It is also possible to come to the same conclusion if it is assumed there is an interdependence of the electronic and vibrational wavefunctions. One can expand the electronic transition moment as a Taylor Series in terms of the equilibrium position of the vibrational coordinates, Q:

$$\boldsymbol{R}_{\mathrm{e}}(Q) = (\boldsymbol{R}_{\mathrm{e}})_{\mathrm{eq}} + \sum_{i} \left(\frac{\partial \boldsymbol{R}_{\mathrm{e}}}{\partial Q_i}\right)_{\mathrm{eq}} Q_i + \frac{1}{2!} \sum_{i,j} \left(\frac{\partial^2 \boldsymbol{R}_{\mathrm{e}}}{\partial Q_i \partial Q_j}\right)_{\mathrm{eq}} Q_i Q_j + \cdots$$

Equation 2.20

Where Q_i and Q_j are the vibrational coordinates of modes i and j in a polyatomic molecule. If this is then combined with the vibronic transition moment, as written in Equation 2.16, one obtains:

$$\boldsymbol{R}_{\mathrm{ev}}(Q) = (\boldsymbol{R}_{\mathrm{e}})_{\mathrm{eq}} \langle \psi''_{\mathrm{v}} | \psi'_{\mathrm{v}} \rangle + \sum_{i} \left(\frac{\partial \boldsymbol{R}_{\mathrm{e}}}{\partial Q_i}\right)_{\mathrm{eq}} Q_i \langle \psi''_{\mathrm{v}} | \psi'_{\mathrm{v}} \rangle$$
$$+ \frac{1}{2!} \sum_{i,j} \left(\frac{\partial^2 \boldsymbol{R}_{\mathrm{e}}}{\partial Q_i \partial Q_j}\right)_{\mathrm{eq}} Q_i Q_j \langle \psi''_{\mathrm{v}} | \psi'_{\mathrm{v}} \rangle + \cdots$$

Equation 2.21

Which also implies that there is some dependence of $\boldsymbol{R}_{\mathrm{e}}$ on both the electronic and vibrational wavefunctions, as in Equation 2.18.

From this, one can see that, if there is an electronic transition that is electric dipole allowed, $(\boldsymbol{R}_{\mathrm{e}})_{\mathrm{eq}}$ is non-zero and therefore the first term in this Taylor series will be dominant, and if one truncates the Taylor series at the first term, this is analogous to the case in which the Born-Oppenheimer approximation is valid, as described in Sections 2.2 and 2.3. However, if one acknowledges that the electronic and vibrational wavefunctions are not fully separable, one would also expect to see some structure arise as a result of the higher-order terms in the Taylor series; although one expects that the influence of these higher-order terms of Equation 2.21 to be significantly smaller than the leading term.

However, in a situation in which the electronic transition is electric dipole forbidden, such as the $\tilde{A}^1A_2 \leftarrow \tilde{X}^1A_1$ transition in NMP, $(\boldsymbol{R}_\mathrm{e})_\mathrm{eq}$ is zero, thus the first term in the Taylor expansion (Equation 2.21) must also be zero. However, as will be seen later in this work, despite this electronic transition being symmetry-forbidden, some structure is still observed. This structure originates from the second term of the Taylor series in Equation 2.21 as a result of the dependence of the electronic transition moment ($\boldsymbol{R}_\mathrm{e}$) on the vibrational coordinates, Q_i. If one varies the vibrational coordinates, $\boldsymbol{R}_\mathrm{e}$ will vary from $(\boldsymbol{R}_\mathrm{e})_\mathrm{eq}$ and therefore $\sum_i \left(\frac{\partial \boldsymbol{R}_\mathrm{e}}{\partial Q_i}\right)_\mathrm{eq} Q_i$ may be non-zero; this is provided there is some displacement, Q_i, which perturbs the geometry of the upper state in a direction at which a transition from ψ''_e is not forbidden. Therefore, there is some mixing of an allowed transition, and is the origin of the term 'intensity stealing', which is often used in descriptions of the Herzberg-Teller vibronic coupling scheme as the 'forbidden' transition 'steals' some intensity from an allowed transition. Again, this logic is analogous to that which was derived qualitatively in Equations 2.18 and 2.19.

To summarise, one cannot completely separate the electronic and vibrational wavefunctions, as one has some effect on the other, although what is observed will depend on the vibrational coordinate excited and which term of the Taylor expansion in Equation 2.21 is dominant.

This is discussed in depth in the books by Herzberg[123], Hollas[127] and Bunker and Jensen[124]. Henceforth, Herzberg-Teller (vibronic) coupling will now be discussed in terms of molecular spectra and symmetry, looking first at NMP, which is similar to benzene in that the $S_1 \leftarrow S_0$ transition is symmetry forbidden.

NMP is of *pseudo*-C_{2v} symmetry and its $\tilde{A}^1A_2 \leftarrow \tilde{X}^1A_1$ electronic transition is electric dipole forbidden, as discussed. If one considers a b_1 vibration in the $\tilde{A}^1A_2$ electronic state, the symmetry of this vibronic state can be given as the product of the electronic and vibrational state symmetries and thus, overall, the vibronic state has B_2 symmetry. Energetically close to this vibronic state is the $\tilde{B}^1B_2$ electronic state (see Figure 2.2), and the $\tilde{B}^1B_2 \leftarrow \tilde{X}^1A_1$ transition is electric dipole allowed (polarised in the y-direction) and has $\boldsymbol{R}_e > 0$. As the B_2 vibronic states associated with the $\tilde{B}^1B_2$ electronic state (*i.e.*, a_1 symmetry vibrations within the $\tilde{B}^1B_2$ vibrational manifold) and a B_2 vibronic state associated with the $\tilde{A}^1A_2$ state are of the same symmetry, they can interact, and intensity of the B_2 vibronic state can be gained from the $\tilde{B}^1B_2$ electronic state. Hence one can observe intensity *via* the b_1 vibrations built upon the $\tilde{A}^1A_2$ state, as a result of this vibronic coupling. This is illustrated pictorially in Figure 2.2, as well as other vibronic coupling routes in NMP associated with the $\tilde{A}^1A_2$ electronic state.

In a similar way, vibrations of a_2 and b_2 symmetry in the $\tilde{A}^1A_2$ electronic state become Herzberg-Teller (HT) allowed, owing to the interactions with nearby $^1A_1$ and $^1B_1$ electronic states, respectively, gaining intensity (Figure 2.2). One should note that one would not expect to observe the a_1 vibrations in the $\tilde{A}^1A_2$ electronic state as this would require coupling to a $^1A_2$ electronic state and, as established, these electronic states have zero oscillator strength – in order to steal intensity, there must be something to steal!

The strength of the vibronic coupling, and therefore the intensity of a vibronically-induced vibration, is dependent on:

i. the electronic transition moment of the electronic state to which coupling occurs (*i.e.*, the probability of a transition to that electronic state) and;

ii. how well the two vibronic states couple, which is partially dependent on how close in energy the two electronic states are (a vibration in the $\tilde{A}^1A_2$ electronic state is going to couple more strongly if the inducing electronic state is close in energy, compared to if it were energetically far removed).

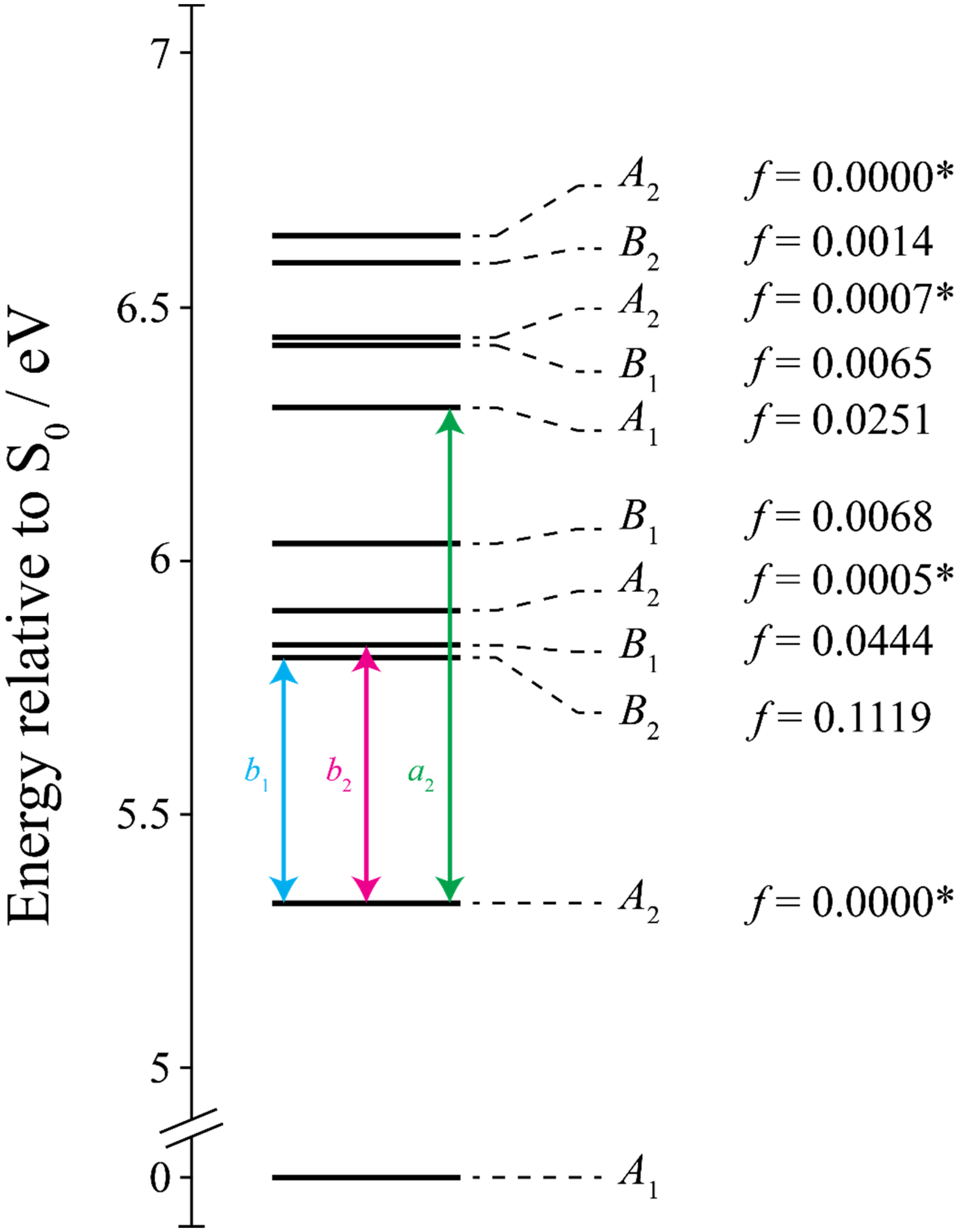

Figure 2.2. Schematic, to scale, showing the vertical excitation energies to the first ten excited singlet states of NMP. These were calculated using the TD-CAM-B3LYP level of theory with the aug-cc-pVTZ basis set (see Section 5.6) from the ground state, optimised geometry of NMP. The effective-C_{2v} symmetries of the electronic states are given, alongside the symmetries of the vibrations within the $\tilde{A}^1A_2$ state (lower case, in colour) that induce vibronic coupling with higher lying electronic states. The calculated oscillator strengths (f) of the electronic states are also given, and those indicated with an asterisk (*) are those expected to be zero if the point group symmetry of NMP were truly C_{2v} (the point group symmetry of ground state NMP is C_s owing to the staggered conformation of the methyl rotor, thus some oscillator strength is calculated where it is not necessarily expected). For more details, see Section 12. Adapted from Figure 3 of Section 12.

2.5. Vibrations of diatomic molecules

Coupling between molecular vibrations is an important way in which excess energy can be redistributed through a molecular system. Initially, molecular vibrations can be considered as normal modes which are motions in which a molecule oscillates with its centre of mass remaining stationary and these all conform to an irreducible representation, which is determined by the point group of the molecule. Furthermore, all normal modes of vibration are orthogonal, meaning when one mode is excited, under the harmonic approximation, no motion in any other normal mode is induced. The simplest picture for looking at molecular vibrations is the classical, Hookean model in a diatomic molecule.

2.5.1. Hooke's law and the harmonic oscillator

When a molecular vibration is treated within Hooke's law, it oscillates with harmonic motion and this scheme is thus termed the 'harmonic oscillator'. Initially considering a diatomic molecule, if one treats this as two point masses, connected by a spring of a given stiffness, Hooke's Law describes a 'restoring force', which acts to return the system to equilibrium after any perturbation by an applied force, *F*:

$$F = \frac{-dV(x)}{dx} = -k_{\mathrm{F}}x$$

Equation 2.22

Here, it is possible to describe the 'restoring force' in terms of the 'stiffness' of the spring (which is determined by a force constant, k_{F}), and its displacement, *x*. Often, the displacement is given as a perturbation from the equilibrium bond length, r_{e}, such that $x = |r - r_{\mathrm{e}}|$, where r is the internuclear separation. In the case of polyatomic molecules, the displacement will be expressed in terms of nuclei in all three spatial dimensions, and therefore have *x*-, *y*- and *z*-components. Equally, noting that a force is simply the *negative* derivative of the potential energy, $\frac{dV(x)}{dx}$, with respect to displacement, if one integrates Equation 2.22 the resulting function describes the vibrational potential in terms of displacement from r_{e}:

$$V(x) = \frac{1}{2} k_{\mathrm{F}} x^2$$

Equation 2.23

Firstly, one should note that the potential energy is dependent on the square of the displacement. This means that, when one plots a harmonic potential energy curve, it takes the form of a parabola, centred about the equilibrium bond distance, r_e. Intuitively, one can see this is not very realistic as when one stretches the string more and more, such that $r \rightarrow \infty$, the system described by Equation 2.23 implies the potential energy of the system also tends to infinity. In a diatomic molecule, one would expect that the two atoms become less and less influenced by one another as they are moved further and further apart, where the potential energy between them tends to zero.

If one solves the diatomic Schrödinger equation (in one dimension), using the harmonic oscillator Hamiltonian:

$$\hat{H} = -\frac{\hbar}{2\mu} \frac{d^2\psi(x)}{dx^2} + \frac{1}{2} k_{\mathrm{F}} x^2$$

Equation 2.24

Where $\hbar$ is the reduced Planck's constant and μ is the reduced mass of the system:

$$\mu = \frac{m_a m_b}{m_a + m_b}$$

Equation 2.25

With m_a and m_b being the masses of the two atoms, a and b, in the system. The resultant eigenvalues are the permitted, quantised vibrational levels of a harmonic system where these take the form:

$$E_{\mathrm{vib}} = hc\omega_{\mathrm{e}} \left(v + \tfrac{1}{2}\right) \text{ where } \omega_{\mathrm{e}} = \tfrac{1}{2\pi c} \sqrt{\tfrac{k_{\mathrm{F}}}{\mu}}$$

Equation 2.26

The energy of the vibrational level, in terms of its vibrational quantum number, v (where v is an integer, v = 0, 1, 2, 3, …), is dependent on the force constant and the reduced mass of the system; the heavier the point masses on the spring and the weaker the spring, the lower the vibrational energy will be.

In Equation 2.26, the only variable which describes the energy of the vibrational levels is the vibrational quantum number, v. Therefore, the solutions to the Schrödinger equation, using the harmonic oscillator Hamiltonian, imply that all the energy levels are equally spaced by $E = hc\omega_e$ (ω_e is the fundamental harmonic vibrational wavenumber for a diatomic molecule), with a zero-point vibrational energy (ZPVE) of $\frac{hc\omega_e}{2}$; these energy levels continue infinitely up the potential well. However, this is not physically accurate and, in reality, the energy levels will converge to a dissociation limit whereby, when the particles are pulled far enough away, they cease to interact strongly enough with each other for the attractive forces to restore the system to equilibrium.

The failure of the harmonic oscillator is stark; it fails to provide an accurate representation of reality. Despite this, it is a reasonable approximation for any small displacements that do not deviate very far in either direction from r_e, such that $x = |r - r_e| \approx 0$ – see Figure 2.3.

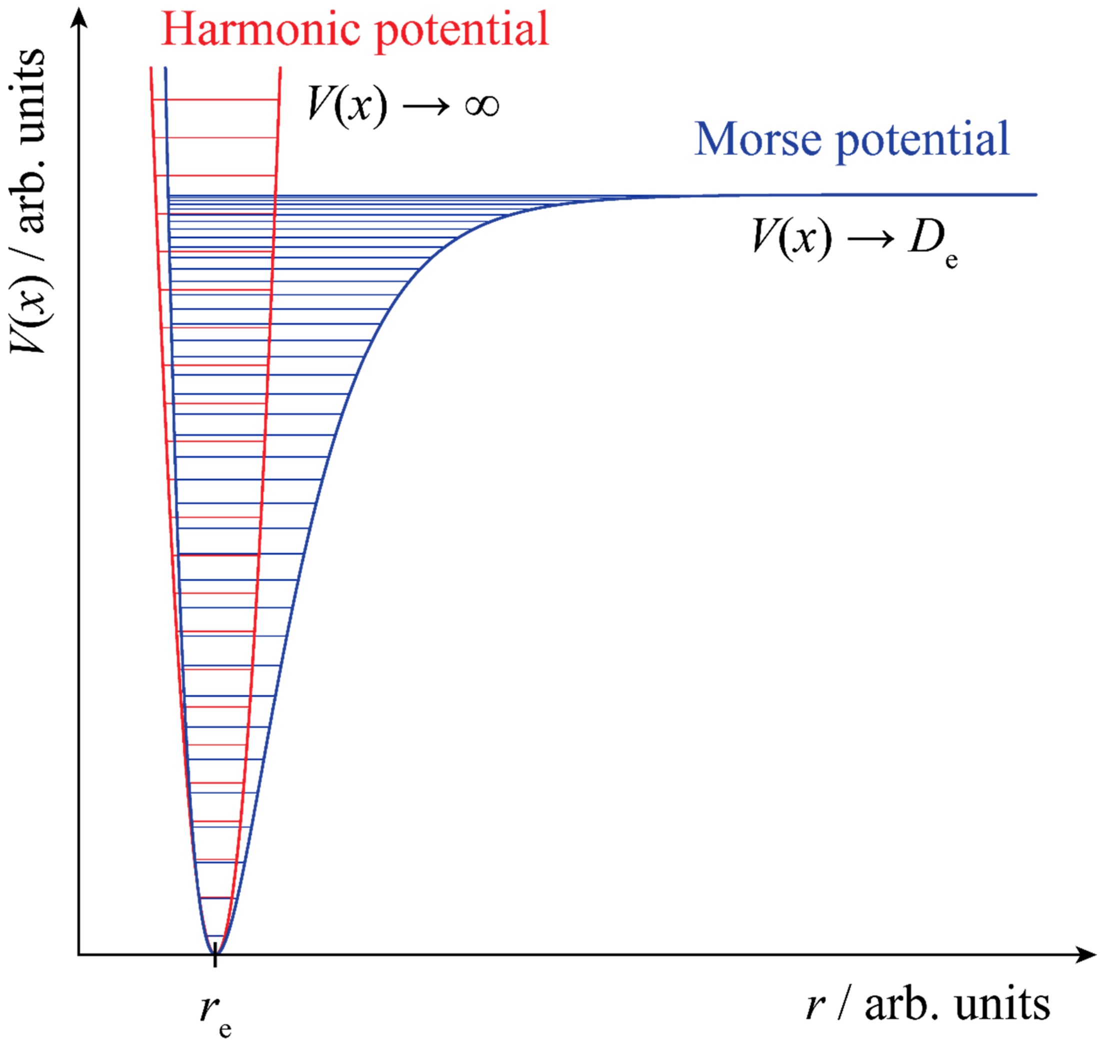

Figure 2.3. A schematic description showing the differences between the harmonic potential (red) and the Morse potential (blue), centred about the same equilibrium bond length, r_e. One can see that, with the Morse potential, the vibrational levels converge rapidly to the dissociation limit, but continue infinitely upwards, equally spaced in the harmonic potential.

2.5.2. The anharmonic oscillator and the Morse potential

One can begin to rectify the failure of the harmonic model by considering anharmonicity. Now, one can begin to devise a model in which the vibrational levels of a diatomic species will begin to converge to a limit, after which the two particles are said to have dissociated and are no longer interacting with one another.

One can see the vibrational levels actually do converge – this can be seen by simply observing overtones in experimental spectra: these are not at exactly twice the energy of the fundamental vibration (as would be predicted by the harmonic oscillator), but instead, the energy gaps between vibrational levels get smaller with each increment of v, see Figure 2.3. (Indeed, under the harmonic treatment, overtones would be forbidden as the general selection rule is $\Delta v = \pm 1$, so seeing overtones at all from the zero-point level is evidence of anharmonicity in itself!) This is particularly noticeable in the spectra of metal-rare gas complexes[130–136], where the vibrational levels can be seen to converge rapidly, owing to the (generally) highly anharmonic nature of physically bound species.

Mechanical anharmonicity, as the name implies, affects the mechanical properties of system and this largely affects the shape of the potential and the force constants associated with it. The harmonic approximation assumes that the force constant is not dependent on the internuclear separation, however one can see in Figure 2.3 that this cannot be true. In the anharmonic case, as $r \rightarrow \infty$, the potential flattens out, so $k_F \rightarrow 0$, and the bond gets weaker owing to the interactions between the nuclei getting smaller. Conversely, the anharmonic depiction in Figure 2.3 also shows that as one decreases the internuclear separation below r_e, the anharmonic potential rises more steeply than does the harmonic potential. This arises from the mutual repulsion between the nuclei which becomes larger as the nuclei get closer together. This increases the strength of the bond, as the repulsive forces try to push the atoms away, such that $k_F \rightarrow \infty$ as $r \rightarrow 0$, requiring more and more energy to push the atoms ever closer together.

Mechanical anharmonicity relaxes the general $\Delta v = \pm 1$ selection rule to yield $\Delta v = \pm 1, \pm 2, \pm 3$, *etc.*, although as Δv increases, the intensities of such vibrational bands decrease rapidly. There is also electrical anharmonicity[*]; the effects of this are generally small, but it also serves to relax the $\Delta v = \pm 1$ selection rule. Unlike electrical anharmonicity, mechanical anharmonicity changes the forms of the vibrational wavefunctions, discussed below, and is often far more significant to a system than is electrical anharmonicity.

---

[*] Briefly, there is a dependence of the dipole moment and polarisability of the molecule on the displacement during a vibration. These are effects on the electrical properties of the molecules which are not considered in this thesis, so are not described in depth here. The book by Hollas[128] is a good starting point for further details.

One of the simpler depictions of the anharmonic oscillator, taking into account such mechanical anharmonicity, is the Morse potential (also shown in Figure 2.3), which takes the form[137]:

$$V(x) = D_\mathrm{e}\,[1 - \exp(-ax)]^2$$

Equation 2.27

Where D_e is the dissociation energy from the bottom of the potential well, 'x' is displacement from the equilibrium geometry, as above, and 'a' is a constant that defines the shape of the potential. One can see that, in contrast to the harmonic oscillator (Figure 2.3), as $x \to \infty$, $V(x) \to D_\mathrm{e}$, which is more realistic.

One can describe the vibrational term values, and therefore vibrational energy levels, $\tilde{G}(v)$, by an infinite, converging power series[128] in terms of $\left(v + \frac{1}{2}\right)$:

$$\tilde{G}(v) = \omega_\mathrm{e}\left(v + \frac{1}{2}\right) - \omega_\mathrm{e}x_\mathrm{e}\left(v + \frac{1}{2}\right)^2 + \omega_\mathrm{e}y_\mathrm{e}\left(v + \frac{1}{2}\right)^3 + \cdots$$

Equation 2.28

As before, ω_e is the harmonic vibrational wavenumber, and x_e, y_e, *etc.*, are anharmonicity terms. This series converges rapidly as the power increases; therefore, one anharmonicity term, x_e, is often sufficient for most spectroscopic purposes and studies obtaining spectroscopic constants often report only ω_e and $\omega_\mathrm{e}x_\mathrm{e}$. Furthermore, if one solves the Schrödinger equation using the Morse potential as a basis, *the solution is exact* if the series is truncated at the $\omega_\mathrm{e}x_\mathrm{e}$, without any higher powers of $\left(v + \frac{1}{2}\right)$[138]. It is the inclusion of these anharmonicity terms that cause the vibrational energy levels to converge to the dissociation limit as a positive $\omega_\mathrm{e}x_\mathrm{e}$ term is subtracted from ω_e. Generally, $\omega_\mathrm{e} \gg \omega_\mathrm{e}x_\mathrm{e} > \omega_\mathrm{e}y_\mathrm{e}$ and higher-order anharmonic terms will therefore only slightly modify the separations.

2.5.3. Extension to polyatomic molecules

Most molecules, however, are polyatomic. For all non-linear molecules, there are $3N$-6 degrees of vibrational freedom, or vibrational modes, where N is the number of atoms in the system. This arises by subtracting the three translational degrees of freedom in three dimensions and the three rotational degrees of freedom about three principal inertial axes. In linear molecules, the rotation about the internuclear axis is neglected owing to the moment of inertia being zero for this mode and there is no energy associated with this. Hence, this rotational degree of freedom does not contribute so there are 3*N*-5 vibrational modes in linear molecules.

In the harmonic picture, if one distorts the molecule from its equilibrium geometry and then allows it to relax (*i.e.*, impart some vibrational motion), this excitation will occur in only one normal mode, as all normal modes are orthogonal. However, upon the consideration of anharmonicity, it is possible for this excitation to couple to several normal modes because these vibrational modes are no longer orthogonal, and are interdependent to some degree.

If one treats the vibrations of a polyatomic molecule in the same way as was done for diatomic molecules in Section 2.5.1, the overall harmonic vibrational potential, $\tilde{G}(v)$, is described as a sum of the vibrational terms, $\tilde{G}(v_i)$, for each normal mode, *i*:

$$\tilde{G}(v) = \sum_i \tilde{G}(v_i) = \sum_i \omega_i \left(v_i + \frac{1}{2}\right)$$

Equation 2.29

Where there is a harmonic vibrational wavenumber, ω_i, for each of the *i* vibrations, analogous to ω_e in the diatomic case. One can then take this further to consider anharmonicity, as presented in Section 2.5.2. The expression then becomes:

$$\tilde{G}(v) = \sum_i x_i \left(v_i + \frac{1}{2}\right) + \sum_{i \le j} x_{ij} \left(v_i + \frac{1}{2}\right)\left(v_j + \frac{1}{2}\right) + \sum_{i \le j \le k} x_{ijk} \left(v_i + \frac{1}{2}\right)\left(v_j + \frac{1}{2}\right)\left(v_k + \frac{1}{2}\right) + \cdots$$

Equation 2.30

Analogous to Equation 2.28, this is a converging power series which considers anharmonicity to describe more accurately the overall vibrational potential, with anharmonic effects considered between pairs, triplets, *etc.*, of normal modes. This time, however, the anharmonicity constants are given as x_{ij}, *etc.*, where i and j, *etc.* are different vibrational modes. Generally, x_i, x_{ij} and x_{ijk} are analogous to the ω_e, $\omega_e x_e$ and $\omega_e y_e$ diatomic terms, respectively, when $i = j = k$. This is often referred to as diagonal anharmonicity as it considers the anharmonicity of an individual vibrational mode.

However, the series also has non-diagonal cross-terms when $i \neq j$. In these cases, one must consider that the motions of the vibrations are not completely independent of one another *i.e.*, they become coupled in some manner. In this scenario, two or more vibrational modes become coupled as a consequence of anharmonicity. This coupling also occurs between more than two vibrational modes, for example between i, j and k, coupled *via* the parameter x_{ijk}, although the magnitude of these higher-order off-diagonal coupling effects is generally very small so are not considered here. Vibrational coupling in this way means a vibrational excitation in one coordinate may be dispersed through multiple vibrational modes, and is the basis of the Fermi resonance and, by extension, IVR (*vide infra*).

2.6. Anharmonic coupling

As has been shown, the breakdown of the harmonic oscillator model leads to the anharmonic picture becoming more important as larger, more complex perturbations displace the system further away from equilibrium. As discussed above, in the case of polyatomic molecules, higher-order off-diagonal anharmonicity terms must be considered, and these terms mean individual vibrational modes are no longer necessarily independent of one another.

Before discussing the ways in which levels may interact, the types of levels one would expect to excite in a polyatomic molecule should be discussed, since some of these arise owing to anharmonicity and whose definitions are pertinent to the forms of mode coupling described below. After this, discussion shall move onto the simplest form of anharmonic mode coupling: the Fermi resonance.

i. Electronic origin:

In electronic spectroscopy, there is often reference to the electronic origin and, indeed, many vibrational wavenumbers presented in this thesis are given relative to the corresponding electronic origin. As discussed in Section 2.2, an electronic transition may occur when a photon (with the correct energy) is absorbed or emitted. If this energy exactly corresponds to the energy gap between the zero-point vibrational and rotationless level of both electronic states, this is considered a pure electronic transition (as there is no vibrational, torsional or rotational excitation associated with this transition). The band that one would observe in such a spectrum is called the electronic origin.

However, the electronic origin is not always allowed (Sections 2.4, 10 and 12), and a band may not always be observed (*cf.* NMP *versus* *m*FT) even if there is a photon with the appropriate energy. In these cases, one may infer the energy of the forbidden electronic origin, whether through progressions in vibrational or torsional levels or by observing electronic origins and dissociation asymptotes in other electronic states. Alternatively, one can use other experimental techniques to modify the selection rules (such as a multiphoton excitation[82] scheme), see Sections 5.2 and 12.

ii. Vibrational fundamental:

There will be vibrational levels associated with an electronic state and, with vibrationally-resolved electronic spectroscopy techniques, one may populate and identify these individual vibrational levels in the excited state, dependent on the spectroscopic technique employed. A number of these vibrational levels will correspond to vibrational fundamental transitions, which occur when *a single quantum* of a normal mode of a vibration is excited alongside an electronic transition. In the electronic spectroscopy of polyatomic molecules, however, there are multiple normal modes that can be excited;

indeed, there are 30 ring-localised modes in *m*FT and 24 in NMP. Whether these vibrational transitions are allowed or not depends on the electronic state to which one excites. In the context of the spectroscopic techniques detailed in Section 5, a vibrational transition may occur simultaneously with an electronic transition and therefore, under the jet-cooled conditions, $S_1 v_i' \leftarrow S_0$ is considered a fundamental vibrational transition, where v_i' is a vibration in the excited electronic state; the vibrational wavenumber of the transition is then reported relative to the S_1 state electronic origin.

iii. Vibrational overtone:

The term 'vibrational overtone' generally means that *more than one quantum* of a particular vibration has been excited. As before, we consider a vibrational transition occurring simultaneously with an electronic transition: the first overtone will occur when two quanta of an excited state vibration are excited, the second overtone when three quanta are excited, third overtone when four quanta are excited, *etc*.

There are multiple vibrational modes that can be excited, each with their own symmetries. In the case of a symmetry-allowed fundamental vibration (*vide supra*) such as those in *m*FT, all overtones of the vibration are allowed. However, if the fundamental vibration is symmetry-forbidden but the electronic transition is electric dipole allowed (*e.g.*, the a'' vibrations in the S_1 state of *m*FT), only excitations of even quanta of the vibration are allowed and thus observable, as these will always transform as the totally-symmetric symmetry class of the corresponding point group. From the example above, as the a'' vibrational fundamental is forbidden, the first overtone (*i.e.*, two quanta of the vibration) is allowed as $a'' \times a'' = a'$ and a' is the totally-symmetric symmetry class of the C_s point group. Going further, the second overtone is symmetry forbidden as, like the fundamental, it also has a'' symmetry and the third overtone is allowed as this has a' symmetry, again, and so forth.

Additionally, for small, diatomic van der Waals (vdW) complexes, the change in geometry may be large between electronic states and one may expect to see higher overtones of the intermolecular stretch, and not the fundamental vibration owing to the location of the Franck-Condon window (this is a generalised name for the parts of the potential energy surface that can be accessed through a vertical transition). However, in cases where the change between two electronic states is relatively small, the FC window is located around the zero-point vibrational level of the molecule in the upper electronic state; hence, one would not necessarily expect to observe higher-order overtones owing to the anticipated low intensity, but would expect to observe vibrational fundamental transitions. Nonetheless, if such an overtone is symmetry allowed and signal to noise is good, there is no *prima facie* reason not to expect to observe first and second overtones, *etc.*, if one scans high enough in wavenumber, although their intensities will diminish with the FCFs.

In photoelectron spectra, one may expect to observe higher overtones compared to in electronic excitation spectra of the neutral molecule as the removal of an electron can lead to a significant change in electronic structure, and therefore geometry. This may lead to a greater displacement of the potential energy surfaces between the neutral molecule and the cation, such that the FCF maximum may be expected to have shifted from the zero-point vibrational level of the cation.

iv. Vibrational combination band

It has been discussed above that polyatomic molecules have multiple vibrational modes, indeed, for a non-linear molecule, there are $3N$-6 (N is the number of atoms) vibrational degrees of freedom. What has not been discussed is that more than one vibrational mode in a molecule may be excited simultaneously. Similarly to overtones, dependent on symmetry, one may expect to observe such transitions, and these are referred to as vibrational combination bands.

One can use the direct product table for the appropriate point group to deduce the overall symmetry of the combination band and then consider the selection rules presented throughout this section to assess if the combination band is symmetry allowed. For example, a combination band comprising of one quantum of an a_1 vibration and one quantum of a b_2 vibration (with C_{2v} symmetry) will have the overall symmetry of $a_1 \times b_2 = b_2$. Additionally, one quantum of an a_1 vibration in combination with *two* quanta of a b_2 vibration will have the symmetry: $a_1 \times b_2 \times b_2 = a_1$.

v. Vibration-torsion combination bands

Also referred to as ‘vibtors’, these will be discussed in more detail in Sections 3 and 4. Briefly, these are similar to vibrational combination bands – this time, one or more quanta of a vibration can be excited simultaneously with a torsion. The torsional selection rules are slightly different to those of vibrations so one must use the symmetries of the vibration and torsion (and electronic state if a vibration-torsion-electronic, or vibtoronic, state is considered) in the corresponding molecular symmetry group (*e.g.*, G_6 or G_{12}; Section 3.4) in order to deduce if a vibtor transition is symmetry allowed.

vi. Hot bands

Lastly, one may observe hot bands in electronic spectra. These are transitions originating in a vibrational level that is *not* the zero-point level of the initial electronic state. As discussed further in Section 5, the experiments conducted as part of this thesis employ a supersonic jet expansion to cool internally the vibrational (and rotational) degrees of freedom. As such, given these conditions, vibrational hot bands are not expected. Conversely, in experiments conducted at room temperature or where cooling is ineffective, then observing hot bands is likely.

Owing to incomplete internal cooling of the torsional degrees of freedom of the sample in the free-jet expansion, some population remains in a low-lying, but nonetheless excited, torsional level in the ground electronic state.

Therefore, a small number of torsional hot bands are observed in the REMPI and LIF spectra presented herein.

viii. False origin:

While this is not strictly a ‘type’ of level one may observe in spectroscopy, it remains something of which one should be aware. As mentioned above, the electronic origin transition may not always be electric dipole allowed and the vibrations of this electronic state may be allowed through vibronic coupling methods (or otherwise) and may be rather intense, such as P_{16} in NMP and ν_6 (Wilson[139] label) in benzene[83,84]. Hence, it is possible that one may, at first glance, mistake such a vibrational transition to be the electronic origin, hence the term ‘false origin’.

Despite the following not being, by definition, a false origin, it is worth noting that some vibrational fundamentals may appear to behave in a similar way to the electronic origin in the spectra of polyatomic molecules, even when the electronic origin is allowed. Such bands may have similar vibrational activity built upon them, reminiscent to that observed for the origin band. For example, the vibrational fundamental $^{+}18^{1}$, observed in the ZEKE spectra *via* m^0 and m^1 (both torsional components of the S_1 electronic origin) in *m*FT, was observed in combination with all vibrations overserved for the cationic electronic origin, $^{+}0^{0}$. This was also the case for 15^1 in the S_1 state (see Ref. 76 and Section 8).

2.6.1. Fermi resonance

The simplest manifestation of anharmonic coupling is the Fermi resonance and was first proposed by Fermi[140] in 1931. To the first-order, two fundamental vibrations cannot interact with one another, so the Fermi resonance considers solely an interaction between a fundamental vibration and either an overtone or a combination band. The two states that comprise the Fermi resonance (the states in absence of the interaction) are referred to as zero-order states (ZOSs). These two interacting ZOSs must be of the same symmetry and close in energy to interact.

When the two ZOSs interact, this can be thought of as the ZOSs perturbing one another. The strength of the interaction, and therefore the degree of mutual perturbation, is dependent on how close in energy the ZOSs are: two ZOSs that are close in energy will usually perturb each other considerably more than two ZOSs energetically distant. This means one is unlikely to observe a Fermi resonance if two ZOSs are far apart in energy apart, unless the ZOSs are particularly strongly coupled.

In a frequency-resolved photoelectron or fluorescence spectrum, such as those considered in this thesis, one would not directly observe the ZOSs that form the Fermi-resonance, instead one would observe two resultant eigenstates of mixed character *i.e.*, the end-product of the interaction. Consider two ZOSs, $|1\rangle$ and $|2\rangle$. Provided they are energetically close and of the same symmetry, they can interact, and perturb one another, and two eigenstates of mixed character will be formed:

$$|a\rangle = c_i|1\rangle + c_j|2\rangle$$
$$|b\rangle = c_i|2\rangle + c_j|1\rangle$$

Equation 2.31

These eigenstates, $|a\rangle$ and $|b\rangle$, are a linear combination of the ZOSs, $|1\rangle$ and $|2\rangle$, and c_i and c_j are the mixing coefficients. If the coefficients, c_i and c_j, were both exactly 0.5, this is indicative of perfect mixing, and the resultant eigenstates will be equally mixed. Resonant-intermediate photoelectron or fluorescence spectra *via* $|a\rangle$ and $|b\rangle$ will be indistinguishable, in the absence of other couplings or vibrational mixing between electronic states (Section 2.7). It should be reiterated that the ZOSs will not be observed; the Fermi-resonance is an intrinsic interaction and the eigenfunctions are already mixed in this way and the ZOSs are a convenient basis to describe the interaction. Should the mixings be unequal, one will observe one eigenstate as being ‘more’ of a particular ZOS than the other. Should the energy spacing be large, then $c_i >> c_j$ and the mixing of the two ZOSs becomes negligible, and one will observe intensity almost completely arising from one particular ZOS.

Not only do the characters of these ZOSs become mixed in the formation of the mixed eigenstates, but the resultant states will also appear displaced from the expected energetic location of the contributing ZOSs, which can be thought of as a repulsion. How much the eigenstates are repelled also depends on how far apart in energy the ZOSs were and how strongly they couple. This is illustrated, schematically, in Figure 2.4.

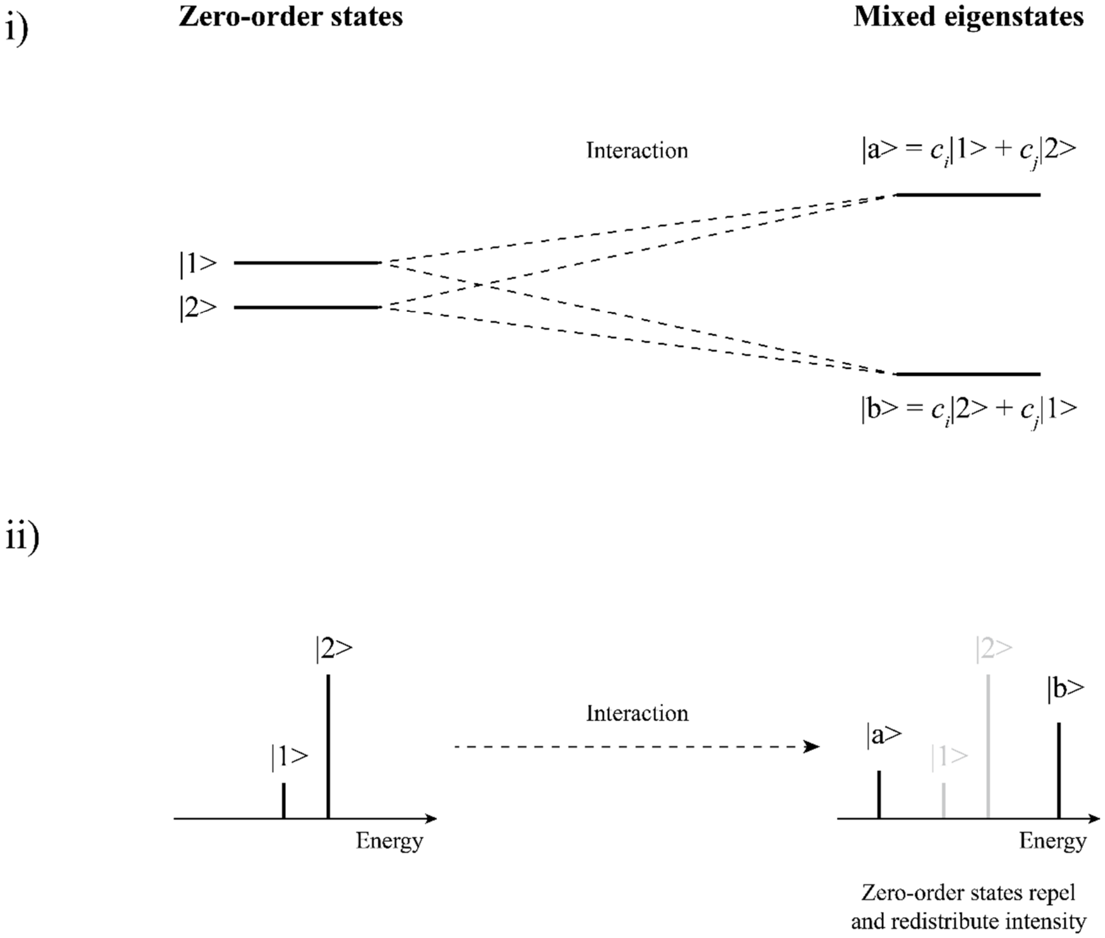

Figure 2.4. Depiction of the perturbation of two zero-order states, $|1\rangle$ and $|2\rangle$, which interact owing to a Fermi resonance. Panel (i) is a schematic energy level diagram, showing the mixing of the characters, and perturbations, of the ZOSs. Panel (ii) is a schematic representation of a spectrum showing what one may observe arising from the Fermi resonance (the original intensities and positions of the ZOSs are in grey on the right-hand side).

The two eigenstates in Fermi resonance can be useful to the spectroscopist as the ZOSs need not, necessarily, be allowed. Fermi's original paper[140] considered the Raman spectrum of CO_2. The first overtone of the bending mode has symmetry Σ_g^+ (as $\Pi_u \times \Pi_u = \Sigma_g^+$) and as does the symmetric stretch; one would initially expect these vibrational modes to appear as near-degenerate. However, only one intense band in this region of the spectrum is expected as the overtone of the bending mode expected to be weak. Fermi, however, observed two sizeable bands noticeably displaced from the expected positions of the ZOSs, suggesting there was a strong interaction that was not only repelling the two eigenstates, but also allowing the band (mostly) due to the overtone bending mode to gain significant intensity, and the resultant eigenstate contains some character from the symmetric stretch.

Furthermore, while a Fermi resonance is, by definition, between the fundamental of a vibration and an overtone or combination band, an identical coupling scheme may occur between two overtones, or two combination bands, or a mixture of the two, and these are often referred to as Darling-Dennison resonances[141].

Typically, when talking about coupling in this manner, the ZOSs may be referred to as either a zero-order bright (ZOB) state or a zero-order dark (ZOD) state. The ZOB state is a ZOS which, when excited would have inherent intensity; conversely, the ZOD state will not have any inherent intensity and, in absence of any coupling, one would not expect to observe this in an experimental spectrum.

In experiments such as 2D-LIF and ZEKE (see Sections 5.4 and 5.5, respectively), one can project the populations of these mixed-character eigenstates onto the vibrational levels of another electronic state, which allows for the elucidation of the character of the states that comprise the Fermi resonance, even though it would not be possible to observe the ZOD state directly.

2.6.2. Restricted IVR

Where a Fermi resonance is often described through the involvement of two interacting ZOSs, one can also consider a scenario in which a small number of ZOSs and/or eigenstates may couple together. While this is necessarily more complicated than the Fermi resonance, there is not a total redistribution of vibrational energy throughout the molecule. This has been observed in *m*FT at low internal energy, and in NMP, at ~800 cm^{-1} in S_1, and will be discussed in detail in Sections 8-13. Although in these cases, there are few enough states coupling together to unravel the nature of this coupling and for the identities of the ZOSs involved to be proposed. This is termed ‘restricted IVR’, as the coupling, and therefore dispersal of energy, is only between a handful of levels.

In a frequency-resolved experiment, such as those conducted herein, one would be able to observe the resultant eigenstates and make deductions about the identities of the ZOSs. However, even in these scenarios, it may be difficult to ascertain which states are coupling to which, as the coupling may be direct, or indirect. If one has three ZOSs that are coupled as $|a\rangle \rightarrow\ |b\rangle \leftarrow |c\rangle$, where the arrow represents direct coupling, one can say that states $|a\rangle$ and $|c\rangle$ are indirectly coupled through $|b\rangle$. If one probes $|a\rangle$, one should be able to see Franck-Condon activity due to both states $|b\rangle$ and $|c\rangle$ as well, despite $|a\rangle$ and $|c\rangle$ not being coupled directly.

While it was stated in Section 2.6.1 that, to the first order, fundamental vibrations may not couple, they may indirectly couple together through a state that is not a vibrational fundamental. Despite this, generally, one may describe a restricted IVR scenario as one in which the individual ZOSs involved in the coupling, whether direct or indirect, may be identified and assigned.

A time-resolved technique, however, would be able to see how the population propagates and oscillates between the coupled ZOB and ZOD states in the form of quantum beating. Such an experiment would be able to distinguish between coupled ZOSs and those which are simply Franck-Condon active or Duschinsky mixed – see below. However, a time-resolved experiment will not necessarily be able to ascertain the identity and characteristics of the mixed eigenstates; alternatively, a frequency-resolved experiment, such as those conducted as a part of this work, should be able to determine the identities of the eigenstates and propose identities for the ZOSs involved.

2.6.3. Statistical (dissipative) IVR

IVR is often described in terms of the 'tier model'[142], in which there is a cascading coupling of eigenstates; two ZOSs couple, forming two new eigenstates (see Figure 2.4), which will then go on to couple with other ZOSs or eigenstates, and these will couple again, *etc*. Indeed, this often occurs when the density of same-symmetry states is high. In fact, it is one of the reasons that full, statistical (or dissipative) IVR is achieved in *m*FT far faster than it is in *p*FT: the decrease in symmetry from the G_{12}

molecular symmetry group to G_6 means that states that were formerly the wrong symmetry to interact, now can. This is described very well by Parmenter *et al.*[74,143–145] in the context of substituted benzenes, following the addition of a methyl rotor, and will also form part of the discussion of the papers in this thesis.

Statistical IVR is more complex than the restricted IVR regime, in that there will be many direct and indirect couplings such that any excited eigenstate, when probed, will give rise to significant activity in a spectrum, making it difficult to discern the nature of the individual states that have coupled. Furthermore, this can continue to the point whereby the vibrational population is widely distributed between multiple modes, so one primarily observes coupling to a 'bath' of states yielding a broad, structureless spectrum. In this case, the activity becomes indistinguishable and unresolved, except, perhaps some activity due to the excited eigenstate and a small number of other strongly coupled states[†], such as for the 11^1 band in S_1 *m*FT – see Section 8. This, however, happens more frequently at high internal energy (>1500 cm^{-1}), unless there are 'aggravating' factors such as (multiple) methyl rotors or a low symmetry (*e.g.*, C_s or C_1).

2.7. Duschinsky mixing

Anharmonic coupling is not the only way in which the appearance of unexpected activity in a spectrum can be facilitated. Duschinsky mixing (also referred to as Duschinsky rotation) manifests itself in a molecular spectrum in a similar way to anharmonic coupling, in which one may see strong activity arising from another vibration that is not the one pumped; however, anharmonic coupling and Duschinsky mixing have very different origins. This type of mode mixing was first described by Duschinsky[146] in 1937. As mentioned previously, two fundamental vibrations may not couple together directly, however, there is no such limitation on fundamental vibrations being involved in Duschinsky mixing as this is not a coupling mechanism. Through Duschinsky mixing, it is possible to observe activity in a spectrum *via* one

---

[†] Should a ZOB state be coupled particularly strongly to a ZOD state, and this ZOD state is coupled to another state in a 'bath of states' that leads to statistical IVR, this is referred to as 'doorway IVR' as the ZOD state acts as a 'doorway' to statistical IVR. This is generally considered separately from both statistical and restricted IVR, despite often exhibiting characteristics of both.

fundamental vibration that arises from other fundamental vibrations. As anharmonic coupling and Duschinsky mixing possess similar hallmarks in molecular spectra, caution must be applied in the interpretation of such spectra. They differ in that Duschinsky mixing arises from changes in the forms of the vibrations between two electronic states, rather than being an inherent interaction between vibrational modes arising from anharmonicity.

Briefly, the Duschinsky effect is based on the observation that, owing to the geometry change between two electronic states, the accompanying change in the nuclear coordinates and charge densities will lead to a change in the forms of the normal modes between these two states. As such, it is assumed that the vibrations of the final electronic state can be represented as a weighted linear combination of the vibrations of the initial state and is often referred to as ‘mixing’. Normally, as the changes in geometry between two electronic states for small, aromatic molecules are generally small, the extent of the vibrational mixing is expected to be limited. However, in some cases, it can be rather extensive, especially if the change in geometry between the two electronic states in question is along the same coordinate as one or more vibrations. Furthermore, only vibrations of the same symmetry can be mixed in this way[‡].

A common way of representing the extent of such mixing is through the use of a Duschinsky matrix (DM). This is essentially a plot of how well the vibrational wavefunctions of the normal modes in an initial and final state overlap, as calculated through quantum chemical calculations (noting that these are often harmonic vibrational calculations and so are an approximate picture). A perfectly diagonal matrix (*i.e.*, where the diagonal elements are unity, and all off-diagonal elements are

---

[‡] It should be noted, here, that in the work presented in Sections 11 and 12, the Duschinsky matrices presented indicate that there is some ‘mixing’ of vibrations of different symmetries, seemingly in contrast to what is written here. This arises from the fact that the reported point group symmetry for NMP is only the *approximate* point group. As a result of the methyl rotor, NMP is not strictly C_{2v} and quantum chemical calculations will use the C_s point group symmetry. As such, the Duschinsky matrix arising from these calculations leads to the conclusion that there is some mixing of modes of ‘different’ symmetry; this is not allowed if the point group is representative of the true symmetry of the molecule.

zero) occurs when there is no vibrational mixing between states, and the vibrations of both electronic states have identical motions and amplitudes. The introduction of off-diagonal elements to the DM arises when there is some degree of mixing present, and hence differences in the vibrational motions between electronic states.

Figure 2.5 depicts two, generalised, DMs for nine vibrations between an initial state, $\tilde{X}$, and a final state, $\tilde{A}$. These describe how mixed the vibrations, v_n, between these two electronic states are, in terms of the initial state vibrations. Matrix (i) depicts a case in which there is no mixing of the vibrations between the two electronic states, such that each final state vibration is perfectly in correspondence with the equivalent initial state vibration; therefore, if one were to visualise the atomic motions, one would not be able to distinguish between the two electronic states. In essence, one observes purely diagonal character in the Duschinsky matrix with no off-diagonal elements.

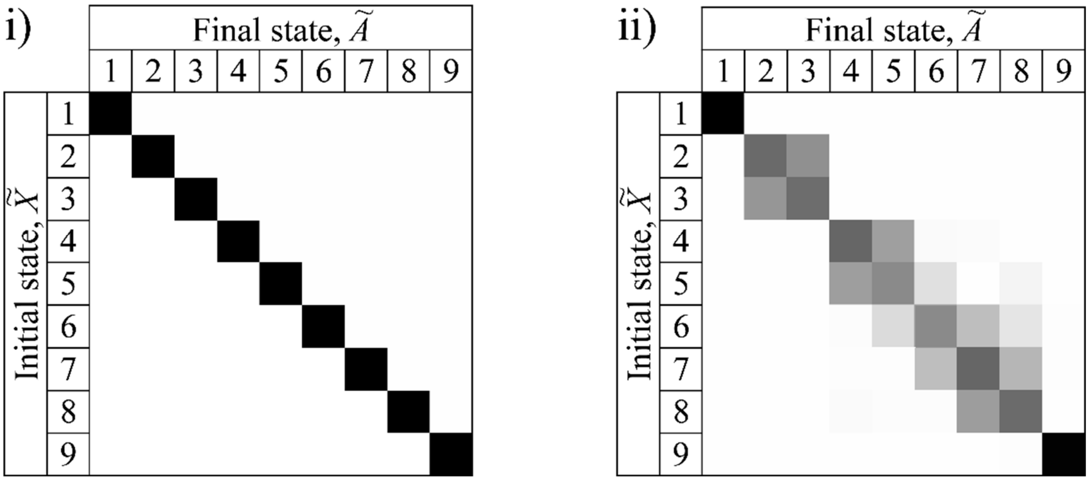

Figure 2.5. Generalised Duschinsky matrices depicting how import the Duschinsky effect can be in determining the changes in the characters of the vibrational modes between two electronic states. The vibrational labelling is consistent between states and vibrations are given by a number, see, for example, the $^{m}D_i$ and P_i scheme for *m*FT and NMP in Section 4. DM (i) depicts a scenario in which there is no vibrational mixing between the electronic states and DM (ii) represents a scenario in which there is mixing of the vibrational modes between the electronic states, such that the vibrations in the final state can be represented as an admixture of more than one initial state vibration. The depth of shading is representative of the coefficients of mixing, where black is 1 and white is 0.

However, in reality, there will likely be some mixing of the vibrational modes between the excited and final states owing to the different electronic structures and there will be some off-diagonal elements to the DM. In matrix (ii) of Figure 2.5, this is represented by the off-diagonal entries being greater than zero (off-white or light grey), indicating small quantities of mixing, and the on-diagonal elements become less than one (less black) as a result. The darker the colour in the square, the larger the contribution of that initial state vibration to the linear combination of the final state vibration. It should be noted that all mixing coefficients for the various initial state modes that make up the final state vibration will always sum to one.

In a spectroscopic context, if one projects the population of a vibrational fundamental in the S_1 state (ν_1') onto the D_0^+ state, as one would for a ZEKE experiment, when one looks at the ZEKE spectrum recorded while pumping ν_1', one may observe more than one transition to vibrational fundamentals of the cation state (ν_1^+, ν_2^+, ν_3^+, *etc.*), arising from Duschinsky mixing between S_1 and D_0^+. One can represent this linear combination as $|v_1'\rangle = c_i|v_1^+\rangle + c_j|v_2^+\rangle + c_k|v_3^+\rangle$ where $c_i \gg c_j \sim c_k$. The mixing coefficient, c_i, is expected to be the largest as v_1' and v_1^+ are, qualitatively, the 'same' vibration in the S_1 and D_0^+ states, respectively, and this would correspond to the diagonal element in the DM. Therefore, one would expect the most intense band in such a ZEKE spectrum to arise from $|v_1^+\rangle$. However, off-diagonal elements *i.e.*, arising from vibrations v_2^+ and v_3^+, in the absence of coupling and assuming FCFs are equal, will show intensities in the spectrum proportional to c_j and c_k, respectively. Additionally, a similar picture would be seen if one pumped different vibrations in the S_1 state (*e.g.*, ν_2', ν_3', *etc.*) that were involved in the mixing.

In terms of the observed spectra, this means one may observe significant intensity due to vibrations that are not expected from the $\Delta\nu = 0$ (diagonal element) propensity rule, which do not arise from FC activity or mode coupling. As such, this is another way in which vibrational fundamentals can gain intensity in a spectrum, meaning simple Franck-Condon arguments are no longer wholly reliable.

3. The effect of the methyl rotor in molecular spectroscopy

There has been significant interest in the effects of the addition of a methyl rotor on internal coupling routes within small, aromatic molecules in recent years. Pioneering experimental work by Weisshaar[68,147] and Parmenter[74,144,145] discussed this issue, and has been considered further, more recently, by Lawrance and co-workers[36,75,148]. Significant theoretical developments by Longuet-Higgins[149] and Bunker and Jensen[124] have facilitated the use of permutation-inversion molecular symmetry groups (MSGs) to describe the torsional motions of the methyl rotor. It is these symmetry groups that provide the basis for understanding the rules that govern how the methyl rotor can couple and interact with the rest of the molecule. There is also a very detailed review by Spangler[150] which provides a good background on the role of the methyl rotor in spectroscopy.

By adding a methyl rotor onto a benzene or pyrrole moiety, one opens up new ways in which ring localised modes can interact with the motions of the methyl rotor. First targeted by Parmenter *et al.* in terms of substituted benzenes, it was shown that the rate of IVR increased significantly upon addition of a methyl rotor[74]. For example, they determined that the replacement of a fluorine atom of *p*DFB, yielding *p*FT, increased the rate of IVR by a factor of ~40. Then, decreasing the symmetry of the molecule from effective-C_{2v} to effective-C_s, as in *m*FT, further increased the rate of IVR by a factor of ~12. Therefore, in comparison to *p*DFB, the rate of IVR increases in *m*FT by a factor of ~480.

In this section, aspects of the addition of the methyl rotor will be discussed, in the context of both *m*FT and NMP, from the free-rotor, through to the hindered-rotor. The quantised nature of the torsional energy levels is discussed and also, briefly, permutation-inversion MSGs. Owing to the nature of these molecules, only the single-rotor case will be considered as the addition of a second rotor (*e.g.*, in *o*-/*m*-/*p*-Xyl) complicates the matter significantly, as well as further increasing the rate of IVR. For discussion on the double rotor, the reader is directed to Refs. 48 and 55, and the thesis of Tuttle[151], which discusses the impact of the double rotor in great detail.

3.1. The free rotor

Initially, the simplest case shall be considered, which is the free rotor. A model for this is an internally-rigid methyl group, which is not perturbed in any way as it rotates about the bond connecting it to an infinitely heavy point mass. This scenario is analogous to that of the particle-on-a-ring model. In this case, the Hamiltonian can be written as:

$$H = F\frac{\partial^2}{\partial\phi^2}$$

Equation 3.1

Where F is the effective rotational constant for the rotor and ϕ is the torsional angle. For a molecule containing a freely-rotating methyl rotor, the effective rotational constant can be written in terms of the reduced moment of inertia, I:

$$F = -\frac{\hbar^2}{2I}$$

Equation 3.2

$$I = \frac{I_\mathrm{m} I_\mathrm{r}}{I_\mathrm{m} + I_\mathrm{r}}$$

Equation 3.3

Where I_m is the moment of inertia of the $-CH_3$ group, and I_r is the moment of inertia of the rest of the molecule; for *m*FT and NMP, this is the aromatic ring, which is treated as a point mass. The reduced moment of inertia is used since the rotor and the rest of the molecule are both freely rotating about the same bond, in this two-body picture.

As mentioned above, the rest of the molecule must be viewed as being of infinite mass compared to the rotor in order to treat the rotor in such a way and, indeed, in the case of substituted pyrroles and especially substituted benzenes, the mass of the parent molecule is significantly greater than that of the single methyl rotor. If this assumption is followed through, the reduced moment of inertia, I, as presented in Equation 3.3, can be approximated as I_m. Therefore, we determine F, the internal rotation constant as, approximately:

$$F \cong \frac{\hbar^2}{2I_\mathrm{m}}$$

Equation 3.4

If one solves the Schrödinger equation with the free-rotor Hamiltonian, the obtained eigenvalues give the energies of the free-rotor torsional levels:

$$E = m^2F$$

Equation 3.5

Where m is the torsional quantum number, which takes values of 0, ±1, ±2, ±3, …, and so forth, with the accompanying eigenfunctions[126]:

$$\psi = \exp(im\phi)$$

Equation 3.6

Notably, due to the quadratic dependence on the torsional quantum number, the free-rotor torsional energy levels, for $m \neq 0$, are all doubly degenerate (one can view this as rotating the methyl rotor clockwise or anticlockwise with respect to the parent molecule), and the energy increases as a function of m^2. Also, one can see there is no zero-point energy associated with the free-rotor torsional levels as, from Equation 3.5, the energy is zero for $m = 0$.

Here, a number of assumptions have been made that seem unrealistic at first glance, notably the assumption that the pyrrolyl or benzene ring is infinitely heavy compared to the methyl rotor. However, in general, for qualitative purposes, the majority of the torsional levels calculated in this manner are sufficient to get an idea of the energies of the torsional levels, which can be useful in distinguishing between the internal rotations of the methyl rotor and low-energy vibrations of the parent molecule in molecular spectra, with some caveats, as discussed below.

3.2. The hindered rotor

Out of all the assumptions made in the free-rotor case, the most significant one is that the methyl rotor is not perturbed by any hindering potential arising from the rest of the molecule. Indeed, there will always be a hindering potential exhibited by the rest of the molecule as it will never be a non-interacting, infinitely heavy, point mass and there will always be some form of electronic or steric influence on the methyl rotor. Therefore, one should consider what occurs when a hindering potential is applied.

If one assumes the three hydrogen atoms, and their corresponding C-H bonds, of the methyl rotor are equivalent (while there may be some distortion of bond lengths and angles as the methyl group rotates, this approximation holds as these perturbations are very small), it can be inferred that there will be a three-fold symmetry of the rotor relative to the ring, so the overall, hindered, torsional potential would be expected to be periodic with $3n$ minima (n = 0, 1, 2, 3, …), and, as such, the 'n' of the V_n potential terms increases by $3n$ as well. It should be noted, however, that the precise nature of the number of minima is also dependent on the symmetry of the rest of the molecule. Therefore, we can model the torsional potential, $V(\phi)$, generally, as:

$$V(\phi) = \frac{V_3}{2}[1 - \cos(3\phi)] + \frac{V_6}{2}[1 - \cos(6\phi)] + \frac{V_9}{2}[1 - \cos(9\phi)] + \cdots$$

Equation 3.7

Where the V_n terms are the potential terms of the overall torsional potential, which arise from the three-fold symmetry of the methyl rotor. As above, ϕ is the torsional angle.

The first non-zero term in the expansion in Equation 3.7, as mentioned previously, is dependent on the symmetry of the overall system. For *m*FT, there is three-fold rotational symmetry of the methyl rotor (about the bond connecting the rotor to the ring), but only one-fold rotational symmetry of the *meta*-fluorinated benzyl ring about the connecting bond; as such, there is a three-fold symmetric torsional potential and, therefore, the V_3 term is the first non-zero term and this gives rise to three minima per 360º rotation of the methyl rotor.

In the case of NMP, in addition to the three-fold symmetry of the methyl rotor, there is two-fold rotational symmetry from the pyrrolyl ring. Therefore, to the first order, one expects the torsional potential to have six minima – three from the methyl rotor, multiplied by two as each hydrogen atom of the methyl rotor passes either side of the ring. Furthermore, the V_3 parameter is zero and the V_6 term is then the first non-zero term of the torsional potential in Equation 3.7.

In general, the first non-zero term of the potential determines the height of the potential barrier to rotation (which is notably large in *m*FT$^+$), whereas higher-order terms influence the shape of the potential. Spangler[150] highlights in his review that, owing to the rapidly converging nature of the potential series (Equation 3.7), one term tends to fit very well to experimental data (which can be seen is true for NMP in Section 10). It is very rare for more than two terms to be required to describe the torsional potential accurately (as an example, both V_6 and V_3 terms are used to describe the torsional potential of *m*FT), as the contribution of higher-order V_n terms to the potential gets smaller, rapidly, as *n* increases[§].

Figure 3.1 depicts the torsional potential of *m*FT (in the S_0 state), using calculated V_3 and V_6 parameters values[75], truncated at the V_6 term, and how the V_3 and V_6 terms contribute individually to the potential, as a function of torsional angle, ϕ. As the torsional potential of NMP is accurately described by only the V_6 term, the red trace in Figure 3.1 will (qualitatively) depict the appearance of the torsional potential of NMP; however, one notes that the magnitude of the V_6 parameter is different between *m*FT and NMP in the S_0 state.

[§] If the magnitudes of these higher-order terms are significant, they may have the effect of introducing additional local minima between those arising from the highest V_n term, although this is often only appreciable for the V_6 parameter when the value of V_3 is small. If V_3 is present and large, then the torsional potential generally looks like it would if there were only a V_3 parameter.

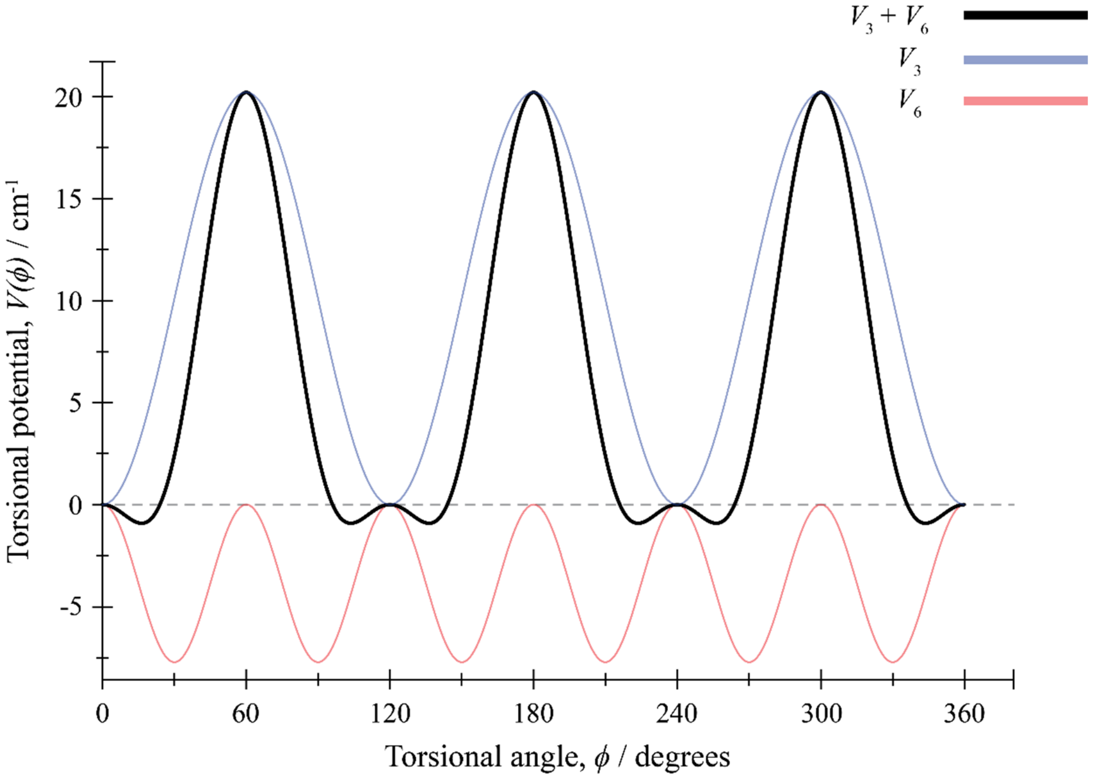

Figure 3.1. Hindered torsional potential for one full 360° rotation of the methyl rotor of *m*FT, as a function of torsional angle, in the S_0 state, with 0° defined as one hydrogen atom of the methyl rotor being eclipsed and *pseudo-trans* (see Figure 3.2) to the fluorine of the fluorobenzyl ring. V_3 = 20.2 cm^{-1} and V_6 = -7.7 cm^{-1}, as determined by Lawrance *et al.*[75]; these parameter values are calculated and do not account for vibration-torsion interactions.

From Figure 3.1, one can see that it is the V_3 term that determines the height of the torsional potential barrier in *m*FT, with V_6 simply altering the shape and adding the small, local minima near where the V_3 and V_6 plots meet out-of-phase. One should note that the signs of the V_3 and V_6 terms are important and the overall torsional potential, $V(\phi)$, would appear strikingly different should either V_3 or V_6 be negative. Comparatively, in NMP, there is no V_3 term due to the two-fold rotational symmetry of the pyrrolyl ring, such that it is the V_6 term instead that describes the height of the potential barrier. Additionally, the value of V_6 parameter for NMP in its S_0 state is comparatively much larger than it is in *m*FT[118] at -(40-45) cm^{-1}.

One should note that there is a level of uncertainty in the V_3 and V_6 parameters used to produce Figure 3.1; Lawrance and co-workers[75] report an error of one standard deviation, as they use calculated line-positions of the torsional levels and fit them to the potential. They also note that their V_3 and V_6 parameters do not include correction for vibtor interactions, therefore, any torsional levels calculated using these values will not exactly reproduce the levels one observes experimentally, particularly if there is a strong vibration-torsion interaction.

If the torsional potential of a molecule has a leading V_3 term, such as for *m*FT, the sign of the V_3 term is assigned based on the conformation of the methyl rotor with respect to the parent ring. By convention, the sign of the V_3 term is considered to be *positive* if the minimum energy conformation is when the methyl rotor is eclipsed with respect to the ring, and the in-plane rotor hydrogen and *meta*-substituted fluorine atom of the ring are *pseudo-trans* with respect to one another[68]. This is generally also taken as a torsional angle of 0º, as it has been in Figure 3.1. This is shown diagrammatically in Figure 3.2.

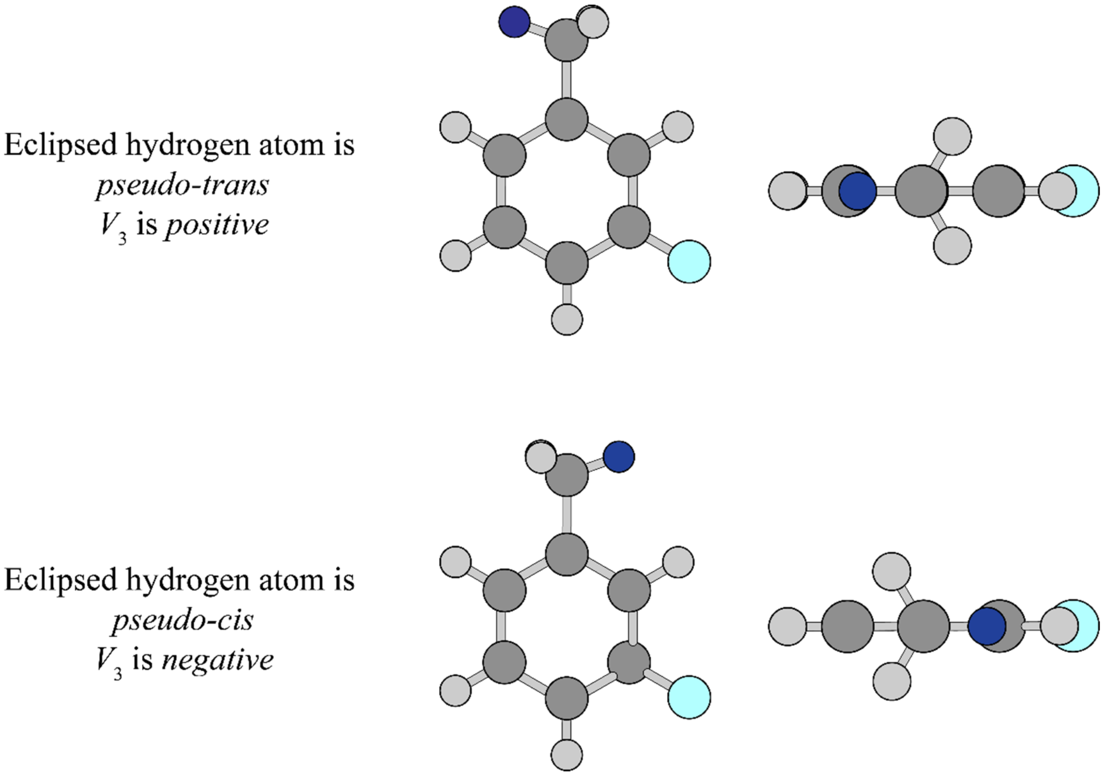

Figure 3.2. Schematic showing the conformations of the methyl rotor with respect to the *meta*-substituted fluorine atom in *m*FT, the correspondence between these and the sign of the V_3 parameter. The fluorine atom is sky-blue, carbon atoms are grey and hydrogen atoms are off-white. The methyl rotor hydrogen, eclipsed with respect to the parent ring, is coloured ultramarine for clarity.

Conversely, the sign of V_3 is taken as *negative* if the minimum energy conformation of the methyl rotor has an eclipsed geometry with respect to the ring, with the in-plane methyl hydrogen atom *pseudo-cis* to the *meta*-substituted fluorine atom[68,77]; this is also depicted in Figure 3.2. From this, one can expect a three-fold periodic V_3 potential, with a minimum each time a methyl rotor hydrogen becomes eclipsed *pseudo-cis* or *pseudo-trans* (depending on the sign of V_3) to the substituent in the *meta* position, every 120º of rotation[**].

One must emphasise that the *sign* of the V_3 term cannot be determined in the experiments conducted as part of this thesis, as the energies of the torsional levels are not directly affected by the sign of the potential, however it is possible to determine if there is a *change* in sign between electronic states with these experiments. [Notably, the sign of the V_3 term changes between the S_0 and S_1 state, and the cation (D_0^+) in *m*FT, leading to a breakdown of the $\Delta(v, m) = 0$ propensity that one expects when the torsional potentials are in-phase, see Sections 7-9 and Ref. 76 for further discussion.] Quantum chemical calculations, however, can assist in locating the global energy minimum of the potential energy surface and, from this, the sign of the V_3 term can be determined for the electronic state investigated. In spite of this, the *sign* of the V_6 term does affect the energy ordering of some of the terms, and its *magnitude* affects the spacings of the energy levels. This will be discussed in further detail below.

For a molecule with a leading V_6 term, such as NMP, the definitions of the sign of the V_6 term are different, although simpler. The V_6 term is *negative* if the methyl rotor is *staggered* with respect to the parent ring, and *positive* if the methyl rotor is *eclipsed* with respect to the parent ring. In these cases, one would expect the V_6 potential to be six-fold periodic over a 360º rotation of the methyl rotor, with a minimum every 60º of rotation (see the red trace of Figure 3.1).

[**] The *overall* torsional potential, in which we consider other V_n terms, may not have a minimum every 120º (as in Figure 3.1.) because this depends on how the V_3 potential is perturbed by the addition of higher-order V_n terms. See the blue trace of Figure 3.1 for the V_3 potential in isolation.

3.3. The splitting of the free-rotor torsional levels upon the application of a hindering potential

As noted above, if the internal rotation of the methyl rotor becomes hindered, one may expect this to affect the energies of the torsional levels. In the following, and the work presented in Sections 7-13, it is assumed that any vibrational-torsional coupling is small, meaning that the torsional quantum number, *m*, remains a ‘good’ quantum number to describe the torsions of the hindered rotor. The energy levels discussed can be simply viewed as perturbed versions of the initial free rotor levels and, therefore, the hindered rotor torsional levels retain the same *m*-label as in the free-rotor case, with a couple of differences detailed below.

The most obvious way to solve the hindered rotor problem is to apply perturbation theory to a Hamiltonian matrix, using the free rotor eigenfunctions as a basis [recall from Equation 3.6 the free rotor eigenfunctions take the form $\psi = \exp(im\phi)$]. Therefore, one can take the perturbing potential to the free rotor eigenfunctions as:

$$\int \mathrm{e}^{-im\phi} \left\{ \frac{V_n}{2} [1 - \cos(n\phi)] \right\} e^{im\phi} \, d\phi = -\frac{V_n}{4} \delta_{m,m' \pm n}$$

Equation 3.8

Where $\delta_{m,m'\pm n}$ is the Kronecker delta and is one when m and $m' \pm n$ are the same and zero when they are different. Considering each V_n term (for which we use V_3 and V_6 for *m*FT and V_6 only for NMP) independently, we can determine the non-zero Hamiltonian matrix elements as:

$$H_{m,m'} = \frac{V_n}{2} \delta_{m,m'} - \frac{V_n}{4} \delta_{m,m' \pm n}$$

Equation 3.9

Following through for the V_3 and V_6 terms only, the non-zero matrix elements become:

$$H_{m,m'} = \left(m^2F + \frac{V_3 + V_6}{2}\right)\delta_{m,m'} - \frac{V_3}{4}\delta_{m,m'\pm 3} - \frac{V_6}{4}\delta_{m,m'\pm 6}$$

Equation 3.10

Where m^2F are the unperturbed free rotor eigenvalues (Equation 3.5), the $\left(\frac{V_3+V_6}{2}\right)$ term serves as the perturbation to all of the free rotor eigenstates and the $\frac{V_n}{4}$ terms serve as cross-coupling terms, which couple together states dependent on the V_n term under consideration. This is to say that the $\frac{V_3}{4}$ term couples together torsional levels whose m quantum number differs by three and the $\frac{V_6}{4}$ term couples those levels where the m quantum number differs by six. These two terms form the non-zero off-diagonal terms, and the first term in Equation 3.10 is the diagonal term of such a Hamiltonian matrix. If this matrix is then diagonalised, the hindered rotor energy levels are obtained as the corresponding eigenvalues. Using this method to calculate the hindered rotor torsional levels, one should use a basis set of free rotor functions significantly larger than the number of hindered rotor levels required, to allow for reasonable convergence to the hindered rotor eigenfunctions.

There are numerous texts[122,147,152–155] that discuss these effects in detail and the reader is urged to refer to these for a more comprehensive picture of the mathematical background.

In Equation 3.10, one can see that only m-levels corresponding to $m = \pm 3n$ (where $n = 0, 1, 2, \ldots$) can couple. As a result of this coupling, the $m = \pm 3n$ levels split from degeneracy, with each component of the level becoming a symmetric and antisymmetric linear combination of the $m = +3n$ and $-3n$ components which, throughout this thesis, are denoted as the $m = 3n(+)$ and $3n(-)$ levels [*e.g.* 3(+), 6(-), *etc.*]. The strength of the coupling, and therefore how far removed from degeneracy the $m = 3n(+/-)$ levels are, depends on n and also the torsional barrier height; the splitting of the degenerate levels decreases as n increases *i.e.*, the $m = 3(+)$ and 3(-) levels are split more than the $m = 6(+)$ and 6(-) levels. As the $m \neq \pm 3n$ are uncoupled due to the three-fold symmetry of the methyl rotor, they remain degenerate as $m = \pm 1, \pm 2, \pm 4, \pm 5, \ldots$ However, as these degenerate levels are signed, one may still observe interactions between *m* = -1, say, and *m* = +2, *etc.*, as these levels are separated by Δ*m* = 3. Despite this, these interactions do not split these levels as the degeneracy of these levels means there is an equal interaction between *m* = +1 and *m* = -2, in the opposite direction, thus the perturbation is cancelled out.

One should note that *m*FT is a particularly interesting system from the point of view of torsional potentials and the induced splitting of the non-degenerate torsional levels. In *m*FT, the approximate values of V_3 and V_6 are known from previous work[68,69,71,72,75], although, owing to vibration-torsion interactions, their exact value is still debated. In S_0, the V_3 barrier is markedly low – it is only ~20 cm^{-1}. Therefore, the majority of the torsional levels are above the potential barrier, and as such, these levels essentially behave as free rotor levels. In contrast, the V_3 barrier in the D_0^+ state is approximately -300 cm^{-1}, with most of the torsional levels observed in the ZEKE spectra[71,72,76] below the torsional potential. The S_1 state has V_3 ~ 115 cm^{-1} and its magnitude is thus intermediate to the S_0 and D_0^+ cases. Hence, these three electronic states evolve from the methyl rotor being essentially freely rotating in S_0, through a moderately hindered internal rotation in S_1 to a highly hindered internal rotation in the ground state cation. Furthermore, the change in sign of the V_3 term between S_0/S_1 and D_0^+ gives rise to different structure being observed in the ZEKE spectra, which may make assignments of the torsional levels (and indeed vibrational levels where they appear as a progression of vibration-torsion combinations) easier, owing to a distinctive pattern of intensities of torsional (and vibtor) transitions.

In Figure 3.3, the variation of the energies of the *m*-levels are shown as a function of V_6. This scenario is akin to that of a G_{12} molecule, such as NMP, where there is no V_3 term. As such, the symmetries of the *m*-levels are given using the G_{12} symmetry labels with the C_{2v} equivalent in parentheses (where appropriate). Although, at this stage, the symmetry of the *m*-level is not strictly relevant for the discussion in this section (although one should appreciate the degenerate *m*-levels have *e* symmetry and the non-degenerate *m* = 3*n* levels do not), and molecular symmetry groups shall be discussed later in this section.

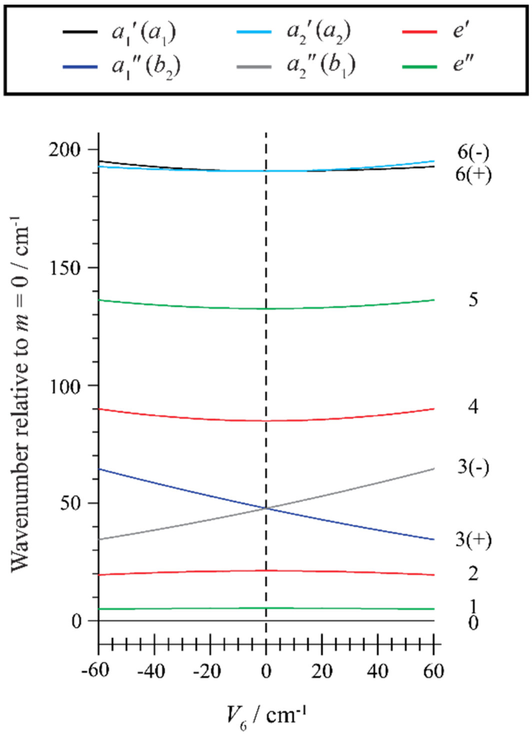

Figure 3.3. Variations in the energy levels as a function of the V_6 parameter. The energies strictly relate to *N*-methylpyrrole, although the qualitative picture holds for any G_{12} symmetry molecule. Symmetries of the torsional energy levels are given based on the colours of the lines, using the G_{12} symmetry labels in the legend (the G_{12} MSG is isomorphic to that of D_{3h}), with the corresponding C_{2v} symmetry label (if applicable) in parentheses. It should be noted that V_6 is positive for the eclipsed conformation of the methyl rotor with respect to the parent ring and $F = 5.3$ cm^{-1}. See Figure 4 of Section 10.

Starting with $V_6 = 0$ cm^{-1}, the $m = 3n$ levels are degenerate although any deviation from $V_6 = 0$ cm^{-1} leads to the splitting of these levels. It is the sign of the V_6 parameter that determines which of the $m = 3n(+)$ or $3n(-)$ levels is perturbed to higher energy. In the case of a positive V_6 (eclipsed methyl rotor), the $m = 3n(-)$ is the higher energy of the non-degenerate pair and, conversely, has the lower energy of the pair in the case of a negative V_6 (staggered methyl rotor). Additionally, it is the magnitude of V_6 that determines the degree of splitting between these levels.

As one increases the magnitude of V_6 to infinity, these $m = 3n$ levels will converge towards an ‘adjacent’ doubly degenerate level of e' or e'' symmetry, leading towards sets of triply degenerate levels. For example, in Figure 3.3, one can see that $m = 3(+)$ approaches $m = 2$, and $m = 3(-)$ approaches $m = 4$, as $V_6 \rightarrow +\infty$. The arguments are reversed if $V_6 \rightarrow -\infty$.

As a result of the torsional levels splitting in this manner, one can establish the *relative* geometries of the methyl rotor, with respect to the aromatic ring, by elucidating the ordering of the m = 3(+) and m = 3(-) transitions in experimental spectra. However, one requires more information to determine their definitive ordering if the only information one has is a single spectrum. For example, it is possible to make deductions based on intensities and by invoking symmetry arguments[75,156] as the torsional levels have different symmetries (see Figure 3.3), and one may expect to observe transitions to different torsional levels in different electronic states. Despite this, one has to take care with intensities as these can be dependent on the conditions in the free-jet expansion at the time of scanning, and also the dye/grating in that energy region if using a dye laser; furthermore, in the ZEKE spectra, it is common to see some transitions to symmetry-forbidden levels (see Ref. 76). A more convenient and definitive method is to use quantum chemical calculations to deduce the minimum energy conformation of the methyl rotor in the state of interest.

Perhaps more importantly, for a molecule in the G_{12} MSG, the splitting of the m = 3(+) and m = 3(-) levels can allow the determination of the magnitude of the V_6 parameter as this directly controls the splitting of the non-degenerate m = 3n levels. Earlier, the matrix formalisation of the particle on a ring in a basis set of free rotor eigenfunctions was discussed as this yields the hindered rotor eigenvalues. From Equation 3.10, one can see that, for any terms separated by m = 6 [*e.g.*, m = 3(+) and m = 3(-)], are directly coupled by the $\frac{V_6}{4}$ term, meaning that the m = 3(+) and m = 3(-) levels move away from their zero-order position (*i.e.*, when they are degenerate) by $\frac{V_6}{4}$ in opposing directions, such that the overall splitting between the m = 3(+) and m = 3(-) levels is $\frac{V_6}{2}$. Hence, one can determine V_6 as twice the splitting of these levels. However, one should be aware that this can only be considered an *effective* V_6 parameter value if deduced experimentally in this way: in reality, owing to vibration-torsion and rotation-torsion coupling, the splitting of the m-levels in question may couple to other vibtor levels or rotational levels, perturbing them from their hindered-rotor energetic locations. Furthermore, the assumption that higher-order V_n terms do not indirectly couple these torsional levels is not entirely true and will also have some effect, although the influence of higher-order V_n terms does diminish rapidly with increasing n.

However, in a molecule with lower symmetry, such as *m*FT which belongs to the G_6 MSG, the V_3 parameter value is not zero, so this must also be considered if one wishes to understand how the torsional levels behave when influenced by a hindering potential. In comparison with the G_{12} case, the V_3 barrier is generally much larger than the V_6 barrier, and this leads to a more rapid convergence of one of the $m = 3n$ to a pair of $m \neq 3n$ levels; despite this, the behaviour of the convergence is similar to that of purely varying V_6. Similarly to Figure 3.3, if one fixes $V_6 = 0$ and varies the V_3 parameter, the scenario depicted in Figure 3.4 is observed.

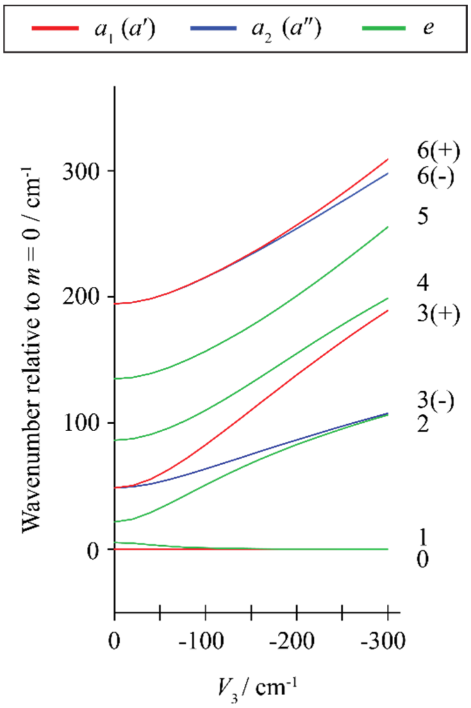

Figure 3.4. Diagram showing how the energies of the torsional levels vary as a function of V_3 for a molecule belonging to the G_6 MSG, such as *m*FT. Here, the V_3 parameter is varied in the negative direction, owing to the conformation of the methyl rotor in D_0^+ *m*FT, which has a large, negative value of V_3 of ~-300 cm^{-1}. Despite this, the variation of the torsional levels, when treated in this manner, will be symmetric about $V_3 = 0$ cm^{-1}. One can see that, in comparison to Figure 3.3, varying the V_3 parameter value in isolation (*i.e.*, fixing V_6 at 0 cm^{-1}) causes the *m*-levels to converge far more rapidly than by varying V_6 alone. This figure is adapted from panel (a) of Figure 1 in Ref. 76.

In this case, the m = 3(+) and m = 3(-) levels are still directly coupled by the V_6 parameter, but now they are also coupled indirectly *via* the V_3 parameter *via* $m = 0$.

This means that, in the case of a system where there is a V_3 term in the torsional potential, it is difficult to directly deduce the magnitude of V_6 as one did in the G_{12} case, because both the V_3 and V_6 terms serve to couple the non-degenerate torsional levels, noting that V_3 is simply the height of the torsional potential barrier. As a result of this, the easiest way to estimate the V_3 and V_6 terms from experimental data is to extract the wavenumbers of numerous torsional levels (as many as one can observe) and vary the V_n parameters heuristically in a model until one can reproduce the torsional energies and the correct splitting, while being aware of the fact that any vibtor interaction will also perturb the *m*-levels, yielding effective V_3 and V_6 parameter values.

3.4. Molecular symmetry groups

Point groups are a very convenient way to describe the ring localised vibrations of species such as NMP and *m*FT, and this is generally a good approximation if one considers the methyl rotor as a point-mass whose electronic structure does not notably impact the forms of these vibrations. Indeed, this is largely a satisfactory approximation; however, the work presented in this thesis demonstrates that this is not always true, and, in some circumstances, one must consider the ring-localised vibrations, the torsional motion, and any interactions these two sets of motions may have. As such, when discussing the torsional modes and vibtor modes, the point group approximation breaks down, largely because one must describe the interchange of the hydrogen atoms of the methyl rotor, as well as the ring.

If we consider the methyl rotor explicitly, we have three equivalent hydrogen atoms, rotating about the bond connecting them to the pyrrolyl (NMP) or fluorobenzyl (*m*FT) ring. In order to describe the motions of the torsions correctly, as well as the symmetries of these motions, one has to use the so-called permutation-inversion molecular symmetry groups, or MSGs. As the name suggests, this treatment of the molecule considers all feasible permutations of the positions of identical nuclei (such as the hydrogens in the methyl rotor) as well as all feasible permutation-inversions, which are essentially an operation in which a permutation (as before) is performed, followed by an inversion through the centre of mass. Longuet-Higgins asks in his original paper[149], how one should classify the symmetry of a molecule when there is a transformation that alters the molecular symmetry either on such a short timescale it should be noticeable in a laboratory experiment or if there a very small barrier to such a transformation that it can occur readily? This latter point is the principle that underpins the use of the MSGs to describe the torsional motions of both *m*FT and NMP.

The explicit treatment of non-rigid molecules in this way was first considered by Longuet-Higgins[149] and expanded upon later by Bunker and Jensen[124]. Furthermore, the theses of Tuttle[151] and Kemp[157] provide a more detailed description of the intricacies of these permutation-inversion groups (in a more accessible way than in Refs. 124 and 149), therefore, only an outline of the G_6 and G_{12} molecular symmetry groups – as these are pertinent to *m*FT and NMP, respectively - shall be given here.

The next subsections will commence with a brief description and explanation of the G_6 MSG, building up towards the G_{12} MSG. The operations in the G_{12} MSG are encompassed within the G_6 MSG, so beginning with the G_6 MSG provides a good foundation, upon which complexity can be added later.

3.4.1. The G_6 molecular symmetry group

The character table of the G_6 MSG is shown in Table 3.1. From this, we can see that there are three symmetry operations required to describe this class: E, (123) and (23)*, which shall be discussed in turn. Furthermore, the symmetry operations above, and in Table 3.1 are shown in context of *m*FT in Figure 3.5.

Table 3.1. Character table for the G_6 MSG. T represent translations, and J represents rotations around the principal inertial axes, a, b and c, see Figure 3.5.

G_6	E	(123)	(23)*	
A_1	1	1	1	T_a, T_b, J_c
A_2	1	1	-1	T_c, J_a, J_b
E	2	-1	0	

- E – This is identical to the corresponding symmetry operation with the same name in point group symmetry. It is the ‘identity’: it represents doing nothing.

- (123) – This simply relates to the interchange of the hydrogen atoms of the methyl rotor. If one labels the rotor hydrogen atoms as in Figure 3.5, (123) is simply replacing hydrogen 1 with hydrogen 2, 2 with 3, and 3 with 1. This is essentially a clockwise cyclic permutation of the nuclei.
- (23)* - This is essentially a swapping of hydrogens 2 and 3 (as labelled in Figure 3.5) followed by an inversion, which is denoted by the asterisk, ‘*’, through the *centre of mass*; the positions of all particles are inverted.

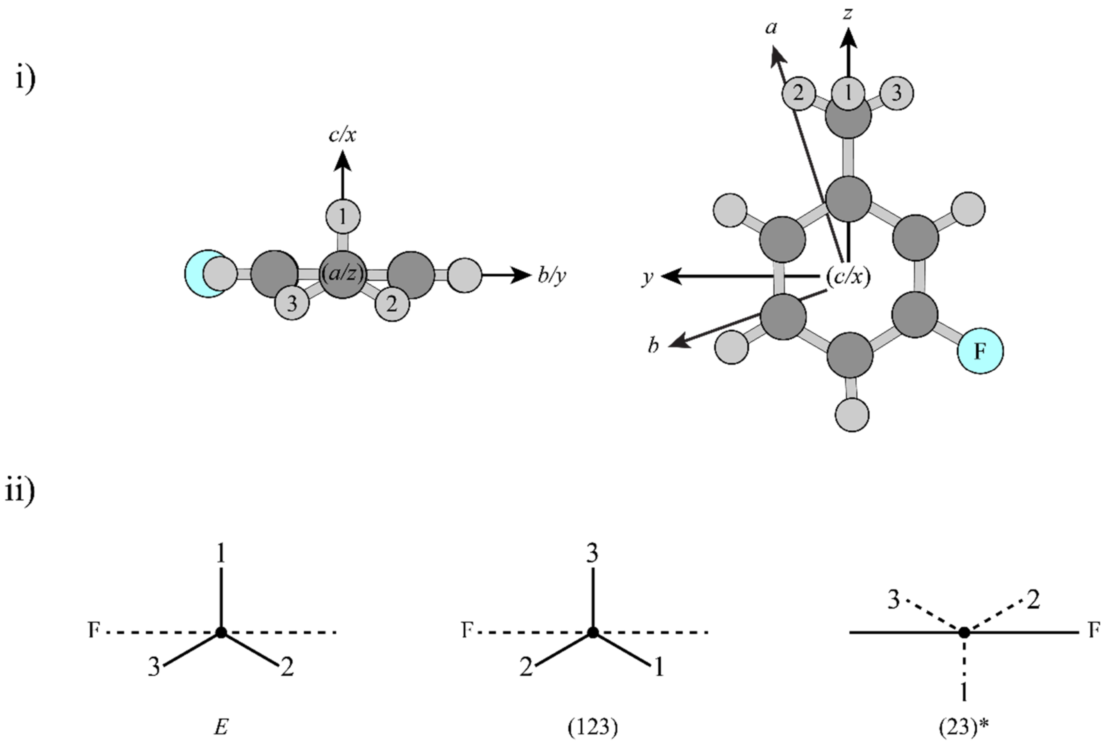

Figure 3.5. Schematics of *m*FT undergoing the symmetry transformations that make up the G_6 MSG, as well as showing the principal inertial axes (*a*, *b* and *c*) and the corresponding Cartesian axes (*x*, *y* and *z*). Axes in parentheses represent the axis protruding into or out of the plane of the paper. Hydrogen atoms are numbered consistently throughout. **Part i)** view of *m*FT looking along the methyl rotor (axis *z*) and a view of *m*FT looking from above the fluorobenzene ring (axis *c*/*x*). A sky-blue atom represents fluorine, grey represents carbon and off-white represents hydrogen. **Part ii)** Newman projection-like schematics of *m*FT undergoing symmetry operations *E*, (123) and (23)*. A solid line represents the foreground and a dashed line represents the background with a single line depicting the plane of the fluorobenzyl ring. The black circle represents the carbon atom of the methyl rotor.

It can be seen that these permutations will all leave the molecule appearing unchanged, with the exception of a rotation, without distortion, back to the original coordinates. Furthermore, it does not matter in which order the permutations and inversions are made. For example, with the operation (23)*, it does not matter whether one replaces the nuclear coordinates of hydrogens 2 and 3 first followed by the inversion, or whether one inverts all atoms through the centre of mass first followed by the interchanging of the positions of hydrogens 2 and 3.

Finally, it is useful to note that the G_6 MSG is isomorphic to the C_{3v} point group, such that the character tables and irreducible representations (but not the translational and rotational operations) are identical. As such, one can use a C_{3v} character table and direct product table to calculate the symmetries of vibrations and vibtor modes for the G_6 MSG.

3.4.2. The G_{12} molecular symmetry group

Having considered the G_6 MSG, the additional symmetry operations present in the G_{12} MSG can be considered. For example, in NMP, the ring also brings two-fold rotational symmetry about the axis passing through N-CH_3 bond in addition to the three-fold rotational symmetry from the methyl rotor.

The G_{12} character table is given in Table 3.2. Notably, three more symmetry operations are added: (ab)(cd), (123)(ab)(cd), and (23)(ab)(cd)*. The rest of the symmetry operations are identical to those in the G_6 MSG and permute the atoms in the same way. Figure 3.6 illustrates the G_{12} MSG operations and their impact on NMP. Here, the hydrogens of the pyrrolyl ring are labelled a, b, c and d to distinguish them from those of the methyl rotor, although in many texts, they are labelled sequentially (*i.e.*, 4, 5, 6 and 7).

Table 3.2. Character table for the G_{12} MSG. T represents translations and J represents rotations around the principal inertial axes, *a*, *b* and *c*; see Figure 3.6.

G_{12}	E	(123)	(23)*	(ab)(cd)	(123)(ab)(cd)	(23)(ab)(cd)*	
A_1'	1	1	1	1	1	1	T_a
A_1''	1	1	1	-1	-1	-1	T_b, J_c
A_2'	1	1	-1	1	1	-1	J_a
A_2''	1	1	-1	-1	-1	1	T_c, J_b
E'	2	-1	0	2	-1	0	
E''	2	-1	0	-2	1	0	

As can be seen from Figure 3.6:

- (ab)(cd) – This operation represents the interchange of the pyrrolyl ring hydrogens a with b, c with d.
- (123)(ab)(cd) – This is a combination of the operations (123) and (ab)(cd). The nuclear coordinates of the hydrogen atoms in the methyl rotor are cyclically permuted, and the hydrogen atoms either side of the parent pyrrolyl ring are exchanged, noting again that the order of operations is not important.
- (23)(ab)(cd)* - This is a combination of the (ab)(cd) and (23)* symmetry operations. The rotor hydrogens 2 and 3 are interchanged, the hydrogens on either side of the pyrrolyl ring are interchanged, and an inversion through the centre of mass is performed.

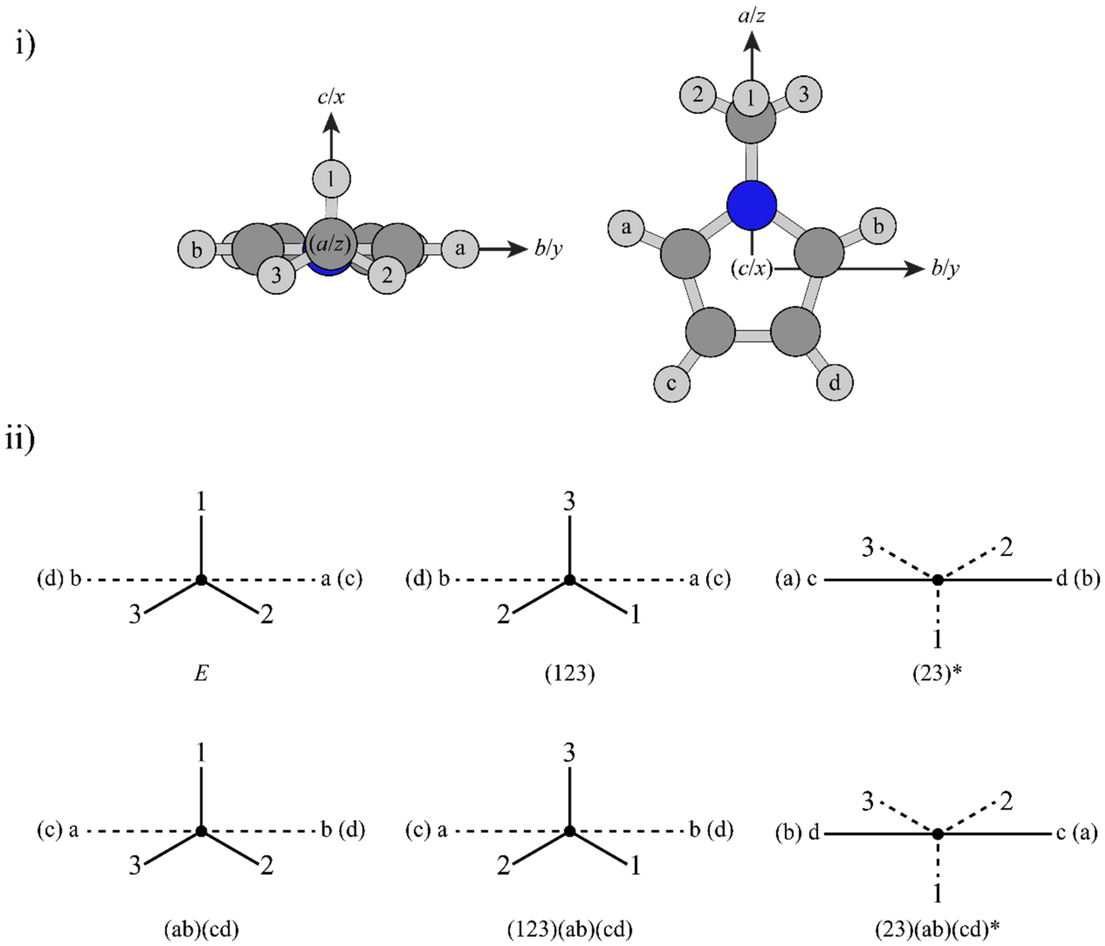

Figure 3.6. Schematics of NMP undergoing the symmetry transformations that make up the G_{12} MSG, as well as showing the principal inertial and Cartesian axes. Axes in parentheses represent the axis protruding into or out of the plane. Hydrogen atoms are numbered consistently throughout (hydrogen atom labellings a, b and c should not be confused with the principal axes which are labelled in italics: *a*, *b* and *c*). The pyrrolyl ring is located in the *yz*-plane, which is important in the discussion below. **Part i)** view of NMP looking along the methyl rotor (axis *a*) and a view of NMP looking from above the pyrrolyl ring (axis *c*). Royal blue represents nitrogen, grey represents carbon and off-white represents hydrogen. **Part ii)** (clockwise from top left) Newman projection-like schematics of NMP undergoing symmetry operations *E*, (123), (23)*, (23)(ab)(cd)*, (123)(ab)(cd) and (ab)(cd). A solid line represents the foreground and a dashed line represents the background, with a single line representing the plane of the pyrrolyl ring. The hydrogen atom labels in parentheses represent the hydrogen atoms are located behind those outside of the parentheses. A black circle represents the carbon atom of the methyl rotor.

Similarly to the G_6 MSG, it is useful to note that the G_{12} MSG is isomorphic with the D_{3h} point group, such that the irreducible representations are identical, although the translational and rotational operations are not the same.

3.4.3. The symmetries of vibrational and vibrational-torsional levels using MSGs

It is often convenient to continue to use the approximate point group symmetry of these molecules for the discussion of both electronic states and vibrations. However, as discussed in the previous two sub-sections, when one considers the internal rotations of the methyl group, one must consider the symmetries within the MSGs.

Generally, this is not a problem, yet it is something of which the reader should be aware. In the discussion of vibtor levels, one simply takes the MSG symmetry label of the vibration and combines it with the MSG symmetry of the torsion, and then uses the corresponding direct product table of the MSG (or that of an isomorphic point group) to yield the overall symmetry of the vibtor. In Table 3.3, the correspondence between the C_s and G_6 symmetry labels of *m*FT is given, alongside the symmetries of the vibrations and torsions. Table 3.4 is similar to this but shows correspondence between the C_{2v} and G_{12} symmetry labels of NMP.

Table 3.3. Correspondence between the C_s and G_6 symmetry classes and the symmetries of vibrations and the pure torsional levels considered in this work.

C_s	G_6[a]	^mD_i[b]	*m*
a'	a_1	D_1 - D_{21}	0, 3(+), 6(+), 9(+), …
a''	a_2	D_{22} - D_{30}	3(-), 6(-), 9(-), …
	e		1, 2, 4, 5, 7, …

[a] There are no corresponding C_s irreducible representations, or indeed any vibrations, with *e* symmetry. This is purely a requirement for the consideration of the torsional and vibrational-torsional levels.

[b] The ^mD_i labels for the vibrations are discussed in Ref. 158 as well as, briefly, in Section 4. See also Appendices 1 and 3.

Table 3.4. Correspondence between the C_{2v} point group and the G_{12} MSG, alongside the symmetries of the P_i vibrations and pure torsional levels considered in this work.

C_{2v}	G_{12}[a]	P_i[b]	m
a_1	a_1'	$P_1 – P_9$	0, 6(+)
a_2	a_2'	$P_{10} – P_{12}$	6(-)
b_1[c]	a_2''	$P_{13} – P_{16}$	3(-)
b_2[c]	a_1''	$P_{17} – P_{24}$	3(+)
	e'		2, 4
	e''		1, 5

[a] There are no corresponding C_{2v} irreducible representations, or vibrations, associated with e' and e'' symmetry in the G_{12} scheme.

[b] The P_i labels are discussed briefly in Section 4 and in detail in Section 11. See also Appendices 1 and 3.

[c] The b_1 and b_2 labels (and by extension a_2'' and a_1'') swap over dependent on whether one locates the plane of the molecule in either the *yz*-plane or the *xz*-plane. For clarity, it should be noted that the pyrrolyl ring is *always* located in the *yz*-plane in this thesis. This means that there are four out-of-plane, ring-localised b_1 vibrations, and there are eight in-plane b_2 vibrations. A similar argument holds for the torsional levels in the G_{12} MSG. It is easy to confuse axis systems, so the reader should exercise caution when consulting the literature on NMP, as some authors have switched axis systems unintentionally!

As an example, if one wants to know the overall symmetry of the vibtor level in *m*FT comprising one quantum of the D_{21} vibration in combination with $m = 2$, one should take the symmetry of D_{21} in the G_6 symmetry class, which is a_1, and the symmetry of $m = 2$, which is e. Consulting the direct product table for the G_6 MSG, it is possible to determine the overall symmetry of this vibtor level as e. Another example, this time for NMP: the symmetry of a vibtor level, comprising P_{16} in combination with m = 3(+) is a_2'. This arises from the symmetry of P_{16}, which is of b_1 symmetry under the C_{2v} scheme and corresponds to a_2'' in the G_{12} MSG, and combines it with the symmetry of the torsion m = 3(+), which is a_1''. Therefore, by taking the direct product of these irreducible representations, the overall symmetry of the vibtor level is a_2'. One can further extend the MSG treatment to electronic states as well, to arrive at the overall symmetry for a vibrationally and torsionally excited electronic state. In *m*FT, the first electronic excited state has A' symmetry if one treats it using the C_s point group but this becomes A_1 if one treats the methyl rotor explicitly, using the G_6 MSG. Similarly, the S_1 state of NMP has A_2 symmetry under the C_{2v} scheme, but is A_2' if one treats the molecule with the G_{12} MSG.

4. Labelling schemes and notations

This section lays out the background to the methodology used, and the rationale behind the labelling schemes used to describe both the torsions and vibrations in this thesis. Clearly, the comparison of the ring-localised vibrations between molecules of different forms, such as between *m*FT and NMP, is not generally feasible owing to the change in the number of atoms, the inclusion of heteroatoms and the differences in locations of the centre of masses; all of which change the forms of the vibrations significantly. However, molecules in a given group, such as the *meta*-disubstituted benzenes, *m*FT, *m*DFB and *m*ClT, may be considered together and compared.

4.1. Vibrational labelling

Putting aside the torsions for now, as these will be considered separately, consistent labelling schemes have been derived for *meta*-disubstituted benzenes and *N*-substituted pyrroles, to overcome the weaknesses of the schemes most commonly used in spectroscopy today. These fall into two distinct types, and both are discussed in turn.

4.1.1. The Wilson/Varsányi labelling scheme

The Wilson[139,159]/Varsányi[160,161] labels are based on the vibrations of benzene. Here, the vibrations of benzene are compared to forms of the substituted benzene molecule under study. The main issue with such a scheme is that the addition of any substituent, particularly if there are multiple heavy-atom or asymmetric substituents, can radically alter the form of the ring-localised vibrations. This is proposed to be driven by two major mechanisms:

a. Firstly, mass effects from the substituent can affect the form of the vibration as, during the vibration of a normal mode, the centre of mass must stay the same. If the centre of mass shifts from the centre of the ring owing to the substitution, some amplitudes of atomic motion may either be exaggerated or suppressed, dependent on the position of the centre of mass relative to the substituent(s).

b. Secondly, electronic effects. Adding any substituent to benzene (or pyrrole) that is not hydrogen will have some form of electronic effect on the ring, whether that is strongly or weakly electron-withdrawing or electron-donating. Such effects can alter the force constants of the bonds in the ring, leading to differences in the forms of vibrations as the amplitudes of the atomic motions will change.

This can lead to some ambiguities in determining which vibration is 'the same' between benzene and the substituted species. Varsányi[160], in his scheme, attempted to ameliorate this by using chemical insight and analysing multiple spectra, to determine certain, approximate, energy regions in which certain vibrations may exist. He also used symmetry arguments to bring consistency into what motions constitute a given vibration. However, there are still weaknesses with this scheme, mainly arising from Varsányi splitting molecules into groups (somewhat arbitrarily) based on those with 'light' and 'heavy' substituents. This means that two differently substituted species (such as fluorobenzene and bromobenzene), despite having similar vibrational modes, may have different labels and this will make it more difficult to compare the vibrational modes between these molecules.

4.1.2. The Mulliken/Herzberg labelling scheme

The Mulliken[162]/Herzberg[123] scheme is scheme is relatively simple and takes the vibrational modes of a molecule, separates them by symmetry (for a C_{2v} molecule: a_1, a_2, b_1, b_2; for a C_s molecule: a', a''), orders them in descending energy for each symmetry group and finally assigns a number for the vibration from 1 through x, where 'x' is the total number of vibrations for that molecule (*i.e.*, 30 modes for benzene and 24 for pyrrole). This relies on the ordering of the symmetry classes in the labelling scheme being agreed or established beforehand.

The major weaknesses of this scheme are that, if the substituent is more complex than a single atom, extra vibrational modes are added, and also the symmetry of the molecule may change. As the vibrations are ordered in terms of symmetry and then energy, any additional vibrations from substituents will lead to the 'same' vibration in a different molecule (perhaps the ring-puckering mode of *p*DFB and *p*FT) having a different label. Furthermore, if the symmetry is lowered, the vibrations will have to be re-assigned, for example, in *m*DFB, if a fluorine substituent is changed to make *meta*-chlorofluorobenzene (*m*ClFB), the symmetry will be lowered from C_{2v} to C_s, and therefore a_1 and b_2 modes become a' and a_2 and b_1 modes become a''. (Although, what is labelled b_1 and b_2 will change dependent on the axis system used for C_{2v} molecules which complicates things further.) Therefore, all vibrations under the C_{2v} scheme will have their label changed, despite being the 'same' vibration as before, making the comparisons of the vibrations between similar molecules less than straightforward.

4.1.3. The $^{m}D_i$ and P_i labelling schemes

As both of the aforementioned schemes lead to difficulties in comparing between differently substituted species, even of the same isomeric class, this research group has derived a new set of vibrational labels, acknowledging the weaknesses of both schemes and improving upon them. This leads to a scheme where the ring-localised vibrations of molecules of the same isomeric class may be compared, as vibrations of the same symmetry and form will have the same label, regardless of how far-removed they are in energy from those vibrations in the reference molecule.

These labelling schemes are based of the vibrations of the corresponding fluorinated isomer [the vibrational modes of *m*DFB and *N*-fluoropyrrole (NFP) are presented in Appendix 1], rather than unsubstituted benzene as in the Wilson/Varsányi scheme. The fluorine substituent was selected as it is *generally* the lightest, stable single-atom substituent (excluding deuterium; for reasons which become apparent in Section 11). The vibrations are then separated by symmetry and ordered in terms of energy and designated a new label (either $^{m}D_{\mathrm{i}}$, for *meta*-disubstituted benzenes, or P_i, for *N*-substituted pyrroles, where '*i*' is an index for the vibration). The vibrations of the substituent are also considered separately, and in the case of a methyl rotor, are similarly assigned and given a Me_i label, where '*i*' is the index number for each of the methyl-localised vibrations.

In terms of mass effects, it is found that the forms of the vibrations have largely settled down by a substituent mass of ~14 m_u, which is around the lower-bound of mass of the vast majority of realistic substituents. The labels indicate the motions of the vibrations so, unlike in the Mulliken/Herzberg scheme, one vibration will have the same label for multiple molecules in the same isomeric class, even if that molecule has a different symmetry or its substituent has more/fewer atoms. Furthermore, if applicable, these labels are based on the point group of an asymmetrically substituted species (in the case of disubstituted molecules[158,163,164]) and so the labels can be modified to be consistent between molecules with higher symmetry, such as symmetrically substituted species, in contrast to the Wilson/Varsányi labels which started with a reference molecule with higher symmetry than the substituted molecules in question.

One must also note that, while these schemes are believed to be rigorous for most purposes, it is appreciated that there may be significant mixing of the vibrations between electronic states arising from the Duschinsky effect (Section 2.7). Therefore, it can be difficult to assign the vibrations of an excited electronic state of a molecule in terms of the vibrations of the ground state reference molecule. Hence, drawing comparisons between molecules becomes more difficult (see Sections 7 and 11). However, these cases appear to be few and far between and, nonetheless, the reliability and usability of these labelling schemes are maintained over the Wilson/Varsányi or Mulliken/Herzberg schemes, as labelling in this manner will always be more consistent between similar molecules.

The ${}^{m}D_i$ and P_i labels, their symmetries and calculated harmonic vibrational wavenumbers for neutral ground state *m*DFB and *m*FT for the ${}^{m}D_i$ labels, and NFP and NMP for the P_i labels, are presented in Appendix 3 and the forms of NFP and *m*DFB are presented in Appendix 1.

4.2. The labelling of vibrational, vibtor and torsional transitions

As has become common usage, the vibrational, torsional and vibtor levels will be denoted using the notation of a transition, with the specific level given by the quantum numbers associated with it. For *m*FT, the vibration will be given as the index, *i*, of the ${}^{m}D_i$ labels and for NMP, the vibration shall be given as the index, *i*, of the P_i labels. A torsion will be denoted using its *m* quantum number. Vibtor levels will be described as a combination of both vibrational and torsional transitions

In the case of the REMPI and LIF experiments, the number of quanta excited will be indicated by a superscript following the vibration index, *i*, of the vibration excited. Levels in the cation, as determined through ZEKE spectroscopy, shall be denoted in the same way, although with a preceding, superscripted '+' symbol, which is on occasion (in figures) omitted for clarity. In the DF and 2D-LIF experiments, the levels of the ground state are accessed by emissions from an electronically excited state and the number of quanta of the *emitted* radiation shall be given by a subscript following the index number of the vibration. Additionally, for combination bands, it is conventional to give the indices of the vibrations, and their respective quantum numbers, in increasing order of the index of the vibration.

For example, an excitation of two quanta of the D_{30} vibration in *m*FT and one quantum of m = 3(+) will be given as $30^2m^{3(+)}$ and an emission to the pure torsion, m = 4, in the ground state will be denoted m_4. An excitation of a single quantum of the P_{16} vibration and a single quantum of the P_{15} vibration of cationic NMP will be denoted as ${}^{+}15^{1}16^{1}$. In the REMPI and ZEKE spectra of NMP, we cannot resolve the m = 0 and m = 1 levels separately, and so both are excited simultaneously, unlike in *m*FT where it is possible to distinguish between the m = 0 and m = 1 levels in S_1 and D_0^+. As such, we use ${}^{(+)}m^{0,1}$ or $m_{0,1}$ to indicate the band contains contributions from both the m = 0 and m = 1 levels.

This notation strictly requires a definition of the starting level, rather than just the final level as discussed above. However, this is omitted for clarity as the initial level should be obvious from either the jet-cooled conditions (m = 0 and m = 1 are not interconvertible for symmetry reasons) or the pumped level in the DF, 2D-LIF or ZEKE experiments. We do observe some residual population in the m = 2 level in the free-jet expansion, and torsional hot bands are one case in which it is necessary to specify both an initial and a final level. In such cases, these shall be denoted as m_a^b

where ‘*a*’ is the initial state torsional quantum number and ‘*b*’ is the torsional quantum number for the final state. For example, a hot band in the REMPI spectrum from S_0 $m = 2$ to S_1 $m = 2$ will be denoted as m_2^2. Indeed, no residual population in excited vibrational levels is observed in the molecular beam – cooling to the zero-point vibrational level is achieved.

Finally, in the 2D-LIF experiments, it is often necessary to describe a band using a pair of levels: an excitation and emission. These assignments are represented in the form (*a*, *b*), in parentheses, where ‘*a*’ is the excited level and ‘*b*’ is the emitted level. For example, if one were to probe the $17^1m^{3(+)}$ level in *m*FT and observe the diagonal, $\Delta v = 0$, emission, one would express the observed band as ($17^1m^{3(+)}$, $17_1m_{3(+)}$).

5. Experimental methods

For the work presented as part of this thesis, multiple experimental methods are employed: resonance-enhanced multiphoton ionisation (REMPI), zero-electron-kinetic-energy (ZEKE), laser-induced fluorescence (LIF), dispersed fluorescence (DF) and two-dimensional laser-induced fluorescence (2D-LIF) spectroscopies. These are undertaken on two apparatuses, with the REMPI and ZEKE experiments being performed on one apparatus and the LIF/DF/2D-LIF experiments being performed on another. In the following subsections, the individual spectroscopic techniques will be discussed, with a brief commentary on their capabilities and drawbacks, followed by a more detailed description of each of the apparatuses, and finally their individual configurations for the different molecules studied.

5.1. Supersonic jet expansions

If one considers a room-temperature molecular sample, there will be significant excited rotational state populations. It is less likely for there to be significant population in higher vibrational states as a result of the greater energy spacings for vibrational levels than for rotational levels, although one may expect to observe some vibrationally excited molecules (especially with low-frequency vibrational modes). Therefore, if one conducts a spectroscopic experiment on a sample at room temperature, it is possible to excite from several rotational and vibrational levels that are not the lowest in energy. This has the impact of complicating the spectra by introducing vibrational hot bands as well as there being a wide rotational envelope leading to the broadening of the bands, which may lead to significant band overlap. This makes it more difficult to assign spectra as it is not only harder to identify individual bands, but also more difficult to identify which are hot bands or those that originate from the zero-point vibrational level. Therefore, it would be desirable to cool a molecule down to its lowest vibrational and rotational levels to achieve the narrowest bands as possible, to aid the assignment and hence to elucidate the vibrational and torsional structure. (One should note here, however, that with the resolution of the experiments conducted herein, and owing to the size of the molecules under investigation, it is not expected that the rotational profile will be fully resolved, although it is possible to make certain deductions about the rotational structure from the shape of the unresolved rotational envelope.)

Firstly, one may consider cooling the sample physically, perhaps using an ice bath or liquid nitrogen. A sample of an aromatic molecule, however, is likely to freeze under these conditions; if the technique relies on sample in the gas phase, this is clearly a problem as the partial pressure of the vapour above a frozen sample is very low. So, the question is, how does one get a sample into the gas phase and then cool it down internally such that spectrum is not congested? A solution to this is the supersonic jet expansion.

The basic principle of the supersonic jet expansion relies on there being a large pressure gradient across two sides of an orifice, through which the sample is passed. Typically, one would have a gas reservoir at a pressure of a few bar above atmospheric pressure on one side of the orifice and a high vacuum (10^{-5} mbar or below) on the other side. If the orifice diameter is significantly greater than the mean free path of the gas at the higher pressure (noting that a gas at a higher pressure will have a lower mean free path), the individual gaseous molecules will collide with one another as they pass through the orifice, which leads to the depopulation of rotationally and vibrationally excited energy levels, and also promotes a unidirectional gas flow. The orifice is generally a small hole, often countersunk, to provide more control over the directionality of the gas on the low-pressure side. The molecular sample in the jet expansion becomes significantly internally cooled, such that it is possible to achieve rotational populations characteristic of a molecule held at temperatures as low as 1 K[127,165]. Vibrational levels are more difficult to depopulate, although vibrational temperatures of ~40-50 K in such jet expansions are typical and more than acceptable for most applications.

The free-jet expansion significantly narrows the distribution of velocities of the gas compared to the Boltzmann distribution at room temperature (see Figure 5.1) as the centre of the gas flow is essentially unidirectional, with the molecules moving close to a uniform speed. Furthermore, as the gas is expanded into a high vacuum (in which the mean free path is large), the free-jet expansion propagates through the vacuum and is unlikely to encounter and collide with molecules, which may cause shockwaves and turbulence in the flow. Gas molecules inside the free-jet expansion, on the low-pressure side of the orifice, thus do not collide with one another as a result of the unidirectionality of the gas flow in the pulse.

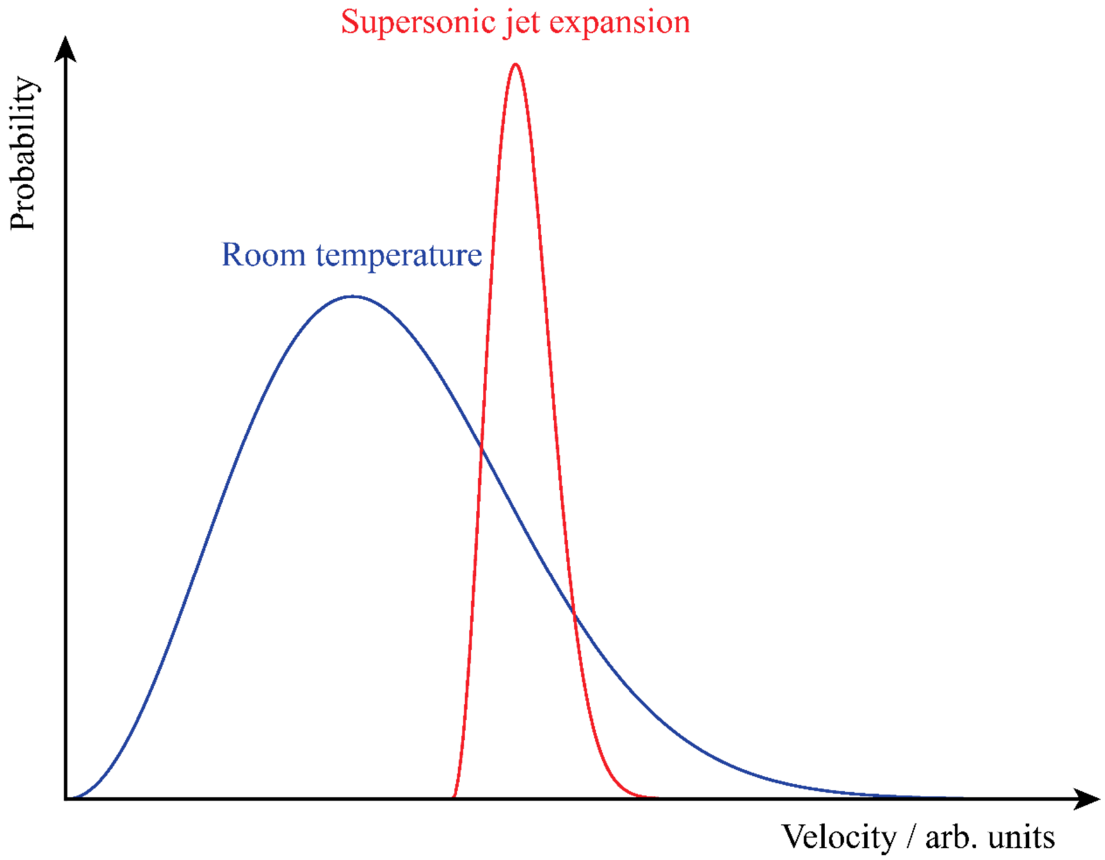

Figure 5.1. A schematic plot showing the distribution of velocities for a molecule at room temperature *versus* a molecule in a supersonic jet expansion. Note the significant narrowing of the distribution in the jet expansion.

Consequently, the speed of sound decreases since the effective temperature of the medium decreases and is accompanied by a modest increase in average speed of the gas during the jet expansion. As the Mach number is simply the ratio of the average speed of the gas to the local speed of sound of the medium, Mach numbers $\gg 1$ can be achieved, and hence the jet expansion is referred to as ‘supersonic’.

Furthermore, one can employ a ‘seeded expansion’ to internally cool the sample of interest, based on the principles above. To do this, one would require a sufficient vapour of the sample and an excess of a carrier gas. If the vapour pressure of the sample is relatively high, one may rely on the diffusion of the vapour above a room temperature sample, otherwise one may have to heat the sample. Briefly, the carrier gas, such as Ar, passes through the sample vapour and picks it up, which ‘seeds’ it in the carrier gas. The collisions between the carrier gas and the sample, as it passes through the pulsed valve orifice, then cool the molecular sample internally. One should, however, exercise caution in choosing the carrier gas; heavier carrier gases such as Kr and Xe will cool more efficiently, but they are more polarisable (and expensive) and have a tendency to form vdW complexes with the molecular sample. Lighter gases, such as He and Ne, are less likely to form vdW complexes with the sample, but are generally less efficient at collisionally cooling the sample, owing to their low mass. As such, a common carrier gas for a seeded expansion, such as those employed in the work in this thesis, is Ar. This is not only cheap, as it is readily distillable from air, but is also a good balance between effective internal cooling of the sample and not forming too many complexes.

As the supersonic jet expansion is relatively easy to build into an apparatus that already employs a vacuum chamber and, given the advantages of probing an internally-cooled molecule *versus* one at room temperature, all the experiments herein are conducted on jet-cooled *m*FT and NMP. Therefore, in the work presented in the later sections, owing to the jet-cooled conditions, we observe transitions arising from the zero-point vibrational level and lowest torsional levels (which correspond to $m = 0$ or $m = 1$), although we occasionally observe some torsional hot bands arising from residual population in the $m = 2$ levels owing to incomplete cooling.

5.2. Resonance-enhanced multiphoton ionisation (REMPI) spectroscopy

Conceptually, resonance-enhanced multiphoton ionisation spectroscopy is a rather simple experiment. This technique allows us to study and understand the vibrational and torsional levels of an excited electronic state of a molecule, which in our experiments, is often the first singlet excited state, or S_1 state. Despite this, in principle, any electronic state with an appreciable oscillator strength or HT-allowed vibronic states can be accessed. REMPI can not only be used to study isolated molecules, but also complexes and clusters of molecules, such as the NMP-RG (RG = Kr, Ar) vdW complexes, discussed in Section 13.

In the work presented herein, three distinct REMPI schemes are applied: (1 + 1), (1 + 1′) and (2 + 2). These schemes are generally denoted as (*x* + *y*)-REMPI, where ‘*x*’ is the number of photons driving the excitation of the molecule to the state of interest, and ‘*y*’ is the number of photons used to ionise the sample from its excited electronic state. One can also indicate that the energies of the photons for the excitation and ionisation steps are different by including a prime symbol, ′. In this case, the experiment is described as ‘two-colour’ (as two ‘colours’ of light are used).

Firstly, we shall discuss the one-colour (1 + 1) REMPI scheme. Here, only one laser is required, which is scanned across the transition energies corresponding to the vibrational and torsional manifold of the excited electronic state in question, and a second photon, of identical energy to the first, from the same laser pulse, will ionise the molecule and it is then these ions that are detected. This is shown pictorially in Figure 5.2.

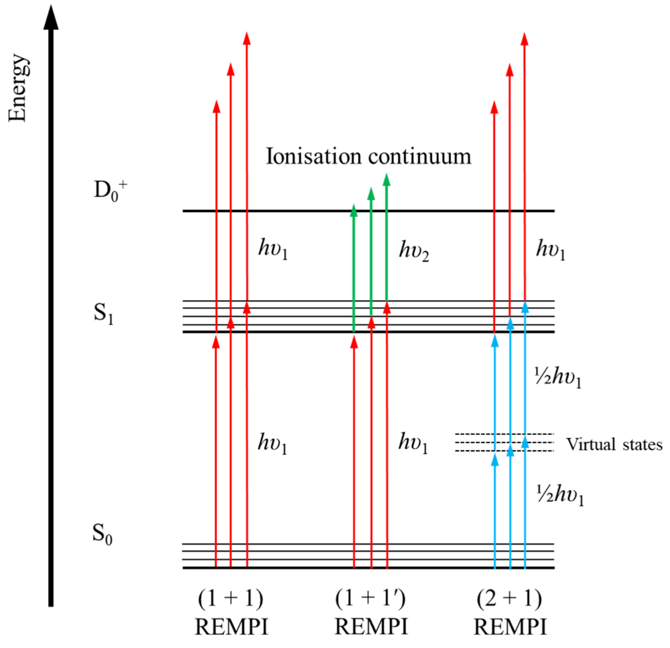

Figure 5.2. Schematic depiction of the various REMPI schemes used in the experiments detailed in this thesis. The symbols representing the electronic state on the left-hand side are for illustrative purposes only, and simply represent excitation, followed by ionisation.

In a two-colour REMPI experiment, one can use a second photon with an energy different to the first in a so-called (1 + 1′) process. This is useful in the case where the excited state is less than half-way to the AIE, *i.e.*, the gap between the ground state and the excited state is less than that between the excited state and the ionisation energy. [A (1 + *n*) REMPI scheme (where *n* > 1) is also possible in this instance, although a (1 + 1′) REMPI scheme is often more efficient.] Hence, one laser is scanned across the vibrational and torsional levels of the electronic state and a photon from a second laser of a different energy then ionises the molecule from these intermediate excited levels. A two-colour experiment is often more difficult in comparison to a one-colour experiment, as one must ensure that the ionisation laser pulse is both spatially and temporally overlapped with the excitation laser pulse, such that the ionising photon arrives *after* the excitation photon, otherwise no signal will be observed.

If one does not need, strictly, to conduct a two-colour (1 + 1′) experiment as a (1 + 1) REMPI experiment is feasible, then the power of the excitation laser needs to be attenuated such that the photon flux of the excitation laser beam is not high enough to efficiently ionise the populated excited state. This is also depicted pictorially in Figure 5.2. One may wish to conduct such a two-colour experiment as greater control of the excess energy in the produced ions can be achieved, which is useful should the ions fragment; this also forms the basis of two-colour ZEKE spectroscopy (discussed in a following subsection). Furthermore, a (1 + 1′) REMPI spectrum generally has a better signal to noise ratio than does a (1 + 1) REMPI spectrum, owing to the much lower power of the excitation laser, additionally, the attenuated excitation laser will minimise the impact of power broadening on the bands in the spectrum.

We can also consider a (2 + *n*)-REMPI scheme, where two photons are used to excite the sample to an excited state, and '*n*' photons are used in subsequent ionisation. One may specifically consider attempting a (2 + 1′) REMPI experiment in place of this, where a single photon of different energy, from a second laser, may be used to ionise the prepared excited state. Often, the photon flux of the first laser must be high to drive the two-photon excitation. Therefore, it becomes likely that a one-colour multiphoton ionisation will also occur, caused by the same laser pulse as the excitation, as opposed to the absorption of a single photon of a different energy from the second laser. Hence, a (2 + 1′) REMPI experiment requires a careful balance of the relative laser powers and this technique is more challenging than a (2 + 2) or a (1 + 1′) REMPI experiment.

A (2 + 2) REMPI spectrum was recorded for NMP, and is presented in Section 12, which used the visible fundamental output of the dye laser, rather than the frequency-doubled, UV, output. One can, conceptually, think of a two-photon absorption in two ways: firstly, the two photons can be thought of as being absorbed simultaneously, or it can be thought of as an absorption, first to a very short-lived ‘virtual state’ (see Figure 5.2), followed by rapid, subsequent absorption of another photon to the excited state of interest. Either way, a two-photon absorption modifies the selection rules of the transition so, despite the $\tilde{A}^1A_2 \leftarrow \tilde{X}^1A_1$ electronic transition of NMP being one-photon forbidden, it is two-photon allowed. Consequently, a (2 + 2) REMPI experiment will access the FC allowed levels of the S_1 state, with the intensities of the transitions determined by the FCFs, allowing one, in this case, to obtain vibrational wavenumbers for a_1 symmetry vibrations[82] directly. Therefore, a two-photon excitation, while more difficult to conduct since it requires tight focusing of the laser beam in the interaction region and relies on a far less probable process, can yield further information about the electronic structure of a system.

While the states accessible *via* a vibronically-allowed, one-photon transition in NMP remain two-photon allowed, two-photon absorptions have a much lower absorption cross section than do one-photon absorptions, thus the vibronic structure becomes too weak to observe in the two photon process, although it is expected to be observed given high enough powers.

In all cases discussed above, the REMPI spectrum is essentially a plot of (mass-selected) ion yield *versus* the energy of the scanning excitation laser. Each peak, therefore, represents the energy of a vibrational or torsional transition (often with unresolved rotational structure in our experiments) of the excited electronic state.

Two major advantages of the REMPI technique are that:

(i) it can be coupled with a time-of-flight (ToF) mass spectrometer (as is the case here), permitting mass-resolution, so one can monitor only the ion of interest, and record signal arriving in a single mass-channel. This is in contrast to LIF, where all the fluorescence is detected, without the ability to directly determine from which species in the jet expansion it is arising.

(ii) it relies on the absorption of a photon and subsequent ionisation, and so, if the photon flux is high enough and the timings of the lasers in a two-colour experiment are correct, the second photon is absorbed almost immediately. Therefore, one is less reliant on the excited states produced being long-lived, meaning it is, in principle, easier to study short-lived species *via* REMPI spectroscopy than it is using LIF. In spite of this, LIF can give information regarding excited state lifetimes whereas this is a lot more difficult to reproduce in a REMPI experiment.

5.3. Laser-induced fluorescence (LIF) spectroscopy

As mentioned in the previous subsection, LIF spectroscopy (also known as ‘fluorescence excitation’ spectroscopy) is a technique in which one can obtain similar information to that obtained using REMPI spectroscopy. Whilst a laser also scans across the vibrational and torsional structure of an electronically excited state, instead of ionising the molecule immediately with another photon, one waits for the molecule to fluoresce. This fluorescence originates (in a collisionless environment) from whatever level is excited and occurs to multiple levels in the ground electronic state with intensities of the emissions dependent on the FCFs.

With LIF, we can collect all of this fluorescence using a photomultiplier tube (PMT), and an LIF spectrum is a plot of total fluorescence yield *versus* scanning wavenumber. This is shown schematically in Figure 5.3.

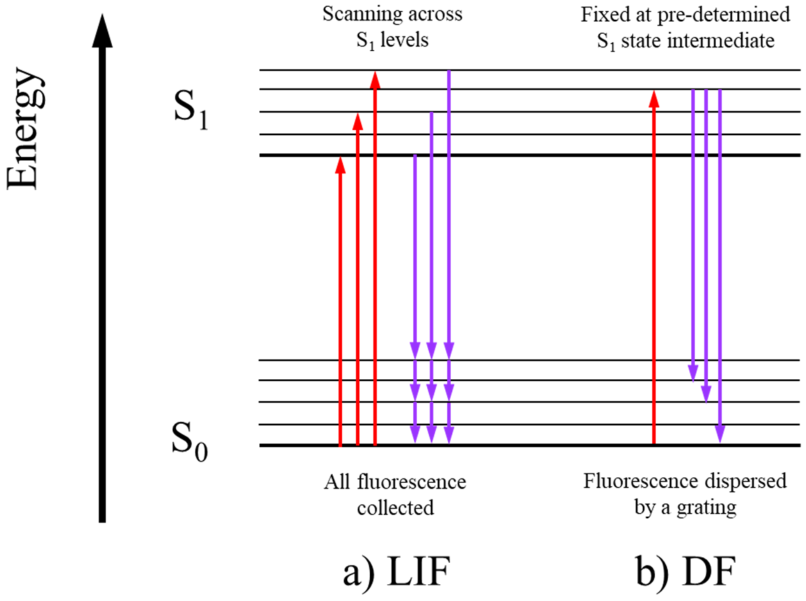

Figure 5.3. A schematic showing (a) the laser-induced fluorescence technique in which the output of a dye laser scans across the vibrational and torsional structure of an excited electronic state and all fluorescence from the resonant level is collected by a PMT; (b) the dispersed fluorescence technique in which a pre-determined level is pumped and the fluorescence that is emitted is dispersed by a grating in a monochromator. The two-dimensional laser-induced fluorescence technique is, essentially, a combination of these two techniques. See Section 5.4 for further details.

Qualitatively, one would expect a REMPI spectrum and an LIF spectrum to look identical since the selection rules to the excited levels are the same, as it is the same excitation process. However, the difference is in the detection technique, so there will be some variation between them. As mentioned, LIF requires the excited state to fluoresce and further relies on the excited state lifetime being long enough for fluorescence to be emitted. In this time, it is possible for the excited state population to decay (this could include predissociation, internal conversion or, slower, intersystem crossing), which could cause lifetime broadening of the spectral bands. For example, in NMP, the lifetime of the S_1 excited state is rather short and, as one increases the internal energy in the excited state (scans to higher wavenumber), the excited state lifetime gets shorter still. This is hypothesised to arise through the excited state having a potential barrier caused by orbital mixing involving a σ* orbital (the 3s Rydberg orbital evolves into a σ* orbital along the N-CH_3 coordinate) leading to predissociation at higher energies which would reduce the probability of fluorescence as the population is being ‘drained’ from the S_1 state. Hence, the LIF spectrum of the $\tilde{A}^1A_2 \leftarrow \tilde{X}^1A_1$ transition of NMP becomes weaker and less resolved at higher internal energy and its appearance begins to deviate from that of the REMPI spectrum (which is less susceptible to excited state lifetime effects, such as predissociation, owing to the almost immediate ionisation), with bands losing intensity or disappearing entirely. In contrast, the electronic excited state lifetime of *m*FT is much longer than that of NMP, therefore, the LIF spectra presented herein for *m*FT (and also the vertically-integrated 2D-LIF spectra) more closely resemble the REMPI spectrum – see Sections 8 and 9.

Additionally, the fluorescence is emitted isotropically allowing the PMT to be placed where it is least affected by scattered radiation of the laser. Further, an LIF apparatus will benefit from having baffles on the excitation laser entrance and exit windows, to minimise the amount of scattered laser light in the chamber.

Owing to the fluorescence being emitted to multiple ground state vibrational levels, laser-induced fluorescence may be coupled with a technique known as dispersed fluorescence, which is discussed below.

5.4. Dispersed fluorescence (DF) and two-dimensional laser-induced fluorescence (2D-LIF) spectroscopy

Dispersed fluorescence spectroscopy, also known as single vibronic level fluorescence (SVLF) spectroscopy, is a technique in which one can project the population of an electronic excited state back onto the ground electronic state.

One can fix a laser at a transition found *via* LIF to prepare a vibrational/torsional level in an excited electronic state and, as mentioned above, this may fluoresce to multiple levels in the ground electronic state, with the intensity of these transitions being dependent on the FCFs. These are, in turn, dependent on the vibrational level prepared, from which the fluorescence is emitted. Instead of collecting the fluorescence with a PMT, the fluorescence is dispersed by the grating of a monochromator to separate spatially (or disperse) the emitted photons of different energies. This radiation can then be captured on a charge-coupled device (CCD) camera, allowing one to collect windows of the emitted fluorescence to see to which levels the excited state emits, and how strongly (*i.e.* how large the FCFs are between the emitting level and the ground state level). A dispersed fluorescence spectrum is, therefore, fluorescence intensity *versus* the energy of the emitted photons. From this, one can draw conclusions about the identity of the excited state level pumped, but also to gain information on the ground state vibrational and torsional levels which will not be populated in the free-jet expansion.

As the area of the CCD is rather small compared to the width of the dispersed fluorescence, a DF spectrum will have to be collected in ‘windows’ where one moves the grating of the monochromator to vary which part of the fluorescence profile is directed onto the CCD. One will often collect the signal from the CCD for each window over a few thousand laser shots, allowing the signal to build up for a better signal to noise ratio. These windows of fluorescence can then be spliced together to create a DF spectrum as wide as desired. A benefit of this technique is that there is a very wide dynamic range of the CCD, meaning it is often possible to zoom-in far into the baseline and see small peaks, barely visible amongst very intense bands. This is often not possible in ZEKE (*vide infra*), where one must turn down the sensitivity of the MCPs to keep intense transitions on-scale, losing any weaker bands to the baseline. This means that spectra must be recorded multiple times with different sensitivity settings to ensure no data is lost. Furthermore, the quality of the DF spectrum is often mostly dependent on the number of laser shots over which the fluorescence is accumulated.

A natural extension to this is the 2D-LIF technique, which combines both the DF and LIF techniques, where a dispersed fluorescence spectrum is recorded for each excited state wavenumber during a scan over the vibrational and torsional structure of the excited electronic state. In this case, a two-dimensional spectrum of emission intensity to the ground state *via* a variety of excited state intermediates is produced. Both the DF and, by inference, the 2D-LIF techniques are depicted schematically in Figure 5.3 alongside the LIF technique (*vide supra*).

The 2D-LIF technique is a powerful tool as it combines the ability to project the population of an electronically excited state levels back onto the ground electronic state, with the ability to observe this over a wide dynamic range. Therefore, one can observe changes in the dispersed fluorescence over the scan and hence identify any cross activity, which can be indicative of coupling and/or Duschinsky mixing, *etc.*, in the ground and/or excited electronic states. One can also use 2D-LIF to deduce the contribution of overlapping bands in excitation, as well as *m*-specific interactions.

The apparatus in place in the laboratory is set up such that we can record 2D-LIF spectra over a wide scanning range, at the cost of some resolution. Naturally, if one wants to get the highest resolution spectra, one requires to have an extremely fine scanning step size (< 0.2 cm^{-1}) as well as a long path length in the monochromator. The latter has two effects: firstly, this means smaller windows of dispersed fluorescence can be collected over the CCD, which has a fixed size; secondly, the fluorescence intensity diminishes as the path length inside the monochromator increases (this is key to achieving the best dispersion and, so, emission resolution) so one will also have to accumulate the fluorescence for longer. This two-fold issue means that, in order to achieve the best resolution possible (*i.e.*, to see highly-resolved band structure[166]), one is limited by the region that can realistically be investigated in a given timeframe.

If one shortens the monochromator path length to collect larger windows of fluorescence, one can scan over a wider energy range in the same time and investigate a larger part of the excitation spectrum, at the cost of increasing band width and the loss of the ability to resolve some rotational structure. As modern monochromators can either be operated in single-pass or double-pass modes (*viz.* increasing the path length and adding a second grating, therefore increasing the dispersion of the fluorescence), one can, in principle, perform a higher-resolution scan over a small, selected, region identified in a lower-resolution scan. However, owing to the amount of work required to change a monochromator from operation in single-pass mode to double-pass mode, and then back again, is often prohibitive for most users and retaining the chosen configuration is commonplace. The work presented as part of this thesis shows that single-pass operation of the monochromator is more than sufficient to identify and elucidate nuanced interactions between ZOSs (see Section 2.6).

5.5. Zero-electron-kinetic-energy (ZEKE) spectroscopy

Zero-electron-kinetic-energy spectroscopy is a threshold ionisation technique which allows one to investigate the vibrational and torsional energy levels of the cation. In a two-colour ZEKE experiment, such as the ones conducted herein, one can pump a level in an excited electronic state (such as one identified in a REMPI experiment), using this as an intermediate state and ionise from there. This projects the population of the pumped intermediate state onto the cation, allowing control of the FCFs between the excited state and the cation, permitting deductions to be made about the nature of the excited intermediate level as well as the levels in the cation. This means one can explore interactions involving the intermediate state, as well as interactions in the cation. Combining the data obtained from 2D-LIF, ZEKE and REMPI one can gain a comprehensive insight into the ground electronic state, ground state cation, as well as the nature of the pumped intermediate level.

Although not conducted as part of this thesis, it is possible to conduct non-resonant, multiphoton ZEKE experiments[167–170] and one-colour ZEKE experiments (using VUV or XUV radiation as one has to ionise the sample with a single photon)[171–174]. In addition, ZEKE spectra of anions[175–178] and on systems where the initial state is also a cation[179,180] are also possible. From here on, the discussion of ZEKE spectroscopy will only be in context of a two-photon, resonant ZEKE experiment.

In a typical ZEKE experiment, one would fix the energy of a laser to be resonant with an intermediate state, and then the output of a second dye laser, aligned spatially and temporally with the first, scans across the energy levels in the cation, as depicted in Figure 5.4.

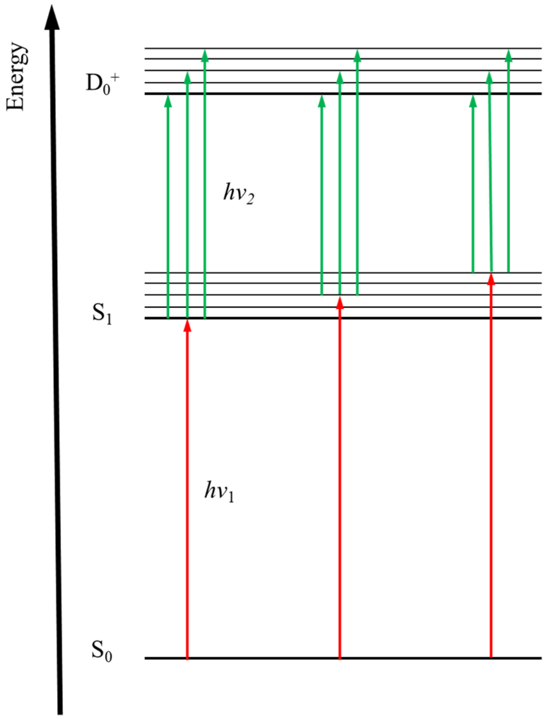

Figure 5.4. A schematic description of the two-colour resonant ZEKE technique. Here, an intermediate level in an excited electronic state is pumped and the output of a second laser scans across the energy levels in the cation. This schematic is applicable to both ‘true’ ZEKE and PFI-ZEKE (see below). Note that the intermediate state, as with REMPI spectroscopy, does not necessarily need to be the S_1 excited state.

In ‘true’ ZEKE, when the scanning laser becomes exactly resonant with a level in the cation, electrons are produced with zero kinetic energy, and one simply has to wait for any non-resonantly produced electrons (those with non-zero kinetic energy) to disperse and then pulse an electric field to direct the zero-kinetic-energy electrons towards a detector (often a set of MCPs). Threshold ionisation techniques such as ZEKE offer a significant improvement on resolution compared to traditional photoelectron techniques, in which a resolution of > 100 cm^{-1} is commonplace[165,181–184]. Theoretically, the resolution of ‘true’ ZEKE is simply the linewidth of the laser used which is often 0.5 cm^{-1} or better. However, most experiments conducted today are not ‘true’ ZEKE experiments, owing to various difficulties which will be discussed below.

In practice, ‘true’ ZEKE is rather difficult to achieve as any small, stray magnetic or electric fields, such as those produced by electronics in a laboratory environment and, indeed, the Earth’s own magnetic field, can disperse the zero-kinetic-energy electrons, leading to a significant reduction in signal or a total loss of signal. It is possible to line the apparatus in μ-metal, as indeed occurred in early ZEKE experiments. However, a minor modification to the experimental set-up can be made, which deviates from the ‘true’ ZEKE regime, but significantly increases the level of signal achieved, whilst retaining a very reasonable resolution.

Pulsed-field ionisation ZEKE (or PFI-ZEKE) is the major form of ZEKE spectroscopy used today and is used in the experiments considered in this thesis. Simply, one can install a set of electrical grids, connected to a delay generator to pulse an electric field in the interaction region of the experimental apparatus, as one may have in a ‘true’ ZEKE apparatus. One scans the output of a laser across the energy levels in the cation, and instead of being perfectly resonant with these, an electron is promoted to a high-lying Rydberg orbital (often $n > 100$) in a Rydberg series that lies just below each ionisation threshold and is associated with the energy level of the cation in question. This electron is still bound to the molecule, albeit very weakly, and these Rydberg states are very long-lived (μs). As such, these states are, and therefore the technique is, much less affected by small, stray magnetic and electric fields in the laboratory. After a short delay, to allow non-resonant prompt electrons to disperse, one can apply a pulsed electric field to the grids which perturbs the Coulombic potential in which the Rydberg electron is bound, allowing the electron to overcome the potential, and be directed towards a detector.

The two main disadvantages of the PFI-ZEKE technique are that there may be a small discrepancy between the AIE reported and the ‘true’ AIE, as one is detecting the electrons removed from the Rydberg states which converge to the cationic energy levels, and this may spread out the lower-energy band profile, making it more difficult to ascertain the true AIE. Secondly, the resolution of PFI-ZEKE is limited to the bandwidth of the pulsed field as the nature of the rapidly converging Rydberg series lead to multiple states being populated and anything within the bandwidth of the pulsed field will be pulsed-field ionised; despite this, it is still a marked improvement on traditional photoelectron spectroscopy. The full-width at half-maximum (FWHM) bandwidth of typical bands in our ZEKE experiment is 5-7 cm^{-1}, being a combination of the rotational envelope and a small contribution arising from the PFI process. This means it is possible to report adiabatic ionisation energies and energies of vibrational and torsional levels to within approximately ±5 cm^{-1}.

For molecules such as *m*FT and NMP, the low-lying Rydberg states are sufficiently short-lived that they do not contribute to those extracted by the ZEKE pulsed field. This means the only Rydberg states being extracted by the pulsed field, and therefore detected, are the highest-lying Rydberg states which occupy a very small energy region below the cation. Hence, for these molecules, it is not necessary to report a pulsed-field correction to the AIEs or cationic energy levels reported[185–188]. This is contrary to the case of small molecules like atoms/diatomics/triatomics in which case one must be careful regarding correction of the energies as a result of the pulsed field as these lower-lying Rydberg states become more long-lived.

5.6. Quantum chemical calculations

In the work presented in this thesis quantum chemical calculations have often been employed to assist in the assignment and interpretation of the spectra. Both density functional theory (DFT) and *ab initio* methods have been considered. We find that the scaled harmonic vibrational wavenumbers calculated at the B3LYP level of theory with the aug-cc-pVTZ basis set are more than sufficient for this purpose. The harmonic vibrational wavenumbers calculated using the B3LYP functional are scaled by 0.97 in all cases, to account for anharmonicity and deficiencies with the basis set and/or level of theory. It has been shown that scaling in this way gives frequencies in very good agreement with calculations which explicitly calculated anharmonic frequencies[189,190], although the harmonic frequency calculations are significantly less costly, justifying this procedure.

Prior to this, the geometry is optimised using the same basis set and level of theory. Generally, the scaled harmonic vibrational wavenumbers for the neutral and cationic ground states are in good agreement with the experimental values derived from ZEKE and 2D-LIF spectra, although the quality of the harmonic vibrational wavenumbers for excited state calculations [time-dependent (TD) DFT for open-shell singlet excited states] can vary significantly, as has been reported by this group[46,191]. Here, it is found that for *m*FT and NMP, the TD-B3LYP vibrational wavenumbers are largely reliable, with a few notable exceptions. Spin-unrestricted DFT methods were employed for calculations on the cation, and the $\langle S^2 \rangle$ values are almost always ~0.76 suggesting there is little spin contamination and this method is reasonable.

In the case of the NMP-RG (RG = Ar, Kr) the CAM-B3LYP functional was used in order to better describe the long-range dispersive forces[192], characteristic of weakly-bound complexes. (Ref. 192 also notes that TD-B3LYP is also largely unsuccessful at calculating excited state energies, hence the TD-CAM-B3LYP method was used for this purpose for NMP in Section 12.) The harmonic vibrational frequencies calculated using the CAM-B3LYP functional are scaled in the same manner as those calculated at the B3LYP level of theory. The harmonic frequencies for the intermolecular modes are expected to be largely unreliable, as these modes are highly anharmonic, which is discussed in Section 13; although, as expected, the scaled harmonic frequencies calculated for the ring-localised vibrations remain reliable and are affected little by complexation.

Generally, all geometry optimisations, frequency calculations and vertical excitation calculations were conducted using the Gaussian 16[193] package of quantum chemical programs, with MOLPRO 2015[194] being used to calculate binding energies at the (R)CCSD(T) level of theory, and for calculations for which specifying an explicit electronic state in terms of its symmetry and orbital occupancy was required, where MOLPRO was found to offer more control over the specification of the wavefunction. Standard basis sets, found within the libraries of the computational chemistry programs, were employed and, within the work on NMP-RG, the small-core fully-relativistic effective core potential, ECP10MDF, was used for Kr alongside the corresponding aug-cc-pVTZ-PP core-valence basis set[195], obtained from the Basis Set Exchange database[196].

5.7. Experimental apparatus: REMPI/ZEKE

In our laboratory, the REMPI and ZEKE experiments are conducted on a single apparatus. We use a ‘standard’ REMPI spectrometer, modified slightly to be able to perform the ZEKE experiments. The specifics of the apparatus are described below, as well as shown pictorially in Figure 5.5.

The REMPI/ZEKE apparatus consists of two connected, differentially pumped vacuum chambers. The first chamber contains the pulsed valve (Parker solenoid valve, 750 μm orifice, 10 Hz) which introduces the sample to the spectrometer and generates the supersonic jet expansion. Separated by a gate valve is the second vacuum chamber, which contains the electrical plates, which make up the ion lens for REMPI or, for ZEKE, the pulsed-field ionisation, and microchannel plate detectors (MCPs). The supersonic jet expansion comprises the vapour above room-temperature NMP or *m*FT, seeded in 1 – 3 bar Ar (above atmospheric pressure), which expands into the first vacuum chamber and proceeds, unskimmed, into the second chamber where it is intercepted by (one or) two laser beams, overlapped spatially and temporally, collinear and counterpropagating, between the two electrical plates. In a REMPI experiment, the produced ions are directed upwards, through a custom-built ion lens assembly, into a time-of-flight (ToF) tube in which the ions are separated by mass and are detected when they strike a set of MCPs.

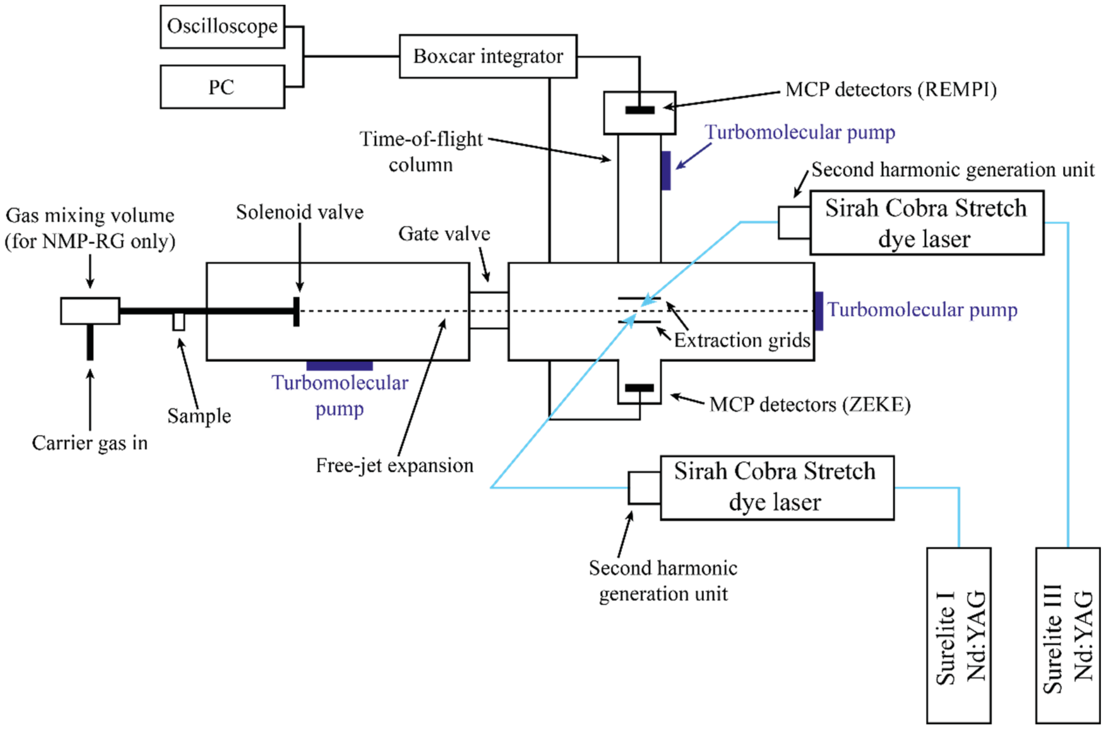

Figure 5.5. Schematic of the REMPI/ZEKE apparatus. The blue lines represent laser beams.

In the ZEKE experiments, the electrical plates are re-purposed such that, instead of the plates holding a large, positive voltage, one of the plates is grounded and the other is subject to a programmed pulse consisting of a small positive voltage (generating fields of ~10 V cm^{-1}), after a delay of about 1.5 – 2 μs, to extract the electrons from the long-lived Rydberg states, and direct them to a second set of MCPs, located below the interaction region.

Both the source chamber and ionisation chamber were held at ~10^{-7} mbar (~10^{-5} mbar working pressure), by turbomolecular pumps, backed by large, Edwards M40 rotary pumps. The source chamber had a large turbomolecular pump (Oerlikon Leybold Turbovac TW1600) attached to the bottom of the chamber. The ionisation chamber had two small turbomolecular pumps: one in line with the jet expansion (Leybold Turbovac 1000 C) and the other was connected to the ToF tube (Leybold Turbovac 151); both turbomolecular pumps in this chamber were backed by a single Edwards M40 rotary pump.

The experiments employed two Sirah Cobra Stretch dye lasers, both capable of frequency doubling the fundamental laser radiation with either a BBO or KDP crystal (dependent on the wavelength range of the dye used), steered with quartz turning prisms to direct the output laser beams towards the interaction region of the vacuum chamber. These lasers had different gratings in the resonator: one was 1800 lines mm^{-1} and the other was 2400 lines mm^{-1}, meaning the grating anomalies (both resonance and Rayleigh anomalies, see Sections 5.9 and 12.1) lie in a different energetic region for each dye laser. One of these dye lasers was pumped by a Continuum Surelite III Nd:YAG laser and the other by a Continuum Surelite I Nd:YAG laser (later switched to a second Surelite III Nd:YAG laser). Dependent on the dye used, the fundamental 1064 nm radiation was either frequency doubled to 532 nm, or frequency tripled to 355 nm radiation.

The timings of the lasers and pulsed valve were controlled using digital delay generators (SR535), and the signals from the MCPs for both the ZEKE and REMPI experiments were sent to a boxcar integrator (SR250), gated, averaged, and then sent to an oscilloscope for visualisation and to a PC, *via* a computer interface (SR245), for recording and storage. The ZEKE signal is also amplified (SR445A) before being processed by the boxcar integrators.

Specifically:

i. *m*FT – the excitation laser was operated with Coumarin 503, pumped with the third harmonic (355 nm) of a Surelite III Nd:YAG laser. The dye laser output was frequency doubled into the UV region and directed into the vacuum chamber. For ZEKE and (1 + 1′)-REMPI experiments, the ionisation laser was operated with Pyrromethene 597 or Pyrromethene 580 and pumped with the second harmonic of a Surelite I Nd:YAG laser. The output of this dye laser was frequency doubled as well, before being directed into the vacuum chamber, timed to arrive after the excitation laser pulse.

ii. NMP – the excitation laser was operated with Coumarin 480, pumped with the third harmonic of a Surelite III Nd:YAG laser. For most of the experimental work, the dye laser output was frequency doubled before being directed into the vacuum chamber, but for the (2 + 2)-REMPI spectrum, the dye laser output was left undoubled, and the visible radiation was directed into the vacuum chamber and tightly focused. The ionisation laser was operated with Coumarin 440 or Stilbene 420, and was pumped by the third harmonic of a Surelite I Nd:YAG laser, and the dye laser output was left undoubled.

iii. NMP-RG – for these experiments, the same laser configuration was used as in (ii), but a gas mixing volume was used in order to produce a mixture of Kr in Ar and this was connected to the high-pressure side of the pulsed valve to generate the NMP-Kr complexes. For these complexes, a mixture of 20 – 40% Kr in Ar was used at a pressure of ~3 bar above atmospheric pressure. The amount of uncomplexed NMP$^+$ ion signal, especially for the NMP-Ar complexes, in the REMPI experiments ‘contaminated’ the NMP-Ar mass channel, so a small piece of copper wire was suspended down the ToF tube, close to, and in front of the MCPs, and connected to a high-voltage power supply. This was programmed to put a large (0.5 – 1.5 kV), positive voltage across the wire and was timed to reduce the number of uncomplexed NMP$^+$ ions striking the MCP, being detected, and thus reducing the signal contamination, leading to a better background subtraction in the NMP$^+$-RG mass channel. A longer ToF tube was trialled, although it was determined this reduced the signal to levels too low to produce publishable-quality data reliably.

Photoionisation efficiency (PIE) spectra can also be recorded using this apparatus. The PIE spectrum is a plot of ion yield versus laser wavelength, in which one scans over the ionisation threshold of a molecule while pumping a pre-selected level in a neutral electronically excited state. When the combined energy of the laser outputs become greater than (or equal to) the AIE, ions are produced, and these can be detected on the same set of MCPs as one would use when recording a REMPI spectrum. As one continues to scan, and every time another cationic level is accessed, the ionisation efficiency increases further, more ions are produced (with the number of extra ions proportional to the intensity of the transition) and, hence, a typical spectrum would look a bit like a staircase, with steps at the energies of the levels in the cation. However, for the PIE spectra presented in this work, these onsets are more gradual than this and are more 'sloping', with a large, single rise at the $\Delta v = 0$ vibration, followed by a gradual increase in the ion signal.

Owing to the large electric fields required to push the ions up the ToF tube, the onset of the PIE curves is often below the true AIE (*cf.* the ZEKE technique where only small electric fields are applied). This arises as the range of Rydberg states that can be ionised in the electric field is large. An advantage of PIE curves, however, is that, unlike in ZEKE, there is mass resolution so one can verify whether any signal seen in a ZEKE experiment is due to the species of interest or anything else excited in the molecular beam. PIE curves were used as a diagnostic tool in verifying the AIE of the NMP-RG complexes. Like the ZEKE spectra, the PIE curves were also affected by the grating anomalies (see Sections 5.9, 12 and 12.1) so that it could be verified that, in the regions of the ZEKE spectra in which there was a lack of structure, this was a result of a total loss in ion yield and confirming that the grating anomalies were the cause.

Owing to these significant caveats, PIE spectra were used for ‘survey’ work, although they were a useful compromise in the absence of being able to conduct mass-analysed threshold ionisation (MATI) experiments. PIE curves were also used to obtain an approximate wavenumber for an unknown AIE to guide the ZEKE experiments, of a previously unstudied molecular system, towards the true AIE.

5.8. Experimental apparatus: 2D-LIF

This apparatus consists of only one vacuum chamber and one laser system, and a schematic of the apparatus is given in Figure 5.6. A Continuum Surelite III Nd:YAG laser (third harmonic, 355 nm) was used to pump a Sirah Cobra Stretch dye laser, operating with Coumarin 480 for NMP or Coumarin 503 for *m*FT, and the output was frequency doubled (by a BBO crystal) and then directed into the vacuum chamber, pumped by a turbomolecular pump (Oerlikon Leybold Turbovac TMP361; previously a Pfeiffer turbomolecular pump with an unknown model), backed by an Edwards M40 rotary pump. The laser beam entered and exited the chamber through a set of baffles, to minimise the amount of scattered radiation from the laser inside the chamber. The timing of the laser pulse with respect to the pulsed valve (Parker solenoid valve, 750 μm orifice, 10 Hz) was controlled by a delay generator (SR535).

In the LIF experiments, the emitted fluorescence passes through a set of collection optics which focuses the fluorescence onto a photomultiplier tube (Hamamatsu H10721-01) and then the signal is simultaneously sent to a boxcar integrator (SR250), where it is gated, integrated and averaged, and to an oscilloscope for visualisation. The signal from the boxcar integrator is sent to a PC, *via* a computer interface (SR245) for recording and storage.

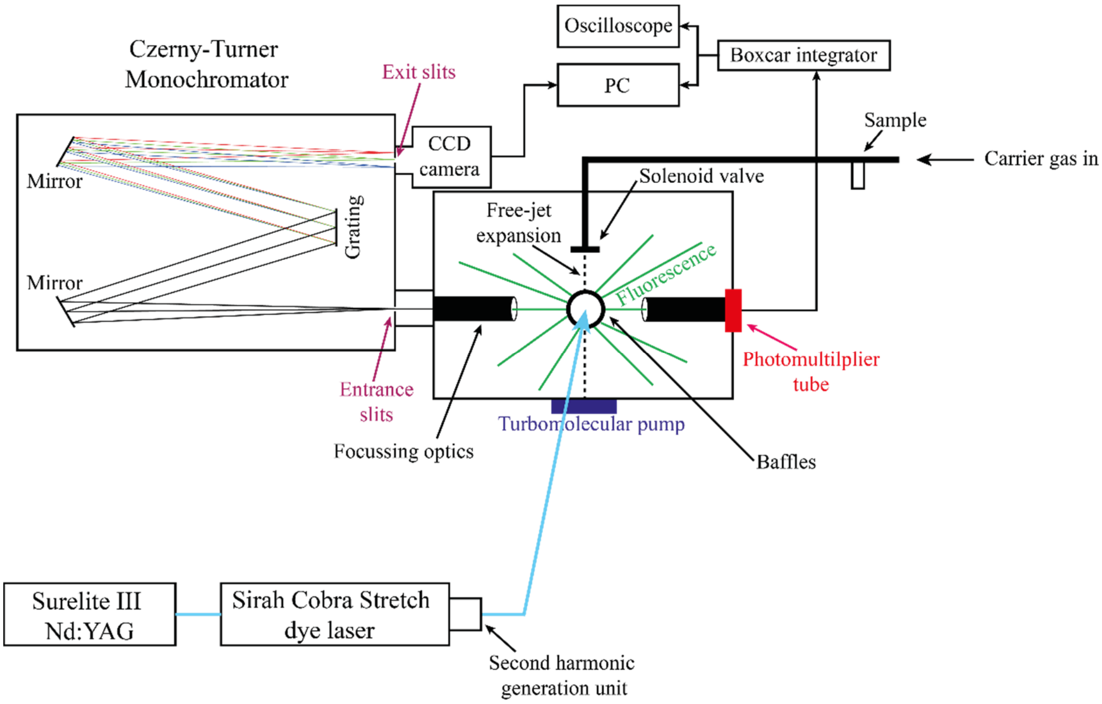

Figure 5.6. A schematic of the 2D-LIF apparatus. Blue lines represent the laser beam, green lines represent the fluorescence of the sample, which is isotropically emitted from the interaction region. Some light is focused by the collection optics and directed towards either the photomultiplier tube, or the monochromator.

For the DF and 2D-LIF experiments, a set of collection optics (identical to those used in the LIF experiments and positioned on the opposite side of the vacuum chamber) focuses the fluorescence through entrance slits into a Czerny-Turner style monochromator (Sciencetech 9150), operating in single pass mode. The different wavelengths of light are dispersed spatially by the grating and directed towards a CCD camera (Andor iStar DH334T), which can collect ~300 cm^{-1} windows of fluorescence. The camera was internally cooled to -20°C, to maintain a wide dynamic range, good signal to noise and prevent internal electrical discharges and is directly connected to a PC for data visualisation, collection and storage.

5.9. A note on gratings and grating anomalies

The grazing-incidence gratings that make up the part of the resonator of the dye laser are a key part of its operation, responsible for wavelength selection from the broadband emission from the dye. However, the grating one requires depends on a number of desired properties:

i. The energetic region over which one requires tuneable radiation,

ii. The linewidth, and therefore, resolution one wishes to achieve and
iii. The polarisation of light one uses.

In order to achieve the maximum efficiency of the laser cavity, one must select the right grating for the desired dye region. One dye laser on the REMPI/ZEKE apparatus and the dye laser on the 2D-LIF apparatus both contain a 2400 line mm^{-1} grazing incidence grating; the other dye laser on the REMPI/ZEKE apparatus has an 1800 line mm^{-1} grazing-incidence grating, which offers a different effective tuning range. These effective tuning regions vary and are dependent on various grating anomalies (first reported in-depth by Wood in 1902[197], although grating anomalies had been identified before this[198], see also Ref. 199).

Two different types of grating anomaly have been observed in the ZEKE spectra and PIE curves of NMP: the Rayleigh[200,201] and resonance anomalies[202,203]; these (especially the former) initially led us astray in the analysis of the NMP and NMP-RG ZEKE spectra. The resonance anomaly causes a significant deterioration in the efficiency of the grating, and dramatically reduces the power output of the dye laser in certain energy regions with a given grazing incidence angle, and this is what is generally referred to as the “Wood’s anomaly”; these are generally thought to arise from surface phonons that occur across the grating at certain wavelengths, which depend on the groove spacing, amongst other factors. Additionally, the Rayleigh anomaly redirects the energy into other propagating orders, thus reducing the efficiency of the grating which is generally aligned to only allow for the propagation of first-order diffracted light. In our systems, this occurs when incoming radiation is polarised *perpendicularly* to the grooves on the grating - this is required for the grating to operate.

For the propagation of a given order of light, n, on a grating at wavelength λ, the following equation must be true[204]:

$$gn\lambda = \sin(\theta_{\mathrm{i}}) + \sin(\theta_{\mathrm{d}})$$

Equation 5.1

Where g is the groove density of the laser, θ_i is the angle of incidence and θ_d is the angle of diffraction. For first-order (*i.e.*, $n = 1$) diffraction to occur efficiently, the wavelength of light must be between some minimum and maximum bound, which is dependent on the groove density:

$$\frac{\lambda_{\mathrm{max}}}{2} \leq \frac{1}{g} \leq \lambda_{\mathrm{min}}$$

Equation 5.2

Where λ_max is the theoretical maximum wavelength a grating, with groove density g, can output. Conversely, λ_min is the theoretical wavelength at which second-order (*i.e*, $n = 2$) diffraction can occur. These values are given in Table 5.1, alongside the useful tuning range which is feasible for these dye lasers. This differs somewhat to λ_max and λ_min as these are ideal values, and at λ_min, there is not a sharp cut-off where first-order diffraction stops and second-order begins; λ_min is more an indication as to where second-order diffraction from the grating becomes important. Furthermore, it is reasonable to operate a dye laser with higher-order diffraction for a better linewidth, although the efficiency of the cavity decreases dramatically. Thus, the useful tuning range is more an empirical guideline as to the range in which a dye laser, with a given grating, may operate efficiently and as expected.

Table 5.1. The tuning range for the two configurations of Sirah Cobra Stretch dye laser used in our laboratory. The regions in which there is no ‘useful’ tuneability is where the efficiency of the grating for first-order diffraction drops and higher-order diffraction becomes important; in our ZEKE spectra of NMP, this was the energetic region which was accessed, and hence the spectra recorded did not appear as anticipated. This table is reproduced from the dye laser manual, see Ref. 204.

g (groove density)	λ_max / nm	λ_min / nm	Useful tuning range[a] / nm
1800 line mm^{-1}	1100	555	900 - 575 *and* 555 - 400
2400 line mm^{-1}	833	417	740 - 434 *and* 423 - 350

[a] Empirically deduced operating region, see text.

Therefore, a combination of the resonance anomaly (which decreases the efficiency of grating), coupled with an inopportune Rayleigh anomaly, led us to believe that, when we observed identical structure to higher energy, this was genuine structure, rather than the same bands arising from radiation diffracted in a higher-order. Later, it was recognised that these other signals seen showed the same spectrum, but with 50% the bandwidth and spacing. Notably, we were led astray by the assumption that the *only* grating anomaly one would observe is the resonance anomaly, which causes a decrease in the efficiency of the grating (*viz*. a blind spot) and not *also* the redirection the light into higher-order propagations.

In general, such grating anomalies are regarded as a minor nuisance of which to be aware as they only exist over a small region of the tuneable range of the grating and lasers with more than one (switchable) grating in the cavity are now commercially available. It was only when the roles of the dye lasers were swapped over in the REMPI/ZEKE experiment (owing to the 'fortuitous' breakage of the motor coupling in the second harmonic generation unit corresponding to the excitation laser) that this issue was resolved and the ZEKE spectra recorded thereafter were more in-line with expectations. We believe that, for the first time, we have reported the effect of both grating anomalies on resolved molecular spectra simultaneously, although Kessel has noted anomalies in the intensities of bands in fluorescence emission spectra of porphyrins under certain conditions[205] (the author also noticed that polarisers could be placed before the grating to ameliorate the effect). Interestingly, it has been suggested that such anomalies may find a purpose in the production of sensors[206].

6. Introduction to the published papers

The publications presented in the following sections make up the results and discussion of this thesis. All the fundamental background theory required for the understanding and interpretation of the work presented henceforth has been detailed in the previous sections.

The first three papers cover the first ~1350 cm^{-1} of the $S_1 \leftarrow S_0$ transition of *m*FT, with assignments presented for the majority of these levels, aided by the interpretation and assignment of ZEKE and 2D-LIF spectra. This has been split into a number of distinct parts. The first part, not included as part of this thesis, covers the first ~350 cm^{-1} of the $S_1 \leftarrow S_0$ transition and includes the pure torsions and a handful of the low-energy vibrations. This work (Ref. 76) and that by Lawrance and co-workers (Ref. 75) provide key background to the work on *m*FT presented herein. Next, the ~350-500 cm^{-1} of the $S_1 \leftarrow S_0$ transition of *m*FT is discussed, where evidence is found of an unusually strong case of Duschinsky mixing of the D_{18}, D_{19} and D_{20} vibrations within the $D_0^+ \leftrightarrow S_1 \leftrightarrow S_0$ transitions and comparisons are drawn to *m*ClT. The second paper presented covers the remainder of the bands seen in the spectrum of the $S_1 \leftarrow S_0$ transition, up to about ~1350 cm^{-1}, which discusses the build-up from purely localised coupling of vibrational and vibrational-torsional ZOSs towards dissipative coupling. Discussion is also made, drawing comparisons to *p*FT, and referring to the original conclusions made by Parmenter *et al.*[74] noting that it will always be difficult to compare *meta*- and *para*-substituted toluenes owing to the significant change in vibrational motions between *meta*- and *para*-substituted molecules. The final paper focusing on *m*FT considers the ~650 – 750 cm^{-1} region of the $S_1 \leftarrow S_0$ transition, in which one can observe transitions to 17^1, $26^1 28^1$ and 27^2 (amongst others), noting that there are some rather complex vibration-torsion interactions, as well as *m*-specific couplings, which makes it difficult to determine the exact identities of the eigenstates excited from the REMPI spectrum alone, further evidencing the power of ZEKE and 2D-LIF as methods to elucidate the natures of rather complicated interactions.

The next four papers pertain to the analysis of the vibrational activity of the first ~1100 cm^{-1} of the symmetry-forbidden $S_1 \leftarrow S_0$ transition of NMP. Furthermore, ZEKE spectra are presented *via* almost all bands below this wavenumber, whose appearance in the spectrum of the $S_1 \leftarrow S_0$ transition is a result of vibronic coupling to higher-lying electronic states. The ZEKE spectra demonstrate the largely diagonal activity, as expected given the nature of the intermediate electronic state in the FC-region, although some unexpected activity is observed when exciting *via* the b_1 vibrations. The 2D-LIF and DF spectra are interesting owing to the plethora of activity observed, in direct contrast to the ZEKE spectra.

The first paper in this section focuses on the first ~120 cm^{-1} of the $S_1 \leftarrow S_0$ transition of NMP, in which the pure torsional transitions are observed. Presented is a 2D-LIF spectrum over this region, as well as ZEKE spectra *via* the four observable torsional levels in S_1; these allow the determination of values of V_6 and F in each electronic state considered, as well as the derivation of a precise AIE for NMP. The second paper presents the rationale behind the P_i labelling scheme that is used throughout the work on NMP in this thesis, as well as how it improves on the commonly used Mulliken/Herzberg and Wilson/Varsányi labelling schemes. The third paper forms the most significant portion of work on NMP, in which ZEKE spectra are reported for (almost) all bands below ~1100 cm^{-1} of the $S_1 \leftarrow S_0$ transition, excluding the torsions, and 2D-LIF and DF spectra are presented for certain bands. Furthermore, there is discussion on the vibronic coupling routes expected within NMP that give rise to the intensity of these bands in S_1, given the transition is electric dipole forbidden for a one-photon absorption. The final paper of this section discusses the impact of the resonance and Rayleigh anomalies on the ZEKE spectra presented in Section 12, as well as offering an insight into the appearance of these spectra in absence of the grating anomalies.

Finally, the final paper presents REMPI and ZEKE spectra for the NMP-RG (RG = Ar, Kr) vdW complexes, reporting an unusually localised and largely unstructured REMPI spectrum and the ‘clean’, but rich in structure, ZEKE spectra for these species, noting that the inclusion of the RG atom is sufficient to perturb the electronic structure of the S_1 state to allow the electronic origin transition to be observed. This work enabled the deduction of binding energies in the S_0, S_1 and D_0^+ states, which are compared to high-level *ab initio* calculations, and also AIEs for these complexes.

7. Variations in Duschinsky rotations in *m*-fluorotoluene and *m*-chlorotoluene during excitation and ionization

Abstract: "We investigate Duschinsky rotation/mixing between three vibrations for both *m*-fluorotoluene (*m*FT) and *m*-chlorotoluene (*m*ClT), during electronic excitation and ionization. In the case of *m*FT, we investigate both the $S_1 \rightarrow S_0$ electronic transition and the $D_0^+ \leftarrow S_1$ ionization, by two-dimensional laser-induced fluorescence (2D-LIF) and zero-electron-kinetic energy (ZEKE) spectroscopy, respectively; for *m*ClT, only the $D_0^+ \leftarrow S_1$ ionization was investigated, by ZEKE spectroscopy. The Duschinsky mixings are different in the two molecules, owing to shifts in vibrational wavenumber and variations in the form of the fundamental vibrations between the different electronic states. There is a very unusual behavior for two of the *m*FT vibrations, where apparently different conclusions for the identity of two S_1 vibrations arise from the 2D-LIF and ZEKE spectra. We compare the experimental observations to the calculated Duschinsky matrices, finding that these successfully pick up the key geometric changes associated with each electronic transition and so are successful in qualitatively explaining the vibrational activity in the spectra. Experimental values for a number of vibrations across the S_0, S_1, and D_0^+ states are reported and found to compare well to those calculated. Assignments are made for the observed vibration-torsion ("vibtor") bands, and the effect of vibrational motion on the torsional potential is briefly discussed."

Authors: Alexander R. Davies, David J. Kemp, Lewis G. Warner, Elizabeth F. Fryer, Alan Rees and Timothy G. Wright.

Submitted: to Journal of Chemical Physics, 30th March 2020

Published: 1st June 2020

Reference: A. R. Davies, D. J. Kemp, L. G. Warner, E. F. Fryer, A. Rees and T. G. Wright, *J. Chem. Phys.*, 2020, **152**, 214303.

DOI: 10.1063/5.0009391

Summary: In this work, we present REMPI, 2D-LIF and ZEKE spectra for a small region of the $S_1 \leftarrow S_0$ transition for both *m*FT and *m*ClT, focusing on ~0^0 + 350 – 500 cm^{-1}. Here, we see evidence of very strong Duschinsky mixing between the D_{18}, D_{19} and D_{20} fundamentals between the S_0 and S_1 electronic states, as well between S_1 and D_0^+. As such, it is not possible to unambiguously assign an ${}^{m}D_i$ label for the D_{19} and D_{20} vibrations in S_1, as one would apparently reach different conclusions to their identities based on the ZEKE and 2D-LIF spectra thus, in S_1, they are assigned as D_X and D_Y. Interestingly, we note that it is possible to assign D_{18} unambiguously in all three states, despite also being mixed with the other vibrations. The Duschinsky mixing of these modes in *m*ClT is also stark, although nowhere near as strong as it is in *m*FT. It is noted, in Section 2.7, that Duschinsky mixing is to be expected to some degree between electronic states, owing to the inevitable change in electronic structure and, therefore, geometry; however, it is noted that such strong Duschinsky mixing is unusual. This paper describes a remarkable instance of Duschinsky mixing and forms a good comparison to the anharmonic coupling and mode mixing in the other papers presented herein.

Contributions: The spectra for *m*FT were recorded by myself and EFF, under supervision of DJK during a Master's project. The spectra for *m*ClT were recorded by LGW and DJK. Despite having limited influence on the analysis of the *m*ClT spectra, I include this paper as part of this thesis as the majority of the analysis of the *m*FT spectra was conducted by myself at the very beginning of my PhD, in collaboration with DJK and TGW, and this analysis comprises the most significant part of this work. I also made Figures 2, 4 and 6 for publication, making edits to Figures 1, 3 and 5 following discussion with TGW and departure of DJK from the group after completing his own PhD. Furthermore, I read and commented on multiple iterations of the manuscript, as well as discussing and implementing the reviewers' comments to the final version of the paper.

Reproduced from *J. Chem. Phys.*, 2020, 152, 214303, with the permission of AIP Publishing.

The Journal of Chemical Physics ARTICLE scitation.org/journal/jcp

Variations in Duschinsky rotations in *m*-fluorotoluene and *m*-chlorotoluene during excitation and ionization

Cite as: J. Chem. Phys. **152**, 214303 (2020); doi: 10.1063/5.0009391
Submitted: 30 March 2020 • Accepted: 12 May 2020 •
Published Online: 1 June 2020

Alexander R. Davies, David J. Kemp, Lewis G. Warner, Elizabeth F. Fryer, Alan Rees, and Timothy G. Wright[a)]

AFFILIATIONS

School of Chemistry, University of Nottingham, University Park, Nottingham NG7 2RD, United Kingdom

[a)]**Author to whom correspondence should be addressed:** Tim.Wright@nottingham.ac.uk

ABSTRACT

We investigate Duschinsky rotation/mixing between three vibrations for both *m*-fluorotoluene (*m*FT) and *m*-chlorotoluene (*m*ClT), during electronic excitation and ionization. In the case of *m*FT, we investigate both the $S_1 \rightarrow S_0$ electronic transition and the $D_0^+ \leftarrow S_1$ ionization, by two-dimensional laser-induced fluorescence (2D-LIF) and zero-electron-kinetic energy (ZEKE) spectroscopy, respectively; for *m*ClT, only the $D_0^+ \leftarrow S_1$ ionization was investigated, by ZEKE spectroscopy. The Duschinsky mixings are different in the two molecules, owing to shifts in vibrational wavenumber and variations in the form of the fundamental vibrations between the different electronic states. There is a very unusual behavior for two of the *m*FT vibrations, where apparently different conclusions for the identity of two S_1 vibrations arise from the 2D-LIF and ZEKE spectra. We compare the experimental observations to the calculated Duschinsky matrices, finding that these successfully pick up the key geometric changes associated with each electronic transition and so are successful in qualitatively explaining the vibrational activity in the spectra. Experimental values for a number of vibrations across the S_0, S_1, and D_0^+ states are reported and found to compare well to those calculated. Assignments are made for the observed vibration-torsion ("vibtor") bands, and the effect of vibrational motion on the torsional potential is briefly discussed.

I. INTRODUCTION

An analysis of the vibrational activity in electronic and photoelectron spectra is often used as a signature of vibrational coupling between fundamentals, overtones, and combination levels. This occurs through anharmonic coupling, which leads to the dispersal, and so delocalization, of internal energy within a molecule, an important aspect to enhance photostability.[1–4] Sometimes, activity in fundamentals other than that excited can be seen in the experimental spectra; however, to first order, vibrational fundamentals do not couple anharmonically. Such an activity can be induced by changes in the geometry that lead to significant Franck–Condon factors (FCFs) or as a result of a Duschinsky rotation,[5] with the cross-activity between vibrations being a signature of the latter. Understanding the intensities of vibrational features in electronic and photoelectron spectra is key to understanding electronic and geometric changes between electronic states. A Duschinsky rotation occurs when the vibrational motions and/or force constants vary significantly between two electronic states; then, each of the affected vibrations in one electronic state has a motion that can be expressed as a linear combination of more than one vibrational motion in the other electronic state. This is sometimes termed the Duschinsky effect, with the resulting vibrations said to have undergone Duschinsky mixing. This would mean, for example, that the activity arising when exciting from a particular vibration would be more extensive than expected, owing to the excitation of further vibrations in the final electronic state. Of course, both Franck–Condon (FC) and Duschinsky effects will operate simultaneously, which can complicate the interpretation of the spectra.

Very recently, we published resonance-enhanced multiphoton ionization (REMPI) and zero-electron-kinetic-energy (ZEKE) studies of the low-wavenumber regions of *m*-fluorotoluene (*m*FT)[6] and *m*-chlorotoluene (*m*ClT),[7] which mainly focused on torsions and vibration-torsion (vibtor) levels. The *m*FT study complemented the two-dimensional laser-induced fluorescence (2D-LIF) study of Stewart *et al.*, who examined the first 350 cm^{-1} of the $S_1 \leftarrow S_0$ transition.[8] The spectra of both molecules were assigned in terms of torsion and vibtor levels in the S_0 and S_1 states. Earlier, Okuyama and co-workers[9–12] reported laser-induced fluorescence (LIF), dispersed fluorescence (DF), REMPI, and ZEKE spectra of the low-wavenumber region of *m*FT. In addition, Ichimura *et al.*[13] have published LIF and DF spectra of *m*ClT, while Feldgus *et al.*[14] reported REMPI and ZEKE spectra of *m*ClT, restricted to the torsional region.

In the present work, we focus on a set of three vibrations that are active in the $S_1 \leftarrow S_0$ transition and are found to have a high degree of cross-activity, as ascertained by 2D-LIF and ZEKE spectroscopy. These three vibrations are designated D_{18}, D_{19}, and D_{20}, as described in Ref. 15, and their explicit motions will be discussed later.

II. EXPERIMENTAL

The ZEKE[16] apparatus and 2D-LIF[17] apparatus are the same as those employed recently. In both experiments, for *m*FT, a free-jet expansion of *m*FT (Sigma-Aldrich, 98% purity) in 1.5 bar Ar was employed. For the ZEKE experiments on *m*ClT, a free jet expansion was also used, consisting of *m*ClT (Alfa Aesar, 98% purity) in 2 bars Ar, where the *m*ClT sample was heated to ~50 °C in order to introduce sufficient vapor to the expansion.

For the 2D-LIF spectra, the free-jet expansion was intersected at *X*/*D* ~20 by the frequency-doubled output of a single dye laser (Sirah CobraStretch), operating with Coumarin 503 and pumped with the third harmonic of a Surelite III Nd:YAG laser. The fluorescence was collected, collimated, and focused onto the entrance slits of a 1.5 m Czerny–Turner spectrometer (Sciencetech 9150) operating in single-pass mode, dispersed by a 3600 groove/mm grating, and ~300 cm^{-1} windows of the dispersed fluorescence collected by using a CCD camera (Andor iStar DH334T). At a fixed grating angle of the spectrometer, the excitation laser was scanned, and at each excitation wavenumber, the camera image was accumulated for 2000 laser shots. This allowed a plot to be produced of fluorescence intensity vs both the excitation laser wavenumber and the wavenumber of the emitted and dispersed fluorescence, termed a 2D-LIF spectrum.[18,19]

For the ZEKE spectra, the focused, frequency-doubled outputs of two dye lasers (Sirah CobraStretch) were overlapped spatially and temporally and passed through a vacuum chamber coaxially and counterpropagatively, where they intersected the free jet expansion. The excitation laser was operated with Coumarin 503 and was pumped with the third harmonic (355 nm) of a Surelite III Nd:YAG laser, while the ionization laser was operated with Pyrromethene 597 and pumped with the second harmonic (532 nm) of a Surelite I Nd:YAG laser. The jet expansion passed between two biased electrical grids located in the extraction region of a time-of-flight mass spectrometer, which was employed in the REMPI experiments. These grids were also used in the ZEKE experiments by application of pulsed voltages, giving typical fields of ~10 V cm^{-1}, after a delay of up to 2 μs; this delay was minimized while avoiding the introduction of excess noise from the prompt electron signal. The resulting ZEKE bands had widths of ~5 cm^{-1} to 7 cm^{-1}. Electron and ion signals were recorded on separate sets of microchannel plates.

III. RESULTS AND ASSIGNMENTS

A. Nomenclature and labeling

1. Vibrational and torsional labeling

We shall employ the D_i labels[15] for the vibrations, as used in Refs. 6–8, since neither Wilson[20]/Varsányi[21] nor Mulliken[22]/Herzberg[23] notations are appropriate for the vibrations of *m*FT or *m*ClT. The C_s point group labeling scheme[15] is based on the vibrations of the *meta*-difluorobenzene (*m*DFB) molecule.

We shall also refer to the methyl torsional motion for *m*FT and *m*ClT, for which the G_6 molecular symmetry group (MSG) is appropriate, and we shall use those symmetry labels throughout. The torsional levels will be labeled via their *m* quantum number,[6,8] and the correspondence between the C_s point group labels and the G_6 MSG ones is given in Table I. To calculate the overall symmetry of a vibtor level, it is necessary to use the corresponding G_6 label for the vibration and then find the direct product with the symmetry of the torsion (Table I), noting that a C_{3v} point group direct product table can be used, since the G_6 MSG and the C_{3v} point group are isomorphic.

Under the free-jet expansion conditions employed here, almost all of the molecules are expected to be cooled to their zero-point vibrational level, and thus, essentially all $S_1 \leftarrow S_0$ pure vibrational excitations are expected to originate from this level. In contrast, owing to nuclear-spin and rotational symmetry, the molecules can be in one of the $m = 0$ or $m = 1$ torsional levels,[24] with residual population in the $m = 2$ levels also seen.[6–8]

2. Transitions

When designating excitations, we shall generally omit the lower level, since it will be obvious from either the jet-cooled conditions or the specified intermediate level. In the usual way, vibrational transitions will be indicated by the cardinal number, *i*, of the D_i vibration, followed by a superscript/subscript specifying the number of quanta in the upper/lower states, respectively; torsional transitions will be indicated by *m* followed by its value. Finally, vibtor transitions will be indicated by a combination of the vibrational and torsional transition labels.

TABLE I. Correspondence of the C_s point group symmetry classes with those of the G_6 molecular symmetry group. Also indicated are the symmetries of the D_i vibrations and the different pure torsional levels.[a]

C_s	G_6	D_i[b]	*m*
a'	a_1	D_1–D_{21}	0, 3(+), 6(+), 9(+)
a''	a_2	D_{22}–D_{30}	3(−), 6(−), 9(−)
	e		1, 2, 4, 5, 7, 8

[a] Symmetries of vibtor levels can be obtained by combining the vibrational symmetry (in G_6) with that of the pure torsional level, using the C_{3v} point group direct product table.

[b] The D_i labels are described in Ref. 15, where the vibration mode diagrams can also be found.

As has become a common usage, we will generally refer to a level using the notation of a transition, with the level indicated by the specified quantum numbers, with superscripts indicating levels in the S_1 state and, when required, subscripts indicating levels in the S_0 state. Since we will also be referring to transitions and levels involving the ground state cation, D_0^+, we shall indicate those as superscripts, but with a single, additional, preceding, superscripted "+" sign. Relative wavenumbers of the levels will be given with respect to the relevant zero-point vibrational level with $m = 0$ in each electronic state.

For cases where both the geometry and the torsional potential are similar in the S_1 and D_0^+ states, the most intense transition is usually expected to be that for which no changes in the torsional and/or vibrational quantum numbers occur: designated as $\Delta m = 0$, $\Delta v = 0$, or $\Delta(v, m) = 0$ transitions, as appropriate. However, as will be seen (and as reported in Refs. 6, 7, 12, and 14), the $\Delta m = 0$ and $\Delta(v, m) = 0$ transitions are almost always not the most intense bands in the ZEKE spectra for *m*FT and *m*ClT, indicative of a significant change in the torsional potential upon ionization.

B. Overview of the REMPI spectra

In Fig. 1, we show the REMPI spectra of the first 500 cm^{-1} above the origin of the $S_1 \leftarrow S_0$ transition in *m*FT and *m*ClT. The 0–350 cm^{-1} region of the *m*FT spectrum has been discussed in detail previously, in terms of 2D-LIF and ZEKE spectroscopy,[6,8] while the corresponding region of the *m*ClT spectrum has also been discussed relating to ZEKE spectroscopy.[7] Because of the consistent vibrational labeling used for both molecules,[15] it can be seen that the activity in both spectra is similar. In the present work, we shall concentrate on the two expanded regions of Fig. 1, between 400 cm^{-1} and 480 cm^{-1} for *m*FT and 350–470 cm^{-1} for *m*ClT. In the case of *m*ClT, the spectrum was recorded in two mass channels, corresponding to the ^{35}Cl and ^{37}Cl isotopologues, where some bands

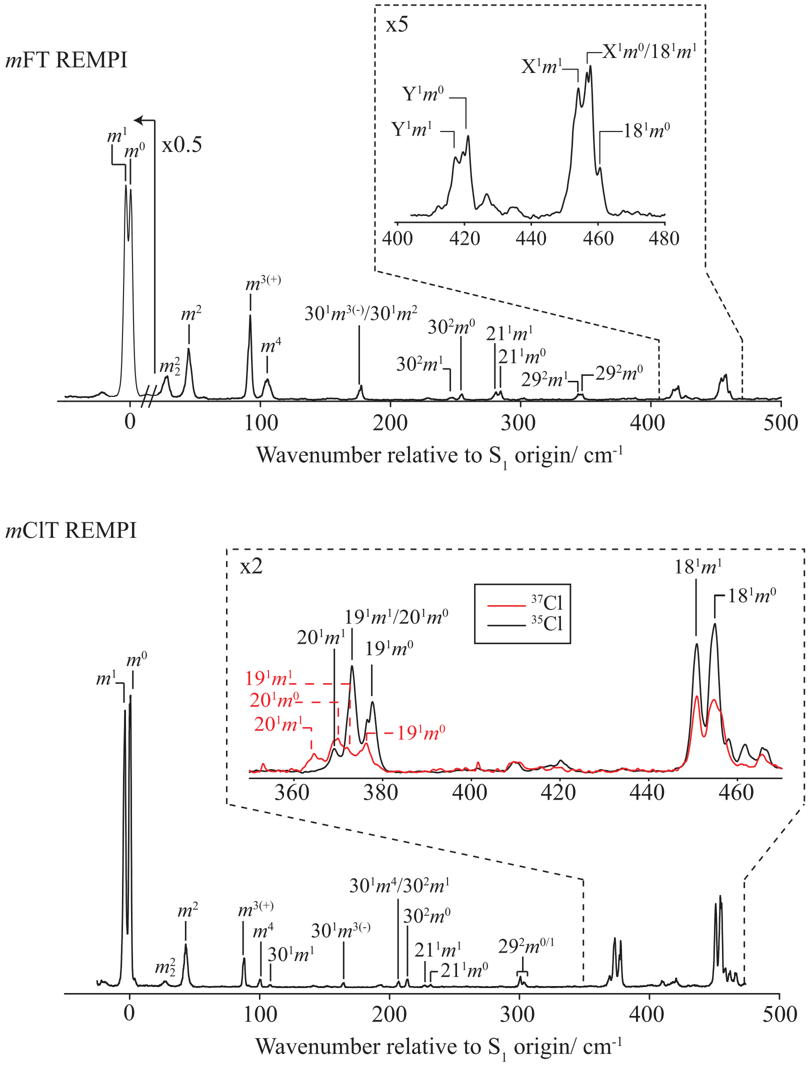

FIG. 1. REMPI spectra of the 0–500 cm^{-1} region above the origin for the $S_1 \leftarrow S_0$ transition for (a) *m*FT and (b) *m*ClT. In each case, the expanded views of the regions corresponding to the $18^1m^{0,1}$, $19^1m^{0,1}$, and $20^1m^{0,1}$ transitions are shown. In the case of *m*ClT, traces for both the ^{35}Cl and ^{37}Cl isotopologues are presented. Note that for *m*FT, the region around the origin to lower wavenumber than the indicated break has been scaled by a factor of 0.5.

around 370 cm^{-1} can be seen to undergo isotopic shifts (compare the red and black traces in the expanded region in the lower portion of Fig. 1), but there are essentially no shifts for the lower-wavenumber bands.[7] For both *m*FT and *m*ClT, these regions are dominated by activity involving three vibrations, D_{18}, D_{19}, and D_{20}. As we shall see below, these vibrations are significantly Duschinsky mixed in the S_1 state.

We shall first concentrate on the assignment of the 2D-LIF and ZEKE spectra of *m*FT, before moving on to the ZEKE spectra of *m*ClT (no 2D-LIF spectra were recorded for this molecule). We shall then discuss the observations for both molecules.

C. 2D-LIF and ZEKE spectra of *m*FT

In Fig. 2, the 2D-LIF spectrum of *m*FT in the range 412–466 cm^{-1} is presented, while the ZEKE spectra recorded at various excitation positions across the same region are shown in Fig. 3. The calculated wavenumbers for a selection of pertinent vibrations for both molecules and for the three different electronic states considered are presented in Table II: the level of theory utilized has generally been shown to be sufficient for these molecules in our previous work.

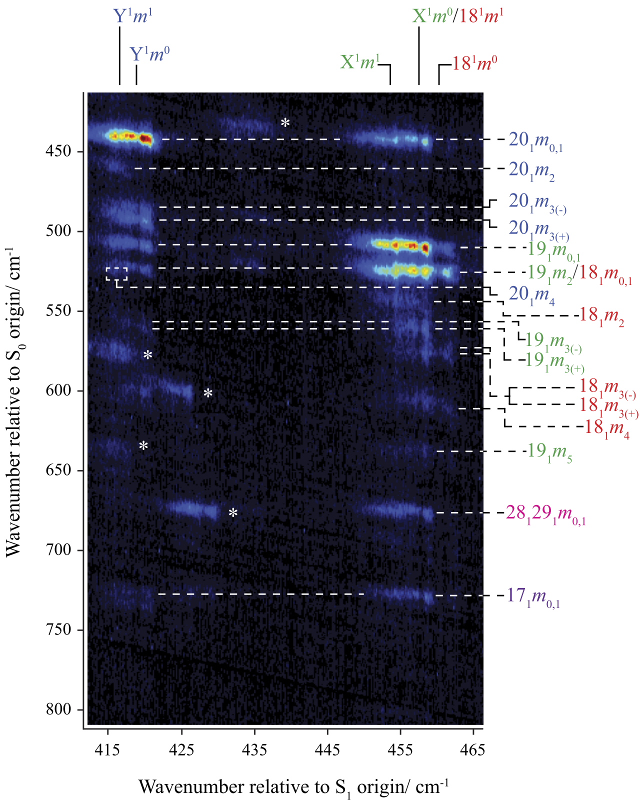

FIG. 2. 2D-LIF spectrum for *m*FT, where the excitation range covers the $18^1m^{0,1}$, $X^1m^{0,1}$, and $Y^1m^{0,1}$ transitions. The emission range covers the main $\Delta(v, m) = 0$ regions, extending to a higher wavenumber to include other key features. Assignments for related bands (e.g., vibtor and combination levels of the same vibration) are shown in the same color. Features marked with an asterisk are not assigned here, but these will be addressed in a future publication.

It will be seen in the discussion below that the D_{19} and D_{20} vibrations become very mixed in the S_1 state. For this reason, we have designated the S_1 mixed vibrations, D_X and D_Y, in the following. The strongest features in the 2D-LIF spectrum (Fig. 2) are seen when exciting via 18^1, X^1, and Y^1, each comprising $m = 0$ and $m = 1$ components, as indicated; significant cross-activity is evident. The strong emission bands seen when exciting via 18^1 are partially overlapped with those seen when exciting via X^1. Associated with each of the strong emission bands is a series of vibtor transitions, which have distinctive structure, as seen in the low-wavenumber region.[8] These consist of strong $m_{3(+)}$ and weaker $m_{3(-)}$ bands when exciting via the $m = 0$ components, as well as a strong m_2 band, with weaker m_4 and m_5 bands, when exciting via the $m = 1$ components; some of these are overlapped by other features in the 2D-LIF spectrum.

In Fig. 3, we present the ZEKE spectra recorded via the $m = 0$ and $m = 1$ components of the 18^1, X^1, and Y^1 vibrations of *m*FT. It can be seen from Fig. 1 that the X^1m^0 and 18^1m^1 transitions overlap, and so the ZEKE spectrum recorded for these overlapped features is included in both the upper and lower portions of Fig. 3, but located on the correct scale in each case. Again, significant cross-activity is seen when exciting via 18^1, X^1, and Y^1, for both *m* levels.

To aid in the understanding of the activity of the spectra, Duschinsky matrices were calculated (using the FC-LAB II program)[25] for a selection of the vibrations. This was performed for the three pairings of the S_0, S_1, and D_0^+ electronic states for *m*FT, and these are shown in Fig. 4. Additionally, we show the calculated motions of the three Duschinsky-mixed vibrations of interest, in each of the three electronic states. First, we point out that the D_i labels are defined with respect to the S_0 motion (the motions of *meta*-disubstituted benzenes in the S_0 state, on which the D_i labeling is based, were discussed in detail in Ref. 15). Second, the S_0/D_0^+ matrix indicates that the vibrational motions in the ground state cation are very similar to those in the ground state neutral molecule, so that the S_0 vibrational labels, D_i, can also be used for the cationic vibrations to a very good approximation (it is highlighted that the wavenumber ordering of the D_{19} and D_{20} vibrations has switched in the cation relative to the S_0 state, see Table II).

We now turn to the S_0/S_1 matrix for *m*FT in Fig. 4. This indicates that the motions of the S_1 vibrations corresponding to the D_{18}, D_{19}, and D_{20} S_0 vibrations are significantly altered, and each of these S_1 vibrations can be thought of as being significant admixtures of the corresponding S_0 ones, i.e., they are Duschinsky mixed; a similar picture holds when these S_1 vibrations are expressed in terms of the D_0^+ vibrations. In contrast, the D_{17} and D_{21} vibrations exhibit extremely similar motions in the three electronic states and so are not considered to be Duschinsky mixed. We now point out that the S_1 D_{18} vibration is dominated by the same motion as in the S_0 state (and the D_0^+ state), and so these are recognizably the same vibrations, even though the S_0 and S_1 motions are not precisely the same, with a noteworthy contribution in S_1 from D_{19}. Hence, we retain the D_{18} label for this vibration across the three electronic states. This is not true for the D_{19} and D_{20} vibrations, where the two S_1 vibrations have motions that can be expressed as significant admixtures of the corresponding S_0 (or D_0^+) vibrations; as such, the D_{19} and

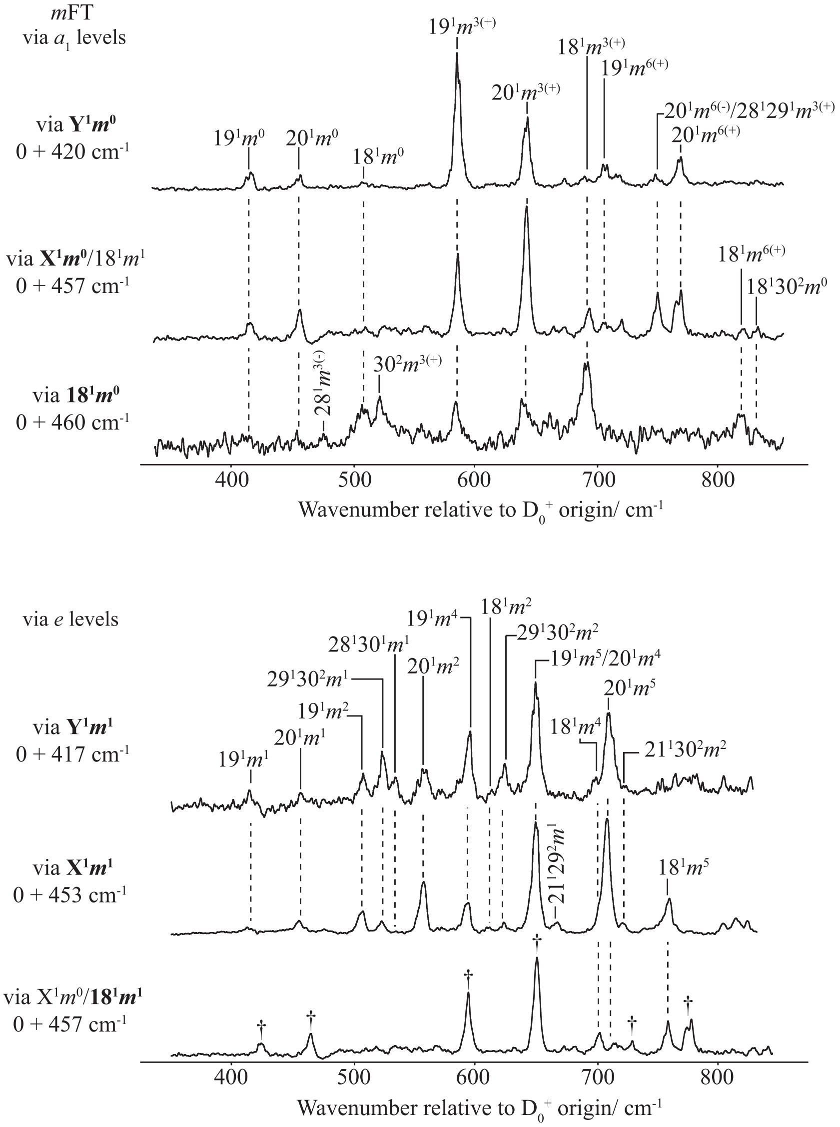

FIG. 3. ZEKE spectra of *m*FT recorded at different $S_1 \leftarrow S_0$ excitation positions, separated into $m = 0$ and $m = 1$ components. For clarity, the preceding superscripted "+" used in the text is omitted from the transition labels. Since the 18^1m^1 and 19^1m^0 transitions are overlapping, the corresponding ZEKE spectrum has been included in both parts of the figure; the bold label indicates the pertinent level for that part of the figure. We have added obeli (†) to bands that arise from the overlapping transition and which are labeled on the duplicate trace. The relative energy scales are given with respect to the $^+m^0$ and $^+m^1$ transitions; in absolute terms, the $^+m^1$ transition is ~5 cm^{-1} lower in wavenumber, owing to the $m_1 \leftarrow m_0$ spacing in the S_0 state.

D_{20} labels cannot be used for these two S_1 vibrations, which is why we have designated them D_X and D_Y, in an increasing wavenumber order.

We now look at the activity in the 2D-LIF and ZEKE spectra in more detail. In Fig. 2, we can see that there is significant cross-activity in the 2D-LIF spectrum involving the D_{18}, D_{19}, and D_{20} vibrations, as indicated by the (X^1, 18_1), (X^1, 19_1), and (X^1, 20_1) bands, together with (Y^1, 18_1), (Y^1, 19_1), and (Y^1, 20_1), which appear for each of the two *m* levels. A definite (18^1m^0, 19_1m_0) band can be seen, as well as (18^1m^0, 18_1m_0), but there is only the faintest activity for (18^1m^0, 20_1m_0); there do, however, appear to be ($Y^1m^{0,1}$, $18_1m_{0,1}$) bands, albeit overlapped by (Y^1m^1, 20_1m_4), indicating a lesser contribution of D_{18} to the S_1 state Y^1 vibration, compared to the X^1 vibration, see further discussion below.

With regard to the *m*FT ZEKE spectra in Fig. 3, clear $^+19^1$ and $^+20^1$ activity can be seen when exciting via each of X^1 and Y^1, for both $m = 0$ and $m = 1$ levels, with the $^+19^1$ wavenumber being *lower* than that of $^+20^1$, i.e., the opposite order to the S_0 and S_1 states, see Table II (there is also $^+18^1$ activity, but this is less prominent). The $^+19^1m^x$ vibtor activity is the greatest when exciting via Y^1 and that of $^+20^1m^x$ when exciting via X^1, with this being most clear from the $^+19^1m^{3(+)}$ and $^+20^1m^{3(+)}$ bands. The dual activity of both vibrations is consistent with the vibrational character of the D_X and D_Y vibrations in the S_1 state being highly mixed versions of the corresponding D_0^+ vibrations. The assignment of the various vibtor transitions is relatively straightforward, with the $^+20^1m^x$ transitions being very close to the expected positions; however, the $^+19^1m^x$ bands are somewhat shifted from the expected positions, but can be identified by their relative intensities and by comparison to

TABLE II. Calculated and experimental wavenumbers for *m*FT and *m*ClT vibrations pertinent to the present study.

	S_0		S_1		D_0^+	
D_i	Calculated[a]	Experimental	Calculated[b]	Experimental	Calculated[c]	Experimental
			*m*FT			
17	718	728[d,f]	685	685[d,f]	700	
18	519	527[d,f,g]	459	460[e,f]	509	510[e,f]
19 (X)	505	512[d,f,g]	448	457[d,e,f]	410	415[f]
20 (Y)	435	445[d,f,g]	410	420[d,e,f]	442	456[f]
21	285	292[d,f,g]	281	284[d,e,f,g]	290	296[e,f]
28	443	438[d,f,g]	241	258[d,e,f,g]	373	375[e,f]
29	236	236[f,g]	184	173[d,e,f,g]	190	190[e,f]
30	199	201[f,g]	122	127[d,e,f,g]	167	167[e,f]
			*m*ClT			
18	513	524[h,j]	446	455[h]	455	457[i]
19	402	409[h,j]	373	378[h]	391	396[i]
20	376	387[h,j]	368	373[h]	377	387[i]
21	226	221[h,j]	226	231[i]	233	240[i]
28	432	431[j]	241		366	
29	213	234[j]	159	151[i]	176	176[i]
30	171	185[j]	80	111[i]	150	149[i]

[a] B3LYP/aug-cc-pVTZ, scaled by 0.97. For *m*ClT, the results are for the ^{35}Cl isotopologue.

[b] TD-B3LYP/aug-cc-pVTZ, scaled by 0.97. For *m*ClT, the results are for the ^{35}Cl isotopologue.

[c] UB3LYP/aug-cc-pVTZ, scaled by 0.97; $\langle S^2 \rangle = 0.76$. For *m*ClT, the results are for the ^{35}Cl isotopologue.

[d] Ref. 9. Small updates to some of these values have been made in Refs. 3 and 8 and the present work.

[e] Ref. 6.

[f] Present work. The experimental values for D_{27} were obtained from the observed vibtor bands. In the case of D_{19} and D_{20} in the S_1 state, which we have designated D_X and D_Y in the text, we have allocated these to the D_i label that has the maximum S_0 contribution from the Duschinsky matrix in Fig. 4.

[g] From Ref. 8.

[h] From Ref. 13.

[i] From Ref. 7.

[j] Ref. 15.

the $^+20^1m^x$ bands. Further discussion on the shifted $^+19^1m^x$ band spacings for *m*FT is given in Sec. IV B.

At this point, we note that for a symmetric, disubstituted benzene, such as *m*DFB, the point group is C_{2v}, where the D_{19} and D_{20} vibrations are both of b_2 symmetry, while D_{18} is of a_1 symmetry; thus, D_{19} and D_{20} can be thought of as mixing with one another during their evolution as the mass of the substituents changes,[15] while D_{18} cannot. In the asymmetric *m*FT, we note that the masses of CH_3 and a fluorine atom are very similar, and this may be an explanation of why there is strong Duschinsky mixing between D_{19} and D_{20}. Also, as the mass difference between the two substituents increases for an asymmetric disubstitution, D_{18} and D_{19} evolve into localized motions containing symmetric and asymmetric stretches, respectively, each involving the substituents, both being of a' symmetry (in the C_s point group).[15] In the present case, this is exhibited as the mixing between the D_{18} and D_{19} modes, for which the localization of the motion is not complete, and the extent of this varies between the electronic states (see Fig. 4). We now compare and contrast the activity in the 2D-LIF and ZEKE spectra seen when exciting via the 18^1, X^1, and Y^1 levels.

The initial interpretation of the 2D-LIF spectrum (Fig. 2) is that D_Y in the S_1 state is dominated by S_0 D_{20} character, with a sizable contribution from D_{19} and a smaller one from D_{18}; furthermore, D_X has the largest contribution from D_{19} but with large contributions from D_{18} and (to a lesser extent) D_{20}. We can also see that D_{18} in the S_1 state has a significant contribution from S_0 D_{19}. These conclusions are largely in line with the calculated S_0/S_1 Duschinsky matrix (Fig. 4).

If we now look at the ZEKE spectra in Fig. 3, then we would reach a different conclusion in that exciting via Y^1 gives the largest contribution from $^+D_{19}$ (i.e., the D_{19} vibration in the cation) with a significant contribution from $^+D_{20}$, while exciting via X^1 gives the largest contribution from $^+D_{20}$, with a significant contribution from $^+D_{19}$. Again, these conclusions are in line with the calculated S_1/D_0^+ Duschinsky matrix—see Fig. 4. As a consequence, at first sight, it seems that the conclusions from the 2D-LIF and ZEKE spectra are

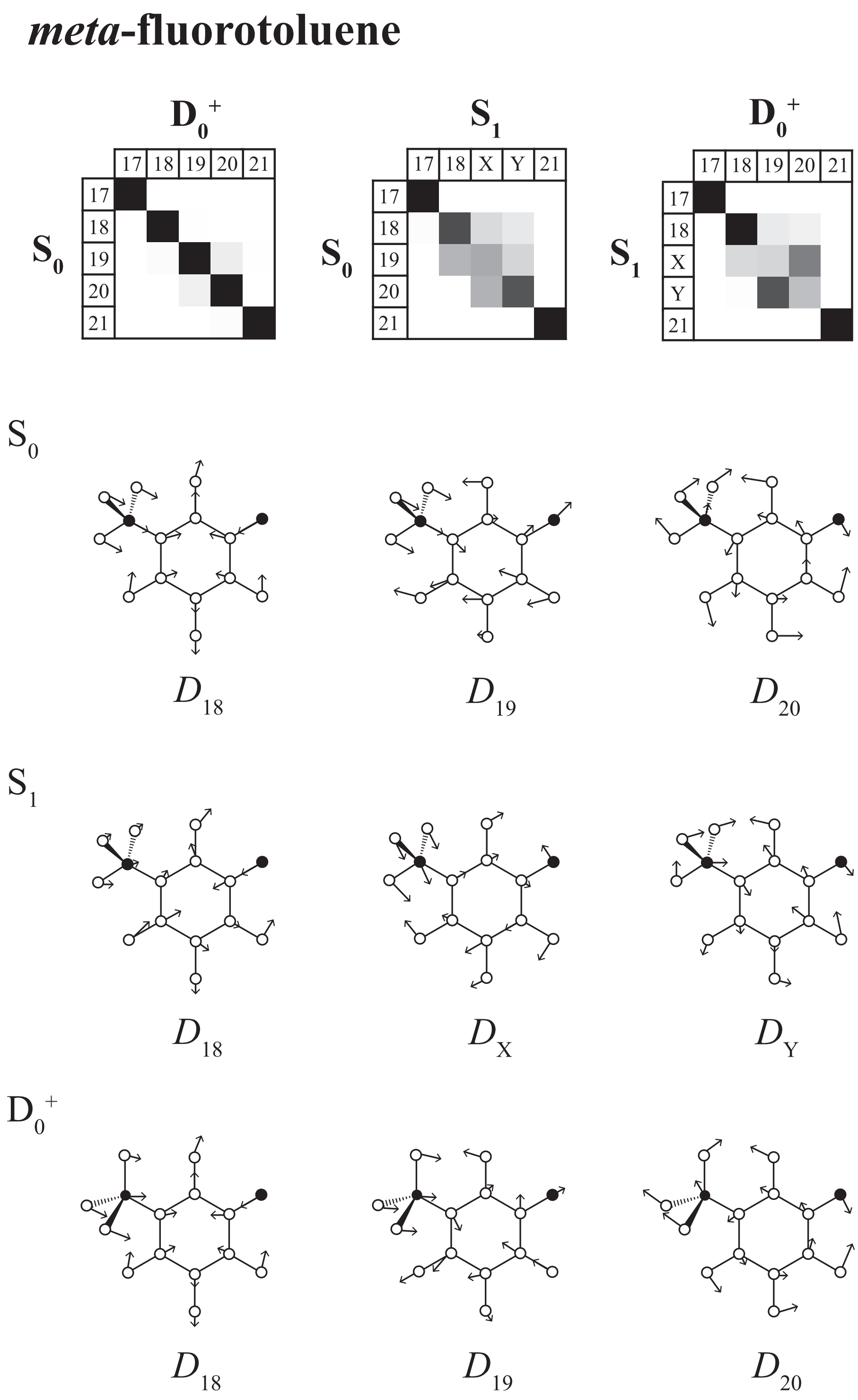

FIG. 4. *Top*. Duschinsky matrices for selected vibrations of *m*FT for combinations of the S_0, S_1, and D_0^+ electronic states. The depth of gray shading represents the coefficients of the mixing between the vibrations in the two electronic states, with white representing 0 and black representing 1. *Bottom*. Calculated mode diagrams for the three vibrations corresponding to D_{18}, D_{19}, and D_{20} in the three different electronic states. See text for further discussion.

contradictory with regard to the make-up of the D_X and D_Y S_1 vibrations. This must arise from the small, but notable, differences in the motions of the D_{18}, D_{19}, and D_{20} vibrations in the S_0 and D_0^+ electronic states, which cause the expression of the S_1 motions as admixtures of these vibrations in the different electronic states to differ. In addition, the Franck–Condon factors between the vibrations and associated vibtor levels will differ for the $S_1 \rightarrow S_0$ and $D_0^+ \leftarrow S_1$ transitions, depending on the main geometry changes between the respective pair of electronic states. These have been discussed previously[6,7] for *m*FT and *m*ClT, where the changes are very similar. Notably, for *m*FT, both C–CH$_3$ and C–F bond lengths increase significantly during the S$_1$ → S$_0$ transition; however, the C–CH$_3$ bond length is almost unchanged during the $D_0^+ \leftarrow S_1$ ionization, while the C–F bond shortens. Also, a shortening of all ring C–C bond lengths occurs during the S$_1$ → S$_0$ transition, while there is an asymmetric change in those bond lengths during the $D_0^+ \leftarrow S_1$ ionization. These are consistent with the 18^1, X^1, and Y^1 activity seen during the S$_1$ ← S$_0$ and S$_1$ → S$_0$ transitions (Figs. 1 and 2, respectively) and the activity of $^+18^1$ in the ZEKE spectra via the vibrationless m^0 and m^1 levels (see Ref. 6).

We now consider the calculated motions of these three vibrations. Looking first at D_{18} and D_{19} (Fig. 4), we see motions in the S$_0$ and D_0^+ states that have significant in-phase C–CH$_3$ and C–F stretches for D_{18}, but these are out-of-phase for D_{19}; moreover, the motions of the other atoms are very similar for these states. For D_{18} in the S$_1$ state, although the motion of the methyl group and of some of the ring carbon atoms is different than that of the other two electronic states, it is dominated by the in-phase C–CH$_3$ and C–F stretches: this is our justification for employing the same vibrational label. Similarly, for D_{20} in the S$_0$ and D_0^+ states, the motion can be identified by the in-phase, in-plane bending of the C–CH$_3$ and C–F bonds. However, in the S$_1$ state, the motions of two of the vibrations, the ones labeled X and Y, can be seen to be significant mixtures of the motions of the D_{19} and D_{20} vibrations. In particular, the motions of the C–CH$_3$ and C–F bonds for D_X and D_Y are similar to those of D_{19} and D_{20}, respectively, while the motions of the carbon atoms in the aromatic rings for D_X and D_Y largely resemble D_{20} and D_{19}, respectively. Thus, different aspects of the D_X and D_Y motions resemble different parts of the D_{19} and D_{20} vibrations. This shows that the D_{19} and D_{20} motions have indeed become mixed in S$_1$, in line with the Duschinsky matrices (Fig. 4), and this is reflected in the activity in the 2D-LIF and ZEKE spectra (Figs. 2 and 3). Of course, each entry in the Duschinsky matrix is a distillation of the comparisons of all angular and radial displacements between two vibrations; nonetheless, even though the subtleties of the different changes are not necessarily evident, the entry is expected to reflect the most important geometry changes for a particular electronic transition. This case shows that, in fact, the Duschinsky matrix does give a good qualitative picture of the observed spectral activity, although, for very mixed vibrations, caution is merited in the interpretation of the matrix in establishing how vibrations of one electronic state map onto another. Clearly, for the S$_1$ → S$_0$ emission, it is the motions of the C–CH$_3$ and C–F bonds that dominate the overlap of the S$_1$ D_X and D_Y vibrations with the S$_0$ D_{19} and D_{20} ones; while for the $D_0^+ \leftarrow S_1$ ionization, the relative motions of the carbon atoms in the aromatic ring are more important in determining the activity.

Summarizing, we conclude that the D_{18}, D_X, and D_Y vibrations are heavily mixed in the S$_1$ state, with the D_{19} and D_{20} contributions to X^1 and Y^1, each, being particularly significant; however, when distilled into Duschinsky matrix entries, these are different when expressed in terms of the S$_1$ or D_0^+ vibrations, but in agreement with the observed vibrational activity.

D. ZEKE spectra of *m*ClT

The ZEKE spectra of *m*ClT were recorded when exciting at various positions in the region indicated in the expanded view in the bottom half of Fig. 1. These spectra are shown in Fig. 5, for the $m = 0$ and $m = 1$ components, respectively; note that the 19^1m^1 and 20^1m^0 transitions overlap, and so the spectrum recorded for these overlapped features is included in both the upper and lower portions of the figure, each shifted to be on the correct relative wavenumber scale. The S_0/D_0^+ Duschinsky matrix shown in Fig. 6 indicates that although the D_{18}, D_{19}, and D_{20} vibrations of the D_0^+ state are mixed versions of the corresponding S$_0$ ones, there is sufficient dominant character to employ the same labels for both states, notably with respect to the motions of the C–CH$_3$ and C–Cl bonds. With regard to the aromatic ring carbon atoms, although the motions are not precisely the same in the S$_1$ state as the other two states, they are largely correspondent with that expected for the D_{19} or D_{20} vibrations, and this gives a more diagonal Duschinsky matrix, allowing the same vibrational labels to be used in the three states. Although the 2D-LIF spectrum was not recorded, the S$_0$/S$_1$ Duschinsky matrix indicates that there would likely be significant cross-activity between the 19_1 and 20_1 emissions, but with 18_1 being largely pure.

For *m*ClT, the ZEKE spectra recorded via 19^1m^0 and 19^1m^1 are relatively clean, with activity associated almost exclusively with this mode, with only small contributions from $^+21^1$ when exciting via 19^1m^0 and $^+30^2$ when exciting via 19^1m^1 (the $^+30^1m^2$ contribution, seen when exciting via 19^1m^1, is consistent with the observation of this band when exciting via m^1, see Refs. 7 and 14). We observe that the wavenumber of $^+21^1m^0$ is very close to that of $^+m^5$; however, the latter is symmetry forbidden when exciting via 19^1m^0 (although we have discussed previously[6] the possible activity of $^+m^5$ when exciting via m^0 for *m*FT in terms of a possible deviation away from the G_6 MSG, we currently favor the $^+21^1m^0$ assignment here). On the other hand, it is clear that there is significant cross-activity between 18^1 and 20^1, although this is much clearer when exciting via the $m = 0$ components: for the $m = 1$ components, the spectra are less clean and there are severely overlapped features (see Fig. 5). In particular, 20^1m^0 is overlapped by 19^1m^1 for the ^{35}Cl isotopologue, as is evident from the REMPI spectra of the ^{35}Cl and ^{37}Cl isotopologues, Fig. 1 (bottom trace). It can also be seen from Fig. 1 that 20^1m^1 for the ^{35}Cl isotopologue is overlapped by 20^1m^0 for the ^{37}Cl isotopologue, but we cannot see definitive evidence for the latter in the ZEKE spectra. No attempts were made to record the ZEKE spectra via 20^1m^1 for the ^{37}Cl isotopologue.

We comment that the activity seen in the ZEKE spectra when exciting via 19^1m^0 and 19^1m^1 is similar to that observed[7] via the pure torsional levels, m^0 and m^1, although the $^+19^1m^x$ bands are relatively more intense here, as expected. We highlight that no evidence was seen for the $^+18^1m^x$ bands observed via the pure torsional levels;[7] additionally, there was a similar lack of $^+20^1m^x$ band activity. This suggests that the D_{19} vibration in the cation has a motion very similar to that of the S$_1$ state, which is largely supported by the Duschinsky matrix shown in Fig. 6. In contrast, when exciting via 18^1m^0 and 18^1m^1, bands attributable to both $^+18^1m^x$ and $^+20^1m^x$ are present, which is in line with the Duschinsky matrix. That said, the activity of $^+18^1m^x$ bands when exciting via 20^1m^1 is less clear, although there is plausible evidence for the presence of a $^+18^1m^{3(+)}$ band when exciting via 20^1m^0. Since some of the $^+19^1m^x$ and $^+20^1m^x$ bands are very close in wavenumber, it is possible that $^+19^1m^x$ bands are hidden, but these are not expected, according to the Duschinsky matrix. Concomitantly, when exciting via 20^1m^0 and 20^1m^1, both

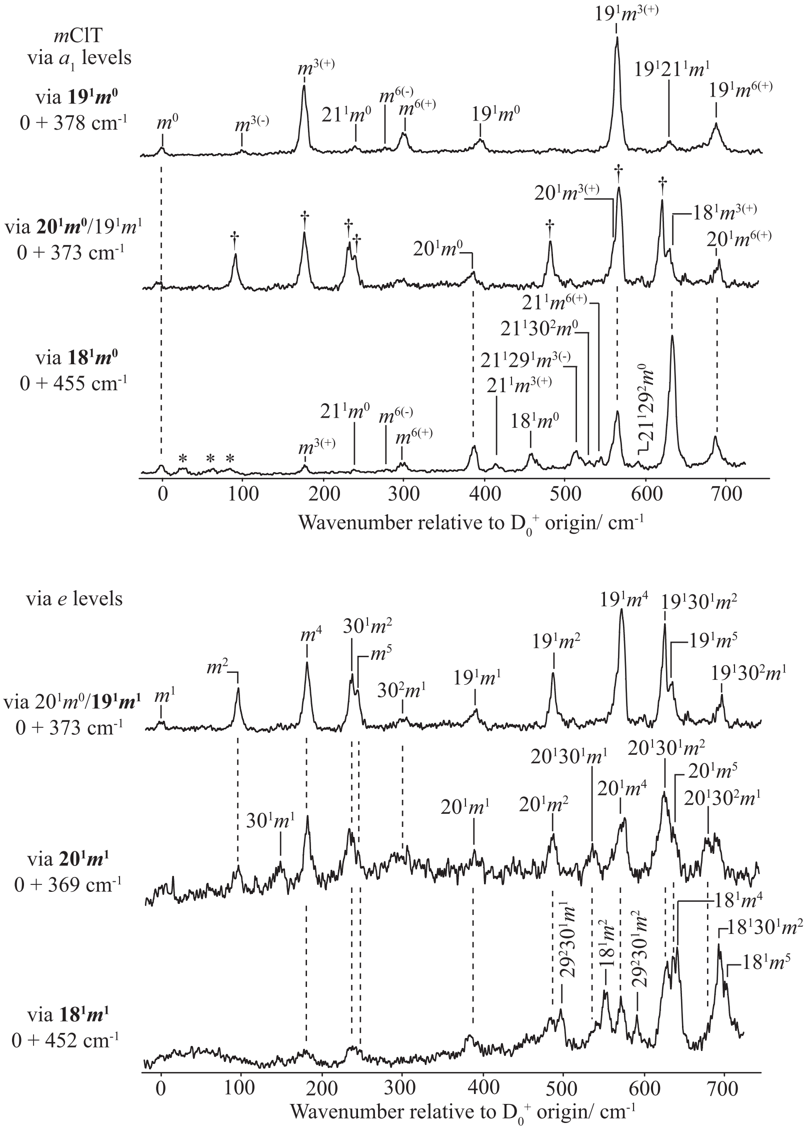

FIG. 5. ZEKE spectra of *m*ClT recorded at different $S_1 \leftarrow S_0$ excitation positions, separated into $m = 0$ and $m = 1$ components. For clarity, the preceding superscripted "+" used in the text is omitted from the transition labels. Since the 19^1m^1 and 20^1m^0 transitions are overlapping, the corresponding ZEKE spectrum has been included in both parts of the figure; the bold label indicates the pertinent level for that part of the figure. We have added obeli (†) to bands that arise from the overlapping transition and which are labeled on the duplicate trace. The low-wavenumber bands marked with asterisks (*) are spurious. The relative energy scales are given with respect to the $^+m^0$ and $^+m^1$ transitions; in absolute terms, the $^+m^1$ transition is ~5 cm^{-1} lower in wavenumber, owing to the $m_1 \leftarrow m_0$ spacing in the S_0 state.

$^+18^1m^x$ and $^+20^1m^x$ activities are present. The implication is that the D_{18} and D_{20} vibrations undergo Duschinsky mixing between the S_1 state and the cation, in line with the presented S_1/D_0^+ Duschinsky matrix.

From Fig. 1, the 20^1m^0 transition is expected to be largely coincident with the 19^1m^1 transition for the ^{35}Cl isotopologue. The strongest ZEKE band expected from 20^1m^0 is $^+20^1m^{3(+)}$; this can be seen as a shoulder on the lower wavenumber side of the $^+19^1m^4$ band in Fig. 5, providing evidence for this overlap. Similarly, the 19^1m^0 band for the ^{37}Cl isotopologue is mostly overlapping the same band for the ^{35}Cl isotopologue; however, since we do not expect significant isotopic shifts for the $^+19^1m^x$ bands, there is not expected to be any obvious evidence for this overlap, and indeed, none is seen. We also note that the 20^1m^0 band for the ^{37}Cl isotopologue is expected to coincide with the 20^1m^1 band for the ^{35}Cl isotopologue, and there is a slight broadening of the main $^+20^1m^4$ band, but this is merely consistent with the $^+20^1m^{3(+)}$ activity from the ^{37}Cl isotopologue, rather than being definitive.

Comparing the motions of the three vibrations shown in Figs. 4 and 6, it is clear that, in the S_0 and D_0^+ states, the C–CH$_3$ and C–Cl stretches have become more localized for *m*ClT, as per the discussion given in Ref. 15, see the forms of the D_{18} and D_{19} modes; however, there is more bending motion of the methyl group in D_{19} of *m*ClT caused by the more pronounced asymmetry in mass in the molecule.

In summary, between the S_1 and D_0^+ states for *m*ClT, the corresponding Duschinsky matrix suggests that all three of the D_{18}, D_{19}, and D_{20} states undergo a small amount of Duschinsky

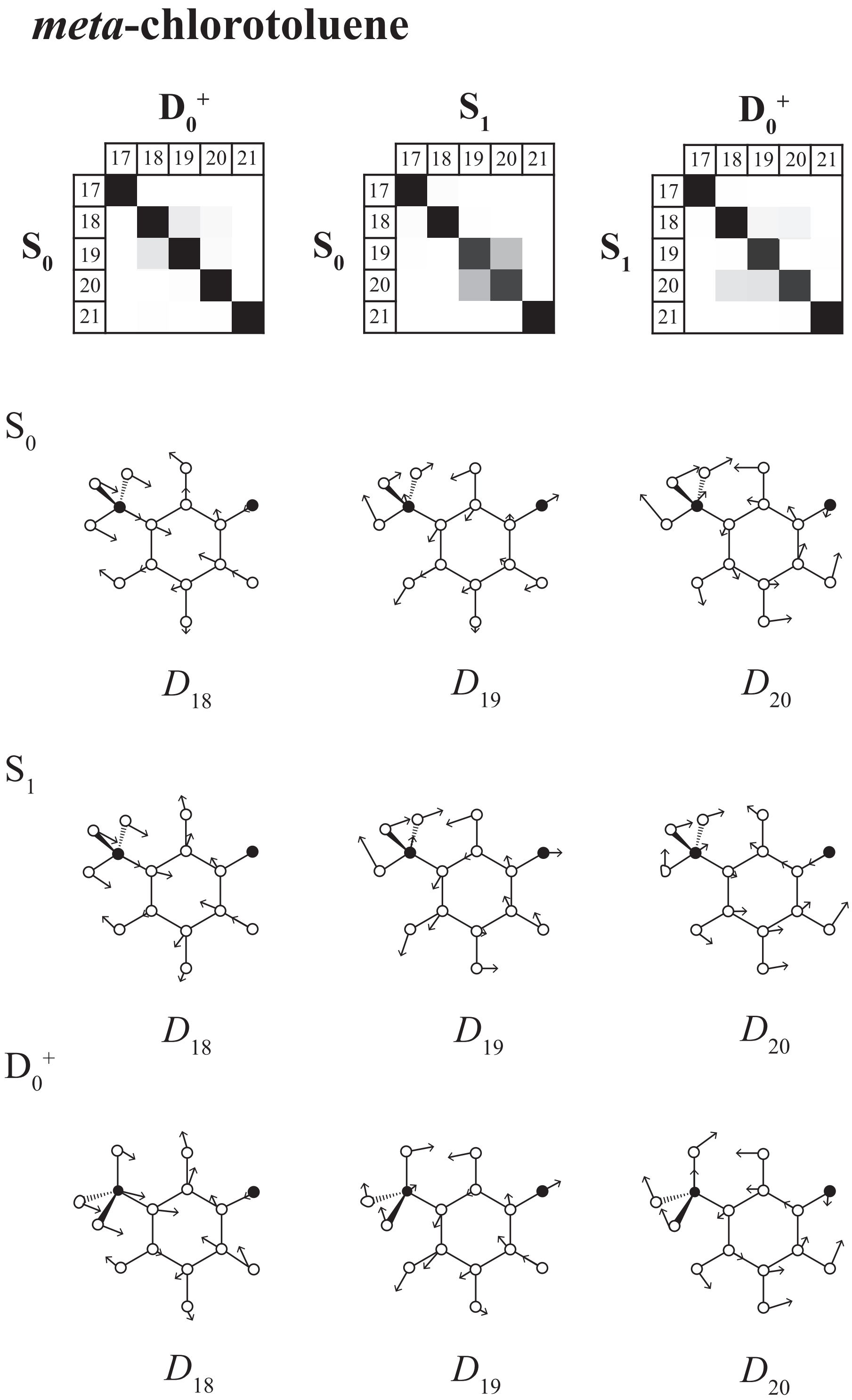

FIG. 6. *Top*. Duschinsky matrices for *m*ClT between combinations of the S_0, S_1, and D_0^+ electronic states. The depth of gray shading represents the coefficients of the mixing between the vibrations in the two electronic states, with white representing 0 and black representing 1. *Bottom*. Calculated mode diagrams for the three vibrations corresponding to D_{18}, D_{19}, and D_{20} in the three different electronic states. See text for further discussion.

mixing so that activity in each of the three modes is expected in the cation, whichever is excited, and this will, of course, apply to both of the $m = 0$ and $m = 1$ components. The spectra recorded when exciting via $18^1m^{0,1}$ do support a greater mixing between D_{18} and D_{20}. The spectra recorded when exciting via $19^1m^{0,1}$ appear to show little evidence of activity involving the other two vibrations, while those recorded via $20^1m^{0,1}$ suffer from significant overlap, but do not exclude involvement of activity of the other two vibrations. Hence, these observations are only qualitatively in line with the Duschinsky matrices. Overall, however, the situation for *m*ClT appears to be clearer cut than for *m*FT. We note our discussion of the geometry changes for *m*FT in Sec. III C, which complicates the expected vibrational activity and which also applies, but to a more limited extent, to *m*ClT. We highlight the consistency between the molecules with the activity of 18^1, 19^1, and 20^1 in the $S_1 \leftarrow S_0$ excitation (Fig. 1). Furthermore, we saw the activity of both $^{+}18^1$ and $^{+}19^1$ when exciting via the vibrationless m^0 and m^1 levels,[7] which is expected from the anticipated changes in bond lengths; note that only $^{+}18^1$ was active in the case of *m*FT,[6] again illustrating activity differences between two very similar molecules.

IV. FURTHER DISCUSSION

A. Duschinsky rotation

The assumed linear and orthogonal relationship between the vibrations of different electronic states[5] is only an approximation,[26] and neither of these conditions strictly holds; moreover, when the geometries of the electronic states differ from each other, axis switching can occur,[27] which can further complicate the matter. On top of this, the entries in a Duschinsky matrix are a single number summarizing all of the changes in angular and radial motions of the bonds between two electronic states. If the vibrational motions are largely similar, the diagonal entries will be the largest. If some of the vibrations become very mixed, significant off-diagonal elements will be present, but still the diagonal elements would be expected to be the largest. The case is unusual here in that some off-diagonal elements are the largest for particular vibrations. Normally, this would suggest a misassignment of the vibrational labels; however, here, these labels have been established from the S_0/D_0^+ Duschinsky matrix. Hence, we interpret these large off-diagonal elements as reflecting particular aspects of the geometry changes that occur as a result of the electronic excitation. In such a scenario, as happens here for *m*FT, there is no longer a clear 1:1 correspondence between the vibrations in the S_1 state and the other two states. This is, indeed, largely borne out by the calculated matrices and the experimental observations as discussed in the present work, with the strong mixing between the D_{19} and D_{20} modes for *m*FT being the most notable and that between D_{18} and D_{20} being significant for *m*ClT.

Different Duschinsky mixings between the molecules will arise from the slightly different motions of the vibrations, owing to the different masses of the halogen atoms in the two cases, plus slightly different electronic effects caused by the different electronegativities of the halogen atoms, and the different overlap of the halogen orbitals with the aromatic π system. For *m*FT, the motions of two of the S_1 vibrations become strong mixtures of the S_0 (and D_0^+) vibrations, preventing the same labels being used; although the mixing is also significant for *m*ClT, the motions are similar enough to employ the same labels. These changes in motions are reflected in the activity in the ZEKE spectra and, for *m*FT, also in the 2D-LIF spectra.

B. Vibtor coupling and torsional potential changes

TABLE III. Separations of vibtor levels built on different vibrations for *m*FT (cm^{-1}).

	Vibrational level[a,b]			
Torsion[c]	$^{+}0^0$ [0]	$^{+}18^1$ [510]	$^{+}19^1$ [415]	$^{+}20^1$ [456]
$^{+}m^{0,1}$	0	0	0	0
$^{+}m^2$	101	100 (610)	94 (509)	102 (558)
$^{+}m^{3(-)}$	103	102 (612)		
$^{+}m^{3(+)}$	185	184 (694)	172 (587)	187 (643)
$^{+}m^4$	192	193 (703)	181 (596)	195 (651)
$^{+}m^5$	250	250 (760)	235 (650)	254 (710)
$^{+}m^{6(-)}$	292	292 (802)		294 (750)
$^{+}m^{6(+)}$	311	312 (822)	293 (708)	312 (768)
$^{+}m^7$	368	370 (880)		

[a] Torsional spacings are given with respect to the band position of the $m = 0$ level of the indicated vibration.

[b] Values in square brackets in the column headers are the wavenumbers of the $m = 0$ level of the indicated vibration.

[c] The $^{+}m^0$ and $^{+}m^1$ levels are degenerate at our resolution. Levels with $m \neq 3n$ have degenerate + and − levels.

In Tables III and IV, we give the wavenumbers of the different vibtor transitions in the cation for *m*FT and *m*ClT, respectively, and the separation of each of these levels from the $m = 0$ level of each vibration. Previously,[6,7] we have discussed the fact that the torsional potential of the out-of-plane D_{30} vibration and its first overtone in the cation is altered compared to the pure torsional potential for both *m*FT and *m*ClT, while the potentials for the observed in-plane (totally symmetric) vibrations were not affected. Here, we find that the vibtor spacings of the cation involving the in-plane D_{19} vibration are reduced compared to those of the pure torsional levels (Table IV), suggesting that the torsional barrier experienced during this vibration is lower, while some of those involving D_{20} are largely

TABLE IV. Separations of vibtor levels built on different vibrations for *m*ClT (cm^{-1}).

	Vibrational level[a,b]			
Torsion[c]	$^{+}0^0$ [0]	$^{+}18^1$ [457]	$^{+}19^1$ [396]	$^{+}20^1$ [387]
$^{+}m^{0,1}$	0	0	0	0
$^{+}m^2$	98	97 (555)	94 (490)	105 (492)
$^{+}m^{3(-)}$	98			
$^{+}m^{3(+)}$	175	177 (633)	171 (563)	182 (569)
$^{+}m^4$	186	186 (642)	177 (573)	193 (584)
$^{+}m^5$	246	248 (704)	240 (636)	254 (641)
$^{+}m^{6(-)}$	284	278 (734)	272 (668)	
$^{+}m^{6(+)}$	300	300 (756)	294 (690)	300 (687)
$^{+}m^7$	363			

[a] Torsional spacings are given with respect to the band position of the $m = 0$ level of the indicated vibration. The values in parentheses are the actual band position with respect to $^{+}m^0$.

[b] Values in square brackets in the column headers are the wavenumbers of the $m = 0$ level of the indicated vibration.

[c] The $^{+}m^0$ and $^{+}m^1$ levels are degenerate at our resolution. Levels with $m \neq 3n$ have degenerate + and − levels.

unaltered. However, it is difficult to rationalize, from the vibrational motions shown in Figs. 4 and 6, why the CH_3 torsional barrier is particularly sensitive to the D_{19} vibrational motion in the cation, and this may reflect a more complicated explanation in terms of electronic- and vibration-induced steric interactions.

V. CONCLUSIONS

In this work, we have focused on the activity and character of three vibrations for the closely related molecules, *m*FT and *m*ClT. In particular, we examined the change in the character of a subset of the vibrations upon electronic excitation, $S_1 \leftarrow S_0$, which was deduced via the activity not only in the ZEKE spectra but also in the 2D-LIF spectra for *m*FT. Even though the activity in the REMPI spectra was very similar for these two molecules, the details of the changing vibrational character showed that, in fact, there were significant differences in the mixings occurring as a result of electronic excitation and ionization. This could be seen from the calculated form of the vibrations, as well as the differences in the vibrational activity exhibited in the spectra. In general terms, the calculated Duschinsky matrices were in line with the observed spectral activity, even though such matrices are only expected to be approximate reflections of the vibrational character change between electronic states. Unusually, for *m*FT, if one were to deduce the correspondence between the S_1 vibrations and those in the S_0 and D_0^+ states, reverse conclusions would be reached. This was identified as being due to the motions of the carbon atoms in the aromatic ring pairing with the switched C–CH_3 and C–F bond motions in the S_1 state for two of the vibrations. Remarkably, the Duschinsky matrices picked up the subtlety of the different electronic transitions affecting different geometric aspects of the molecule and, in a qualitative way, correctly predicted the switched intensities of the transitions involving the D_{19} and D_{20} vibrations. We conclude that Duschinsky matrices, even though they are a rather coarse distillation of all of the changes in atomic motions between electronic states, are actually very sensitive to the aspects of the geometry that are most affected by the electronic transition.

Understanding such changes in detail, via assignment of vibrational structure as a result of electronic excitation and photoionization, is clearly key to understanding the photo-physico-chemical behavior.

ACKNOWLEDGMENTS

The authors are grateful to the EPSRC for funding (Grant No. EP/L021366/1). L.G.W. is grateful for an Undergraduate Summer Bursary funded via a University of Nottingham School of Chemistry 1960 scholarship. The EPSRC and the University of Nottingham are thanked for providing studentships to D.J.K. and A.R.D.

DATA AVAILABILITY

The data that support the findings of this study are available from the corresponding author upon reasonable request.

REFERENCES

[1] D. J. Nesbitt and R. W. Field, J. Phys. Chem. **100**, 12735 (1996).

[2] G. M. Roberts and V. G. Stavros, in *Ultrafast Phenomena in Molecular Sciences*, edited by R. de Balda and L. Bañares (Springer, Dordrecht, 2014).

[3] Y. He, C. Wu, and W. Kong, J. Phys. Chem. A **107**, 5145 (2003).

[4] C. S. Byskov, F. Jensen, T. J. D. Jørgensen, and S. B. Nielsen, Phys. Chem. Chem. Phys. **16**, 15831 (2014).

[5] F. Duschinsky, Acta Physicochim. URSS **7**, 551 (1937).

[6] D. J. Kemp, E. F. Fryer, A. R. Davies, and T. G. Wright, J. Chem. Phys. **151**, 084311 (2019).

[7] D. J. Kemp, L. G. Warner, and T. G. Wright, J. Chem. Phys. **152**, 064303 (2020).

[8] L. D. Stewart, J. R. Gascooke, and W. D. Lawrance, J. Chem. Phys. **150**, 174303 (2019).

[9] K. Okuyama, N. Mikami, and M. Ito, J. Phys. Chem. **89**, 5617 (1985).

[10] K. Takazawa, M. Fujii, T. Ebata, and M. Ito, Chem. Phys. Lett. **189**, 592 (1992).

[11] M. Ito, K. Takazawa, and M. Fujii, J. Mol. Struct. **292**, 9 (1993).

[12] K. Takazawa, M. Fujii, and M. Ito, J. Chem. Phys. **99**, 3205 (1993).

[13] T. Ichimura, A. Kawana, T. Suzuki, T. Ebata, and N. Mikami, J. Photochem. Photobiol., A **80**, 145 (1994).

[14] S. H. Feldgus, M. J. Schroeder, R. A. Walker, W.-K. Woo, and J. C. Weisshaar, Int. J. Mass Spectrom. Ion Processes **159**, 231 (1996).

[15] D. J. Kemp, W. D. Tuttle, F. M. S. Jones, A. M. Gardner, A. Andrejeva, J. C. A. Wakefield, and T. G. Wright, J. Mol. Spectrosc. **346**, 46 (2018).

[16] V. L. Ayles, C. J. Hammond, D. E. Bergeron, O. J. Richards, and T. G. Wright, J. Chem. Phys. **126**, 244304 (2007).

[17] A. M. Gardner, W. D. Tuttle, L. E. Whalley, and T. G. Wright, Chem. Sci. **9**, 2270 (2018).

[18] N. J. Reilly, T. W. Schmidt, and S. H. Kable, J. Phys. Chem. A **110**, 12355 (2006).

[19] J. R. Gascooke and W. D. Lawrance, Eur. Phys. J. D **71**, 287 (2017).

[20] E. B. Wilson, Jr., Phys. Rev. **45**, 706 (1934).

[21] G. Varsányi, *Assignments of the Vibrational Spectra of Seven Hundred Benzene Derivatives* (Wiley, New York, 1974).

[22] R. S. Mulliken, J. Chem. Phys. **23**, 1997 (1955).

[23] G. Herzberg, *Molecular Spectra and Molecular Structure II. Infrared and Raman Spectra of Polyatomic Molecules* (Krieger, Malabar, 1991).

[24] A. M. Gardner, W. D. Tuttle, P. Groner, and T. G. Wright, J. Chem. Phys. **146**, 124308 (2017).

[25] I. Pugliesi and K. Müller-Dethlefs, J. Phys. Chem. A **110**, 4657 (2006), A free download of the software can be found at http://www.fclab2.net.

[26] See, for example G. M. Sando and K. G. Spears, J. Phys. Chem. A **105**, 5326 (2001).

[27] J. T. Hougen and J. K. G. Watson, Can. J. Phys. **43**, 298 (1965).

8. Methyl-torsion-facilitated internal energy delocalization following electronic excitation in *m*-fluorotoluene: can *meta* and *para* substitution be directly compared?

Abstract: “Coupling between vibrations, and between vibrations and torsions—a generalization of intramolecular vibrational redistribution (IVR)—provides routes to internal energy delocalization, which can stabilize molecules following photoexcitation. Following earlier work on *p*-fluorotoluene (*p*FT), this study focuses on *m*-fluorotoluene (*m*FT) as probed *via* the $S_1 \leftrightarrow S_0$ electronic transitions and the $D_0^+ \leftarrow S_1$ ionization, using two-dimensional laser-induced fluorescence and zero-electron-kinetic energy spectroscopy, respectively. Wavenumbers are reported for a number of vibrations in the S_0, S_1, and D_0^+ states and found to compare well to those calculated. In addition, features are seen in the *m*FT spectra, not commented on in previous studies, which can be assigned to transitions involving vibration–torsion (“vibtor”) levels. Comparisons to the previous work on both *m*-difluorobenzene and *m*FT are also made, and some earlier assignments are revised. At lower wavenumbers, well-defined interactions between vibrational and vibtor levels are deduced—termed “restricted IVR,” while at higher wavenumbers, such interactions evolve into more-complicated interactions, moving toward the “statistical IVR” regime. It is then concluded that a comparison between *m*FT and *p*FT is less straightforward than implied in earlier studies.”

Authors: Alexander R. Davies, David J. Kemp and Timothy G. Wright.

Submitted: to AIP Advances, 6th October 2020.
Published: 1st December 2020
Reference: A. R. Davies, D. J. Kemp and T. G. Wright, *AIP Adv.*, 2020, **10**, 125206.
DOI: 10.1063/5.0032146

Summary: Here, we investigate further the $S_1 \leftarrow S_0$ transition of *m*FT, assisted by 2D-LIF and ZEKE spectroscopy. The activity in the ZEKE and 2D-LIF spectra is assigned and discussed, for all major bands $\lesssim$1350 cm^{-1} above the S_1 origin (with a notable exception, see Section 9), drawing comparisons to the activity of *m*DFB. Notably, the complexity of the spectra associated with several bands at intermediate internal energy is discussed. It is hypothesised that there is a Fermi resonance between two states, accessible through the $m = 0$ component, causing one of these eigenstates to overlap with the $m = 1$ component of the vibration, explaining the appearance of structure arising from both $m = 0$ and $m = 1$ components in the ZEKE and 2D-LIF spectra. This complicates the interpretation of what, *prima facie*, should be a relatively simple pair of bands. Owing to the number of spectra presented over a wide range of internal energies in S_1, we are able to show the build-up of IVR, from no such evidence in the case of the origin, through Fermi resonances at intermediate energies, to widespread IVR by ~950 cm^{-1} above the S_1 origin. We also use the results of quantum chemical calculations to present density-of-states (DoS) plots, which supports this build-up of IVR, to assist the discussion of how symmetry effects and the methyl rotor can accelerate this, while also drawing comparisons to both *m*DFB and *p*FT as well. Comparing the spectra presented herein to those of previous work on *p*FT, we conclude that, despite these two molecules being isomers, their spectra and activity are noticeably different, likely due to the forms of the vibrational modes being different, and caution that it is not so straightforward to draw direct comparisons between the build-up of IVR of molecules in different isomeric classes.

Contributions: The spectra were recorded by both myself and DJK, with the exception of the REMPI spectrum of *m*DFB, which is an historical spectrum recorded by AMG and WDT, who were previous members of the group. The analysis was conducted by both myself and TGW independently, cross-checking for consistency and to discuss ideas/assignments. All the data was processed, with all figures created by myself, with input from TGW and DJK. Additionally, I read and commented on multiple iterations of the manuscript, and discussed and implemented the reviewers’ comments to form the final version of the text.

AIP Advances ARTICLE scitation.org/journal/adv

Methyl-torsion-facilitated internal energy delocalization following electronic excitation in *m*-fluorotoluene: Can *meta* and *para* substitution be directly compared?

Cite as: AIP Advances 10, 125206 (2020); doi: 10.1063/5.0032146
Submitted: 6 October 2020 • Accepted: 10 November 2020 •
Published Online: 1 December 2020

Alexander R. Davies, David J. Kemp, and Timothy G. Wright[a)]

AFFILIATIONS

School of Chemistry, University of Nottingham, University Park, Nottingham NG7 2RD, United Kingdom

[a)] Author to whom correspondence should be addressed: Tim.Wright@nottingham.ac.uk

ABSTRACT

Coupling between vibrations, and between vibrations and torsions—a generalization of intramolecular vibrational redistribution (IVR)—provides routes to internal energy delocalization, which can stabilize molecules following photoexcitation. Following earlier work on *p*-fluorotoluene (*p*FT), this study focuses on *m*-fluorotoluene (*m*FT) as probed via the $S_1 \leftrightarrow S_0$ electronic transitions and the $D_0^+ \leftarrow S_1$ ionization, using two-dimensional laser-induced fluorescence and zero-electron-kinetic energy spectroscopy, respectively. Wavenumbers are reported for a number of vibrations in the S_0, S_1, and D_0^+ states and found to compare well to those calculated. In addition, features are seen in the *m*FT spectra, not commented on in previous studies, which can be assigned to transitions involving vibration–torsion ("vibtor") levels. Comparisons to the previous work on both *m*-difluorobenzene and *m*FT are also made, and some earlier assignments are revised. At lower wavenumbers, well-defined interactions between vibrational and vibtor levels are deduced—termed "restricted IVR," while at higher wavenumbers, such interactions evolve into more-complicated interactions, moving toward the "statistical IVR" regime. It is then concluded that a comparison between *m*FT and *p*FT is less straightforward than implied in earlier studies.

I. INTRODUCTION

Anharmonic coupling in molecules leads to delocalization, and so dispersal, of internal energy within a molecule—an important aspect to enhanced photostability.[1–4] Which of the vibrations in a molecule can couple, and to what extent, depends on a number of factors, but having the same symmetry and being close in energy are two key considerations,[1] along with the relative motions of the atoms in those vibrations. Such coupling leads to actual vibrational motions having mixed character, and this can be discerned through an analysis of the vibrational activity in electronic and photoelectron spectra, where vibrational eigenfunctions of one electronic state are projected onto those of another. To first order, vibrational fundamentals do not couple anharmonically, but sometimes activity in fundamentals other than that excited can be seen in experimental spectra. This can be caused by changes in geometry that lead to significant Franck–Condon factors (FCFs), or as a result of Duschinsky rotations.[5]

Methylation in biomolecules has been invoked as a key factor in photoinduced carcinogenicity,[6] and consequently, an understanding of the role of methyl groups in the modification of a molecule's photobehavior is of key importance. Parmenter and coworkers have published numerous studies on the effect of methylation on intramolecular vibrational redistribution (IVR), with the most pertinent study here being that of Timbers *et al.*[7] In that work, it was concluded that *m*-fluorotoluene (*m*FT) undergoes intramolecular vibrational redistribution (IVR) more than an order of magnitude faster than *p*-fluorotoluene (*p*FT) and, hence, that the location of substituents is important in internal energy delocalization.

Recently, we published resonance-enhanced multiphoton ionization (REMPI) and zero-electron-kinetic-energy

(ZEKE) studies of the low-wavenumber regions of *m*FT[8] and *m*-chlorotoluene (*m*ClT),[9] which mainly focused on torsions and some vibration–torsion (vibtor) levels. The *m*FT study complemented the two-dimensional laser-induced fluorescence (2D-LIF) study of Stewart *et al.*,[10] who examined the first 350 cm^{-1} of the $S_1 \leftarrow S_0$ transition and the first 550 cm^{-1} of the $S_1 \rightarrow S_0$ transition via a mixture of LIF, dispersed fluorescence (DF), and 2D-LIF. In these studies, the spectra were assigned in terms of transitions involving torsional, vibtor, and vibrational levels in the S_0 and S_1 states. Earlier, Ito and co-workers[11–14] reported laser-induced fluorescence (LIF), DF, REMPI, and ZEKE spectra of the low-wavenumber region of *m*FT. Very recently, we compared the activity of three Duschinsky-mixed vibrations for *m*FT and *m*ClT, using a combination of 2D-LIF and ZEKE spectroscopy, finding that the spectra were exquisitely sensitive to small changes in molecular mass and electronic structure.[15]

Previously, we have studied the *p*FT molecule using REMPI, ZEKE, and 2D-LIF spectroscopy, showing how IVR evolves through the restricted to statistical regimes. It was seen that this is not a smooth evolution and that the methyl group plays a key role in this. We were able to identify key interactions and energy delocalization routes.[16–23]

In the present work, we extend our studies to the $S_1 \leftarrow S_0$ spectrum of *m*FT in the range 0 cm^{-1}–1350 cm^{-1} above the origin, using 2D-LIF, REMPI, and ZEKE spectroscopy. This encompasses a number of fundamental, overtone, combination, and vibtor levels. As with *p*FT, it is found that there is again an evolution from interactions between small numbers of levels, termed restricted IVR, at low wavenumber to widespread interactions, approaching statistical IVR, at higher wavenumbers. We identify specific interactions and derive wavenumbers for a number of vibrations across the S_0, S_1, and $D_0{}^+$ electronic states.

Over several years, our group has been examining the spectroscopy of fluoro-substituted and methyl-substituted benzene molecules. In doing so, we have examined the vibrational labeling of these molecules, putting forward general schemes for the ring-based vibrations of monosubstituted benzene molecules[24] and for each of the three isomeric classes of disubstituted benzene molecules.[25–27] These schemes were developed since neither Wilson[28]/Varsányi[29] nor Mulliken[30]/Herzberg[31] notations are appropriate. Indeed, separate schemes were required for these four classes of substituted benzene molecules, since the forms of the vibrations differ substantially between them. This implies that the comparison of vibrational activity between classes of substituted benzene molecules poses difficulties; however, the schemes do allow for direct comparison within each isomeric class. These labeling schemes are based on monofluorobenzene and difluorobenzene molecules, with consistent labels across both symmetric and asymmetric substitutions in the latter cases. They have allowed vibrational activity to be compared across spectra of *p*-difluorobenzene (*p*DFB), *p*-chlorofluorobenzene (*p*ClFB), *p*FT, and *p*-xylene (*p*Xyl)—see Refs. 17 and 32—although these ideas flow through our recent work across these molecules.

In the present case, a comparison will be made between the previously published detailed laser fluorescence study of *m*-difluorobenzene (*m*DFB)[33] and *m*FT, for which we expect the vibrational activity to be similar if the same vibrational numbering scheme is used—as will be seen, this expectation is largely borne out. Of course, the spectrum of *m*FT will be complicated by the contributions from torsion and vibtor levels, as noted above.

II. EXPERIMENTAL

The REMPI/ZEKE[34] and 2D-LIF[18] apparatuses are the same as those employed recently. In both experiments for *m*FT, a free-jet expansion of *m*FT (Sigma-Aldrich, 99% purity) in 2 bar Ar was employed.

For the 2D-LIF spectra, the free-jet expansion was intersected at $X/D \sim 20$ by the frequency-doubled output of a single dye laser (Sirah Cobra-Stretch), operating with Coumarin 503 and pumped with the third harmonic of a Surelite III Nd:YAG laser. The fluorescence was collected, collimated, and focused onto the entrance slits of a 1.5 m Czerny–Turner spectrometer (Sciencetech 9150) operating in single-pass mode, dispersed by a 3600 groove/mm grating, allowing ~300 cm^{-1} windows of the dispersed fluorescence to be collected by a CCD camera (Andor iStar DH334T). At a fixed grating angle of the spectrometer, the excitation laser was scanned, and at each excitation wavenumber, the camera image was accumulated for 2000 laser shots. This allowed a plot to be produced of fluorescence intensity vs both the excitation laser wavenumber and the wavenumber of the emitted and dispersed fluorescence, termed a 2D-LIF spectrum.[35,36] Band positions for the 2D-LIF spectra are given for the estimated band center.

For the REMPI and ZEKE spectra of *m*FT, the focused, frequency-doubled outputs of two dye lasers (Sirah Cobra-Stretch) were overlapped spatially and temporally and passed through a vacuum chamber coaxially and counterpropagating, where they intersected the free-jet expansion. The excitation laser was operated with Coumarin 503 and pumped with the third harmonic (355 nm) of a Surelite III Nd:YAG laser, while the ionization laser was operated with Pyrromethene 597 and pumped with the second harmonic (532 nm) of a Surelite I Nd:YAG laser. The jet expansion passed between two biased electrical grids located in the extraction region of a time-of-flight mass spectrometer, which was employed in the REMPI experiments. These grids were also used in the ZEKE experiments by application of pulsed voltages, giving typical fields of ~10 V cm^{-1}, after a delay of up to 2 μs; this delay was minimized while avoiding the introduction of excess noise from the prompt electron signal. The resulting ZEKE bands had widths of ~5 cm^{-1}–7 cm^{-1}. Electron and ion signals were recorded on separate sets of microchannel plates. Band positions for REMPI and ZEKE bands are given for the maximum, and ZEKE spectra were generally obtained when exciting through the intermediate band maximum.

For the REMPI spectrum of *m*DFB, a free-jet expansion of *m*DFB (Sigma-Aldrich, 99% purity) in 5 bar Ar was employed.

III. RESULTS AND ASSIGNMENTS

A. Nomenclature and labeling

1. Vibrational and torsional labeling

We shall employ the D_i labels[27] for the *m*FT vibrations, as used in Refs. 8–10; this C_s point group labeling scheme is based on the vibrations of the *m*DFB molecule. As such, we shall transcribe the Wilson/Varsányi labels in Ref. 11 and the C_{2v} Mulliken labels used in Ref. 33 for *m*DFB to the D_i labels for the purposes of comparison with the present work. These, and the available experimental vibrational wavenumbers for *m*DFB, are presented in Table I, alongside the calculated wavenumbers—the calculated and experimental S_0 values are generally taken from Ref. 27 (some of which were deduced from Refs. 33 and 37), while the experimental values for the S_1 state were obtained from Ref. 33, with the calculated values for this electronic state being obtained in the present work.

TABLE I. Calculated and experimental wavenumbers (cm^{-1}) for the vibrations of *m*-difluorobenzene.

	S_0		S_1	
D_i (C_{2v})[a]	Calculated[b]	Expt.[c]	Calculated[d]	Expt.[e]
	a_1			
D_1 (1)	3122	3095		
D_2 (2)	3116	3086		
D_3 (21)	3112	3086		
D_4 (3)	3090			
D_5 (4)	1597	1611	1529	(1519)
D_6 (22)	1592	1613	1480	
D_7 (23)	1475	1490	1375	
D_8 (5)	1439	1435	1378	(1346)
D_9 (24)	1304	1337	1435	
D_{10} (6)	1255	1277	1250	
D_{11} (25)	1252	1292[f]	1228	1267[f]
D_{12} (26)	1145	1157	1118	1145
D_{13} (27)	1102	1120	1094	(1206)
D_{14} (7)	1058	1068	995	998
D_{15} (8)	994	1012	958	966
D_{16} (28)	941	956	883	936
D_{17} (9)	726	739	698	701
D_{18} (10)	514	522	438	442
D_{19} (29)	502	513	440	444
D_{20} (30)	467	477	462	468
D_{21} (11)	320	329	315	317
	a_2			
D_{22} (15)	963	957	719	(581)
D_{23} (12)	871	876	724	672
D_{24} (16)	856	857	362	480
D_{25} (17)	767	771	502	(479)
D_{26} (18)	671	680	457	422
D_{27} (13)	597	603	406	369
D_{28} (19)	455	454	241	260
D_{29} (14)	239	252	196	176
D_{30} (20)	222	227	98	127

[a] The D_i labels are described in Ref. 27, where the vibration mode diagrams can also be found. The values in parentheses are the Mulliken C_{2v} numbers used in Ref. 33 with 1–11 being a_1, 12–14 being a_2, 15–20 being b_1, and 21–30 being b_2.

[b] B3LYP/aug-cc-pVTZ, scaled by 0.97.[27]

[c] Taken from Ref. 27, where the selection and assignments are discussed; some of the values originate from Ref. 33. For D_{10}, we have reverted to the original liquid-phase value,[37] since we deduce that the reassignment of D_{11} in Ref. 33 is likely incorrect.

[d] TD-B3LYP/aug-cc-pVTZ, scaled by 0.97. Present work.

[e] Taken from Ref. 33; values in parentheses are those about which the authors of that work were less certain.

[f] Reassigned in the present work.

Since we shall also be referring to the methyl torsional motion for *m*FT, for which use of the G_6 molecular symmetry group (MSG) is appropriate, we shall employ those symmetry labels throughout. The torsional levels will be labeled via their m quantum number,[8,10] and the correspondence between the C_s point group labels and the G_6 MSG labels is given in Table II. To calculate the overall symmetry of a vibtor level, it is necessary to use the corresponding G_6 label for the vibration and then find the direct product with the symmetry of the torsion (Table II), noting that a C_{3v} point group direct product table can be used, since the G_6 MSG and the C_{3v} point group are isomorphic. The torsional levels in *m*FT are labeled with the signed quantum number m ($m = 0, 1, 2, \ldots$). The $m = 0$ level is singly degenerate, while levels with $|m| \neq 3n$ ($n = 1, 2, \ldots$) are doubly degenerate, consisting of +/− pairs, and levels with $m = 3n$ form linear combinations of the +/− pairs that split in energy under the influence of the torsional potential; these are labeled $m = 3(+)$ and $m = 3(-)$.[8]

Under the free-jet expansion conditions employed here, almost all molecules are expected to be cooled to their zero-point vibrational level, and thus essentially, all $\mathrm{S}_1 \leftarrow \mathrm{S}_0$ excitations are expected to originate from this level. In contrast, owing to nuclear-spin and rotational symmetry, the *m*FT molecules can be in one of the $m = 0$ or $m = 1$ torsional levels, with approximately equal population in each;[38] residual population in the $m = 2$ level is also seen.[8–10]

The available experimental vibrational wavenumbers for *m*FT are presented in Table III, alongside the calculated wavenumbers—the experimental S_0 values are generally taken from Ref. 27, while the experimental values for the S_1 state were obtained from Refs. 8 and 10 and the present work; the calculated S_0 and S_1 values are obtained in the present work and generally agree well with those presented in Ref. 10. The experimental values for the D_0^+ state are from Ref. 8 and the present work, while the calculated values are from the present work.

The level of theory employed is given in the footnotes of Tables I and III, and Gaussian 16[39] was used for all of these calculations.

2. Coupling and transitions

In the usual way, vibrational transitions will be indicated by the number, i, of the D_i vibration, followed by a superscript/subscript specifying the number of quanta in the upper/lower states, respectively. When required, torsional transitions will be indicated by m

TABLE II. Correspondence of the C_s point group symmetry classes with those of the G_6 molecular symmetry group. Also indicated are the symmetries of the D_i vibrations and the different pure torsional levels.[a]

C_s	G_6	D_i[b]	m
a'	a_1	D_1–D_{21}	0, 3(+), 6(+), 9(+)
a''	a_2	D_{22}–D_{30}	3(−), 6(−), 9(−)
	e		1, 2, 4, 5, 7, 8

[a] Symmetries of vibtor levels can be obtained by combining the vibrational symmetry (in G_6) with those of the pure torsional level, using the C_{3v} point group direct product table.

[b] The D_i labels are described in Ref. 27, where the vibration mode diagrams can also be found.

TABLE III. Calculated and experimental wavenumbers (cm^{-1}) for the vibrations of *m*-fluorotoluene.

	S_0		S_1		D_0^+	
D_i[a]	Calculated[b]	Expt.[c]	Calculated[d]	Expt.[e]	Calculated[f]	Expt.[g]
a_1						
D_1	3107	[3081]	3128		3119	
D_2	3088	[3060]	3114		3107	
D_3	3086		3123		3111	
D_4	3072		3084		3092	
D_5	1578	[1595]	1512		1541	1569
D_6	1603	[1623]	1494		1490	
D_7	1479	[1492]	1392		1444	
D_8	1420	[1460]	1363		1385	
D_9	1302	[1295] 1294	1411		1356	
D_{10}	1239	[1251] 1254	1243		1299	1290
D_{11}	1271	[1266] 1271	1252	1260	1258	1275
D_{12}	1148	[1160] 1132	1122	[h]	1143	
D_{13}	1126	[1143] 1115	1113	[h]	1101	
D_{14}	1071	[1079] 1081	1023		1074	
D_{15}	988	[1003] 1004	958	965	997	984
D_{16}	912	[924] 930	866	840	873	874
D_{17}	720	[728] 731	685	684	700	710
D_{18}	519	[527] 525	459	460	509	510
$D_{19(X)}$	505	[513] 512	448	457	410	415
$D_{20(Y)}$	435	[450] 445	410	420	442	456
D_{21}	285	[296] 294	281	285	290	298
a_2						
D_{22}	967	[970]	760		988	
D_{23}	886	[886]	705		916	
D_{24}	859	[858]	501		855	
D_{25}	773	[778] 775	575		787	780
D_{26}	683	[683]	468		592	592
D_{27}	557	[556] 554	377	367	514	517
D_{28}	443	[442] 441	241	253	373	380
D_{29}	236	[243] 237	184	174	190	190
D_{30}	199	[212] 201	122	128	167	169

[a] Labels are discussed in Ref. 27, where mode diagrams are presented. For D_{19} and D_{20}, the motions are very mixed in the S_1 state, as discussed in Ref. 15, and are denoted D_X and D_Y, respectively.

[b] B3LYP/aug-cc-pVTZ, scaled by 0.97. Present work—essentially the same as the values published in Ref. 10, which employed the same quantum chemical method.

[c] The values in square brackets are IR/Raman values that have been discussed in Ref. 27. Updates to some of these values have been made in gas-phase studies: Ref. 15 and the present work, in some cases confirming a value reported in Ref. 10.

[d] TD-B3LYP/aug-cc-pVTZ, scaled by 0.97. Present work—these values are close to the TD-B3LYP/cc-pVTZ values presented in Ref. 10, but several of the values do seem to be sensitive to the addition of diffuse functions to the basis set.

[e] Gas-phase values taken from Refs. 8 and 15 and the present work, in some cases confirming a value reported in Ref. 10.

[f] UB3LYP/aug-cc-pVTZ, scaled by 0.97; $\langle S^2 \rangle = 0.76$. Present work.

[g] Values taken from Refs. 8 and 15 and the present work.

[h] Experimental values for these two vibrations were reported in Ref. 11 but have been concluded to have been misassigned,[10] and we concur with this conclusion.[43].

followed by its superscripted value, and vibtor transitions will be indicated by a combination of the vibrational and torsional transition labels. When designating transitions, we shall generally omit the initial level, since it will be evident from either the jet-cooled conditions or the specified intermediate level.

As has become common usage, we will generally refer to a level using the notation of a transition, with the level indicated by the specified quantum numbers, with superscripts indicating levels in the S_1 state and subscripts indicating levels in the S_0 state. Since we will also be referring to transitions and levels involving the ground state cation, D_0^+, we shall indicate those as superscripts, but with a single, additional, preceding superscripted "+" sign. Relative wavenumbers of the levels will be given with respect to the relevant zero-point vibrational level with $m = 0$, in each electronic state.

For cases where the geometry and the torsional potential are both similar in the S_1 and D_0^+ states, the most intense transition is usually expected to be that for which no changes in the torsional and/or vibrational quantum numbers occur, designated as $\Delta m = 0$, $\Delta v = 0$, or $\Delta(v, m) = 0$ transitions, as appropriate. However, as will be seen (and as reported in Refs. 8, 9, 14, and 15), the $\Delta m = 0$ and $\Delta(v, m) = 0$ transitions are almost always not the most intense bands in the ZEKE spectra for *m*FT, indicative of a significant change in the torsional potential upon ionization. The intensities of low-wavenumber features in the $S_1 \leftrightarrow S_0$ transitions have been discussed in Ref. 10, and reference will be made to that work when appropriate.

If two levels are close in wavenumber and have the same overall symmetry, then (except between vibrational fundamentals, to first order) interactions can occur, with the simplest example being the anharmonic interaction between two vibrational levels—the classic Fermi resonance.[40] Such couplings are only expected to be significant for small changes in the vibrational quantum number, $\Delta v \approx 3$, and for levels that lie close in energy.[41] For molecules that contain a hindered internal rotor, such as *m*FT and *p*FT, and if vibration–torsion coupling occurs, then interactions can also involve torsional or "vibtor" levels. This is expected to be significant only for changes in the torsional quantum number, Δm, of ±3 or ±6 in descending order of likely strength.[42] The result of such interactions is the formation of eigenstates with mixed character. Often, the resulting eigenstates will be referred to by the dominant contribution, with the context implying if an admixture is present.

B. An overview of the REMPI spectrum

In Fig. 1, we show the $S_1 \leftarrow S_0$ REMPI spectrum of *m*FT over the range 0 cm^{-1}–1350 cm^{-1}. It may be seen to be rich in structure, some of which has been assigned previously.[8,10–15] We note the good agreement with the appearance of the LIF spectrum in Ref. 11, which covers a similar range. Wavenumbers of some of the S_1 vibrations are in dispute.[10] We highlight that the 0 cm^{-1}–350 cm^{-1} region has been discussed in depth in Refs. 8 and 10, and the 400 cm^{-1}–480 cm^{-1} region was the focus in Ref. 15. Also in Fig. 1, we present the corresponding REMPI spectrum of *m*DFB, which compares very well with the LIF spectrum presented in Ref. 33.

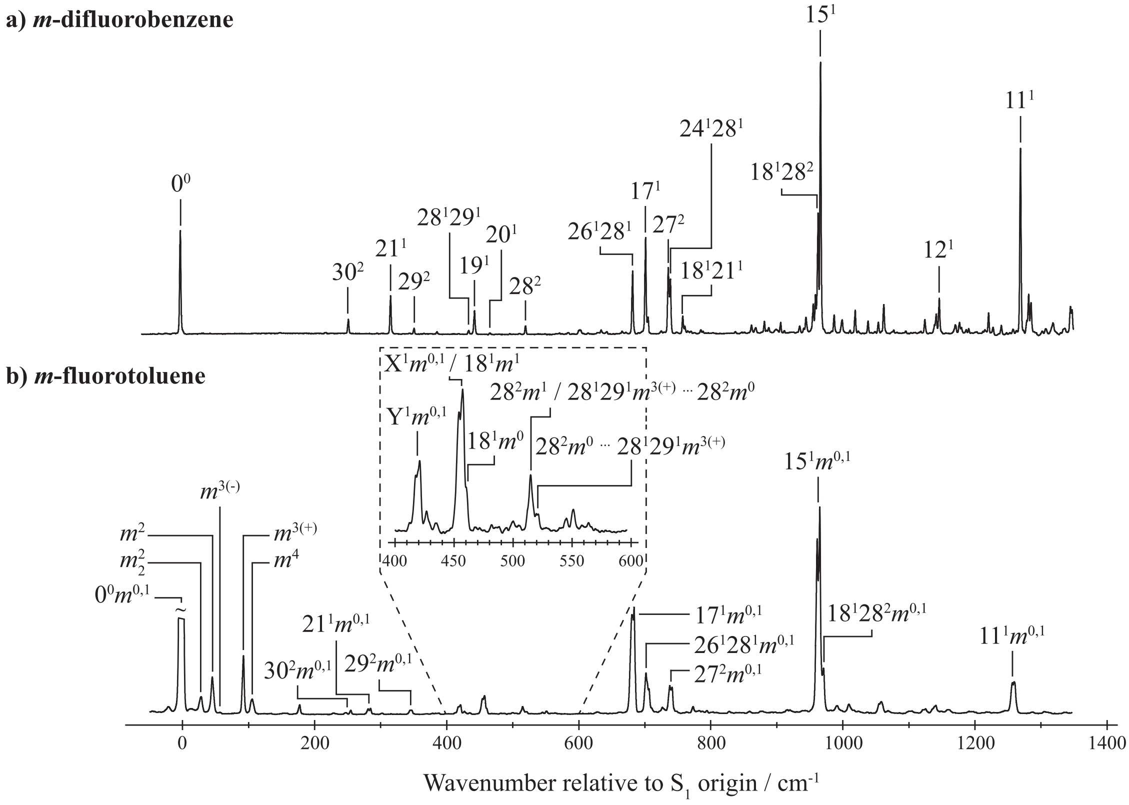

FIG. 1. Overview of the REMPI spectrum of the $S_1 \leftarrow S_0$ transition in the range 0 cm^{-1}–1350 cm^{-1} for (a) *m*DFB and (b) *m*FT. Only selected assignments are shown—see the text. For *m*FT, the origin bands, m^0 and m^1, have been truncated—see Ref. 8 for the 0 cm^{-1}–350 cm^{-1} region of the spectrum. The most intense bands in the expanded view were discussed and assigned in Ref. 15. See the text for further discussion on the assignments.

Overall, ignoring the torsional transitions for *m*FT, the correspondence between the main activity in both REMPI spectra in Fig. 1 is striking and adds confidence to the assignments for *m*FT discussed later.

A number of values and assignments in Table III are from the present work and will be discussed in Subsections III C–III G, where we break the discussion up into five main regions. Through these five regions, it will be seen that the coupling evolves from being absent, through well-defined coupling between a small number of levels at low wavenumber, into widespread coupling, approaching statistical IVR at higher wavenumbers.

In some of the figures, vertically integrated traces of the 2D-LIF spectra are presented. Each of these looks very similar to the corresponding section of the REMPI spectrum, confirming that the fluorescence collected is representative of the absorption spectrum in that region.

C. 2D-LIF and ZEKE spectra via the origin m = 0 and m = 1 levels

In Fig. 2, we show the 2D-LIF spectrum recorded when exciting through the pure torsional m^0 and m^1 excitations, and many assignments are also shown. The 0 cm^{-1}–550 cm^{-1} region of the emission spectrum has been assigned and discussed in depth by Stewart *et al.*,[10] and we concurred with those assignments in our ZEKE study.[8] In Ref. 10, only the 0 cm^{-1}–65 cm^{-1} region of the 2D-LIF spectrum via the m^0 and m^1 bands was presented, although DF spectra were presented up to 550 cm^{-1}, with full assignments. These will prove useful in assigning the 2D-LIF spectra in the present work, when we excite at higher wavenumbers.

The assignment of these vibrational bands allows S_0 vibrational wavenumbers to be established, which are included in Table III, some of which were reported by Stewart *et al.*[10] These values are close to those established by IR and Raman spectroscopy[37] and those discussed in Ref. 27, providing further confirmation of the assignments. Other features can be identified as vibtor levels associated with these vibrational transitions, and indeed, subject to sensitivity, we expect to see the main pattern of vibtor and related transitions that are observed for the origin, for each vibrational transition.

In Fig. 3, we show the ZEKE spectra recorded via both m^0 and m^1. The regions up to ∼850 cm^{-1} were assigned in Ref. 8; in the present work, the spectra are extended up to ∼1850 cm^{-1} and show more vibrational bands with their associated vibtor structure. As will be seen, these help in the assignment of other ZEKE spectra presented later. The vibrational wavenumbers arising from these spectra are also included in Table III.

D. The 410 cm^{-1}–555 cm^{-1} region

The integrated 2D-LIF trace covering this region of the $S_1 \leftarrow S_0$ excitation is shown at the top of Fig. 4. The three most intense features in this region are Y^1 and the overlapped X^1 and 18^1 bands. The S_1 D_X and D_Y vibrations are highly mixed forms of the S_0 D_{19} and D_{20} vibrations, and these assignments, alongside the Duschinsky mixing that gives rise to the mixed character, have been discussed in Ref. 15. In Fig. 4, we also show an extended 2D-LIF spectrum recorded across this region. It can be seen that numerous features can be identified in the 2D-LIF image that are not obviously associated with discrete features in the integrated 2D-LIF (nor REMPI) spectrum; this highlights one aspect of the extra information that 2D-LIF spectra provide. The assignments of many of the bands are straightforward, combining the knowledge of the torsional levels from Refs. 8 and 10 and the vibrational levels from Ref. 15, and these are indicated in the figure, with numerous features arising from Δ(v, m) = 0 transitions. However, there were also numerous cases where the assignment was less obvious, and some of these will be discussed in the following.

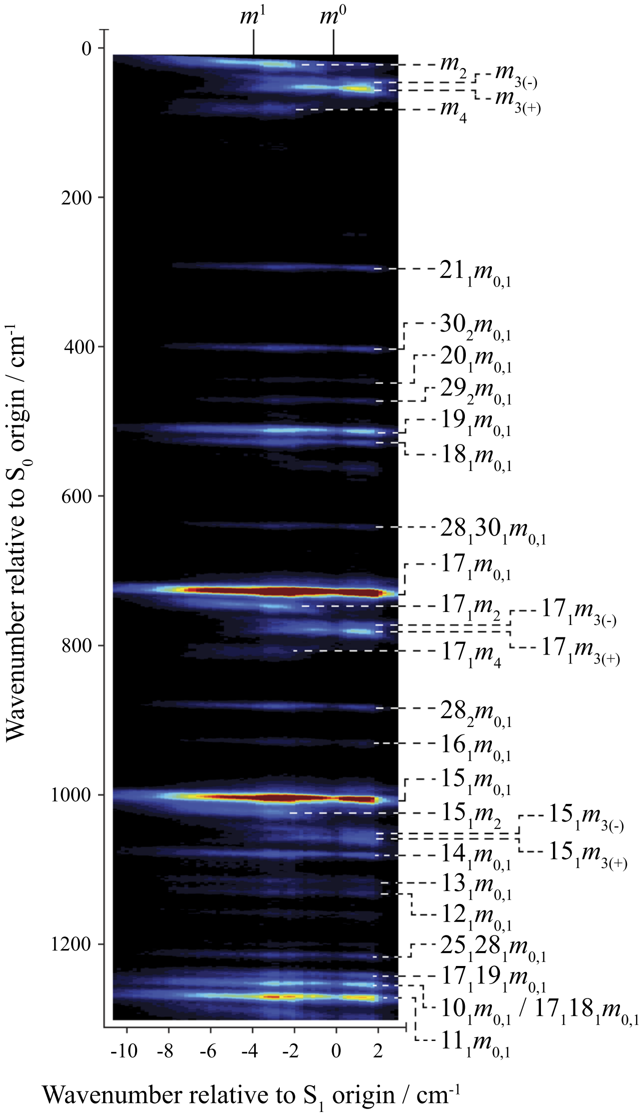

FIG. 2. 2D-LIF over the m^0 and m^1 excitation bands, showing the 0 cm^{-1}–1300 cm^{-1} emission region. Selected assignments are shown, with each main vibrational emission band being associated with a set of vibtor levels, many of which are indicated. See the text for further discussion on the assignments.

We see a 2D-LIF feature at (428, 675) cm^{-1}, whose assignment is to the Δ(v, m) = 0 band ($28^1 29^1 m^0$, $28_1 29_1 m_0$). This assignment is reached on the basis of a weak associated band in the expected

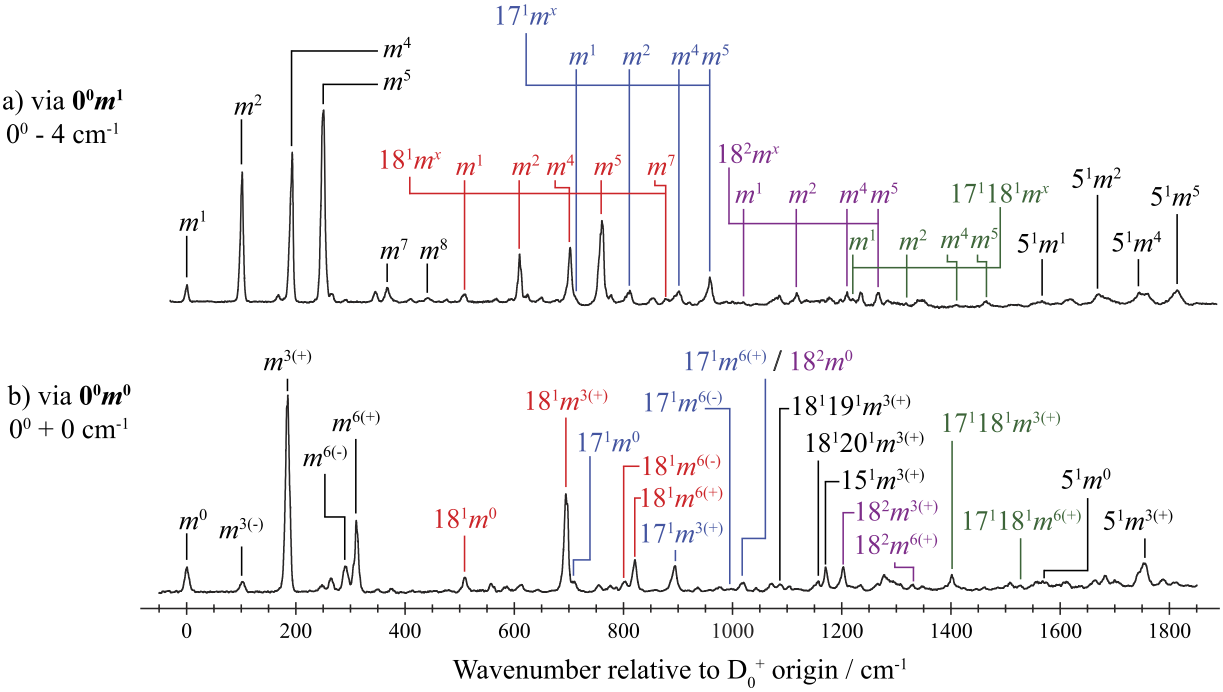

FIG. 3. ZEKE spectra via the (a) m^1 and (b) m^0 excitation bands. The preceding "+" sign used in the text is omitted from the assignments for clarity. These cover a wider range than those presented in Ref. 8, where further ZEKE spectra are shown when exciting though other torsional levels.

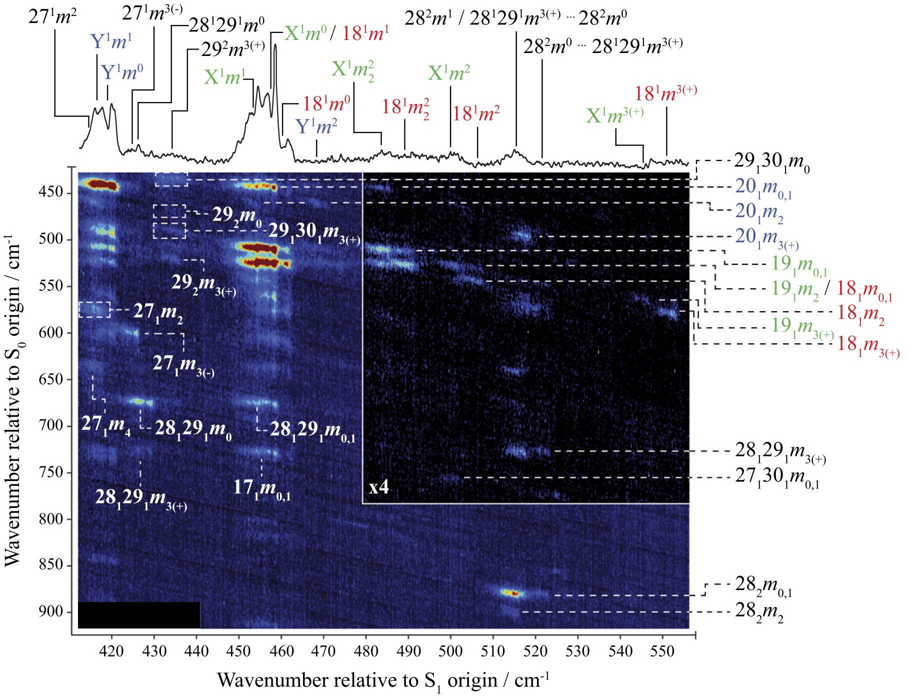

FIG. 4. 2D-LIF over the excitation range 410 cm^{-1}–555 cm^{-1}. At the top of the 2D-LIF spectrum, the trace shows the result of integrating vertically over the presented section of the 2D-LIF spectrum and closely resembles the corresponding region of the REMPI spectrum. The 415 cm^{-1}–465 cm^{-1} excitation range of the spectrum has been shown, and the main features are discussed and assigned, in Ref. 15. The majority of the vibtor structure and other 2D-LIF features whose assignments are indicated in white on the spectrum are presented here for the first time. The region between ~480 cm^{-1} and 550 cm^{-1}, as indicated, has been enhanced by 4× to highlight the weaker bands present in this region. Colored text is used for clarity. See the text for further discussion on the assignments.

position for $28_1 29_1 m_{3(+)}$ and also the ZEKE spectrum [Fig. 5(a)], which only shows the structure that is consistent with an $m = 0$ component. Furthermore, this is consistent with the observation of $28^1 29^1$ by Graham and Kable in the case of *m*DFB[33]—see Fig. 1(a).

Interestingly, there is no evidence for the corresponding ($28^1 29^1 m^1$, $28_1 29_1 m_1$) $\Delta(v, m) = 0$ band at this excitation position, and as just noted, the lack of the expected *e* symmetry bands in the ZEKE spectrum excludes the possibility of its being overlapped with the $m = 0$ component. It is interesting to note, however, that dual $m = 0$ and 1 component activity is observed for the corresponding emission when exciting at ~449 cm^{-1}–459 cm^{-1}. [This observation precludes an alternative assignment of the (428, 675) cm^{-1} band to a vibtor transition.]

Overall, this behavior is reminiscent of the fact that the ($29^1 30^1 m^1$, $29_1 30_1 m_1$) band was also observed to be very much weaker than ($29^1 30^1 m^0$, $29_1 30_1 m_0$).[10] The reason for the weakness of the transition involving $m = 1$ was not entirely clear, but the assigned ($29^1 30^1 m^1$, $29_1 30_1 m_1$) band was suggested as being significantly shifted from its expected excitation position,[10] and it was hypothesized that there could be a $29^1 30^1 m^1 \ldots m^7$ interaction, although this would be a ($\Delta v = 2$, $\Delta m = 6$) interaction, and so perhaps this is not expected to be strong. In general terms, although we do expect more widespread vibtor coupling involving *e* symmetry torsions, there is no evidence of such coupling for the $28^1 29^1 m^1$ level in the 2D-LIF spectrum, and so the absence of the $m = 1$ component is somewhat puzzling.

In Fig. 5(a), we show the ZEKE spectrum recorded when exciting at 427 cm^{-1}, which shows a strong $\Delta m = 3$ band, $^{+}28^1 29^1 m^{3(+)}$, in line with expectations when exciting through totally symmetric vibrations;[8] there are also the expected weaker $^{+}28^1 29^1 m^0$ and $^{+}28^1 29^1 m^{6(+)}$ bands. There is no clear evidence for the ZEKE bands expected to arise from ionization from $28^1 29^1 m^1$, confirming that the major contribution to the REMPI spectrum at this wavenumber is indeed $28^1 29^1 m^0$.

We also see evidence in the 2D-LIF spectrum (Fig. 4) for bands associated with excitation of $27^1 m^2$ and $27^1 m^{3(-)}$. Evidence for the former arises from observation of $27_1 m_2$ and $27_1 m_4$ emission bands at excitation positions close to 415 cm^{-1}. We speculate that the $27^1 m^2$ level is interacting weakly with $\mathrm{Y}^1 m^1$, which both have *e* symmetry; this is supported by their proximity in wavenumber, but also the extension of the emission bands underneath the $27^1 m^2$ excitation region. The $27^1 m^{3(-)}$ band is symmetry allowed [and is in line with $28^1 m^{3(-)}$ and $30^1 m^{3(-)}$ activity reported previously[8]], but this level could also be interacting with $\mathrm{Y}^1 m^0$. The latter is supported by

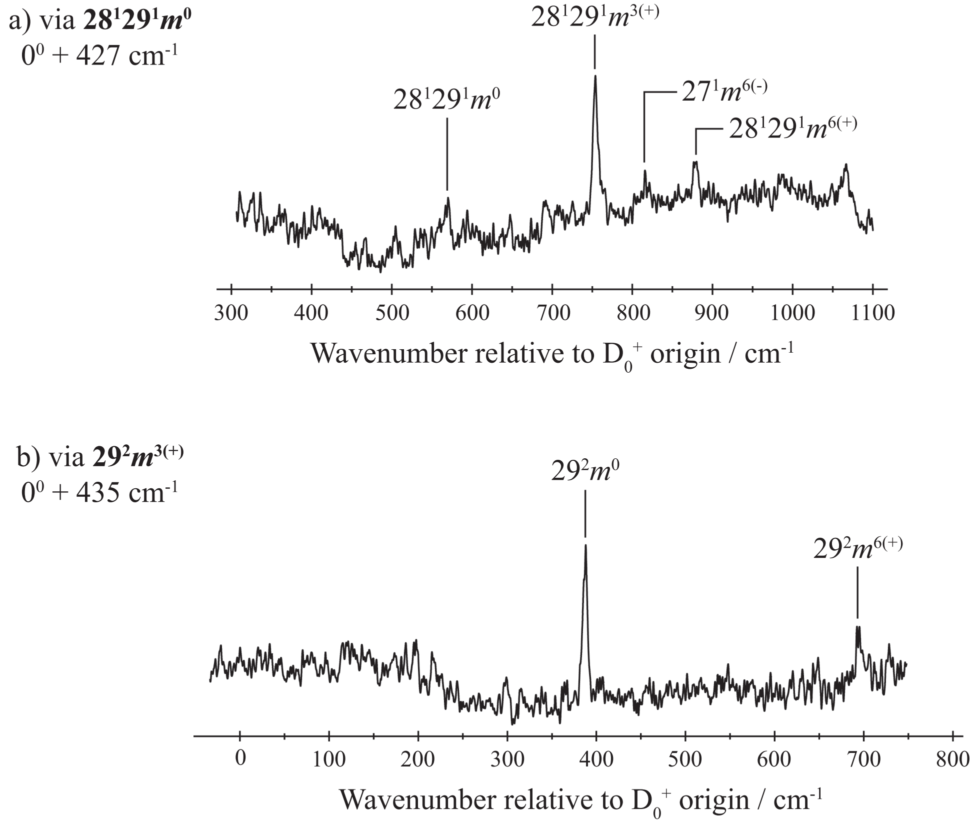

FIG. 5. ZEKE spectra recorded when exciting via the S_1 levels at (a) $0^0 + 427$ cm^{-1} and (b) $0^0 + 435$ cm^{-1}. The preceding "+" sign used in the text is omitted from the assignments for clarity. See the text.

there being $27_1m_{3(-)}$ activity also at the Y^1m^0 excitation position, and the "reverse" activity with the 20_1m_0 band extending to higher excitation wavenumbers. The width of the bands, and their limited activity, makes it difficult to ascertain whether shifts from expected band positions have occurred, which would be another signature of such an interaction.

Owing to the energetic closeness of the $27^1m^{3(-)}$ and $28^129^1m^0$ bands in the S_1 state (Fig. 4), it may be expected that when recording ZEKE spectra when exciting at $0^0 + 427\ \mathrm{cm}^{-1}$, we might also observe bands arising from excitation of $27^1m^{3(-)}$. The weak feature at 816 cm^{-1} in the ZEKE spectrum when exciting here, shown in Fig. 5(a), is at about the expected wavenumber for the $\Delta m = 3$ band, $^{+}27^1m^{6(-)}$, to which it is tentatively assigned. This is in line with the increased propensity of $\Delta m = 3$ transitions seen in the ZEKE spectra.[8] Overall, therefore, the ZEKE spectrum recorded when exciting at 427 cm^{-1} is consistent with the assignments shown in the 2D-LIF spectrum in Fig. 4 but is not definitive. In addition, even though the $27^1m^{3(-)}$ and $28^129^1m^0$ transitions overlap to some extent, no evidence of an interaction is seen.

A reasonable assignment for the weak 2D-LIF features in Fig. 4 that appear at an excitation wavenumber of 435 cm^{-1} can be proposed. This is close to the expected excitation wavenumber for $29^2m^{3(+)}$, and a ZEKE spectrum recorded at this position, see Fig. 5(b), shows bands that are assignable to $^{+}29^2m^0$ and $^{+}29^2m^{6(+)}$. In line with observations in our previous paper,[8] the $^{+}29^2m^{3(+)}$ band is expected to be weak and is not discernible in the spectrum.

The prominent feature at (514, 880) cm^{-1} in Fig. 4 is straightforwardly assignable as (28^2m^1, 28_2m_1), based on the appearance of the corresponding $m = 2$ component at (515, 899) cm^{-1}. This is consistent with the observation of 28^2 in the case of *m*DFB.[33] Accompanying the prominent band is a weaker feature at (522, 879) cm^{-1}, which can be assigned as (28^2m^0, 28_2m_0). It is initially surprising that this feature is so weak, as usually the $m = 0$ and $m = 1$ components for a vibrational band have comparable intensities, with the $m = 1$ band being slightly more intense (see Fig. 2). A clue as to the interpretation of these anomalous relative intensities comes from the ZEKE spectra, presented in Fig. 6, recorded at positions corresponding to the maxima of each of these features. The spectrum when exciting at 515 cm^{-1} is seen to be more complicated than the spectrum recorded at 520 cm^{-1}. With insight from the appearance of the ZEKE spectrum via m^1 [see Fig. 3(a)],[8] which demonstrates prominent $^{+}m^2$, $^{+}m^4$, and $^{+}m^5$ vibtor bands, and those via m^0 levels, which show prominent $^{+}m^{3(+)}$ and $^{+}m^{6(+)}$ vibtor bands [Fig. 3(b)], the bands arising from both the 28^2m^1 and 28^2m^0 levels can be straightforwardly identified. Two aspects of the spectra then become clear: first, there are bands arising from 28^2m^0 in both spectra, and second, there are other bands in the spectra. The $^{+}19^1m^1$ and $^{+}20^1m^1$ bands in the 515 cm^{-1} ZEKE spectrum, and the $^{+}21^129^1m^{3(-)}$ band in the 520 cm^{-1} spectrum, arise from Franck–Condon (FC)-like activity; however, there are some other relatively intense bands that appear in both sets of spectra. Our favored assignment of these is to $^{+}28^129^1m^x$ vibtor transitions, and their assignment suggests their source is $28^129^1m^{3(+)}$, with the $^{+}28^129^1m^{3(+)}/^{+}28^2m^0$ band being clearly seen in Fig. 6(a), but not immediately in Fig. 6(b), where its position is indicated.

The expected position of $28^129^1m^{3(+)}$ in S_1 is around 522 cm^{-1}, and this has the same symmetry, a_1, as the 28^2m^0 level, which is also expected to be close to this position; consequently, these two levels can interact. Furthermore, they differ by $\Delta v = 2$ and $\Delta m = 3$, making the suggested interaction sensible. We thus suggest a

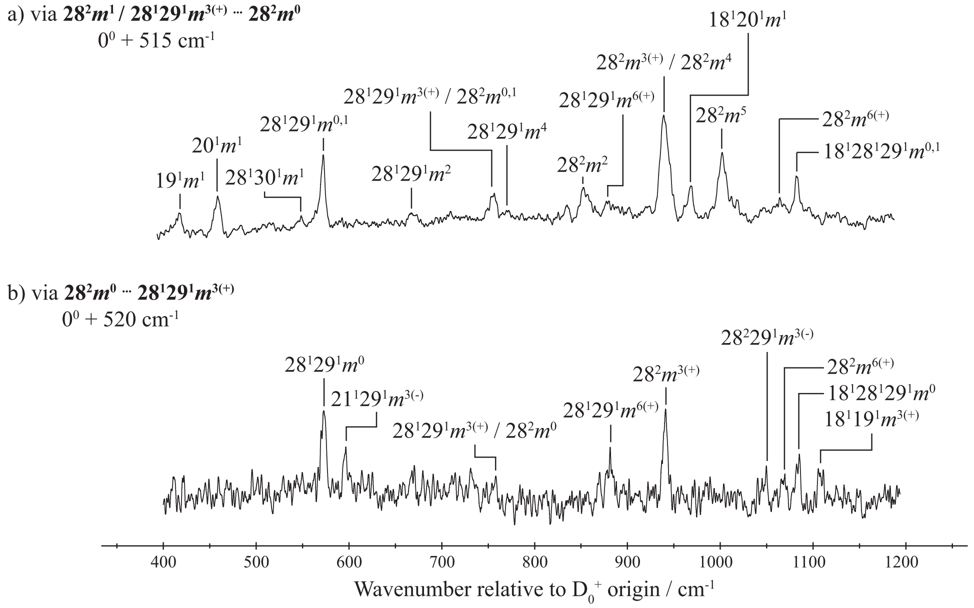

FIG. 6. ZEKE spectra of the $28^2m^{0,1}$ bands: (a) $0^0 + 515\ \mathrm{cm}^{-1}$ and (b) $0^0 + 520\ \mathrm{cm}^{-1}$. The preceding "+" sign used in the text is omitted from the assignments for clarity.

$28^2m^0\ldots28^129^1m^{3(+)}$ interaction that gives rise to two eigenstates of mixed composition. The relative intensities of the ZEKE bands suggest that the $28^2m^0\ldots28^129^1m^{3(+)}$ state (note that the leading term implies the dominant contribution to the eigenstate) gives rise to the higher, ~520 cm^{-1}, feature, while the $28^129^1m^{3(+)}\ldots28^2m^0$ eigenstate gives the lower feature; its transition is overlapped with that of 28^2m^1 at ~515 cm^{-1}, explaining the more-complicated structure in the ZEKE spectrum recorded at that position, Fig. 6(a).

This assignment is also consistent with the appearance of the 2D-LIF spectrum (Fig. 4), where the $28_129_1m_{3(+)}$ emission band has intensity across the 513 cm^{-1}–523 cm^{-1} region, consistent with the proposed interaction. We note the coincidence in the wavenumber of 17_1 and $28_129_1m_{3(+)}$, which makes the interpretation of the 2D-LIF spectrum less straightforward initially, but we accept the $28_129_1m_{3(+)}$ assignment based upon the ZEKE spectra and the $28_2m_{0,1}$ band profiles.

E. The 670 cm^{-1}–750 cm^{-1} region

The region of the REMPI spectrum of *m*FT between 670 cm^{-1} and 750 cm^{-1} can be seen to consist of three main features (Fig. 1), with the lowest wavenumber of these excitation bands being assigned to 17^1 (designated 1^1 by Okuyama *et al.*[11]). The other two features were assigned to 12^1 and 13^1 (designated $9b^1$ and $18b^1$ by Okuyama *et al.*[11]), but these two assignments have been questioned by Stewart *et al.*[10] When comparing to the *m*DFB spectrum (see Fig. 1), it can be seen that similar activity is seen, with Graham and Kable[33] having assigned these four main features to 26^128^1, 17^1, 27^2 and an overlapped feature consisting of 24^128^1 and 25^128^1. In a future paper,[43] we shall examine the two higher-wavenumber features in this region of the *m*FT spectrum in more detail, but for the purposes of the present work, we concentrate on the lowest wavenumber feature.

The integrated 2D-LIF trace is shown at the top of Fig. 7(c), which closely resembles the corresponding section of the REMPI spectrum. This excitation feature is assigned to the two *m* components of the 17^1 transition, in agreement with the assignment of Okuyama *et al.*[11] and consistent with the *m*DFB spectrum[33] (Fig. 1). Both the 2D-LIF spectrum [Fig. 7(c)] and the ZEKE spectra [Fig. 7(b)] support the 17^1m^1 and 17^1m^0 assignments; however, there are significant additional features in both spectra. Furthermore, although, when the 2D-LIF spectrum is examined, the strongest emission does indeed correspond to the two *m* components of 17_1, it is clear that the 17_1m_0 emission band is more intense

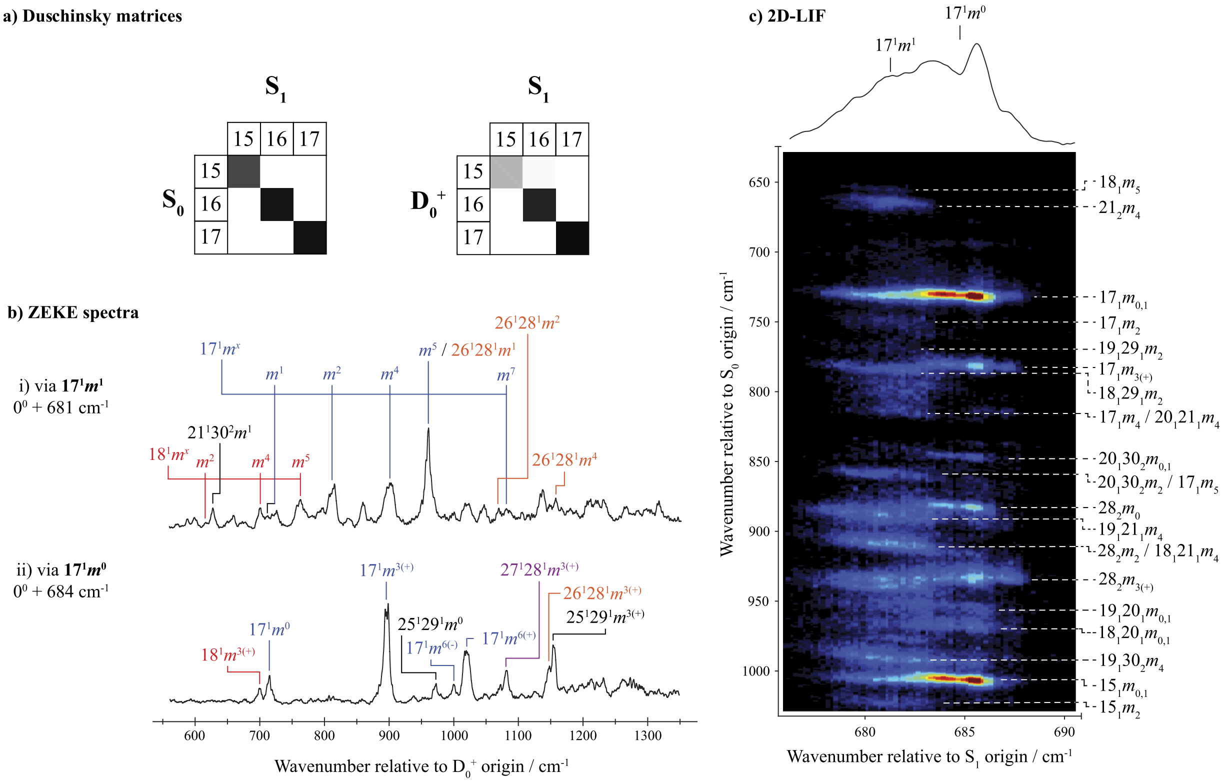

FIG. 7. (a) Duschinsky matrices showing the character of selected vibrations between excitation and ionization. The depth of shading represents the coefficients of mixing between vibrations in the two electronic states, between 0 (white) and 1 (black). (b) ZEKE spectra recorded at 0^0 + 681 and 0^0 + 684 cm^{-1}, which correspond to the m^1 and m^0 components of 17^1, respectively. The preceding "+" sign used in the text is omitted from the assignments for clarity. (c) 2D-LIF over the excitation range 673 cm^{-1}–690 cm^{-1}. At the top of the 2D-LIF spectrum, the trace shows the result of integrating vertically over the presented section of the 2D-LIF spectrum and closely resembles the corresponding region of the REMPI spectrum. Colored text is used for clarity. Selected assignments are shown, and the spectra are discussed further in the text.

than 17_1m_1—also reflected in the associated vibtor levels. The 15_1 bands are notably intense—cf. the 960 cm^{-1} feature (Sec. III F). Despite these observations, the Duschinsky matrices [Fig. 7(a)] indicate that there is almost no mixing between these modes during excitation or ionization. (In the matrices, the depth of shading of D_{15} implies that there is some predicted mode mixing of D_{15} between electronic states, but this is composed of several minor contributions from vibrational modes other than D_{17} and so is not discussed further here.) In contrast, via the origin, the m^1 band is more intense than m^0 (see Fig. 2), and this is the case with each vibrational emission band. We interpret this as an indication that the 17^1m^1 (e symmetry) S_1 level emits to more S_0 levels than 17^1m^0 (a_1 symmetry); furthermore, the ZEKE spectrum recorded via 17^1m^1 shows more bands than that recorded via 17^1m^0. Taken together, it is concluded that the 17^1m^1 level is likely interacting with other e symmetry levels.

In the 0 cm^{-1}–550 cm^{-1} emission region (not shown) of the 2D-LIF spectrum recorded via $17^1m^{0,1}$, essentially all of the features seen via the origin (see Fig. 2 and Ref. 10) can also be seen. In the region shown in Fig. 7(c), emission to a number of vibrational levels and their associated vibtor levels can be seen, and a selection of assignments is shown.

The largely discrete nature of the emission spectrum suggests interactions will be between a small number of levels, and we initially considered an interaction with an $m = 2$ level for the most efficient coupling with 17^1m^1 ($\Delta m = 3$, recalling that the m quantum number is signed) and with $\Delta v \leq 3$. This led to the assignment of the emission band at (682, 784) cm^{-1} to $18_1 29_1 m_2$, which is supported by the observation of the weaker $19_1 29_1 m_2$ emission band at (682, 767) cm^{-1}. There are other emission bands that can be assigned when exciting at 682 cm^{-1}—these can be associated either with activity from $18^1 29^1 m^2$ or with further interactions between e symmetry levels in S_1. Although it is not possible to be definitive, the latter is supported by the fact that a number of levels are at a wavenumber position in S_1 that suggests that they could interact with $18^1 29^1 m^2$, each related by ≤ 3 changes in v and/or m. As such, we conclude that a number of concurrent stepwise interactions are occurring, which link 17^1m^1 to a number of e symmetry levels, explaining the significantly lower 17_1m_1 intensity compared to that of 17_1m_0. For example, $18^1 29^1 m^2$ can interact with $21^1 29^2 m^2$ via a $\Delta v = 3$ interaction, and the latter can then undergo a further $\Delta v = 3$ interaction with $29^3 30^1 m^2$. That multiple interactions are likely to be occurring is supported by the significant amount of underlying activity that can be seen in the 2D-LIF and ZEKE spectra in Fig. 7.

Another prominent band in the 2D-LIF spectrum is the band at (681, 665) cm^{-1}, which is assigned to (21^2m^4, 21_2m_4), and we suggest 21^2m^4 is interacting with other e symmetry bands, including 17^1m^1, which would be $\Delta v = 3$, $\Delta m = 3$. At this excitation position, we also see other active bands, including $18_1 21_1 m_4$, $19_1 21_1 m_4$, and the overlapped $20_1 21_1 m_4$; at higher emission wavenumbers, we also see the $19_1 30_2 m_4$ band. We suggest that these bands arise from the 21^2m^4 activity.

In general, for solely anharmonic vibrational coupling, each m level of a particular vibration would behave similarly. However, in the case under discussion, the coupling is with a vibtor level that can only interact with one of the m levels of 17^1, and generally, there is a greater likelihood of coupling between e symmetry levels than for a_1 (or a_2)—see Sec. IV. Another possibility for an m-specific interaction with 17^1m^1 would be with the $m = 1$ level of an a_2 symmetry vibrational energy level, as the vibtor symmetry would then be e in both cases. However, the coupling mechanism could not simply be anharmonicity but would have to result from a breakdown in the separability of vibrational and torsional motions. It is also possible for m-specific interactions to occur with other vibtor levels of a_1 symmetry, but we do not see evidence of such interactions here.

The ZEKE spectrum via 17^1m^1, presented in Fig. 7(b)(i), is consistent, but not definitive, with regard to the suggested couplings: for example, although we do see $^+18^1m^2$, we do not see a clear band for $^+18^1 29^1 m^2$, which would be expected at 805 cm^{-1} and, if present, would be overlapped by the $^+17^1m^2$ band. Furthermore, the expected $\Delta m = 3$ ZEKE band would be $^+18^1 29^1 m^5$, anticipated at 952 cm^{-1}, which would overlap the $^+17^1m^5$ band, and could contribute to the higher-than-expected intensity for this feature. In addition, bands associated with ionization from 21^2m^4 are all expected in positions that overlap with other bands. However, the greater complexity of the $m = 1$ ZEKE spectrum compared to that of $m = 0$ is consistent with m-specific coupling. Part of the difficulty in reaching definitive conclusions from the ZEKE spectra is that the significant change in the magnitude of the torsional barrier, coupled with the change in phase upon ionization, leads to activity arising from a number of m levels in the ZEKE spectrum for a specific m intermediate level.[8] For a limited amount of vibrational activity, this is actually a good assignment tool, as distinct patterns of bands can be identified for each FC active vibration. However, when interactions in S_1 have occurred, particularly those involving vibtor levels, the resulting increase in the number of bands leads to difficulties in reaching a definitive assignment. In both ZEKE spectra in Fig. 7(b), we have given suggested assignments to most of the intense bands at lower wavenumbers, and a number of these also appear in combination with $^+18^1$ at higher wavenumbers (not indicated). Also present in those spectra are bands that are assigned to combinations, and these appear to arise from FC-like activity.

F. The 952 cm^{-1}–976 cm^{-1} region

The relevant region of 2D-LIF and three ZEKE spectra recorded across this region are shown in Fig. 8. Okuyama *et al.*[11] assigned the main feature to 15^1 (denoted 12^1 in their work), and we concur with this assignment of the main excitation bands to $15^1m^{0,1}$.

The integrated 2D-LIF spectrum is shown at the top of Fig. 8(b), which closely resembles this region of the REMPI spectrum. The 2D-LIF spectrum consists of a number of well-defined bands, falling into two main columns of activity, centered at excitation wavenumbers of 960 cm^{-1} and 964 cm^{-1}; a weaker column of activity is seen at excitation wavenumbers close to 970 cm^{-1}. Above about 1000 cm^{-1} in emission, there is a less well-defined structure extending across the spectrum, suggesting that this emission originates from coupled levels, which will be discussed below.

The band intensities in the 2D-LIF spectrum are not as expected, with the 17_1m_x emission bands being significantly more intense than the 15_1m_x emission bands; the assignment is clear, however, since the 17_1 bands were straightforwardly assigned above in Sec. III E, where we also commented that the 15_1 emission bands were unexpectedly intense when exciting 17^1. The assignment is also supported by the ZEKE spectra recorded at positions of the intermediate band maxima, 0^0 + 961 cm^{-1} and 0^0 + 965 cm^{-1} [Fig. 8(a)(i)

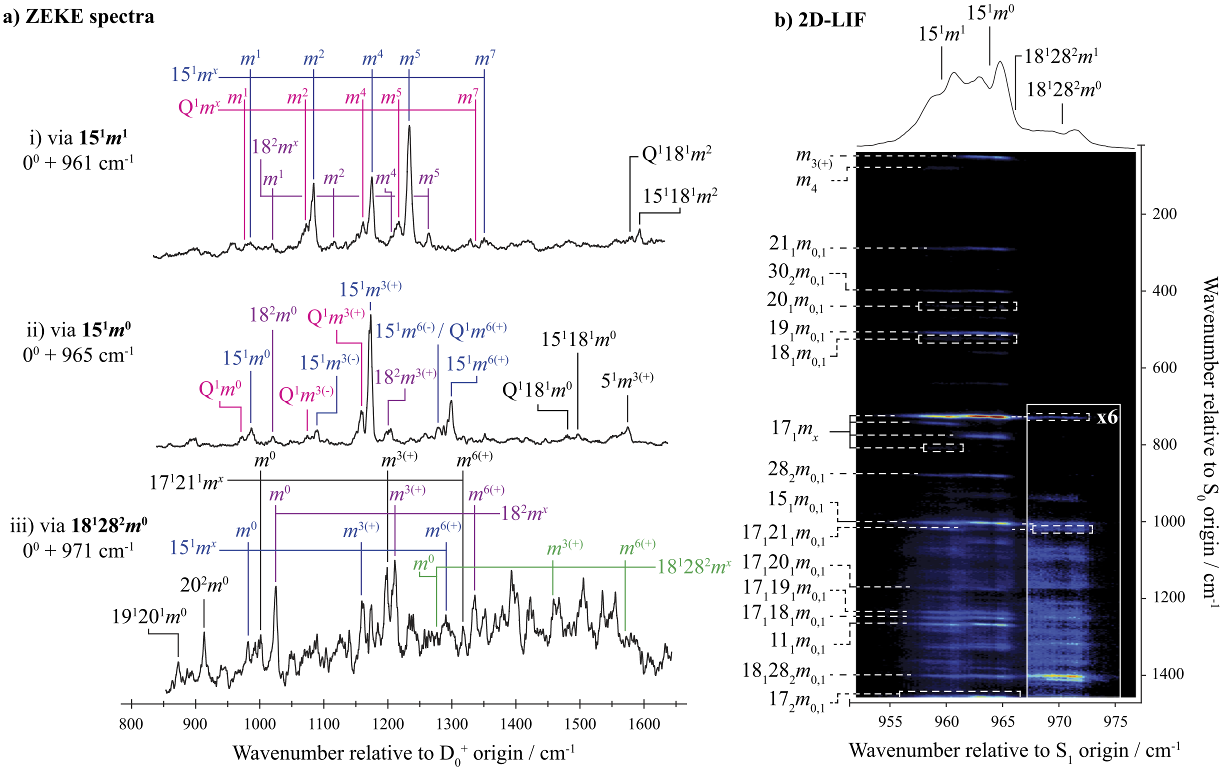

FIG. 8. (a) ZEKE spectra via 15^1m^1, 15^1m^0, and the feature at $0^0 + 971$ cm^{-1}. In the ZEKE spectra, the preceding "+" sign used in the text is omitted from the assignments for clarity—see the text regarding the Q^1m^x bands. Colored text is used for clarity. (b) 2D-LIF over the excitation range 950 cm^{-1}–978 cm^{-1}. At the top of the 2D-LIF spectrum, the trace shows the result of integrating vertically over the presented section of the 2D-LIF spectrum and closely resembles the corresponding region of the REMPI spectrum. The region between $0^0 + 967$ and $0^0 + 975$ cm^{-1} has been enhanced by a factor of six, as indicated, as this structure is weak compared to the main activity. Selected assignments are shown—see the text for further discussion.

and Fig. 8(a)(ii)], which show the expected strong vibtor bands associated with $^{+}15^1$. We thus conclude that there are non-diagonal FCFs associated with emission from 15^1, which must be related to geometry changes, since we do not see evidence of a Duschinsky rotation between these vibrations in the Duschinsky rotation matrix [see Fig. 7(a)], and indeed, the ZEKE spectra [Fig. 8(a)] do not exhibit $^{+}17^1m^x$ bands; neither do we see $^{+}15^1m^x$ bands when exciting via $17^1m^{0,1}$ [see Fig. 7(b)]. The 2D-LIF spectrum [Fig. 8(b)] also shows significant torsional bands, together with vibtor bands associated with the main emissions. These are largely as expected, and their assignments are straightforwardly obtained both by the 2D-LIF spectrum obtained via m^0 and m^1 (Fig. 2) and by comparison with the work of Stewart *et al.*,[10] as well as the wavenumbers of other vibrations, obtained in the present work (see Table III).

When exciting at 970 cm^{-1}, the strongest 2D-LIF band is at (970, 1402) cm^{-1}. The assignment of this band to the $\Delta(v, m) = 0$ band ($18^1 28^2 m^0$, $18_1 28_2 m_0$) is relatively straightforward, fitting the expected wavenumbers in both the S_0 and S_1 states, and also being consistent with the $18^1 28^2$ band seen for *m*DFB (Fig. 1). Furthermore, vibtor bands associated with $^{+}18^1 28^2 m^0$ are seen in the ZEKE spectrum recorded when exciting via the intermediate band maximum $0^0 + 971$ cm^{-1}, although it is noted that $^{+}18^1 28^2 m^{3(+)}$ is not the most intense band in the spectrum, as would be expected. We note that the strongest emissions seen when exciting across 957 cm^{-1}–966 cm^{-1} all extend to higher excitation wavenumbers, consistent with either coincidental FC activity or an interaction between one or both $15^1m^{0,1}$ levels and a level at 970 cm^{-1}. Since the profile of the $18_1 28_2$ emission band is strongest for the m_0 component, we suggest there is a $15^1 \ldots 18^1 28^2$ interaction for both m components, but for the $m = 1$ levels, further interactions cause a dissipation of the emission intensity across numerous transitions. In contrast, the interaction with $18^1 28^2 m^0$ is weaker and less profligate, and so the emission band is more pronounced.

At this excitation wavenumber, we can also anticipate possible activity from other levels, including $17^1 21^1 m^{0,1}$ and the vibtor levels $18^1 19^1 m^{3(+)}$ and $18^1 20^1 m^{3(+)}$. Relatively weak, but clearly observable bands at the correct wavenumbers for the $17_1 21_1 m_{0,1}$ emissions can be seen in the 2D-LIF spectra; moreover, bands arising from $^{+}17^1 21^1 m^x$ vibtor levels can also be seen in the ZEKE spectrum in Fig. 8(a)(iii). In addition, $^{+}18^2 m^x$ ZEKE bands are seen, but these are thought to arise from FC activity, since these are also seen in other spectra when exciting fundamentals. In summary, it seems clear that interactions are occurring, and the evidence is that this predominantly involves the $m = 1$ components and involves widespread coupling; the coupling with the $m = 0$ component is less definitive and is at best restricted in nature. The main activity comes from $15^1m^{0,1}$, but there is clear activity from $18^128^2m^{0,1}$ and persuasive evidence for involvement of $17^121^1m^{0,1}$; however, whether these levels are interacting significantly or not is less clear, but if they are, then the stronger interaction might be expected to be between 15^1 and 17^121^1, which is $\Delta v = 3$, while the other interaction would be $\Delta v = 4$.

The ZEKE spectrum recorded via $0^0 + 971$ cm^{-1} [Fig. 8(a)(iii)] is rich in structure, and its assignment is challenging. We highlight that there are ZEKE bands at the correct position for $17^121^1m^0$ activity, for example, the intense $^+17^121^1m^{3(+)}$ band, but the corresponding activity expected for $17^121^1m^1$ is not seen, in line with comments in the previous paragraph. We note a strong series of bands at 1026 cm^{-1}, 1212 cm^{-1}, and 1338 cm^{-1} that appear to be the $m = 0$, 3(+), and 6(+) components associated with $^+18^2$, which are indicated in the figure. Although possible assignments could be put forward for other bands in this spectrum, we generally refrain from doing so, since these are not definitive. For example, in cases where an interaction can be suggested, such as $19^121^129^1m^{3(-)}$ and $18^121^129^1m^{3(-)}$, each being ($\Delta v = 3$, $\Delta m = 3$) from $17^121^1m^0$, it is not possible to identify all of the expected bands in this complicated spectrum.

Looking at the ZEKE spectra via 15^1m^x [Fig. 8(a)(i) and Fig. 8(a)(ii)], there are a series of bands labeled "Q^1m^x" and we show the $\Delta v = 0$ band as well as the corresponding vibtor structure. Despite these bands being well-resolved and prominent in both ZEKE spectra, there is no evidence for corresponding activity in the 2D-LIF spectrum. Although it is difficult to determine the identity of "Q," it may be associated with a level that is in Fermi resonance with $^+15^1$ in the cation (and so each corresponding pair of vibtor levels is also interacting); one promising candidate is $Q = {}^+25^129^1$. This could also simply arise from FC-like activity, of course, and we noted the appearance of $^+25^129^1m^x$ bands when exciting via 17^1m^1 [Fig. 7(b)].

In summary, at the very least, the 2D-LIF and ZEKE spectra suggest that there are likely numerous interactions occurring with the 15^1 level, supported by the appearance of many bands alongside those of $^+15^1m^x$ in the ZEKE spectrum recorded at $0^0 + 971$ cm^{-1}. We also see clear evidence for $18^128^2m^0$ activity and persuasive evidence for $17^121^1m^0$.

G. The 1251 cm^{-1}–1266 cm^{-1} region

The 2D-LIF spectrum [Fig. 9(c)] consists of several well-defined bands on top of a broad background emission, particularly above

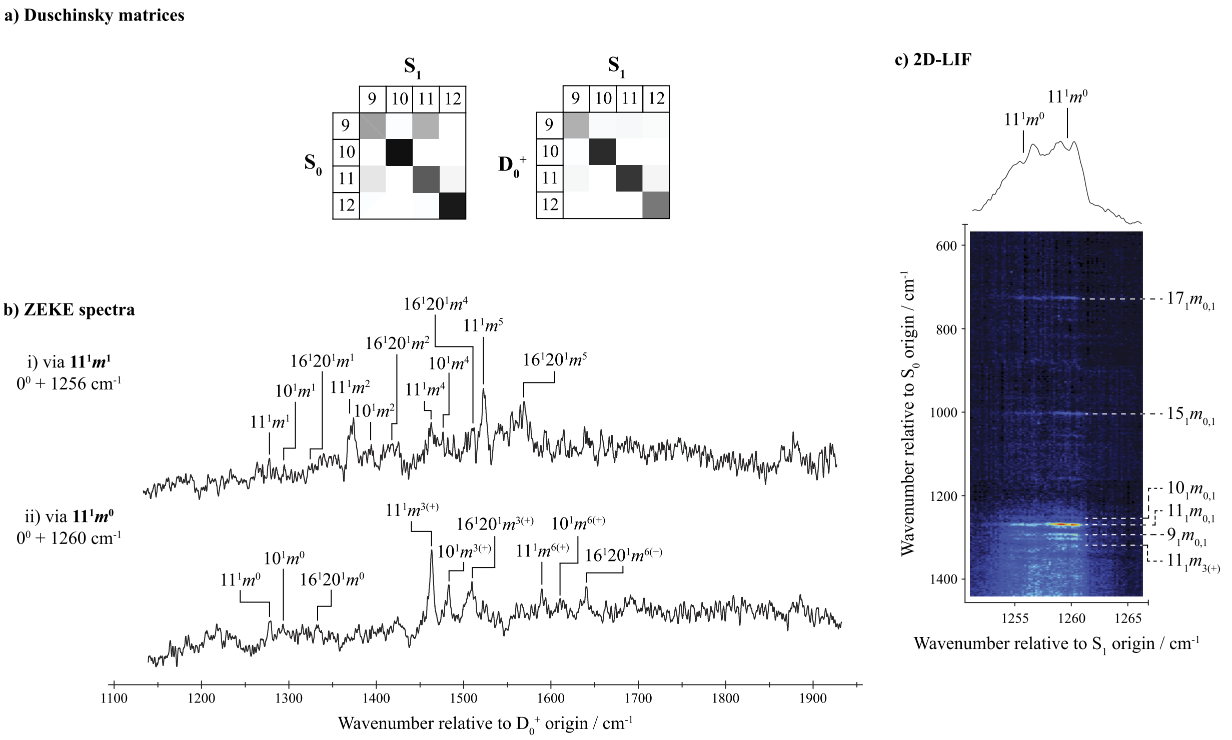

FIG. 9. (a) Duschinsky matrices showing the character of selected vibrations between excitation and ionization. The depth of shading represents the coefficients of mixing between vibrations in the two electronic states, between 0 (white) and 1 (black). (b) ZEKE spectra via 11^1m^1 and 11^1m^0. In the ZEKE spectra, the preceding "+" sign used in the text is omitted from the assignments for clarity. (c) 2D-LIF over the excitation range 1250 cm^{-1}–1267 cm^{-1}. At the top of the 2D-LIF spectrum, the trace shows the result of integrating vertically over the presented section of the 2D-LIF spectrum and closely resembles the corresponding region of the REMPI spectrum. Selected assignments are shown, and the spectra are discussed further in the text.

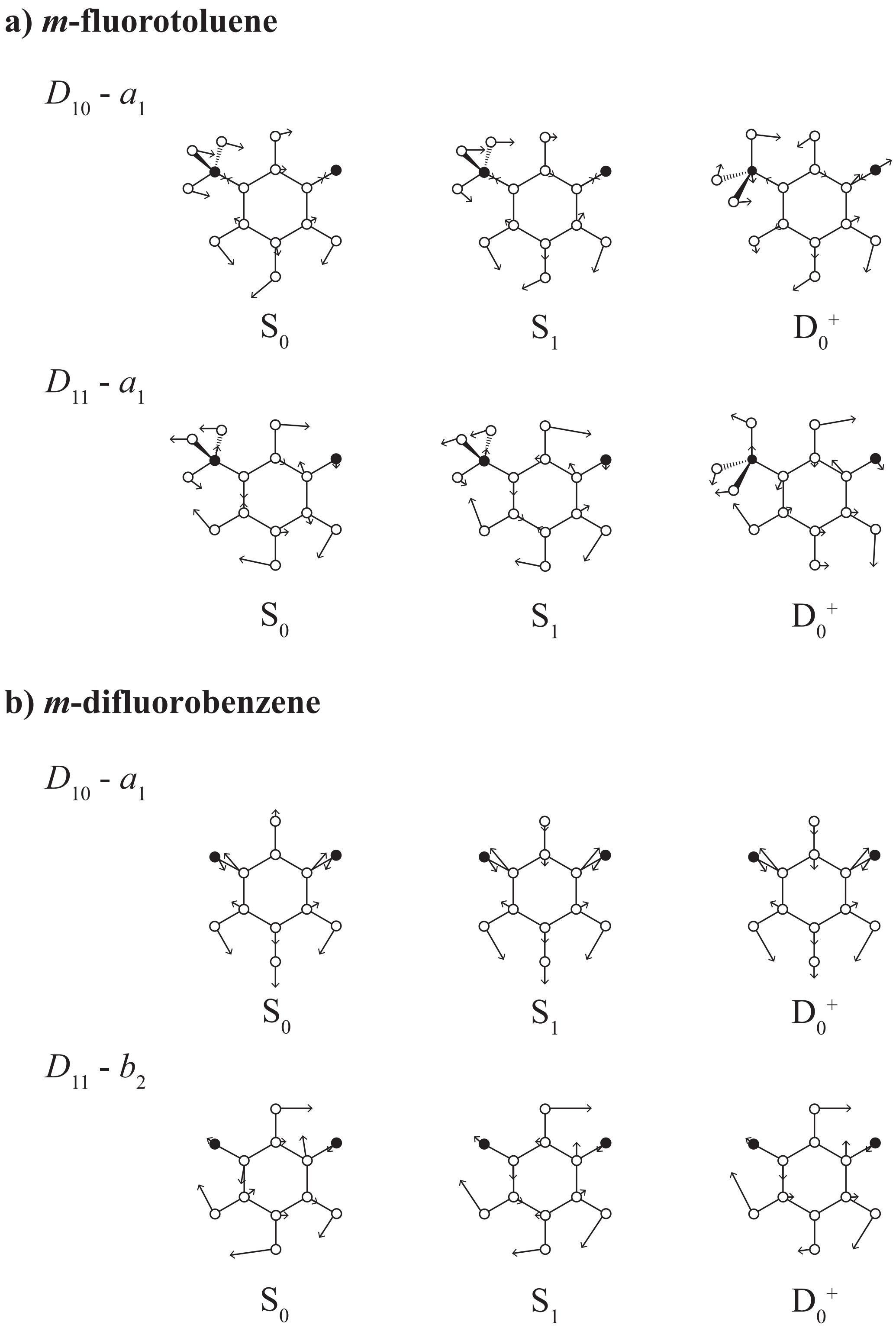

FIG. 10. Calculated mode diagrams for the D_{10} and D_{11} vibrations of (a) *m*FT (G_6) and (b) *m*DFB (C_{2v}) in the three electronic states under consideration, obtained using quantum chemistry calculations, as indicated in Tables I and III (for *m*DFB, the level of theory used for the cation was the same as that used for *m*FT). The motions are distinctive, and hence, assigning each vibration from the mode diagram is straightforward.

1200 cm^{-1}, and the integrated spectrum at the top of the spectrum closely resembles this region of the REMPI spectrum.

The main emission band for *m*FT, when exciting across 1254 cm^{-1}–1262 cm^{-1}, is at 1271 cm^{-1}. Comparing this value with the liquid-phase IR/Raman values suggests an assignment of the emission to 11_1, and this would be in line with the calculated wavenumbers. Note that Okuyama *et al.*[11] assigned a value of 1267 cm^{-1} to an S$_0$ vibration, which they labeled ν_{14} in Varsányi[29] notation and would correspond to *m*DFB mode ν_{25} in Mulliken notation[33] and, hence, D_{11} here; however, it was shown in previous work that Varsányi modes ν_3 and ν_{14} have got confused over the years and, further, that these labels do not describe the motions of the atoms in disubstituted benzene molecules.[24,25] With these caveats, the present assignment and that of Ref. 11 are in agreement. In Fig. 10, we show the calculated motions of D_{10} and D_{11} for *m*DFB and *m*FT in each of the three electronic states, showing that their motions are distinctive and, hence, assignment of each from the calculations is unambiguous.

A comparison of the REMPI spectrum of *m*FT with that of *m*DFB also suggests that the excitation at 1267 cm^{-1} should be assigned as 11^1; however, this was assigned as 10^1 (denoted 6^1) in the fluorescence study.[33] In *m*DFB, under C_{2v} point group symmetry, the D_{10} vibration is of a_1 symmetry, while that of D_{11} is b_2; thus, the 10^1 transition would be symmetry allowed. However, other transitions involving b_2 symmetry vibrations were assigned in Ref. 33, with 21^1, 19^1, and 20^1 transitions being notable; these are likely to be vibronically induced. These are also all seen in *m*FT[15] (where they all become symmetry allowed), but also the 18^1 transition is moderately intense in *m*FT but is absent in the *m*DFB spectrum (see Fig. 1 and Ref. 33), even though D_{18} is totally symmetric in both molecules. Hence, there is no prima facie reason not to assign the *m*DFB transition at 1267 cm^{-1} to 11^1, which would bring consistency with the *m*FT assignment. We highlight that Table I shows that the calculated values for D_{10} and D_{11} in the S$_0$ state of *m*DFB are too close to be discriminant (but their motions and so identities are clear—see Fig. 10), and with either assignment, there is a 40 cm^{-1} difference between the calculated value and the experimental value. Additionally, we are particularly cautious regarding the calculated S$_1$ values, which we have found to be often less reliable than those for the S$_0$ and D$_0{}^+$ states.[23,44]

Further evidence is gleaned from related symmetrically substituted molecules: in Ref. 27, vibrational wavenumbers are presented for five such molecules. Excluding *m*DFB, the wavenumber for the D_{10} vibration lies below that of D_{11} for both the experimental and calculated values for all of the other molecules. For *m*DFB, as noted, the calculated values are only a few cm^{-1} apart, but the experimental values, as assigned, are clearly reversed compared to those of the other molecules. Given the variation in these wavenumbers with mass—and given that the corresponding values for *m*-xylene and resorcinol are consistent with each other, but the reverse of the previously assigned values for *m*DFB—we suggest that the D_{10} and D_{11} assignments need to be reversed as well, and this has been done in Table I. This is then consistent with the *m*FT results obtained herein. Consequently, as with 18^1, it appears that 10^1 simply is not active in *m*DFB, despite being totally symmetric, while we conclude that 11^1 must be vibronically active. Furthermore, we note that Graham and Kable[33] have commented that previous assignments of the b_2 symmetry vibrations of *m*DFB are questionable, noting that the assignment of 11^1 in S$_1$ to a value of 1608 cm^{-1} does not seem to be correct, and indeed, this would not agree well with the calculated value in Table I.

In summary, the most intense 2D-LIF band for *m*FT in Fig. 9(c) at (1260, 1271) cm^{-1} is assigned as (11^1m^0, 11_1m_0) and is significantly more intense than the corresponding $m = 1$ band. The ZEKE spectra [Fig. 9(b)] are consistent with this assignment, with the main bands being assigned as the expected vibtor levels via the two *m* components. Several other fundamentals are also seen, and, where the sensitivity allows, the expected associated vibtor structure is seen.

With the assignment of the excitation to 11^1, the observed structure in the ZEKE spectrum allows a vibrational wavenumber of 1275 cm^{-1} to be obtained for ${}^+11^1$. (We note that, unhelpfully, the experimental value for this vibration falls between the calculated values for ${}^+11^1$ and ${}^+10^1$, and so this cannot be used as further evidence for this assignment, which is largely based on the 2D-LIF spectrum—see Table III.) The ZEKE spectra have a significant underlying unstructured signal, which is akin to the broad background in the 2D-LIF spectrum and again is consistent with significant IVR occurring. Another progression of vibtor levels is also seen in both ZEKE spectra, consistent with a vibration with the wavenumber 1330 cm^{-1}, which can be plausibly assigned to ${}^+16^1 20^1$, which could be arising from a $\Delta\nu = 3$ interaction; the activity in ${}^+10^1$ likely arises from FC activity, since the Duschinsky matrices, Fig. 9(a), show that D_{10} and D_{11} are not significantly mixed upon ionization. If the ${}^+16^1 20^1 m^x$ assignments are correct and an interaction is indeed occurring, then this suggests a value for D_{16} in S$_1$ of ~840 cm^{-1}, which is in fair agreement with the calculated value. The interaction would be expected for both *m* components, which is consistent with the ZEKE spectrum. The $16_1 20_1$ bands, expected at ~1370 cm^{-1}, are in a region of the 2D-LIF spectrum that consists of unstructured emission, effectively ruling out the possibility of definitive identification. This emission, together with the unstructured background in the ZEKE spectra, suggests significant interactions are occurring, but we cannot provide unambiguous assignments for all of the bands nor identify the likely myriad of interacting levels in the spectrum.

IV. FURTHER DISCUSSION

In the above, we have looked at the assignment of a selection of bands across the lowest ~1350 cm^{-1} of the S$_1$ state of *m*FT. Clearly, IVR cannot occur for the origin and the very lowest levels, but as discussed in Ref. 10, even below 350 cm^{-1}, there are interactions occurring between vibrations, torsions, and vibtor levels. Here, we have extended the examination of levels, where we see limited interactions are present for levels below 950 cm^{-1}, but significant IVR occurs above this, moving toward the statistical (dissipative) IVR regime; the latter is demonstrated by the presence of a largely unstructured underlying background in both the 2D-LIF and ZEKE spectra recorded at ~960 cm^{-1} and ~1260 cm^{-1}. On top of this underlying background, there are numerous well-resolved bands, showing that in the present experiments, some energy remains localized to particular vibrations, while some is dissipated through a range of motions.

We noted above that Timbers *et al.*[7] have compared the behavior of *m*FT and *p*FT, concluding that at about 1200 cm^{-1}, the rate of IVR was an order of magnitude faster for *m*FT than for *p*FT, based upon quenching experiments. We have studied *p*FT in a range of internal energies, and we have found that below 1000 cm^{-1}, limited IVR occurs involving both anharmonic and vibration–torsional coupling.[16–18,20,21] At ~1015 cm^{-1}, we found that coupling occurred involving two largely separate overtone levels, providing two routes for energy delocalization in *p*FT,[23] while in the region 1190 cm^{-1}–1240 cm^{-1}, there was more widespread IVR, but two levels less than 40 cm^{-1} apart behaved significantly differently.[17,22] In both of the latter, there were still structured bands on top of a broad background, suggesting at least some energy remains localized. In the case of *p*Xyl, however, at these energies, most structure was lost in the ZEKE spectra recorded, suggesting almost complete delocalization of energy; these observations were discussed in terms of symmetry and the density of states (DOS).[17] It was concluded that although the DOS buildup is critical in providing pathways to widespread IVR, this is determined largely by the presence of one or more methyl groups, rather than the symmetry per se. On top of this, the DOS buildup is not smooth, and so at lower internal energies, serendipity can play a large role in determining whether a particular vibration is located in a "clump" of levels; even then, there needs to be a means of efficient coupling to these. Such coupling will clearly depend on symmetry, but also on the motions involved; such considerations lead to the "Tier Model" of IVR, whereby coupling between particular levels is efficient and facilitates pathways to coupling with a wide range of "bath states."[1]

Here, we make further comparison between *m*FT and *p*FT. In Fig. 11, we show their DOS plots for totally symmetric vibrations, and also when including torsions and vibtor levels. It is clear that for *m*FT, there are more totally symmetric vibrations, as all in-plane vibrations are totally symmetric, while for *p*FT, these split into a_1' (a_1 in C_{2v}) and a_1'' (b_2 in C_{2v}) subgroups— this is evident in Fig. 11.

a) *m*FT - vibrations **b) *p*FT - vibrations**

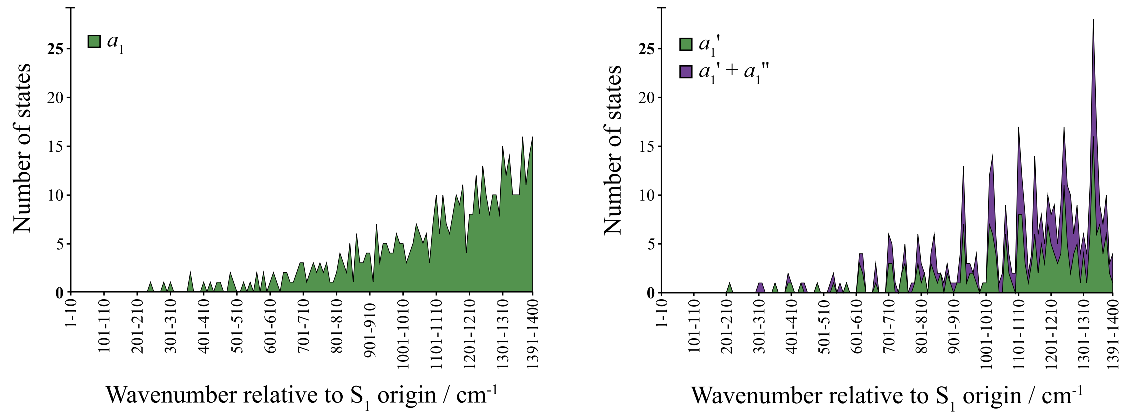

c) *m*FT - vibration, torsion, and vibtor states **d) *p*FT - vibration, torsion, and vibtor states**

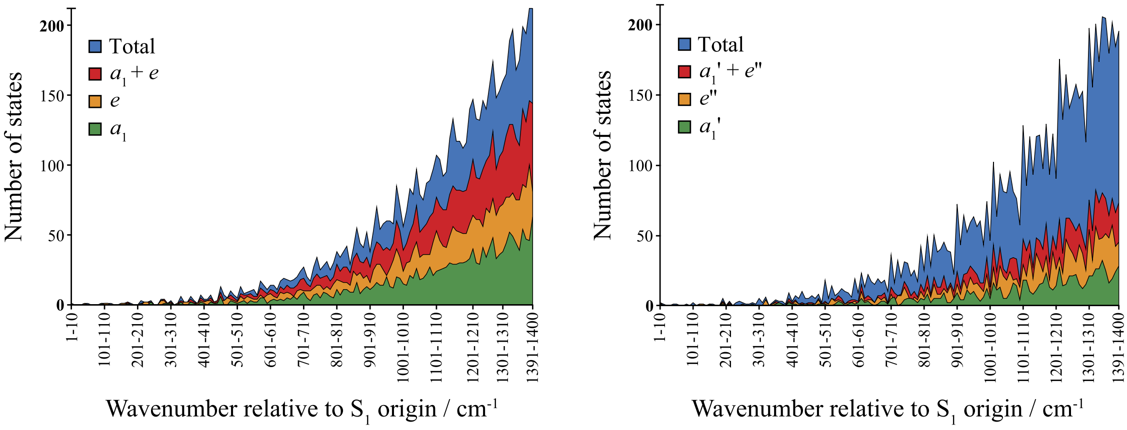

FIG. 11. Density of states (DOS) plots for *m*FT and *p*FT, using calculated vibrational wavenumbers from Table III and Ref. 23. In plots (a) and (b), only vibrational levels are included, while in plots (c) and (d), vibrations and vibtor and torsional levels are included. In both plots, we indicate levels that are accessible from the $m = 0$ and $m = 1$ levels, which are those that are the most populated in the free-jet expansion ($a_1 + e$ for *m*FT and $a_1' + e''$ for *p*FT), together with all levels. Note that we do not consider rotational levels in this work.

Notably, the buildup in the DOS is more erratic for *p*FT than for *m*FT. This difference is clearer once vibtor levels are included, where again an approximate doubling of the available energy levels is seen for *m*FT compared to *p*FT, for levels accessible from $m = 0$ and $m = 1$. Furthermore, it can be seen that the buildup of levels is generally more continuous once vibtor levels are included compared to only the vibrations, which is somewhat erratic, particularly for the totally symmetric levels in *p*FT.

With regard to previous IVR experiments on *p*FT, there has been some uncertainty regarding the vibrations excited, which has been discussed.[45] For *p*FT, there are two main fundamentals at 1196 cm^{-1} and 1232 cm^{-1}, but there are other levels nearby, as examined in depth in our recent work.[22] In Ref. 7, it seems the latter level is excited, which is the 5^1 vibration, mainly corresponding to an in-phase stretch of the C–F and C–CH_3 bonds, with the former motion dominating.[25] As we have discussed in the present work, for *m*FT, the 1260 cm^{-1} transition is assigned as the vibronically induced 11^1, which is largely a ring-based distortion. As such, the vibrational motion is quite different for the two molecules, making the comparison less straightforward. Indeed, the motion of D_{11} (see Fig. 10) in *m*FT will involve the adjacent C–H bonds interacting with the methyl group more strongly than for the 5^1 vibration in *p*FT, which would be one explanation for the increased IVR as a result of vibration–torsional coupling.

In the experiments by Parmenter's group,[7] reliance is placed upon collisional quenching with O_2. The idea is that the excited electronic state is vibrationally excited following laser excitation and that there is time dependence for the IVR to occur. In addition, the higher the partial pressure of O_2, the more rapid the quenching, and the less the time molecule had to undergo IVR. However, this can only occur with levels that are excited coherently within the width of the laser pulse, which will be a few cm^{-1} for a nanosecond pulse (not stated in Ref. 7, but the laser system mentioned suggests this was the case). In Ref. 7, a fit is made to the data to determine k_{IVR}, with electronic and vibrational collision quenching, k_{V}, included. Various assumptions were made in determining k_{IVR}, with the end conclusion being that this was roughly an order of magnitude larger than that for *p*FT. A discussion of the possible rationalization of this observation was then made, including the DOS of the coupled vibrational levels, the effect of the methyl rotor not being on a principal axis, and the magnitude of the torsional barrier.

With regard to the DOS, we note that there are two factors that increase this in *m*FT relative to *p*FT, both related to the reduction in molecular (point group) symmetry from G_{12} (C_{2v}) for *p*FT to G_6 (C_s) for *m*FT. For the vibrations, using molecular symmetry group labels, *m*FT will have a greater number of totally symmetric vibrations as both the $a_1{}'$ and $a_1{}''$ symmetry vibrations in *p*FT have the same symmetry (a_1) in *m*FT; Fig. 11 indicates that the number of a_1 vibrations in *m*FT is comparable to the number of $a_1{}' + a_1{}''$ symmetry vibrations in *p*FT but with a smoother buildup for *m*FT. Furthermore, considering molecular symmetry, the number of *e* torsional levels in *m*FT is about the same as the number of $e' + e''$ torsional levels in *p*FT. Taken together, see Fig. 11, it can be seen that the *total* number of vibrational + vibtor levels is about the same in *p*FT and *m*FT. However, considering only the states that have the same symmetries as the $m = 0$ and $m = 1$ levels (the ones with the dominant populations in the free-jet expansion), then there are about twice as many levels for *m*FT as for *p*FT.

The aforementioned DOS does not include rotational levels, and it was argued in Ref. 7 that coupling with rotational levels would be more significant in *m*FT than *p*FT; if so, then it may be that there is an effect from the use of room temperature and high pressure conditions in Ref. 7, where rotational effects would be expected to be more significant than they would be in jet-cooled, gas-phase studies.[45] It was also commented in that work[7] that at the internal energies employed, *p*FT will couple to 10–50 levels, while *m*FT will couple to essentially an infinite number. The DOS plots in Fig. 11 do not support this latter comment and, further, the 2D-LIF spectra do not either, where the structure is seen, albeit on a background, for both *p*FT (Ref. 19) and *m*FT (present work); this is in contrast to the fluorescence spectrum for *m*FT reported in Ref. 7, where no structure is evident when the quencher is absent.

We concur with the comments in Ref. 7 that the significantly higher barrier in *m*FT is expected to produce larger torsion–vibration coupling terms. One rationale for the higher barrier in *m*FT compared to *p*FT is in terms of hyperconjugation: in *p*FT, hyperconjugation is not expected to be a large effect and weaker van der Waals type interactions are thus expected to dominate, explaining the lower torsional barrier.

As noted above, there has been some ambiguity in the levels employed for IVR studies on *p*FT,[45] which is pertinent as the vibrational motion is expected to be critical in the observed coupling. For *p*FT, at 1200 cm^{-1}, a rather different time-dependent behavior has been observed for the two main levels,[46,47] which was discussed in terms of a rotation-dependent vibration–torsion interaction that occurred specifically for one of the *m* levels. Rotational dephasing was concluded to be a time-dependent effect only and is not seen in frequency-resolved experiments.[19]

In summary, direct comparison between different isomers of substituted benzene molecules is difficult because of the different forms of the vibrations, even if the observed activity seems quite similar. Furthermore, the conditions used in an experiment are expected have a strong bearing on the results,[45] and so caution is strongly advised when making general deductions from a single experiment. Having the ability to resolve vibrational, vibtor, and torsional structures in a spectrum does seem to give the ability to identify explicit coupling channels, but only when the coupling is reasonably limited. Once the coupling becomes widespread, however, this advantage is lost in frequency-resolved experiments if the resolution is not sufficient to resolve all features, or if the spectrum becomes too complicated to assign definitively. Time-resolved photoelectron spectroscopy experiments with picosecond pulses can, however, still be useful in picking out zero-order state contributions in such circumstances, as long as the frequency resolution can be maintained at tens of cm^{-1}.[46,47]

V. CONCLUSIONS

We have presented 2D-LIF and ZEKE spectra obtained when exciting through selected levels up to 1350 cm^{-1} in the lower wavenumber region of the $S_1 \leftarrow S_0$ excitation in *m*FT. We have assigned the majority of the main features observed, but there are many weak features and also broad unstructured backgrounds in some cases. The assigned features confirm that there is widespread vibtor coupling occurring in this molecule, as well as some anharmonic vibrational coupling; these become more prevalent to higher internal energies and are more common for the *e* symmetry torsional levels than for the a_1 symmetry levels. Explicit couplings can be identified in some cases, while, in others, only potential couplings have been suggested, based upon some of the observed 2D-LIF bands. When there are numerous couplings, the ZEKE spectra become very difficult to assign, owing to the number of bands arising, also causing each to have a lower intensity, and these are located on a rising unstructured background.

Comparing *p*FT and *m*FT, we agree with many, but not all, of the ideas expressed in Ref. 7, but we have highlighted that both the number of vibrations and also torsions, and so vibtor, levels are responsible for the stark increase in the DOS; of course, all of these levels will have an associated set of rotational levels, and hence in room temperature studies, this difference will be exacerbated compared to experiments employing a free-jet expansion. We have emphasized that it is difficult to compare these molecules directly, with the particular vibration excited at ~1250 cm^{-1} being different for the two molecules. Moreover, relying on Wilson/Varsányi labels to identify a vibration can be misleading, since the motions of the atoms for a particular vibrational wavenumber can be very different for *meta* and *para* substituted molecules as discussed in Ref. 27. Last, the buildup in vibrational levels is somewhat erratic at these low wavenumbers, and this suggests that at low energies, notwithstanding the more-rapid buildup in the DOS for *m*FT, the rapidity with which IVR efficiency can increase is restricted since coupling elements will still depend on Δv being small.

Our conclusion is that it seems clear that *m*FT undergoes more rapid IVR than *p*FT, but ascertaining the precise reasons for this, and quantifying them, is far from straightforward.

ACKNOWLEDGMENTS

We are grateful to the EPSRC for funding (Grant No. EP/L021366/1). The EPSRC and the University of Nottingham are thanked for studentships to D.J.K. and A.R.D. Alan Rees, Lewis G. Warner, and Elizabeth F. Fryer are thanked for helping with the recording of some of the spectra during undergraduate projects, with L.G.W. also being grateful for an Undergraduate Summer Bursary funded via a University of Nottingham School of Chemistry 1960 scholarship. The REMPI spectrum of *m*DFB was recorded in our laboratory by Adrian M. Gardner and William D. Tuttle. We are grateful for access to the High-performance computing resource at the University of Nottingham.

DATA AVAILABILITY

The data that support the findings of this study are available from the corresponding author upon reasonable request.

REFERENCES

[1] D. J. Nesbitt and R. W. Field, J. Phys. Chem. **100**, 12735 (1996).
[2] G. M. Roberts and V. G. Stavros, in *Ultrafast Phenomena in Molecular Sciences*, edited by R. de Balda and L. Bañares (Springer, Dordrecht, 2014).
[3] Y. He, C. Wu, and W. Kong, J. Phys. Chem. A **107**, 5145 (2003).
[4] C. S. Byskov, F. Jensen, T. J. D. Jørgensen, and S. B. Nielsen, Phys. Chem. Chem. Phys. **16**, 15831 (2014).
[5] F. Duschinsky, Acta Phys. - Chim. U.R.S.S. **7**, 551 (1937).
[6] L. Martinez-Fernandez, A. Banyasz, L. Esposito, D. Markovitsi, and R. Improta, Signal Transduct. Target Ther. **2**, 17201 (2017).
[7] P. J. Timbers, C. S. Parmenter, and D. B. Moss, J. Chem. Phys. **100**, 1028 (1994).
[8] D. J. Kemp, E. F. Fryer, A. R. Davies, and T. G. Wright, J. Chem. Phys. **151**, 084311 (2019).
[9] D. J. Kemp, L. G. Warner, and T. G. Wright, J. Chem. Phys. **152**, 064303 (2020).
[10] L. D. Stewart, J. R. Gascooke, and W. D. Lawrance, J. Chem. Phys. **150**, 174303 (2019).
[11] K. Okuyama, N. Mikami, and M. Ito, J. Phys. Chem. **89**, 5617 (1985).
[12] K. Takazawa, M. Fujii, T. Ebata, and M. Ito, Chem. Phys. Lett. **189**, 592 (1992).
[13] M. Ito, K. Takazawa, and M. Fujii, J. Mol. Struct. **292**, 9 (1993).
[14] K. Takazawa, M. Fujii, and M. Ito, J. Chem. Phys. **99**, 3205 (1993).
[15] A. R. Davies, D. J. Kemp, L. G. Warner, E. F. Fryer, A. Rees, and T. G. Wright, J. Chem. Phys. **152**, 214303 (2020).
[16] A. M. Gardner, W. D. Tuttle, L. Whalley, A. Claydon, J. H. Carter, and T. G. Wright, J. Chem. Phys. **145**, 124307 (2016).
[17] W. D. Tuttle, A. M. Gardner, L. E. Whalley, D. J. Kemp, and T. G. Wright, Phys. Chem. Chem. Phys. **21**, 14133 (2019).
[18] A. M. Gardner, W. D. Tuttle, L. E. Whalley, and T. G. Wright, Chem. Sci. **9**, 2270 (2018).
[19] D. J. Kemp, W. D. Tuttle, A. M. Gardner, L. E. Whalley, and T. G. Wright, J. Chem. Phys. **151**, 064308 (2019).
[20] W. D. Tuttle, A. M. Gardner, L. E. Whalley, and T. G. Wright, J. Chem. Phys. **146**, 244310 (2017).
[21] D. J. Kemp, A. M. Gardner, W. D. Tuttle, and T. G. Wright, Mol. Phys. **117**, 3011–3026 (2019).
[22] D. J. Kemp, L. E. Whalley, A. M. Gardner, W. D. Tuttle, L. G. Warner, and T. G. Wright, J. Chem. Phys. **150**, 064306 (2019).
[23] A. M. Gardner, L. E. Whalley, D. J. Kemp, W. D. Tuttle, and T. G. Wright, J. Chem. Phys. **151**, 154302 (2019).
[24] A. M. Gardner and T. G. Wright, J. Chem. Phys. **135**, 114305 (2011).
[25] A. Andrejeva, A. M. Gardner, W. D. Tuttle, and T. G. Wright, J. Mol. Spectrosc. **321**, 28 (2016).
[26] W. D. Tuttle, A. M. Gardner, A. Andrejeva, D. J. Kemp, J. C. A. Wakefield, and T. G. Wright, J. Mol. Spectrosc. **344**, 46 (2018).
[27] D. J. Kemp, W. D. Tuttle, F. M. S. Jones, A. M. Gardner, A. Andrejeva, J. C. A. Wakefield, and T. G. Wright, J. Mol. Spectrosc. **346**, 46 (2018).
[28] E. B. Wilson, Jr., Phys. Rev. **45**, 706 (1934).
[29] G. Varsányi, *Assignments of the Vibrational Spectra of Seven Hundred Benzene Derivatives* (Wiley, New York, 1974).
[30] R. S. Mulliken, J. Chem. Phys. **23**, 1997 (1955).
[31] G. Herzberg, *Molecular Spectra and Molecular Structure. II. Infrared and Raman Spectra of Polyatomic Molecules* (Krieger, Malabar, 1991).
[32] W. D. Tuttle, A. M. Gardner, and T. G. Wright, Chem. Phys. Lett. **684**, 339 (2017).
[33] P. A. Graham and S. H. Kable, J. Chem. Phys. **103**, 6426 (1995).
[34] V. L. Ayles, C. J. Hammond, D. E. Bergeron, O. J. Richards, and T. G. Wright, J. Chem. Phys. **126**, 244304 (2007).
[35] N. J. Reilly, T. W. Schmidt, and S. H. Kable, J. Phys. Chem. A **110**, 12355 (2006).
[36] J. R. Gascooke and W. D. Lawrance, Eur. Phys. J. D **71**, 287 (2017).
[37] J. H. S. Green, Spectrochim. Acta. **26A**, 1523 (1970).
[38] A. M. Gardner, W. D. Tuttle, P. Groner, and T. G. Wright, J. Chem. Phys. **146**, 124308 (2017).
[39] M. J. Frisch, G. W. Trucks, H. B. Schlegel, G. E. Scuseria, M. A. Robb, J. R. Cheeseman, G. Scalmani, V. Barone, G. A. Petersson, H. Nakatsuji, X. Li, M. Caricato, A. V. Marenich, J. Bloino, B. G. Janesko, R. Gomperts, B. Mennucci, H. P. Hratchian, J. V. Ortiz, A. F. Izmaylov, J. L. Sonnenberg, D. Williams-Young, F. Ding, F. Lipparini, F. Egidi, J. Goings, B. Peng, A. Petrone, T. Henderson, D. Ranasinghe, V. G. Zakrzewski, J. Gao, N. Rega, G. Zheng, W. Liang, M. Hada, M. Ehara, K. Toyota, R. Fukuda, J. Hasegawa, M. Ishida, T. Nakajima, Y. Honda, O. Kitao, H. Nakai, T. Vreven, K. Throssell, J. A. Montgomery, Jr., J. E. Peralta, F. Ogliaro, M. J. Bearpark, J. J. Heyd, E. N. Brothers, K. N. Kudin, V. N. Staroverov, T. A. Keith, R. Kobayashi, J. Normand, K. Raghavachari, A. P. Rendell, J. C. Burant, S. S. Iyengar, J. Tomasi, M. Cossi, J. M. Millam, M. Klene, C. Adamo, R. Cammi, J. W. Ochterski, R. L. Martin, K. Morokuma, O. Farkas, J. B. Foresman, and D. J. Fox, Gaussian 16, Revision A.03, Gaussian, Inc., Wallingford CT, 2016.

[40] E. Fermi, Z. Phys. **71**, 250 (1931).

[41] N. T. Whetton and W. D. Lawrance, J. Phys. Chem. **93**, 5377 (1989).

[42] J. R. Gascooke and W. D. Lawrance, J. Chem. Phys. **138**, 134302 (2013).

[43] A. R. Davies, D. J. Kemp, and T. G. Wright (unpublished).

[44] D. J. Kemp, A. M. Gardner, W. D. Tuttle, J. Midgley, K. L. Reid, and T. G. Wright, J. Chem. Phys. **149**, 094301 (2018).

[45] C. J. Hammond, V. L. Ayles, D. E. Bergeron, K. L. Reid, and T. G. Wright, J. Chem. Phys. **125**, 124308 (2006).

[46] J. A. Davies, A. M. Green, A. M. Gardner, C. D. Withers, T. G. Wright, and K. L. Reid, Phys. Chem. Chem. Phys. **16**, 430 (2014).

[47] J. A. Davies, L. E. Whalley, and K. L. Reid, Phys. Chem. Chem. Phys. **19**, 5051 (2017).

9. Unpicking vibration-vibration and vibration-torsion interactions in *m*-fluorotoluene

Abstract: "Two-dimensional laser-induced fluorescence (2D-LIF) spectra are reported for a set of features in the $S_1 \leftrightarrow S_0$ electronic spectrum of *m*-fluorotoluene. Two transitions previously assigned to fundamentals are reassigned in the present work. The main reassignments are confirmed with zero-electron-kinetic-energy (ZEKE) spectroscopy. Interactions in the S_0, S_1 and D_0^+ electronic states involving vibrational and vibration-torsional ("vibtor") levels are identified *via* observed activity. The obtained vibrational wavenumbers compare well to the results of quantum chemical calculations."

Authors: Alexander R. Davies, David J. Kemp and Timothy G. Wright.
Submitted: to Journal of Molecular Spectroscopy, 9th June 2021.
Published: 25th August 2021
Reference: A. R. Davies, D. J. Kemp and T. G. Wright, *J. Mol. Spectrosc.*, 2021, **381**, 111522.
DOI: 10.1016/j.jms.2021.111522

Summary: In this paper, we investigate a small portion (~150 cm^{-1}) of the $S_1 \leftarrow S_0$ transition of *m*FT that was only mentioned in passing in Section 8, and whose analysis followed the recording of more spectra subsequent to the publication of that material. The three major regions of structure were formerly assigned as fundamental vibrations by Okuyama *et al.*[69], and the work presented herein shows that this is not the case and actually arises from some rather complicated anharmonic interactions (and overlapping features) between these and other, nearby dark states and vibtor levels. Notably, we observe the $17^1m^{0,1}$ and $26^128^1m^{0,1}$ levels in Fermi resonance, although we conclude that the majority of the activity observed *via* 17^1 in the 2D-LIF and ZEKE spectra arises from the m = 1 component, in direct contrast to the 26^128^1 combination band in which the majority of activity arises from the m = 0 component;

this arises from further couplings. It is further noted that S_1 $26^1 28^1 m^0$ is also interacting with $26^1 29^1 m^{3(+)}$, an example of a torsion-facilitated interaction. Such interactions, however, are not localised to the S_1 state and it is proposed that there is an interaction in the cation of $^{+}26^1 29^1 m^0$…$^{+}18^1 29^1 m^{3(-)}$, which arises owing to the interaction in S_1, which brings $29^1 29^1 m^{3(+)}$ character into the excited eigenstate.

However, the most significant (and strongest) interaction occurs in the ground state, whereby we see the $\Delta(v, m) = (2, 3)$ interaction, $27_2 m_0$…$19_1 27_1 m_{3(-)}$, which perturbs the energy of the ZOSs comprising the corresponding emission bands in the 2D-LIF spectrum. Consequently, the $27_2 m_0$…$19_1 27_1 m_{3(-)}$ eigenstate is lowered in emission energy and the $19_1 27_1 m_{3(-)}$…$27_2 m_0$ eigenstate is pushed up in energy. Therefore, the latter is then, serendipitously, located where one would expect the pure $27_2 m_0$ level to lie. Again, this is an example of an *m*-specific interaction and there are no significant *e* symmetry levels nearby in energy to $27_1 m_1$ to yield such an interaction. There is, remarkably, a very similar $26_1 27_1 m_0$…$19_1 26_1 m_{3(-)}$ interaction, ~100 cm^{-1} higher in emission energy. This is, again, another study that shows the power of the 2D-LIF technique in aiding the understanding of overlapping and interacting states, as one can separate out both the emission and excitation transitions, to get a wider view of these interactions. We further highlight that the complexity of this region of the excitation spectrum is remarkable as is still relatively low in internal energy.

Contributions: The original 2D-LIF spectrum was collected by myself and DJK as a part of my MSci project with the group. While writing up the paper presented as Section 8, it was realised that the ZEKE spectra we had previously recorded were not sufficient in number or quality to unpick the origins of these remarkable interactions, as such, all the ZEKE spectra presented in this paper were recorded by myself, much later. All figures were created by myself, and the analysis of the data was a collaboration between myself, DJK and TGW. I read and commented on multiple versions of the manuscript, and discussed and helped implement reviewers' comments to the final version of the paper.

Reproduced from *J. Mol. Spectrosc.*, 2021, 381, 11152, as permitted by Elsevier.

Journal of Molecular Spectroscopy 381 (2021) 111522

Contents lists available at ScienceDirect

Journal of Molecular Spectroscopy

journal homepage: www.elsevier.com/locate/yjmsp

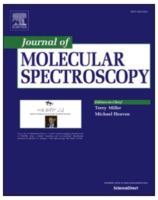

Unpicking vibration-vibration and vibration-torsion interactions in *m*-fluorotoluene

Alexander R. Davies, David J. Kemp, Timothy G. Wright [*]

School of Chemistry, University of Nottingham, University Park, Nottingham NG7 2RD, UK

ARTICLE INFO

Keywords:
m-Fluorotoluene
REMPI
ZEKE
Dispersed fluorescence
2D-LIF
LIF
Torsion

ABSTRACT

Two-dimensional laser-induced fluorescence (2D-LIF) spectra are reported for a set of features in the $S_1 \leftrightarrow S_0$ electronic spectrum of *m*-fluorotoluene. Two transitions previously assigned to fundamentals are reassigned in the present work. The main reassignments are confirmed with zero-electron-kinetic-energy (ZEKE) spectroscopy. Interactions in the S_0, S_1 and D_0^+ electronic states involving vibrational and vibration-torsional ("vibtor") levels are identified via observed activity. The obtained vibrational wavenumbers compare well to the results of quantum chemical calculations.

1. Introduction

In previous work [1–3] we have presented assignments of bands seen in the $S_1 \leftrightarrow S_0$ electronic spectra of *m*-fluorotoluene (*m*FT), based on activity seen in resonance-enhanced multiphoton ionization (REMPI), two-dimensional-LIF (2D-LIF) and zero-electron-kinetic-energy (ZEKE) spectra, together with quantum chemical calculations. The first work [1] focused on the low-energy region, the second [2] on unusual intensities caused by Duschinsky rotations, with the most recent one [3] tackling the majority of the bands in the 0–1350 cm^{-1} region of the $S_1 \leftarrow S_0$ transition. In the latter paper, we examined the evolution of the interactions that underpin intramolecular vibrational energy redistribution (IVR) from the restricted regime through to that of statistical; furthermore, the validity of directly comparing the IVR behaviour of *m*- and *p*-fluorotoluene was considered. Omitted from Ref. [3] was a detailed consideration of the bands in the 650–800 cm^{-1} region, shown in Fig. 1, except for the assignment of the $17^1m^{0,1}$ contributions. In the present work, we consider this region of the spectrum further. We present both 2D-LIF and ZEKE spectra, and discuss evidence for the assignment of the main contributions to these features, together with evidence for interactions in the S_0, S_1 and D_0^+ states.

Our first paper on the low-wavenumber region [1] complemented the 2D-LIF study of that region by Stewart, Gascooke and Lawrance [4] and information from both papers is useful in aiding the assignment of the spectra reported in the present work. Also in Ref. [4], quantum chemistry calculations suggested that several of the assignments by Okuyama et al. [5] may be incorrect, and this was supported by similar calculations by ourselves [3]. The present work will consider two of these, providing spectroscopic evidence for the reassignments. The activity will then be seen to be consistent with that observed in the corresponding region for *m*-difluorobenzene (*m*DFB) [6] – see Fig. 1.

2. Experimental

The REMPI/ZEKE [7] and 2D-LIF [8] apparatuses are the same as those employed recently. In all of the present experiments, a free-jet expansion of the vapour above room-temperature *m*FT (Sigma-Aldrich, 98% purity) in 2 bar Ar was employed.

For the 2D-LIF spectra, the free-jet expansion was intersected at *X/D* ~ 20 by the frequency-doubled output of a single dye laser (Sirah CobraStretch), operating with Coumarin 503 and pumped with the third harmonic of a Surelite III Nd:YAG laser. The fluorescence was collected, collimated, and focused onto the entrance slits of a 1.5 m Czerny-Turner spectrometer (Sciencetech 9150) operating in single-pass mode, dispersed by a 3600 groove/mm grating. This allowed ~300 cm^{-1} windows of the dispersed fluorescence to be collected by a CCD camera (Andor iStar DH334T). At a fixed grating angle of the spectrometer, the excitation laser was scanned, and at each excitation wavenumber the camera image was accumulated for 2000 laser shots. This allowed a plot to be produced of fluorescence intensity versus both the excitation laser wavenumber and the wavenumber of the emitted and dispersed fluorescence, termed a 2D-LIF spectrum [9,10].

---

[*] Corresponding author.
E-mail address: Tim.Wright@nottingham.ac.uk (T.G. Wright).

https://doi.org/10.1016/j.jms.2021.111522
Received 9 June 2021; Received in revised form 18 August 2021; Accepted 20 August 2021

The REMPI and ZEKE spectroscopic experiments employed focused, frequency-doubled dye laser outputs (Sirah CobraStretch). For the ZEKE experiments, two such outputs were overlapped spatially and temporally, and passed through a vacuum chamber coaxially and counter-propagating, where they intersected the free-jet expansion. The excitation laser (also used in the REMPI experiments) operated with Coumarin 503 and was pumped with the third harmonic (355 nm) of a Surelite III Nd:YAG laser, while the ionization laser operated with Pyrromethene 597, pumped with the second harmonic (532 nm) of a Surelite I Nd:YAG laser. The jet expansion passed between two biased electrical grids located in the extraction region of a time-of-flight mass spectrometer, which was employed in the REMPI experiments. These grids were also used in the ZEKE experiments by application of pulsed voltages, giving typical fields of ~ 10 V cm^{-1}, after a delay of up to 2 μs; this delay was minimized while avoiding the introduction of excess noise from the prompt electron signal. The resulting ZEKE bands had widths of ~ 5–7 cm^{-1}. Electron and ion signals were recorded on separate sets of microchannel plates.

3. Nomenclature

3.1. Vibrational and torsional labelling

When referring to vibrations, the C_s point group may be used, under the assumption that the methyl group is treated as a point mass. To consider the methyl torsional motion explicitly, use of the G_6 molecular symmetry group (MSG) is appropriate. In Table 1, we provide the correspondence between the C_s and G_6 symmetry labels. The torsional levels will be labelled via their m quantum number [1,4]. We shall employ the D_i labels [11] for the vibrations, as used in previous work [1–4]. That labelling scheme is based on the vibrations of the *m*DFB molecule, but treated within the C_s point group. The available experimental vibrational wavenumbers for *m*FT and *m*DFB are presented in Table 2, alongside the calculated wavenumbers – the majority of the calculated values have been presented previously [3]. Diagrams of the atomic motions associated with each D_i label can be found in Ref. [11]. One caveat to this is that the D_{19} and D_{20} the motions are very mixed in

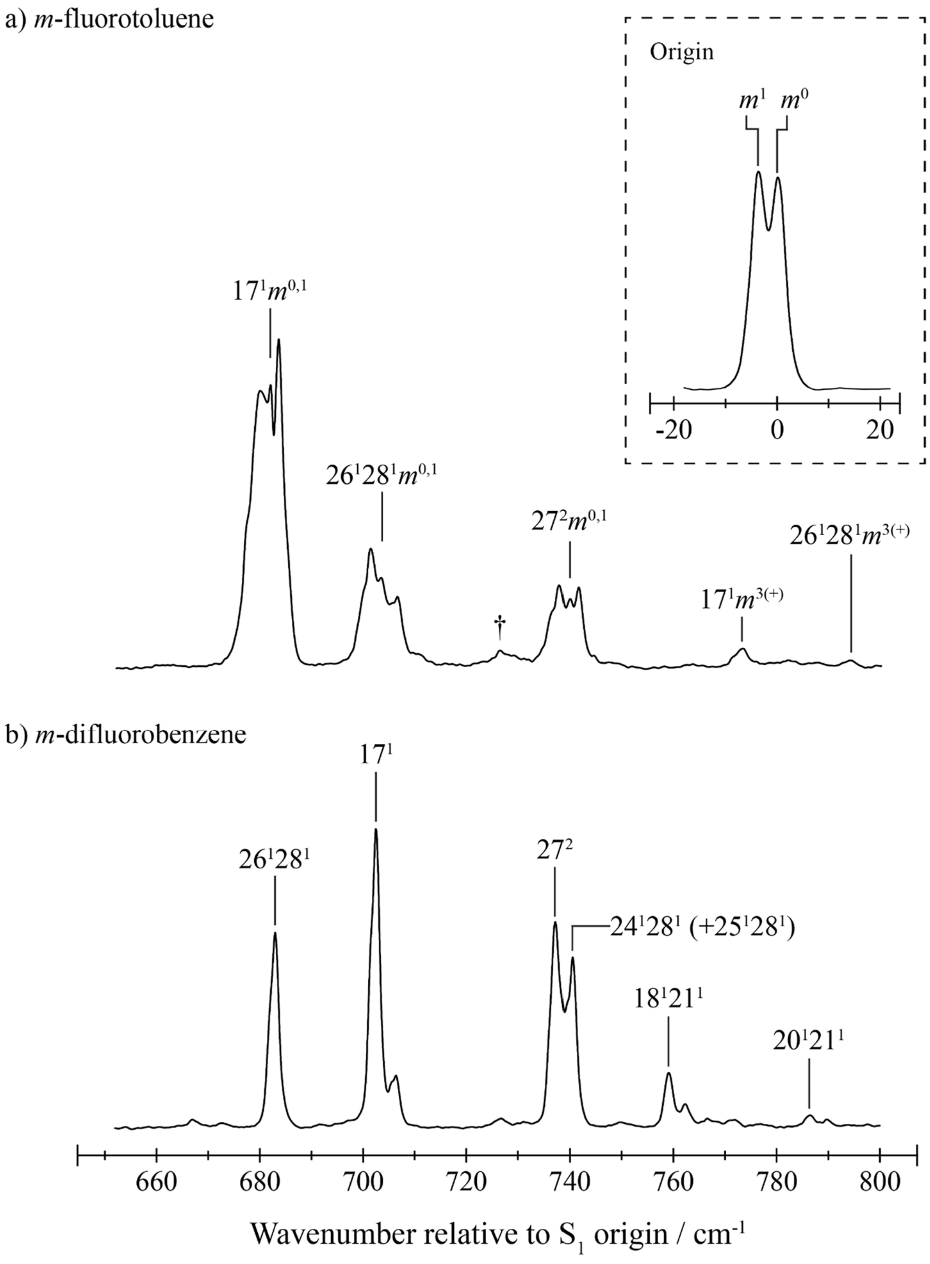

Fig. 1. REMPI spectrum of (a) *m*-fluorotoluene; and (b) *m*-difluorobenzene. The REMPI assignments of *m*-fluorotoluene are discussed in the text, while those of *m*-difluorobenzene were presented and discussed by Graham and Kable for their LIF spectrum [6], and commented on in Ref. [3]. The band marked with an obelus in the top trace is discussed in the text, and the corresponding band is also indicated in the integrated 2D-LIF spectrum at the top of Fig. 2. In the insert, top right, we show the origin bands on the same wavenumber scale, to allow band shapes to be compared – see text.

Table 1
Correspondence of the C_s point group symmetry classes with those of the G_6 molecular symmetry group. Also indicated are the symmetries of the D_i vibrations and the different pure torsional levels.[a]

C_s	G_6	D_i[b]	m
a'	a_1	D_1–D_{21}	0, 3(+), 6(+), 9(+)
a''	a_2	D_{22}–D_{30}	3(–), 6(–), 9(–)
	e		1, 2, 4, 5, 7, 8

[a] Symmetries of vibtor levels can be obtained by combining the vibrational symmetry (in G_6) with those of the pure torsional level, using the C_{3v} point group direct product table.

[b] The D_i labels are described in Ref. [11], where the vibration mode diagrams can also be found.

the S_1 state (only) of *m*FT, as discussed in Ref. [2], and are denoted therein as D_X and D_Y respectively in that state; we retain that labelling here.

To establish the overall symmetry of a vibtor level, it is necessary to use the corresponding G_6 label for the vibration, and then find the direct product with the symmetry of the torsion, noting that a C_{3v} point group direct product table can be used, since the G_6 MSG and the C_{3v} point group are isomorphic.

Under the free-jet expansion conditions employed here, almost all molecules are expected to be cooled to their zero-point vibrational level, and thus essentially all $S_1 \leftarrow S_0$ pure vibrational excitations are expected to originate from this level. In contrast, owing to nuclear-spin and rotational symmetry, the molecules can be in one of the $m = 0$ or $m = 1$ torsional levels [12], with close-to-equal populations in each; additionally, residual population in the $m = 2$ level of *m*FT is sometimes present [1,4,5].

3.2. Coupling and transitions

In the usual way, vibrational transitions will be indicated by the number, *i*, of the D_i vibration, followed by a super-/subscript specifying the number of quanta in the upper/lower states, respectively; torsional

Table 2
Calculated and experimental wavenumbers (cm^{-1}) for the vibrations of *m*-difluorobenzene and *m*-fluorotoluene.

D_i	C_{2v}[a]		S_0				S_1				D_0^+	
			*m*DFB		*m*FT		*m*DFB		*m*FT		*m*FT	
			Calc[b]	Expt[c]	Calc[b]	Expt[c]	Calc[b]	Expt[c]	Calc[d]	Expt[e]	Calc[f]	Expt[g]
							a' (a_1)[h]					
D_1	1	a_1	3122	3095	3107	[3081]	3157		3128		3119	
D_2	2	a_1	3116	3086	3088	[3060]	3141		3114		3107	
D_3	21	b_2	3112	3086	3086		3115		3123		3111	
D_4	3	a_1	3090		3072		3113		3084		3092	
D_5	4	a_1	1597	1611	1578	[1595]	1529	(1519)	1512		1541	1569
D_6	22	b_2	1592	1613	1603	[1623]	1480		1494		1490	
D_7	23	b_2	1475	1490	1479	[1492]	1375		1392		1444	
D_8	5	a_1	1439	1435	1420	[1460]	1378	(1346)	1363		1385	
D_9	24	b_2	1304	1337	1302	1294	1435		1411		1356	
D_{10}	6	a_1	1255	1277	1239	1254	1250		1243		1299	1290
D_{11}	25	b_2	1252	1292	1271	1271	1228	1267	1252	1260	1258	1275
D_{12}	26	b_2	1145	1157	1148	1132	1118	1145	1122	[i]	1143	
D_{13}	27	b_2	1102	1120	1126	1115	1094	(1206)	1113	[i]	1101	
D_{14}	7	a_1	1058	1068	1071	1081	995	998	1023		1074	
D_{15}	8	a_1	994	1012	988	1004	958	966	958	965	997	984
D_{16}	28	b_2	941	956	912	930	883	936	866	840	873	874
D_{17}	9	a_1	726	739	720	731	698	701	685	684	700	710
D_{18}	10	a_1	514	522	519	525	437	442	459	460	509	510
$D_{19(X)}$	29	b_2	502	513	505	512	439	444	448	457	410	415
$D_{20(Y)}$	30	b_2	467	477	435	445	462	468	410	420	442	456
D_{21}	11	a_1	320	329	285	294	314	317	281	285	290	298
							a'' (a_2)[h]					
D_{22}	15	b_1	963	957	967	980	719	(581)	760		988	
D_{23}	12	a_2	871	876	886	[886]	723	672	705		916	
D_{24}	16	b_1	856	857	859	842[j]	362	480	501	514[j]	855	
D_{25}	17	b_1	767	771	773	766	500	(479)	575	580	787	780
D_{26}	18	b_1	671	680	683 [k]	683	458	422	468	453	592	592
D_{27}	13	a_2	597	603	557	557	400	369	377	371	514	517
D_{28}	19	b_1	455	454	443	441	239	260	241	253	373	380
D_{29}	14	a_2	239	252	236	237	187	176	184	174	190	190
D_{30}	20	b_1	222	227	199	201	97	127	122	128	167	169

[a] Labels discussed in Ref. [11], where mode diagrams are presented. The numbers are the Mulliken C_{2v} numbers used in Ref. [6] for *m*DFB. For D_{19} and D_{20} the motions are very mixed in the S_1 state of *m*FT, as discussed in Ref. [2], and are denoted therein as D_X and D_Y respectively.

[b] B3LYP/aug-cc-pVTZ, scaled by 0.97 – see Ref. [3].

[c] S_0 values are those obtained in jet-cooled expansion experiments or, when such values are not available, those from IR/Raman studies of liquids or solutions are given in square brackets – see Refs. [3] and [11]. For the S_1 state, values that were deemed uncertain in Ref. [6] are given in parentheses.

[d] TD-B3LYP/aug-cc-pVTZ, scaled by 0.97. These values have been recalculated here, and are almost identical to those reported in Ref. [3], but where the four highest wavenumber values were omitted. (These values are also close to the TD-B3LYP/cc-pVTZ values presented in Ref. [4], but several of the values may be seen to be sensitive to the addition of diffuse functions to the basis set.)

[e] Gas phase values taken from Refs. [1–4] and the present work, in some cases confirming a value reported in Ref. [5].

[f] UB3LYP/aug-cc-pVTZ, scaled by 0.97; $\langle S^2 \rangle = 0.76$ [3].

[g] Values taken from Refs. [1–3] and the present work.

[h] Symmetry label in the C_s point group, with G_6 molecular symmetry group label in parentheses.

[i] Experimental values for these two vibrations were reported in Ref. [5], but have been concluded to have been misassigned [4].

[j] Value obtained in the present work from the assignment of the ($24^1 29^1$, $24_1 29_1$) emission – see text.

[k] Slightly different values are obtained from the $26_1 28_1$ and $26_1 27_1$ bands; the average value is given here.

transitions will be indicated by *m* followed by its value. Finally, vibtor transitions will be indicated by a combination of the vibrational and torsional transition labels. When designating transitions, we shall generally omit the initial level, since it will be obvious from either the jet-cooled conditions or the specified intermediate level. When we refer to a “vibrational transition” it is understood to refer to both the $m = 0$ and $m = 1$ components, unless otherwise specified.

As has become common usage, we will generally refer to a level by specifying quantum numbers; thus, superscripts indicate levels in the S_1 state and subscripts indicate levels in the S_0 state. Since we will also be referring to transitions and levels involving the ground state cation, ${D_0}^+$, we shall indicate those as superscripts, but with a single, additional, preceding superscripted “+” sign. Relative wavenumbers of the levels will be given with respect to the relevant zero-point vibrational and *m* level in each electronic state.

For cases where the geometry and the torsional potential are both similar in the S_1 and ${D_0}^+$ states, the most intense transition is usually expected to be that for which no changes in the torsional and/or vibrational quantum numbers occur, designated as $\Delta m = 0$, $\Delta v = 0$, or $\Delta(v, m) = (0, 0)$ transitions, as appropriate. Where we are denoting the difference in quantum numbers between a pair of interacting levels as $\Delta(v, m) = (x, y)$, where *x* denotes the change in the vibrational quantum number, and *y* that in the torsional quantum number.

However, as will be seen (and as reported in Refs. [1,4,5]), the $\Delta m = 0$ and $\Delta(v, m) = (0, 0)$ transitions are almost always not the most intense bands in the ZEKE spectra for *m*FT, indicative of a significant change in the torsional potential upon ionization. The assignments and intensities of low-wavenumber features in the $S_1 \leftrightarrow S_0$ transitions have been discussed in Ref. [4], and reference will be made to that work when appropriate; the corresponding ZEKE spectra have been considered in depth in Ref. [1].

When we need to refer to the wavenumbers of a 2D-LIF band, this will be done as an (excitation, emission) cm^{-1} pair of numbers; similarly, a pair of transitions can be explicitly given [4] if required to identify a 2D-LIF band.

If two levels are close in wavenumber, and have the same overall symmetry, then (except between vibrational fundamentals, to first order) interactions can occur. The simplest example of this is the anharmonic interaction between two vibrational levels – the classic Fermi resonance [13], where the intensity of an optically bright state – a zero-order bright (ZOB) state – may be thought of as being shared with an optically dark state – i.e. zero-order dark (ZOD) state; ZOB and ZOD states can be referred to collectively as zero-order states (ZOSs). Further couplings can also occur, and multiple couplings can be considered within the “tier model” [14], with the overall process being termed intramolecular vibrational redistribution (IVR). Direct couplings are only expected to be significant for small changes, $\Delta v \approx 3$, of the vibrational quantum number [15]. For molecules that contain a hindered internal rotor, and if vibration-torsion coupling occurs, then interactions can also involve torsional and/or “vibtor” levels. This is expected to be significant only for changes in the torsional quantum number Δm, of 0, ±3 or ±6, in descending order of likely strength [16]. The end result of such interactions is the formation of eigenstates with mixed character. Often the resulting eigenstates will be referred to herein by the dominant contribution, with the context implying if an admixture is present. If this process involves only a handful of states, this is known as restrictive IVR whereas, if there is widespread dispersal of internal energy, this is known as statistical IVR.

4. Assignments

The assignments of the majority of the bands in the ~ 0–1350 cm^{-1} region of the electronic spectrum of the $S_1 \leftarrow S_0$ transition in *m*FT have been discussed in our previous work [1–3]. Here we focus on the 650–800 cm^{-1} region, for which the REMPI spectrum is shown in Fig. 1, together with the corresponding section of the *m*DFB spectrum. (Scans of the wider ~0–1350 cm^{-1} regions have been presented in Ref. [3], where the activities were compared between these two molecules.)

We shall consider each main feature of the *m*FT spectrum by discussing the 2D-LIF spectra, considering pertinent bands and regions, before moving onto the ZEKE spectra. The latter turn out to be less useful in the initial identification of the assignments of the various contributions to the spectra, owing to the change in phase and other torsional parameters between the S_1 state and the cation. This aspect leads to several ZEKE bands arising for each contribution, and while this is a useful diagnostic in cases where there is a highly dominant contribution [1–3], it leads to complicated spectra; even so, the ZEKE spectra provide useful confirmatory evidence for the main assignments.

We have recorded 2D-LIF spectra of *m*FT across the excitation range 676–748 cm^{-1}, and in the emission range 25–1300 cm^{-1}; this latter range is expected to cover the $\Delta(v, m) = (0, 0)$ regions, as well as showing other activity indicative of interactions with vibtor levels. In Fig. 2, we show two sections of the overview of the 2D-LIF spectrum where the richness of the emission activity can be seen. The larger region covers the $\Delta(v, m) = (0, 0)$ regions, while the smaller section shows the low-wavenumber emission region when exciting across the same region of bands. At the top of Fig. 2 we show the result of vertically integrating the 2D-LIF spectrum, producing a spectrum that is very similar to the corresponding region of the REMPI spectrum shown in Fig. 1; this suggests that the range of the fluorescence collected in the 2D-LIF image is representative of the absorption spectrum. It is relatively straightforward to see columns of emission activity in the 2D-LIF spectrum, and to associate these with the individual excitation features; however, it can be seen that there is extra complexity underlying each feature.

The change in the torsional potential between the S_0 and S_1 states leads to the origin, and other vibrational bands in the REMPI and integrated fluorescence spectrum (see Fig. 1), to comprise a pair of bands corresponding to $\Delta m = 0$ transitions involving the $m = 0$ and $m = 1$ components, of roughly equal intensity, and separated by ~4 cm^{-1} [1,4,5]. As such, it is expected that there will be columns of emission bands in the 2D-LIF spectrum, arising from pairs of approximately equal intensity transitions. Additionally, there are various vibtor transitions, some of which are those accessible from each of the S_1 $m = 0, 1$ components [1–5]. Interestingly, for the 675–690 cm^{-1} and 734–746 cm^{-1} excitations, there is not a single pair of obvious $\Delta(v, m) = (0, 0)$ bands corresponding to each ZOB state. Furthermore, across the 2D-LIF spectrum, in the cases where they are present, the intensities of the $m = 0$ and $m = 1$ components of various 2D-LIF bands may be seen to be markedly different to one another (Fig. 2). Not so obvious, is that there are various emission bands that are not directly associated with an active vibrational level, and so must arise as a result of interactions; for the most part, these are assigned to vibtor levels.

In previous work [3], we have discussed the 2D-LIF and ZEKE spectra recorded across the 675–690 cm^{-1} absorption region. The ZEKE spectra were clear that the main contribution to this region was $17^1m^{0,1}$, with the distinctive pattern of associated $^{+}17^1m^x$ vibtor bands. Interestingly, as may be seen from Fig. 2, as well as the clear $17_1m_{0,1}$ emission bands in the 2D-LIF spectrum, there are other fairly strong emission bands to higher wavenumber, in particular $15_1m_{0,1}$, even though the calculated Duschinsky mixing of the D_{15} and D_{17} vibrations was minimal – indeed, when exciting $15^1m^{0,1}$, the $17_1m_{0,1}$ bands were actually more intense than the $15_1m_{0,1}$ ones [3]. Although these transitions are allowed, it is possible that the vibrational potentials are affected by vibronic coupling, which was not included in the calculation of the Duschinsky matrix.

If we use the same labelling scheme for *m*DFB and *m*FT, then, since the masses of the substituents are very similar, we expect the corresponding vibrational wavenumbers to be close for these molecules, although some differences may arise from electronic/steric factors [11]. As a consequence, in assigning the REMPI spectrum of *m*FT, we expect activity to resemble that seen in corresponding spectra of other similar molecules, such as the LIF and REMPI spectra of *m*DFB [3,6]. In Fig. 1, we have included the corresponding section of the REMPI spectrum of

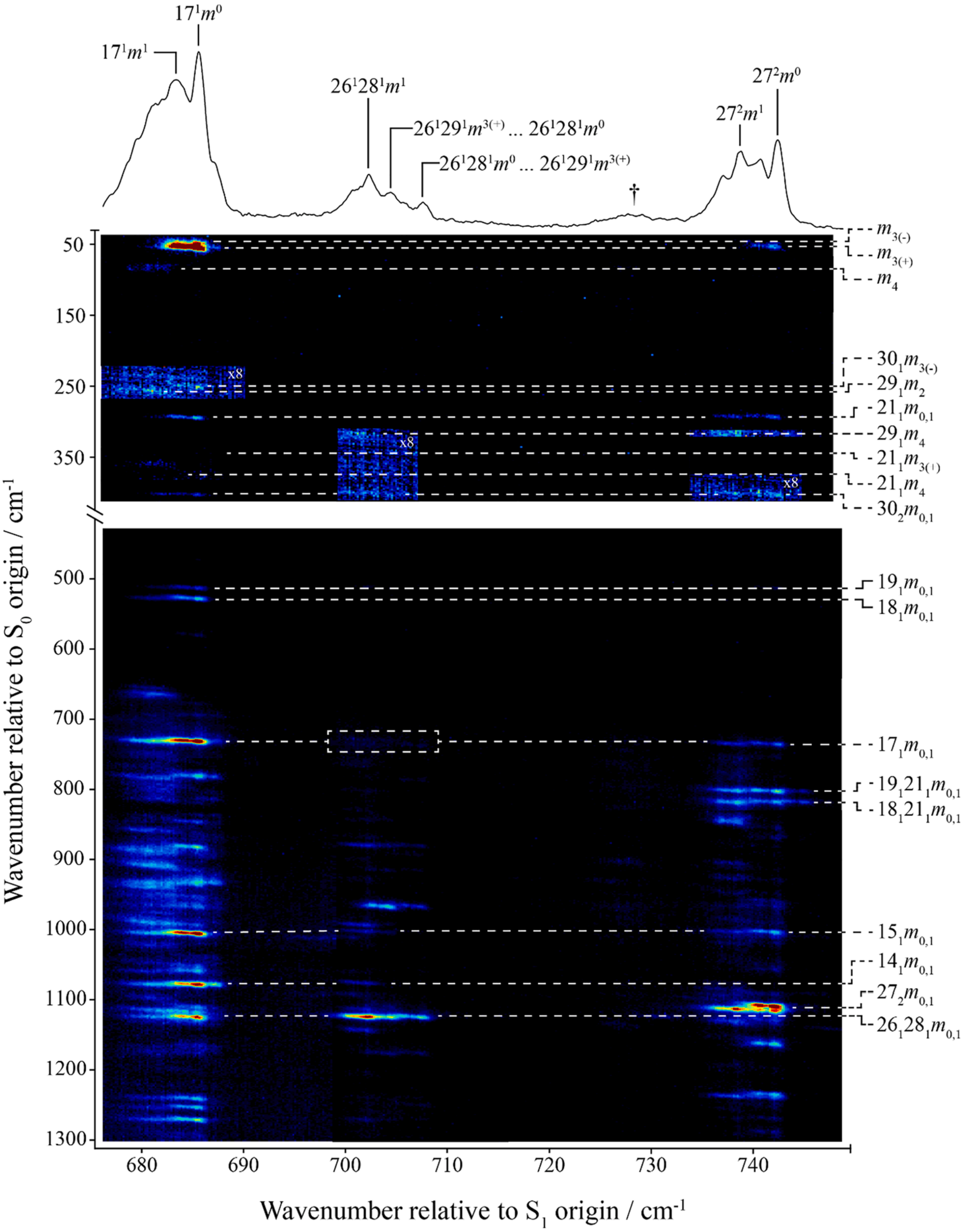

Fig. 2. The top trace, which can be seen to resemble closely the REMPI spectrum of *m*FT in Fig. 1(a), is the vertically-integrated version of the whole 2D-LIF spectrum. Below this, two sections of the 2D-LIF spectrum are presented: the top section shows the low-wavenumber emission region; the bottom section shows the main $\Delta(v, m) = (0, 0)$ activity. In the integrated trace at the top, the main contributions are indicated – see text for further discussion of interactions. Only selected main emission assignments are given on the 2D-LIF sections, with further assignments discussed in the text and shown in Figs. 3, 6, and 8. The band marked with an obelus in the integrated 2D-LIF trace is discussed in the text, and the corresponding band is also indicated in the REMPI spectrum of *m*FT at the top of Fig. 2; it may be seen that there are weak features in the 2D-LIF spectrum, particularly evident in the 850–1150 cm^{-1} emission wavenumber range.

*m*DFB, which is similar in appearance to that of the LIF spectrum of Ref. [6], where assignments of a number of bands are given, and with which we largely concurred; [3] the additional *m*FT assignments will be discussed in the following subsections.

Stewart et al. [4] reported scaled harmonic wavenumbers for the vibrations of *m*FT obtained with quantum chemistry calculations, and we reported very similar calculated values [1–3]. These calculations indicated that the two main higher-wavenumber, 698–714 cm^{-1} and 734–746 cm^{-1}, excitation features are not assignable to the fundamentals suggested by Okuyama et al. [5] We will reassign these bands herein, based on the activity seen in the 2D-LIF and ZEKE spectra, and consistent with the quantum chemical calculations.

4.1. The 17^1 level

Concentrating first on the activity in the absorption range 675–690 cm^{-1} – see expanded view of the 2D-LIF image in Fig. 3 – the strongest emission may be seen to be at a wavenumber of 731 cm^{-1}, which has been assigned [3,5] to 17_1. However, the intensity of the 17_1m_0 band is significantly stronger than that of 17_1m_1, suggesting that the 17^1m^1 level is interacting with other S_1 levels and/or is emitting to more levels than 17^1m^0. Clearly, the overall intensity profile of the REMPI/LIF feature suggests that the integrated emissions for the two m components are relatively similar (see traces at the top of Fig. 2 and Fig. 3), although the $17^1m^{0,1}$ band profiles are significantly different to those of the $m^{0,1}$ band associated with the adiabatic transition (see insert in Fig. 1), suggestive of an interaction occurring for one or both of the $17^1m^{0,1}$ levels. In Fig. 3, we have given assignments of many of the more-intense bands – it is clear that there are many other weaker bands in the spectrum, but we refrain from discussing all of these, concentrating on establishing the main assignments and hence interactions.

Since D_{17} is a totally-symmetric vibration, then it is not surprising that the most intense emission bands correspond to Franck-Condon (FC)-active totally-symmetric vibrations, many of which were also seen when exciting the origin; [3] indeed, the 17_1 emission was the strongest emission observed when exciting via the origin [3]. Each vibrational band in the REMPI and 2D-LIF spectra has the expected “double band” structure, arising from m^0 and m^1 component transitions, and also associated vibtor levels, similar to those seen on the origin; [1,4] and although some are too weak to discern in Fig. 3, many can be seen on “zoomed-in” views (not shown). In Fig. 2, the low-wavenumber emission region of the 2D-LIF spectrum is presented, and we highlight the clear $m_{3(+)}$ band when exciting 17^1m^0, and the m_4 band seen when exciting 17^1m^1 (the expected m_2 band was obscured by scatter from the excitation laser, and is not present in Fig. 2).

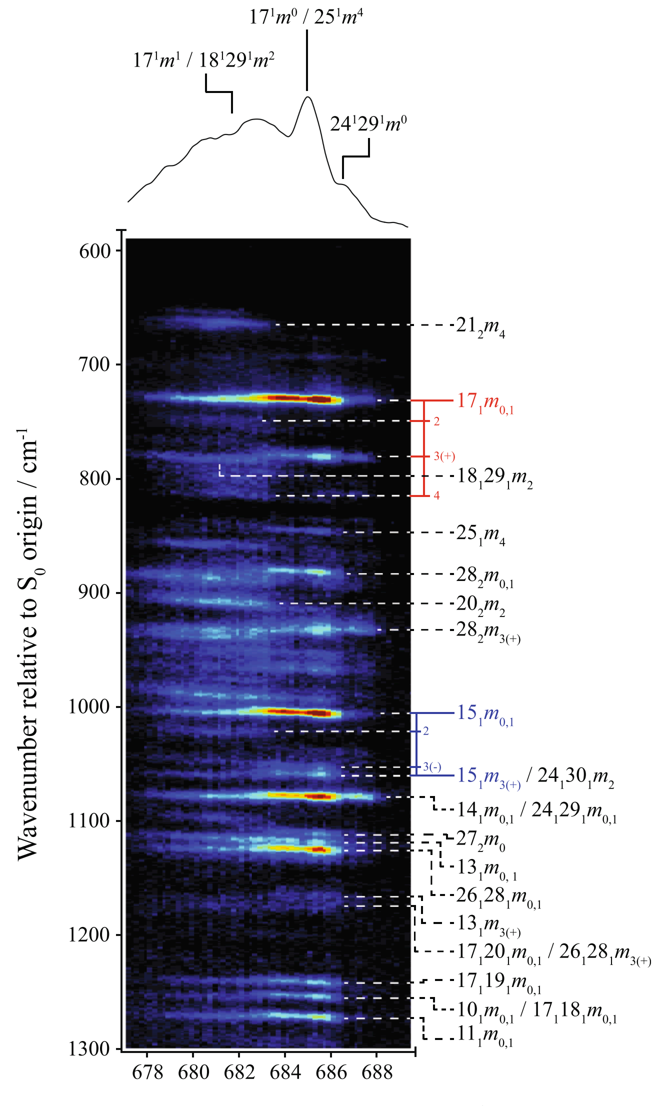

Fig. 3. Section of the 2D-LIF spectrum corresponding to the $17^1m^{0,1}$ region. The intensity scale has been adjusted from that in Fig. 2 to emphasise some of the key weaker features. The top trace is the vertically-integrated version of the 2D-LIF spectrum, with the main excitation assignments shown; these and the main emission assignments are discussed further in the text. The colouring of some labels is merely for clarity.

It is evident from Fig. 3, that the bands corresponding to totally-symmetric vibrations all have a m_0 component that is more intense than the m_1 one. Examination of other activity reveals that there are a number of 2D-LIF bands that are not associated with FC activity, primarily corresponding to S_1 levels of e symmetry, and so arising directly from, or potentially via interaction with, 17^1m^1. Furthermore, several of the bands have activity extending to higher excitation wavenumber than 17_1m_0, notably the emission band at 1079 cm^{-1}.

Since the wavenumbers of the majority of the S_0 fundamentals have been established [1–5], and since the torsional spacings are also known, then the majority of the emission bands can be assigned with a fair degree of confidence, noting that anharmonicity together with vibrational and vibration-torsion interactions may lead to bands being slightly displaced from their expected positions [4].

We now move on to consider other bands in the 2D-LIF spectrum, that do not appear to be associated with emissions arising from the FC-active totally-symmetric vibrations and their vibtors. These “additional” bands can arise as a result of interactions, in which case we should be able to identify them from a combination of their excitation and emission wavenumbers, or as activity associated with the main excitations. We first address the feature that appears as a shoulder on high-wavenumber side of the 17^1m^0 band (see trace at top of Fig. 3), which is consistent with emission producing the high-wavenumber contribution to the band at (687, 1079) cm^{-1}. (We associate the majority of the lower-excitation portion of the 1079 cm^{-1} emission feature with FC-activity arising from 14_1 following excitation of 17^1, as seen via the origin, and assigned in Ref. [3].)

As the (687, 1079) cm^{-1} feature corresponds to the most intense emission at this excitation wavenumber, we conclude this 2D-LIF feature is a $\Delta(v, m) = (0, 0)$ band, and so corresponds to a level that involves one or more vibrations that have a significant shift between the S_0 and S_1 states. Consideration of the possibilities reveals two contenders: ($24^130^1m^2$, $24_130_1m_2$) and ($24^129^1m^{0,1}$, $24_129_1m_{0,1}$). Considering initially the $24^130^1m^2$ level, this can interact with 17^1m^1, consistent with the lower intensity of the 17^1m^1 transition, and associated transitions; this would be a $\Delta(v, m) = (3, 3)$ interaction. This would then imply that the FC-active emission bands that occur at an excitation wavenumber of 681 cm^{-1} arise from $17^1m^1 \ldots 24^130^1m^2$, while those that occur at an excitation wavenumber of 687 cm^{-1} arise from $24^130^1m^2 \ldots 17^1m^1$, where the first term indicates the dominant contribution to that eigenstate; other contributions to these eigenstates would also likely be occurring. However, the band profiles of other emission bands at this excitation wavenumber are more in line with a totally-symmetric level, and particularly that there is an additional overlapping contribution to the m_0 components, and an extended activity to higher excitation wavenumber (most clearly seen on the 1079 cm^{-1} emission). The most convincing evidence for assigning this emission to a totally-symmetric level is that this extends to higher emission wavenumber for $17_1m_{3(+)}$. This observation suggests that a better assignment is ($24^129^1m^{0,1}$, $24_129_1m_{0,1}$). The 24^129^1 level can interact with 17^1 via both the $m = 0$ and $m = 1$ levels, and so would not directly be the cause of the asymmetry between the 17_1m_1 and 17_1m_0 intensity profiles, which must be due to m-specific interactions; in particular, it can also be seen (Fig. 3) that the 17^1m^1 band has an altered shape compared to that of the m^1 origin band (see inset in Fig. 1), while the 17^1m^0 band is similar.

The $24^130^1m^2$ assignment would yield a value for 24_1 of 860 cm^{-1}, which would be in excellent agreement with the calculated and previous

IR/Raman spectroscopic values. Notwithstanding this, the implication that the contribution is more likely totally-symmetric leads us to favour the $24^1 29^1$ assignment, with $24_1 29_1 m_0$ being attributable to the (687, 1079) cm^{-1} feature. This then yields a value for 24^1 of 514 cm^{-1}, which is in good agreement with the calculated value (Table 2), and a value for 24_1 of 842 cm^{-1}, which is still in reasonable agreement with the quantum chemical and IR/Raman values – particularly considering possible liquid/solvatochromic shifts compared to the present gas-phase value. This would then locate $24_1 30_1 m_2$ at 1061 cm^{-1}, and indeed there is an emission band at that wavenumber, which partially overlaps the $15_1 m_{3(+)}$ band. In summary, we assign the 1079 cm^{-1} emission to $24_1 29_1 m_0$ arising from a $24^1 29^1 \ldots 17^1$ interaction; the corresponding $24_1 29_1 m_1$ component is likely overlapped by the 14_1 emission. The value of 842 cm^{-1} for D_{24} in the S_0 state is thus adopted.

We now consider the band at (682, 664) cm^{-1}, which is consistent with an assignment to the $21_2 m_4$ emission. Since only a very faint band is seen at the expected wavenumber for $21_2 m_{0,1}$, this cannot be just a FC-active vibtor band. The $21_2 m_4$ emission is not at quite the expected excitation wavenumber for the $\Delta(v, m) = (0, 0)$ band, expected at 675 cm^{-1}, and although it may arise as a result of emission from other levels, such as $17_1 m_1$, its intensity does not support this. To be the $\Delta(v, m) = (0, 0)$ band the transition would have to gain intensity from interaction with $17^1 m^1$ via a $\Delta(v, m) = (3, 3)$ transition, which is plausible, but the inconsistency with the expected excitation position makes us cautious on this point.

A band that appears at (682, 785) cm^{-1} can be associated with the $18^1 29^1 m^2$ excitation, with a $\Delta(v, m) = (0, 0)$ assignment suggested by the absence of other associated vibtor bands, and the good agreement with expected excitation and emission wavenumbers. This is consistent with obtaining intensity from $17^1 m^1$ via a $\Delta(v, m) = (3, 3)$ interaction.

The next band considered is that at (685, 847) cm^{-1}, which can be assigned as involving the $25^1 m^4$ excitation. We suggest that this is a $\Delta(v, m) = (0, 0)$ band, gaining intensity following interaction with $17^1 m^1$ in a $\Delta(v, m) = (2, 3)$ interaction. This assignment yields values for 25^1 of 580 cm^{-1} and for 25_1 of 766 cm^{-1}, both of which are in good agreement with previous and/or calculated values – see Table 2. In our previous paper [3], we assigned an emission band at 1217 cm^{-1} to $25_1 28_1$ that was seen when exciting via the origin, giving a slightly lower value for 25_1. We now proffer an alternative assignment to that emission band, $22_1 29_1$, giving a value for 22_1 of 980 cm^{-1}.

There are other bands that cannot be associated as vibtor activity from the $17^1 m^{0,1}$ levels, nor are at the correct excitation wavenumbers to be associated with levels that are interacting with the $17^1 m^{0,1}$ levels. We currently assume that these are associated with activity arising from some of the other interacting levels, mostly those that have *e* symmetry. One example is the band at (682, 909) cm^{-1}, which has a possible assignment to a $20_2 m_2$ emission, but is not in the correct excitation position to be a $\Delta(v, m) = (0, 0)$ band.

We now examine the ZEKE spectra in the light of the above assignments, which are presented in Fig. 4, and where the main activity was discussed in Ref. [3], and the majority of the bands were assigned to vibtor transitions, $^{+}17^1 m^x$, with the expected pattern of intensities.

Bands assignable to $^{+}26^1 28^1 m^0$ and $^{+}26^1 28^1 m^{3(+)}$ are also present in the ZEKE spectrum when exciting at the wavenumber of $17^1 m^0$ (684 cm^{-1}), and $^{+}26^1 28^1 m^{1,2,4}$ bands are assignable when exciting at the wavenumber of $17^1 m^1$. As such, this is evidence that there is an interaction between $26^1 28^1$ and 17^1; this seems clearer from the ZEKE spectrum than the 2D-LIF spectrum. Other activity in the ZEKE spectrum is present, but definitive evidence for activity from the other posited interactions deduced from the 2D-LIF spectrum is elusive, because of the overlapping bands and other activity. Thus, it is only by dual consideration of the 2D-LIF and the ZEKE spectra that a more-complete picture of the activity in this region of the $S_1 \leftarrow S_0$ spectrum can be established.

We finish by noting that we assigned some $^{+}25^1 29^1 m^x$ transitions in Ref. [3], but we are now less certain of these, and so omit them here.

4.2. ZEKE spectrum via $17^1 m^{3(+)}$

In the REMPI spectrum shown in Fig. 1, there is a weak band to higher wavenumber that is in the correct position to be assigned to $17^1 m^{3(+)}$, and there are a few other weak bands to higher wavenumber. Owing to the weakness of the bands, we have only recorded a ZEKE

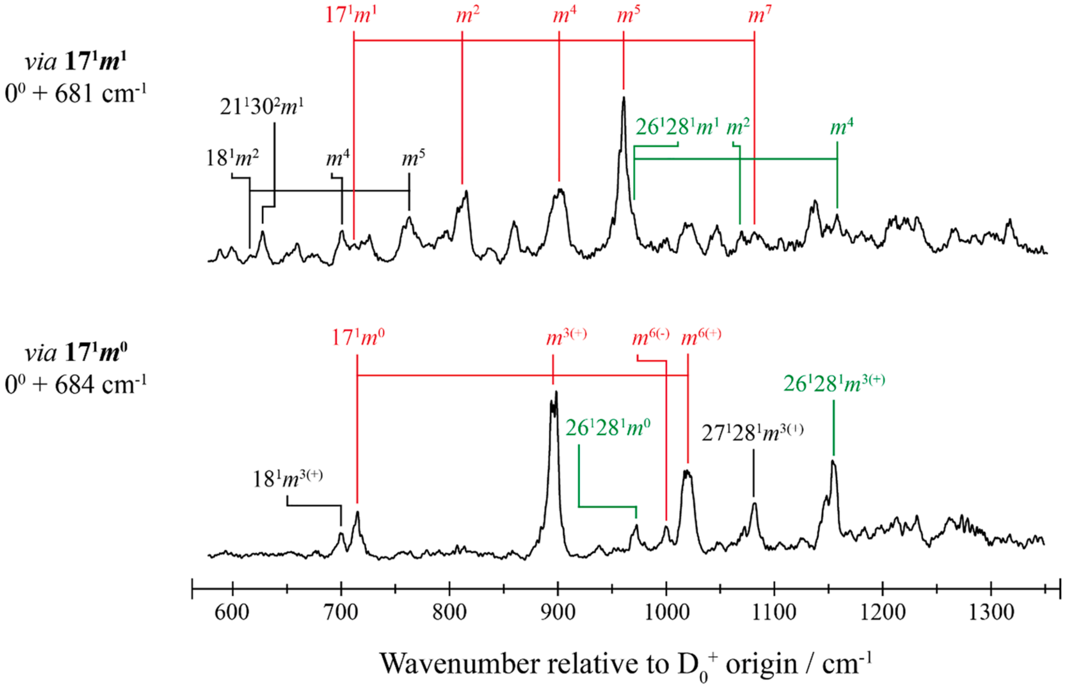

Fig. 4. ZEKE spectra recorded at the indicated excitation positions across the $17^1 m^{0,1}$ region. Key assignments are indicated and discussed further in the text. The preceding superscripted "+" is omitted from the assignments to avoid congestion. Each spectrum has been normalized to the most intense band. The colouring of the labels and combs is merely for clarity.

spectrum via $17^1m^{3(+)}$, and this is shown in Fig. 5. Remarkably, there is significant structure in this spectrum, with the expected [1–3] $\Delta m = 3$ bands, $^{+}17^1m^0$ and $^{+}17^1m^{6(+)}$ being clearly seen and the $\Delta(v, m) = (0, 0)$ band, $^{+}17^1m^{3(+)}$ being very weak , and not unambiguously identifiable in this spectrum. Interestingly, there is a significant band assignable as $^{+}26^128^1m^0$ and a band assignable to $^{+}26^128^1m^{6(+)}$ can also be identified to higher wavenumber. These are consistent with a $17^1m^{3(+)}\ldots26^128^1m^{3(+)}$ interaction in the S_1 state, mirroring the $17^1\ldots26^128^1$ interaction. Other bands in the ZEKE spectrum are consistent with reasonable assignments involving totally-symmetric levels, and so attributed to FC activity; however, there are several for which the only possible assignments do not appear to be consistent with the intensity of the bands, and those bands are left unassigned in Fig. 5.

We saw no clear evidence of activity from other 17^1m^x vibtor levels, such as 17^1m^2 and 17^1m^4, in the REMPI or 2D-LIF spectra.

4.3. *The 26^128^1 level*

In the LIF spectrum of *m*FT reported by Okuyama et al. [5] the band we observe at 706 cm^{-1} was assigned as 12^1 (denoted ν_{9b} in that work, using Wilson notation). As Table 2 shows, and in agreement with comments in Ref. [4], this band is far too low in wavenumber for this assignment to be correct, although the value for 12_1 reported in Ref. [5] is close to that calculated (Table 2) and previous IR/Raman values (see the tables and discussion in Ref. [11]).

The main features in the 2D-LIF spectrum, Fig. 6, are at an emission wavenumber of 1125 cm^{-1} and are concluded to be the $\Delta v = 0$ bands. Comparison with the spectrum of *m*DFB in Fig. 1, and the calculated vibrational wavenumbers (Table 2) allows the excitation to be straightforwardly identified as 26^128^1. From the $\Delta(v, m) = (0, 0)$ bands and the established value for 28_1 of 441 cm^{-1}, a value for 26_1 of 684 cm^{-1} is obtained, which is in good agreement with the calculated and IR/Raman values in Table 2; the value is also reasonably close to 12_1, which is likely the reason for the misassignment of the excitation in Ref. [5]. In addition, with the value of 253 cm^{-1} for 28^1, then 26^1 may be derived as 453 cm^{-1}, in good agreement with the calculated value (Table 2). Even though the 17_1 emission, when exciting 26^128^1 (Fig. 6), is weak, the previous subsection discussed some evidence for a $17^1\ldots26^128^1$ interaction, and we shall return to this point shortly, when we consider the ZEKE spectra. In Fig. 2, it can be seen that when exciting via $26^128^1m^0$, we do not see $m_{3(+)}$, and we also do not see bands corresponding to *e* symmetry torsional levels from $26^128^1m^1$. These observations are consistent with the weakness of the 17_1 emission.

There is another fairly intense band at (706, 968) cm^{-1} in Fig. 6. Looking at the activity seen in *m*DFB (see Fig. 1), we considered (25^128^1, 25_128_1) and (24^128^1, 24_128_1) as possible assignments, however, neither of these agree with the expected band positions for these two bands.

We then considered a possible assignment for this feature of (25^130^1, 25_130_1), which would be consistent with the values in Table 2 for both the S_0 and S_1 states. This could arise from inherent activity, or via a $26^128^1\ldots25^130^1$ interaction, but which would be $\Delta v = 4$, and so not expected to be strong. Also, given that the 25^130^1 band was not active in the LIF spectrum of *m*DFB [6], then it would be surprising if this were so prominent in *m*FT, unless there were an interaction. Also, examining the spectrum in more detail, we find that we cannot discern the associated vibtor bands that are expected to be associated with the (706, 968) cm^{-1} band, if it were assigned to emission to a vibrational level. Furthermore, if the activity arose from an interaction, then this would give rise to two eigenstates for $m = 0$, namely $25^130^1\mathrm{m}^0\ldots26^128^1m^0$ and $26^128^1m^0\ldots25^130^1m^0$, and a corresponding pair for $m = 1$. It would then be expected for both of the emissions at 968 cm^{-1} and 1125 cm^{-1} to extend over the same excitation range, which is not the case: the 968 cm^{-1} emission has a narrower extent than the 1125 cm^{-1} emission.

These aspects of the spectrum are what led us to seek another assignment involving a vibtor level: since a vibtor transition would be consistent with the absence of associated vibtor bands mentioned hereinbefore. The appearance and locations of the associated m_2 and the two $m_{3(+)}$ bands associated with the 1125 cm^{-1} emission leads to the conclusion that the interacting vibtor level in the S_1 state needs to be totally symmetric, and so interacts with $26^128^1m^0$, but not $26^128^1m^1$. We currently favour the assignment of the interacting level as $26^129^1m^{3(+)}$, which is consistent with the 968 cm^{-1} emission. That band is at a significantly lower excitation wavenumber than expected for $26^129^1m^{3(+)}$, and we currently assume that its interactions with $26^128^1m^0$ and other levels have produced eigenstates in significantly shifted positions – some vibration-torsion interactions can be sizeable [4].

Although $26^128^1m^1$ is at the lowest excitation wavenumber, the ordering of the other two states is less clear, but the intensities of the bands suggest $26^129^1m^{3(+)}\ldots26^128^1m^0$ is the lower wavenumber component of this $\Delta(v, m) = (2, 3)$ interaction. Looking at the REMPI band profile in Figs. 2 and 3, and comparing this to the appearance of the origin band (Fig. 2), it can be seen that the higher wavenumber side of the $26^128^1m^{0,1}$ feature has an altered shape, and is displaced from the expected $26^128^1m^0$ band position, in line with an *m*-specific interaction involving $m = 0$. As such, we tentatively assign the S_1 levels between 698 cm^{-1} and 709 cm^{-1} to: $26^128^1m^1$, $26^129^1m^{3(+)}\ldots26^128^1m^0$, and $26^128^1m^0\ldots26^129^1m^{3(+)}$, in order of increasing wavenumber (see Fig. 6).

We now consider the ZEKE spectra obtained when exciting across the excitation region containing the $26^128^1m^{0,1}$ bands. These are shown in

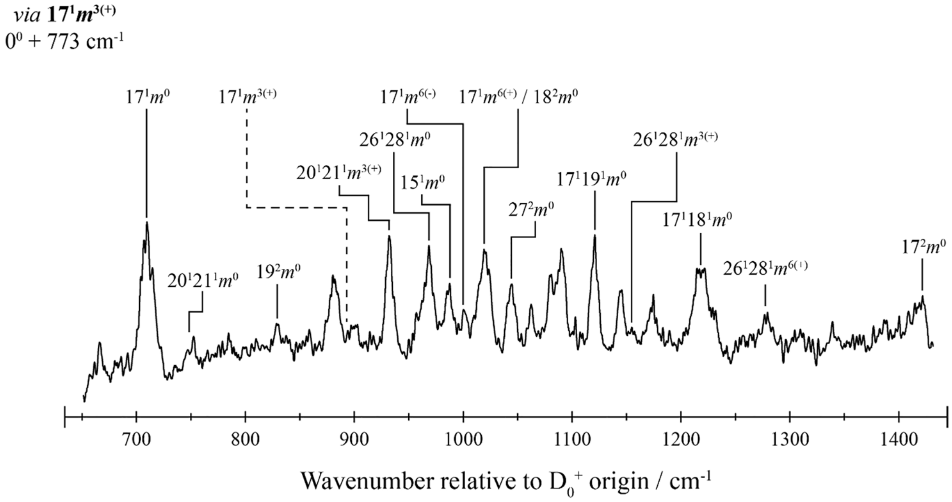

Fig. 5. ZEKE spectrum recorded via $17^1m^{3(+)}$. Key assignments are indicated and discussed further in the text. The preceding superscripted "+" is omitted from the assignments to avoid congestion. There are several sizeable bands for which there are possible assignments, but these are troublesome owing to their unexpected intensity; as such, we refrain from indicating these at the present time. We have indicated the expected position for $^{+}17^1m^{3(+)}$ with a dashed line, as there is no definitive band at this position.

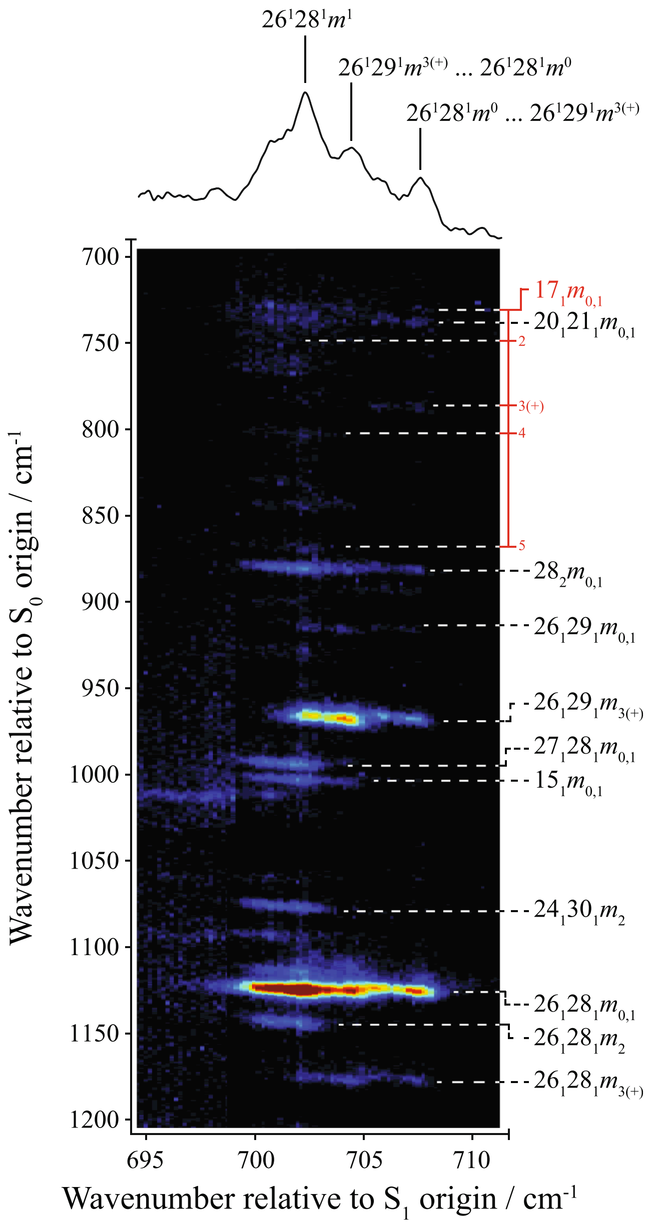

Fig. 6. Section of the 2D-LIF spectrum corresponding to the $26^1 28^1 m^{0,1}$ region. The intensity scale has been adjusted from that in Fig. 2 to emphasise some of the key weaker features. The top trace is the vertically-integrated version of the 2D-LIF spectrum, with the main excitation assignments shown; these and the main emission assignments are discussed further in the text. The colouring of the labels is merely for clarity.

Fig. 7, where six excitation positions have been employed, scanning down to cover the low wavenumber region of the ZEKE spectrum. The appearance of the torsional bands $^{+}m^2$, $^{+}m^4$ and $^{+}m^5$ are characteristic of an intermediate level that involves m^1, and as such support the assignment of the low-wavenumber section of the REMPI band to $26^1 28^1 m^1$; moreover, there are a series of corresponding $^{+}26^1 28^1 m^x$ bands providing definitive evidence for this. Interestingly, each of the latter bands is a doublet, and the other component can be identified as the equivalent $^{+}15^1 m^x$ band. Although these doublets could all be associated with FC activity, we suggest that $^{+}15^1$ and $^{+}26^1 28^1$ are in Fermi resonance in the cation, and that this occurs for each of the associated vibtor levels; this would be reminiscent of the discussed $17^1 \ldots 26^1 28^1$ interaction in the S_1 state.

For the higher-wavenumber excitations, it can be seen that the activity arises from levels associated with $m = 0$, where $^{+}m^{3(+)}$, can be seen at each of the four excitation positions, with $^{+}m^{6(-)}$ and $^{+}m^{6(+)}$ bands also sometimes being identified. It is also clear that the $^{+}26^1 28^1 m^{3(+)}$ band is more intense on the high-wavenumber end of the band, supporting the contribution to the REMPI spectrum here of $26^1 28^1 m^0 \ldots 26^1 29^1 m^{3(+)}$. The intense ZEKE band at 787 cm^{-1} may be assigned to $^{+}26^1 29^1 m^0$, supporting the involvement of $26^1 29^1 m^{3(+)}$ to the S_1 eigenstates with the contribution from $26^1 29^1 m^{3(+)} \ldots 26^1 28^1 m^0$ being located in the centre of the REMPI band, consistent with the 2D-LIF spectrum discussed earlier. The ZEKE band at 802 cm^{-1} appears to arise from a Fermi resonance in the cation: $^{+}26^1 29^1 m^0 \ldots 18^1 29^1 m^{3(-)}$, and its intensity follows that of the 787 cm^{-1} band.

It is also clear that at the higher excitation wavenumbers, we see bands that are assignable to $^{+}20^1 21^1 m^{3(+)}$ and $^{+}20^1 21^1 m^{6(+)}$, which would be consistent with $Y^1 21^1 m^0$ activity, even though the corresponding 2D-LIF bands are weak (see Fig. 3). Unambiguous identification of the *e* symmetry $^{+}20^1 21^1 m^x$ bands when exciting at the lower wavenumbers, where $Y^1 21^1 m^1$ would be expected, is less straightforward, owing to the large amount of structure in the spectrum.

In summary, the strong activity of the $^{+}17^1 m^x$ bands, taken together with the complementary activity seen when exciting via $17^1 m^{0,1}$, is highly suggestive of a $17^1 \ldots 26^1 28^1$ interaction occurring for both $m =$ 0 and 1 levels, with a further $26^1 28^1 m^0 \ldots 26^1 29^1 m^{3(+)}$ interaction occurring. The evidence for the $17^1 \ldots 26^1 28^1$ interaction is much clearer in the ZEKE spectra than it is in the 2D-LIF spectra; however, taken together, this is persuasive.

4.4. The 27^2, $18^1 21^1$ and $X^1 21^1$ levels

In the LIF spectrum of *m*FT reported by Okuyama et al. [5] a band at 746 cm^{-1} was assigned as 13^1 (denoted ν_{18b} in Wilson notation, in that work), which we find is at 741 cm^{-1}. As Table 2 shows, and in agreement with comments in Ref. [4], this band is far too low in wavenumber for this assignment to be correct, although the value for 13_1 reported in Ref. [5] is close to the calculated (Table 2) and previous IR/Raman values (see tables and discussion in Ref. [11]).

In the 2D-LIF spectrum in Fig. 8, the most intense features occur across a range of emission wavenumbers of 1104–1122 cm^{-1} – see the inset to Fig. 8. Comparison with the spectrum of *m*DFB (see Fig. 1), and the calculated vibrational wavenumbers (Table 2), allows the main excitation to be assigned as 27_2. The emission band (1114 cm^{-1}) at lower excitation wavenumber is straightforwardly assignable as $27_2 m_1$, but it is noteworthy that there are two such bands to higher excitation wavenumber, and the lower of these emission bands (1110 cm^{-1}) is the more intense. In addition, the other band is displaced to slightly higher emission wavenumber (1116 cm^{-1}) than $27_2 m_1$. As such, we conclude that at the higher excitation wavenumber, the lower-wavenumber of the two emission bands mainly arises from $27_2 m_0$, and is moved to lower emission wavenumber, owing to an interaction in the S_0 state (see inset to Fig. 8). Looking at the possibilities for a totally-symmetric vibtor level, we identify the interacting level as $19_1 27_1 m_{3(-)}$ – a $\Delta(v, m) = (2,3)$ interaction; this then gives rise to the pair of observed bands. Interestingly, a similar pattern of emission bands appears in the range 1231–1245 cm^{-1}, which is interpreted as a analogous interaction between $26_1 27_1 m_0$ and $19_1 26_1 m_{3(-)}$ – see Fig. 8. The observed wavenumbers are consistent with the calculated values (Table 2) and those derived from the ($26^1 28^1$, $26_1 28_1$) band discussed in the previous subsection.

The REMPI (Fig. 1) or integrated 2D-LIF (Fig. 8) band profiles are each different from those of the origin, suggesting that other activity is present at this wavenumber, and this is also demonstrated by the 2D-LIF spectrum in Fig. 8. Bands associated with $18_1 21_1$ and $19_1 21_1$, are clearly seen in the 2D-LIF spectrum, and are unlikely to simply be due to FC activity. Comparison with the values in Table 2, together with the similarity of the pattern of 2D-LIF bands seen when exciting 18^1 and X^1 – see Ref. [2] – makes it clear that these are $\Delta v = 0$ bands arising from

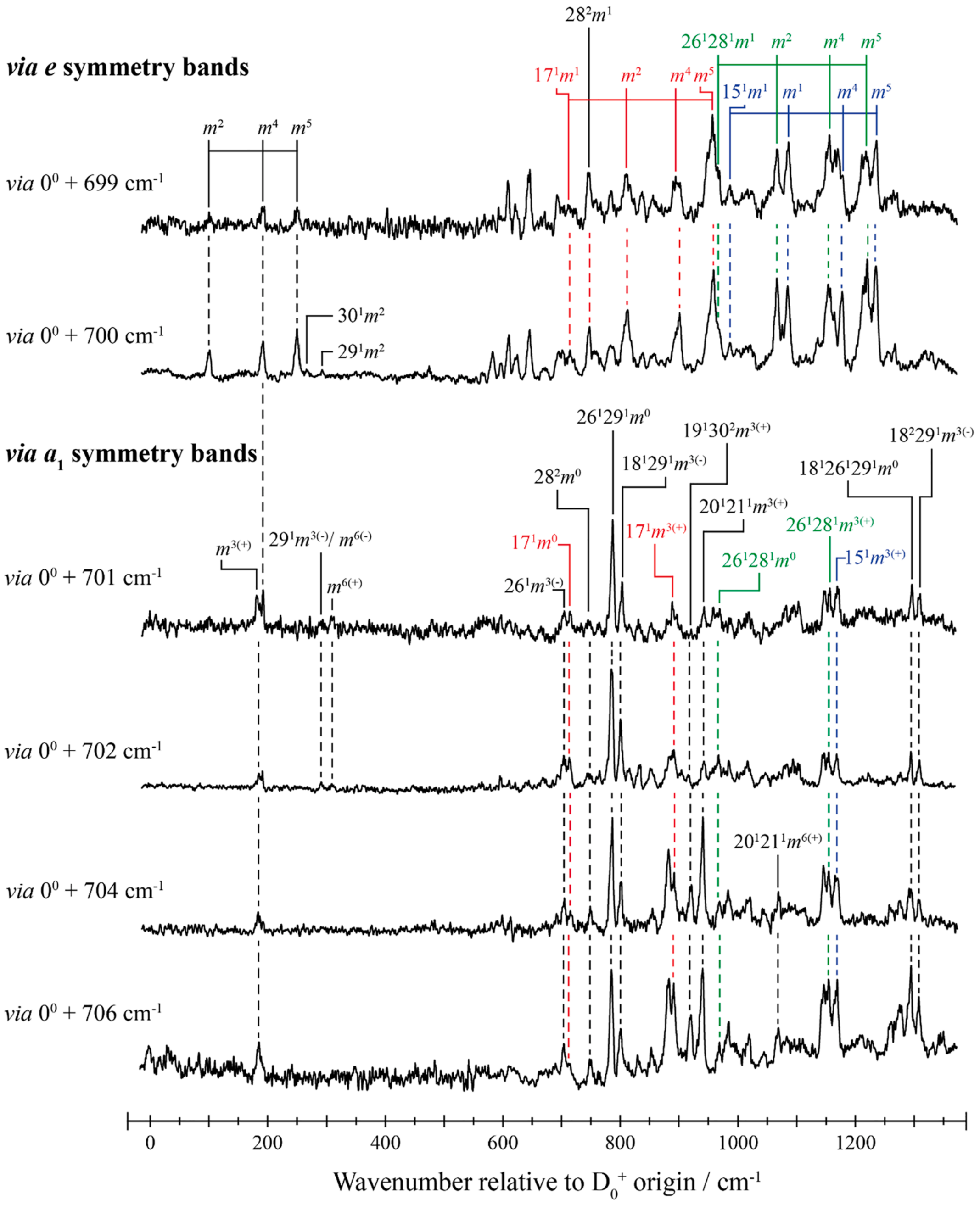

Fig. 7. ZEKE spectra recorded at the indicated excitation positions across the $26^128^1m^{0,1}$ region. Key assignments are indicated and discussed further in the text. The preceding superscripted “+” is omitted from the assignments to avoid congestion. Each spectrum has been normalized to the most intense band. The colouring of the labels and combs is merely for clarity.

18^121^1 and X^121^1 excitations. At around 705 cm^{-1}, the excitation spectra reported in Ref. [2] suggest we should see the Y^121^1 band also whose emission features are at ~736 cm^{-1}. These are seen to be very weak (Fig. 6) although the corresponding ZEKE bands in Fig. 7 are more prominent; it may also be that the 18^121^1 and X^121^1 levels are interacting weakly with 27^2, and hence gaining some intensity from it.

Since we did not observe pure torsional emission bands when exciting via 26^128^1, we may not expect to see these via 27^2; however, we do see a weak $m_{3(+)}$ band at the corresponding excitation energy (see Fig. 2) and so we hypothesise that this arises from activity associated with the 18^121^1 and X^121^1 levels, which are made up of totally-symmetric vibrations. We do not see any *e* symmetry pure torsional emission bands arising from 27^2m^1, but these may simply be too weak to see.

ZEKE spectra have been recorded at four positions across the feature that includes the $27^2m^{0,1}$ transitions, and these are shown in Fig. 9. It is immediately apparent that two of the spectra are associated with the $m = 1$ component, as ascertained from the $^+m^1$, $^+m^2$, $^+m^4$ and $^+m^5$ bands, while the other two cover $m = 0$, as ascertained from the $^+m^{3(+)}$, $^+m^{6(-)}$ and $^+m^{6(+)}$ bands (with the $^+m^0$ band being barely discernible) [1–3]. The high-wavenumber region of each spectrum shows the corresponding $^+27^2m^x$ bands. It is notable in all spectra that there is significant additional structure than the expected bands, and this is particularly the case for those corresponding to $m = 1$ where there are numerous bands, including at low wavenumber.

As noted, we expect some activity from 18^121^1 and X^121^1 in this region, and indeed bands supporting this activity are present, although these are more difficult to identify definitively in the $m = 1$ case. In

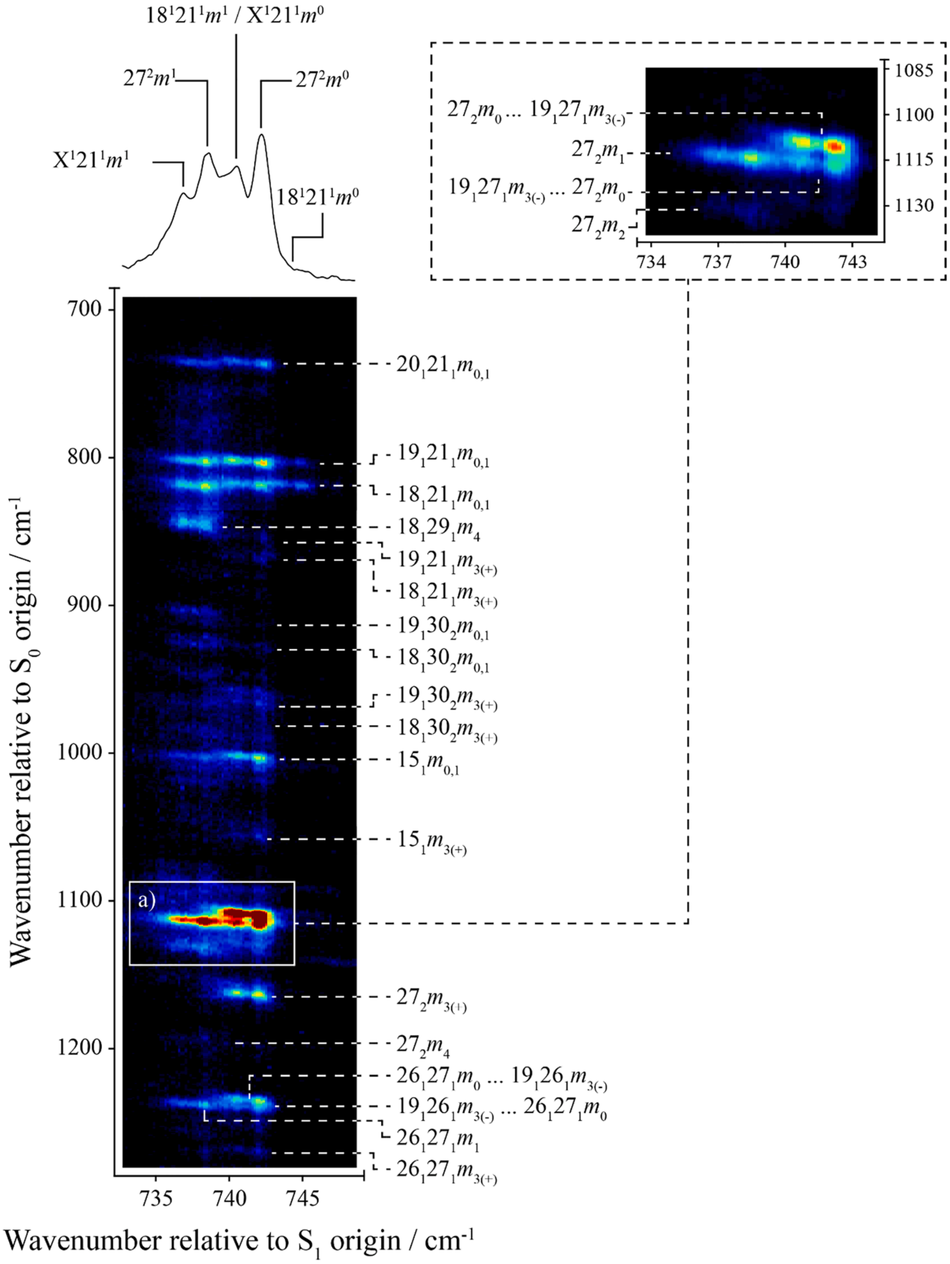

Fig. 8. Section of the 2D-LIF spectrum corresponding to the $27^2 m^{0,1}$ region. The intensity scale has been adjusted from that in Fig. 2 to emphasise some of the key weaker features. The top trace is the vertically-integrated version of the 2D-LIF spectrum, with the main excitation assignments shown; these and the main emission assignments are discussed further in the text. In the inset, top right, and expanded view is shown of the 27_2 emission region, indicating the presence of a Fermi resonance in the S_0 state – see text for further comment.

previous work on *m*FT [1–3], *p*FT [8,17–23], and *N*-methylpyrrole (NMP) [24], we have noted how the low-wavenumber region of ZEKE spectra can often give strong hints as to the assignment, since bands assignable to torsions, vibrations or vibtors that form part of combination bands are often seen. The low-wavenumber region of the spectra in Fig. 9 suggests that there is little interaction involving the $27^2 m^0$ level, but significant interactions involving $27^2 m^1$, in line with the activity seen in these spectra; identification of explicit interactions in this case has not, however, been possible, except the interactions with $X^1 21^1$ and $18^1 21^1$. As mentioned earlier, the significant change in the torsional potential upon ionization causes each contributing level to give rise to a number of ZEKE bands and this makes a full assignment “challenging”. As such, we have restricted ourselves to highlighting the main contributions, as discussed above and labelled in Fig. 9.

Finally, we comment on a weak excitation feature at 727 cm^{-1} that appears in the REMPI spectrum (Fig. 1), as well as in the integrated 2D-LIF spectrum (top of Fig. 2) – marked with an obelus in both cases. It can be seen from the 2D-LIF spectrum in Fig. 2 that there are some weak features associated with this band, for example at (727, 902) cm^{-1} and (725, 930) cm^{-1}. A possible, tentative $\Delta(v, m) = 0$ assignment of the first feature is ($25^1 m^5$, $25_1 m_5$), while two possible $\Delta(v, m) = 0$ assignments for the second one are ($26^1 m^7$, $26_1 m_7$) and ($20^1 28^1 m^{3(-)}$, $20_1 28_1 m_{3(-)}$), with the transitions involving *e* symmetry levels that can each gain intensity via interaction with one or more of $27^2 m^1$, $X^1 21^1 m^1$, $18^1 21^1 m^1$, which would be $\Delta(v, m) = (3, 6)$; while the transition involving the *a′* symmetry levels can gain intensity from interacting with one or more of $27^2 m^0$, $X^1 21^1 m^0$, $18^1 21^1 m^0$, which would be $\Delta(v, m) = (4, 3)$. These interactions are not expected to be especially strong, in keeping with the weak nature of the excitation feature. Other weak features in the REMPI and integrated LIF spectra are not considered further here.

5. Further remarks and conclusions

In the present work, we have investigated a ~150 cm^{-1} region of the $S_1 \leftarrow S_0$ REMPI spectrum of *m*FT. By recording 2D-LIF and ZEKE spectra, we have gained significant insight into the S_1 levels that give rise to this

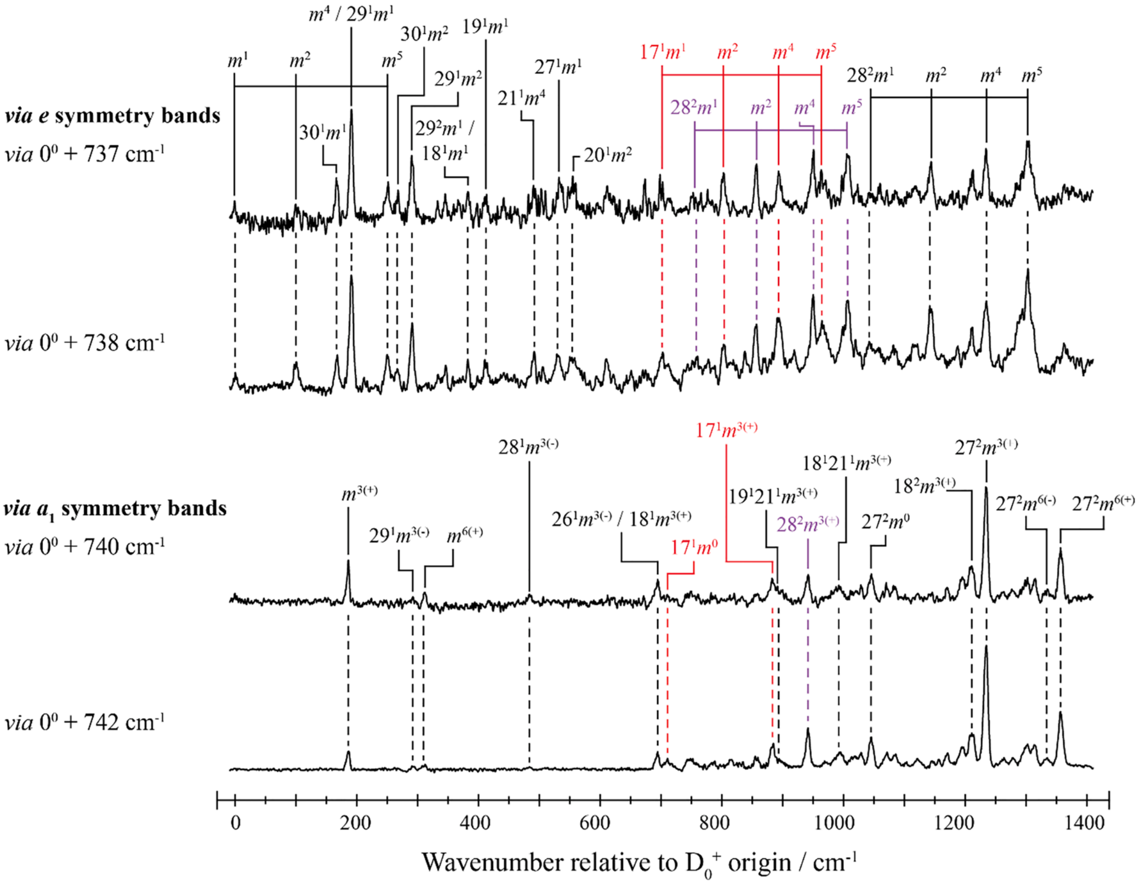

Fig. 9. ZEKE spectra recorded at the indicated excitation positions across the $27^2m^{0,1}$ region. Key assignments are indicated and discussed further in the text. The preceding superscripted "+" is omitted from the assignments to avoid congestion. Each spectrum has been normalized to the most intense band. The colouring of the labels and combs is merely for clarity.

spectrum; a summary of the transitions discussed are presented in Table 3. In addition, these spectra have revealed interactions in the S_0 and D_0^+ states. Even with these detailed spectra, it is clear that unpicking all of the interactions is complicated, although we feel confident that we have identified the main interactions. In the S_1 state, we have identified that the main *m*-specific interactions for the 17^1 level are via the $m = 1$ component, while for $26^1 28^1$, the main interaction is via the $m = 0$ component. Furthermore, there is evidence for a Fermi resonance between 17^1 and $26^1 28^1$ in the S_1 state, but this occurs in tandem with the $26^1 28^1 m^0 \ldots 26^1 29^1 m^{3(+)}$ interaction, and other interactions involving $17^1 m^1$. As a consequence, providing a comprehensive and quantitative picture of the interactions is difficult. The ZEKE spectrum of $17^1 m^{3(+)}$ also supports the $17^1 \ldots 26^1 28^1$ Fermi resonance, with evidence also presented for the corresponding interaction for the vibtor levels: $17^1 m^{3(+)} \ldots 26^1 28^1 m^{3(+)}$. Of course, such interactions are expected for all such vibtor levels [4] (in the same way as they would be expected for vibrational combinations), and notably will be occurring for the corresponding m^0 and m^1 levels; this means that, to first order, all vibtor levels will shift in sync as a result of vibrational interactions, such as a Fermi resonance. As a particular example, the ZEKE spectra in Fig. 7 reveal that there is likely a $^{+}15^1 \ldots ^{+}26^1 28^1$ interaction that occurs for each of the observed vibtors for a particular *m* value. The caveat to this is that any particular vibtor level may also be undergoing additional level-specific interactions, of the type identified for torsional and vibtor levels by Stewart et al. [4] As one example, we commented on the $^{+}26^1 29^1 m^0 \ldots ^{+}18^1 29^1 m^{3(-)}$ interaction seen in the ZEKE spectra presented in Fig. 7, recorded at the higher excitation wavenumbers.

Table 3
Summary of transitions.

Excitation wavenumber/cm^{-1}	Main contributor[a]
681	17^1m^1
682	$(21^2m^4/18^1 29^1 m^2)$
684	17^1m^0
685	25^1m^4
687	$24^1 29^1 m^0$
702	$26^1 28^1 m^1$
704	$26^1 29^1 m^{3(+)} \ldots 26^1 28^1 m^0$
706	$26^1 28^1 m^0 \ldots 26^1 29^1 m^{3(+)}$
727	$(25^1m^5/ 26^1m^7/ 20^1 28^1 m^{3(-)})$
737	$X^1 21^1 m^1$
738	27^2m^1
740	$18^1 21^1 m^1/X^1 21^1 m^0$
742	27^2m^0
745	$18^1 21^1 m^0$
773	$17^1m^{3(+)}$
795	$26^1 28^1 m^{3(+)}$

[a] Interactions between a number of states of the same symmetry are expected and are discussed in the text. Significant interactions in the S_1 state are indicated by "…". A solidus (/) indicates overlapping contributions. See Tables 1 and 2 for symmetries of vibrational and torsional levels. Tentative assignments are indicated by parentheses.

To slightly higher wavenumber is the 27^2 transition, and it is found that there are likely some weak $\Delta v = 4$ interactions with $18^1 21^1$ and $X^1 21^1$ in the S_1 state; however, the most significant interaction is $27_2 \ldots 19_1 27_1 m_{3(-)}$ in the S_0 state, and a corresponding $26_1 27_1 \ldots 19_1 26_1 m_{3(-)}$ interaction is also seen.

We have commented here, and in previous work [2,3], that there are complications in the interpretation of the spectra of *m*FT, with the strong cross-activity in the 2D-LIF spectra of 15^1 and 17^1, even though these two vibrations are not obviously Duschinsky mixed [3]. We have also noted the complications posed by the non-$\Delta(v, m) = (0, 0)$ activity that occurs upon ionization; this, coupled with the various interactions in the S_1 state leads to some ZEKE spectra showing a cornucopia of activity, and some 2D-LIF spectra also show a range of weaker activity. Considering also that various other higher-order interactions are likely occurring, is it probably a fruitless task to try and assign every weak band in the spectra. Taking this pragmatic view, we have tried to restrict ourselves to reporting the main interactions, while giving a flavour of the more-complicated underlying picture.

We highlight that the region of the excitation spectrum considered here corresponds to relatively low internal energies, and so the complexity is quite surprising, particularly as the density of states is still quite low [3], probably only a few levels per cm^{-1} at most. However, the lower symmetry of *m*FT compared to other molecules, such as *p*DFB [18,25] *p*FT [8,16–23] and NMP [24] gives more possibilities for interaction, especially those corresponding to odd-*m* vibtor levels, which all have the same *e* symmetry in the G_6 MSG [3]. Although only limited wavenumber region of the excitation spectrum of the *m*-chlorotoluene molecule have been studied [2,26], evidence for such interactions were also seen in that molecule. The serendipitous nature of IVR at low wavenumber was discussed in Ref. [18] in relation to *para*-disubstituted benzenes, and the present results, in tandem with those in Refs. [1–3], particularly the latter, confirm that this is also the case in *m*FT.

In summary, even at the low internal energy considered herein, a rather complicated picture of interacting levels emerges. However, a great deal of insight is possible using a partnership of fluorescence and ionization spectroscopies. Of course, for the vast majority of larger (bio) molecules, the symmetry will drop further, opening up more coupling routes.

CRediT authorship contribution statement

Alexander R. Davies: Investigation, Writing – review & editing, Visualization, Data curation. **David J. Kemp:** Investigation, Writing – review & editing, Data curation. **Timothy G. Wright:** Conceptualization, Writing – original draft, Investigation, Validation, Supervision, Project administration, Funding acquisition.

Declaration of Competing Interest

The authors declare that they have no known competing financial interests or personal relationships that could have appeared to influence the work reported in this paper.

Acknowledgements

We are grateful to the EPSRC for funding (grant EP/L021366/1). The EPSRC and the University of Nottingham are thanked for studentships to D.J.K. and A.R.D. Continuing discussions on vibration-torsional couplings with Warren Lawrance and Jason Gascooke (Flinders University) are gratefully acknowledged.

References

[1] D.J. Kemp, E.F. Fryer, A.R. Davies, T.G. Wright, J. Chem. Phys. 151 (2019), 084311.
[2] A.R. Davies, D.J. Kemp, L.G. Warner, E.F. Fryer, A. Rees, T.G. Wright, J. Chem. Phys. 152 (2020), 214303.
[3] A.R. Davies, D.J. Kemp, T.G. Wright, AIP Adv. 10 (2020), 125206.
[4] L.D. Stewart, J.R. Gascooke, W.D. Lawrance, J. Chem. Phys. 150 (2019), 174303.
[5] K. Okuyama, N. Mikami, M. Ito, J. Phys. Chem. 89 (1985) 5617.
[6] P.A. Graham, S.H. Kable, J. Chem. Phys. 103 (1995) 6426.
[7] V.L. Ayles, C.J. Hammond, D.E. Bergeron, O.J. Richards, T.G. Wright, J. Chem. Phys. 126 (2007), 244304.
[8] A.M. Gardner, W.D. Tuttle, L.E. Whalley, T.G. Wright, Chem. Sci. 9 (2018) 2270.
[9] N.J. Reilly, T.W. Schmidt, S.H. Kable, J. Phys. Chem. A 110 (2006) 12355.
[10] J.R. Gascooke, W.D. Lawrance, Eur. Phys. J. D 71 (2017) 287.
[11] D.J. Kemp, W.D. Tuttle, F.M.S. Jones, A.M. Gardner, A. Andrejeva, J.C. A. Wakefield, T.G. Wright, J. Molec. Spectrosc. 346 (2018) 46.
[12] A.M. Gardner, W.D. Tuttle, P. Groner, T.G. Wright, J. Chem. Phys. 146 (2017), 124308.
[13] E. Fermi, Z. Phys. 71 (1931) 250.
[14] D.J. Nesbitt, R.W. Field, J. Phys. Chem. 100 (1996) 12735.
[15] N.T. Whetton, W.D. Lawrance, J. Phys. Chem. 93 (1989) 5377.
[16] J.R. Gascooke, W.D. Lawrance, J. Chem. Phys. 138 (2013), 134302.
[17] A.M. Gardner, W.D. Tuttle, L. Whalley, A. Claydon, J.H. Carter, T.G. Wright, J. Chem. Phys. 145 (2016), 124307.
[18] W.D. Tuttle, A.M. Gardner, L.E. Whalley, D.J. Kemp, T.G. Wright, Phys. Chem. Chem. Phys. 21 (2019) 14133.
[19] D.J. Kemp, W.D. Tuttle, A.M. Gardner, L.E. Whalley, T.G. Wright, J. Chem. Phys. 151 (2019), 064308.
[20] W.D. Tuttle, A.M. Gardner, L.E. Whalley, T.G. Wright, J. Chem. Phys. 146 (2017), 244310.
[21] D.J. Kemp, A.M. Gardner, W.D. Tuttle, T.G. Wright Molec, Phys. 117 (2019) 3011.
[22] D.J. Kemp, L.E. Whalley, A.M. Gardner, W.D. Tuttle, L.G. Warner, T.G. Wright, J. Chem. Phys. 150 (2019), 064306.
[23] A.M. Gardner, L.E. Whalley, D.J. Kemp, W.D. Tuttle, T.G. Wright, J. Chem. Phys. 151 (2019), 154302.
[24] A.R. Davies, D.J. Kemp, T.G. Wright, J. Chem. Phys. 15 (2021), 224305.
[25] D.J. Kemp, A.M. Gardner, W.D. Tuttle, J. Midgley, K.L. Reid, T.G. Wright, J. Chem. Phys. 149 (2018), 094301.
[26] D.J. Kemp, L.G. Warner, T.G. Wright, J. Chem. Phys. 152 (2020), 064303.

10. Torsions of *N*-methylpyrrole and its cation

Abstract: "Torsional levels in *N*-methylpyrrole are investigated in the ground (S_0) and first excited (S_1) neutral states using two-dimensional laser-induced fluorescence (2D-LIF), and in the ground state cation (D_0^+) using zero-electron-kinetic-energy (ZEKE) spectroscopy. The ZEKE spectra confirm the largely Rydberg nature of the S_1 state. The activity seen in both the 2D-LIF and ZEKE spectra are indicative of vibronic (including torsional) interactions and torsional potentials in the three electronic states are deduced, and are consistent with calculated geometries. The adiabatic ionization energy of *N*-methylpyrrole is derived as 64250 ± 5 cm^{-1}."

Authors: Alexander R. Davies, David J. Kemp and Timothy G. Wright.
Submitted to: Chemical Physics Letters, 3rd November 2020
Published: 7th December 2020
Reference: A. R. Davies, D. J. Kemp and T. G. Wright, *Chem. Phys. Lett.*, 2020, **763**, 138227.
DOI: 10.1016/j.cplett.2020.138227

Summary: In this paper, we publish the first 2D-LIF spectrum of the torsional region of *N*-methylpyrrole, and from this determine that there is a change in the conformation of the methyl group between the S_0 and S_1 states by observing a reversal in the energy ordering of the $15^1m^{3(+)}$ and $15^1m^{3(-)}$ vibtor absorptions and their corresponding emissions (see the 2D-LIF spectrum, Figure 3). While we could not directly observe the $\Delta(v, m) = 0$ bands for the torsions themselves, owing to these being very weak transitions in an unfavourable region in the laser dye, the observation of various strong vibtor transitions allows us to glean some vibrational wavenumbers for the ground state as well as a deduction of the change in geometry.

Furthermore, we also present ZEKE spectra *via* the torsional levels for the first time and note that these are perfectly in line with the S_1 state of NMP being a 3s Rydberg-state in the FC region. These show highly diagonal FCFs, with the $\Delta m = 0$ band being the strongest, with a weak $^{+}m^{0}$ or $^{+}m^{1}$ band, dependent on the symmetry of the torsion excited, allowing the determination of the AIE, which is derived as 64250 ± 5 cm^{-1}. From the ZEKE spectra, we determine vibrational wavenumbers for $^{+}m^{2}$, $^{+}m^{3(+)}$, $^{+}m^{3(-)}$ and $^{+}m^{4}$, relative to $^{+}m^{0}$ or $^{+}m^{1}$, noting these wavenumbers are almost identical to the corresponding torsional wavenumbers in the S_1 state. Furthermore, it is also deduced that the methyl rotor conformation is the same in D_0^+ as it is in S_1. From these experimental observations and quantum chemical calculations, it was possible to determine values of F, the effective rotational constant, and the V_6 parameter. [Noting the latter is only the effective V_6 parameter as it is solely based on the observed splitting of the m = 3(+) and m = 3(-) levels. Additionally, the V_6 value in the S_0 state is given as a range as it was not possible to observe m = 3(+) and 3(-) directly.]

Contributions: The 2D-LIF spectrum was collected by myself. The ZEKE spectra were collected by myself, alongside DJK. Quantum chemical calculations were conducted by myself, with the initial calculations by DJK; all figures were made by myself. TGW calculated the values of F for each state. The analysis of the data was a collaboration between myself and TGW. Furthermore, all figures were created by myself. I also read and commented on multiple versions of the manuscript, and discussed and helped implement reviewers’ comments to the final version of the paper. This paper was selected as an Editor’s Choice Article, based on the highly favourable referee reviews and being recognised as being a ‘significant contribution to the field’, with our graphical abstract being featured on the front cover of this issue of *Chem. Phys. Lett.*

Reproduced from *Chem. Phys. Lett.*, 2020, 763, 138277, as permitted by Elsevier.

Chemical Physics Letters 763 (2021) 138227

Contents lists available at ScienceDirect

Chemical Physics Letters

journal homepage: www.elsevier.com/locate/cplett

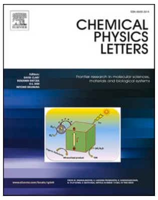

Editor's Choice

Torsions of *N*-methylpyrrole and its cation

Alexander R. Davies, David J. Kemp, Timothy G. Wright *

School of Chemistry, University of Nottingham, University Park, Nottingham NG7 2RD, UK

ARTICLE INFO

Keywords:
N-methylpyrrole
REMPI
ZEKE
2D-LIF
Torsion
Fluorescence
Ionization

ABSTRACT

Torsional levels in *N*-methylpyrrole are investigated in the ground (S_0) and first excited (S_1) neutral states using two-dimensional laser-induced fluorescence (2D-LIF), and in the ground state cation (D_0^+) using zero-electron-kinetic-energy (ZEKE) spectroscopy. The ZEKE spectra confirm the largely Rydberg nature of the S_1 state. The activity seen in both the 2D-LIF and ZEKE spectra are indicative of vibronic (including torsional) interactions and torsional potentials in the three electronic states are deduced, and are consistent with calculated geometries. The adiabatic ionization energy of *N*-methylpyrrole is derived as 64250 ± 5 cm^{-1}.

1. Introduction

Pyrroles, including *N*-methylpyrroles, are key building blocks of many biomolecules, medicines [1,2] and molecular wires [3]. As such, an understanding their energy-level structure underpins their photophysics and photodynamics. *N*-methylpyrrole (NMP), has been the subject of a number of spectroscopic and photodissociation studies.

The absorption spectrum at ambient temperature has been reported by Milazzo [4], McDiarmid and Xing [5], and Cooper et al. [6]. Spectra of supersonic-jet-cooled molecules have been presented by McDiarmid and Xing [5], Philis [7,8] and Biswas et al. [9]. A theoretical study of the torsional levels in NMP was published by Kanamaru [10], although we shall question the conclusions of that work. In addition, the photodynamics of NMP have been the subject of a number of studies [11–15].

The low-lying electronic states of NMP are interesting, with occupied orbitals that are mixtures of valence and Rydberg-character. Initially treating the methyl group as a point mass, the point group symmetry is C_{2v} and the ground electronic state configuration may be written as … $a_1^2 b_1^2 a_2^2$, where the a_1 symmetry orbital is σ bonding, and the two outermost occupied orbitals are π bonding. At the S_0 optimized geometry, the lowest lying electronic states are largely Rydberg-like, and are formed following vertical excitations from the two outermost orbitals into these. Here, we locate the pyrrolyl ring in the *yz*–plane, with the N–CH_3 bond lying along the *z*–axis, then the symmetry of the Rydberg states are 3s (a_1), $3p_x$ (b_1), $3p_y$ (b_2) and $3p_z$ (a_1). We shall come back to these later, but here we note that the lowest-energy vertical excitation is the 3s ← a_2 excitation, yielding the S_1 $^1A_2$ first excited state; the highest occupied orbital in the S_1 state evolves from 3s character in the Franck-Condon region, to σ* character at extended N–CH_3 bond lengths [14]. Accessing this state is electronically forbidden in a one-photon transition, although it has been seen in two-photon transitions in some of the above-cited work; as such, the activity seen in the one-photon spectrum arises from vibronic interactions.

The main focus of the present work will be the torsional levels in the S_0, S_1 and D_0^+ electronic states. The torsional levels in the S_1 state have been assigned on the basis of activity seen in the resonance-enhanced multiphoton ionization (REMPI) spectrum of internally cold NMP by Philis [7]; further, the observation of hot-band structure also allowed information on the S_0 state to be obtained; we shall compare our results to those. For the first time, we shall also present zero-electron-kinetic energy (ZEKE) spectra using S_1 torsional levels as intermediates, allowing the torsional levels in the cation to be investigated.

2. Experimental

The REMPI/ZEKE [16] and 2D-LIF [17] apparatuses are the same as those employed recently. In both experiments, a free-jet expansion of NMP (Sigma-Aldrich, 99% purity) in 2 bar Ar was employed.

For the 2D-LIF spectra, the free-jet expansion was intersected at *X/D* ~ 20 by the frequency-doubled output of a single dye laser (Sirah CobraStretch), operating with Coumarin 480 and pumped with the third harmonic of a Surelite III Nd:YAG laser. The fluorescence was collected, collimated, and focused onto the entrance slits of a 1.5 m Czerny-Turner spectrometer (Sciencetech 9150) operating in single-pass mode,

---

* Corresponding author.
E-mail address: Tim.Wright@nottingham.ac.uk (T.G. Wright).

https://doi.org/10.1016/j.cplett.2020.138227
Received 3 November 2020; Received in revised form 24 November 2020; Accepted 25 November 2020

dispersed by a 3600 groove/mm grating, allowing ~ 300 cm^{-1} windows of the dispersed fluorescence to be collected by a CCD camera (Andor iStar DH334T). At a fixed grating angle of the spectrometer, the excitation laser was scanned, and at each excitation wavenumber the camera image was accumulated for 2000 laser shots. This allowed a plot to be produced of fluorescence intensity versus both the excitation laser wavenumber and the wavenumber of the emitted and dispersed fluorescence, termed a 2D-LIF spectrum [18,19].

For the REMPI and ZEKE spectra of NMP, the focused outputs of two dye lasers (Sirah CobraStretch) were overlapped spatially and temporally, and passed through a vacuum chamber coaxially and counter-propagating, where they intersected the free-jet expansion. The excitation laser operated with Coumarin 480 and was pumped with the third harmonic (355 nm) of a Surelite III Nd:YAG laser and was frequency doubled while the ionization laser operated with Coumarin 440, pumped with the third harmonic (355 nm) of a Surelite I Nd:YAG laser, and was undoubled. The jet expansion passed between two biased electrical grids located in the extraction region of a time-of-flight mass spectrometer, which was employed in the REMPI experiments. These grids were also used in the ZEKE experiments by application of pulsed voltages, giving typical fields of ~ 10 V cm^{-1}, after a delay of up to 2 μs; this delay was minimized while avoiding the introduction of excess noise from the prompt electron signal. The resulting ZEKE bands had widths of ~ 5–7 cm^{-1}. Electron and ion signals were recorded on separate sets of microchannel plates.

3. Results and discussion

3.1. Overview

In Fig. 1 we show the (1 + 1) REMPI spectrum of NMP over the first ~ 1000 cm^{-1}; the origin transition is located at 41193 cm^{-1} (Ref. [15]). Here we concentrate on the 0–120 cm^{-1} wavenumber region, which is shown as an expanded trace. There are four cold bands in this region, which are assigned to transitions involving torsional levels. The (2 + 2) spectrum is also shown in Fig. 1, and although this is somewhat power broadened, as with other published versions of this [9,15], it does allow the origin to be seen, as well as different vibrational structure to the (1 + 1) spectrum.

The torsional levels are described by the m quantum number, which is signed. Levels with $|m| \neq 3n$ ($n = 0, 1, 2\ldots$) are degenerate for a molecule that belongs to the G_{12} molecular symmetry group (MSG), while levels with $|m| = 3n$ are non-degenerate, forming linear combinations for $n \neq 0$; the $m = 0$ level is singly degenerate. The splitting of the

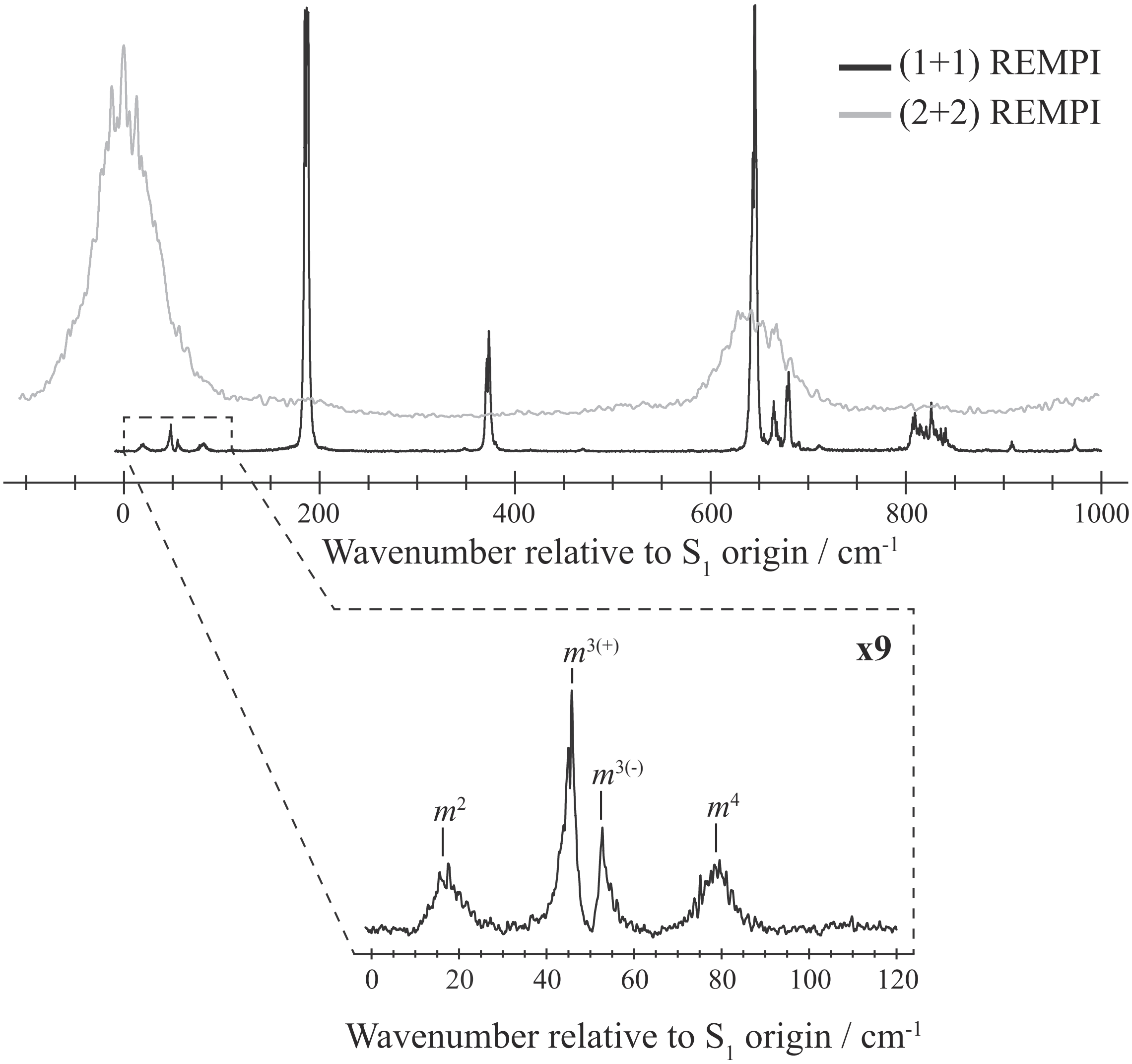

Fig. 1. Black trace: (1 + 1) REMPI spectrum of NMP; grey trace (2 + 2) REMPI spectrum of NMP; full assignments will be presented in a forthcoming publication [29]. The origin transition is located at 41193 cm^{-1} (Ref. 15). An expansion of the low-wavenumber region of the (1 + 1) REMPI spectrum of NMP is also shown, which includes the torsional transitions. Assignments are discussed in the text.

$|m| = 3n$ ($n \neq 0$) levels occurs as a result of hindered rotation, caused by a torsional potential characterized by a parameter V_6. For example, the $m = +3$ and –3 levels, form combinations that are denoted 3(+) and 3 (–), with their relative energy ordering determined by the sign of V_6, which arises from the minimum energy geometry. For geometries where the methyl group is eclipsed, with a C–H bond of the methyl group in the same plane as the pyrrolyl ring, V_6 is positive; while for a staggered geometry, where one of the methyl C–H bonds is perpendicular to the pyrrolyl ring, V_6 is negative.

As is well known, nuclear spin and symmetry considerations mean that it is not possible to cool the $m = 1$ torsional population into the $m = 0$ level, and hence under the jet-cooled conditions employed herein, both levels have roughly equal populations. As a consequence, transitions can occur from either the $m = 0$ or $m = 1$ level of the S_0 zero-point vibrational level. Since the separations of these two levels are very similar in the S_1 and S_0 electronic states, then the m^0 and m^1 bands are essentially coincident in the REMPI spectrum, and this will be true for all vibrational bands. (We will often refer to a level using the notation of a transition, e.g. a transition to S_1 $m = 0$ will be given by m^0; furthermore, we shall generally omit the initial level when designating a transition – with transitions to $m = 3n$ originating from the S_0 $m = 0$ level, and those for $m \neq 3n$ originating from S_0 $m = 1$ – subscripts refer to the S_0 state, superscripts to the S_1 state, and for cationic levels we use a pre-superscripted "+".)

In Fig. 2, we show the low wavenumber region of the ZEKE spectra recorded via the four torsional levels in S_1 accessed via cold $S_1 \leftarrow S_0$ transitions. If the torsional potentials are very similar in the two electronic states, then we generally expect transitions that involve $\Delta m = 0$ to be the most intense, with $\Delta m = 3$ transitions possible, but expected to be much weaker; and the spectra clearly demonstrate this. From these ZEKE spectra, we can deduce the positions of the $^+m^0$, $^+m^1$, $^+m^2$, $^+m^{3(+)}$, $^+m^{3(-)}$ and $^+m^4$ levels. Note that, although the identification of the m^2 and m^4 bands in the REMPI spectrum are unambiguous, this is not the case for the $m^{3(+)}$ and $m^{3(-)}$ bands, which will be discussed below, although we can deduce that the ordering is the same in the S_1 and D_0^+ states.

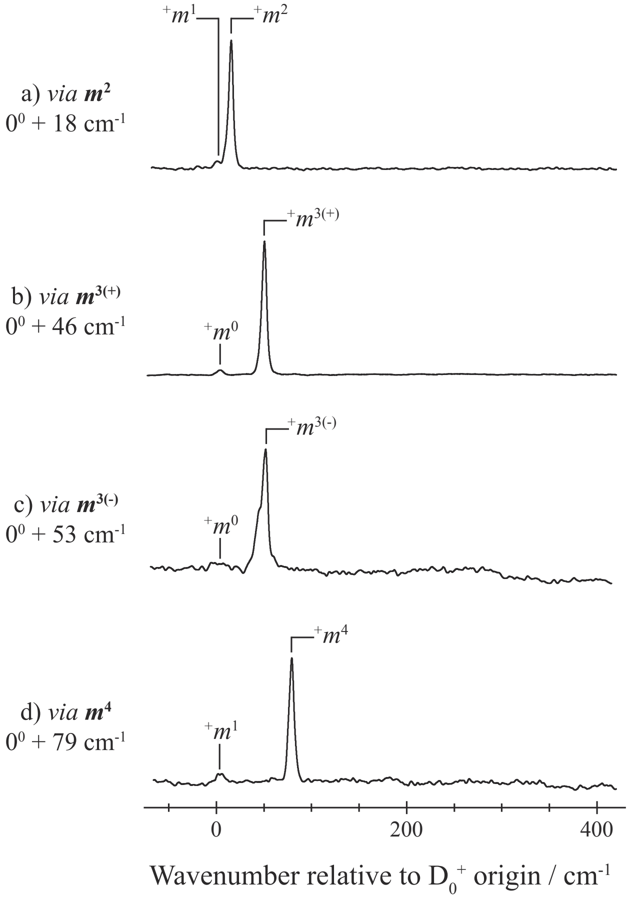

Fig. 2. ZEKE spectra via the S_1 torsional levels of NMP. Assignments are discussed in the text. The band positions relative to the $^+m^0$ or $^+m^1$ band positions are: $^+m^2$ (15 cm^{-1}); $^+m^{3(+)}$ (46 cm^{-1}); $^+m^{3(-)}$ (51 cm^{-1}); and $^+m^4$ (77 cm^{-1}). Derived F and V_6 values are given in Table 3.

In Fig. 3, we present a 2D-LIF spectrum recorded over the region of the S_1 torsional levels, with the lowest excitation band only partially scanned. At the top of the 2D-LIF spectrum, we show the corresponding section of the REMPI spectrum from Fig. 1, to indicate the excitation positions. Note that we have omitted the regions of the emission below ~ 60 cm^{-1}, where the $\Delta m = 0$ bands would be expected, as no features were discernible, suggesting that these are weak. We can see, however, emission bands to S_0 vibtor levels, and we see clear vibtor bands associated with several S_0 vibrational levels.

Again, the ordering of the S_1 $m^{3(+)}$ and $m^{3(-)}$ levels is not immediately clear, but we can deduce that the ordering is reversed between the S_0 and S_1 states, from the intensities of the emission bands in Fig. 3.

3.2. Assignments and discussion

We shall now switch the symmetry labels to those of the G_{12} MSG. (The correspondence between G_{12} and C_{2v} labels is given in Table 1.) We have noted in the above that electronic excitations and ionizations of a molecule that belongs to the G_{12} MSG generally obey a $\Delta m = 0$ selection rule. When referring to vibrations, we shall use a revised numbering based on the ring vibrations [29], but the correspondence to the numbering employed in the work of Biswas et al. [9] is given in Table 2 for selected vibrations.

The REMPI spectrum for the $S_1 \leftarrow S_0$ transition corresponds to a $A\ ^1A_2' \leftarrow X\ ^1A_1'$ transition. The pure electronic transition is forbidden for a one-photon absorption, and hence the electronic origin does not appear in the (1 + 1) REMPI spectrum; furthermore, the torsional activity is expected to correspond to that which is facilitated by vibronic (Herzberg-Teller) coupling.

Philis [7] has given assignments of the four features in the expanded region of the (1 + 1) REMPI spectrum in Fig. 1. We note that Kanamaru [10] has put forward a reinterpretation of the torsional transitions seen in Philis's work [7]; however, almost all of the proposed transitions are symmetry forbidden, and so we do not concur with this reassignment. We will conclude that the assignments given by Philis [7] are correct on the basis of the 2D-LIF and ZEKE spectra discussed herein.

In commenting on the torsional activity seen in the REMPI spectrum, we note that the missing electronic origin corresponds to the absence of both m^0 and m^1 transitions, which would be almost completely overlapped, since the effective rotational constant for CH_3 torsional motion is very similar in the two electronic states. As the one-photon $S_1 \leftarrow S_0$ transition is forbidden, the present bands must arise from a form of vibronic coupling which encompasses the torsional levels. (We generalize the use of the term "vibronic" to cover vibration-electronic, torsion-electronic and vibration-torsion-electronic interactions.) There has been some slight confusion in discussing the vibrations and vibronic coupling in NMP, owing to different axis systems being employed, with the molecule having been located in the *yz*– and *xz*–planes (and perhaps both, on occasion!). In the present work, the pyrrolyl ring is located in the *yz*–plane throughout.

Wu et al. [14] have studied the low-lying states of NMP to explain observed photodynamics. The electronically-excited states of NMP are interesting, since they exhibit both Rydberg and valence character. Briefly, the ground electronic state of NMP is $\ldots(a_2'')^2(a_2')^2$, with the HOMO–1 and HOMO orbitals corresponding to π orbitals. The lowest electronically-excited states are formed following excitation of electrons from these two orbitals into orbitals that are mostly Rydberg in character in the Franck-Condon region. The lowest Rydberg orbitals are 3s and $3p_{x,\,y,\,z}$ and the HOMO–HOMO-1 energy gap is quite similar to the

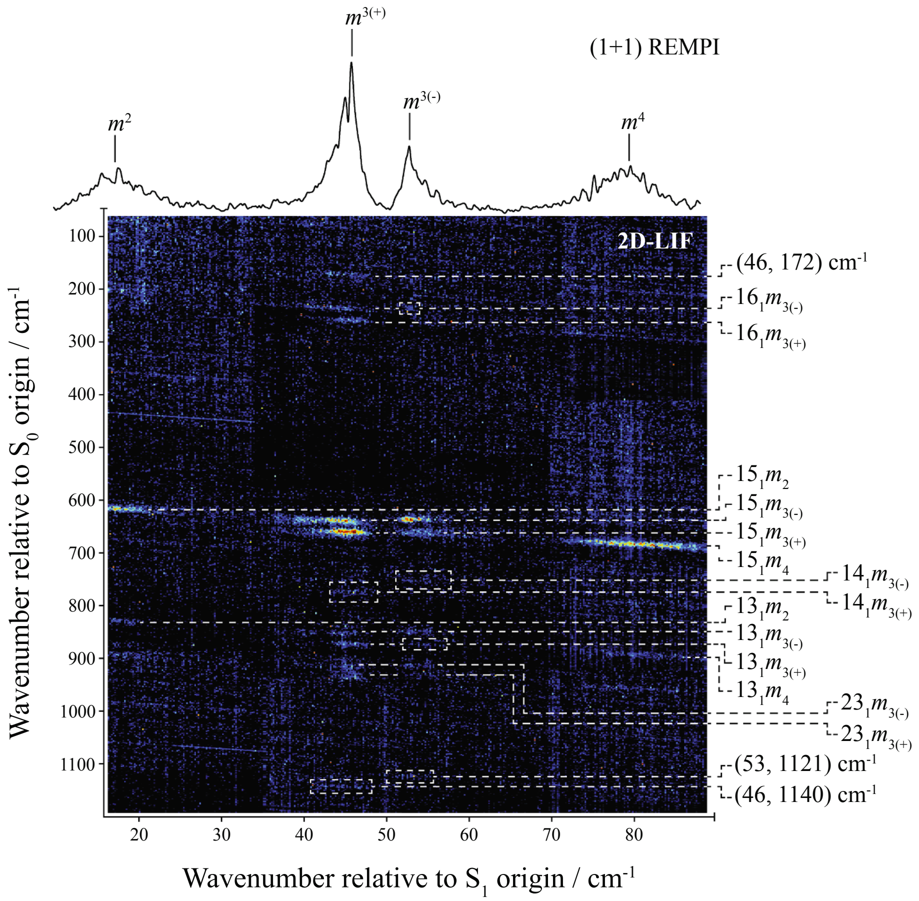

Fig. 3. 2D-LIF spectrum spanning the $S_1 \leftarrow S_0$ excitation region corresponding to the torsions. The origin transition is located at 41193 cm^{-1} (Ref. 15). Note that the m^2 level is only partially only partially shown, though it is expected from the band profiles in the REMPI trace (shown at the top of the figure) that the full band profile of the emissions from m^2 will closely resemble those from m^4. Assignments are discussed in the text. The lower-wavenumber emission region extending to the origin has not been included as no discernible features were seen.

Table 1
Correspondence of the C_{2v} point group symmetry classes with those of the G_{12} molecular symmetry group. Also indicated are the symmetries of the P_i vibrations and the different pure torsional levels.[a]

C_{2v}	G_{12}	P_i[b]	m
a_1	a_1'	$P_{1–9}$	0, 6(+)
a_2	a_2'	$P_{10–12}$	6(−)
b_1	a_2''	$P_{13–16}$	3(−)
b_2	a_1''	$P_{17–24}$	3(+)
	e'		2, 4
	e''		1, 5

[a] Symmetries of vibtor levels can be obtained by combining the vibrational symmetry (in G_{12}) with those of the pure torsional level, using the D_{3h} point group direct product table.

[b] The P_i vibrational labels will be described in a forthcoming publication [29].

Table 2
Correspondence between the vibrational numbers used in the present work with those of Biswas et al. [9].

G_{12} (C_{2v}) symmetry	Vibration numbering (present work)[29]	Vibrational numbering (Ref. 9)
a_1' (a_1)	6	8
a_2'' (b_1)	13	19
	14	20
	15	21
	16	22
a_1'' (b_2)	23	32

3s–3p energy gap. It was found [14] that the S_1 $^1A_2'$ state was the lowest in energy, and it is energetically well-separated from any higher states (by ~ 0.4 eV), while the states that arose from the $3p_{x,y,z} \leftarrow a_2'$ and $3s \leftarrow a_2''$ excitations all lay within a 0.5 eV window, when considering vertical excitations. The main character of these states and the oscillator strengths were also given for the transitions from the ground state. The S_2 state was calculated to arise mainly from the $3s \leftarrow a_2''$ excitation (yielding a $^1A_2''$ state), while the S_3–S_5 states arose mainly from the $3p_{x,y,z} \leftarrow a_2'$ excitations. Since the $3p_{x,y,z}$ orbitals have respective symmetries a_2'', a_1'' and a_1', then the resulting respective Rydberg states are $^1A_1''$, $^1A_2''$ and $^1A_2'$. (These correspond to the S_5, S_3 and S_4 states given in Ref. [14], respectively, but note that the symmetry for the S_5 state given therein is incorrect – this should be B_2 in C_{2v} symmetry, not A_1 as given.) The S_2 and S_3 states were calculated to be closest in wavenumber to the S_1 state, and vibronic coupling would be expected to induce activity for transitions that involved torsional/vibrational levels of a_1'' symmetry. On the other hand, the S_5 state has an oscillator strength three times higher and is only 0.2 eV further removed in energy and this would be expected to induce activity for transitions that involved torsional/vibrational levels of a_2'' symmetry. Thus, interactions between S_1 and the $^1A_2''$ and $^1A_1''$ states can be used to rationalize the appearance of the $m^{3(+)}$ and $m^{3(-)}$ transitions, respectively – see below.

The symmetry arguments presented in the preceding paragraph refer to the $m = 0$ level of the interacting electronic state, however, similar arguments hold for the $m = 1$ level, which has e' vibronic symmetry for the S_2, S_3 and S_5 states. This means torsional (or vibtor) levels of the S_1 state of e' symmetry can have intensity induced through vibronic coupling, and this explains the appearance of the m^2 and m^4 transitions, as well as the absence of m^1 and m^5. We comment that the S_4 state cannot induce any activity, since transitions to it are also one-photon forbidden. Finally, the S_6 state of Ref. [14], arising largely from a $3p_x \leftarrow a_2''$

excitation, is an $^1A_1'$ state, and so could induce activity in transitions to the S_1 state involving torsion/vibrational levels of a_2' symmetry, which would include $m^{6(-)}$, but this would be expected to be weak, as the S_1 and S_6 states are ~0.8 eV apart, and also the oscillator strength for the latter electronic state is fairly low. A very strong band at ~ 184 cm^{-1} in the REMPI spectrum (see Fig. 1) was initially hypothesised to be the $m^{6(-)}$ transition [7], but this assignment was revised in a later publication [9] – we shall comment on this further in due course [29].

We now address the ordering of the $m = 3(+)$ and $m = 3(-)$ levels in the three electronic states. We have plotted the variation of the energies of the m levels with V_6 in Fig. 4. (Note that the ordering of the $m = 3n$ levels in Fig. 4 is the reverse of that in Ref. [20].) We have already noted that the ordering is the same for the S_1 and D_0^+ states, but the reverse for the S_0 state. To establish the ordering, we have optimized the geometry of NMP in each of the three electronic states, and the optimized geometries are shown in Fig. 5; Gaussian 16 [21] was used for these calculations, with the level of theory and basis set shown. It is clear that the S_0 state is staggered, and both the S_1 and D_0^+ states are eclipsed. On this basis, the V_6 parameter is negative for the S_0 state and positive for the S_1 and D_0^+ states, consistent with the intensities in the 2D-LIF spectrum (Fig. 3). This conclusion for the S_0 and S_1 states agree with the values deduced by Philis on the basis of hot and cold torsional transitions [7]. The ordering of the $m = 3(+)$ and 3(–) levels in the three states is thus established and are labelled appropriately in Figs. 1–3. The concurrence of the ordering in the S_1 and D_0^+ states is unsurprising, since the S_1 state is largely of 3s Rydberg character close to the Franck-Condon region, with its ionic core being the D_0^+ state; this is further confirmed by the largely diagonal nature of the torsional transitions during the ionization (see Fig. 2). It is interesting to note that the $m^{3(+)}$ transition more intense than $m^{3(-)}$. This can gain intensity from $^1A_2'' \leftarrow S_0$ transitions, and there are two such transitions close to the $S_1^1A_2'$ state [14]. Further, the $m^{3(-)}$ transition is more intense than it appears in similar spectra of substituted benzenes [20,23], where its intensity arises from rotation-torsion coupling, (which is temperature dependent), since it cannot be vibronically induced. Here, this transition can gain intensity vibronically from a $^1A_1'' \leftarrow S_0$ transition, which (once the correct symmetry is noted), corresponds to the strongest transition calculated in Ref. [14]. This then explains why both the $m^{3(+)}$ and $m^{3(-)}$ transitions are observed. That the former is the more intense, presumably arises from the fact that there are two transitions from which to steal intensity, and these are energetically closest to the S_1 state; these two factors must outweigh the higher oscillator strength of the slightly higher-energy $^1A_1'' \leftarrow S_0$ transition.

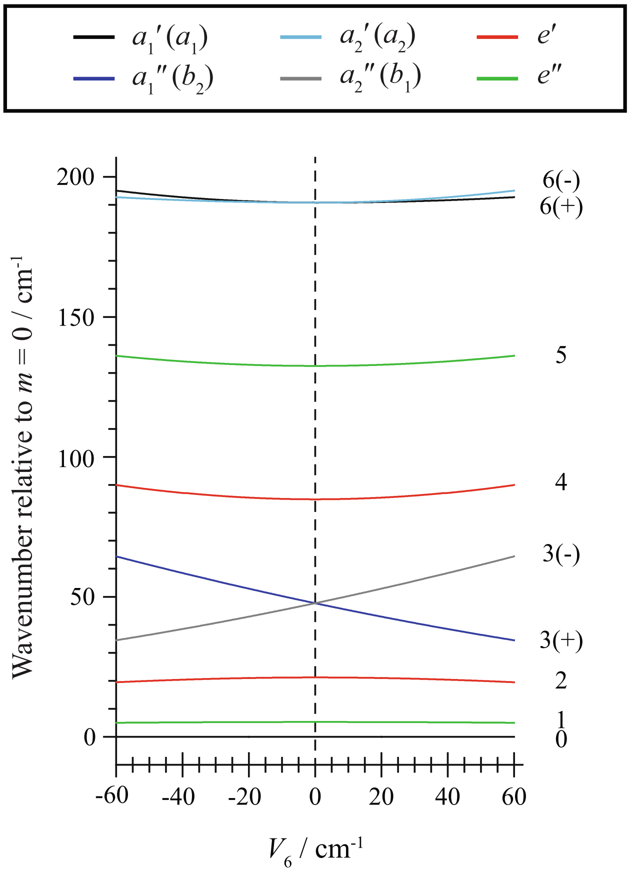

Fig. 4. Variation of the energies of the m levels for different values of V_6. Notice the switch in ordering of the $m = 3n$ ($n = 1, 2$) levels with the sign of V_6. V_6 is positive for the eclipsed confirmation (S_1 and D_0^+) states, and negative for the staggered conformation (S_0) – see Fig. 5. For this plot, the torsional angle is taken as zero for the eclipsed conformation, and the effective torsional rotational constant was taken as 5.3 cm^{-1}. (Note that the ordering of the $m = 3(+)$ and 3(–) levels is the reverse of that shown in Ref. 20.)

With regard to the magnitude of V_6, values of –45 cm^{-1} and 17 cm^{-1} have been deduced by Philis [7] for the S_0 and S_1 states, respectively; these gave a reasonable agreement with the observed line positions, with the former value agreeing with a microwave study [22]. We have calculated the effective rotational constant, F, using the optimized geometries in Fig. 5, and deduced the V_6 parameter from the positions of the $m = 3(+)$ and $m = 3(-)$ bands in the appropriate spectra. These values are given in Table 3, and for the S_0 and S_1 states agree well with those of Philis [7]. Caution is merited, however, since Lawrance and coworkers have shown that vibration-torsion interactions can affect the deduced V_6 (and F) values [23,24], and so without further analysis, the present V_6 values must be viewed as being “effective” values. We note here that for the D_0^+ state, very similar potential parameters as the S_1 state provide satisfactory agreement with the observed ZEKE band positions, which is not unexpected as the S_1 state is Rydberg-like in the Franck-Condon region. For both the S_1 and D_0^+ states there is a low-lying a_2'' symmetry vibration (16^1 at ca. 200 cm^{-1}) lying above the $m = 3(+)$ and $m = 3(-)$ levels [29], with the latter level the higher. Comparing this situation to that of *p*FT (see Figure 6 of Ref. [23]), we can expect vibration-torsion interactions to push the $m = 3(-)$ level down towards the $m = 3(+)$ level, with the latter remaining in approximately the same position; thus, the V_6 values in the S_1 and D_0^+ states are expected to be lower bounds to the true value. The opposite situation holds in the S_0 state, where the 3(–) level is the lower, so here the V_6 value is expected to be an upper bound.

The observation of the $^+m^0$ band in the ZEKE spectra (Fig. 2) allows the adiabatic ionization energy (AIE) to be deduced. This value is 64250 ± 5 cm^{-1} (7.9660 ± 0.0006 eV), which compares well with previous experimental values of 7.94 ± 0.02 eV [6] and 7.95 ± 0.05 eV [25]. Although we have no explanation why, we comment that we do not observe $\Delta m = +3$ bands in the ZEKE spectrum, only $\Delta m = -3$ bands, even though both symmetry-forbidden bands can be induced by vibronic coupling in the cation/high-lying Rydberg states, or by intrachannel coupling [26].

Going back to the 2D-LIF spectrum in Fig. 3, we have noted that we do not see emission to the torsional levels in S_0, only to vibtor levels. These are assigned based on previous IR/Raman values [27,28] (see also Ref. [9]) and further fluorescence spectra to be published [29]. They are consistent with a value of V_6 in S_0 in the range –40 cm^{-1} to –45 cm^{-1}, with the caveat that the vibtor levels are likely to be interacting. We particularly note the three bands to low emission wavenumber. The 236 and 259 cm^{-1} bands are in the correct position to be $16_1m_{3(-)}$ and $16_1m_{3(+)}$, respectively. The (46, 172) cm^{-1} band is difficult to assign, since it is not in the correct position for any calculated torsional level, and is lower than any vibrational wavenumber for the S_0 state. The only plausible explanation is that it arises from $m_{6(+)}$ or $m_{6(-)}$, which are perhaps interacting with one of the $16_1m_{3(-)}$ and $16_1m_{3(+)}$ levels, respectively; however, without a full analysis of the vibration-torsion interaction, this remains speculative.

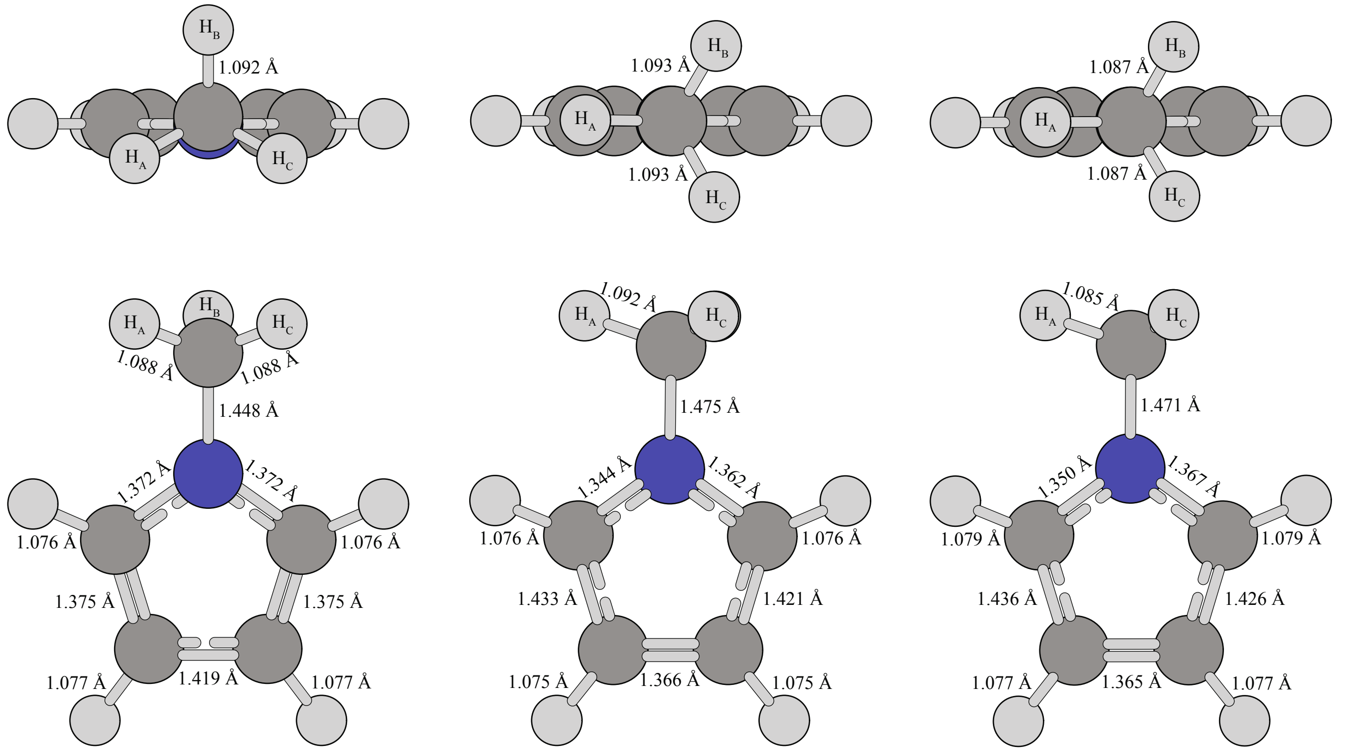

***N*-Methylpyrrole - S_0**
B3LYP / aug-cc-pVTZ
Geometry: staggered

***N*-Methylpyrrole - S_1**
TD-B3LYP / aug-cc-pVTZ
Geometry: eclipsed

***N*-Methylpyrrole - D_0^+**
U-B3LYP / aug-cc-pVTZ
Geometry: eclipsed

Fig. 5. Optimized geometries of NMP and its cation, at the indicated levels of theory. Note that the methyl group of the S_0 state has an optimized staggered geometry, while the methyl group of the S_1 and D_0^+ states are both eclipsed, with respect to the pyrrolyl ring. These geometries were ascertained as minima by calculating the vibrational wavenumbers, which were all real – these will be discussed further in later work [29].

Table 3
Calculated F and experimental V_6 values (cm^{-1}) in the S_0, S_1 and D_0^+ states[a].

m	S_0	S_1	D_0^+
F	5.39	5.27	5.35
V_6	–(40–45)[b]	14	10

[a] The F values used here have been calculated from the optimized geometries presented in Fig. 5. The V_6 values are effective values (see text), and merely reproduce the spacing between the $m = 3(+)$ and $m = 3(–)$ states, with the appropriate sign. In the S_0 state, we have not observed the torsional levels themselves, but do see vibtor levels for different vibrations. The vibtor spacings could be affected by vibration-induced changes to the torsional potential and/or interactions between levels.

[b] Values vary slightly for vibtor levels associated with different vibrations – see Ref. 20 for a comment on vibration-modified torsional potentials.

4. Conclusions

It has been established that the torsional levels in the NMP cation are almost identical to those in the S_1 state, and that the $\Delta m = 0$ propensity rule is closely followed, confirming that the latter is Rydberg-like in the Franck-Condon region. The observation of some $\Delta m = \pm 3$ transitions allows the accessing of the $^{+}m^{0}$ level in the ZEKE spectra, and this allows the AIE to be established as 64250 ± 5 cm^{-1}. The 2D-LIF spectrum confirms the S_1 state assignments and activity involving several ground state vibrations is observed. Furthermore, the observed (and unobserved) torsional activity has been rationalized both in terms of the calculated geometries, and via the vibronic interactions.

In future work, a wide-ranging analysis of the S_0, S_1 and D_0^+ energy levels will be presented in a combined fluorescence and ZEKE study [29].

CRediT authorship contribution statement

Alexander R. Davies: Investigation, Writing - review & editing, Visualization, Data curation. **David J. Kemp:** Investigation, Writing - review & editing, Data curation. **Timothy G. Wright:** Conceptualization, Writing - original draft, Investigation, Validation, Supervision, Project administration, Funding acquisition.

Declaration of Competing Interest

The authors declare that they have no known competing financial interests or personal relationships that could have appeared to influence the work reported in this paper.

Acknowledgements

We are grateful to the EPSRC for funding (grant EP/L021366/1). The EPSRC and the University of Nottingham are thanked for studentships to D.J.K. and A.R.D.

Data Availability Statement

The data that support the findings of this study are available from the corresponding author upon reasonable request.

References

[1] V. Bhardwaj, D. Gumber, V. Abbot, S. Dhiman, P. Sharma, RSC Adv. 5 (2015) 15233.
[2] S. Chavda, K. Mulder, T. Brown, H. Makay, B. Babu, L. Westrate, A. Ferguson, S. Lin, K. Kiakos, J.P. Ramos, M. Munde, W.D. Wilson, J.A. Hartley, M. Lee, Med. Chem. 6 (2010) 150.
[3] Y. Fu, X. Cheng, J. Zhao, T. Kong, C. Chi, X. Zhang, Polymer J. 44 (2012) 1048.
[4] G. Milazzo, Gazz. Chim. Ital. 74 (1944) 152.
[5] R. McDiarmid, X. Xing, J. Chem. Phys. 105 (1996) 867.
[6] C.D. Cooper, A.D. Williamson, J.C. Miller, R.N. Compton, J. Chem. Phys. 73 (1980) 1527.
[7] J.G. Philis, Chem. Phys. Lett. 353 (2002) 84.
[8] J.G. Philis, J. Molec. Struct. 651–653 (2003) 567.
[9] N. Biswas, S. Wategaonkar, J.G. Philis, Chem. Phys. 293 (2003) 99.
[10] N. Kanamaru, J. Molec. Struct. (Theochem) 686 (2004) 15.
[11] A.G. Sage, M.G.D. Nix, M.N.R. Ashfold, Chem. Phys. 347 (2008) 300.
[12] L. Blancafort, V. Ovejas, R. Montero, M. Fernández-Fernández, A. Longarte, J. Phys. Chem. Lett. 7 (2016) 1231.
[13] G. Piani, L. Rubio-Lago, M.A. Collier, T. Kitsopoulos, M. Becucci, J. Phys. Chem. A 113 (2009) 14554.
[14] G. Wu, S.P. Neville, O. Schalk, T. Sekikawa, M.N.R. Ashfold, G.A. Worth, A. Stolow, J. Chem. Phys. 142 (2015), 074302.
[15] K.C. Woo, S.K. Kim, PCCP 21 (2019) 14387.
[16] V.L. Ayles, C.J. Hammond, D.E. Bergeron, O.J. Richards, T.G. Wright, J. Chem. Phys. 126 (2007), 244304.
[17] A.M. Gardner, W.D. Tuttle, L.E. Whalley, T.G. Wright, Chem. Sci. 9 (2018) 2270.
[18] N.J. Reilly, T.W. Schmidt, S.H. Kable, J. Phys. Chem. A 110 (2006) 12355.
[19] J.R. Gascooke, W.D. Lawrance, Eur. Phys. J. D 71 (2017) 287.
[20] D.J. Kemp, E.F. Fryer, A.R. Davies, T.G. Wright, J. Chem. Phys. 151 (2019), 084311.
[21] Gaussian 16, Revision A.03, M. J. Frisch, G. W. Trucks, H. B. Schlegel, G. E. Scuseria, M. A. Robb, J. R. Cheeseman, G. Scalmani, V. Barone, G. A. Petersson, H. Nakatsuji, X. Li, M. Caricato, A. V. Marenich, J. Bloino, B. G. Janesko, R. Gomperts, B. Mennucci, H. P. Hratchian, J. V. Ortiz, A. F. Izmaylov, J. L. Sonnenberg, D. Williams-Young, F. Ding, F. Lipparini, F. Egidi, J. Goings, B. Peng, A. Petrone, T. Henderson, D. Ranasinghe, V. G. Zakrzewski, J. Gao, N. Rega, G. Zheng, W. Liang, M. Hada, M. Ehara, K. Toyota, R. Fukuda, J. Hasegawa, M. Ishida, T. Nakajima, Y. Honda, O. Kitao, H. Nakai, T. Vreven, K. Throssell, J. A. Montgomery, Jr., J. E. Peralta, F. Ogliaro, M. J. Bearpark, J. J. Heyd, E. N. Brothers, K. N. Kudin, V. N. Staroverov, T. A. Keith, R. Kobayashi, J. Normand, K. Raghavachari, A. P. Rendell, J. C. Burant, S. S. Iyengar, J. Tomasi, M. Cossi, J. M. Millam, M. Klene, C. Adamo, R. Cammi, J. W. Ochterski, R. L. Martin, K. Morokuma, O. Farkas, J. B. Foresman, and D. J. Fox, Gaussian, Inc., Wallingford CT, 2016.
[22] W. Arnold, H. Dreizler, H.D. Rudolph, Naturforsh. 23a (1968) 301.
[23] J.R. Gascooke, E.A. Virgo, W.D. Lawrance, J. Chem. Phys. 143 (2015), 044313.
[24] J.R. Gascooke, W.D. Lawrance, J. Molec. Spectrosc. 318 (2015) 53.
[25] A.D. Baker, D. Betteridge, N.R. Kemp, R.E. Kirby, Anal. Chem. 42 (1970) 1064.
[26] D.J. Kemp, A.M. Gardner, W.D. Tuttle, J. Midgley, K.L. Reid, T.G. Wright, J. Chem. Phys. 149 (2018), 094301.
[27] D.W. Scott, J. Mol. Spectrosc. 37 (1971) 77.
[28] T.J. Dines, L.D. MacGregor, C.H. Rochester, J. Coll. Int. Sci. 245 (2002) 221.
[29] A. R. Davies, D. J. Kemp, and T. G. Wright (to be published).

11. Vibrations of pyrrole, *N*-substituted pyrroles, and their cations

Abstract: "The vibrations of pyrrole, *N*-deuteropyrrole, *N*-fluoropyrrole, *N*-aminopyrrole and *N*-methylpyrrole are studied. The evolution of the vibrational wavenumbers of pyrrole is examined, as the mass of the nitrogen-bonded hydrogen atom is artificially increased. It is found that some vibrations are very sensitive to the mass of the substituent bonded to the nitrogen, and this can be viewed as vibrations mixing as that mass increases; however, these mixings stablilize by the time a mass of 14 m_u is reached. A consistent numbering scheme for the ring-localized vibrations of *N*-substituted pyrroles is then put forward. A discussion of the vibrations of the cations of pyrrole and *N*-substituted pyrroles is then presented. Calculated vibrational wavenumbers are compared to experimental ones for pyrrole, *N*-deuteropyrrole and *N*-methylpyrrole, as well as the pyrrole cation."

Authors: Alexander R. Davies, David J. Kemp and Timothy G. Wright

Submitted to: Journal of Molecular Spectroscopy, 1st December 2020

Published: 3rd January 2021

Reference: A. R. Davies, D. J. Kemp and T. G. Wright, *J. Mol. Spectrosc.*, 2021, **376**, 111410.

DOI: 10.1016/j.jms.2020.111410

Supplementary material: see Appendix 4

Summary: In this paper, we propose a labelling system for the ring-localised vibrations, based on the similar schemes proposed by Wright *et al.*[158,163,164,207] for substituted benzenes, which we denote the P_i labels. This labelling scheme is based on the forms of the vibrations of an *N*-substituted pyrrole, treating any vibrations of the substituent independently; this approach has been shown to resolve numerous flaws with the commonplace Wilson[139]/Varsányi[160,161] and Mulliken[162]/Herzberg[123] schemes for substituted benzene molecules. Despite this, we note the proposed labelling scheme is exclusive of *unsubstituted* pyrrole as comparisons of its vibrations cannot be made easily to those of *N*-substituted species, owing to significant changes in the forms of the vibrations largely arising from the change in mass of the *N*-bonded atom (or group) between pyrrole and various *N*-substituted pyrroles. Additionally, this scheme excludes other species, such as 2- or 3-substituted pyrroles as, again, the forms of the vibrations are expected to change significantly from those of the *N*-substituted pyrroles.

Herein, we calculate the vibrational frequencies and forms of the vibrational modes explicitly for the *N*-substituted species, taking into account both mass and electronic effects, as well as calculating the forms and frequencies of the vibrational modes of pyrrole while artificially increasing the mass of the *N*-bonded hydrogen atom (retaining the pyrrole force field). These sets of calculations allow the separation of mass and electronic effects, and we also consider the Duschinsky effect to identify any vibrational mixing that may occur between the neutral and cationic ground states. Here, we find that, even for normal modes which induce a significant displacement of the substituent, the forms of the vibrations have largely settled down by a substituent mass of approximately 14 m_u, which is below the mass of a fluorine atom, and so justify the use of NFP as the basis for this scheme. We expect this to be a consistent, general-purpose scheme for labelling the ring-localised vibrations of *N*-substituted pyrroles and use this scheme as a basis for all our other work on NMP. We found that certain extreme cases (such as in *N*-aminopyrrole$^+$) may lead to two vibrations becoming heavily mixed versions of more than one NFP S_0 vibration, therefore it becomes difficult to assign a P_i label, but stress we expect these cases to be in a small minority.

Contributions: All quantum chemical calculations were conducted by myself, with the exception of the initial calculations on NMP, which were conducted by DJK. All figures were created by myself with input from TGW. Analysis was conducted by myself and TGW. Furthermore, I read and commented on multiple versions of the manuscript, and discussed and helped implement reviewers' comments to the final version of the paper.

Reproduced from *J. Mol. Spectrosc.*, 2021, 376, 111410, as permitted by Elsevier.

Journal of Molecular Spectroscopy 376 (2021) 111410

Contents lists available at ScienceDirect

Journal of Molecular Spectroscopy

journal homepage: www.elsevier.com/locate/jms

Vibrations of pyrrole, *N*-substituted pyrroles, and their cations

Alexander R. Davies, David J. Kemp, Timothy G. Wright *

School of Chemistry, University of Nottingham, University Park, Nottingham NG7 2RD, UK

ARTICLE INFO

Article history:
Received 1 December 2020
Accepted 21 December 2020
Available online 3 January 2021

Keywords:
Pyrrole
N-substituted pyrroles
Vibrations
Cation

ABSTRACT

The vibrations of pyrrole, *N*-deuteropyrrole, *N*-fluoropyrrole, *N*-aminopyrrole and *N*-methylpyrrole are studied. The evolution of the vibrational wavenumbers of pyrrole is examined, as the mass of the nitrogen-bonded hydrogen atom is artificially increased. It is found that some vibrations are very sensitive to the mass of the substituent bonded to the nitrogen, and this can be viewed as vibrations mixing as that mass increases; however, these mixings stablilize by the time a mass of 14 m_u is reached. A consistent numbering scheme for the ring-localized vibrations of *N*-substituted pyrroles is then put forward. A discussion of the vibrations of the cations of pyrrole and *N*-substituted pyrroles is then presented. Calculated vibrational wavenumbers are compared to experimental ones for pyrrole, *N*-deuteropyrrole and *N*-methylpyrrole, as well as the pyrrole cation.

1. Introduction

Pyrroles are key building blocks of many biomolecules and medicines [1,2], and can also be used in the formation of molecular wires [3]. There are various *N*-substituted pyrroles, but here we focus on *N*-deuteropyrrole (NDP), *N*-aminopyrrole (NAP), *N*-methypyrrole (NMP), and *N*-fluoropyrrole (NFP), in our analysis of the vibrations.

A compilation of the vibrational wavenumbers of ground state pyrrole (Pyr) from liquid/solution studies has been given by Scott [4]. More precise information on ground state vibrations would be obtained from dispersed fluorescence (DF) studies; however, these are hampered by the rapid dissociation of the excited electronic states of pyrrole following photoexcitation [5]. Further, we examine Pyr^+ and compare with the results of one-photon zero-electron-kinetic-energy (ZEKE) spectra of Pyr [6]. Although infrared spectroscopy has been used to study complexes of Pyr^+, these have focused on the N—H stretching region [7]. Vibrational wavenumbers have been reported for the ground state of NDP [4], but we are unaware of any values for the cation.

There has been little work on NAP to date, with the calculated geometry and harmonic vibrational wavenumbers published, albeit at a low level of theory [8].

There have been several early studies on the vibrations of NMP, with many of the values being tabulated from these by Scott [4], alongside a force field model. Further work on IR spectroscopy of NMP absorbed on oxide surfaces has also been published [9]. Some data relevant to the vibrations of NMP^+ are available via the observation of Rydberg states in absorption and resonance-enhanced multiphoton ionization (REMPI) spectra [10–16]; DF spectra from the first excited state have also been reported [13]. We have been examining the vibrations of NMP in its ground and first excited neutral states and ground state cation, as part of a combined laser-induced fluorescence and ZEKE study [15,17], for which the present work is preparatory. As such, we refrain from a detailed examination of the vibrations of NMP and NMP^+ herein, restricting ourselves to reporting the calculated wavenumber values for each vibrational mode. In forthcoming work [17], we shall comment on the DF spectra of Biswas et al. [13], and the proposed assignments of the first excited neutral state vibrations [13,16], as well as report vibrational wavenumbers and assignments for vibrations of the cation.

We also find that there has been very little work on NFP, with its geometry having been reported using low-level *ab initio* [18] and semi-empirical [19] calculations.

2. Calculational details

All geometry optimization and harmonic vibrational frequency calculations were undertaken using Gaussian 16 [20]. We employ (U)B3LYP/aug-cc-pVTZ calculations, with the unrestricted version being used for the cations. Geometries are optimized, and vibrational wavenumbers calculated, at the respective minima; the harmonic vibrational wavenumbers are scaled by a factor of 0.97 [21], which we have also used successfully in previous studies on substituted benzenes. We have based our methodology upon that we employed when putting forward a consistent labelling scheme

---

* Corresponding author.
E-mail address: Tim.Wright@nottingham.ac.uk (T.G. Wright).

https://doi.org/10.1016/j.jms.2020.111410
0022-2852/

for the ring-based vibrations of the monosubstituted benzenes [22], and for each of the three isomeric classes of disubstituted benzenes [23–25]. Such schemes allow comparison of vibrational activity across molecules from the same isomeric class. Here, we wish to examine the evolution of the vibrations of pyrrole as the nitrogen-bonded hydrogen atom is changed to different substituents. We do this by initially performing "artificial isotope" calculations whereby the mass of the nitrogen-bonded hydrogen atom is increased through 1 to 19 m_u, to observe how the mass of the substituent affects these vibrations without introducing any changes as a result of electronic effects associated with explicitly changing the substituent. The variations in the vibrational wavenumbers can then be tracked as a function of this mass. The values obtained with that approach can then be compared to the actual calculated values for NDP, NAP, NFP and NMP. We then repeat the calculations for the cations.

3. Results and discussion

3.1. Optimized geometries: Neutrals

All structures were optimized, with the resultant geometries shown in Fig. 1, with a complete set of values for the geometric parameters given in the Supplementary Material.

For pyrrole, excellent agreement is obtained between the present calculated geometry [Fig. 1(a)] and the structure determined from microwave studies on various isotopologues [26]; good agreement is also seen with the B3LYP-D3/aug-cc-pVTZ calculated structure reported in Ref. [7].

For NAP, agreement is reasonable between the present geometry [Fig. 1(c)] and the calculated one presented in Ref. [18]; it is also consistent with that discussed in an X-ray and NMR study [19]. Very good agreement is seen with the results of B3LYP/6-31+G** calculations [8]. It is notable that the hydrogens of the NH_2 group lie perpendicular to the plane of the pyrrolyl ring, in contrast to aniline, where the NH_2 group is rotated by 90° relative to NAP. A suggested rationale [18] for the NAP geometry was that this is a balance between the repulsion of the nitrogen lone pairs, and the energy gained by delocalization of the $–NH_2$ lone pair into the ring π system. It thus appears that, for aniline, there is more to be gained from the delocalization, while for NAP the repulsion remains the larger term and hence the amino group rotates, so that the lone pairs on the nitrogen atoms are orthogonal. We note that the $–NH_2$ group in NAP is tilted slightly off-vertical, to the left as viewed in Fig. 1(c) – see Supplementary Material.

For NMP, good agreement is seen between the present structure [Fig. 1(d)] and that deduced in microwave studies [27]; in particular, the ground state geometry has a staggered confirmation of the methyl group, which agrees with other work [14,15]. Biswas et al. [13] have reported the results of MP2 and B3LYP calculations on NMP, using D95++ and 6-311G** basis sets; the latter basis set gave the better agreement with the results obtained herein, with fairly similar results obtained with both levels of theory. Good agreement is also seen with the B3LYP/6–31+G** results of Ref. [8].

To our knowledge, there have been no experimental determinations of the geometry of NFP, but very good agreement between the present geometry [Fig. 1(b)] and that obtained with B3LYP/6–31+G** calculations [8] is evident, although no vibrational wavenumbers were reported.

3.2. Vibrations: Neutrals

Calculated vibrational wavenumbers for Pyr and NDP are presented in Table 1, and compared to experimental values, taken from Scott [4], where available. In that work, the reported wavenumbers are separated into symmetry classes, which have been used here to assign to a particular mode. The numbering here follows the Mulliken [28]/Herzberg [29] scheme, and the vibrational modes of pyrrole are shown in Fig. 2; these also agree with the modes reported in Ref. [4], obtained from a force field model. Generally, very good agreement is found, noting that the experimental data was obtained in liquids/solutions, and so are expected to be shifted from gas-phase values. Overall though, as has been shown with our previous work [22–25], the modest level of theory employed here performs surprisingly well.

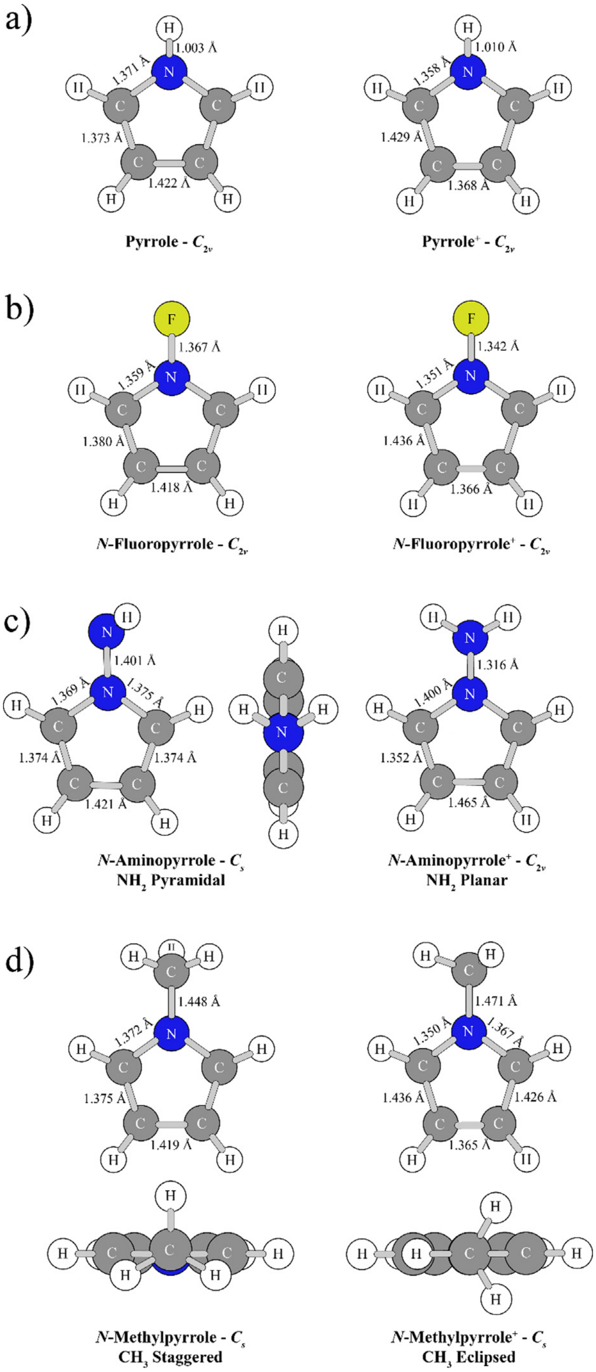

Fig. 1. Optimized geometries of the neutral (left) and cation (right) geometries of: (a) Pyr; (b) NFP; (c) NAP; and (d) NMP. Selected bond lengths are given here; a more complete set of geometric parameters is given as Supplementary Material.

Table 1
Calculated and experimental vibrational wavenumbers (cm^{-1}) for pyrrole, and *N*-deuteropyrrole in C_{2v} symmetry.

Symmetry	Mulliken[a]	Pyrrole		*N*-deuteropyrrole	
		Calculated[b]	Experiment[c]	Calculated[b]	Experiment[c]
a_1	1	3561	3531	3166	3145[d]
	2	3166	3145[d]	3146	3131[d]
	3	3146	3129[d]	2622	2607
	4	1454	1467	1449	1460
	5	1372	1382	1372	1388
	6	1137	1144	1129	1139
	7	1057	1074	1056	1071
	8	1002	1016	998	1011
	9	875	881	863	869[d]
a_2	10	867	869	867	869[d]
	11	682	710	682	708
	12	612	618	612	618
b_1	13	826	826	823	824
	14	715	721	713	718
	15	623	601	599	
	16	483	474	375	
b_2	17	3160	3145[d]	3160	3145[d]
	18	3135	3129[d]	3135	3131[d]
	19	1527	1530	1507	
	20	1400	1422	1337	1410[e]
	21	1276	1287	1256	1210
	22	1121	1134	1061	
	23	1035	1048	898	909
	24	855	865	819	827

[a] Mulliken [28]/Herzberg [29] labels.
[b] This work – B3LYP/aug-cc-pVTZ, scaled by 0.97.
[c] Taken from the compilation in Ref. [4]. (Note that an alternate axis system is used in Ref. [4] such that b_1 is b_2 in the present work and vice versa.)
[d] These values were not assigned uniquely in Ref. [4], and so each appears twice in a column.
[e] This assignment looks to be incorrect; in the text we have suggested a reassignment to the first overtone of P_{11}.

In Tables 2 and 3, we show the calculated vibrational wavenumbers for NAP, NFP and NMP, where the numbering will be discussed later in this subsection.

Vibrational wavenumbers have previously been calculated for NAP using a small basis set, where the ring-localized and NH_2-localized vibrations were listed together in C_s symmetry classes [18]; no scaling was performed, but if a scaling factor of 0.9 is applied [21], many of the values are in close agreement with those presented herein (Tables 2 and 3). An IR spectroscopic study in CCl_4 solutions [30] reported symmetric and asymmetric stretch values for the NH_2-localized vibrations, obtaining values of 3300 cm^{-1} and 3371 cm^{-1}, respectively; the present calculated values (Table 3), 3368 cm^{-1} and 3444 cm^{-1}, suggest that the experimental values have undergone a solvatochromatic shift.

We have been unable to locate any experimental or calculated vibrational wavenumber values for NFP, but present our calculated values in Table 2.

Calculated values for the vibrational wavenumbers of NMP have been reported by Biswas et al. [13] at the B3LYP/6-311G** level of theory; these were unscaled and, despite the fact that the methyl group breaks the C_{2v} symmetry, both the methyl- and ring-localized vibrations were collected together in C_{2v} symmetry classes. These agree with the values obtained here (Tables 2 and 3), provided a similar scaling factor similar is employed. Vibrational wavenumbers for the ground state neutral molecule have also been reported by Kanamaru [31], at the MP2/6-31G** level (unscaled), separated into both point group and molecular symmetry group classes; good agreement is seen with the present values. The available experimental values have been collated by Scott [4], with very similar values having been obtained for some vibrations by Dines et al. [9] in a surface IR study – see Table 2. In Ref. [4], the vibrations were separated into a' and a'' symmetry classes, but no specific assignments were made; in Ref. [9], a very brief description of each mode was given. In Table 2, we have associated each wavenumber with the best match to the calculated value, taking into account symmetry. Overall, good agreement is obtained between the present calculated values and the majority of the reported experimental ones. One exception is that for ν_{20} for NDP; we suggest that this assignment is incorrect, with a possible reassignment to the first overtone of P_{11}.

Of note is that there are three a_1 symmetry vibrations with wavenumbers > 3000 cm^{-1} for Pyr, but only two such for NDP, NAP, NMP and NFP, and as discussed below, this is because the N–X stretch vibration decreases sharply in wavenumber as the mass of the substituent, X, increases; other vibrations will also be seen to be highly mass dependent.

In earlier work, we have put forward a consistent labelling scheme for monosubstituted benzenes [22]. The ideas underpinning this are that when substituents are added, both the wavenumber and vibrational motion can alter as a result of both mass and electron density changes, but also extra vibrations are present when the substituent is larger than a single atom. The former means that labelling schemes based upon the vibrational motions in the unsubstituted species, such as the Wilson labels [32] for benzene, can be highly misleading when applied to the substituted species; the latter means that labels based upon a wavenumber ordering of the vibrations, such as the Mulliken [28]/Herzberg [29] scheme, will lead to different numbers for the same vibrational motion. Varsányi [33] attempted to bring order to the labels in substituted benzenes, but we have shown that those still contain significant labelling inconsistencies between similar molecules [22–25]. As such, in the present work, using a similar approach to Ref. [22], we put forward labels that will prove useful both in labelling the vibrations of *N*-substituted pyrroles, but we also will show how the vibrations of the parent pyrrole molecule are related to these. The scheme is based on the twenty-four ring-based vibrations, with those that are largely localised on the substituent being deemed to be separate from these: essentially, we are treating the substituent as a point mass. We calculate the vibrations as the mass of the nitrogen-bonded sub-

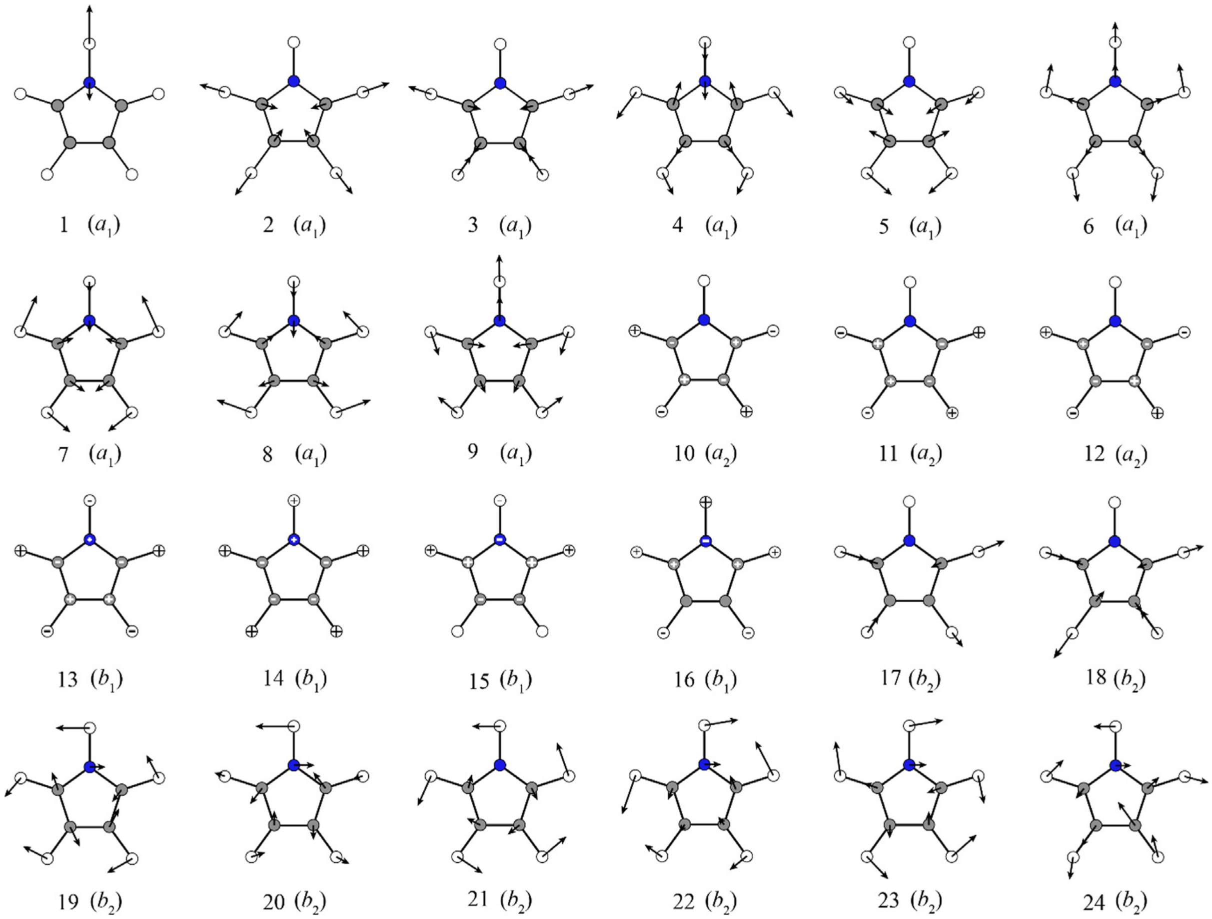

Fig. 2. Vibrational mode diagrams for pyrrole. The numbering follows the Mulliken [28]/Herzberg [29] labelling scheme. Nitrogen atoms are blue, carbon atoms are dark grey, and hydrogen atoms are white. The lengths of the arrows and sizes of the +/- signs are approximate indications of the magnitudes of the atomic displacements. The calculated wavenumbers can be found in Table 1.

stituent changes. It has previously been found that, for ground state neutral substituted benzenes, there is relatively little mixing of the substituent-localized and ring-based vibrations, and similarly that electronic effects are usually small [22–25].

In Fig. 3(a) we show the variations in the calculated vibrational wavenumbers of pyrrole, where the mass of the nitrogen-bonded hydrogen is artificially increased from 1 to 19 m_u. We also show expanded views of the 1–3 m_u region in Fig. 3(b) for the a_1 and b_2 vibrations that are particularly mass dependent; we highlight that all of the a_2 symmetry vibrations are only weakly mass dependent – see Fig. 3(a). On the left-hand side of each plot, the vibrations are those of ^{1}H–Pyr, while upon moving across to the right-hand side, we expect these vibrations to resemble closely those of the *N*-substituted pyrroles. The plots show behaviour that is reminiscent of interactions and avoided crossings that one would see in potential energy curves of diatomic molecules. We interpret such behaviour as vibrations becoming mixed versions of each other, with the mixing particularly marked close to an "avoided crossing" region; these then evolve further, in some cases closely resembling their original forms, but with altered energy ordering (see Refs. [22;23] for further, similar discussion and commentary); others largely lose their original identity and become significant mixtures of the original pyrrole modes. The mixing of the modes is indicated via a Duschinsky matrix in Fig. 4 where the ^{15}H-Pyr modes are expressed in terms of the ^{1}H-Pyr modes; this, and other such matrices were created with the FC-LabII program [34]. The Duschinsky matrix in Fig. 4 indicates that the vibrations of ^{15}H–Pyr are very different to those of ^{1}H–Pyr; however, from Fig. 3, it is clear that, in all but one case, the curves do not undergo any further avoided crossings after 3 m_u, and all become largely parallel at masses greater than 14 m_u. In our earlier work [22–25], we used similar observations to propose consistent labelling schemes based on monofluoro- or difluoro-substituted benzenes, such that the labels were good representations of the ring motions, whatever the substituents. Some of the largest changes occurred in the low mass region, and the same behaviour is seen here; this region represents the largest relative changes in mass, so this is not unexpected – see Fig. 3(b). We thus propose a set of labels for the vibrations of *N*-substituted pyrroles that we expect to be valid for all commonly-occurring nitrogen-bonded substituents, except for commonly-occurring isotopes of hydrogen; we denote these vibrations, P_i, with the index, i, being determined by the Mulliken [28]/Herzberg [29] numbering for ground state neutral NFP. The calculated vibrational motions for NFP and the P_i labels are shown in Fig. 5.

In Table 2 we have given both the vibrational wavenumbers calculated for ^{19}H–Pyr and those calculated for NFP, and similarly for NAP and ^{14}H–Pyr, and NMP and ^{15}H–Pyr. The agreement between the two sets is generally very good, showing that the majority of the wavenumber variations result from the mass change; this is emphasised by the ratios presented, which show values close to 1.00. There are a few exceptions, which suggests that these modes are sensitive to electronic effects caused by the substitutions; these could include hyperconjugation and inductive effects. These effects, however, are not sufficient to cause any ambiguities in the assignment of the modes.

Table 2
Calculated and experimental wavenumbers (cm^{-1}) for the ring-localized vibrations of *N*–aminopyrrole, *N*–methylpyrrole, *N*-fluoropyrrole, and the corresponding ^{x}H–Pyr in C_{2v} symmetry.

Symmetry	P_i	NAP		NMP			NFP	
		^{14}H–Pyr[a]	Calculated[b]	^{15}H–Pyr[a]	Calculated[b]	Experiment[c]	^{19}H–Pyr[a]	Calculated[b]
a_1	1	3166 (0.997)	3174	3166 (1.00)	3160	3130[d] (3126)	3166 (0.993)	3187
	2	3146 (1.00)	3146	3146 (1.00)	3141	3103[d] (3101)	3146 (0.997)	3155
	3	1573 (1.07)	1470	1566 (1.05)	1492	1504 (1509)	1548 (1.07)	1446
	4	1374 (0.999)	1377	1374 (1.00)	1375	1416 (1419)	1373 (1.00)	1367
	5	1362 (1.06)	1282	1358 (1.06)	1278	1286 (1288)	1343 (1.07)	1254
	6	1080 (1.01)	1066	1079 (1.00)	1075	1088 (1091)	1076 (1.03)	1048
	7	1048 (1.01)	1042	1048 (1.00)	1045	1058 (1055)	1047 (1.01)	1033
	8	969 (1.01)	957	968 (1.01)	956	966	964 (1.02)	948
	9	680 (1.03)	658	668 (1.02)	652	662	627 (0.992)	632
a_2	10	867 (1.00)	865	867 (1.00)	863	858	867 (1.01)	858
	11	682 (1.02)	667	682 (1.01)	675	688	682 (1.08)	629
	12	612 (0.994)	616	612 (1.00)	610		612 (1.01)	608
b_1	13	821 (1.00)	818	821 (1.01)	814	815	821 (1.03)	796
	14	712 (1.00)	712	712 (1.00)	712	720	712 (1.05)	681
	15	590 (1.01)	587	590 (0.978)	603	601	590 (1.12)	527
	16	207 (1.10)	188	204 (1.10)	186	186	196 (1.39)	141
b_2	17	3160 (1.00)	3158	3160 (1.00)	3152	3130[d] (3126)	3160 (0.992)	3184
	18	3135 (1.00)	3134	3135 (1.00)	3132	3103[d] (3101)	3135 (0.997)	3143
	19	1503 (0.999)	1504	1503 (0.999)	1505	1547	1503 (1.01)	1493
	20	1321 (0.990)	1334	1321 (0.979)	1350		1321 (0.962)	1373
	21	1245 (1.00)	1242	1245 (0.987)	1262	1232	1245 (1.00)	1239
	22	1055 (1.00)	1052	1055 (0.983)	1073	1043	1055 (1.01)	1046
	23	865 (1.01)	855	865 (1.00)	864	868	865 (1.02)	845
	24	422 (1.07)	394	415 (1.20)	347	354	391 (1.01)	388

[a] This work. These are obtained using the B3LYP/aug-cc-pVTZ force constants for Pyr and calculating the vibrational wavenumbers with the mass of the nitrogen-bonded hydrogen atom changed to the indicated mass, in m_u; the vibrational wavenumbers were then scaled by 0.97. The values in parentheses are the ratio of the ^{x}H–Pyr value to that calculated for the actual molecule.

[b] This work – B3LYP/aug-cc-pVTZ, scaled by 0.97.

[c] Taken from the compilation in Ref. [4], with the values in parenthesis being from a surface IR study [9].

[d] This value was not assigned uniquely in Ref. [4].

Table 3
Calculated wavenumbers (cm^{-1}) for the substituent-localized vibrations[a].

Mode[a]	Description[b]	Neutral	Cation	
		Calculated[c]	Experiment	Calculated[c]
	N-aminopyrrole			
Am_1	*asym* str	3444	3371[d]	3560
Am_2	*sym* str	3368	3300[d]	3422
Am_3	bend	1635		1600
Am_4	rock	1284		1212
Am_5	inversion	882		197
Am_6	torsion	253		355
	N-methylpyrrole			
Me_1	*asym* CH_2 str	3026	2942[e,f]	3051
Me_2	*sym* CH_2 str	2996	2942[e,f]	3071
Me_3	*sym* CH_3 str	2935	2819[f]	2976
Me_4	*asym*. bend	1467	(1464)[f]	1442
Me_5	*sym* bend	1447	1382[e,f]	1463
Me_6	umbrella	1409	1382[e,f]	1408
Me_7	*sym* rock[g]	1111	(1120)[e]	1117
Me_8	*asym* rock[g]	1029	(1127)[e]	993
Me_9	torsion	69		28

[a] The amine (Am) and methyl (Me) modes, numbered in decreasing wavenumber order in the neutral state, with cation vibrations given the same label for the corresponding motion. These motions are very distinct, and it is clear that the vibrational ordering changes upon ionization.

[b] Approximate description of the main motion.

[c] This work – B3LYP/aug-cc-pVTZ for the neutrals and UB3LYP/aug-cc-pVTZ for the cations, each scaled by 0.97.

[d] IR studies in CCl_4 solution [30].

[e] Taken from the compilation in Ref. [4]. Values in parentheses were estimated using a force field model derived from the available experimental data. This is our best attempt at associating the presented wavenumbers with these methyl-localized vibrations.

[f] This value was not assigned uniquely in Ref. [4].

[g] Of the two methyl rocks the higher wavenumber one (*sym*) is rocking towards and away from the ring in the cation, maintaining C_s symmetry, while the lower wavenumber one (*asym*) is rocking either side of the reflection plane.

3.3. Optimized geometries: Cations

Very little information is available on the cations. Cursory information is available in the one-photon ZEKE spectrum of pyrrole on the approximate change in geometry [6], with a more-detailed structure for Pyr^+ being available at the B3LYP-D3/aug-cc-pVTZ level in Ref. [7]; the present structure, Fig. 1(a), is in excellent agreement with that.

We have been unable to find any information on the geometry of NAP^+, although its first and second vertical ionization energies

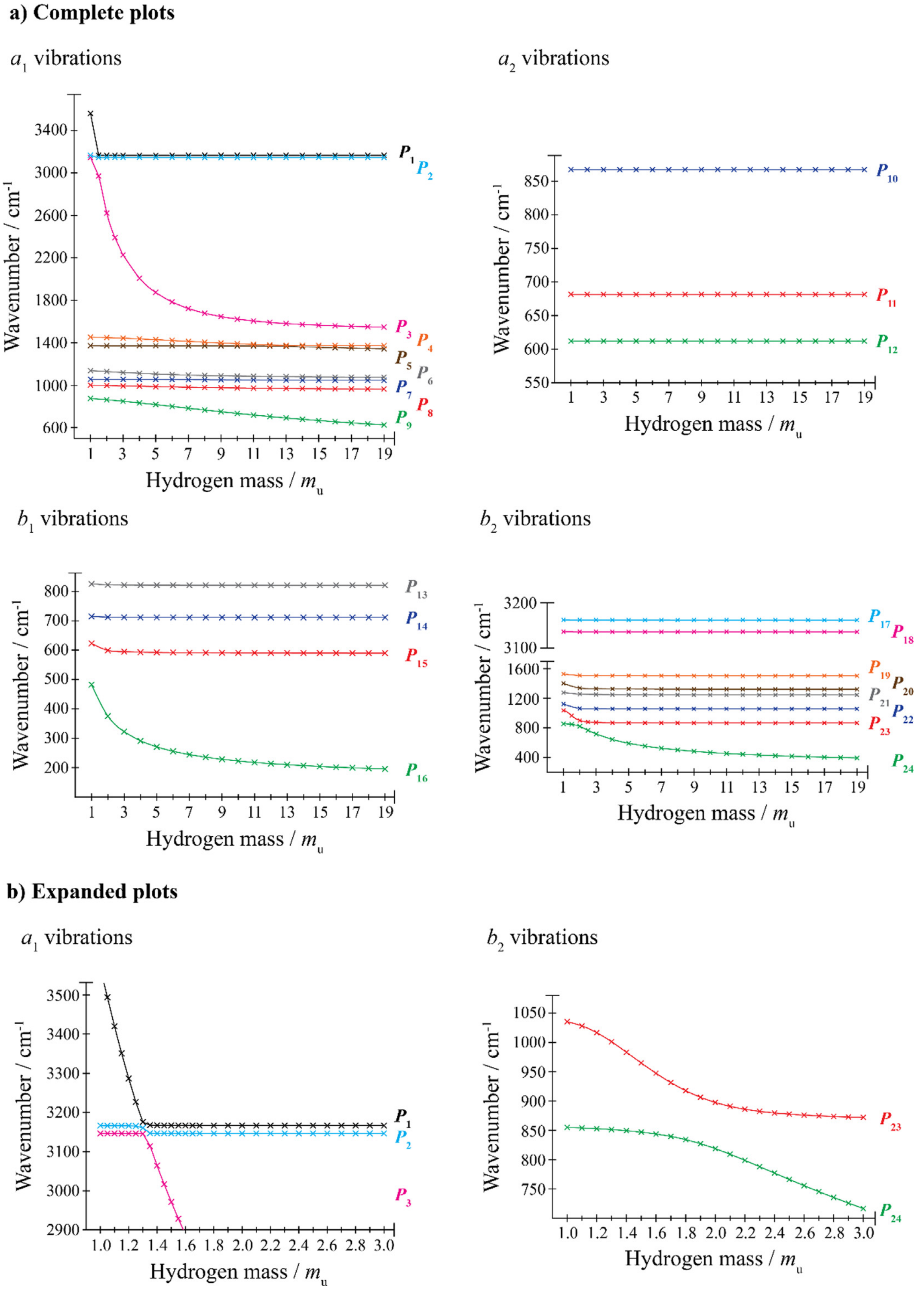

Fig. 3. Mass correlation diagram for the neutral molecules, ^{1}H–Pyr → ^{19}H–Pyr. (a) Complete plots for ^{x}H–Pyr, x = 1–19 m_u, showing the variation of the vibrational wavenumbers for each C_{2v} symmetry class. (b) Expanded views of the ^{x}H–Pyr (x = 1–3 m_u) vibrational wavenumber variation for selected vibrations. The colours are merely a guide to the eye.

have been measured as 8.36 eV and 9.03 eV, respectively [35]. We find that the amino group in the cation is planar, in contrast to the pyramidal structure in the neutral [Fig. 1(c)], which is reminiscent of the planar ← pyramidal geometry changes that occurs upon ionization for ammonia [36] and aniline [37]; although, as noted above, the NH_2 group in the neutral NAP is rotated 90° compared to neutral aniline. Our rationale for the planar geometry of NAP$^+$ is that the positive charge, mainly localized in the pyrrolyl ring π system, makes it more favourable for the –NH_2 lone pair to become involved in the π system, causing partial double-bond character in the N—N bond; this is confirmed by the significant shortening of this bond [Fig. 1(c)] upon ionization. This also forces both N atoms to have a hybridization close to sp^2, and so producing a planar geometry.

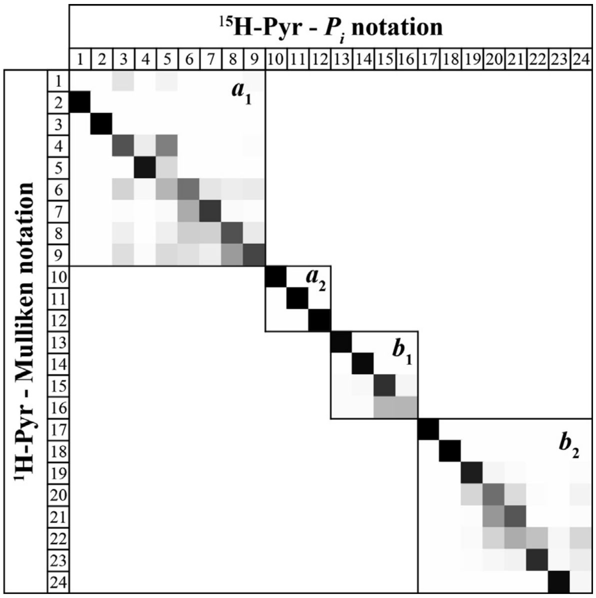

Fig. 4. Duschinsky matrix showing how the ^{1}H–Py and ^{15}H–Py vibrations can be expressed as mixtures of each other.

For NMP$^+$, there is a change in conformation of the methyl group upon ionization, with there being a staggered geometry in the ground state neutral, while the cation has an eclipsed geometry – see Fig. 1(b). This is in agreement with the results of recent ZEKE and two-dimensional laser-induced fluorescence (2D-LIF) spectroscopy from our group [15,17].

We are unaware of any calculated or experimental information on the structure of NFP$^+$.

3.4. Vibrations: Cations

In Fig. 6, we show plots similar to those in Fig. 3, but now for the cation, where we are varying the mass of the nitrogen-bonded hydrogen atom of Pyr$^+$ artificially from 1 to 19 m_u. In general terms, very similar behaviour is observed for the cation and the neutral, although there are some differences, owing to the different force fields in these species. Importantly, however, the main conclusion holds: namely, that the vibrations have settled down in form to higher mass and hence the ring-localized motions will be very similar for different substituents, excluding for commonly-occurring hydrogen isotopes. In Fig. 7(a), we show Duschinsky matrices that express the ^{1}H–Pyr$^+$ vibrations in terms of the ^{1}H–Pyr ones, using the standard Mulliken [28]/Herzberg [29] labelling scheme for each of these. It can be seen that there is significant mixing of the vibrations between these two states, so much so that many of the cation vibrations cannot be straightforwardly identified with a single ground state vibration. This is true both from the Duschinsky mixing matrix, but also upon examining animations of the modes of the vibration. As such, for pyrrole, and NDP, we conclude that the ground state neutral and cation vibrations must be labelled separately.

Yang et al. [6] have recorded a one-photon ZEKE spectrum of Pyr and assigned a significant number of the fundamental vibrations of Pyr$^+$, which are shown alongside the present calculated

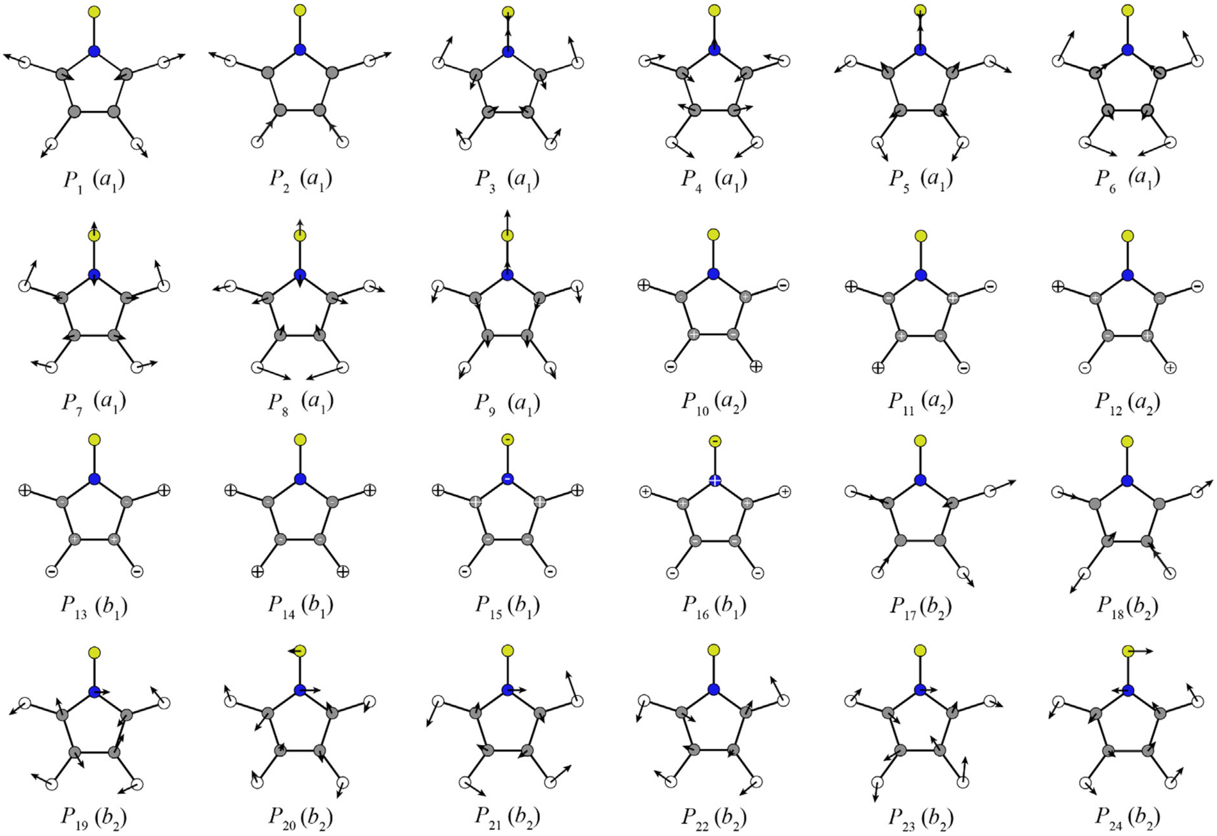

Fig. 5. Vibrational mode diagrams for *N*–fluoropyrrole. The numbering follows the Mulliken [28]/Herzberg [29] labelling scheme, which is then designated the P_i labelling scheme for *N*–substituted pyrroles herein, with the label remaining fixed for the same atomic motions. The C_{2v} symmetries of each mode are given. Nitrogen atoms are blue, fluorine atoms are yellow-green, carbon atoms are dark grey, and hydrogen atoms are white. The lengths of the arrows and the sizes of the +/− signs are approximate indications of the magnitudes of the atomic displacements. The calculated wavenumbers can be found in Table 2.

a) Complete plots

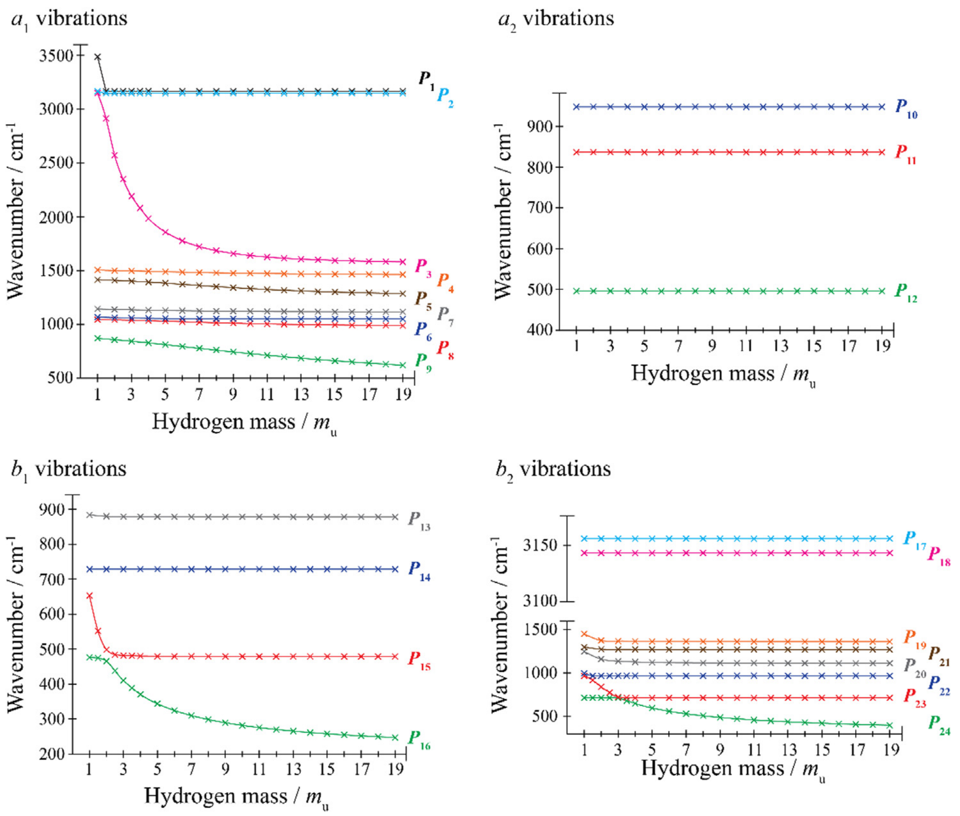

b) Expanded plots

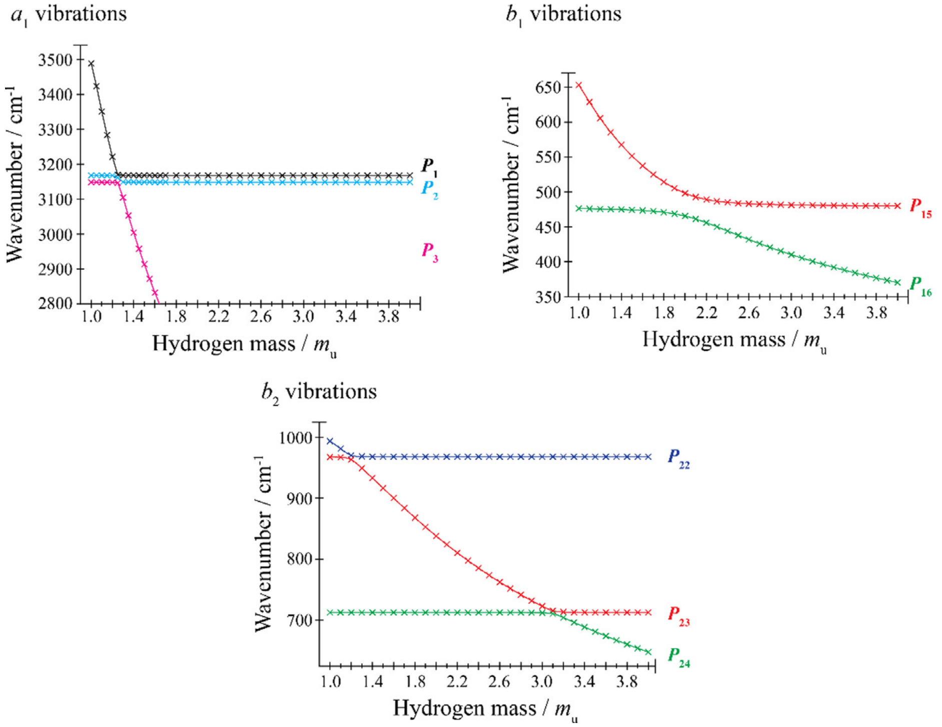

Fig. 6. Mass correlation diagram for the cations, ^{1}H–Pyr^{+} → ^{19}H–Pyr^{+}. (a) Complete plots for ^{x}H–Pyr^{+}, x = 1–19 m_u, showing the variation of the vibrational wavenumbers for each C_{2v} symmetry class. (b) Expanded views of the ^{x}H–Pyr^{+} (x = 1–4 m_u) vibrational wavenumber variation for selected vibrations. The colours are merely a guide to the eye. Note that P_6 and P_7, and P_{20} and P_{21} have switched order in the cation, from that in the neutral.

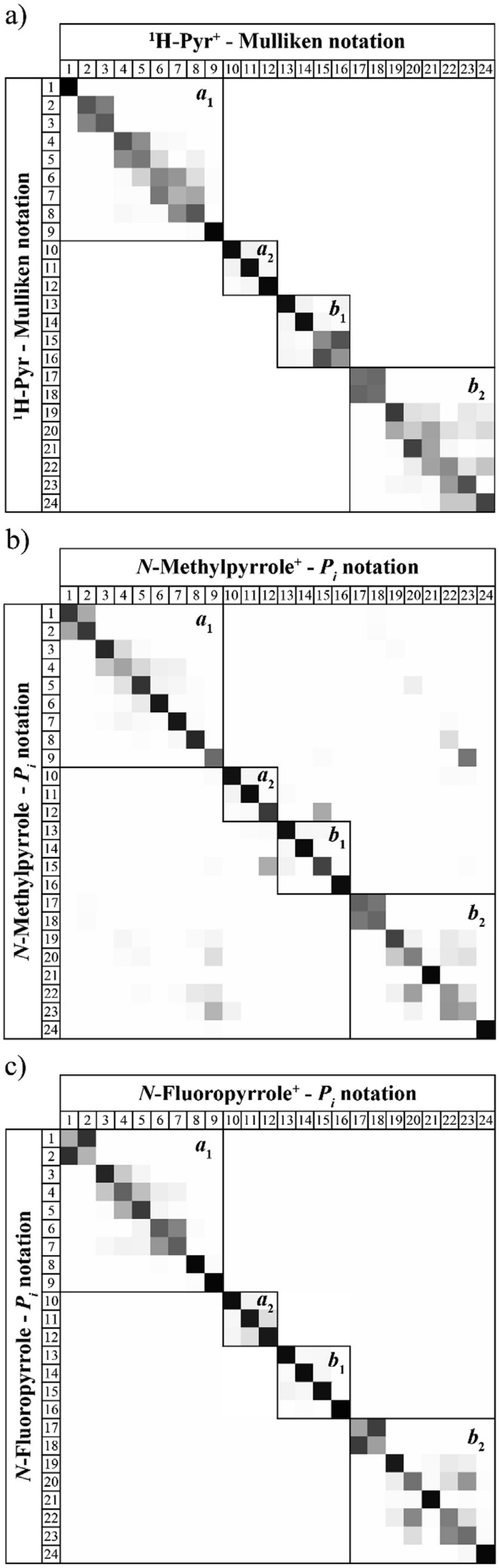

Fig. 7. Duschinsky matrices showing how the neutral and cation vibrations can be expressed as mixtures of each other: (a) for ^{1}H–pyrrole/^{1}H–pyrrole$^+$; (b) for *N*–methylpyrrole/*N*-methylpyrrole$^+$; and (c) *N*-fluoropyrrole/*N*-fluoropyrrole$^+$. For (a), separate Mulliken [28]/Herzberg [29] labels have been used for the neutral and cation vibrations, while for (b) and (c) the cation vibrations have been labelled with the P_i labels of the neutral; however, there is significant mixing, and we have generally used the label that indicates the greatest contribution – see text.

values in Table 4. Interestingly, as well as the expected totally-symmetric vibrations being active in the spectrum, a number of formally symmetry-forbidden bands were also observed, although mechanisms exist to explain this [38]. The agreement between the experimental values and those calculated here and in Ref. [6] (if scaled similarly), using the same DFT method and similar basis sets, supports the assignments offered, in terms of Mulliken [28]/Herzberg [29] labels, but with the caveat that many of the cation vibrations will be significantly altered from those of the neutral molecule. The calculated value of the N—H stretch vibration in gas-phase Pyr$^+$ was 3459 cm^{-1} in Ref. [7], which is in good agreement with the present calculated value (3489 cm^{-1}) – Table 4.

In Table 5 we present the calculated values for the ring-localized vibrations of *N*-substituted pyrrole cations, and compare those calculated by artificially changing the nitrogen-bonded hydrogen atom in Pyr$^+$. (The substituent vibrational wavenumbers for NAP, NMP and their cations, are given in Table 3.) Although many of the vibrations compare well between the two approaches, there are some notable differences, indicating more significant perturbations to the electronic structure; this is particularly true for NAP$^+$, where we have noted that there is a significant change in geometry (pyramidal → planar) upon ionization. We highlight that amongst the a_1 vibrations, except for NAP$^+$, P_6 and P_7 have switched wavenumber order upon ionization, while for the b_2 symmetry vibrations, P_{20} and P_{21} have changed order for all species – these points have been confirmed by careful examination of the motions. These comments are borne out by the Duschinsky matrices presented in Fig. 7(b) and (c) that, despite showing some mixing, are largely dominated by the diagonal elements. It is also the case that P_{20} and P_{23} in NAP$^+$ have become heavily mixed so that the ring and hydrogen motions do not completely correspond to the anticipated motion (Fig. 5); as such, it was difficult to assign a P_i label based on the forms of the vibration alone and use has also been made of the wavenumber order. (Technical difficulties meant that it has not been possible to create the Duschinsky matrix for NAP/NAP$^+$.) Also, there is significant mixing between P_9 and P_{23} in *N*-methylpyrrole [see Fig. 7(b)], suggesting that the interaction with the methyl group is enough to cause the true point group symmetry, C_s, to be experienced, even though the torsional barrier is ~10 cm^{-1} in the cation [15]. The geometry can be seen to deviate from C_{2v} [Fig. 1(b)], and a_1 and b_2 symmetries in C_{2v} both become a' in C_s symmetry. Despite these points, it was still possible to assign a P_i label upon visualization of the vibrational mode.

4. Further remarks and conclusions

In the above we have presented a complete set of geometries and vibrational wavenumbers for Pyr, NAP, NMP and NFP, together with those for their cations. We have shown that there is a strong mass dependence for some of the vibrations as the mass of the nitrogen-bonded substituent increases. This can be viewed as mixing of the pyrrole modes, and this means that many of the vibrations of the substituted pyrroles are very different to those of pyrrole itself; this is the case for both the neutral and cation species. The implication is that one cannot use the same labels for the vibrations of pyrroles and substituted pyrroles, in a similar way to that demonstrated in the corresponding case of benzenes [22–25]. However, for substituents with masses > 14 m_u (i.e. most commonly-occurring substituents), the forms of the vibrations are very similar – see Fig. 3 – making it meaningful to label these with the same number. Indeed, even though the Duschinsky matrix might sometimes indicate a fair amount of mixing, for almost all vibrations it is relatively straightforward to identify the motion that corresponds to that in NFP from visualization, and so to associate a P_i label with it.

Table 4
Calculated and experimental vibrational wavenumbers (cm^{-1}) for pyrrole$^+$ and *N*-deuteropyrrole$^+$ in C_{2v} symmetry.

Symmetry	Mulliken[a]	Pyr$^+$			NDP$^+$
		Calculated		Experiment	Calculated
		YLM[b]	Present[c]	YLM[b]	Present[c]
a_1	1	3602	3489		3168
	2	3271	3168		3149
	3	3253	3149		2574
	4	1549	1504	1508	1500
	5	1459	1415	1418	1409
	6	1177	1142	1150	1138
	7	1100	1066	1078	1062
	8	1075	1043	1060	1041
	9	897	869	874	856
a_2	10	974	948	943	948
	11	858	836	838	836
	12	509	496	495	496
b_1	13	904	884	895	880
	14	750	729	728	729
	15	670	653	679	498
	16	486	476		466
b_2	17	3259	3156		3156
	18	3247	3143		3143
	19	1496	1450	1480	1374
	20	1336	1299	1353	1273
	21	1286	1247		1160
	22	1025	994	1003	968
	23	997	968	979	838
	24	735	713	715	713

[a] Mulliken [28]/Herzberg [29] labels.
[b] From a one-photon ZEKE spectroscopic study by Yang et al. [6].
[c] This work – UB3LYP/aug-cc-pVTZ, scaled by 0.97.

Table 5
Calculated and experimental wavenumbers (cm^{-1}) for the ring-localized vibrations of *N*-aminopyrrole$^+$, *N*–methylpyrrole$^+$ and *N*-fluoropyrrole$^+$ and the corresponding ^{x}H–Pyr$^+$ in C_{2v} symmetry.

Symmetry	P_i	^{14}H–Pyr$^+$ [a]	NAP$^+$ [b]	^{15}H–Pyr$^+$ [a]	NMP$^+$ [b]	^{19}H–Pyr$^+$ [a]	NFP$^+$ [b]
a_1	1	3168 (0.997)	3176	3168 (1.00)	3167	3168 (1.00)	3165
	2	3149 (0.997)	3159	3149 (1.00)	3144	3149 (1.00)	3148
	3	1599 (1.07)	1494	1594 (1.04)	1527	1580 (1.05)	1508
	4	1467 (1.10)	1334	1466 (1.01)	1456	1463 (1.02)	1435
	5	1305 (0.912)	1431	1300 (1.07)	1218	1285 (1.04)	1239
	6	1050 (0.960)	1094	1050 (0.998)	1052	1050 (1.03)	1018
	7	1117 (1.13)	989	1116 (1.01)	1107	1114 (1.01)	1104
	8	995 (1.10)	906	993 (1.03)	968	987 (1.02)	970
	9	672 (0.984)	683	660 (1.08)	609[d]	619 (0.964)	642
a_2	10	948 (1.05)	906	948 (1.01)	942	948 (1.01)	939
	11	836 (1.24)	676	836 (1.00)	833	836 (1.03)	809
	12	496 (0.917)	541	496 (1.00)	495	496 (0.992)	500
b_1	13	878 (1.02)	865	878 (1.01)	868	878 (1.03)	854
	14	729 (1.01)	723	729 (1.01)	721	729 (1.05)	697
	15	479 (0.813)	589	479 (0.978)	490	479 (1.13)	425
	16	261 (1.09)	240	258 (1.20)	215	247 (1.20)	206
b_2	17	3156 (0.995)	3171	3156 (1.00)	3155	3156 (1.00)	3154
	18	3143 (0.997)	3154	3143 (1.00)	3138	3143 (1.00)	3143
	19	1361 (0.877)	1551	1361 (0.995)	1368	1361 (0.997)	1365
	20	1112 (0.869)	957[c]	1112 (0.942)	1180	1111 (1.03)	1081
	21	1270 (1.33)	1280	1270 (0.995)	1275	1270 (1.01)	1252
	22	968 (0.902)	1073	968 (1.01)	955	968 (1.03)	938
	23	713 (1.26)	567[c]	713 (1.10)	646[d]	713 (1.39)	514
	24	428 (1.14)	374	421 (1.24)	340	397 (1.01)	392

[a] This work. These are obtained using the force constants for Pyr$^+$ calculated using UB3LYP/aug-cc-pVTZ and calculating the vibrational wavenumbers with the mass of the nitrogen-bonded hydrogen atom changed to the indicated mass, in m_u, scaled by 0.97. The values in parentheses are the ratio of the ^{x}H–Pyr$^+$ value to that calculated for the actual molecule.
[b] This work – UB3LYP/aug-cc-pVTZ, scaled by 0.97.
[c] Modes P_{20} and P_{23} become very mixed in NAP$^+$, and have been assigned here on the basis of wavenumber.
[d] Although assignable, there is a significant amount of mixing between P_9 and P_{23} in NMP$^+$ – see Fig. 7 and text for more details.

Remarkably, many of the vibrational wavenumbers calculated from the pyrrole force field, while artificially increasing the mass of the nitrogen-bonded hydrogen atom, are in very good agreement with the "explicitly calculated" values, showing that electronic effects are generally small, particularly in the neutral molecules; indeed any deviations can be used as a signature that such vibrations are sensitive to substituent-induced electronic density changes. Further, although there was significantly more mixing of the modes upon ionization, it was still possible to use the P_i labels for the cation vibrations in almost all cases. For pyrrole itself, however, the modes changed substantially upon ionization, such that it is not straightforward to use the same labels for the neutral and cation.

We emphasise that the P_i labels are only expected to be applicable to the nitrogen-substituted species since, in our work on disubstituted benzenes, the vibrational motions change significantly between the *ortho*, *meta* and *para* cases [22–25]. This means that comparing vibrational activity upon excitation or ionization can be less than straightforward for different isomers [39], but is a useful framework for assigning the spectra, and identifying phenomena such as Duschinsky mixing. Therefore, we expect the P_i labels will be useful in assigning the spectra of other *N*-substituted pyrroles, including alkyl pyrroles (in addition to NMP), *N*–borylpyrrole, *N*-phosphinylpyrroles, and alkali metal pyrrolides.

As indicated in the above, we shall soon publish our work on the vibrations of NMP in the ground and first excited neutral states, as well as the ground state cation [17], following on from our work on the NMP torsions in the same three electronic states [15].

Declaration of Competing Interest

The authors declare that they have no known competing financial interests or personal relationships that could have appeared to influence the work reported in this paper.

Acknowledgements

The EPSRC and the University of Nottingham are thanked for studentships to D.J.K. and A.R.D. We are grateful for access to the High-Performance Computing (HPC) resource at the University of Nottingham.

Appendix A. Supplementary material

Supplementary data to this article can be found online at https://doi.org/10.1016/j.jms.2020.111410.

References

[1] V. Bhardwaj, D. Gumber, V. Abbot, S. Dhiman, P. Sharma, RSC Adv. 5 (2015) 15233.

[2] S. Chavda, K. Mulder, T. Brown, H. Makay, B. Babu, L. Westrate, A. Ferguson, S. Lin, K. Kiakos, J.P. Ramos, M. Munde, W.D. Wilson, J.A. Hartley, M. Lee, Med. Chem. 6 (2010) 150.

[3] Y. Fu, X. Cheng, J. Zhao, T. Kong, C. Chi, X. Zhang, Polymer J. 44 (2012) 1048.

[4] D.W. Scott, J. Molec. Spectrosc. 37 (1971) 77.

[5] G. Wu, S.P. Neville, O. Schalk, T. Sekikawa, M.N.R. Ashfold, G.A. Worth, A. Stolow, J. Chem. Phys. 142 (2015) 074302.

[6] J. Yang, J. Li, Y. Mo, J. Chem. Phys. 125 (2006) 174313.

[7] M. Schütz, Y. Matsumoto, A. Bouchet, M. Öztürk, O. Dopfer, Phys. Chem. Chem. Phys. 19 (2017) 3970.

[8] K. Zborowski, I. Alkora, J. Elguero, Struct. Chem. 18 (2007) 797.

[9] T.J. Dines, L.D. Macgregor, C.H. Rochester, J. Coll. Interf. Sci. 245 (2002) 221.

[10] G. Milazzo, Gazz. Chim. Ital. 74 (1944) 152.

[11] R. McDiarmid, X. Xing, J. Chem. Phys. 105 (1996) 867.

[12] C.D. Cooper, A.D. Williamson, J.C. Miller, R.N. Compton, J. Chem. Phys. 73 (1980) 1527.

[13] N. Biswas, S. Wategaonkar, J.G. Philis, Chem. Phys. 293 (2003) 99.

[14] J.G. Philis, Chem. Phys. Lett. 353 (2002) 84.

[15] A.R. Davies, D.J. Kemp, T.G. Wright, Chem. Phys. Lett. 763 (2021) 138227.

[16] K.C. Woo, S.K. Kim, Phys. Chem. Chem. Phys. 21 (2019) 14387.

[17] A.R. Davies, D.J. Kemp, T.G. Wright, work in progress.

[18] N.V. Riggs, L. Radom, Although not stated explicitly in this work, these appear to be Hartree-Fock (HF) theory calculations, Aust. J. Chem. 241 (1988) 397.

[19] M. de al Conceptión Foces-Foces, F. Hérnandez Cano, R.M. Claramunt, D. Sanz, J. Catalán, F. Abero, A. Fruchier, J. Elguero, J. Chem. Soc. Perkin Trans. 2 (1990) 237.

[20] Gaussian 16, Revision A.03, M.J. Frisch, G.W. Trucks, H.B. Schlegel, G.E. Scuseria, M.A. Robb, J.R. Cheeseman, G. Scalmani, V. Barone, G.A. Petersson, H. Nakatsuji, X. Li, M. Caricato, A.V. Marenich, J. Bloino, B.G. Janesko, R. Gomperts, B. Mennucci, H.P. Hratchian, J.V. Ortiz, A.F. Izmaylov, J.L. Sonnenberg, D. Williams-Young, F. Ding, F. Lipparini, F. Egidi, J. Goings, B. Peng, A. Petrone, T. Henderson, D. Ranasinghe, V.G. Zakrzewski, J. Gao, N. Rega, G. Zheng, W. Liang, M. Hada, M. Ehara, K. Toyota, R. Fukuda, J. Hasegawa, M. Ishida, T. Nakajima, Y. Honda, O. Kitao, H. Nakai, T. Vreven, K. Throssell, J. A. Montgomery, Jr., J.E. Peralta, F. Ogliaro, M.J. Bearpark, J.J. Heyd, E.N. Brothers, K.N. Kudin, V.N. Staroverov, T.A. Keith, R. Kobayashi, J. Normand, K. Raghavachari, A.P. Rendell, J.C. Burant, S.S. Iyengar, J. Tomasi, M. Cossi, J.M. Millam, M. Klene, C. Adamo, R. Cammi, J.W. Ochterski, R.L. Martin, K. Morokuma, O. Farkas, J. B. Foresman, D.J. Fox, Gaussian, Inc., Wallingford CT, 2016.

[21] P. Sinha, S.E. Boesch, C. Gu, R.A. Wheeler, A.K. Wilson, J. Phys. Chem. A 108 (2004) 9213.

[22] A.M. Gardner, T.G. Wright, J. Chem. Phys. 135 (2011) 114305.

[23] A. Andrejeva, A.M. Gardner, W.D. Tuttle, T.G. Wright, J. Molec. Spectrosc. 321 (2016) 28.

[24] W.D. Tuttle, A.M. Gardner, A. Andrejeva, D.J. Kemp, J.C.A. Wakefield, T.G. Wright, J. Molec. Spectrosc. 344 (2018) 46.

[25] D.J. Kemp, W.D. Tuttle, F.M.S. Jones, A.M. Gardner, A. Andrejeva, J.C.A. Wakefield, T.G. Wright, J. Molec. Spectrosc. 346 (2018) 46.

[26] L. Nygaard, J.T. Nielsen, J. Kirchheiner, G. Maltesen, J. Rastrup-Andersen, G. Ole Sørensen, J. Molec. Struct. 3 (1969) 491.

[27] W. Arnold, H. Dreizler, H.D. Rudolph, Z. Naturforsh. 23a (1968) 301.

[28] R.S. Mulliken, J. Chem. Phys. 23 (1955) 1997.

[29] G. Herzberg, Molecular Spectra and Molecular Structure II. Infrared and Raman Spectra of Polyatomic Molecules, Krieger, Malabar, 1991.

[30] L.K. Dyall, Spectrochim. Acta. A 44 (1988) 283.

[31] N. Kanamaru, J. Molec. Struct. (Theochem) 686 (2004) 15.

[32] E.B. Wilson Jr, Phys. Rev. 45 (1934) 706.

[33] G. Varsányi, Assignments of the Vibrational Spectra of Seven Hundred Benzene Derivatives, Wiley, New York, 1974.

[34] I. Pugliesi, K. Müller-Dethlefs, J. Phys. Chem. A 110 (2006) 4657. http://www.fclab2.net.

[35] W. Flitsch, H. Peeters, W. Schulten, P. Radelmacher, Tetrahedron 34 (1978) 2301.

[36] G. Reiser, W. Habenicht, K. Müller-Dethlefs, J. Chem. Phys. 98 (1993) 8462.

[37] X. Song, M. Yang, E.R. Davidson, J.P. Reilly, J. Chem. Phys. 99 (1993) 3224.

[38] D.J. Kemp, A.M. Gardner, W.D. Tuttle, J. Midgley, K.L. Reid, T.G. Wright, J. Chem. Phys. 149 (2018) 094301.

[39] A.R. Davies, D.J. Kemp, T.G. Wright, AIP Advances (in press). https://doi.org/10.1063/5.0032146.

12. Electronic, vibrational and torsional couplings in *N*-methylpyrrole: ground, first excited and cation states

Abstract: "The electronic spectrum associated with the $S_1 \leftarrow S_0$ ($\tilde{A}^1A_2 \leftarrow \tilde{X}^1A_1$) one-photon transition of jet-cooled *N*-methylpyrrole is investigated using laser-induced fluorescence (LIF) and (1 + 1) resonance-enhanced multiphoton ionization (REMPI) spectroscopy; in addition, the (2 + 2) REMPI spectrum is considered. Assignment of the observed bands is achieved using a combination of dispersed fluorescence (DF), two-dimensional LIF (2D-LIF), zero-electron-kinetic energy (ZEKE) spectroscopy, and quantum chemical calculations. The spectroscopic studies project the levels of the S_1 state onto those of either the S_0 state, in DF and 2D-LIF spectroscopy, or the ground state cation (D_0^+) state, in ZEKE spectroscopy. The assignments of the spectra provide information on the vibrational, vibration-torsion (vibtor), and torsional levels in those states and those of the S_1 levels. The spectra are indicative of vibronic (including torsional) interactions between the S_1 state and other excited electronic states, deduced both in terms of the vibrational activity observed and shifts from expected vibrational wavenumbers in the S_1 state, attributed to the resulting altered shape of the S_1 surface. Many of the ZEKE spectra are consistent with the largely Rydberg nature of the S_1 state near the Franck–Condon region; however, there is also some activity that is less straightforward to explain. Comments are made regarding the photodynamics of the S_1 state."

Authors: Alexander R. Davies, David J. Kemp and Timothy G. Wright
Submitted to: Journal of Chemical Physics, 17th March 2021
Published: 10th June 2021
Reference: A. R. Davies, D. J. Kemp and T. G. Wright, *J. Chem. Phys.*, 2021, **154**, 224305.
DOI: 10.1063/5.0050654
Supplementary material: see Appendix 4

Summary: This work comprises the main body of the most comprehensive spectroscopic study, to date, on *N*-methylpyrrole. Here, we present ZEKE and DF spectra (and in a few cases 2D-LIF spectra) *via* almost all bands below ~1100 cm^{-1} of the $S_1 \leftarrow S_0$ transition of NMP. From these spectra, we deduce experimental vibrational wavenumbers for the majority of the normal modes of NMP in the S_0, S_1 and D_0^+ states. As the $\tilde{A}^1A_2 \leftarrow \tilde{X}^1A_1$ electronic transition is symmetry-forbidden, the structure we observe arises from Herzberg-Teller coupling and we discuss the impact this has on the ZEKE and fluorescence spectra. We also discuss the coupling regimes involved as vibronic states of different symmetry (associated with the S_1 electronic state) will gain intensity from different, nearby, electronic states. Furthermore, we discuss, in depth, the spectra for the b_1 symmetry vibrations [these are the out-of-plane with our axis system (the pyrrolyl ring lies in the *yz*-plane)] as these spectra show ZEKE spectra with significantly more activity than one would expect from a (largely) 3s Rydberg excited state.

We also present multiple ZEKE spectra over a rather congested feature at ~800 cm^{-1} above the S_1 origin; this region is notably complicated when compared to the rest of the spectrum, whilst this plethora of activity remains relatively localised. Woo and Kim[110], who have conducted a photodynamical study of NMP, note that this region required multi-exponential fits to describe the lifetime of this feature, requiring three time constants. In the present work, we suggest that this region is actually numerous features arising from multiple interacting ZOSs and conclude that Woo and Kim would be exciting multiple eigenstates coherently within their laser linewidth. This feature is the result of the serendipitous location of two ZOB states that, owing to them being fundamental vibrations of different symmetries, do not themselves interact, but each couples strongly with numerous ZOD states nearby. This region would, initially, be expected to be the perfect candidate for a 2D-LIF spectrum to unpick the nuances of the coupling in this region; however, when individual dispersed fluorescence spectra were recorded, we could only achieve a very weak spectrum, with few noticeable features, and attribute this to a combination of the dramatic reduction in the lifetime of the excited state (LIF is a ‘slower’ process than REMPI, in which the prepared excited state is immediately ionised; see Figure 1, below, for a comparison of the REMPI and LIF spectra) and the presence of multiple

ZOSs involved in the interaction. Therefore, while a 2D-LIF spectrum of this region would be highly desirable, it was not possible to obtain anything of a reasonable quality.

Furthermore, a (2+2)-REMPI spectrum is presented as, in a two-photon absorption regime, the $\tilde{A}^1A_2 \leftarrow \tilde{X}^1A_1$ electronic transition is allowed and the structure observed is now dependent on the FCFs, in direct contrast to the one-photon vibronically allowed structure.

We then discuss the results of previous photodynamics studies, including that of Woo and Kim, considering quantum chemical calculations and the experimental results presented herein, noting the complementarity of time- and frequency-resolved experiments. We also discuss photophysical routes (such as internal conversion and intersystem crossing) in which electronically excited NMP may lose its absorbed energy.

Contributions: REMPI and ZEKE spectra were recorded by myself with some input from DJK. Master's students under my supervision (LGW and AR) are also thanked for their assistance in collecting a few of these spectra. The LIF, DF and 2D-LIF spectra were recorded by myself and DJK. Quantum chemical calculations were conducted by myself, with input from TGW mostly for the TD-DFT calculations on various excited states of NMP. The (2 + 2) REMPI spectrum was recorded solely by myself. The analysis was a collaboration between myself, DJK and TGW owing to the intricacies of the vibrational and torsional coupling and complications arising from the 'ZEKE shadows', see Section 12.1 and 5.9; although the ZEKE spectra *via* the b_2 and a_2 vibrations were rather straightforward to assign. All figures were created by myself, with input from TGW. I have also read and commented on multiple iterations of the manuscript and discussed and implemented the reviewers' comments to the final version of the paper.

Pre-scriptum: Shortly after publication when recording spectra with a different dye laser configuration, it was noticed that certain anomalies in our spectra were a result of resonance and Rayleigh anomalies of a dye laser grating, owing to an oversight relating to the effective tuning region of the ionisation dye laser grating used in the ZEKE and PIE experiments. We discuss our results of this paper in light of the identification of these anomalies, as well as publishing ZEKE spectra in absence of these anomalies for three b_1 vibrations and one b_2 vibration. This is detailed in the comment in Section 12.1, which immediately follows this section, see also Section 5.9. It is emphasised that *this is not an erratum* as the discussion and assignments presented in the original paper are unaffected by these findings, it is simply the appearance of the PIE and ZEKE spectra, to higher scanning wavenumber, that change, on which we comment in Section 12.1.

The Journal of Chemical Physics ARTICLE scitation.org/journal/jcp

Electronic, vibrational, and torsional couplings in *N*-methylpyrrole: Ground, first excited, and cation states

Cite as: J. Chem. Phys. 154, 224305 (2021); doi: 10.1063/5.0050654
Submitted: 17 March 2021 • Accepted: 12 May 2021 •
Published Online: 10 June 2021

Alexander R. Davies, David J. Kemp, and Timothy G. Wright[a)]

AFFILIATIONS

School of Chemistry, University of Nottingham, University Park, Nottingham NG7 2RD, United Kingdom

[a)]**Author to whom correspondence should be addressed:** Tim.Wright@nottingham.ac.uk

ABSTRACT

The electronic spectrum associated with the $S_1 \leftarrow S_0$ ($\tilde{A}^1A_2 \leftarrow \tilde{X}^1A_1$) one-photon transition of jet-cooled *N*-methylpyrrole is investigated using laser-induced fluorescence (LIF) and (1 + 1) resonance-enhanced multiphoton ionization (REMPI) spectroscopy; in addition, the (2 + 2) REMPI spectrum is considered. Assignment of the observed bands is achieved using a combination of dispersed fluorescence (DF), two-dimensional LIF (2D-LIF), zero-electron-kinetic energy (ZEKE) spectroscopy, and quantum chemical calculations. The spectroscopic studies project the levels of the S_1 state onto those of either the S_0 state, in DF and 2D-LIF spectroscopy, or the ground state cation (D_0^+) state, in ZEKE spectroscopy. The assignments of the spectra provide information on the vibrational, vibration-torsion (vibtor), and torsional levels in those states and those of the S_1 levels. The spectra are indicative of vibronic (including torsional) interactions between the S_1 state and other excited electronic states, deduced both in terms of the vibrational activity observed and shifts from expected vibrational wavenumbers in the S_1 state, attributed to the resulting altered shape of the S_1 surface. Many of the ZEKE spectra are consistent with the largely Rydberg nature of the S_1 state near the Franck–Condon region; however, there is also some activity that is less straightforward to explain. Comments are made regarding the photodynamics of the S_1 state.

I. INTRODUCTION

Pyrroles, including *N*-methylpyrroles, are key building blocks of many biomolecules (e.g., tryptophan, haem B, melatonin, and phycobiliproteins), a range of medicines (including photomedicines),[1,2] metalloporphyrin-based metal–organic frameworks (MOFs),[3] and molecular wires.[4] *N*-methylpyrrole (NMP) has been the subject of a number of photodissociation studies,[5–11] which have compared and contrasted its behavior with that of pyrrole.[12] A detailed understanding of the photophysics and photodynamics of molecules relies on establishing the energy-level structure; as such, there have been a number of spectroscopic studies of NMP.

The absorption spectrum of gaseous NMP molecules at ambient temperature has been reported by Milazzo,[13] McDiarmid and Xing,[14] and Cooper *et al.*[15] Spectra of supersonic-jet-cooled molecules have been presented by McDiarmid and Xing,[14] Philis,[16,17] and Biswas *et al.*;[18] additionally, suggested assignments of the S_1 vibrational and torsional levels were given by Woo and Kim.[11] A theoretical study of the torsional levels in NMP was published by Kanamaru,[19] although we have questioned some of the conclusions of that work.[20]

The low-lying electronic states of pyrrole and NMP are interesting, with occupied orbitals that are mixtures of valence and Rydberg character; for pyrrole and other molecules, the ramifications of such Rydberg-valence character on photodynamics have been discussed by Paterson and Townsend.[21]

Initially, treating the methyl group as a point mass, the point group symmetry of NMP is C_{2v}. Here, we locate the pyrrolyl ring in the *yz*-plane, with the $N–CH_3$ bond lying along the *z*-axis. The ground electronic state configuration may then be written as $\ldots a_1^2 b_1^2 a_2^2$, where the a_1 symmetry orbital is mainly σ bonding ($N–CH_3$) and the two outermost occupied orbitals are *π* bonding. At the S_0 optimized geometry, the lowest-lying unoccupied orbitals are largely Rydberg-like and are accessed following vertical excitation from the two outermost occupied orbitals into these. The symmetry of the lowest Rydberg states are 3s (a_1), 3p$_x$ (b_1), 3p$_y$ (b_2), and 3p$_z$ (a_1). We shall come back to these later, but here we note that the lowest-energy vertical excitation is the 3s ← a_2 excitation, yielding the S_1 $^1A_2$ first excited state. In addition, the highest occupied orbital in the S_1 state evolves from 3s character in the Franck–Condon region to σ* character at extended N–CH_3 bond lengths.[9] Accessing this state is electronically forbidden in a one-photon transition,[22] although it has been seen in two-photon transitions in some of the above-cited work[11,14–16] and herein; as such, the activity seen in the one-photon spectrum arises from vibronic interactions. We shall consider both the one- and two-photon $\tilde{A} \leftarrow \tilde{X}$ spectra of NMP in the present work.

The main focus here will be the vibrational and vibration-torsional (vibtor) levels in the S_0, S_1, and D_0^+ electronic states of NMP, building on our earlier two-dimensional LIF (2D-LIF) and zero-electron-kinetic energy (ZEKE) study that concentrated on the torsional levels[20] and where we reported the adiabatic ionization energy (AIE) as 64 250 ± 5 cm^{-1}. Here, we extend the earlier spectroscopic work to provide more definitive assignments of the S_1 levels, via both fluorescence and ZEKE spectroscopies. The latter allows vibrational wavenumbers for ground electronic state NMP$^+$ to be established for the first time. In addition, we obtain gas-phase S_0 vibrational wavenumbers, a number for the first time, from the dispersed fluorescence (DF) and 2D-LIF spectra; these values are largely similar to liquid-/solution-phase IR and Raman values.[23–25] By comparing the results of quantum chemical calculations for the S_1 and D_0^+ states with experimental vibrational wavenumbers, it is concluded that the shape of the S_1 potential energy surface is modified by the vibronic interactions, particularly along out-of-plane coordinates.

II. EXPERIMENTAL

The REMPI/ZEKE[26] and 2D-LIF[27] apparatuses are the same as those employed earlier and in the recent study addressing the torsional levels in NMP and NMP$^+$.[20] In all of the present experiments, a free-jet expansion of the vapor above room-temperature NMP liquid (Sigma-Aldrich, 99% purity) seeded in 2 bars Ar was employed.

For the fluorescence experiments, the free-jet expansion was intersected at $X/D \sim 20$ by the frequency-doubled output of a single dye laser (Sirah CobraStretch), operating with Coumarin 480 and pumped with the third harmonic of a Surelite III Nd:YAG laser. For the LIF spectra, the fluorescence was focused onto a photomultiplier tube (Hamamatsu H10721-01). For the 2D-LIF spectra, the fluorescence was collected, collimated, and focused onto the entrance slits of a 1.5 m Czerny–Turner spectrometer (Sciencetech 9150) operating in single-pass mode, dispersed by a 3600 groove/mm grating, allowing ~380 cm^{-1} windows of the dispersed fluorescence to be collected by a CCD camera (Andor iStar DH334T). At a fixed grating angle of the spectrometer, the excitation laser was scanned, and at each excitation wavenumber, the camera image was accumulated for 2000 laser shots. This allowed a plot to be produced of fluorescence intensity vs both the excitation laser wavenumber and the wavenumber of the emitted and dispersed fluorescence, termed a 2D-LIF spectrum.[28,29]

For the ZEKE spectra of NMP, the focused outputs of two dye lasers (Sirah CobraStretch) were overlapped spatially and temporally and passed through a vacuum chamber coaxially and counterpropagating, where they intersected the free-jet expansion. The excitation laser operated with Coumarin 480 and was pumped with the third harmonic (355 nm) of a Surelite III Nd:YAG laser. The fundamental of the excitation laser was used to record the (2 + 2) REMPI spectrum, while for the (1 + 1) REMPI and the ZEKE spectra, that output was frequency doubled. In the ZEKE experiments, the ionization laser operated with Coumarin 440, pumped with the third harmonic (355 nm) of a Surelite I Nd:YAG laser, and the output was undoubled. The jet expansion passed between two biased electrical grids located in the extraction region of a time-of-flight mass spectrometer, which was employed in the REMPI experiments. These grids were also used in the ZEKE experiments by application of pulsed voltages, giving typical fields of ~10 V cm^{-1}, after a delay of ~2 μs; this delay was minimized while avoiding the introduction of excess noise from the prompt electron signal. The resulting ZEKE bands had widths of ~5–7 cm^{-1}. Electron and ion signals were recorded on separate sets of microchannel plates.

We also report photoionization efficiency (PIE) curves for some selected levels, where we fix the excitation laser on a particular S_1 level and then scan the ionization laser across the ionization threshold, recording the NMP$^+$ ion yield. The PIE curves were recorded with the same setup used for the REMPI experiments.

III. RESULTS AND DISCUSSION

A. Nomenclature

1. Electronic states

Generally, we shall refer to electronic and vibrational symmetries using C_{2v} point group symmetry labels. When we consider torsional and vibration-torsion (vibtor) levels, we shall employ G_{12} molecular symmetry group (MSG) labels.[30] In Table I, we give the correspondence between these two sets of labels. Both the symmetry labels employed will be clear from the context since the G_{12} labels have prime (′) or double prime (″) embellishments, while the C_{2v} labels do not; occasionally, we give both the C_{2v} and G_{12} symmetry labels to aid the reader.

TABLE I. Correspondence of the C_{2v} point group symmetry classes with those of the G_{12} molecular symmetry group. Also indicated are the symmetries of the P_i vibrations and the pure torsional levels.[a]

C_{2v}	G_{12}	P_i[b]	m
a_1	a_1'	P_{1-9}	0, 6(+)
a_2	a_2'	P_{10-12}	6(−)
b_1	a_2''	P_{13-16}	3(−)
b_2	a_1''	P_{17-24}	3(+)
	e'		2, 4
	e''		1, 5

[a] Symmetries of vibtor levels can be obtained by combining the vibrational symmetry (in G_{12}) with those of the pure torsional level using a D_{3h} point group direct product table.

[b] The P_i vibrational labels are described in Ref. 33, where mode diagrams may also be found.

The ground electronic state, S_0, of NMP is $\tilde{X}^1A_1$ and, as given above, has an outermost electronic configuration $\ldots a_1{}^2 b_1{}^2 a_2{}^2$. The lowest energy unoccupied orbitals in the Franck–Condon (FC) region, which are of interest to the present work, are largely Rydberg in character, corresponding to the 3s or $3p_{x,y,z}$ orbitals. The first electronically excited state, S_1, is the $\tilde{A}^1A_2$ state and arises from a 3s ← a_2 excitation. This state is of great interest with regard to the photodynamics of biomolecules, as for the parent pyrrole[12] the HOMO evolves from being Rydberg in character in the FC region to σ^* character for longer N–H bond lengths, allowing for rapid photodissociation when this region of the potential energy surface is accessed; similar behavior occurs for NMP,[9] with regard to the N–CH_3 bond length, and related molecules. This behavior is now accepted as an important mechanism for the photodissociation of biomolecules that contain heterocycles and was pioneered in theoretical work by Domcke and co-workers.[31,32] With this Rydberg character in mind, we expect the torsional and vibrational energy levels in the S_1 state close to its potential minimum to resemble those of the ground state cation. The latter arises from a $a_2{}^{-1}$ ionization, forming the ${}^+\tilde{X}^2A_2$ state, (the $D_0{}^+$ state) with the $b_1{}^{-1}$ ionization forming the ${}^+\tilde{A}^2B_1$ state (the $D_1{}^+$ state). (The $D_1{}^+$ state may also be obtained from a $a_2 \leftarrow b_1$ excitation from the $D_0{}^+$ state.) With regard to the neutral electronic states that lie above the S_1 state, examination of the quantum chemical results of some of the photodynamics studies cited above indicates that their calculated ordering is dependent on the level of theory/basis set employed and/or whether vertical or adiabatic excitation energies are calculated. For these reasons, we refrain from labeling these states as $S_{n(n>1)}$ and instead label them using the following notation, in which the S_1 state is denoted as (a_2, 3s):

$$\begin{aligned}
&\ldots b_1{}^2 a_2{}^1 3p_x && {}^1B_2\left(a_2,\ 3p_x\right),\\
&\ldots b_1{}^2 a_2{}^1 3p_y && {}^1B_1\left(a_2,\ 3p_y\right),\\
&\ldots b_1{}^2 a_2{}^1 3p_z && {}^1A_2\left(a_2,\ 3p_z\right),\\
&\ldots b_1{}^1 a_2{}^2 3s && {}^1B_1\left(b_1,\ 3s\right),\\
&\ldots b_1{}^2 a_2{}^2 3p_x && {}^1A_1\left(b_1,\ 3p_x\right),\\
&\ldots b_1{}^1 a_2{}^2 3p_y && {}^1A_2\left(b_1,\ 3p_y\right),\\
&\ldots b_1{}^1 a_2{}^2 3p_z && {}^1B_1\left(b_1,\ 3p_z\right).
\end{aligned}$$

In the present work, the (b_1, 3s) and the three (a_2, $3p_{x,y,z}$) states are calculated to be close in energy, with the three (b_1, $3p_{x,y,z}$) states being higher in energy; furthermore, the states within each of the (a_2, $3p_{x,y,z}$) and (b_1, $3p_{x,y,z}$) sets of Rydberg states are very close in energy, with the latter states being found to be overlapped by (a_2, 3d) states (see Sec. IV B).

2. Vibrations

The vibrations of NMP are numbered using a scheme that has been developed by studying how the vibrations of the parent pyrrole molecule evolve as a function of the artificially varied mass of the nitrogen-bonded H atom.[33] This method examines the effects of solely changing the mass of a substituent, i.e., without any complications from steric or electronic perturbations. This is analogous to a scheme employed for monosubstituted benzenes[34] and extended to the disubstituted benzenes.[35–37] For NMP, the P_i labels employed are based on the motions of the vibrations in *N*-fluoropyrrole—further details and vibrational mode diagrams can be found in Ref. 33. We label the methyl-localized vibrations Me_i (i = 1–9), in descending wavenumber order, as in Ref. 33. The calculated wavenumbers for the vibrations are presented in Table II. The assignments of the S_0 vibrational wavenumbers obtained from IR and Raman studies from Refs. 23 and 24 were considered in Ref. 33. We have since become aware of another study by Beć *et al.*,[25] where the IR spectra of pure liquid NMP have been reported; the obtained values are quite similar to those reported in Refs. 23 and 24, and in Table II, we retain the IR/Raman values and assignments for the S_0 vibrations presented in Ref. 33.

3. Torsions and vibtor

If the methyl group is now explicitly considered, then NMP belongs to the G_{12} MSG,[30] and the torsional levels are described by the m quantum number, which is signed. Levels with $|m| \neq 3n$ (n = 1, 2, . . .,) are degenerate, with the $m = 0$ level being nondegenerate. As is well known, nuclear spin and symmetry considerations mean that it is not possible to cool the $m = 1$ (strictly $|m| = 1$) torsional population into the $m = 0$ level, and hence, under the jet-cooled conditions employed herein, both levels have roughly equal populations. As a consequence, transitions can occur from either the $m = 0$ or $m = 1$ level of the S_0 zero-point vibrational level, with transitions to $m = 3n$ levels originating from the S_0 $m = 0$ level and those for $m \neq 3n$ originating from S_0 $m = 1$. We will generally refer to a level using the notation of a transition, with subscripts referring to the S_0 state and superscripts to the S_1 state, and for cationic levels, we use superscripts together with a pre-superscripted "+"; furthermore, we shall generally omit the initial level when designating a transition, as it will be clear from the excited intermediate level or the jet-cooled conditions employed. (As an example, a transition from S_0 $m = 0$ to S_1 $m = 0$ will be simply represented as m^0.) Except where explicitly noted, vibrational transitions implicitly include transitions arising from both of the associated $m = 0$ and $m = 1$ levels, which will be almost perfectly overlapped in our spectra, as effective torsional rotational constants are very similar in the S_0, S_1, and $D_0{}^+$ electronic states.[20]

Torsional levels with $|m| = 3n$ are non-degenerate, forming linear combinations for $n \neq 0$. The splitting of the $|m| = 3n$ ($n \neq 0$) levels occurs as a result of the hindered rotation and, in a G_{12} symmetry molecule, is characterized by the parameter V_6. For example, the $m = +3$ and -3 levels form combinations that are denoted as 3(+) and 3(−), with their relative energy ordering controlled by the sign of V_6, which is determined by the minimum energy geometry: for minimum energy geometries where the methyl group is eclipsed, with a C–H bond of the methyl group in the same plane as the pyrrolyl ring, V_6 is positive; while for a minimum staggered geometry where one of the methyl C–H bonds is perpendicular to the pyrrolyl ring, V_6 is negative. NMP has a staggered orientation in its ground electronic state but an eclipsed orientation in the S_1 state and the ground state cation.[20,33]

B. Overview of the REMPI spectra

At the top part of Fig. 1, we show the (1 + 1) REMPI spectrum of NMP over the first ~1110 cm^{-1}. Below this, inverted, is

TABLE II. Calculated and experimental vibrational wavenumbers (cm^{-1}) for NMP in its S_0, S_1, and $D_0{}^+$ states.

		S_0			S_1				$D_0{}^+$	
			Expt.		Calculated					
Sym.[a]	P_i[b]	Calculated[c]	IR/Raman[d]	DF[e]	Kanamaru[f]	Woo and Kim[g]	Present work[c]	Expt.[h]	Calculated[c]	Expt.[i]
a_1	1	3160	3130[j] (3126)				3151		3167	
	2	3141	3103[j] (3101)				3175		3144	
	3	1492	1504 (1509)				1534		1527	
	4	1375	1416 (1419)	1398 (1398)	1622	1510	1459	1468 (1473)	1456	
	5	1278	1286 (1288)	1281			1228		1218	
	6	1075	1088 (1091)	1092 (1083)	1162	1091	1062	1052 (1048)	1052	
	7	1045	1058 (1055)	(1058)			1104	1094	1107	
	8	956	966	933 (925)			971	968	968	
	9	652	662	669 (669)	606	635	613	635 (632)	609	629
a_2	10	863	858	857	931	931	928	907	942	937
	11	675	688	686	801	877	857	830	833	830
	12	610		611	463	520	506	468	495	498
b_1	13	814	815	815 (820)	878	891	875	824	868	861
	14	712	720	710 (718)	742	718	712	677	721	720
	15	603	601	601 (607)	376	491	482	370	490	504
	16	186	186	190 (190)	133	217	210	184	215	220
b_2	17	3152	3130[j] (3126)				3168		3155	
	18	3132	3103[j] (3101)				3157		3138	
	19	1505	1547		1484	1397	1372		1368	
	20	1350		(1388)	1236	1220	1187		1180	
	21	1262	1232		1388	1301	1278		1275	
	22	1073	1043		1114	1042	962	971	955	969
	23	864	868	874 (877)	730	687	659	644	646	636
	24	347	354	359 (354)			340	347	340	351
Methyl	Me_1	3026	2942[j]				2944		3051	
	Me_2	2996	2942[j]				2934		3071	
	Me_3	2935	2819[j]				2858		2976	
	Me_4	1467	1464[j]		1569	1419	1424		1463	
	Me_5	1447	1382[j]		1609	1449	1405		1442	
	Me_6[k]	1409	1382[j]		1489	1405	1386	1390 (1394)	1408	
	Me_7[l]	1111	1120[j]		1219	1138	1115	1100	1117	1113
	Me_8	1029	1127[j]	(1100)	935	988	1013		993	
	Me_9[m]	69					51		28	

[a] C_{2v} symmetry labels, with the pyrrolyl ring lying in the *yz*-plane. The correspondence to G_{12} symmetry labels may be found in Table I.

[b] The P_i vibrational labels are described in Ref. 33, where mode diagrams may also be found. The correspondence between the current labels and those used in Ref. 18 is provided in the supplementary material.

[c] The quantum chemical calculations undertaken for the different states were B3LYP/aug-cc-pVTZ (S_0), TD-B3LYP/aug-cc-pVTZ (S_1), and UB3LYP/aug-cc-pVTZ ($D_0{}^+$). All harmonic vibrational wavenumbers were scaled by 0.97. The calculated values for the S_0 and $D_0{}^+$ states were discussed in Ref. 33.

[d] Taken from Ref. 23 and, in parentheses, Ref. 24; an occasional value comes from the force-field calculations employed in Ref. 23 (see Ref. 33).

[e] From dispersed fluorescence experiments of the present work and, in parentheses, Ref. 18.

[f] CIS/6-31G** values from Ref. 19.

[g] TD-B3LYP/aug-cc-pVDZ (unscaled) values from Ref. 11 (in the supplementary material thereof).

[h] From REMPI experiments in the present work and, in parentheses, of Ref. 11. Some values, such as those for P_{11} and P_{13}, could be affected by interactions between levels.

[i] From ZEKE experiments of the present work. Some values, such as those for ${}^+P_9$, ${}^+P_{11}$, and ${}^+P_{13}$, could be affected by interactions between levels.

[j] A unique assignment was not provided for this wavenumber.

[k] This is the methyl umbrella mode.[33]

[l] This is the in-plane methyl rock.[33]

[m] This is the methyl torsion.[33]

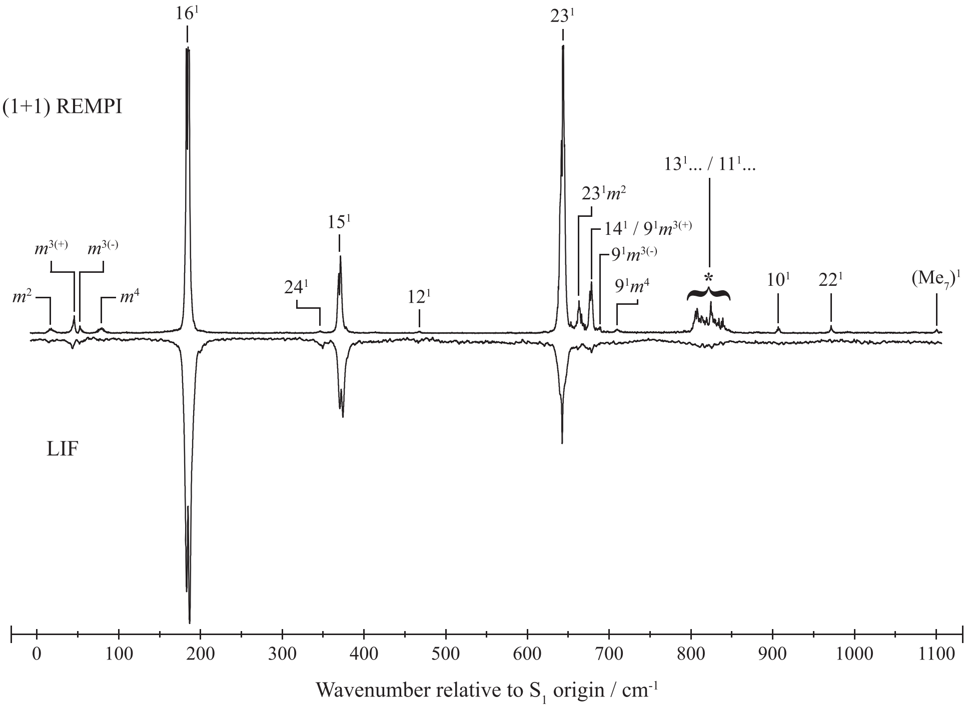

FIG. 1. Upper trace: (1 + 1) REMPI spectrum of the one-photon forbidden $S_1 \leftarrow S_0$ transition of NMP. The feature marked with an asterisk comprises multiple transitions with the associated indicated levels being the anticipated zero-order bright (ZOB) states and is shown in more detail in Fig. 12. Lower trace: reflected LIF spectrum of NMP. The LIF intensity dies off to higher wavenumbers, consistent with shorter lifetimes for the associated S_1 levels.

the corresponding LIF spectrum, and as may be seen, intensity is lost to the increasing wavenumber, particularly above ~600 cm^{-1}, consistent with the lifetimes of the S_1 levels decreasing as the internal energy increases.[9,11] It is the rapid absorption of a second photon in the (1 + 1) REMPI experiment that allows the higher-wavenumber region to be seen more clearly than in the LIF experiment. The (1 + 1) REMPI spectrum looks very similar to the corresponding spectra reported in earlier studies, notably that of Ref. 11, while the LIF spectrum looks similar to the limited range shown in Ref. 18. Transitions neither to the origin nor to a_1 vibrational levels are seen in either spectrum, since these are one-photon forbidden, although we do see some associated torsions.

In Fig. 2, we show the (2 + 2) REMPI spectrum of NMP in the range 0–1500 cm^{-1}, where the now-allowed origin transition[22] is seen and is located at 41 193 cm^{-1} (Refs. 11 and 18). This spectrum has a narrower bandwidth than the spectra reported in earlier studies[11,18] and the region shown in our previous work in Ref. 20, and so a more detailed structure is discernible, allowing other bands to be identified. It is clear that the only totally symmetric fundamentals are observed in the (2 + 2) REMPI spectrum, while only those for non-totally symmetric levels were observed in the (1 + 1) REMPI and LIF spectra (Fig. 1). As well as the fundamentals, some other bands are also seen (see Fig. 2), which are not straightforward to assign. The only reasonable assignment for the band at 542 cm^{-1} is $15^1 16^1$ and suggests significant anharmonicity, since by summing the fundamentals found in the (1 + 1) REMPI spectrum, this is expected at 554 cm^{-1}. The weak band at 665 cm^{-1} is not assignable to any obvious combination band, with the vibtor transition $12^1 m^{6(-)}$ appearing to be the most likely, with it and the adjacent 24^2 band possibly gaining intensity via an interaction with 9^1. A weak band at 1127 cm^{-1} does not have an obvious assignment, and we tentatively opt for $10^1 m^{6(-)}$, with this possibly gaining intensity from 6^1. (Both $12^1 m^{6(-)}$ and $10^1 m^{6(-)}$ correspond to totally symmetric $a_1{}'$ levels.)

C. Vibronic coupling

As pointed out above, the $S_1 \leftarrow S_0$ ($\tilde{A}^1A_2 \leftarrow \tilde{X}^1A_1$) transition is one-photon forbidden. As such, the (1 + 1) REMPI and LIF spectra corresponding to this are dominated by vibronic transitions that are induced by vibrations of particular symmetries. In Fig. 3, a schematic energy-level diagram is shown, which indicates that there are a number of singlet states close to the $\tilde{A}^1A_2$ state: one of B_2 symmetry, two of B_1 symmetry, and, to higher energy, one of A_1 symmetry, as well as other states.

The theory of vibronic coupling is well established,[30,38] with the transition dipole moment (TDM), $\boldsymbol{M}_{\mathbf{evt}}$, being given by the following:

$$\boldsymbol{M}_{\mathbf{evt}} = \int \psi'^{*}_{\mathrm{evt}} \boldsymbol{\mu} \psi''_{\mathrm{evt}} d\tau_{\mathrm{evt}}, \qquad (1)$$

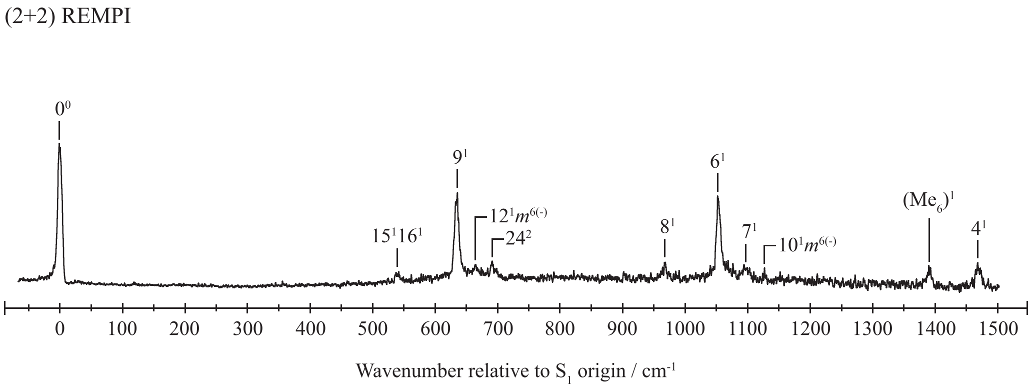

FIG. 2. (2 + 2) REMPI spectrum of the two-photon allowed $S_1 \leftarrow S_0$ transition of NMP.

where ψ_{evt} are vibronic wavefunctions that also describe the torsional motion and $\boldsymbol{\mu}$ is the dipole moment operator. If the wavefunctions are assumed to be completely separable, the TDM can be written as

$$\boldsymbol{M}_{\mathbf{evt}} = \int \left(\psi_{\mathrm{e}}'\psi_{\mathrm{v}}'\psi_{\mathrm{t}}'\right)^{*} \boldsymbol{\mu}\left(\psi_{\mathrm{e}}''\psi_{\mathrm{v}}''\psi_{\mathrm{t}}''\right) d\tau_{\mathrm{evt}}, \tag{2}$$

where the wavefunctions are labeled in an obvious fashion, and the integration is over all electronic, vibrational, and torsional coordinates.

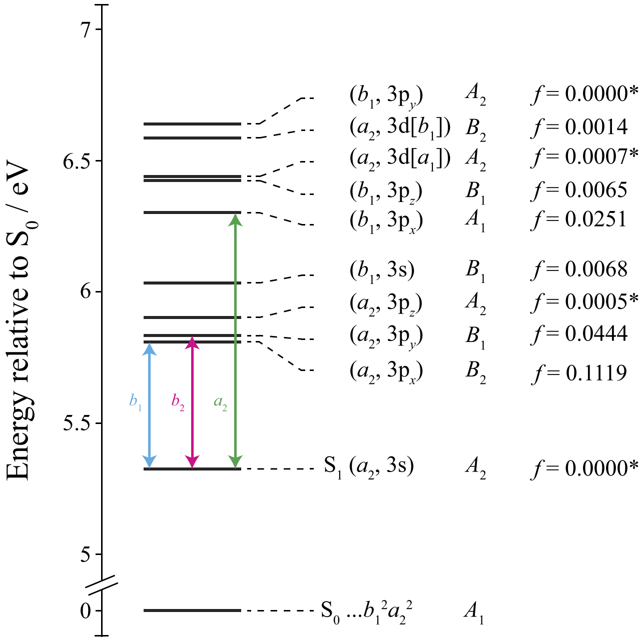

FIG. 3. Schematic, to scale, showing the calculated (TD-CAM-B3LYP/aug-cc-pVTZ) vertical excitation energies of the various singlet excited states of NMP (see also Fig. 15 and Sec. IV B). The electronic configurations are indicated in a concise format, as discussed in the text, with the electronic state symmetry indicated. Also included are the calculated oscillator strengths; those marked with an asterisk would be expected to be zero if the point symmetry were truly C_{2v}; however, for the methyl group, the optimized geometry has C_s symmetry, and only the S_1 state is calculated to have a zero-oscillator strength here. The colored arrows indicate the main vibronic coupling routes expected, together with the symmetries of the vibrations that can induce this coupling. The b_1 symmetry vibrations ($P_{13–16}$) provide the dominant coupling routes, but with activity also seen involving all three a_2 symmetry vibrations ($P_{10–12}$) and the lower-wavenumber b_2 symmetry vibrations (P_{23} and P_{24}) (see Secs. III G 4 and IV A 3 in the text).

If it is assumed that the electronic TDM, $\boldsymbol{M}_{\mathbf{e}} = \int \psi_{\mathrm{e}}'\boldsymbol{\mu}\psi_{\mathrm{e}}'' d\tau_{\mathrm{e}}$, may be expanded about the equilibrium point for a vibrational or torsional coordinate, Q_i, then we can write

$$\boldsymbol{M}_{\mathbf{evt}} = \int \left(\psi_{\mathrm{v}}'\psi_{\mathrm{t}}'\right)^{*} \boldsymbol{M}_{\mathbf{e}}\left(\psi_{\mathrm{v}}''\psi_{\mathrm{t}}''\right) d\tau_{\mathrm{vt}}, \tag{3}$$

with

$$\boldsymbol{M}_{\mathbf{e}} = \left(\boldsymbol{M}_{\mathbf{e}}\right)_{\mathrm{eq}} + \sum_i \left(\frac{\partial \boldsymbol{M}_{\mathbf{e}}}{\partial Q_i}\right)_{\mathrm{eq}} Q_i + \frac{1}{2!}\sum_{i,j}\left(\frac{\partial^2 \boldsymbol{M}_{\mathbf{e}}}{\partial Q_i \partial Q_j}\right)_{\mathrm{eq}} Q_i Q_j + \cdots . \tag{4}$$

Combining these,

$$\begin{aligned}\boldsymbol{M}_{\mathbf{evt}} = {} & \left(\boldsymbol{M}_{\mathbf{e}}\right)_{\mathrm{eq}} \int \left(\psi_{\mathrm{v}}'\psi_{\mathrm{t}}'\right)^{*}\left(\psi_{\mathrm{v}}''\psi_{\mathrm{t}}''\right) d\tau_{\mathrm{vt}} \\ & + \sum_i \left(\frac{\partial \boldsymbol{M}_{\mathbf{e}}}{\partial Q_i}\right)_{\mathrm{eq}} \int \left(\psi_{\mathrm{v}}'\psi_{\mathrm{t}}'\right)^{*} Q_i \left(\psi_{\mathrm{v}}''\psi_{\mathrm{t}}''\right) d\tau_{\mathrm{vt}} \\ & + \frac{1}{2!}\sum_{i,j}\left(\frac{\partial^2 \boldsymbol{M}_{\mathbf{e}}}{\partial Q_i \partial Q_j}\right)_{\mathrm{eq}} \int \left(\psi_{\mathrm{v}}'\psi_{\mathrm{t}}'\right)^{*} Q_i Q_j \left(\psi_{\mathrm{v}}''\psi_{\mathrm{t}}''\right) d\tau_{\mathrm{vt}} + \cdots .\end{aligned} \tag{5}$$

For electronically allowed transitions, the first term in Eq. (5) is non-zero and is usually dominant; the observed structure depends on the overlap integral, whose square is the generalized Franck–Condon factor (FCF). Since we usually start in the (totally symmetric) zero-point vibrational level in jet-cooled experiments, then we would only expect to see transitions involving totally symmetric vibrational levels in the spectrum from this term. (In Ref. 20, we explicitly discussed the "pure" torsional levels.) The second term can also be non-zero for electronically allowed transitions, if there are nearby electronic states to steal intensity. This could affect the observed intensities of bands arising from transitions involving totally symmetric vibrational levels, but it also means that we may see bands arising from transitions involving non-totally symmetric vibrational levels, as often seen in the spectra of substituted benzenes, for example.

For electronically forbidden transitions, such as is the case here for NMP, the first term is zero. The second term is then expected to be dominant and dictates which vibrations can induce activity and how strong the resulting transitions will be. The situation here with NMP is similar to that of benzene,[39–41] where the transition to the first electronic state is electronically forbidden for a one-photon transition. As such, the activity observed in the excitation spectrum arises from vibrations that induce activity via the variation of the electronic dipole moment during those vibrations. An alternative way of viewing this is that the electronically forbidden transition steals intensity from an allowed transition via the inducing vibration. Thus, it is a requirement that there are allowed transitions close in energy to the electronically forbidden transition and of the correct symmetry for interaction (intensity stealing) to occur via non-totally symmetric vibrations.

Referring to Fig. 3, it can be seen that there is a $^1B_2$ state, (a_2, 3p$_x$), closest in energy to the S_1 state, which has the largest oscillator strength; this state can couple to the S_1 state via b_1 symmetry vibrations, as shown. Slightly higher in energy are two $^1B_1$ states, (a_2, 3p$_y$) and (b_1, 3s) that can couple with the S_1 state via b_2 symmetry vibrations; in Fig. 3, we have suggested that the activity of vibrations with b_1 symmetry mainly arises via coupling with the (a_2, 3p$_y$) state, since it is closer in energy and has the higher oscillator strength. Still higher up is an $^1A_1$ state, (b_1, 3p$_x$), and this can couple to the S_1 state via a_2 symmetry vibrations; this is expected to be weaker since the state is energetically further removed. Although there is also a $^1A_2$ state (a_2, 3p$_z$), this is also a forbidden transition, of course, and so no intensity stealing can occur from it. Except for electronic states of A_2 symmetry, the S_1 state can steal intensity from transitions to all of these states, induced by non-totally symmetric vibrations.

Similar arguments hold for torsional or vibtor levels, where the G_{12} symmetries would now need to be considered—see Table I. Hence, for example, we can expect to see a transition to the $m^{3(-)}$ level from the $m = 0$ level in the S_0 state in the one-photon absorption spectrum, via induced intensity stealing from the transition to the lowest-lying $^1A_1''$ ($^1B_2$) state, since the $m = 3(-)$ level has a_2'' symmetry in the G_{12} MSG. In a similar fashion, the $m^{3(+)}$ transition can steal intensity from a transition to a $^1A_2''$ ($^1B_1$) state. The arguments are the same for $m = 1$ levels, and hence, we may expect to see significant transitions to $m = 2$ and 4 levels, which is indeed the case (see Ref. 20 for further discussion). We do not see activity for m^1 nor m^5 transitions, both of which have e'' symmetry, suggesting that intensity stealing from the $^1A_1'$ excited level, via a_2 (a_2') symmetry vibrations, is small.[20]

D. Expected activity in absorption

From Sec. III C and considering the first-order vibronic coupling terms for vibrations, for induced activity in the S_1 state, we require $\Gamma(\psi_{ev}') = \Gamma(\psi_e') \times \Gamma(\psi_v')$ to correspond to an excited electronic state whose transition is one-photon allowed from the S_0 state. Referring to Fig. 3, this means that S_1 vibrations of the b_1 symmetry (P_{13}–P_{16}) can induce intensity stealing from the (a_2, 3p$_x$) $^1B_2$ state, and these are expected to be the strongest, since this electronic transition has the highest calculated oscillator strength as well as being closest in energy to the S_1 state; vibrations of b_2 symmetry (P_{17}–P_{24}) can induce intensity stealing, mainly from the (a_2, 3p$_y$) $^1B_1$ state, and this is expected to be weaker, and vibrations of a_2 symmetry (P_{10}–P_{12}) can induce intensity stealing from the (b_1, 3p$_x$) $^1A_1$ state, which are expected to be the weakest. Similar comments apply to the torsional levels (see Sec. III B).

For the (2 + 2) REMPI spectrum, the situation is different, as now the $S_1 \leftarrow S_0$ transition is two-photon allowed.[22] This means that the dominant vibrational activity is expected to be that determined by the FCFs, generalized to cover both torsional and vibtor transitions and hence totally symmetric levels. Indeed, Fig. 2 (and the work of Ref. 11) demonstrates that this is borne out. It is interesting that no vibronic activity is seen, which is in contrast to the allowed one-photon spectra of substituted benzenes, where both totally symmetric and vibronically induced b_2 vibrational activity is commonplace. As transitions to the required excited electronic states are still allowed in the two-photon transition,[22] we conclude that such transitions must simply be too weak to see with the present sensitivity. Similar comments refer to the torsional levels, where allowed transitions would be expected to be to m^1, as well as $m^{6(+)}$ and m^5—the latter two are $\Delta m = 6$ transitions and so expected to be weak; neither are observed.

E. Expected activity in emission

Similar arguments apply to emission as for one-photon absorption, except now we are commencing at vibrational levels in the S_1 state that are non-totally symmetric. With the excitation laser, we can select levels of different symmetry in the S_1 state and observe the emission from these; in the free-jet expansion, little vibrational or torsional relaxation in the S_1 state will occur. We now expect the dominant emission activity to be that corresponding to the initially excited vibration but in combination with the inducing vibrations of b_1, b_2, and (weaker) a_2 symmetry, with the first of these dominating. As will be seen, again these expectations are largely borne out and are consistent with the activity seen in the corresponding spectra of benzene.[39–41]

We comment that Biswas *et al.*[18] reported DF spectra of NMP when exciting via a number of S_1 torsional levels and also 16^1, 15^1, and 24^1. (We have transcribed their numbering into that employed herein, with the correspondence included in Table SI of the supplementary material.) The presentation of the DF spectra in that work is somewhat difficult to follow, with the same numbered band corresponding to different terminating levels. We have discussed the torsional levels in Ref. 20, and we will see that for many of the vibrational assignments, we agree with those in Ref. 18 for the DF spectra obtained via the three lowest S_1 vibrational levels. In the present work, we shall see evidence for more widespread vibronic coupling, examine more levels by both DF and a selected number with 2D-LIF, and for the first time, report ZEKE spectra of almost all levels having <1110 cm^{-1} internal energy in the S_1 state, observed in the (1 + 1) REMPI spectrum. In so doing, we obtain reliable gas-phase values for a significant number of vibrational wavenumbers in the S_0 and S_1 states and will compare to previous assignments; for the D_0^+ state, we report vibrational wavenumbers for the first time.

We highlight that, although not emphasized in Ref. 20, we found the 2D-LIF spectrum recorded for the torsional levels of NMP to be dominated by 15_1m_x and 16_1m_x bands, at the positions where the m^x transition was excited; this is consistent with activity seen herein for the vibrations.

F. ZEKE spectra

Since it is known that the S_1 state is largely 3s Rydberg-like in the FC region, then we expect the ZEKE spectra to be dominated by $\Delta m = 0$, $\Delta v = 0$, or $\Delta(v, m) = 0$ bands, as appropriate, since the S_1 and D_0^+ geometries are expected to be very similar; this is in line with the results of quantum chemical calculations.[20] This was indeed the case for the ZEKE spectra via the torsional levels,[20] and as will be seen, this is also the case for many of the vibrations and vibtor levels in the present work. Additionally, it would also be expected that the wavenumbers for corresponding vibrations would be very similar for the S_1 and the D_0^+ states. Indeed, looking at the calculated wavenumbers in Table II, the values are very similar across all vibrations for these two electronic states. In contrast, there are some exceptions to this expectation for some of the experimental values, most notably for vibrations of b_1 symmetry but also those of a_2 symmetry, and this will be discussed in Secs. III G 4 and IV A 3.

G. Spectra and assignments

1. DF and 2D-LIF spectra via 16^1

In Fig. 4, we show the DF and 2D-LIF spectra obtained following excitation to the S_1 b_1 symmetry vibration, 16^1. In overall appearance, the DF spectrum is similar to that reported by Biswas *et al.*,[18] except that the present spectrum is of higher resolution. We can see that the two most intense bands are those corresponding to 16_2 and 15_116_1, confirming that P_{15} and P_{16} are the vibrations that induce the majority of the vibronic interaction, via the $(a_2, 3p_x)$ $^1B_2$ state; we also see combination bands involving the other b_1 symmetry vibrations 14_116_1 and 13_116_1, as well as the 15_2 band. In addition, we see activity induced by a b_2 vibration, 16_123_1, and two induced by a_2 vibrations, 11_116_1 and 10_116_1. (If 12_116_1 is present, it would be overlapped by 15_116_1.) There are various other bands, presumably associated with small structural changes, of the same overall vibrational symmetry as the induced bands, but there are multiple possibilities for some of the bands to higher wavenumbers, and so we refrain from giving all of those an explicit assignment. The given assignments allow the wavenumbers for a number of S_0 vibrations to be determined, as well as 16^1 in the S_1 state; these are collected together in Table II and concur with those obtained from other spectra discussed in the present work.

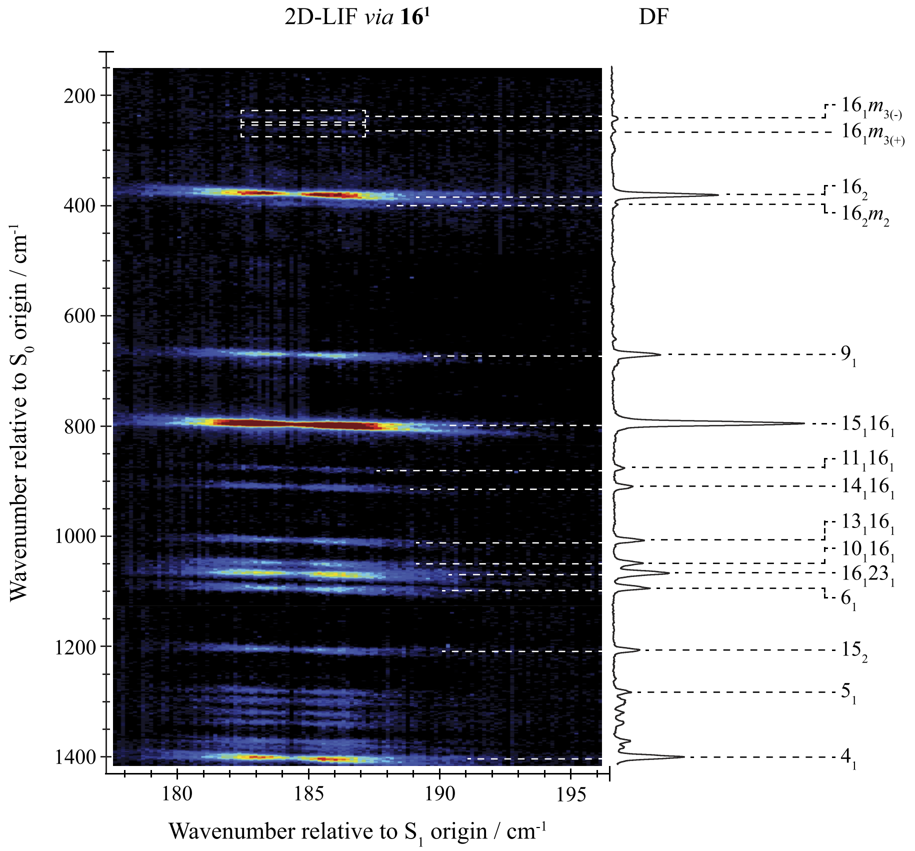

FIG. 4. DF and 2D-LIF spectrum via 16^1. Assignments are given for many of the bands, which are consistent with vibronic coupling, and are discussed further in the text.

We highlight that we see both the $16_1m_{3(-)}$ and $16_1m_{3(+)}$ bands, whose activity could be induced by the corresponding torsions, involving the $(a_2, 3p_x)\ ^1B_2\ (^1A_1'')$ and $(a_2, 3p_y)\ ^1B_1\ (^1A_2'')$ electronic states, respectively. This pair of bands was also seen when exciting the $m^{3(+)}$ and $m^{3(-)}$ levels.[20]

The simple appearance of the isolated 16^1 band in the REMPI and LIF spectra (Fig. 1) indicates that it is unlikely that 16^1 is interacting significantly with any other level in the S_1 state, and the 2D-LIF spectrum supports this, in that the main activity is localized, with a distinctive band shape, and no indications of any overlapping features are apparent.

We shall discuss the ZEKE spectrum from 16^1 in Sec. III G 4.

2. DF and 2D-LIF spectra via 15^1

The DF and 2D-LIF spectra recorded via the S_1 15^1 level, also a b_1 symmetry vibration, are shown in Fig. 5. The DF spectrum is similar to that reported by Biswas *et al.*,[18] and we agree with their assignments, but again the present spectrum is of higher resolution. In a similar way to the DF spectrum from $S_1 16^1$, we see strong activity induced by b_1 symmetry vibrations, with the 15_2 band being the most intense, but we also see combination bands associated with the other b_1 symmetry vibrations, $15_1 16_1$, $14_1 15_1$, and $13_1 15_1$, together with the 16_2 band. Additionally, we see the transition induced by a b_2 symmetry vibration, $15_1 23_1$, as well as $16_1 23_1$; possible bands induced by a_2 vibrations, $11_1 15_1$ and $10_1 15_1$, are very weak and are not marked; in addition, if the $12_1 15_1$ band is present, it would lie under 15_2. There are various other bands, but we refrain from giving explicit assignments when there is more than one reasonable possibility. We do not see the $15_1m_{3(-)}$ and $15_1m_{3(+)}$ vibtor bands, although these were seen when exciting via $m^{3(+)}$ and $m^{3(-)}$.[20] A weak band that is at the correct wavenumber to correspond to the a_1' symmetry $m_{6(+)}$ is tentatively assigned as such. Assignment of the

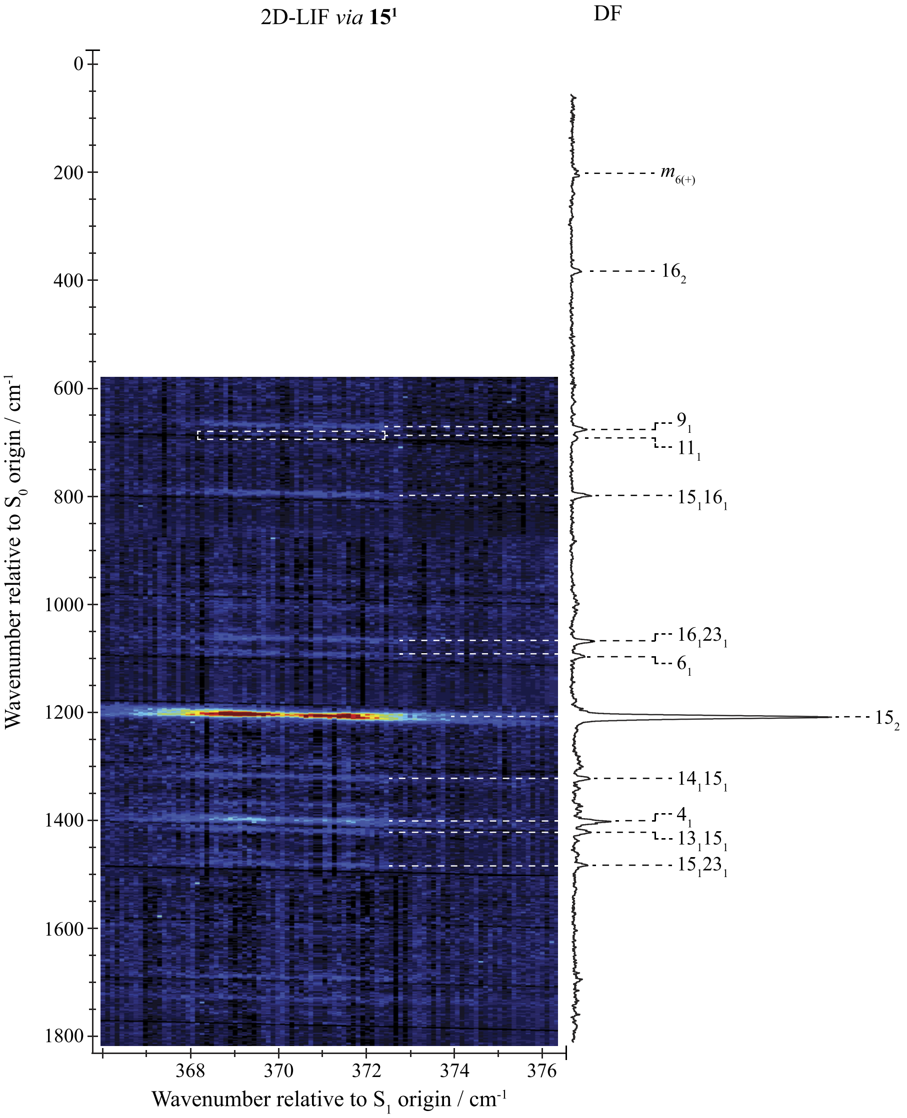

FIG. 5. DF and 2D-LIF spectrum via 15^1. Assignments are given for many of the bands, which are consistent with vibronic coupling, and are discussed further in the text.

spectra allows a number of vibrational wavenumbers for the S$_0$ state to be determined, as well as 15^1 in the S$_1$ state; these are collected together in Table II.

The REMPI and LIF spectra (Fig. 1) indicate that it is unlikely that, as with 16^1, the 15^1 level is interacting with any other level in the S$_1$ state, and the 2D-LIF spectrum again supports this, in that the main activity is localized, with a distinctive band shape, and no indications of any overlapping features are apparent.

We shall discuss the ZEKE spectrum from 15^1 in Sec. III G 4.

3. DF spectrum via 14^1

In Fig. 6, we show the DF spectrum recorded via 14^1. This is dominated by the 14$_1$15$_1$ band, with 14$_1$16$_1$, 14$_2$, and 13$_1$14$_1$ also being seen—all induced by b_1 symmetry vibrations; bands induced by a_2 symmetry vibrations are not observed here, although 12$_1$14$_1$ would be overlapped by the 14$_1$15$_1$ band. Furthermore, bands induced by a_2 and b_2 symmetry vibrations are also present. These assignments allow a number of vibrational wavenumbers for the S$_0$ state to be determined, as well as 14^1 in the S$_1$ state; these are collected together in Table II. This spectrum has not been reported previously.

We shall discuss the ZEKE spectrum from 14^1 in Secs. III G 4 and III G 6.

4. ZEKE and PIE spectra via 16^1, 15^1, and 14^1

In Fig. 7, we show the ZEKE spectra recorded via each of the S$_1$ vibrational levels 16^1, 15^1, and 14^1, all of which are of b_1 symmetry. In addition, for each intermediate, we superimpose the PIE curve for production of NMP$^+$, covering the main activity in each ZEKE spectrum.

The ZEKE spectrum recorded via 14^1 is largely as expected, with the strong $\Delta v = 0$, $^+14^1$, band dominating. There is a weak, symmetry forbidden $^+m^{0,1}$ band, but it is not possible to see other transitions to pure torsional levels. The feature with multiple contributions across the range 635–700 cm^{-1} (marked with an obelus) will be discussed further in Sec. III G 6.

Although there is no clear onset, we see that the PIE curve via 14^1 shows activity close to the AIE, consistent with the weak $^+m^{0,1}$ ZEKE band, and this continues up to a sharp rise at the position of the $\Delta v = 0$ band, $^+14^1$, as expected. Unexpected, however, is the sharp drop-off in the PIE intensity at ~800 cm^{-1}. Indeed, as can be seen in Fig. 7, the PIEs recorded via the 14^1, 15^1, and 16^1 levels all show such a drop-off, albeit at different wavenumbers. Not shown in Fig. 7 is that the PIE intensity picks up again in all cases to higher wavenumbers and appears to be associated with the absorption of more than one photon from the ionization laser. We are currently investigating this behavior, and the structure that appears in some regions of the PIE curves, and will report our findings in due course;[42] for the purposes of the present work, only the regions of the PIE curves before the drop-offs are pertinent.

In some ways, the ZEKE spectrum recorded via 16^1 is largely as expected, with the $\Delta v = 0$ band being by far the most intense—in line with expectations based upon the Rydberg character of the S$_1$ level and activity seen in other ZEKE spectra. Moreover, the wavenumber for $^+16^1$ (220 cm^{-1}) is in very good agreement with the calculated value. It is notable that the experimental wavenumber value for the 16^1 level in the S$_1$ state (184 cm^{-1}) is significantly lower than both the cation value and the calculated value. This will be discussed further in Sec. IV A 3. Also seen in the ZEKE spectrum via 16^1 are bands associated with $^+m^{0,1}$, $^+m^2$ (as a shoulder on the $^+m^{0,1}$ band), and $^+m^4$; a weak band that seems to contain contributions from both $^+m^{3(+)}$ and $^+m^{3(-)}$ is also seen. The torsional potentials in the S$_1$ and D$_0{}^+$ states are very similar, in particular, the sign of the V_6 parameter and its almost identical magnitude.[20] As such, the torsional levels in both states are at very similar wavenumbers. With regard to the PIE curve, we see a clear onset at the AIE, followed by a plateau with some structure, and then a sharp rise at the position of the $\Delta v = 0$ band, $^+16^1$, as expected, followed by the aforementioned drop-off in intensity, this time at ~320 cm^{-1}.

Looking now at the ZEKE spectrum recorded via 15^1, we see unexpected behavior: the $^+15^1$ ZEKE band that is observed at 504 cm^{-1} (Table II) is not the strongest band; this is despite the expected behavior seen for the DF and 2D-LIF spectra recorded from this level (see Sec. III G 2). We actually find the strongest band to be $^+16^1$. As with the 16^1 ZEKE spectrum, we see a reasonably intense origin ($^+m^0$ and $^+m^1$) and bands associated with $^+m^2$ and $^+m^{3(+)}/^+m^{3(-)}$. In the 345–475 cm^{-1} range, marked with an asterisk in Fig. 7(b), there is a complicated set of bands. The only possible NMP contributions to this region would be $^+24^1m^x$ vibtor levels, and although there are possibilities of interactions in the S$_1$ state with the 15^1m^x vibtor levels, such as an indirect $15^1m^1 \ldots 24^1m^1$ interaction, explaining the presence of the $^+24^1m^1$ band, there are no obvious signs of interactions in the 2D-LIF

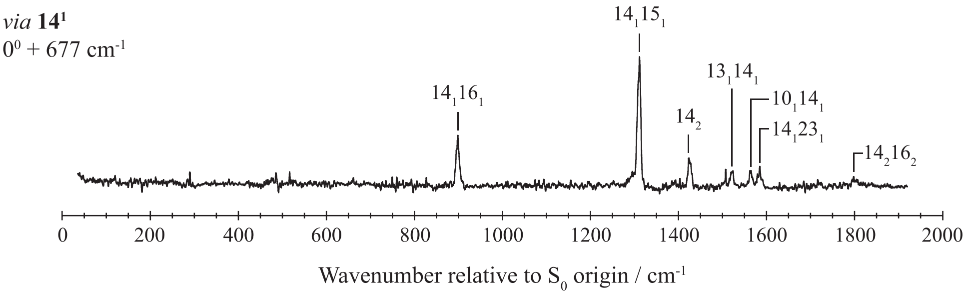

FIG. 6. DF spectra for 14^1. Assignments are given for many of the bands, which are consistent with vibronic coupling, and are discussed further in the text.

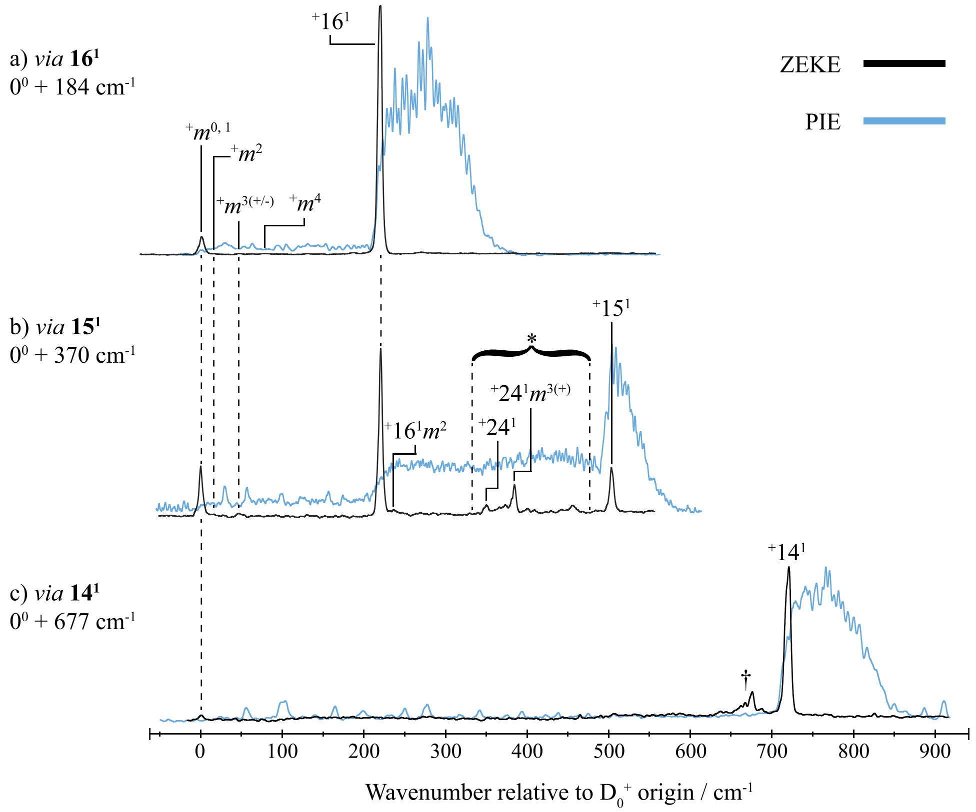

FIG. 7. ZEKE and PIE spectra via (a) 16^1; (b) 15^1; and (c) 14^1. The sharp drop-offs in the intensities of the PIE curves to high wavenumbers are genuine and will be discussed in future work,[42] as will the structure in the low-wavenumber region of the PIE curves. The ZEKE spectrum for 14^1 is that expected for ionization from a Rydberg state, while the other two spectra have unexpected aspects that are discussed further in the text. The relative weakness of the $^{+}15^1$ $\Delta v = 0$ band in (b) is striking and is commented on further in the text. The region marked with an asterisk in (b) is likely due contributions from $^{+}24^1 m^x$ together with a serendipitous overlap with an NMP-Ar resonance at this excitation energy.[42] The 14^1 band is overlapped by $9^1 m^{3(+)}$, which is responsible for the feature marked with an obelus (†) (see Fig. 10 and text).

spectrum (see Sec. III G 2). The $^{+}24^1 m^{3(+)}$ level is totally symmetric, and its presence is consistent with the appearance of the origin band. In fact, ongoing experiments[42] indicate that, as well as the $^{+}24^1 m^1$ and $^{+}24^1 m^{3(+)}$ bands, the 345–475 cm^{-1} region has contributions from NMP-Ar, owing to an overlapping resonance at this excitation energy.

Looking now at the PIE curve recorded via 15^1, we see more-expected behavior. As with the 14^1 and 16^1 PIE curves, we see an onset at the AIE, with structure, followed by a plateau. Although we then see a clear onset corresponding to a non-$\Delta v = 0$ band, $^{+}16$, consistent with the ZEKE spectrum, this is followed by the expected sharp rise corresponding to the $\Delta v = 0$ transition, $^{+}15^1$, with this latter rise being larger than that of the $^{+}16^1$ step. Thus, from the point of view of the PIE curve, this photoionization behavior is as expected, with the strongest rise being the $\Delta v = 0$ band, which appears in the expected position, and consistent with a value for $^{+}15^1$ of 504 cm^{-1} and close to the calculated value (Table II). The less-intense $^{+}15^1$ ZEKE signal is thus highly surprising; indeed, we have recorded this spectrum under a range of conditions, and the band is actually absent on some occasions, suggesting a sensitive dependence on experimental conditions. In addition, the appearance of the $^{+}16^1$ band when exciting via $^{+}15^1$ is also somewhat unexpected as, even though it is symmetry allowed, we are expecting largely diagonal FCFs.

The lack of $^{+}16^1$ and $^{+}15^1$ ZEKE bands when exciting via 14^1 is in line with expectations. However, given the observed strong activity of $^{+}16^1$ when exciting via 15^1, then we might have expected some activity from $^{+}15^1$ when exciting via 16^1, given the aforementioned $^{+}16^1$ activity via 15^1. However, as can be seen in Fig. 7, there is a complete drop-off of ionization cross section for each of the PIE curves to higher wavenumbers; that is, no ions, including fragment ions, are seen that are attributable to ionization of NMP in these regions. This observation is a possible explanation for the absence of the $^{+}15^1$ band when exciting via 16^1, as the $^{+}15^1$ band would appear in this drop-off region. In addition, this may have some bearing on the relative weakness of the $\Delta v = 0$ $^{+}15^1$ band when exciting via 15^1, with other possibilities involving a Rydberg state "window resonance" (i.e., an interaction with a Rydberg state with a low ionization cross section and so reduction of signal) or highly efficient autoionization at the $^{+}15^1$ position (and so depleting the number of ZEKE electrons produced). It is clear that the diminished $^{+}15^1$ ZEKE signal is not directly related to the S_1 state as we see the expected emission activity (Sec. III G 2) and a significant step in the PIE curve at the expected wavenumber of $^{+}15^1$. Further experiments on the photoionization behavior via these features is ongoing.[42]

We highlight the close agreement of the calculated S_1 and D_0^+ wavenumbers for these three b_1 symmetry vibrations (Table II). Furthermore, the experimental D_0^+ wavenumbers are very close to the calculated ones. With these points taken together with the deviation of the experimental values of the S_1 state from the calculated ones, they suggest a change in shape of the actual S_1 potential along b_1 symmetry coordinates away from that expected from its 3s Rydberg character close to the potential minimum. (The experimental S_1 vibrational wavenumber for 15^1 is 370 cm^{-1}, a shift of ~23% from the calculated value; that for 16^1 is slightly lower at ~12%; and for 14^1, the shift is smaller still at ~5%, while for the final b_1 symmetry vibration, 13^1, the shift is ~6%—see Table II.) In Sec. IV A 3, we shall discuss these shifts in wavenumbers in more detail, but this does not seem to be related to evolution of the S_1 HOMO to σ^* character along the N–CH$_3$ coordinate, which would only be expected to change the potential along a_1 symmetry coordinates.

In passing, we comment that although 16^2 is expected to have a value close to the 370 cm^{-1} value in S_1, it is of the wrong symmetry to be active via a one-photon transition, and, furthermore, $^{+}16^2$ in the cation would be expected at 440 cm^{-1} and no such band is seen.

5. DF and ZEKE spectra via 24^1 and fluorescence spectra via 23^1

The DF spectrum recorded via 24^1 is shown in Fig. 8 and shows prominent $16_1 24_1$ and $15_1 24_1$ bands; in addition, we see the weaker $14_1 24_1$, $13_1 24_1$, $10_1 24_1$, and $23_1 24_1$ bands. This confirms that the same b_1 vibrations are inducing the main activity in emission, even when the intermediate has a different symmetry, and that the other vibronic mechanisms are also operating similarly. Interestingly, the $14_1 24_1$ band appears to be ~10 cm^{-1} higher than expected, but no other sensible assignment is apparent: although 24_3 fits better in terms of wavenumber, we do not expect to see this band. (It is a pity that the $14_1 24_1$ band was not observed when exciting 14^1, see Fig. 6, which would have confirmed this shifted band position.) Other bands to higher wavenumbers do not have unambiguous assignments. Assignment of the spectrum allows a number of vibrational wavenumbers for the S_0 state to be determined, as well as S_1 24^1 itself; these are collected together in Table II. The assignment of the DF spectrum largely agrees with that of Biswas *et al.*[18]

In addition, in Fig. 8, we also include the ZEKE spectrum recorded via 24^1. The assignment of this spectrum is clear, since it is dominated by the $\Delta v = 0$ band and yields a wavenumber for the $^{+}24^1$ vibration of 351 cm^{-1}.

The DF and 2D-LIF spectra recorded via 23^1 are presented in Fig. 9. The spectrum is largely as expected, with prominent $15_1 23_1$ and $16_1 23_1$ bands and weaker $14_1 23_1$, $13_1 23_1$, and 23_2 bands; both the 16_1 and 15_1 bands are also seen. In addition, there are various other bands to which we are unable to give unique assignments. The given assignment of the spectra allows a number of vibrational

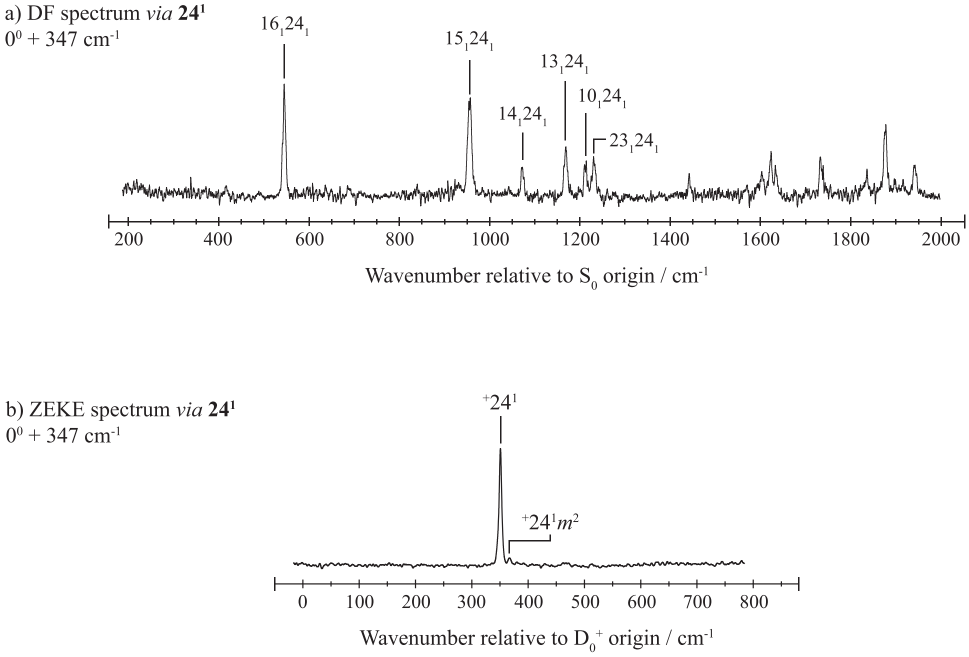

FIG. 8. (a) DF spectrum via 24^1. Assignments are given for many of the bands, which are consistent with vibronic coupling, and are discussed further in the text. (b) ZEKE spectrum via 24^1.

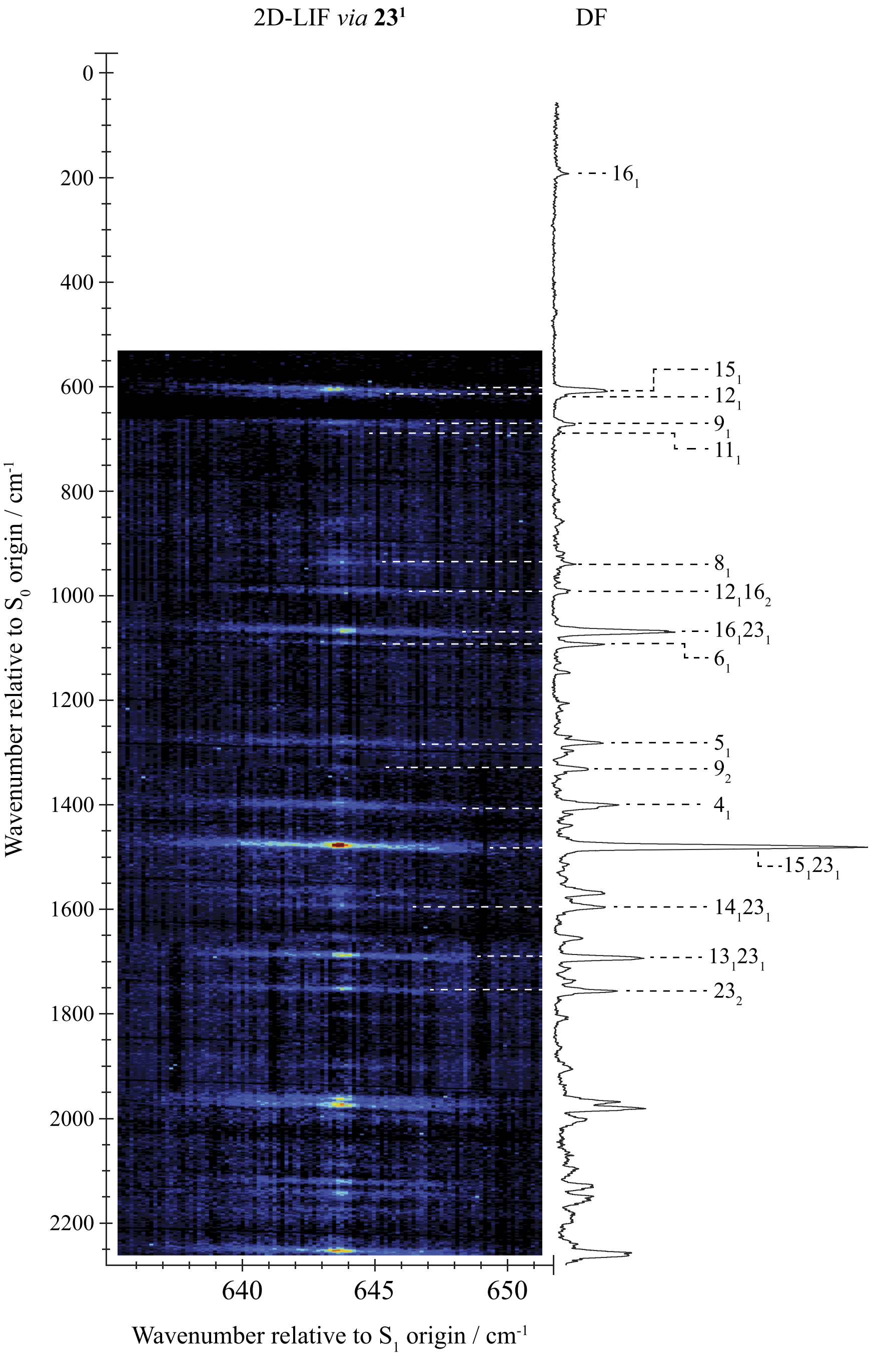

FIG. 9. DF and 2D-LIF spectrum via 23^1. Assignments are given for many of the bands, which are consistent with vibronic coupling, and are discussed further in the text.

wavenumbers for the S_0 state to be determined, as well as 23^1 itself; these are collected together in Table II. These spectra have not been reported previously.

Although there are a number of bands in close proximity in the (1 + 1) REMPI and LIF spectra, over the region scanned, the 2D-LIF spectrum does not give any clear indication that interactions are occurring, with each band showing the same distinctive profile. However, the ZEKE spectra recorded over this region, and which are discussed in Sec. III G 6, do show evidence of some interactions in this region of the spectrum, and it is possible that a 2D-LIF spectrum over the whole 630–720 cm^{-1} region would show further evidence for this, but would be very time consuming to obtain.

6. ZEKE spectra via bands in the 630–720 cm^{-1} region

There is a very intense band in the 630–720 cm^{-1} region, with a number of bands to higher wavenumbers. ZEKE spectra have been recorded through all of the main bands and the observed activity, and these are presented in Fig. 10. The expectation of close-to-diagonal FCFs allows the assignment of the S_1 levels. We have already presented (Fig. 7) the ZEKE spectrum via 14^1 (at 677 cm^{-1}) in Sec. III G 4, together with the PIE curve. We have included the ZEKE spectrum again in Fig. 10 to allow facile comparison with the other spectra in this region and allow discussion of the assignments of the weaker features, which have not already been discussed.

The most intense band at 644 cm^{-1} has been assigned to 23^1 on the basis of the DF and 2D-LIF spectrum, discussed in Sec. III G 5, and again, the ZEKE spectrum confirms that this is the major contributor, yielding the wavenumber for the $D_0{}^+$ vibration of 636 cm^{-1}. We highlight how close the corresponding values are for both the S_1 and $D_0{}^+$ electronic states, in line with the 3s Rydberg character of the former.

The assignment of the other ZEKE spectra are now discussed—no DF spectrum could be recorded for these bands, except for 14^1 (Fig. 6), owing to the diminishing lifetimes of the levels as the internal energy in the S_1 state increases. We first mention that the band at 663 cm^{-1} in the (1 + 1) REMPI and LIF spectra is straightforwardly assignable to 23^1m^2 since, first, the ZEKE spectrum demonstrates a strong $\Delta(v, m) = 0$ band, ${}^+23^1m^2$, at 658 cm^{-1}, as expected, and second also shows a clear ${}^+m^2$ band, with ${}^+23^1m^1$ also clearly observable.

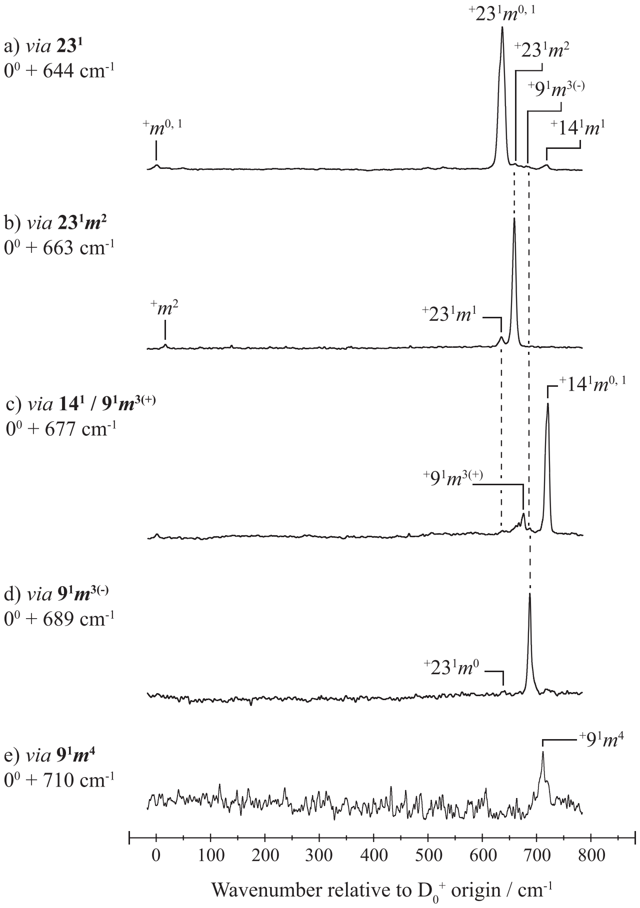

FIG. 10. ZEKE spectra via levels in the 635–715 cm^{-1} region of the (1 + 1) REMPI spectrum.

The other weaker features in the (1 + 1) REMPI spectrum to higher wavenumbers are not in the correct place to be other 23^1m^x vibtor levels, and so another assignment was sought. Aided by the observed torsional structure related to the forbidden origin band in the (1 + 1) REMPI spectrum[20] and by the location of the 9^1 transition at 635 cm^{-1} that is assigned in the (2 + 2) spectrum (Fig. 2 and Ref. 11), we expect to see 9^1m^x vibtor transitions in this region of the spectrum. Indeed, two of the higher wavenumber bands are at the correct wavenumber to be $9^1m^{3(-)}$ and 9^1m^4. The 9^1m^2 band can be seen weakly between 23^1 and 23^1m^2 (not labeled in Fig. 1), while $9^1m^{3(+)}$ will be overlapped by 14^1 [see Figs. 1 and 10(c)]. No ZEKE spectrum was recorded via the very weak 9^1m^2 band, with the ZEKE spectra via 9^1m^4 and $9^1m^{3(-)}$ being dominated by a single band—see Fig. 10. The observation of the weaker feature in the ZEKE spectrum recorded via 14^1, whose wavenumber is consistent with a contribution from ${}^+9^1m^{3(+)}$, confirms that these two bands overlap at ~677 cm^{-1}. There is some slight variation from the vibtor band positions expected, when employing the value for 9^1 obtained from the (2 + 2) REMPI spectrum. This could be partly related to the width of the (2 + 2) REMPI bands but also could be due to interactions, such as $23^1m^0 \ldots 9^1m^{3(+)}$, $14^1m^0 \ldots 9^1m^{3(-)}$, and $23^1m^1 \ldots 9^1m^2 \ldots 14^1m^1$, with the latter allowing an indirect coupling between 23^1m^1 and 14^1m^1. As well as slightly shifted REMPI band positions, the activity in the ZEKE spectra shows some evidence of such interactions. For example, there is a weak band seen in the ZEKE spectrum via 23^1 that can be assigned as ${}^+14^1m^1$; there is also weak cross-activity between the 14^1m^0 and $9^1m^{3(-)}$ spectra. We comment that seeing such interactions in the ZEKE spectra here is made difficult for some levels, since the torsional and in-plane (a_1 and b_2 symmetry) vibrations are almost identical in the S_1 and $D_0{}^+$ states so that any interaction would be expected to occur in both states; hence, vertical transitions will be between the same eigenstates with the same composition. For the out-of-plane vibrations (a_2 and b_1 symmetry), however, there are significant shifts between the two levels, which is consistent with an assignment of ${}^+14^1$ for the weak, higher-wavenumber feature seen in the ZEKE spectrum via 23^1, arising from the indirect $23^1m^1 \ldots 9^1m^2 \ldots 14^1m^1$ interaction.

7. ZEKE spectrum via 12^1

The ZEKE spectrum via the a_2 symmetry 12^1 level is shown in Fig. 11 and demonstrates an essentially perfectly diagonal FCF, with a single band appearing at 498 cm^{-1}, which is in excellent agreement with the calculated wavenumber for ${}^+12^1$, supporting the assignment. Owing to the weakness of the 12^1 band in fluorescence, no DF spectrum could be recorded for this level.

There is some possible ambiguity between the assignment of bands associated with the P_{12} and P_{15} vibrations, as these are calculated to have very similar wavenumbers in all three electronic states under consideration. However, the different symmetries, the expected vibronic coupling, and the DF and 2D-LIF spectra for 15^1

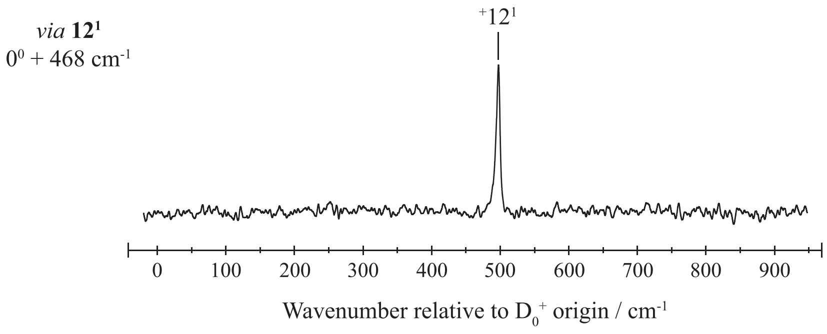

FIG. 11. ZEKE spectrum via 12^1.

are highly supportive of the assignment of 15^1 to the strong 370 cm^{-1} band, supporting a shifted vibrational wavenumber as the result of the vibronic interaction. This makes the assignment of the significantly weaker 468 cm^{-1} band to 12^1 secure and hence also establishes the corresponding vibrational wavenumbers in the S_1 and $D_0{}^+$ states. The 12^1 assignment is also in line with the observation of transitions involving the other two a_2 symmetry vibrations, 10^1 and 11^1, discussed in Secs. III G 8 and III G 9.

8. ZEKE spectra via the 800 cm^{-1} feature

In the 800–850 cm^{-1} region of the (1 + 1) REMPI spectrum, a complicated feature is seen, which is shown in Fig. 1 and in an expanded form at the top of Fig. 12. Although this feature has been referred to previously,[11] the clear complexity of the feature has not; it is evident that there are a number of contributions. To gain insight into these, we have recorded eleven ZEKE spectra at different positions across the band, as indicated in Fig. 12; these have been normalized to the most intense band in each case. Below the $\Delta v = 0$ bands at ∼750 cm^{-1}, we have amplified the intensity by a factor of 4 to highlight the weak structure, which turns out to be crucial to the assignment, and we have also provided expanded views of the $\Delta v = 0$ regions on the right-hand side of Fig. 12. Although an attempt was made at recording a DF spectrum via the most intense part of this band, this yielded a noisy spectrum, with very few features discernible; this is in line with the very stark reduction in intensity in the LIF spectrum compared to the REMPI spectrum—see Fig. 1. Furthermore, the distinct structure seen in the REMPI spectrum over this region was not resolved in the LIF spectrum, meaning that any comparison between DF spectra, or even a 2D-LIF spectrum, over this region would have proved challenging.

The assignment of the ZEKE spectra in Fig. 12 makes use of the fact that we generally expect largely diagonal FCFs. It is clear that there are a number of contributions across this region, and the ZEKE spectra suggest that various interactions are occurring between various zero-order states (ZOSs). The contributions will consist of one or more zero-order bright (ZOB) states, interacting with various zero-order dark (ZOD) states, to produce various eigenstates, which may comprise vibrational and torsional contributions; we do not consider rotations. Inspection of the values in Table II and comparing with the ZEKE spectra, taking into consideration the excitation wavenumber range, suggests that there are two likely fundamental ZOB states, 11^1 and 13^1, each of which has $m = 0$ and $m = 1$ components; both of these were suggested as contributing to this region of the spectrum in Ref. 11. In Table III, we summarize the vibrational and vibtor levels that are of the same symmetry as these ZOB states and that may be contributing to this energy region. These values can only be used as a guide initially, since levels of the same symmetry may interact, leading to slightly shifted eigenstates. As well as the fundamentals, Table III shows that there are also vibrational combinations, which could be either ZOB states or ZOD states, $9^1 16^1$, $12^1 24^1$, and $16^1 23^1$, the first two of which can interact with 13^1, while the latter one can interact with 11^1. Activity involving both 13^1 and 11^1 would be in line with other transitions seen in the REMPI spectrum (see Fig. 1), with the b_1 symmetry 13^1 state expected to be the brighter, owing to the closer proximity and higher oscillator strength of the ${}^1B_2$ state from which it is stealing its intensity (see Fig. 3).

The complicated nature of the 800–850 cm^{-1} excitation feature suggests that there are a number of vibrational/vibtor levels interacting. Taking account of the wavenumbers and symmetries of vibrations in the S_1 state, the expected torsional spacings, and the ZEKE activity, the following vibrational interactions (represented by "…") might be expected, with corresponding interactions occurring for the $m = 1$ levels. The expected strongest ZOB state is indicated in bold, and these couplings are expected to be the strongest, since they have $\Delta v \le 3$, and $\Delta m \le 3$,

$$a_2{}' \text{symmetry} : 16^1 23^1 m^0 \ldots \mathbf{11^1 m^0},$$
$$a_2{}'' \text{symmetry} : 9^1 16^1 m^0 \ldots \mathbf{13^1 m^0} \ldots 12^1 24^1 m^0.$$

We have omitted $12^1 15^1 m^{0,1}$ from the possible interactions above, since $12^1 15^1$ has b_2 symmetry, and hence, its $m = 0$ level cannot interact with the $m = 0$ level of either 13^1 or 11^1, but the $m = 1$ level could be interacting with $13^1 m^1$. Moreover, being a combination band, this transition is not expected to be inherently intense, but we cannot completely rule out a minor contribution to the REMPI feature. The ZEKE band is expected at 1006 cm^{-1}, and since only a very weak band is seen at this wavenumber, we conclude that any involvement is minimal.

In previous ZEKE studies of vibrational and vibtor studies in *p*-fluorotoluene,[27,43] we have found that the low-energy region can often give a good guide as to the contributing levels. Hence, we highlight that the ZEKE spectra recorded here, via the low-wavenumber side of the 800–850 cm^{-1} REMPI feature, show various torsional and

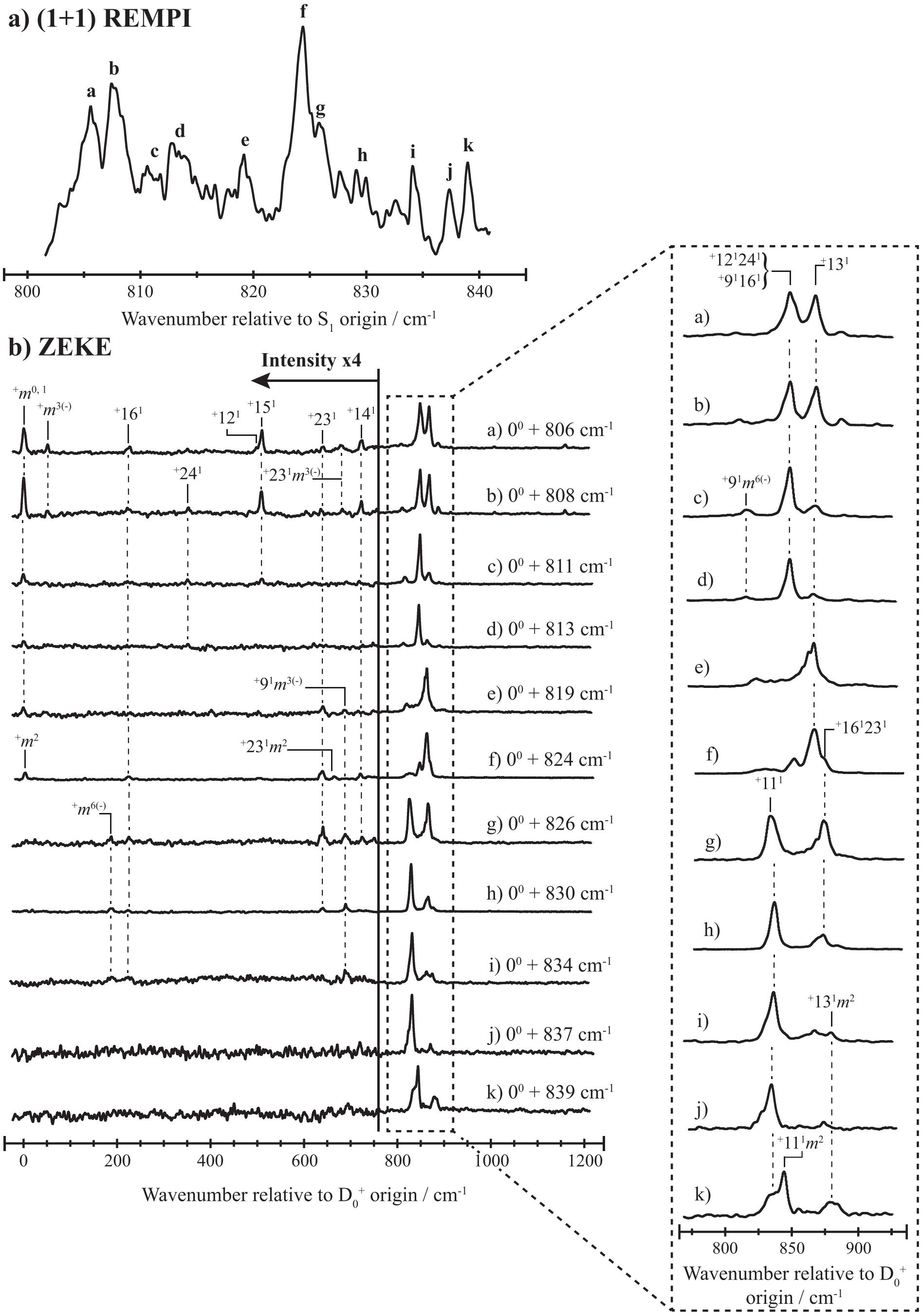

FIG. 12. ZEKE spectra recorded at the indicated positions within the 800–850 cm^{-1} feature in the (1 + 1) REMPI spectrum, with the relevant section shown at the top of the figure. The intensity of the first ~750 cm^{-1} has been enhanced by ×4 to emphasize the low-wavenumber bands. Expansions of the 750–950 cm^{-1} regions of the ZEKE spectra are shown in the side panel on the right. Assignments are indicated by the main zero-order state expected to be contributing to each of the main features. The activity is consistent with vibronic coupling combined with interactions between different zero-order states (see text for further discussion).

fundamental bands. Recall that when we excited via 16^1, then both $^+m^{0,1}$ and $^+16^1$ bands were seen in the ZEKE spectrum (Fig. 7). As such, we conclude that the observation of these bands is consistent with the involvement of the a_2'' symmetry 9^116^1. Similarly, weak $^+12^1$, $^+23^1$, and $^+24$ bands are also seen when exciting on the low-wavenumber side of the 800–850 cm^{-1} REMPI feature, consistent with involvement of 12^124^1. The expected positions of the ZEKE bands from these two combination bands are coincident at 849 cm^{-1} and so consistent with the lower of the two intense bands seen at the lower excitation wavenumbers. The higher-wavenumber band is consistent with $^+13^1$. Hence, we conclude that in this wavenumber region of the S$_1$ state, we have significant contributions from three eigenstates arising from interactions involving 13^1, 9^116^1, and 12^124^1, with the interactions between the 13^1 ZOB state and each of the combinations ($\Delta v = 3$) expected to be stronger than those between the two combinations ($\Delta v = 4$); it appears that the $9^{1}16^{1}$ interaction with 13^{1} is the stronger. From the lower-wavenumber activity, based upon relative intensities, we can also deduce that there is more $9^{1}16^{1}$ character at the very start of the feature, with $12^{1}24^{1}$ then in the ascendent, before the 13^{1} contribution becomes dominant at ~824 cm^{-1}.

TABLE III. Expected wavenumbers of S_1 zero-order states that could contribute to the 800–850 cm^{-1} feature in the (1 + 1) REMPI spectrum.

Level[a,b]		Symmetry[c]		State	
$m = 0$	$m = 1$	$m = 0$ G_{12} (C_{2v})	$m = 1$ G_{12}	S_1[d]	D_0^+[d]
		13^{1}			
$12^{1}24^{1}m^{0}$	$12^{1}24^{1}m^{1}$	$a_2''(b_1)$	e'	815	849
$9^{1}16^{1}m^{0}$	$9^{1}16^{1}m^{1}$	$a_2''(b_1)$	e'	819	849
	$24^{2}m^{5}$		e''	822	831
$\boldsymbol{13^{1}m^{0}}$	$\boldsymbol{13^{1}m^{1}}$	$a_2''(b_1)$	e'	824	861
	$15^{2}m^{4}$		e'	820	1097
$12^{1}16^{1}m^{6(-)}$		a_2''		843	911
$12^{1}15^{1}m^{0}$[e]	$12^{1}15^{1}m^{1}$[e]	$a_1''(b_2)$	e'	838	1006
	$11^{1}m^{2}$		e'	846	846
$23^{1}m^{6(-)}$		a_2''		835	829
		11^{1}			
$9^{1}m^{6(-)}$		a_2'		826	822
	$14^{1}m^{5}$		e'	805	849
$16^{1}23^{1}m^{0}$	$16^{1}23^{1}m^{1}$	$a_2'(a_2)$	e''	828	856
	$12^{1}24^{1}m^{2}$		e''	831	865
$\boldsymbol{11^{1}m^{0}}$	$\boldsymbol{11^{1}m^{1}}$	$a_2'(a_2)$	e''	830	830
	$9^{1}16^{1}m^{2}$		e''	835	865
	$13^{1}m^{2}$		e''	840	877
	$15^{1}24^{1}m^{5}$		e''	845	988
	$16^{1}23^{1}m^{2}$		e'	844	872
$12^{1}24^{1}m^{3(+)}$		a_2'		859	894

[a] The levels have been separated into those vibronically accessible from the $m = 0$ and $m = 1$ levels of the S_0 zero-point vibrational level, which can interact either with the $m = 0$ or $m = 1$ level of the expected zero-order bight states, 13^{1} and 11^{1} (see text for further commentary).

[b] Within each block, levels are given in the expected wavenumber order for the S_1 state, although interactions between the zero-order states could change the ordering.

[c] Symmetries of the levels accessible from the indicated $m = 0$ or $m = 1$ levels. C_{2v} symmetry labels are given for the pyrrolyl ring lying in the yz-plane. For levels where both $m = 0$ and $m = 1$ are possible, both the C_{2v} label for the vibration and the two corresponding G_{12} symmetry labels are given. For other vibtor levels, just the G_{12} label is given.

[d] These are calculated using experimental vibrational values, where they exist, or using a calculated value, where they do not (see Table II). For corresponding $m = 0$ and $m = 1$ levels, the same value applies, under the assumption that there are no interactions between levels. (The given values have been adjusted to be relative to the appropriate $^{+}m^{0}$ or $^{+}m^{1}$ scale.) The torsional energies were obtained from the V_6 and F parameters reported in Ref. 20.

[e] The $12^{1}15^{1}m^{1}$ level could interact with $13^{1}m^{1}$, but the $12^{1}15^{1}m^{0}$ state cannot interact with $13^{1}m^{0}$, as it has a different symmetry. The $12^{1}15^{1}m^{0}$ state could be vibronically active but, being a combination band, is unlikely to be very intense.

From 824 cm^{-1} onwards, we also see activity from $^{+}23^{1}$ and $^{+}16^{1}$ reappearing when exciting in the center of the REMPI feature, where $16^{1}23^{1}$ is expected. We also see that the band at ~860 cm^{-1} becomes more complicated in structure, consistent with overlapping $^{+}13^{1}$ and $^{+}16^{1}23^{1}$ contributions. To slightly higher wavenumbers, $^{+}13^{1}$ is expected to wane in intensity, while $^{+}16^{1}23^{1}$ waxes, and the ZEKE spectra confirm this, with the strongest contribution from $^{+}23^{1}$ bands in the 824–830 cm^{-1} excitation region. We also see a ZEKE band at ~830 cm^{-1}, assigned to $^{+}11^{1}$, which appears in the ZEKE spectra from 0^{0} + 826 cm^{-1}—slightly broadened in that spectrum and then as a narrower band in the spectrum recorded at 0^{0} + 830 cm^{-1}. These observations confirm contributions from eigenstates made up predominantly from 11^{1} and $16^{1}23^{1}$ to the mid- to high-wavenumber end of the 800–850 cm^{-1} feature.

Various other bands can also be seen, some of which may be related to FC activity, but we highlight that there are strong indications that there is a contribution from $9^{1}m^{6(-)}$ to the low-wavenumber end of the feature, expected to interact with $11^{1}m^{0}$. In addition, at the high-wavenumber end of the feature, there are contributions from $13^{1}m^{2}$, via interaction with $11^{1}m^{1}$ and $11^{1}m^{2}$ via interaction with $13^{1}m^{1}$. It is difficult to be definitive about other contributions to the 800–850 cm^{-1} feature, but it is likely that smaller, higher-order interactions are occurring, involving other levels indicated in Table III.

Generally, the discussed interactions appear to give a good correspondence to the observed features seen in the ZEKE spectra (see Fig. 12). On the expanded traces on the right-hand side of Fig. 12, we have indicated the expected positions of the dominant contributions, noting that the eigenstates will be linear combinations of each ZOB state with the coupled ZOD states of the same symmetry. The low-wavenumber side of the REMPI band appears to arise mostly from the transitions involving eigenstates with $13^{1}m^{0,1}$ contributions, while the high-wavenumber side mostly comprises those with $11^{1}m^{0,1}$. The ZEKE spectra clearly indicate that a number of contributions are present and that the REMPI feature therefore comprises transitions to a number of resulting eigenstates. Importantly, a number of these involve vibtor levels that can only interact with one of the two m levels associated with a particular ZOB state. Overall, it means that within this narrow range, four possible independent routes for energy delocalization can occur. This is reminiscent of a feature seen in the REMPI spectrum of p-fluorotoluene, where independent energy delocalization routes of a different symmetry were also identified.[43]

In summary, this is an unusually rich region of the spectrum and arises from the serendipitous location of (at least) two vibronically allowed ZOBs, each with $m = 0$ and $m = 1$ components, which happen to interact strongly with several vibrational and/or vibtor levels. It is notable that this feature is the only one in the REMPI spectrum, in the region scanned, which shows such a complicated structure, although we commented on the likelihood of some interactions in the 630–720 cm^{-1} region (see Sec. III G 6).

9. ZEKE spectra via the >900 cm^{-1} features

To higher wavenumbers, a few other weaker features appear in the REMPI spectrum, which are absent from the LIF spectrum (see Fig. 1). We have recorded ZEKE spectra via these, which are shown in Fig. 13. In each case, there is a single intense $\Delta v = 0$ band consistent with our expectations of largely diagonal FCFs and reminiscent of the ZEKE spectra via 24^1 and 12^1; together with the calculated values in Table II, this allows the assignments to be made, as shown in Fig. 13. The REMPI band at 907 cm^{-1} is assigned to the remaining a_2 symmetry vibration, 10^1, with the 971 cm^{-1} band being assigned to a third b_2 symmetry vibration, 22^1. Both of these provide good agreement with the calculated wavenumbers of the vibrations in the S_1 state and cation and have symmetries consistent with the vibronic coupling mechanisms discussed; they both agree with suggested assignments in Ref. 11. The assignment of the weak structure above the $\Delta v = 0$ band in the 22^1 ZEKE spectrum is unclear.

There is no obvious pyrrolyl-ring localized fundamental of the correct symmetry to assign the band at 1100 cm^{-1}. Interestingly, this band is not apparent in the (1 + 1) REMPI spectrum reported in the picosecond study,[11] and indeed, there seem to be more transitions at these higher wavenumbers, than apparent in our nanosecond spectrum, which may be linked to distinct lifetime behaviors of the different levels.

An assignment of the 1100 cm^{-1} REMPI band to 7^1 is discounted: it would be the only a_1 symmetry fundamental to be active in the one-photon spectrum and is symmetry forbidden; moreover, this transition is observed to slightly lower wavenumbers in the (2 + 2) REMPI spectrum (see Fig. 2, Table II, and Ref. 11). Although a possible assignment to the $9^1 12^1$ combination would be consistent with the excitation wavenumber, this is not consistent with the wavenumber of the corresponding ZEKE band, with the $^{+}12^1$ wavenumber established in Sec. III G 7 and $^{+}9^1$ established in Sec. III G 6. We also reject $6^1 m^{3(-)}$ as it would be the only vibtor transition in this region, which is out of line with the torsional structure seen on the origin (see Fig. 1 and Ref. 20) and the vibtor structure associated with 9^1 (see Sec. III G 6). We finally opt for a transition to a methyl-localized vibration, Me_7, which corresponds to an in-plane rock of the methyl group[33] and would fit with the changing dispersion interactions experienced by the methyl group in the S_0 and S_1 electronic states, consistent with the change in torsional potential between those two states.[16,20]

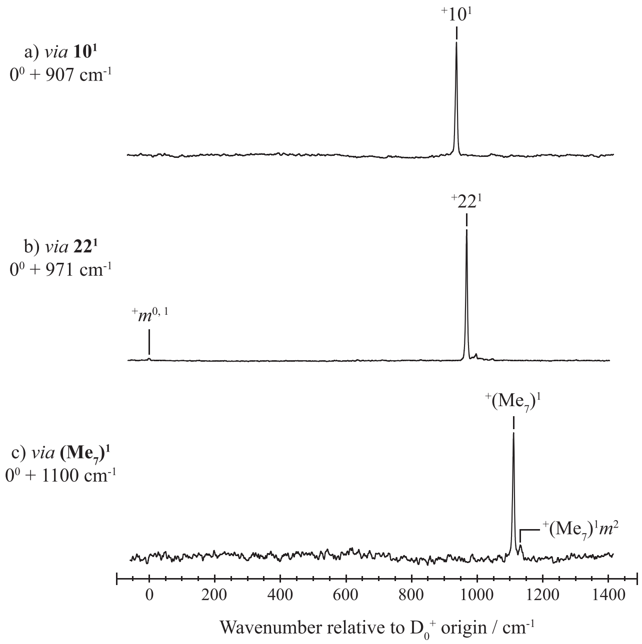

FIG. 13. ZEKE spectra via the three bands that appear in the >900 cm^{-1} region of the (1 + 1) REMPI spectrum, with suggested assignments.

IV. DISCUSSION

A. Vibrations

1. Vibrations in S_0

The ground state IR and Raman data, obtained from liquid, solution, and surface studies,[23,24] were discussed in Ref. 33 and are presented in Table II; in Ref. 33, we also presented calculated S_0 values (B3LYP/aug-cc-pVTZ, scaled by 0.97), which were in very good agreement with the experimental values, and we also discussed previously reported calculated values. We only include our calculated values in Table II, as there was good agreement between the various calculated values, once scaling had been considered. In Table II, we have tabulated the results from the DF study of Biswas *et al.*[18] alongside those obtained in the present work. For the cases where a value was obtained in both studies, the values are in good agreement with each other and with the present calculated values. A couple of the assignments in Ref. 18 appear ambiguous, for example, the value for P_{20} has an alternative assignment to Me_6, the methyl umbrella mode. The assignment of a 1100 cm^{-1} vibration could be assigned to either Me_7 or Me_8.

The present study obtains a number of jet-cooled, gas-phase S_0 vibrational wavenumber values for the first time, which are also in generally good agreement with the previous IR/Raman and calculated values.

2. Vibrations in D_0^+

The wavenumbers for the D_0^+ state of the cation derived from the ZEKE spectra are given in Table II and are the first time any of these values have been reported. (No vibrational structure was reported for the conventional photoelectron spectrum of NMP by Baker *et al.*[44]) The agreement between the calculated and experimental values is exceptionally good, similar to the good agreement seen for the S_0 state, and provides further confidence that the assignments are correct. Of course, the vibrational wavenumbers for the cation are expected to be similar to those of Rydberg states of NMP, and we shall comment on this further in Sec. IV A 3. We provide further commentary on the activity in the ZEKE spectra in Sec. IV A 4. Cooper *et al.*[15] provided some vibrational wavenumbers associated with various Rydberg states of NMP, but although some of these are close to cation values presented in Table II, the assignment of all of these is uncertain.

3. Vibrations in S_1 and vibronic coupling

We have collected the present calculated (TD-B3LYP/aug-cc-pVTZ, scaled by 0.97) and experimental values for the wavenumbers of the S_1 state vibrations together in Table II. Also included are the (TD-B3LYP/aug-cc-pVDZ) calculated values reported in Ref. 11, together with calculated values (CIS/6-31G**) reported in Ref. 19. (We have only included the calculated values from both Refs. 11 and 19 that were included in Ref. 11 and where they were assigned to particular vibrations.) Although the TD-B3LYP/aug-cc-pVDZ and TD-B3LYP/aug-cc-pVTZ results of Ref. 11 and the present work are in close agreement (noting that the former do not appear to have been scaled), there is some disagreement with the CIS/6-31G** values of Ref. 19. Since the S_1 state is Rydberg-like close to the FC region, then we would expect the vibrational wavenumbers for S_1 to be similar to those in the D_0^+ state. Indeed, if the present *calculated* values in Table II are considered, this is indeed the case, with all calculated S_1 vibrational wavenumbers being very close to the corresponding D_0^+ ones for all symmetries, although the wavenumbers of the a_2 symmetry vibrations are slightly more discrepant. Overall, therefore, coupled with the good agreement between the experimental and calculated D_0^+ vibrational wavenumbers, we have more confidence in the TD-B3LYP calculated wavenumbers for the S_1 state than the CIS ones of Ref. 19.

In Fig. 14(a), it may be seen that the calculated vibrational motions of the S_1 state are similar to those in the S_0 state, supporting the use of the same P_i labels for both states, and in Ref. 33, it was shown that similar comments apply to the vibrations of the D_0^+ state. In addition, the $D_0^+ \leftarrow S_1$ Duschinsky matrix shown in Fig. 14(b) is highly diagonal, showing that the calculated vibrational motions in the S_1 state are almost identical to those in the cation, as expected for a Rydberg state with the corresponding ionic core. Given that there is very good agreement between the calculated vibrational wavenumbers for the D_0^+ state and the obtained experimental values (Table II), then we would also expect correspondingly close agreement for the S_1 vibrations. It is noteworthy although this expectation is met for the in-plane a_1 and b_2 vibrations, there are significant differences between the calculated and experimental S_1 vibrational wavenumbers for the out-of-plane b_1 and a_2 vibrations, with the S_1 experimental values all being significantly lower, particularly for P_{15}. We now comment on these observations in the light of the known vibronic interactions in this molecule.

In Fig. 3, we have indicated the approximate vertical energetic locations of the various excited states of NMP, i.e., at the geometry of the $\tilde{X}$ state. The NMP molecule is unusual in two key related aspects: first, in the FC region, its first excited state is Rydberg in character, S_1 (a_2, 3s), yet it fluoresces; and second, there are close-lying states of three different symmetries that each allow distinct vibronic interactions to be induced. In Fig. 3, we have indicated the main excited electronic character of each state and its symmetry, as well as the symmetries of the vibrations that induce the vibronic coupling for each nearby electronic state; furthermore, the calculated oscillator strengths are also indicated, since for intensity to be stolen via vibronic coupling, there must be something to be stolen. Some of the calculated oscillator strengths for some of the A_2 electronic states are not zero (indicated by an "*" in Fig. 3). This is likely because at the potential minimum of the $\tilde{X}$ state of NMP, the geometry is C_s as opposed to C_{2v}, and this breakdown of C_{2v} symmetry means that these states can be calculated as weakly allowed.

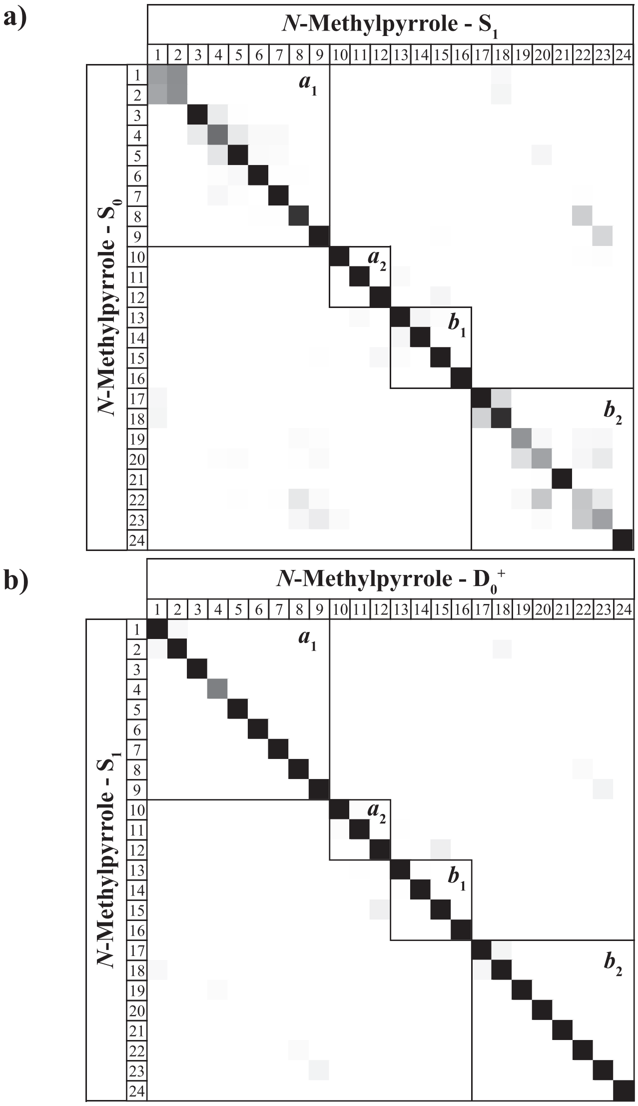

FIG. 14. Duschinsky matrices for the (a) $S_0 \leftrightarrow S_1$, and (b) $S_1 \leftrightarrow D_0^+$ transitions. The depth of shading represents the coefficients of mixing between vibrations in the two electronic states between 0 (white) and 1 (black). The S_1 vibrations can, for the most part, be seen to be dominated by a single S_0 vibration, allowing the P_i labels to be used for those vibrations. The D_0^+ vibrations are calculated to be almost identical to those of the S_1 state; however, the experimental results suggest that some of the S_1 vibrations are affected by vibronic coupling. In Ref. 33, we also discussed the vibrations of D_0^+ expressed in terms of those of the S_0 state.

It is clear from the assignments of the different spectra that there is strong vibronic coupling induced by vibrations of both b_1 and b_2 symmetries. Indeed, all four b_1 vibrations are observed in the REMPI spectrum, as well as the three lowest wavenumber b_2 vibrations (with the others being higher in wavenumber than the region scanned.) The intensity of the b_2 symmetry, 23^1 transition is significant, as are the b_1 symmetry 16^1 and 15^1 bands; some caution is required with the intensities, however, since the lifetimes of the levels are decreasing with the increasing wavenumber, albeit not monotonically.[11] Weaker, but still significant are transitions involving all three a_2 symmetry vibrations. Our resolution is sufficient to discern the rotational band profile type, and we show these in Fig. S1 of the supplementary material for the 16^1, 15^1, and 23^1 bands. These profiles are as expected,[38] being of type *b* for 16^1 and 15^1, which gains intensity from the (a_2, 3p$_x$) $^1B_2 \leftarrow S_0$ transition, and type *c* for 23^1, which gains intensity from the (a_2, 3p$_y$) $^1B_1 \leftarrow S_0$ transition. Bands corresponding to transitions to a_2 symmetry vibrations are expected to show type *a* band profiles, and this is consistent with observations. We find that our REMPI spectra appear to be slightly rotationally colder than our LIF spectra and that we only see some bands clearly in the REMPI spectra; when observed, the band profiles are clearer and slightly wider in the rotationally warmer LIF spectra.

As expected, we see no transitions that involve totally symmetric vibrations in our (1 + 1) REMPI spectrum, since these are forbidden in one-photon transitions, although such transitions are allowed and dominate in the (2 + 2) REMPI spectrum, as can be seen in the spectrum in Fig. 2 and that presented in Ref. 11. The bands in the (2 + 2) REMPI spectrum are broader than those of the (1 + 1) REMPI spectra, likely due to power broadening effects; the bands in the present (2 + 2) REMPI spectrum in Fig. 2 are significantly narrower than those in the corresponding spectrum in Ref. 11, in line with the higher power and pulse width of the picosecond laser employed. Despite the rapidly decreasing lifetimes of the levels,[11] no broadening is evident in the (1 + 1) REMPI spectra, for all bands that we have recorded, up to ~1110 cm^{-1} (see Fig. 1)—consistent with lifetime broadening effects not being significant, in line with the lifetimes cited in Ref. 11.

From the assignments, the (1 + 1) REMPI and LIF spectra display three distinct vibronic coupling mechanisms, with the (2 + 2) REMPI spectrum dominated by FC activity—indeed, no evidence of vibronic coupling is seen in the (2 + 2) REMPI spectrum, although it still can occur. As well as being responsible for the observed intensities in absorption, these vibronic coupling mechanisms will also operate for the emissions and are consistent with the DF and 2D-LIF spectra. As remarked in Sec. III E, the vibrational structure seen will depend upon the symmetry of the level from which emission occurs. The assignment of the DF spectra indicate that the P_{15} vibration is the main inducing mode for the emission, with the strongest band always arising from a combination of P_{15} with the corresponding intermediate S$_1$ vibrational level. In addition, we also see vibronic activity associated with the other b_1 symmetry vibrations, with this being quite strong also for P_{16}, as well as some b_2 and, to a lesser extent, a_2 vibrations, confirming that the same vibronic mechanisms are operating in both emission and absorption. Although the 16^1, 15^1, 23^1, and 14^1 transitions are strong in absorption, with some caution required when considering the intensities of the REMPI and LIF bands because of the lifetime variation, the vibronic coupling involving P_{15} demonstrates by far the strongest bands in emission.

As commented hereinbefore, we expect the S$_1$ and D$_0{}^+$ wavenumbers to be very similar for each vibration, since the S$_1$ state is Rydberg-like, and this expectation is borne out in the calculated wavenumbers, for the most part, and by the corresponding almost perfectly diagonal Duschinsky matrix in Fig. 14(b). This is consistent with the highly diagonal nature of the FCFs for the ionization, as observed for almost all vibrations. The two major exceptions are first in the ZEKE spectrum via 16^1, where the origin transition is clearly seen, and in the ZEKE spectrum via 15^1, where we see both the origin band and a sizeable $^+16^1$ band. We have commented in Sec. III G 4 regarding the absence or relative weakness of $^+15^1$ ZEKE bands in both of these spectra but also the significant step in the PIE curve when exciting via $^+15^1$—these points are the subject of ongoing investigations.[42] Here, we will discuss the effect of vibronic coupling in the S$_1$ state.

Often, two types vibronic effects are described: a dependence of the electronic transition moment on the nuclear coordinates and intensity stealing via vibronic interactions. In the book authored by Bunker and Jensen,[30] it is concluded that these are two manifestations of the Herzberg–Teller effect and can be viewed as vibration-induced mixing of electronic wavefunctions away from the equilibrium position. Hence, for a one-photon forbidden absorption, if we denote the final electronic state of symmetry, *i*, in a transition by $\Phi'_{e,i}(0')$, where $0'$ represents the equilibrium geometry of that state, then for small deviations, δQ_j, along one or more normal modes of symmetry *j*, then we can express the electronic wavefunction of the excited state at the slightly distorted geometry as

$$\Phi'_{e,i}(\delta Q_j) = c_i \Phi'_{e,i}(0') + \sum_j c_j \Phi_{e,j}(0'), \tag{6}$$

where the $\Phi_{e,j}$ are electronic wavefunctions of other excited states of symmetry *j*. For small displacements, we can ignore anharmonic effects and $|c_j|$ will be small and then vanish when all $\delta Q_j = 0$; additionally, $|c_i|$ will be close to, but less than, 1 for $\delta Q_j \neq 0$ and equal to 1 when $\delta Q_j = 0$. Assuming that c_j are proportional to the normal coordinate displacements,[30] then

$$\Phi'_{e,i}(\delta Q_j) = c_i \Phi'_{e,i}(0') + \sum_j C_j Q_j \Phi_{e,j}(0'). \tag{7}$$

Thus, the electronic potential experienced by the molecule will vary along a normal coordinate (more generally, one of the nuclear coordinates could be torsion), and resultant mixings are possible, i.e., C_j is non-zero when the symmetry, *j*, is such that vibronic coupling occurs during a transition from the ground electronic state. It is this variation that can be viewed as mixing in of other excited state characters of symmetry *j*, as a result of a vibronic interaction, away from the equilibrium position of $\Phi'_{e,i}$. Similar arguments apply to emission, although in jet-cooled experiments the emitting state will often be a vibrationally excited level of the upper electronic state; the latter will also be true of the intermediate level employed for the resonant ZEKE transitions.

We have seen that there is good agreement between the calculated b_1 symmetry vibrational wavenumbers for the S$_1$ state and the cation and also between the calculated and experimental values for the cation; in contrast, we find significantly lower values for the experimental S$_1$ b_1 symmetry vibrations. Taken together, these observations strongly suggest in the S$_1$ state, vibronic coupling changes the potential experienced by the molecule along the b_1 coordinates and leads to the observed lowering of those vibrational wavenumbers. A similar, although less marked, scenario emerges for the a_2 symmetry vibrations also. It is extremely interesting that although the in-plane b_2 symmetry vibrations are also involved in inducing vibronic coupling, the experimental values for the three observed vibrations are almost identical in the S$_1$ and

D_0^+ states, and so, apparently, no potential distortion occurs along those coordinates.

4. ZEKE spectra

Considering the ZEKE spectra further, we have highlighted that the majority exhibit very diagonal FCFs, with the Δm, Δv, or $\Delta(v, m) = 0$ band being by far the most intense in the spectrum—the ZEKE spectra recorded via the torsional levels have been discussed in Ref. 20. The main exceptions to this are the ZEKE spectra recorded via the S_1 14^1, 15^1, and 16^1 levels (see Fig. 7), where the origin band appears, which we shall now discuss.

We first comment that the ZEKE spectrum recorded via 14^1 is very much as expected, with very strong diagonal FCF character but with a weak origin band. (The excitation will involve both $m = 0$ and $m = 1$ components, and so the dominant feature is expected to be the overlapped $^+14^1m^{0,1}$ bands; this will be the case for other intermediates vibrational levels also.) The ZEKE spectrum recorded via the much stronger 16^1 level, although being dominated by the $^+16^1$ band, also exhibits a sizeable origin band, as well as a number of weak torsional bands, and the ZEKE spectrum via $^+15^1$ also exhibits a strong origin band, as well as a $^+16^1$ band, with the weakness of the $\Delta v = 0$ ZEKE band commented on in Sec. III G 4.

We have seen that vibronic interactions can cause a change in the potential along coordinates corresponding to vibronic-coupling inducing vibrations, and such a vibrationally excited level could have a slightly distorted average geometry. For b_1 vibrations, this would lead to a small distortion to an out-of-plane averaged geometry and would lead to a C_s symmetry molecule, with the reflection plane being xz in the current axis system; then, the b_1 (a_2'') and a_1 (a_1') symmetry levels become totally symmetric in the C_s point group. Thus, the origin band in the ZEKE spectrum would become weakly allowed via these intermediate levels, as seen, and similarly for the $^+24^1m^{3(+)}$ band via 15^1. Such a mechanism would also lead to e'' symmetry torsional and vibtor levels also becoming allowed, with e' levels already being symmetry allowed from the $m = 1$ levels associated with the b_1 symmetry intermediate vibrational levels. Thus, this is a possible explanation for the appearance of the various torsional bands, particularly evident in the 15^1 and 16^1 ZEKE spectra. That these bands are relatively weak would be in line with the only small geometric distortions expected.

Although symmetry-forbidden bands are prevalent in photoelectron and ZEKE spectra, their origin is not always clear, with the intrachannel-coupling mechanism of Rathbone *et al.*[45] for photoelectron spectroscopy (PES), extended to Rydberg states and ZEKE spectroscopy,[46] being one such mechanism. In outline, the outgoing photoelectron wave (in PES) or the high-n Rydberg electron (in ZEKE) can interact with the vibrations (or torsions and vibtor levels) of the cation core. For NMP, the $np \leftarrow 3s$ excitations are most likely (being $\Delta l = 1$ from the 3s S_1 Rydberg state), with these having the symmetries b_1 for np_x, b_2 for np_y, and a_1 for np_z. Thus, vibrational bands in the ZEKE spectra corresponding to these symmetries, particularly low-frequency, high-amplitude vibrations, can be rationalized by this mechanism.

We now come back to the ZEKE spectrum via 15^1, which has very unexpected activity. First, it is the only ZEKE spectrum recorded for NMP that does not have the dominant $\Delta v = 0$, or equivalent, band; however, the PIE spectrum suggests that this absence is due to some interaction occurring in the cation (Fig. 7 and Sec. III G 4), which is under further investigation.[42] Here, we comment on the appearance of the $^+16^1$ band in this ZEKE spectrum, despite the Duschinsky matrices (Fig. 14) indicating that any mixing between vibrational modes during the ionization is minimal. Earlier, in the present section, we have suggested the possibility that the S_1 potential is affected by the vibronic coupling along the out-of-plane coordinates, particularly those of b_1 symmetry, and this would not be reflected in the calculated Duschinsky matrices; on the other hand, the DF spectra are clear that the intermediate levels are dominated by the expected vibration but indicate that there is cross-activity in the DF spectra recorded via 16^1 and 15^1 (see Figs. 4 and 5). We propose that there is indeed some Duschinsky-type mixing between the 16^1 and 15^1 modes, caused by the vibronically induced change in the S_1 wavefunctions away from their cation-like form, therefore leading to off-diagonal FC activity in both the ZEKE and DF spectra via 15^1 and in the DF spectrum via 16^1; this would not be evident in the calculated Duschinsky matrices. With this in mind, we might therefore expect to have seen $^+15^1$ activity in the ZEKE spectrum recorded via 16^1; however, as we commented on in Sec. III G 4, there is a precipitous drop-off in photoionization cross section of all PIEs recorded to higher wavenumbers, as shown in Fig. 7, followed by further multiphoton activity (not shown and which will be reported at a later date[42]).

B. Comments on photodynamics

The prevalence of the pyrrolyl ring in biomolecules, and the importance of the photostability of biomolecules, has naturally led to the simplest molecules that contain this group, pyrroles and substituted pyrroles, being the targets for photodynamical studies. Of interest is the effect of substituting the N-bonded H atom in pyrrole for a methyl group. It is known that in the S_1 state, pyrrole rapidly loses the N-bound H atom and is presumed to form the pyrrolyl radical and an H atom.[12,21] By analogy, NMP has been suggested to lose a methyl group and also form the pyrrolyl radical.[5] Understanding both how electronically excited molecules fragment and how they efficiently delocalize their energy is the key aspect of understanding the biophysics underpinning solar-radiation-induced radical production, which can lead to cancer formation in living organisms.

As commented on in the above, the first electronically excited state of NMP is Rydberg-like close to the FC region, but at the long range, this state evolves into a σ^* unbound state along the N–CH_3 coordinate. Furthermore, movement along this coordinate involves significant structural changes, mainly involving the CH_3 group evolving from a pyramidal to planar geometry. In Fig. 15, we have optimized the geometry of the S_0 state of NMP at the CAM-B3LYP/aug-cc-pVTZ level and then calculated the vertical excitation energies of excited states at a range of N–CH_3 bond lengths, constraining the rest of the geometric parameters. These plots look similar to those in Ref. 9, and as may be seen, there is a significant barrier to dissociation. We have also optimized the geometries of the ground electronic states of the pyrrolyl radical $(\tilde{X}^2A_2)$ and the CH_3 radical $(\tilde{X}^2A_2'')$ and indicated the energy of this dissociation asymptote in Fig. 15; this confirms that the asymptote of the

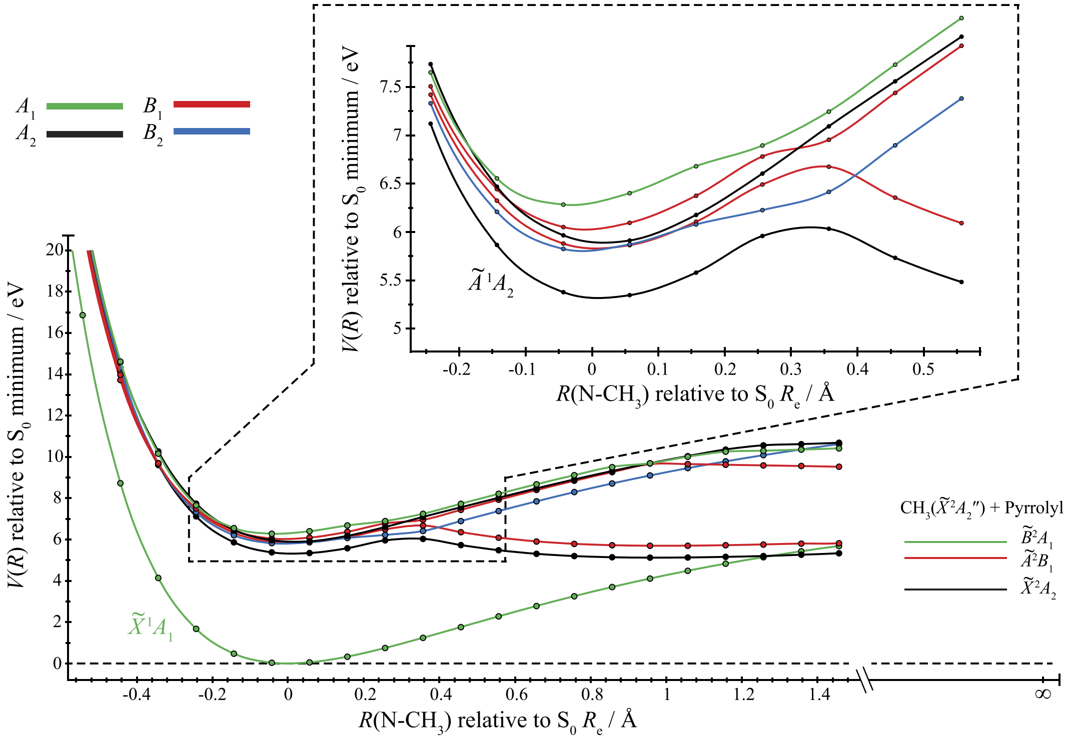

FIG. 15. Calculated, constrained potential energy plots for the ground and lowest six electronically excited states of NMP. TD-CAM-B3LYP/aug-cc-pVTZ level calculations were performed, with the geometry fixed at that optimized for the $\tilde{X}$ state, except for varying the N–CH$_3$ bond length. Vertical excitation energies were calculated at a range of N–CH$_3$ bond lengths for these states to produce the curves shown. In the top right of the figure, an expanded view of the region close to the minima of the excited states is shown. The colors represent the symmetries of the electronic states, as shown in the legend (see also Fig. 3 and text). On the bottom right of the diagram, the lowest three pyrrolyl + CH$_3$ asymptotes are shown. Their energies are obtained by optimizing the geometries of the ground states of the two radicals and then calculating vertical excitation energies. The three lowest asymptotes are found to correspond to ground state CH$_3$, together with three electronic states of pyrrolyl. The coloring indicates the symmetry of the NMP state that correlates with each asymptote. The lowest dissociation asymptote lies significantly below the minimum of the S$_1$ ($^1A_2$) state, consistent with results from photodissociation experiments; relaxed geometry scans would allow these asymptotes to join smoothly to the respective minima.

constrained S$_1$ state is far above the "relaxed" asymptote, with the latter lying below the minimum of the S$_1$ state, in agreement with photodissociation studies.[5,9,11] The optimized geometries of the pyrrolyl and methyl radicals are given in Fig. S2 of the supplementary material; both ground states are found to be planar, with the geometric parameters of pyrrolyl agreeing well with those of Gianola *et al.*[47] Although there are issues with the calculated state ordering in Ref. 8, the relaxed scan shown in Fig. 3 of that work indicates that a barrier still exists to dissociation in the S$_1$ state. In Fig. 15, we have also indicated the positions of the next two dissociation asymptotes, which involve electronically excited pyrrolyl (the pyrrolyl excitation energies used in Fig. 15 are CAM-B3LYP/aug-cc-pVTZ calculated vertical excitations from ground state pyrrolyl). These lie below the asymptotes with electronically excited CH$_3$ (not shown), since the latter are located at >5.7 eV above its ground state.[48] It may be seen that the S$_1$ state of NMP correlates adiabatically with the lowest energy asymptote, pyrrolyl ($\tilde{X}^2A_2$) + CH$_3$ ($\tilde{X}^2A_2''$); we assume that it correlates diabatically to an asymptote involving the 3s Rydberg state of pyrrolyl. The S$_0$ state correlates with the third asymptote and so produces electronically excited pyrrolyl, $\tilde{B}^2A_1$, and ground state CH$_3$. The (a_2, 3p$_y$) $^1B_1$ state presumably dissociates diabatically to produce the 3p$_y$ Rydberg state of pyrrolyl, but adiabatically it produces the first electronic state, $\tilde{A}^2B_1$ plus ground state CH$_3$.

Figure 15 also confirms that the $\tilde{X}$ state potential crosses that of the S$_1$ state along the N–CH$_3$ coordinate; this represents a conical intersection between the S$_1$ and $\tilde{X}$ state surfaces, providing a route for internal conversion (IC) between the two states; the $\tilde{X}$ state also crosses the lowest $^1B_1$ surface. A key route to losing energy in electronically excited NMP (and related molecules) is via IC to the $\tilde{X}$ state. In solution, IC (an isoenergetic process) is followed by subsequent solvent-induced collisional energy loss. If this energy cannot be lost via such mechanisms, for example, in the gas phase under low pressure conditions or in a supersonic jet, then photofragmentation might be expected. We observe that IC to the $\tilde{X}$ state will, of course, produce highly vibrationally excited NMP molecules; although, undoubtedly, this will lead to intramolecular vibrational relaxation (IVR) in the S$_0$ state. As long as the molecule stays on the $\tilde{X}$ state surface, it cannot dissociate, since dissociation on this surface would be to electronically excited pyrrolyl ($\tilde{B}^2A_1$) and CH$_3$

($\tilde{X}^2A_2''$), and this asymptote lies higher in energy than the ground state asymptote (see Fig. 15). Thus, although IC to the $\tilde{X}$ state does represent a population loss mechanism from the S_1 state, it is not a direct route for subsequent dissociation to ground state pyrrolyl + CH_3 products.

Photodissociation can happen on the S_1 surface, but Fig. 15 shows that there would need to be efficient routes around the S_1 state barrier to access the dissociation asymptote, and this may reasonably be expected to depend upon the amount and form of the internal energy and so the molecular motion. It is also possible to envision an indirect mechanism consisting of efficient IC from S_1 to S_0, followed by rapid IVR in S_0, which then leads to a vibrational motion that allows favorable IC back to the S_1 state on the high-R side of the barrier, i.e., with vibrational motion excited that leads to extended vibrationally averaged N–CH_3 bond lengths. This process would be consistent with the observations of Tseng *et al.*[6] and Woo and Kim[11] that there is a time delay before dissociation products are seen. The $S_1 \leftarrow S_0$ IC could thus produce NMP on the other side of the barrier with a longer N–CH_3 bond, which will facilitate unimolecular decay. This process could produce vibrationally excited pyrrolyl and/or CH_3 products, and although some excited CH_3 products have been probed,[5] it would clearly be useful to interrogate other levels and also the pyrrolyl product.

There is very little pyrrolyl$^+$ signal in the mass spectra we record throughout the range of the (1 + 1) REMPI spectrum; furthermore, when we observe the mass spectrum via a two-color process, such as when recording PIE spectra, we only see NMP$^+$ ions (see Figs. S3 and S4 of the supplementary material). The absence of the two-color pyrrolyl$^+$ signal is likely because the ionization energy of pyrrolyl is 9.11 eV;[49] similarly we do not see any significant $CH_3{}^+$ signal, whose ionization energy is 9.84 eV;[50] in both cases, therefore, ionization would require multiple photons. In our one-color experiments, as in Ref. 5, we do see various fragment ions, including weak pyrrolyl$^+$ and $CH_3{}^+$, and this is consistent with the mass spectra shown in Fig. 3 of Ref. 5 (albeit the traces seem to be the wrong way around with respect to the cited excitation wavelengths).

We now comment on some other aspects of the photodynamics studies.

We do not see long progressions involving vibrations that are related to N–CH_3 stretching vibrations over the regions scanned, either in the DF or ZEKE spectra, but this could be because of the limited region of the spectra scanned and that such vibrations would be in-plane. Dissociation of NMP to ground state pyrrolyl + CH_3 products on the S_1 surface will occur along the z-axis of NMP, since pyrrolyl is planar with the unpaired electron in an orbital localized on the nitrogen atom and pointing along the C_2 axis, and the ground state of CH_3 is planar with an electron located in an orbital that is oriented along the methyl C_3 axis. NMP is deduced to dissociate rapidly when in-plane a_1 and b_2 vibrations are excited,[11] and very recent simulations on pyrrole corroborate this observation.[51] It seems clear that once the dissociation asymptote becomes accessible, then dissociation will lead to both fragments experiencing a significant impulse—consistent with the results of photodissociation studies.[5,9,11]

Figure 15 shows that the potential of the lowest excited $^1B_1$ state of NMP has a similar profile as the S_1 state, but correlating to the first excited state of pyrrolyl and ground state CH_3. This state may be playing an intermediate role in other IC processes or, indeed, may be the terminal state, with dissociation on that surface producing electronically excited pyrrolyl. Wu *et al.*[9] have invoked involvement of this state at higher excitation energies. There are various crossings between the lowest $^1B_1$ state and other states, so the IC behavior could be quite complicated. The involvement of excited states at particular excitation energies has also been commented on by others.[5,6,10,11]

Some workers hypothesized that triplet states could be involved in the photodynamics of NMP.[7,10] We observe that each of the open-shell singlet states in Fig. 15 (see also Fig. 3) has an associated triplet state, but since one of the unpaired electrons is in a Rydberg orbital, each of these triplet states would be expected to have potential energy curves that are largely parallel to their corresponding singlets and be close in energy and so exhibit similar behavior. If intersystem crossing (ISC) to the triplet versions of these Rydberg states occurs, we do not think this would lead to dissimilar spectroscopic and dynamical behavior. However, if triplet states are accessed where the two unpaired electrons occupy valence orbitals, this could affect the observed behavior and has been discussed by Blancafort *et al.*[7] for a $\pi\pi^*$ triplet state of NMP.

The Woo and Kim picosecond study[11] appears to be the most comprehensive one to date, in which the lifetimes of many S_1 levels were probed across the internal energy range of ~0–1850 cm^{-1}, with levels accessed by either one- or two-photon excitation. A clear, but non-monotonic, trend was identified of a decrease in lifetime with internal excitation energy of the S_1 state, with occasional small rises in lifetime occurring within the overall downward trend. Furthermore, some of the decay profiles could be fitted with a single time constant, while others required two or three, suggesting different pathways. In particular, IVR was mentioned as a possible explanation for this, with multiple excitations within the width of the picosecond laser being another. We agree with the possibility of the latter for some levels but cannot see that IVR will generally be significant, since the DOS is not very high below 1500 cm^{-1} (Fig. 16); this would be particularly true of levels at very low wavenumbers. However, one exception may be in the 800–850 cm^{-1} region, which was found to have a rather complicated time dependence in Ref. 11, consistent with the excitation of multiple states; the complexity of this feature and the involvement of multiple ZOSs was highlighted in Sec. III G 8.

It was commented in Ref. 11 that the derived lifetimes did not agree with previous work and suggested that this could be associated with different experimental conditions, for example, with regard to the time duration of the laser sources: clearly, very short laser pulses are more likely to excite more than one eigenstate. It is particularly intriguing that only the "fast" CH_3 fragments (with a kinetic energy of ~6000 cm^{-1}) were seen at 183 cm^{-1}, with a slow component (with a kinetic energy ~0 cm^{-1}) appearing weakly at 370 and 641 cm^{-1}; the slow component became dominant at 806 cm^{-1}, with the faster component still sizeable; it was commented[11] that these observations were not wholly in agreement with those of Sage *et al.*[5] A marked change in lifetime was reported at ~700 cm^{-1} ascribed to a non-radiative channel, and it was suggested that this could be the energy at which an S_1/S_n conical intersection could be occurring, but the curves in Fig. 15 seem to suggest that this is unlikely at these low energies, with the caveat that relaxed scans could alter the curves significantly. It is interesting that the "PHOFEX" signal for CH_3 in Ref. 11 decreases significantly at around this internal

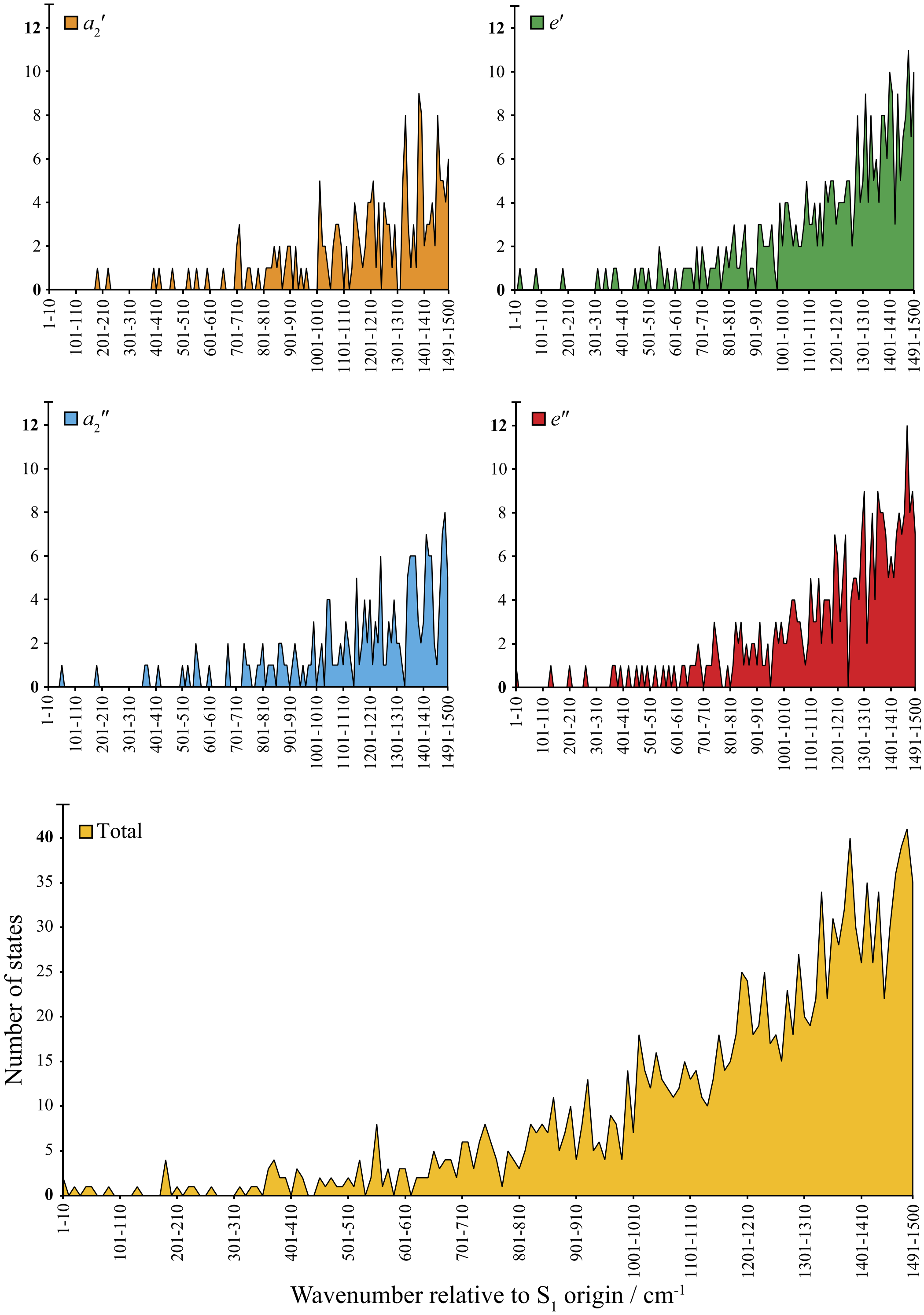

FIG. 16. Density of states (DOS) plots for NMP using calculated vibrational wavenumbers from Table II and torsional levels from Ref. 20; these correspond to the number of states within a 10 cm^{-1} wide window. (The abscissa and ordinate axis labels on the bottom plot of the figure apply to all five plots.) In the top four plots, the DOS has been broken down into the symmetries accessible from $m = 0$ and $m = 1$ of the zero-point vibrational level in the S_1 state and accessing vibrational levels of b_1 (a_2'') or b_2 (a_1'') symmetry, the symmetries of the main inducing vibrations. In the bottom plot, all symmetries are included. In all cases, torsional, vibrational, and vibtor levels have been included. It may be seen that the DOS is relatively low in the 0–1500 cm^{-1} region covered here, and particularly so below 1000 cm^{-1}.

energy, and it was concluded that the dissociation channel decreases in importance as other non-radiative channels open up. We suggest that one explanation for this may be that IC occurs to S_0, followed by IVR and subsequent IC back to S_1, but that at certain energies, it becomes more difficult for the molecule to undergo IC back to the S_1, or perhaps to the $(a_2, 3p_y)\ ^1B_1$ surface, where dissociation can occur. Again, probing the pyrrolyl fragments would be a valuable addition to our knowledge of the photodynamics of this molecule.

V. CONCLUSIONS

In this work, we have presented a detailed assignment of the levels in the S_1 state of NMP based on the appearance of DF, 2D-LIF, and ZEKE spectra. Combined with previous IR and Raman data and quantum chemical calculations, the majority of assignments of the individual S_1 levels are now secure. The assignments largely agree with those of the limited levels studied by Biswas *et al.*[18] as well as many of the suggested assignments put forward by Woo and Kim,[11] with the present work providing either concrete evidence for some of the assignments or new assignments.

We have confirmed the Rydberg nature of the S_1 state in the FC region but have suggested that some vibrationally averaged out-of-plane deviation may occur. This, and other mechanisms discussed, is a possible explanation for the appearance of various "forbidden" bands in some of the ZEKE spectra, particularly when exciting via b_1 vibrations. The main conclusion is that multiple vibronic coupling mechanisms are occurring in the S_1 state.

We find that the DOS build up is relatively slow in this molecule (Fig. 16) and the only significantly congested region of the REMPI spectrum is the 800–850 cm^{-1} region. Even in the latter case, the ZEKE spectra suggest that only limited couplings are occurring, and so this coupling falls into the restricted IVR regime, rather than statistical. Furthermore, different routes for energy delocalization occur under G_{12} symmetry. Some evidence for the involvement of the methyl rotor is seen—this is expected to drive a rapid build-up in the DOS at higher energies, as seen in *p*-fluorotoluene,[52,53] *m*-fluorotoluene,[54] and *p*-xylene.[53]

We have also identified highly unusual behavior following ionization via S_1 15^1 in that the expected $\Delta v = 0$ ZEKE band was surprisingly weak. The appearance of the expected large step in the PIE curve, however, indicates that this is due to unusual photoionization dynamics; this and the drop-offs in the intensities of other PIE curves are currently under further investigation.[42]

In summary, we have confirmed, or obtained for the first time, a number of vibrational wavenumbers for the S_0, S_1, and D_0^+ electronic states and confirmed interactions between vibrational and torsional motion. In principle, therefore, it ought to be possible to gain detailed insight into the photodynamics of NMP, and indeed, level-specific behavior was suggested by Woo and Kim.[11] However, some caution is required relating to both the explicit assignments of that work, particularly as to whether only a single level was excited at particular cited wavelengths; the present study helps that assessment. For example, in the 800–850 cm^{-1} feature, it seems clear that a picosecond laser would have been exciting multiple eigenstates. The present work allows a definitive assignment of the various bands seen in the REMPI spectrum, and hence, the motion of the molecule with particular amounts of internal energy is known. Trying to understand the wealth of photodynamic results will benefit from dynamical modeling, where particular vibrational motion is activated in the S_1 state of NMP, and the effect on the resulting photodissociation studied, as has been reported very recently for pyrrole;[51] this will, of course, require reliable multidimensional potentials, particularly if multiple IC (or ISC) steps occur, as suggested herein. Overall, our results and comments emphasize the utility of knowing which eigenstates are excited in time-dependent experiments and hence reinforces the complementarity of frequency- and time-resolved experiments.

SUPPLEMENTARY MATERIAL

See the supplementary material for correlation between the P_i labels and those of Biswas *et al.*;[18] band profiles of the 16^1, 15^1, and 23^1 LIF bands; optimized geometries of the pyrrolyl and methyl radicals; and mass spectra of NMP recorded in REMPI experiments.

ACKNOWLEDGMENTS

We gratefully acknowledge the EPSRC for funding (Grant No. EP/L021366/1). The EPSRC and the University of Nottingham are thanked for studentships to D.J.K. and A.R.D. In addition, Warren Lawrance (Flinders University) is thanked for useful conversations.

DATA AVAILABILITY

The data that support the findings of this study are available from the corresponding author upon reasonable request.

REFERENCES

[1] V. Bhardwaj, D. Gumber, V. Abbot, S. Dhiman, and P. Sharma, RSC Adv. **5**, 15233 (2015).

[2] S. Chavda, K. Mulder, T. Brown, H. Mackay, B. Babu, L. Westrate, A. Ferguson, S. C. Lin, K. Kiakos, J. P. Ramos, M. Munde, W. D. Wilson, J. A. Hartley, and M. Lee, Med. Chem. **6**, 150 (2010).

[3] C. A. Downes and S. C. Marinescu, ChemSusChem **10**, 4374 (2017).

[4] Y. Fu, X. Cheng, J. Zhao, T. Kong, C. Cui, and X. Zhang, Polym. J. **44**, 1048 (2012).

[5] A. G. Sage, M. G. D. Nix, and M. N. R. Ashfold, Chem. Phys. **347**, 300 (2008).

[6] C.-M. Tseng, Y. T. Lee, and C.-K. Ni, J. Phys. Chem. A **113**, 3881 (2009).

[7] L. Blancafort, V. Ovejas, R. Montero, M. Fernández-Fernández, and A. Longarte, J. Phys. Chem. Lett. **7**, 1231 (2016).

[8] G. Piani, L. Rubio-Lago, M. A. Collier, T. N. Kitsopoulos, and M. Becucci, J. Phys. Chem. A **113**, 14554 (2009).

[9] G. Wu, S. P. Neville, O. Schalk, T. Sekikawa, M. N. R. Ashfold, G. A. Worth, and A. Stolow, J. Chem. Phys. **144**, 014309 (2016).

[10] T. Geng, O. Schalk, T.Hansson, and R. D.Thomas, J. Chem. Phys. **146**, 144307 (2017).

[11] K. C. Woo and S. K. Kim, Phys. Chem. Chem. Phys. **21**, 14387 (2019).

[12] G. Wu, S. P. Neville, O. Schalk, T. Sekikawa, M. N. R. Ashfold, G. A. Worth, and A. Stolow, J. Chem. Phys. **142**, 074302 (2015), and references therein.

[13] G. Milazzo, Gazz. Chim. Ital. **74**, 152 (1944).

[14] R. McDiarmid and X. Xing, J. Chem. Phys. **105**, 867 (1996).

[15] C. D. Cooper, A. D. Williamson, J. C. Miller, and R. N. Compton, J. Chem. Phys. **73**, 1527 (1980).

[16] J. G. Philis, Chem. Phys. Lett. **353**, 84 (2002).

[17] J. G. Philis, J. Mol. Struct. **651–653**, 567 (2003).

[18] N. Biswas, S. Wategaonkar, and J. G. Philis, Chem. Phys. **293**, 99 (2003).

[19] N. Kanamaru, J. Mol. Struct.: THEOCHEM **686**, 15 (2004).

[20] A. R. Davies, D. J. Kemp, and T. G. Wright, Chem. Phys. Lett. **763**, 138227 (2021).

[21] M. J. Paterson and D. Townsend, Int. Rev. Phys. Chem. **39**, 517 (2020).

[22] M. N. R. Ashfold, S. G. Clement, J. D. Howe, and C. M. Western, J. Chem. Soc., Faraday Trans. **89**, 1153 (1993).

[23] D. W. Scott, J. Mol. Spectrosc. **37**, 77 (1971).

[24] T. J. Dines, L. D. Macgregor, and C. H. Rochester, J. Colloid Interface Sci. **245**, 221 (2002).

[25] K. B. Beć, R. Wieczorek, B. Łydżba-Kopczyńska, and J. P. Hawranek, Acta Phys. Pol., A **124**, 115 (2013).

[26] V. L. Ayles, C. J. Hammond, D. E. Bergeron, O. J. Richards, and T. G. Wright, J. Chem. Phys. **126**, 244304 (2007).

[27] A. M. Gardner, W. D. Tuttle, L. E. Whalley, and T. G. Wright, Chem. Sci. **9**, 2270 (2018).

[28] N. J. Reilly, T. W. Schmidt, and S. H. Kable, J. Phys. Chem. A **110**, 12355 (2006).

[29] J. R. Gascooke and W. D. Lawrance, Eur. Phys. J. D **71**, 287 (2017).

[30] P. R. Bunker and P. Jensen, *Molecular Symmetry and Spectroscopy*, 2nd ed. (NRCC, Ottawa, Canada, 1998).

[31] A. L. Sobolewski and W. Domcke, Chem. Phys. **259**, 281 (2000).

[32] A. L. Sobolewski, W. Domcke, C. Dedonder-Lardeux, and C. Jouvet, Phys. Chem. Chem. Phys. **4**, 1093 (2002).

[33] A. R. Davies, D. J. Kemp, and T. G. Wright, J. Mol. Spectrosc. **376**, 111410 (2021).

[34] A. M. Gardner and T. G. Wright, J. Chem. Phys. **135**, 114305 (2011).

[35] A. Andrejeva, A. M. Gardner, W. D. Tuttle, and T. G. Wright, J. Mol. Spectrosc. **321**, 28 (2016).

[36] W. D. Tuttle, A. M. Gardner, A. Andrejeva, D. J. Kemp, J. C. A. Wakefield, and T. G. Wright, J. Mol. Spectrosc. **344**, 46 (2018).

[37] D. J. Kemp, W. D. Tuttle, F. M. S. Jones, A. M. Gardner, A. Andrejeva, J. C. A. Wakefield, and T. G. Wright, J. Mol. Spectrosc. **346**, 46 (2018).

[38] G. Herzberg, *Molecular Spectra and Molecular Structure: III. Electronic Spectra of Polyatomic Molecules* (Krieger, Malabar, 1991).

[39] A. E. W. Knight, C. S. Parmenter, and M. W. Schuyler, J. Am. Chem. Soc. **97**, 1993 (1975).

[40] A. E. W. Knight, C. S. Parmenter, and M. W. Schuyler, J. Am. Chem. Soc. **97**, 2005 (1975).

[41] J. Li, X. Y. Li, C. Y. Zhu, and S. H.Lin, Phys. Chem. Chem. Phys. **12**, 14967 (2010).

[42] A. R. Davies and T. G. Wright, "Unusual photoionization behavior in *N*-methylpyrrole" (unpublished).

[43] A. M. Gardener, L. E. Whalley, D. J. Kemp, W. D. Tuttle, and T. G. Wright, J. Chem. Phys. **151**, 154302 (2019).

[44] A. D. Baker, D. Betteridge, N. R. Kemp, and R. E. Kirby, Anal. Chem. **42**, 1064 (1970).

[45] G. J. Rathbone, E. D. Poliakoff, J. D. Bozek, and R. R. Lucchese, Can. J. Chem. **82**, 1043 (2004).

[46] D. J. Kemp, A. M. Gardner, W. D. Tuttle, J. Midgley, K. L. Reid, and T. G. Wright, J. Chem. Phys. **149**, 094301 (2018).

[47] A. J. Gianola, T. Ichino, R. L. Hoenigman, S. Kato, V. M. Bierbaum, and W. C. Lineberger, J. Phys. Chem. A **108**, 10326 (2004).

[48] G. Herzberg and J. Shoosmith, Can. J. Phys. **34**, 523 (1956).

[49] F. Holzmeier, I. Wagner, I. Fischer, A. Bodi, and P. Hemberger, J. Phys. Chem. A **120**, 4702 (2016).

[50] A. M. Schulenburg, C. Alcaraz, G. Grassi, and F. Merkt, J. Chem. Phys. **125**, 104310 (2006).

[51] D. V. Makhov and D. V. Shalashilin, J. Chem. Phys. **154**, 104199 (2021).

[52] D. J. Kemp, W. D. Tuttle, A. M. Gardner, L. E. Whalley, and T. G. Wright, J. Chem. Phys. **151**, 064308 (2019).

[53] W. D. Tuttle, A. M. Gardner, L. E. Whalley, D. J. Kemp, and T. G. Wright, Phys. Chem. Chem. Phys. **21**, 14133 (2019).

[54] A. R. Davies, D. J. Kemp, and T. G. Wright, AIP Adv. **10**, 125206 (2020).

12.1. Comment on “Electronic, vibrational and torsional coupling in *N*-methylpyrrole: ground, first excited and cation states” [J. Chem. Phys. 154, 224305 (2021)]

Abstract: “Two-color (1 + 1′) zero-electron-kinetic-energy (ZEKE) and photoionization efficiency (PIE) spectra are reported via different levels in the $S_1 \leftarrow S_0$ ($\tilde{A}^1A_2 \leftarrow \tilde{X}^1A_1$) one-photon transition of jet-cooled *N*-methylpyrrole. The laser radiation is produced using two dye lasers, one with an 1800 l/mm grating and one with 2400 l/mm. We report spectra where the excitation and ionization radiation are produced with both combinations of the dye lasers; these spectra differ markedly. This is attributed to Wood’s anomalies with the 2400 l/mm grating: one aspect is a loss in light intensity over a range of wavelengths, attributed to a resonance anomaly. Another is the appearance of a “shadow” ZEKE spectrum and PIE curve at apparently higher ionization wavenumbers; under some conditions, a third ZEKE spectrum was observed—these latter observations arise from higher-order dispersion effects, likely caused by a Rayleigh anomaly. We comment on these observations and report more representative ZEKE and PIE spectra than those presented in a recent paper by our group [A. R. Davies, D. J. Kemp, and T. G. Wright, *J. Chem. Phys.* **154**, 224305 (2021)] for four intermediate S_1 levels.”

Authors: Alexander R. Davies, David J. Kemp and Timothy G. Wright
Submitted to: Journal of Chemical Physics, 13th July 2021
Published: 15th September 2021
Reference: A. R. Davies, D. J. Kemp and T. G. Wright, *J. Chem. Phys.*, 2021, **155**, 117101.
DOI: 10.1063/5.0063264

Summary: Here, we discuss the ZEKE spectra of three b_1 vibrations and one b_2 vibration, in light of our investigation into the ‘ZEKE shadows’ observed in the ZEKE spectra of NMP in Section 12. We conclude it is a combination of a grating resonance anomaly (often referred to as “Wood’s anomaly”), which reduces the efficiency of the grating of the dye laser in a certain energetic region but also, interestingly, the Rayleigh anomaly, which, under certain conditions, redistributes the light into higher propagating orders. It is the latter which is largely responsible for the ‘ZEKE shadows’, which arose from second- and (on occasion) third-order diffraction from the dye laser grating. To support our findings, we present ZEKE spectra and PIE curves ionising with a different dye laser, with a different grating; these are more akin to what one would expect, and we clearly observe a strong $\Delta(v, m) = 0$ band in the ZEKE spectrum *via* 15^1, which was previously absent or very weak. We also present dye curves for the dyes used in the experiment and we clearly see the reduction in efficiency arising from the resonance anomaly in the grating affected, followed by a distinct return of signal due to higher-order dispersion, arising from the Rayleigh anomaly, which are not observed in a dye curve of an unaffected grating. Finally, we discuss the effect of the resonance and Rayleigh anomalies in terms of molecular spectra which, to our knowledge, had not been reported previously.

Contributions: All ZEKE spectra, dye curves and PIE curves were recorded by myself. All figures were produced by myself. Discussions with TGW were had on what data was required for the experiments and how to present them in the figures, with analysis by myself and TGW (which was rather straightforward in light of the work presented in Section 12). Additionally, I read and commented on multiple versions of the manuscript and discussed and implemented the comments from the reviewers to form the final version of the paper.

Reproduced from *J. Chem. Phys.*, 2021, 155, 117101, with the permission of AIP Publishing.

The Journal of Chemical Physics COMMENT scitation.org/journal/jcp

Comment on "Electronic, vibrational and torsional couplings in *N*-methylpyrrole: Ground, first excited and cation states" [J. Chem. Phys. 154, 224305 (2021)]

Cite as: J. Chem. Phys. **155**, 117101 (2021); doi: 10.1063/5.0063264
Submitted: 13 July 2021 • Accepted: 20 August 2021 •
Published Online: 15 September 2021

Alexander R. Davies, David J. Kemp, and Timothy G. Wright[a)]

AFFILIATIONS

School of Chemistry, University of Nottingham, University Park, Nottingham NG7 2RD, United Kingdom

[a)] **Author to whom correspondence should be addressed:** Tim.Wright@nottingham.ac.uk. **Telephone:** +44 115 8467076. **Fax:** +44 115 9513562

ABSTRACT

Two-color (1 + 1′) zero-electron-kinetic-energy (ZEKE) and photoionization efficiency (PIE) spectra are reported via different levels in the $S_1 \leftarrow S_0$ ($\tilde{A}^1A_2 \leftarrow \tilde{X}^1A_1$) one-photon transition of jet-cooled *N*-methylpyrrole. The laser radiation is produced using two dye lasers, one with an 1800 l/mm grating and one with 2400 l/mm. We report spectra where the excitation and ionization radiation are produced with both combinations of the dye lasers; these spectra differ markedly. This is attributed to Wood's anomalies with the 2400 l/mm grating: one aspect is a loss in light intensity over a range of wavelengths, attributed to a resonance anomaly. Another is the appearance of a "shadow" ZEKE spectrum and PIE curve at apparently higher ionization wavenumbers; under some conditions, a third ZEKE spectrum was observed—these latter observations arise from higher-order dispersion effects, likely caused by a Rayleigh anomaly. We comment on these observations and report more representative ZEKE and PIE spectra than those presented in a recent paper by our group [A. R. Davies, D. J. Kemp, and T. G. Wright, J. Chem. Phys. **154**, 224305 (2021)] for four intermediate S_1 levels.

INTRODUCTION

In a very recent paper,[1] we reported (1 + 1) and (2 + 2) resonance-enhanced multiphoton ionization (REMPI) spectra of *N*-methylpyrrole (NMP), as well as a significant number of two-dimensional laser-induced fluorescence (2D-LIF) and zero-electron-kinetic-energy (ZEKE) spectra recorded through a wide range of S_1 intermediate levels—these significantly extended an earlier study of the torsional levels of NMP using 2D-LIF and ZEKE spectroscopy.[2] In that recent study,[1] photoionization efficiency (PIE) spectra were also reported. The collection of spectra reported in Ref. 1 allowed many vibrational fundamental wavenumbers to be established in the S_0, S_1, and D_0^+ states. The work in Refs. 1 and 2 built on the dispersed fluorescence, LIF, and REMPI work by Philis[3,4] and Biswas *et al.*,[5] as well as the time-resolved study by Woo and Kim.[6]

The present work focuses on some unusual observations we made when recording the ZEKE and PIE spectra in Refs. 1 and 2, regarding which we made only passing comment in Ref. 1. These will be described and discussed in the section titled Observations and that titled Wood's Anomalies and their Effect on the ZEKE Spectra.

EXPERIMENTAL

The apparatus used is the same as employed earlier.[1,7] In all of the present experiments, a free-jet expansion of the vapor above room-temperature NMP liquid (Sigma-Aldrich, 99% purity) seeded in 2–3 bar Ar was employed.

For the ZEKE and PIE spectra of NMP, the focused outputs of two dye lasers (Sirah Cobra-Stretch) were overlapped spatially and temporally and passed through a vacuum chamber coaxially and counterpropagating, where they intersected the free-jet expansion. One of these dye lasers had a 2400 l/mm grazing incidence grating, and the other had an 1800 l/mm grazing incidence grating. In our earlier work,[1,2] the excitation laser was always the one with 1800 l/mm, while the ionization laser was always the one with 2400 l/mm. In the present work, we will present ZEKE and PIE spectra, both recorded with the same configuration of lasers and also by reversing the roles of the lasers (also switching the dye, of course); for the latter case, extended wavenumber scans will also be presented. In both cases, the excitation laser was pumped with the third harmonic (355 nm) of a Surelite III Nd:YAG laser (Continuum) operating with Coumarin 480 and was frequency doubled. The ionization laser operated with either Coumarin 440 or Stilbene 420. In the experiments reported in Ref. 1, the dye laser with the 2400 l/mm grating (the ionization laser) was pumped with the third harmonic (355 nm) of a Surelite I Nd:YAG laser (Continuum); however, in the experiments reported here, it was pumped with a second Surelite III Nd:YAG laser (Continuum). In all cases, the output of the ionization laser was always undoubled. During the scans, data were only collected when the grating mirror had stopped moving.

We also report a photoionization efficiency (PIE) spectrum for a selected S_1 level, where we fix the excitation laser on that level and then scan the ionization laser across the ionization threshold, recording the NMP$^+$ ion yield.

The jet expansion passed between two biased electrical grids located in the extraction region of a time-of-flight mass spectrometer, which was employed in the PIE experiments. These grids were also used in the ZEKE experiments by application of pulsed voltages, giving typical fields of ~10 V cm^{-1} after a delay of ~2 μs; this delay was minimized while avoiding the introduction of excess noise from the prompt electron signal. The resulting main ZEKE bands had widths of ~5 to 7 cm^{-1}, although narrower ZEKE bands were seen to have higher wavenumbers in each spectrum—see the section titled Observations. Electron and ion signals were recorded on separate sets of microchannel plates.

OBSERVATIONS

The nomenclature used for vibrations, torsions, and electronic states is explained in Refs. 1, 2, and 8.

To set the scene, we present four pairs of ZEKE spectra in Fig. 1. For each pair, one (upper red trace) was recorded with the 1800 l/mm grating dye laser (frequency doubled output) as the excitation laser and the 2400 l/mm dye laser (fundamental output) as the ionization laser; the second of the pair (lower black trace) was recorded with the roles of the dye lasers switched, viz., the 2400 l/mm dye laser (frequency doubled output) as the excitation laser and the 1800 l/mm grating dye laser (fundamental output) as the ionization laser. It is immediately obvious that for higher wavenumbers, the spectra in each pair are very different. Furthermore, in the cases when the 2400 l/mm grating laser is used as the ionization laser, the low-wavenumber structure appears again at a higher wavenumber but with the bands having half the width of the lower-wavenumber spectrum and the spacing between these bands also halved—we shall refer to this as the first "shadow" ZEKE spectrum. On a number of occasions, this structure appeared again at even higher wavenumbers, but now with the bands a third of the width of the lower-wavenumber spectrum and the spacings also a third—we refer to this as the second "shadow" ZEKE spectrum. ZEKE "shadow" spectra were only seen when the 2400 l/mm dye laser was used as the ionization laser and was seen on all occasions, i.e., via all intermediate S_1 levels considered in Ref. 1, when a scan went high enough in wavenumber to capture this. Note that, pending the further investigations reported herein, we only presented the regions of the ZEKE spectra in Ref. 1 that did not show the "shadow" spectra.

In Ref. 1, we also reported PIE spectra via the S_1 14^1, S_1 15^1, and S_1 16^1 vibrational levels, which showed sharp steps in line with the strongest ZEKE bands, as expected. However, as we commented on in that work, we saw a sudden drop-off in the intensity of the initial PIE band at higher wavenumbers. We also commented on, but did not show, that there was a second PIE spectrum at even higher wavenumbers—we refer to the latter as a PIE "shadow" spectrum. It was postulated in Ref. 1 that the "shadow" PIE and ZEKE bands may have been arising from the absorption of more than one photon from the ionization laser—this is now known not to be the case, as will be demonstrated. At the bottom of Fig. 1, we show the PIE spectrum recorded via the S_1 15^1 vibrational level with the two configurations of the dye lasers; it may be seen that it is only with the 2400 l/mm grating that the large loss of intensity occurs, and for which the shadow PIE band appears. (The decay in the ion signal at the higher wavenumber side of the PIE spectrum, recorded with the 1800 l/mm grating as the ionization laser, is due to the fall-off in the Coumarin 440 dye efficiency at these wavenumbers—see Fig. 2.)

WOOD's ANOMALIES AND THEIR EFFECT ON THE ZEKE SPECTRA

The explanations for our observations are twofold, with the first being an issue we perhaps ought to have identified earlier and the second being an unusual phenomenon that is less well-known. To aid our discussions, in Fig. 2 we present dye curves for the two dyes employed in the ionization laser, Coumarin 440 and Stilbene 420, as recorded with both of the dye lasers used.

The loss of signal in the ZEKE spectra, and its subsequent return when recorded with the 2400 l/mm grating, occurs as a result of the anomalies reported by Wood,[9,10] with there being two main types: Rayleigh anomalies[11,12] and resonance anomalies.[13,14] (Early on, such grating anomalies were considered by Fano[15] and are related to Rowland ghosts.[16,17]) Resonance anomalies cause a dramatic reduction in the efficiency of the 2400 l/mm grating in this region of the spectrum and is generally accepted to arise from surface phonons that occur across the grating at certain incidence angles and at certain wavelengths; they depend upon the groove separation of the grating, among other things. Rayleigh anomalies cause a redistribution of energy into other propagating orders. These effects occur most prominently for light that is polarized perpendicular to the grating groove direction, as is the case in our dye lasers. The resonance anomaly is well known;[14] however, owing to the appearance of the "shadow" ZEKE bands, which we conclude are due to a Rayleigh anomaly, we had not appreciated the role that the 2400 l/mm dye laser output was playing across the range where the ZEKE spectra in Fig. 1 were recorded. (Wood's anomalies for the 1800 l/mm

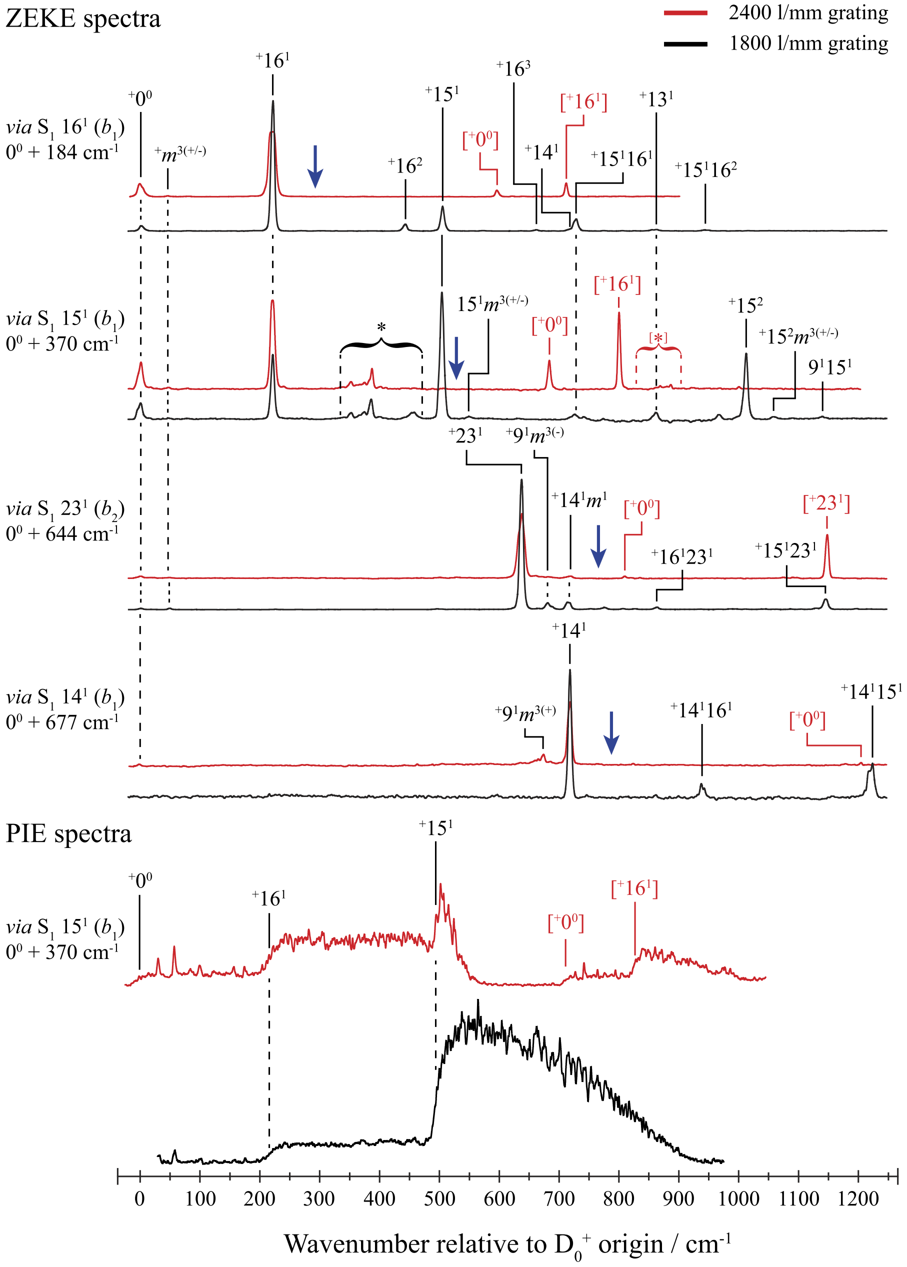

FIG. 1. (Top) ZEKE spectra recorded via four S_1 intermediate levels with their C_{2v} symmetry indicated. Each spectrum was recorded using two configurations of the two dye lasers employed, and the coloring of the traces indicates the grating used for the ionization laser. In the upper (red) traces, the fundamental output of the dye laser with a 2400 l/mm grating was used as the ionization laser. In the lower (black) traces, the fundamental output of the dye laser with an 1800 l/mm grating was used as the ionization laser. The lower-wavenumber regions of the upper traces, up to the arrows, are essentially those reported in Figs. 7 and 10(a) of Ref. 1 and, we now believe, are affected by Wood's anomalies; the higher-wavenumber regions of these spectra after the arrows (not shown in Ref. 1) show "shadow" ZEKE spectra—see text. (The arrows indicate the approximate position at which the spectra were truncated in Ref. 1 and where the first-order light output of the 2400 l/mm grating drops to zero—see Fig. 2.) The lower (black) traces are not affected by Wood's anomalies and hence represent the true ZEKE spectra via the indicated S_1 intermediate levels. Assignments are given for the main bands based on previous work,[1] with the corresponding "shadow" ZEKE band assignments on the upper (red) traces being indicated in square brackets. (Unless explicitly indicated, assignments refer to both $m = 0$ and $m = 1$ components; further discussion is provided in Ref. 1.) The asterisks mark multiple bands, which are discussed in Ref. 1. (Bottom) PIE spectra recorded via the S_1 15^1 level, with the coloring of the traces matching those of the corresponding ZEKE spectra. At higher wavenumbers, the loss of PIE signal in the black trace arises due to the loss of efficiency of the Coumarin 440 dye (see Fig. 2). The loss of the PIE signal in the range ~550 to 700 cm^{-1} in the red trace is due to a resonance anomaly; the PIE signal in the red trace above 700 cm^{-1} arises from higher-order dispersion caused by the Rayleigh anomaly—see text. The PIE spectra have been shifted so that the center of the largest step aligns with the $^+15^1$ ZEKE band—this corrects for the larger electric field used in the PIE experiments compared to that employed in the ZEKE experiments.

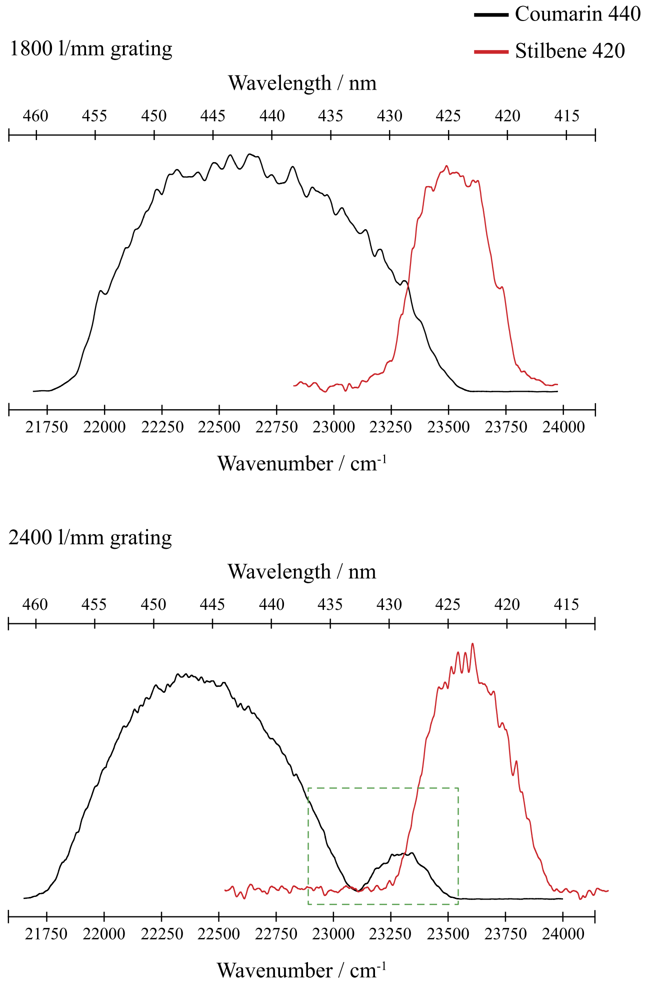

FIG. 2. Dye curves recorded for Coumarin 440 and Stilbene 420—the two dyes employed in the ionization laser—as indicated. (Stilbene 420 was not used in the 2400 l/mm grating dye laser for the photoionization experiments but is included here for completeness.) The dashed box in the bottom part of the figure indicates the approximate position of Wood's anomalies for the 2400 l/mm grating, with the smaller, higher-wavenumber feature being due to higher-order dispersion effects. In all plots, the abscissa scales refer to the expected dye laser outputs over the range of the dye laser resonator scanned.

grating occur in the range 555–575 nm and so are far removed from the spectral regions covered in the present work.)

In the present case, we believe that the resonance anomaly causes a loss of intensity of the main ZEKE bands, as can be clearly seen by comparing the upper and lower traces of each pair of ZEKE spectra in Fig. 1, and echoes the observation made by Wood[9,10] where, for one of the gratings used therein, one of the sodium D lines was absent in the recorded spectrum. Related to this, Kessel[18] has highlighted that in fluorescence emission spectra of solutions, the appearance of spectra can be altered owing to Wood's anomalies and can be detected by re-recording spectra with a second grating with a different l/mm spacing or by adding a polarizer between the emission source and the grating; indeed, the latter is used routinely to avoid this issue.[19] Here, we were able to use an alternative grating, which will be seen to overcome the issue; testing the polarizer solution is impractical with our systems.

ZEKE spectra recorded with the interchanged configuration of the dye lasers such that the ionization laser is now the one with the 1800 l/mm grating are shown as the bottom trace (black) of each pair in Fig. 1. Two things are evident: the "shadow" bands are no longer present, and the new ZEKE spectra have an extended structure at higher wavenumbers. The latter is attributable both to the absence of a resonance anomaly at these wavenumbers for the 1800 l/mm grating and the fact that we have extended the ZEKE spectra to higher wavenumbers than those of Ref. 1 by using the Stilbene 420 dye. In Fig. 1, we also provide assignments for the main bands that were not present in the ZEKE spectra of Ref. 1. It is now evident that, contrary to the surprising appearance of the ZEKE spectra recorded via S_1 16^1 and S_1 15^1 noted in Ref. 1, these ZEKE spectra are as expected, in terms of the dominant $\Delta v = 0$ bands, since the intermediate S_1 electronic state is largely Rydberg-like in the Franck–Condon region. These new observations support the main conclusions of Ref. 1; in particular, both the presence of the origin band and the large change in wavenumber for the P_{15} and P_{16} vibrations upon ionization, contrary to the expectation from the Rydberg character of the S_1 state, are both still significant observations from the ZEKE spectra and were discussed in full detail in Ref. 1. We highlight that when considering the ZEKE spectra recorded with the 1800 l/mm grating in the ionization laser and comparing to those recorded with the 2400 l/mm grating in the ionization laser, together with the dye curves reported in Fig. 2, some of the ZEKE bands at higher wavenumbers ought to have been visible if the second "hump" in the dye curve arose from first-order dispersion. It is clear that ZEKE bands are not present, and it is only the shadow ZEKE bands that are present in that region—we will come back to this below. At the bottom of Fig. 1, the PIE spectrum via S_1 15^1 that was recorded with the 2400 l/mm grating dye laser as the ionization laser, shows a similar effect to the ZEKE spectra, with the loss of signal and then a recurrence of signal at higher wavenumbers, across the region where Wood's anomalies occur; however, such effects are absent when the 1800 l/mm grating dye laser is used as the ionization laser. As we mentioned in Ref. 1, we did not always see the $^{+}15^1$ ZEKE band when exciting via S_1 15^1, as is the case in the spectrum recorded with the 2400 l/mm grating we present in Fig. 1, and it is likely a result of differing performance of the dye, which degrades rapidly with use. Finally, we point out that in the PIE curve in Fig. 1 and as seen in those in Ref. 1, there are some bands seen in the low-wavenumber region. We have still not established the origin of these, but they likely arise from complex resonances involving Rydberg states converging to the various vibrational photoionization limits.

We believe that the "shadow" ZEKE and PIE spectra arise from enhanced intensity in second and third order dispersion from the grating associated with the Rayleigh anomaly. We were initially slightly misled on this since the spacings between the "shadows" were not simply the expected half or a third of the spacings in the main spectrum when viewed *on a wavenumber scale.* In Fig. 3, we plot the ZEKE spectrum recorded via the S_1 16^1 intermediate level on an apparent wavelength scale (i.e., the dye laser wavelength reading, based on the number of grating motor steps from a

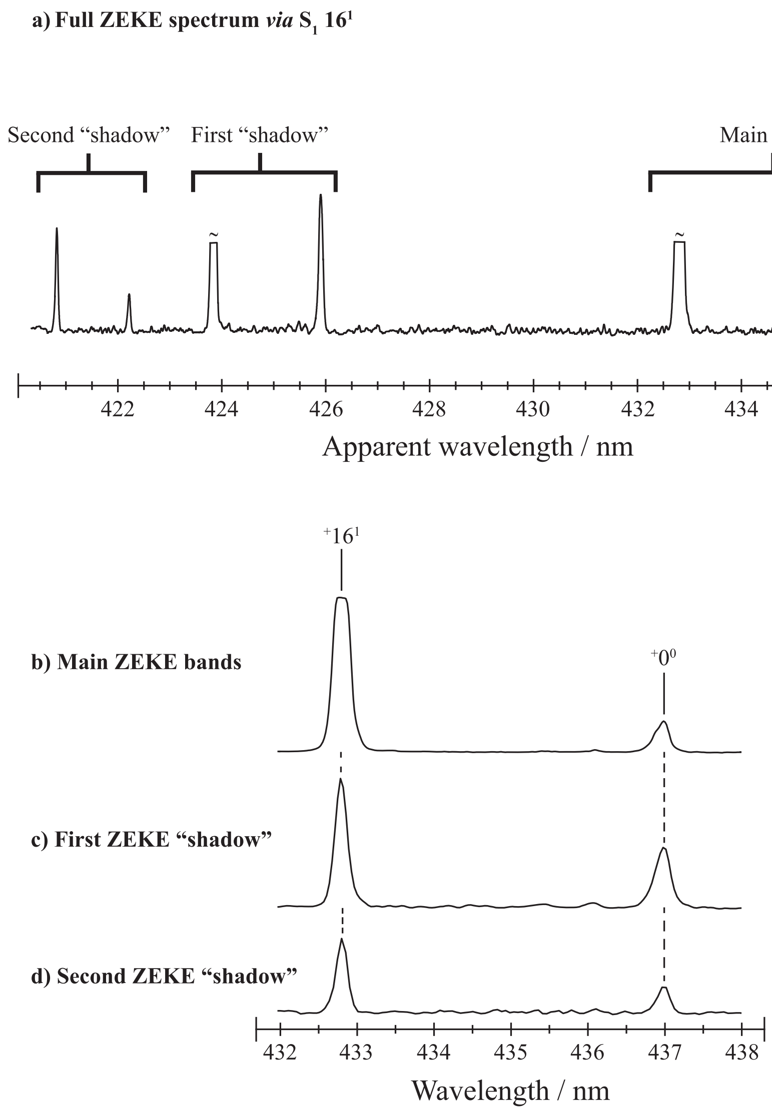

FIG. 3. ZEKE spectra obtained with the 2400 l/mm grating dye laser used as the ionization laser. In (a), the main spectrum is shown, plus the first and second "shadow" spectra presented on a wavelength scale as deduced directly from the dye laser calibration; the most intense bands have been truncated. In (b), the main bands only are shown on the wavelength scale, with the $^{+}16^{1}$ band slightly saturated. In (c), the dye laser wavelength scale has been expanded by a factor of two, and the spectrum shifted to align the first "shadow" spectrum with the main spectrum. In (d), the dye laser wavelength scale has been expanded by a factor of three, and the spectrum shifted to align the second "shadow" spectrum with the main spectrum. It may be seen that the main and two shifted, scaled spectra are essentially the same, indicating that the "shadow" spectra arise from higher-order dispersion.

factory-set "zero"). We then plot this again twice, scaled by factors of two and three and offset so as to match up the first bands of the main and "shadow" spectra. (The wavenumbers reported here are *in vacuo*, while the wavelengths are *in aerem*.) These offset spectra strongly suggest that the source of the "shadow" ZEKE spectra is indeed higher-order dispersion that occurs from the 2400 l/mm grating. Such higher-order spectral lines have, for example, been seen for grazing incidence gratings using X-radiation as a function of the grating angle, where the bands also appear with decreased width.[20]

The non-appearance of the main ZEKE bands at higher wavenumbers, even when the dye curve suggests that light is present, coupled with the appearance of the shadow ZEKE bands, leads us to conclude that the second hump in the dye curve recorded for Coumarin 440 (highlighted in Fig. 2) arises solely from a second-order dispersion effect and actually comprises the same wavelengths of light that produce the main dye band. As can be seen from Fig. 2, the dye curves are slightly misleading, as it initially appears that the Coumarin 440 dye curve from the 2400 l/mm grating is merely missing some of the output, attributed to the resonance anomaly; in fact, the first-order output is missing over a wider range of wavelengths <434 nm (>23000 cm^{-1}), and the apparent recovery of the dye laser output is actually due to the onset of the second-order dispersion effect. (Unfortunately, we do not have dye curves that show the expected additional hump that would correspond to the appearance of the second "shadow," since, as remarked, we only saw these on a few occasions, and we attribute this to favorable dye laser powers on those occasions.)

Although there is a wealth of literature on Wood's anomalies—for example, see Ref. 21—these are often specialist publications in optics, and it is not clear to us that the present behavior has been previously examined explicitly in molecular spectroscopy, in the production of the observed "shadows."

ASSIGNMENT OF THE SPECTRA

The assignments of the ZEKE spectra are included in Fig. 1 based on the experimental and calculated vibrational wavenumbers presented in Ref. 1. For the purposes of discussing the assignments, we shall only refer to the ZEKE spectra recorded with the 1800 l/mm grating dye laser as the ionization laser, i.e., in the absence of the ZEKE "shadows." We can see that the $\Delta v = 0$ band is the most intense feature in all of the spectra shown in Fig. 1, in agreement with the S_1 state being Rydberg-like in the Franck–Condon region and in line with the majority of the spectra shown in Ref. 1; these also confirm the assignments of the S_1 vibrational levels used as intermediate states. In particular, the $^{+}15^{1}$ ZEKE band is the most intense when exciting via S_1 15^1, which was not the case in Ref. 1, and as can also be seen in Fig. 1 when using the 2400 l/mm grating dye laser for ionization. There is now also the expected cross-activity of the $^{+}16^{1}$ and $^{+}15^{1}$ ZEKE bands when exciting through the S_1 16^1 and S_1 15^1 intermediate levels.

We highlight that for intermediate S_1 vibrational bands of b_1 C_{2v} point group symmetry (a_2'' G_{12} molecular symmetry), we see ZEKE bands made up of the $\Delta v = 0$ level but in combination with each of $^{+}16^{1}$, $^{+}15^{1}$, and $^{+}14^{1}$. This is similar to the behavior seen in the 2D-LIF spectra reported in Ref. 1, for which it is even more marked, with the combination emission bands involving 15_1 actually being the most intense. The ZEKE behavior reported in the present work is further confirmation of the vibronic coupling discussed in Ref. 1, which we suggested causes the marked difference in the vibrational wavenumber of P_{15} and P_{16} between the S_1 and ground cationic state, notwithstanding the Rydberg nature of the former; this is in contrast to the majority of vibrations where the wavenumbers were very similar in both states. Moreover, the new ZEKE spectra are now in line with the expected $\Delta v = 0$ behavior.

FINAL REMARKS

Here, we have presented spectra that show an unusual behavior arising from Wood's anomalies. The unusual behavior arises from the use of a particular grating for the ionization step and affects both ZEKE and PIE spectra; the unusual behavior has been shown to be an artifact by recording spectra with a grating with a different groove density (l/mm). Newly reported in the present work, when Wood's anomalies are present, we see a partial ZEKE spectrum that is then repeated at an apparently higher wavenumber, but this has been shown to be spurious due to a higher-order dispersion effect—the Rayleigh anomaly; on occasions, a second such spectrum was observed. Although Wood's anomalies are well known, the effect on a resolved molecular spectrum does not appear to have been reported previously. Interestingly, while this might be regarded as a nuisance to be aware of, such anomalies have been proposed as ways of developing sensors.[22]

ACKNOWLEDGMENTS

We acknowledge the EPSRC for funding (Grant No. EP/L021366/1). The EPSRC and the University of Nottingham are acknowledged for studentships to D.J.K. and A.R.D.

DATA AVAILABILITY

The data that support the findings of this study are available from the corresponding author upon reasonable request.

REFERENCES

[1] A. R. Davies, D. J. Kemp, and T. G. Wright, J. Chem. Phys. **154**, 224305 (2021).

[2] A. R. Davies, D. J. Kemp, and T. G. Wright, Chem. Phys. Lett. **763**, 138227 (2021).

[3] J. G. Philis, Chem. Phys. Lett. **353**, 84 (2002).

[4] J. G. Philis, J. Mol. Struct. **651-653**, 567 (2003).

[5] N. Biswas, S. Wategaonkar, and J. G. Philis, Chem. Phys. **293**, 99 (2003).

[6] K. C. Woo and S. K. Kim, Phys. Chem. Chem. Phys. **21**, 14387 (2019).

[7] V. L. Ayles, C. J. Hammond, D. E. Bergeron, O. J. Richards, and T. G. Wright, J. Chem. Phys. **126**, 244304 (2007).

[8] A. R. Davies, D. J. Kemp, and T. G. Wright, J. Mol. Struct. **376**, 111410 (2021).

[9] R. W. Wood, London, Edinburgh Dublin Philos. Mag. J. Sci. **4**, 396 (1902), the text of this article seems to be the same as that of Ref. 10.

[10] R. W. Wood, Proc. Phys. Soc., London **18**, 269 (1902), the text of this article seems to be the same as that of Ref. 9.

[11] Lord Rayleigh, Proc. R. Soc. London, Ser. A **79**, 399 (1907).

[12] Lord Rayleigh, London, Edinburgh Dublin Philos. Mag. J. Sci. **14**, 60 (1907).

[13] A. Hessel and A. A. Oliner, Appl. Opt. **4**, 1275 (1965).

[14] C. Palmer, *Diffraction Grating Handbook* (MKS Instruments, Rochester, 2020).

[15] U. Fano, J. Opt. Soc. Am. **31**, 213 (1941).

[16] H. A. Rowland, London, Edinburgh Dublin Philos. Mag. J. Sci. **35**, 397 (1893).

[17] H. G. Gale, Astrophys. J. **85**, 49 (1937).

[18] D. Kessel, Photochem. Photobiol. **54**, 481 (1991).

[19] See, for example, E. J. Morgan, J. M. Rippey, and S. A. Tucker, Appl. Spectrosc. **60**, 551 (2006).

[20] Q. Huang, I. V. Kozhevnikov, A. Sokolov, Y. Zhuang, T. Li, J. Feng, F. Siewert, J. Viefhaus, Z. Zhang, and Z. Wang, Opt. Express **28**, 821 (2020).

[21] A. A. Maradudin, I. Simonsen, J. Polanco, and R. M. Fitzgerald, J. Opt. **18**, 024004 (2016), and references therein.

[22] F. Liu and X. Zhang, Biosens. Bioelectron. **68**, 719 (2015).

13. Spectroscopy of *N*-methylpyrrole-RG (RG = Ar, Kr) complexes: first excited neutral and cationic states

Abstract: "*N*-methylpyrrole-RG (RG = Ar, Kr) complexes are investigated using resonance-enhanced multiphoton ionization (REMPI) and zero-electron-kinetic-energy (ZEKE) spectroscopy. The presence of the RG atom makes the electronic transition allowed, and the REMPI spectrum is blue-shifted compared to the *N*-methylpyrrole origin, with no bands associated with vibrational excitation of the *N*-methylpyrrole moiety. The nature of the electronic structure of the S_1 state is discussed. Binding energies are obtained for all three electronic states. Adiabatic ionization energies are obtained from the ZEKE spectra, yielding values of 64077 ± 5 cm^{-1} and 64029 ± 5 cm^{-1} for RG = Ar and Kr, respectively."

Authors: Alexander R. Davies, Jessica T. L. Haynes and Timothy G. Wright
Submitted to: Chemical Physics Letters, 30th March 2022
Published: 19th June 2022
Reference: A. R. Davies, J. T. L. Haynes and T. G. Wright, *Chem. Phys. Lett.*, 2022, **803**, 139800.
DOI: 10.1016/j.cplett.2022.139800
Supplementary material: see Appendix 4

Summary: We present REMPI and ZEKE spectra of NMP-RG (RG = Ar, Kr) and find the structure in the REMPI spectrum of NMP-RG is surprisingly localised in wavenumber, with two distinct bands, followed by a broad, unstructured region. We deduce that we observe the origin of NMP-RG which implies that the addition of RG is sufficient to perturb the electronic structure of NMP from its pseudo-C_{2v} symmetry. Furthermore, the origin of NMP-RG is blue-shifted from the reported origin of NMP, indicating that the S_1 state is less strongly bound than the ground state, in line with the NMP $S_1 \leftarrow S_0$ transition being a $3s \leftarrow \pi$ transition (in the FC region), with the RG competing with the 3s Rydberg electron for the ionic core. We also note the ZEKE spectra are surprisingly ‘clean’, with distinct bands, even as one excites *via* the broad, unstructured part of the REMPI spectrum, although we do observe a multitude of structure that is tricky to assign. We propose this is a result of the intermolecular modes of the S_1 state coupling with the torsional levels and that many transitions become allowed owing to the decrease in symmetry and, additionally, the overlap of m^0 and m^1 in the S_1 state.

From these spectra, we deduce the adiabatic ionisation energies for NMP-Ar and NMP-Kr, as well as determining the binding energies of NMP-RG in the S_1 state (of which is a lower bound in the case of NMP-Kr, owing to the REMPI spectrum gradually decaying into the baseline at higher scanning wavenumber rather than the intensity dropping abruptly as occurs in the REMPI spectrum of NMP-Ar). From this, we then determine the binding energies of the cation and ground state, and compare these to quantum chemical calculations. We note that the (R)CCSD(T) calculations on the CAM-B3LYP geometries yield binding energies in good agreement with the experimental binding energies, even though only a modestly sized basis set was employed.

Contributions: REMPI and ZEKE spectra were recorded by myself assisted by JTLH, a Master’s student under my supervision; quantum chemical calculations were conducted by myself, with analysis between myself, TGW and JTLH. Figures were created by myself, with input from TGW. Furthermore, I have read through multiple iterations of the manuscripts and discussed and implemented the changes requested by the referees to yield the final version of the paper.

Chemical Physics Letters 803 (2022) 139800

Contents lists available at ScienceDirect

Chemical Physics Letters

journal homepage: www.elsevier.com/locate/cplett

Spectroscopy of *N*-methylpyrrole-RG (RG = Ar, Kr) complexes: First excited neutral and ground cationic states

Alexander R. Davies, Jessica T.L. Haynes, Timothy G. Wright

School of Chemistry, University of Nottingham, University Park, Nottingham NG7 2RD, UK

ARTICLE INFO

Keywords:
N-methylpyrrole
Rare gas
Complexes
REMPI
ZEKE
Ionization

ABSTRACT

N-methylpyrrole-RG (RG = Ar, Kr) complexes are investigated using resonance-enhanced multiphoton ionization (REMPI) and zero-electron-kinetic-energy (ZEKE) spectroscopy. The RG atom makes the electronic transition to the S_1 state allowed, and the REMPI spectrum is blue-shifted compared to the *N*-methylpyrrole origin, with no bands associated with vibrational excitation of the *N*-methylpyrrole moiety. The nature of the electronic structure of the S_1 state is discussed. Binding energies are obtained for all three electronic states. Adiabatic ionization energies are obtained from the ZEKE spectra, yielding values of 64077 ± 5 cm^{-1} and 64029 ± 5 cm^{-1} for RG = Ar and Kr, respectively.

1. Introduction

In recent work [1-4], we have examined the electronic spectroscopy of the S_1 electronic state of *N*-methylpyrrole (NMP), probing the vibronic interactions using two-dimensional laser-induced fluorescence (2D-LIF), resonance-enhanced multiphoton ionization (REMPI), and zero-electron-kinetic-energy (ZEKE) spectroscopy. The work built upon earlier spectroscopic [5-9] and photodissociation [10-16] studies by a number of workers; additionally, very recently a far infrared spectrum of NMP has been reported [17]. The S_1 state of NMP is found to be a largely Rydberg-like 3s state in the Franck-Condon region of the S_1 ($^1A_2$) ← S_0 ($^1A_1$) transition, but at extended N–CH_3 bond lengths, the state evolves into a σ* state. Although there has been a microwave study [18] of NMP–Ar, which concluded the Ar atom is located above the pyrrolyl ring in the ground electronic state, we are unaware of any studies on excited or cationic states of complexes of NMP, which we rectify herein by reporting REMPI and ZEKE spectra of NMP–RG (RG = Ar, Kr). Part of the impetus for this is to investigate whether the perturbation of the electronic structure by the RG atom is sufficient to render the origin transition symmetry allowed, as well as to see whether it is possible to observe intermolecular and torsional motion for such complexes. The ZEKE spectra would also be expected to yield ionization energies and, together with the REMPI spectra, binding energies in the different states should be available. This would be the first step in investigating the role of solvation on this forbidden electronic transition. This also opens up the possibility of undertaking ultrafast experiments to see how solvation affects the photophysics of NMP and perhaps pyrrole itself – a key chromophore in many biomolecules.

2. Experimental

The REMPI/ZEKE [19] apparatus is the same as that employed in our recent studies on NMP [1-3]. In all of the present experiments, a free-jet expansion of the vapour above room-temperature NMP liquid (Sigma-Aldrich, 99% purity) was employed. For the NMP–Ar complexes, the backing gas was pure Ar at a pressure of 3 bar, while for the NMP–Kr complexes, mixtures of 20–40% Kr in Ar were employed, with a total pressure of 2–3 bar.

For the one-colour REMPI experiments, we employed the frequency-doubled output of a dye laser (Sirah CobraStretch), operating with Coumarin 480 and pumped with the third harmonic of a Surelite III Nd:YAG laser. For the two-colour REMPI and ZEKE spectra of NMP, the focused outputs of two dye lasers (Sirah CobraStretch) were overlapped spatially and temporally, and passed through a vacuum chamber coaxially and counterpropagating, where they intersected the free-jet expansion. The excitation laser was the same for all REMPI and ZEKE experiments, while the ionization laser for the two-colour REMPI and ZEKE experiments operated with Coumarin 440, pumped with the third harmonic (355 nm) of a Surelite I Nd:YAG laser, and the fundamental output was employed.

The jet expansion passed between two biased electrical grids located in the extraction region of a time-of-flight mass spectrometer, which was employed in the REMPI experiments. These grids were also used in the ZEKE experiments by application of pulsed voltages, giving typical fields

---

E-mail address: Tim.Wright@nottingham.ac.uk (T.G. Wright).

https://doi.org/10.1016/j.cplett.2022.139800
Received 30 March 2022; Received in revised form 13 June 2022; Accepted 15 June 2022

of ~10 V cm^{-1}, after a delay of ~2 μs (this delay was minimized while avoiding the introduction of excess noise from the prompt electron signal). The resulting ZEKE bands had widths of ~5–7 cm^{-1}. The electron and ion signals were each recorded on a separate set of microchannel plates.

3. Quantum chemistry

Quantum chemistry calculations were undertaken using density functional theory, for which we employed the CAM-B3LYP functional [20] to better-describe long-range interactions than the B3LYP functional itself, which we had used previously for NMP [2,3].

We optimized the geometries of three different isomers of the S_0 and D_0^+ states using the (U)CAM-B3LYP/aug-cc-pVTZ level of theory: one with the RG atom above the NMP ring, one with the RG approaching the methyl group, and one with the RG approaching the NMP molecule from the opposite end from the methyl group – see Figure S1 of the Supplementary Material. These calculations indicated that the lowest-energy isomer was the one with the RG atom above the ring, in agreement with the results of a microwave study [18].

We also calculated binding energies for the S_0 and D_0^+ states. This was done at the CAM-B3LYP level by simply subtracting the energy of the complex from that of each of the RG and NMP species, with the latter at its (U)CAM-B3LYP/aug-cc-pVTZ-optimized geometry. Single-point (R) CCSD(T) calculations using the same geometry and basis set were also undertaken, and counterpoise-corrections were undertaken to obtain the basis set superposition error (BSSE). This was obtained for each moiety at the complex geometry and was then subtracted from the aforementioned calculated binding energy. The latter calculations confirmed that the lowest-energy isomer was the ring-bound one, again consistent with the results of a microwave study [18].

Fully optimizing the geometry of the S_1 state of the ring-based structure proved problematic, and so we froze the NMP moiety at the TD-CAM-B3LYP/aug-cc-pVTZ optimized geometry, and then optimized the position of the RG atom for the above-ring structure, again using the TD-CAM-B3LYP method. For NMP–Kr, we then relaxed and fully-optimized the structure, and found a minimum with an intermolecular bond length only 0.02 Å longer; although this procedure was still unsuccessful for NMP–Ar, the NMP–Kr result suggests that the unfreezing of the NMP moiety would make little difference to the calculated intermolecular separation.

4. Results

In Figs. 1 and 2 we present the REMPI spectra of NMP–Ar and NMP–Kr, respectively. In the case of NMP–Ar, these were recorded for the dominant isotopologue involving ^{40}Ar. In the case of NMP–Kr, the combined signals involving all naturally-occurring isotopes of Kr were recorded, since it is not anticipated that any isotopic differences will be discernible with the resolution of our lasers. As noted above, both one-colour and two-colour REMPI spectra were recorded, and these were found to be very similar. The spectra shown in Figs. 1 and 2 have been selected based on their quality and minimal interference from NMP resonances.

Although we scanned > 750 cm^{-1} to lower wavenumber and > 750 cm^{-1} to higher wavenumber, in both cases, signal was only obtained over a narrow range of wavenumbers (see Figs. 1 and 2); in particular, no structure was observed that is associated with excitation of the NMP-localized vibrational modes that were active in NMP itself. [2,16] Although chromophore-localized structure can be seen in the REMPI spectra of complexes of other molecules, such as complexes of phenol with methanol [21] and others,[22,23] often the focus is on the intermolecular bands associated with the origin transition, such as in work on complexes of substituted benzenes.[24,25] Interestingly, for complexes of benzene with rare gases, the symmetry lowers from $D_{6h} \rightarrow C_{6v}$ upon complexation, but the origin transition remains forbidden and so intermolecular modes have been studied in combination with the degenerate ν_6 vibration [26-28], which induces the vibronic activity in $S_1 \leftarrow S_0$ absorption spectrum. In the present case of NMP–RG complexes, the symmetry lowering causes the $S_1 \leftarrow S_0$ origin transition that is forbidden in NMP, to become allowed.

In line with the present quantum chemical calculations and microwave studies of the NMP–Ar complex [18], we assume that we observe the global minimum, with the RG atom above the ring. (Although it is possible that more than one isomer could be produced during the non-equilibrium conditions of the supersonic jet expansion, there is nothing in the REMPI or ZEKE spectra to suggest that there is more than one isomer present in the free-jet expansion.).

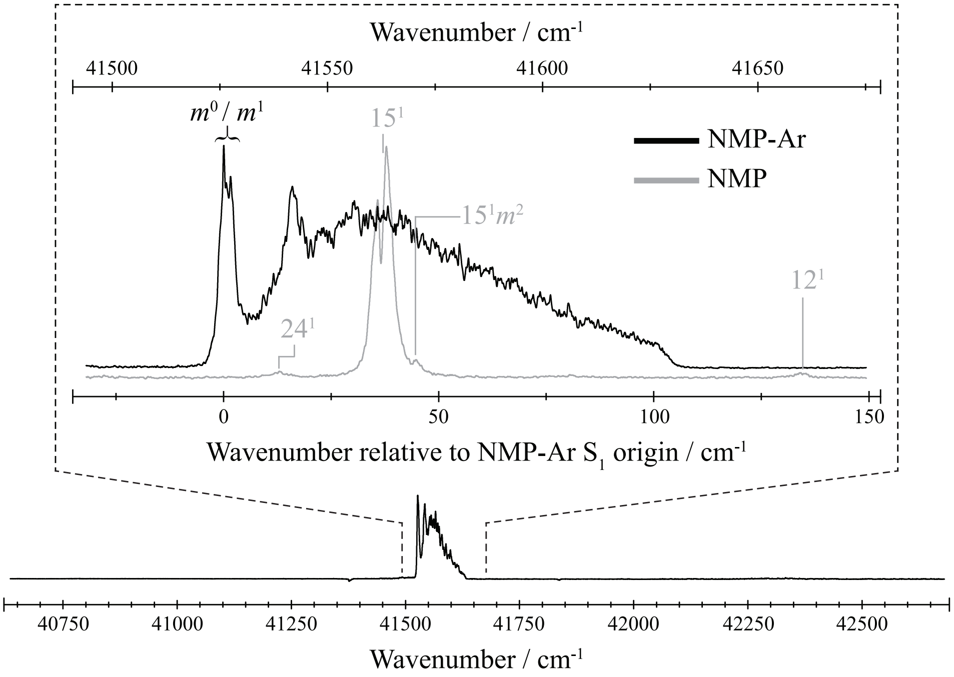

Fig. 1. (1 + 1′) REMPI spectrum of NMP–Ar (with the ionization laser set at 22916 cm^{-1}). The lower trace shows the spectrum over the full range scanned (1 cm^{-1} step size), showing that signals over a very limited wavenumber range were obtained. The upper trace shows a 0.2 cm^{-1} step-size scan of the NMP–Ar spectrum and, in grey, a section of the NMP spectrum, to indicate where accidental excitations of the monomer might occur. Although this is a cold spectrum, it is possible that signals from hot NMP complexes could contribute to the regions around these bands – these would be expected to be significantly weaker than the cold monomer bands, but still potentially significant compared to the much weaker complex signals.

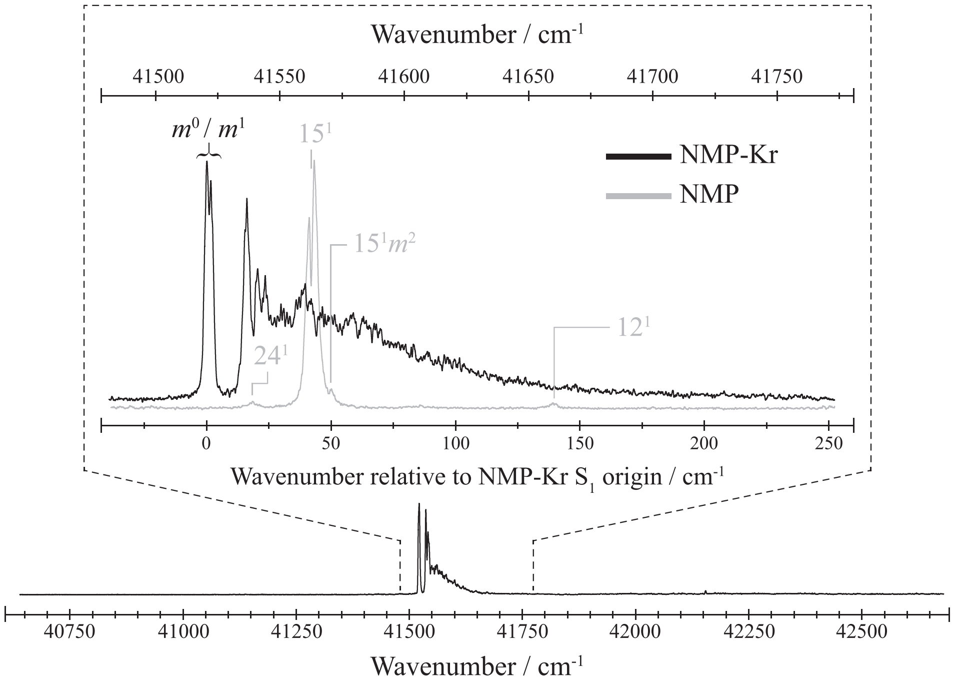

Fig. 2. (1 + 1) REMPI spectrum of NMP–Kr. The lower trace shows the spectrum over the full range scanned (1 cm^{-1} step size), showing that signals over a very limited wavenumber range were obtained (the weak feature at ca. 42240 cm^{-1} is spurious). The upper trace shows a 0.2 cm^{-1} step-size scan of the NMP–Kr spectrum and, in grey, a section of the NMP spectrum, to indicate where accidental excitations of the monomer might occur. Although this is a cold spectrum, it is possible that signals from hot NMP complexes could contribute to the regions around these bands – these would be expected to be significantly weaker than the cold monomer bands, but still potentially significant compared to the much weaker complex signals.

5. Assignments and discussion

5.1. REMPI spectra

The REMPI spectrum of NMP–Ar in Fig. 1 shows a strong band at 41527 cm^{-1}, which we shall conclude is the origin band, based upon the ZEKE spectra discussed in the next subsection; there is then a small gap followed by another discrete band, before a broad feature. To higher wavenumber is a well-defined drop in intensity marking the end of the observed spectrum. As mentioned above, and as shown in Fig. 1, we scanned a wide range of wavenumbers above and below this REMPI spectrum, and no other features were seen. We can immediately make several observations. First, that the appearance of the origin band in the one-photon electronic spectrum suggests that the presence of the Ar atom is sufficient to perturb the NMP electronic structure from its effective C_{2v} symmetry, such that the $\tilde{A}^1A_2 \leftarrow \tilde{X}^1A_1$ transition, dipole forbidden in NMP itself, becomes allowed. Secondly, the observation of the drop in intensity at higher wavenumber gives an estimate of the dissociation energy of the $\tilde{A}$ state of NMP–Ar, D_0', of ≈ 105 ± 2 cm^{-1}. Thirdly, the lack of observation of any other bands to higher or lower wavenumber suggests that the REMPI spectrum in Fig. 1 is associated with vibrationless NMP, and that levels associated with vibrational excitation of NMP in its $\tilde{A}$ state are rapidly depopulated by some mechanism – presumably the presence of the low-frequency, anharmonic intermolecular vibrations accelerates the various processes that have been discussed for the short lifetimes of the NMP excited vibrational levels [2,10,11,12,13,14,15,16]. Fourthly, the spectrum is blue-shifted with respect to the NMP spectrum, whose origin is at 41193 cm^{-1} (Ref. [16]), indicating that the S_1 state of NMP–Ar is less-strongly bound than the S_0 state – see below.

Similar comments apply to the similar-looking REMPI spectrum of NMP–Kr shown in Fig. 2. Again, a strong origin band is seen at 41522 cm^{-1}, with some further structured bands, followed by a broad feature to higher wavenumber. This time there is no clear drop-off in intensity to higher wavenumber, but a gradual decay. Since diminishing Franck-Condon factors, for example, can also cause a loss of intensity in the spectrum, only lower-bound estimate of the dissociation energy of the $\tilde{A}$ state, $D_0' \geq 170$ cm^{-1} can be deduced from where the NMP–Kr REMPI spectrum reaches the baseline at higher wavenumber. Again, the spectrum is blue-shifted with respect to that of NMP itself.

The spectra are very different to those observed previously for complexes of RG atoms with substituted benzenes, where discrete bands are seen with no significant unstructured region – in the case of toluene–RG complexes, which also have a hindered methyl rotor, the bands have been assigned to transitions involving intermolecular vibrations and hindered rotor levels [24,25]. In particular, we note that Gascooke and Lawrance [25] were able to identify contributions from a_1 and e symmetry levels, using 2D-LIF spectroscopy. We will make further comments regarding the REMPI spectra of the NMP–RG complexes, in the light of the ZEKE spectra, in the next subsection.

Regarding the nature of the electronic structure, it is known that the S_1 state of NMP, arising from a 3s ← π excitation, is Rydberg-like in the Franck-Condon region. For the S_1 state of the NMG–RG complexes, we have both a 3s Rydberg electron and the RG atom each competing for the NMP$^+$ cationic core. This situation is reminiscent of the $\tilde{A}\ ^2\Sigma^+$ states of the NO–RG complexes, corresponding to a 3s ← π* excitation on NO, where the state was unbound for RG = Ne [29], and weakly bound for RG = Ar, Kr and Xe [30-32], with the interaction becoming stronger as the polarizability of RG increased, but all significantly more weakly-bound than the corresponding cations. As here, the REMPI spectrum of NO–Ar was blue-shifted with respect to the corresponding transition in NO, indicating the $\tilde{A}$ state was less strongly bound than the $\tilde{X}$ state. This was explained in terms of the competition between the low-lying 3s Rydberg electron and the RG atom for the NO$^+$ cationic core. For the S_1 states of the NMP–RG complexes, we also conclude that the interaction of the RG atom with the NMP$^+$ core is weakened by the presence of the low-lying 3s electron, so that the RG atom largely is interacting with a neutral molecule, rather than wholly with the cationic core. This is in-line with the calculated S_1 optimized geometry, notably the significantly longer intermolecular bond lengths than in the S_0 state.

5.2. ZEKE spectra

We show the low-wavenumber regions of ZEKE spectra recorded for NMP–Ar and NMP–Kr in Figs. 3 and 4, respectively.

When exciting via the origin band, well-defined structure can be seen in the ZEKE spectra at low wavenumber; the structure is somewhat

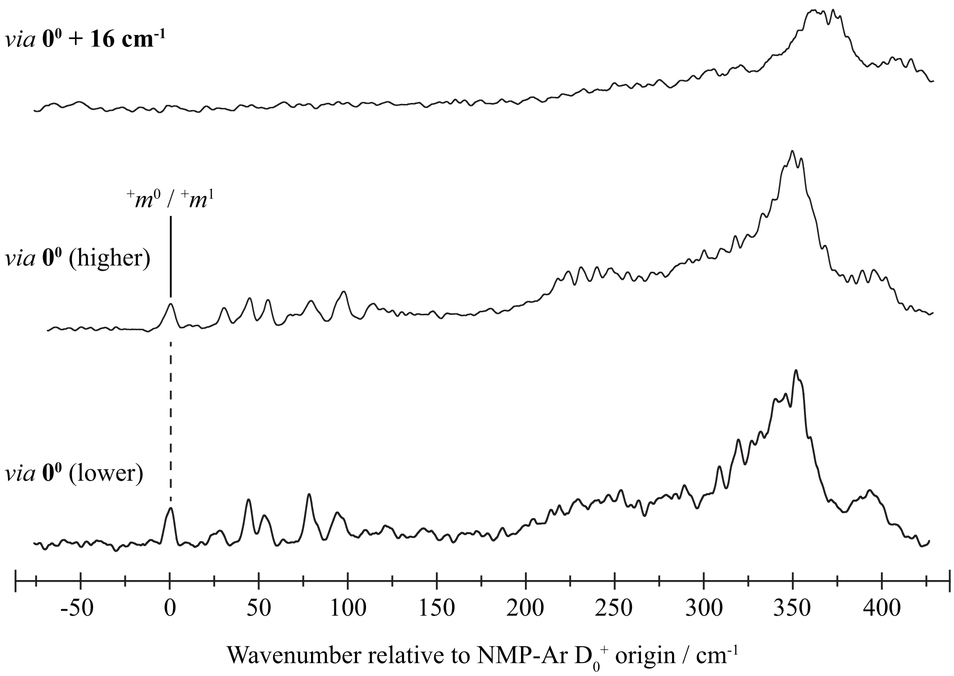

Fig. 3. Low-wavenumber region of ZEKE spectra of NMP–Ar exciting through the indicated levels. Assignments have only been given for the lowest wavenumber band, since many of the levels are expected to have mixed character owing to Fermi resonances and vibration-torsional coupling – see text.

clearer for NMP–Kr than it is for NMP–Ar. This structure is likely to arise from a mixture of torsional and intermolecular vibrations in the D_0^+ state, as seen for the S_0 and S_1 states of toluene–RG (RG = Ar–Xe) by Mons et al. [24] and toluene–Ar by Gascooke and Lawrance [25]. In our previous work on NMP [1], it was found that a $\Delta m = 0$ propensity rule was strongly adhered to – this was in line with the Rydberg-like nature of the S_1 state of NMP in the Franck-Condon region. The NMP–RG complexes differ from NMP in several ways: the symmetry is lowered, making the electronic transition allowed; the torsional potential for NMP–RG will not be the same as for NMP itself, with the introduction of a V_3 term into the torsional potential if the RG atom lies along the z axis of the complex, with other V_n terms arising if the RG atom is positioned asymmetrically; the S_1 state is not expected to be Rydberg-like (see below).

We first address the fact that we might expect to see two different origins, corresponding to the m^0 and m^1 transitions in the REMPI spectrum. The splitting between the first two main REMPI bands is too large to be these, as seen, for example, by comparing to the distinct origins seen for *m*-fluorotoluene [33-35] and *o*-fluorotoluene [33]. The first REMPI bands here do show a small splitting, but the ZEKE spectra from each are essentially identical (see Figs. 3 and 4), and so we associate this with overlapping, unresolved rotational structure. As a consequence, we conclude that the m^0 and m^1 transitions are heavily overlapped in our spectra (we note that these are separated by only 0.9 cm^{-1} in toluene–Ar [25]). For *m*-fluorotoluene, which also has G_6 molecular symmetry, significant torsional structure is seen in the ZEKE spectrum; in addition, there is a change in the sign of the potential upon ionization leading to the $\Delta m = 0$ propensity rule not being followed [35,36]. For NMP, the phase of the potential does not change between the S_1 and D_0^+ states [1], and so we do expect the $\Delta m = 0$ propensity rule to be followed; hence, we would expect to see a strong, overlapped $^{+}m^{0,1}$ ZEKE band, with less-intense, but sizeable $^{+}m^2$, $^{+}m^{3(+)}$ and $^{+}m^4$ ($\Delta m = 3$) bands; contributions from the $\Delta m = 6$ bands and others would be expected to be weak.

We expect the torsional levels will also be similar to those of NMP$^+$ reported in Ref.1. We refrain from giving specific assignments except for the origin bands, since: some bands are overlapped; each band has a width arising from unresolved rotational structure and some are asymmetric; some intermolecular levels are likely to be in Fermi resonance [24,25]; and there is likely to be coupling between torsional and intermolecular vibrational levels forming "vibtor" eigenstates [25] – thus, levels may have varying admixtures of intermolecular and torsional character. Given the preceding discussion, and the present resolution in the ZEKE spectra, we do not feel we can extract any further detailed information of the make-up of the cationic intermolecular vibration/torsion states in the NMP–RG complexes, nor can we determine the V_n and F parameters in the torsional potential. (Even in the microwave study of NMP–Ar [18], the V_6 parameter had to be assumed to be the same as that for NMP within the fit.)

Taking the first band in each ZEKE spectrum as the adiabatic ionization energy (AIE), gives values of 64077 ± 5 cm^{-1} for NMP–Ar, and 64029 ± 5 cm^{-1} for NMP–Kr. These suggest stabilization of the NMP cation by 173 cm^{-1} and 221 cm^{-1} for each of Ar and Kr, respectively. (Note that we do not correct the AIE for the applied field, since such corrections are imprecise, particularly for larger molecules where decay of the lower-lying Rydberg states means the true field-shifted ionization energy onset is seldom seen [37]).

When we excited via the level associated with the second discrete band in the REMPI spectrum for NMP–Ar at $0^0 + 16$ cm^{-1}, we find that the low-wavenumber structure is absent (Fig. 3), with only broad structure to higher wavenumber. We suggest that, comparing with the observations in NMP–Kr, this indicates that the transition intensity to the intermolecular modes has been dissipated to numerous cation levels, but since the transitions are weaker than those in NMP–Kr, each is too weak to be discerned in the present work. In the NMP–Kr spectrum (Fig. 4), however, significant structure can be seen when exciting through other levels, although the intensities of the different bands vary significantly. For example, when exciting the second band ($0^0 + 16$ cm^{-1}), it can be seen that the origin is much less intense, but that there is a plethora of activity up to ∼300 cm^{-1}. This is consistent with a significant change in the intermolecular potential upon ionization. It is possible that the second REMPI band consists of overlapped intermolecular bend and m^2 torsional transitions, for both complexes. We cannot be certain of the assignment of the other two bands in the NMP–Kr REMPI spectrum; but since they are too low in wavenumber to be overtones or other torsional levels, we suggest that one arises from the second bending mode, while the other is the stretch, but the ordering

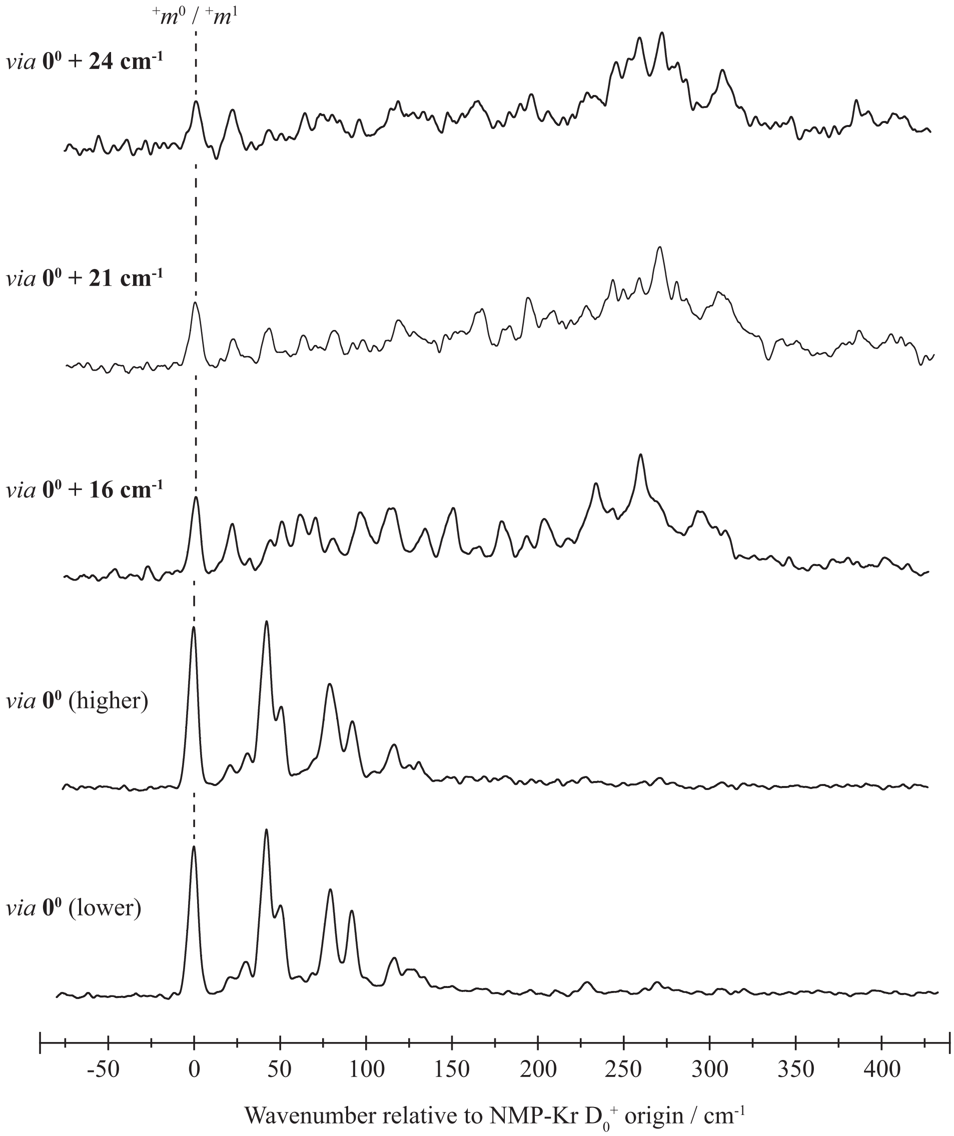

Fig. 4. Low-wavenumber region of ZEKE spectra of NMP–Kr exciting through the indicated levels. Assignments have only been given for the lowest wavenumber band, since many of the levels are expected to have mixed character owing to Fermi resonances and vibration-torsional coupling – see text.

is not obvious.

It is difficult to ascribe the unstructured region of the REMPI spectrum wholly to significant coupling between S$_1$ state intermolecular and torsional levels, and so it may arise from rapid internal conversion, intersystem crossing or from coupling to levels around the barrier to dissociation, i.e. mechanisms discussed in other studies on NMP [2,12,14,16], but all enhanced by both the presence and the anharmonicity of the intermolecular motions. This is notable, since this lack of structure is present at very low internal energies; indeed, even low-energy torsional levels, such as $m^{3(+)}$ and m^4, both observed in uncomplexed NMP [1], are seemingly contained within this broad feature. In other ZEKE spectra (not shown), other bands, often broad, were seen to higher energy than the features shown in Figs. 3 and 4, and this was particularly the case when exciting within the broad features of the REMPI spectra. Several of these appear to be associated with excitation of the NMP monomer – for example, coincidentally exciting the 24^1 band or 15^1 bands (see Figs. 1 and 2). It is not possible that the NMP–RG complexes have dissociated to form NMP + RG at these low energies. In addition, to still higher wavenumber than that shown, effects were seen in all ZEKE spectra arising from the presence of Wood's and Rayleigh anomalies associated with the 2400 l/mm grating employed in the ionization dye laser, as discussed in Ref. 3, to which the reader is referred for further commentary; as such, we do not discuss this further here. In the future, recording higher wavenumber regions of the ZEKE spectra with a different grating and/or mass-analyzed threshold ionization (MATI) spectra, would likely give further insight into whether any NMP-localized vibrational excitation is present in the photoionization spectra of these complexes.

5.3. Binding energies

In the above for NMP–Ar, we have deduced a value of $D_0 \approx 105$ cm^{-1} for the S$_1$ state, and using the T_0' values for NMP and NMP–Ar, we obtain a value for the S$_0$ state, $D_0'' = 440$ cm^{-1}. Similarly, for NMP–Kr, a lower bound value of $D_0 \geq 170$ cm^{-1} is found for the S$_1$ state, and using the T_0' values for NMP and NMP–Kr, we obtain a lower-bound value for D_0'' of ≥ 500 cm^{-1}. It can be seen that both of these values are consistent with the calculated CCSD(T) values in Table 1. In contrast, it can be seen that the CAM-B3LYP binding energies are significantly different to the CCSD(T) ones, and in poor agreement with experiment.

When each AIE is combined with the $D_0^+ \leftarrow S_1$ ionization energy of the relevant complex, and using the AIE of NMP from Ref. 1, then using

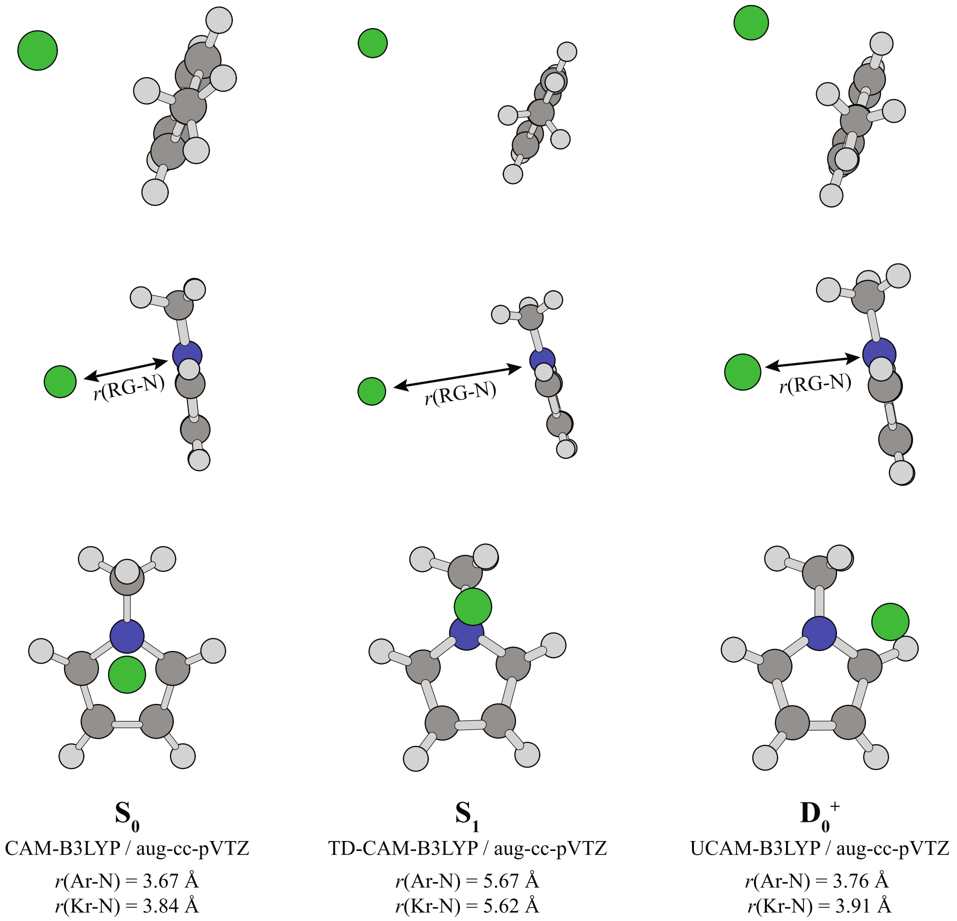

Fig. 5. Calculated geometries of NMP–RG using the indicated levels of theory. Owing to difficulties with the full optimization, for the S_1 state of NMP–Ar, the NMP ring was fixed at its TD-CAM-B3LYP/aug-cc-pVTZ-optimized geometry, and the position of the Ar atom was optimized; for NMP–Kr, a full optimization was successful [with a similarly constrained optimization giving a r(Kr–N) distance only 0.02 Å longer]. Cartesian coordinates for the optimized structures are given in the Supplementary Material.

Table 1
Calculated and experimental binding energies (cm^{-1}) for NMP–Ar and NMP–Kr.

NMP–RG		CAM–B3LYP[a, b]	(R)CCSD(T)[a]			Expt[d]
			BSSE (RG)	BSSE (NMP)	RCCSD (T)[c]	
NMP–Ar	S_0	87	108	31	429	440
	S_1					105
	D_0^+	262	106	27	534	610
NMP–Kr	S_0	85	81	33	517	≥ 500
	S_1					≥ 170
	D_0^+	343	86	28	690	≥ 720

[a] D_e value, i.e. no correction for zero-point energies.

[b] Not counterpoise corrected.

[c] Counterpoise corrected.

[d] Approximate D_0 values – see text. The values for NMP–Kr are based on the high-wavenumber offset in the REMPI spectrum, which is taken as a lower bound for D_0 in the S_1 state; thus, the values for the S_0 and D_0^+ states are also lower bounds. For NMP–Ar, there is a better-defined offset, and so the uncertainty in the S_1 binding energy value is likely ca. ± 2 cm^{-1}, and this uncertainty will contribute to the values for the other states also. For the S_0 state, the uncertainty will be similar, while with regard to the cation, for NMP^+–Ar, the broader ZEKE bands mean that the uncertainty is likely ± 5 cm^{-1}.

the S_1 dissociation energies above, one obtains values for the dissociation energy of the cation complexes as $D_0 \approx 610\ cm^{-1}$ for NMP^+–Ar, and $D_0 \geq 720\ cm^{-1}$ for NMP–Kr. Again, it can be seen that the value for NMP–Kr is close to the calculated RCCSD(T) values in Table 1, while the agreement with the calculated value for NMP–Ar is reasonable, but not as good.

This poor performance of the CAM-B3LYP method with regard to the binding energies, observing that these would be even lower if these were corrected for basis set superposition error, leads us to conclude that the calculated intermolecular wavenumbers should only be used in a qualitative manner, particularly given their low harmonic values, and the expected anharmonicities of the actual vibrations; as such, we do not report these explicitly. Of course, this also suggests that caution is required in employing the CAM-B3LYP geometries in the RCCSD(T) calculations for the binding energies. We note that the calculated intermolecular bond length here of $R_e = 3.67$ Å is not too far from the microwave R value of 3.448 Å for the S_0 state, and so we feel the CAM–B3LYP structures are likely to be fair indications of the actual structures, which is supported by the reasonable agreement of the (R)CCSD(T) binding energies with experiment.

Overall, it is clear that basis set superposition error (BSSE) is playing a significant role here (see Table 1), and so larger basis sets might be expected to be advantageous, as would using geometries optimized at higher levels of theory; however, each of these is computationally expensive.

6. Conclusions

We have reported REMPI spectra for NMP–Ar and NMP–Kr. We believe we have seen the origin transition, implying that the perturbation of the NMP electronic structure is sufficient to render this a dipole-allowed transition. Further, both spectra are blue-shifted with respect to the NMP origin, consistent with the S_1 states being more weakly bound than the S_0 state. In addition, the activity in the REMPI spectra was localized to the region around the origin, with no activity seen for excited NMP-localized vibrations, interpreted in terms of the low-frequency intermolecular modes exacerbating coupling between levels, shortening their lifetimes. It would be interesting to record REMPI spectra of these species using picosecond lasers, to ascertain whether the absence of NMP-localized excited vibrational bands in the present work is due to their short lifetime. It would also be of interest to investigate other ligands.

We have discussed the origin of the low-wavenumber structure in the ZEKE spectra in terms of torsional and intermolecular transitions during the ionization, and we were able to obtain AIEs for both complexes, but not detailed information on the torsional potentials. Possibly 2D-LIF spectra over the electronic absorption spectrum might also prove useful in identifying torsional and intermolecular bands, as it was in the case of toluene–Ar [25]; however, this relies on being able to distinguish between bands of a_1 and e symmetry, and hence on the separation of the m^0 and m^1 bands in the excitation spectrum, which may well not be possible in the present case.

From the REMPI and ZEKE spectra, we were able to deduce estimates of binding energies, and these generally agreed well with calculated values at the (R)CCSD(T) level for the S_0 and D_0^+ states, although those at the CAM-B3LYP level were not in good agreement. MATI spectra would be a means of confirming the deduced binding energies in the cation. Indeed, such binding energies have been measured [38] with the MATI technique to yield values of *p*-fluorotoluene–Ar in the S_0 and D_0^+ states as 329 cm^{-1} and 510 cm^{-1}, respectively; these compare well to the present respective values for NMP–Ar of 440 cm^{-1} and 610 cm^{-1}.

CRediT authorship contribution statement

Alexander R. Davies: Investigation, Writing – review & editing, Visualization, Data curation. **Jessica T.L. Haynes:** Investigation, Data curation. **Timothy G. Wright:** Conceptualization, Writing – original draft, Investigation, Validation, Supervision, Project administration, Funding acquisition.

Declaration of Competing Interest

The authors declare that they have no known competing financial interests or personal relationships that could have appeared to influence the work reported in this paper.

Data Availability Statement

The data that support the findings of this study are available from the corresponding author upon reasonable request.

Acknowledgements

We thank the University of Nottingham for a studentship to A.R.D. We are grateful for access to the University of Nottingham High Performance Computing Facility.

References

[1] A.R. Davies, D.J. Kemp, T.G. Wright, Chem. Phys. Lett. 763 (2021), 138227.
[2] A.R. Davies, D.J. Kemp, T.G. Wright, J. Chem. Phys. 154 (2021), 224305.
[3] A.R. Davies, D.J. Kemp, T.G. Wright, J. Chem. Phys. 155 (2021), 117101.
[4] A.R. Davies, D.J. Kemp, T.G. Wright, J. Molec. Spec. 376 (2021), 111410.
[5] G. Milazzo, Gazz. Chim. Ital. 74 (1944) 152.
[6] R. McDiarmid, X. Xing, J. Chem. Phys. 105 (1996) 867.
[7] J.G. Philis, Chem. Phys. Lett. 353 (2002) 84.
[8] J.G. Philis, J. Molec. Struct. 651–653 (2003) 567.
[9] N. Biswas, S. Wategaonkar, J.G. Philis, Chem. Phys. 293 (2003) 99.
[10] A.G. Sage, M.G.D. Nix, M.N.R. Ashfold, Chem. Phys. 347 (2008) 300.
[11] C.-M. Tseng, Y.T. Lee, C.-K. Ni, J. Phys. Chem A 113 (2009) 3881.
[12] L. Blancafort, V. Ovejas, R. Montero, M. Fernández-Fernández, A. Longarte, J. Phys. Chem. Lett. 7 (2016) 1231.
[13] G. Piani, L. Rubio-Lago, M.A. Collier, T. Kitsopoulos, M. Becucci, J. Phys. Chem. A 113 (2009) 14554.
[14] G. Wu, S.P. Neville, O. Schalk, T. Sekikawa, M.N.R. Ashfold, G.A. Worth, A. Stolow, J. Chem. Phys. 144 (2016), 014309.
[15] T. Geng, O. Schalk, T. Hansson, R.D. Thomas, J. Chem. Phys. 146 (2017), 144307.
[16] K.C. Woo, S.K. Kim, Phys. Chem. Chem. Phys. 21 (2019) 14387.
[17] J.R. Gascooke, W.D. Lawrance, J. Phys. Chem. A 126 (2022) 2160.
[18] S. Huber, J. Makarewicz, A. Bauder, Molec. Phys. 95 (1998) 1021.
[19] V.L. Ayles, C.J. Hammond, D.E. Bergeron, O.J. Richards, T.G. Wright, J. Chem. Phys. 126 (2007), 244304.
[20] T. Yanai, D.P. Tew, N.C. Handy, Chem. Phys. Lett. 393 (2004) 51.
[21] T.G. Wright, E. Cordes, O. Dopfer, K. Müller-Dethlefs, J. Chem. Soc. Faraday Trans. 89 (1993) 1609.
[22] O. Dopfer, T.G. Wright, E. Cordes, K. Müller-Dethlefs, J. Electron Spectrosc. Rel. Phenom. 68 (1994) 247.
[23] K. Müller-Dethlefs, O. Dopfer, T.G. Wright, Chem. Rev. 94 (1845) 1994.
[24] M. Mons, J. Le Calvé, F. Piuzzi, I. Dimicoli, J. Chem. Phys. 92 (1990) 2155.
[25] J.R. Gascooke, W.D. Lawrance, J. Chem. Phys. 138 (2013), 084304.
[26] M. Schmidt, M. Mons, J. Le Calvé, Chem. Phys. Lett. 177 (1991) 371.
[27] T. Weber, E. Riedle, H.J. Neusser, E.W. Schlag, Chem. Phys Lett. 183 (1991) 77.
[28] H. Shinohara, S. Sato, K. Yoshihara, K. Kimura, J. Electron Spectrosc. Rel. Phenom. 88 (1998) 131.
[29] V.L. Ayles, R.J. Plowright, M.J. Watkins, T.G. Wright, J. Kłos, M.H. Alexander, P. Pajón-Suarez, J. Rubayo-Soneira, R. Hernández-Lamoneda, Chem. Phys. Lett. 441 (2007) 181.
[30] S.D. Gamblin, S.E. Daire, J. Lozeille, T.G. Wright, Chem. Phys. Lett. 325 (2000) 232.
[31] J. Lozeille, S.E. Daire, S.D. Gamblin, T.G. Wright, D.M. Smith, J. Chem. Phys. 113 (2000) 7224.
[32] J. Kłos, M.H. Alexander, R. Hernández-Lamoneda, T.G. Wright, J. Chem. Phys. 129 (2008), 244303.
[33] K. Okuyama, N. Mikami, M. Ito, J. Phys. Chem. 89 (1985) 5617.
[34] L.D. Stewart, J.R. Gascooke, W.D. Lawrance, J. Chem. Phys. 150 (2019), 174303.
[35] D.J. Kemp, E.F. Fryer, A.R. Davies, T.G. Wright, J. Chem. Phys. 151 (2019), 084311.
[36] K. Takazawa, M. Fujii, M. Ito, J. Chem. Phys. 99 (1993) 3205.
[37] X. Zhang, J.M. Smith, J.L. Knee, J. Chem. Phys. 97 (1992) 2843.
[38] S. Georgiev, T. Chakraborty, H.J. Neusser, J. Phys. Chem. A 108 (2004) 3304.

14. Final remarks and outlook

The main focus of the work presented in this thesis has been an in-depth spectroscopic study of two very different molecules, namely *m*FT and NMP, in the S_0, S_1 and D_0^+ electronic states. Notably, these two molecules differ by their symmetry (*m*FT belongs to the G_6 MSG and NMP to the G_{12} MSG) and in that $S_1 \leftarrow S_0$ transition in NMP is symmetry-forbidden, meaning all activity observed in the S_1 state is a result of vibronic coupling, whereas the same transition in *m*FT is symmetry-allowed such that the majority of the activity observed is determined by the FCFs. A series of spectroscopic techniques have been used to probe these states, including REMPI, LIF, ZEKE, 2D-LIF and DF. Spectra have been presented for almost all levels up to ~1350 cm^{-1} (*m*FT) and ~1100 cm^{-1} (NMP) above the S_1 origin, to gain insight into the interactions that are occurring within these electronic states and how the methyl rotor affects the build-up of these interactions.

Owing to the lower symmetry of *m*FT, it is perhaps expected that the build-up of IVR is far more rapid than it is for NMP. Significant interactions are seen between vibration-vibration and vibration-torsion modes in *m*FT at even modest internal energies. Arguments for this have been presented in terms of the build-up in the DoS, remarking that this is significantly more rapid in *m*FT than in NMP, and also in terms of the methyl rotor permitting vibration-torsion interactions to further disperse internal energy. Indeed, we note that statistical IVR regime has largely been reached by ~950 cm^{-1} above the S_1 origin, based on the appearance of a broad, unstructured background in the 2D-LIF and ZEKE spectra for the bands at 0^0 + ~960 cm^{-1} and 0^0 + ~1260 cm^{-1} (most notably in the latter) – these also show limited population remains localised to a small number of vibrations, but most is largely dissipated to a range of motions. The onset of statistical IVR makes it a fruitless task to attempt to assign all of the activity, owing to ‘smearing’ of the activity in the 2D-LIF spectra, and the multitude of bands in the ZEKE spectra.

Even at (relatively) low internal energies of ~750 cm^{-1} above the S_1 origin in *m*FT, it is shown that there are still significant and complicated interactions, some of which only arise as a direct result of another interaction, with all spectra showing significant activity. This amount of activity, and its complexity, is surprising given such a low internal energy. Furthermore, owing to the congested nature of the ZEKE spectra, these have not been useful in unpicking the nuances of said interactions, arising from the change in phase of the torsional potential between S_1 and D_0^+ (this leads to the $\Delta m = 3$ propensity occurring upon ionisation), in tandem with the complicated interactions in the S_1 state, leading to significant activity in the ZEKE spectra. Therefore, the ZEKE spectra are difficult to interpret reliably. Nevertheless, these do act as a useful confirmatory tool for determining the identity of the major component of the eigenstate pumped as the expected activity, namely the $\Delta(v, m) = (0, 3)$ activity, remains prominent, even at high S_1 internal energies, although the nuances of any interactions are lost within the structure of the spectra.

It is, however, the 2D-LIF spectra that are the most useful tool for unpicking the interactions in the S_1 state of *m*FT, and indeed, also the S_0 state, arising from the ability to disperse the fluorescence as one scans across various features in the S_1 state. This means that one can see how the emissions vary as one scans across the $m = 0$ and $m = 1$ components of a vibration, noting that a_1 and e symmetry components cannot interact. Therefore, any e symmetry activity extending over an excitation of an a_1 symmetry vibration means there must be some band overlap, whether this arises from serendipitous bright states with the same energy, or an interaction causing an eigenstate to overlap with something else in energy. To distinguish interactions and overlaps in this way is seldom easy in ZEKE spectroscopy.

Furthermore, it is noted that the vibtor interactions are more common for e symmetry vibrations than for a_1 vibrations, largely owing to the more rapid increase in the density of e symmetry states (Sections 8 and 9); it is the $m = 1$ component of a vibration that largely drives *m*-specific couplings. However, a notable exception is the $26^1 28^1$ vibration, where it is actually the $m = 0$ component that interacts, and probing this demonstrates where the majority of the activity is observed.

Moreover, attempts have been made to compare the build-up of IVR between *m*FT and *p*FT (G_{12}), noting that the build-up of the DoS is far more erratic, and slower, in *p*FT than it is in *m*FT, and this largely arises from the higher symmetry of *p*FT leading to a smaller number of same-symmetry levels available to couple that are accessible from either $m = 0$ or $m = 1$, which are both populated in the free-jet expansion. However, caution is recommended in attempting to directly compare such activity, as the forms of the vibrations are significantly different between *para*- and *meta*-disubstituted benzenes. Remarkably, the vibrations probed in the original chemical timing experiments by Parmenter *et al.*[74] are different in *m*FT and *p*FT despite a prominent vibration being pumped at about the same internal energy: in *m*FT, the vibration is largely a ring-based distortion (the D_{11} vibration using the ${}^{m}D_i$ labelling scheme[158]), whereas for *p*FT, it is a symmetric C-F and C-CH_3 stretching mode (the D_5 vibration in using the ${}^{p}D_i$ labelling scheme[164]). As the forms of these vibrations are different, one would expect them to couple to different states; notably, the ${}^{m}D_{11}$ vibration involves an out-of-plane wagging of the ring-localised hydrogen atoms, which one would expect to interact more strongly with the methyl rotor than would the ${}^{p}D_5$ vibration, which is in-plane. Therefore, a direct comparison of the build-up of IVR between *para*- and *meta*-substituted benzenes remains difficult, even when considering vibrations at a similar energy.

While the $S_1 \leftarrow S_0$ transition of NMP was only accessed to ~1100 cm^{-1} above the S_1 origin, compared to ~1300 cm^{-1} in *m*FT, it is notable that the activity observed in all three electronic states is significantly different when compared to that in *m*FT. Naturally, with the S_1 state of NMP being a 3s Rydberg state, one would expect to observe highly diagonal FCFs for the $D_0^+ \leftarrow S_1$ ionisation, however even when looking *via* bands as high as ~1100 cm^{-1} above the S_1 origin, there is little evidence of IVR shown in the ZEKE spectra, in contrast to *m*FT where IVR was approaching the statistical regime at ~950 cm^{-1} above the S_1 origin.

The most significant region of coupling in NMP was the 0^0 + ~800 cm^{-1} region, in which there were two ZOB states, 11^1m^0 (a_2' symmetry in the G_{12} MSG) and 13^1m^0 (a_2'' symmetry in the G_{12} MSG), interacting with numerous ZOD states to produce a surprisingly localised region of activity, in direct contrast to the rest of the $S_1 \leftarrow S_0$ spectrum, even to higher internal energies. Here, it is noted that a degree of serendipity is involved in this region of the REMPI spectrum: while the overall DoS is reasonably high at this internal energy (Figure 16 of Section 12) there just so happens to be the presence of two, nearby ZOB states (each with their own $m = 0$ and $m = 1$ components) which couple strongly to multiple ZOD states; indeed, these ZOB states are required in order to see such coupling. (One should note that the build-up of the DoS is not necessarily smooth but may be somewhat ‘clumpy’ in that there may be a region of low state density, followed by a ‘clump’ of states straight after – *i.e.*, the rise in the number of states in a given energy range is not monotonic.)

It is remarkable that the ZEKE spectra *via* the bands in this region were so ‘clean’ and that, from this, it was possible to use these to determine the nature of the interactions and therefore propose the identities of the ZOB and ZOD states that comprise the interactions. Indeed, it was the low wavenumber region of these ZEKE spectra that assisted in determining the nature of such interactions as there is a tendency for the components of a combination band (if symmetry-allowed in isolation) to be active in a spectrum where one projects the population of that state onto another, such as in ZEKE spectroscopy. Furthermore, it is worth reiterating that, while a 2D-LIF spectrum over this region would have been desirable, it was not possible to achieve anything of sufficient quality.

This is in direct contrast to *m*FT where the 2D-LIF spectra were very useful in the determination of the nature of the couplings, whereas the ZEKE spectra were not. This is put down purely to the nature of the S_1 state of NMP, which is a mixture of a 3s Rydberg and σ^* valance character at extended N-CH_3 bond lengths. At increasing internal energies in S_1, the lifetime of the electronic state decreases significantly, largely due to the population accessing a region beyond a potential barrier, leading to predissociation. This means the ability to resolve various bands in the 2D-LIF spectra decreases with increasing internal energy as the population of the S_1 excited state decays before the molecule can fluoresce. Conversely, in the ZEKE spectra, as this is a much faster process, the population does not have time to decay before ionisation.

Furthermore, in NMP, it is the b_1 symmetry vibrations in S_1 whose ZEKE spectra show the most activity, with some of it being nominally symmetry-forbidden, such as the origin transition. This is proposed to arise from vibronic coupling (the b_1

vibrations are expected to be coupling the strongest in this manner, owing to the high oscillator strength and proximity in energy of the $^1B_2$ electronic state, from which intensity is gained) which leads to a change in the average geometry along the out-of-plane b_1 coordinates. This would reduce the symmetry from effective-C_{2v} symmetry to effective-C_s symmetry, through which one would expect the a_1 symmetry levels to become allowed, and hence may explain the observance of the origin.

It has also been commented that, in order to understand the photodynamics, and thus the fate of an excited state, it is pertinent to know which eigenstates are being excited coherently inside the width of a picosecond (or shorter) laser pulse in time-resolved experiments. This not only reinforces the complementarity of time-resolved and frequency-resolved experiments but also suggests that, in the future, it may be a good idea to reconsider the photodynamics of NMP, knowing which eigenstates are excited in the pulse, in order to determine the fate of the S_1 excited state. Additionally, one could then probe the pyrrolyl fragment to allow one to determine whether a two-step internal conversion from S_1 to a vibrationally excited S_0 state and back to S_1 (or indeed S_2) at long N-CH_3 separations, or whether intersystem crossing to nearby triplet states contributes to the photodynamics and photofragmentation of NMP.

The NMP-RG vdW complexes have proven to be interesting as the presence of the RG allows the origin transition to be observed. As such, it would be of benefit to conduct a time-resolved experiment on these complexes, to elucidate the origins of the broad, unstructured REMPI spectrum and why activity is only observed *via* the NMP origin and not *via* other, excited NMP-localised vibrations, such as P_{16} and P_{23}, as would be expected. MATI experiments would also be useful on these complexes as well, to elucidate whether the broad, higher-wavenumber structure of the ZEKE spectra arises from the complex, or something else in the free-jet expansion.

Although it has been said that it is very difficult to compare directly similar molecules, of different isometric classes, such as *para*- and *meta*-disubstituted benzenes, and this likely to be the case with *N*-substituted *versus* 2- or 3-substituited pyrroles, rudimentary comparisons between the build-up of IVR are possible, albeit with some caveats. As such, it may be interesting to conduct similar experiments to those presented as part of this thesis on 2- or 3-methylpyrrole, to determine how the rate of IVR may change between locations of substitution. Given the lower symmetry of these molecules as well, when compared to NMP, it may be interesting to see if this permits the methyl rotor to facilitate vibration-torsion coupling more efficiently than was seen in NMP. Furthermore, other, related *N*-substituted pyrroles could be studied to confirm that the labelling scheme devised for *N*-substituted pyrroles remains valid, and to also see how changes in mass and electronic structure can further affect the rate of IVR in *N*-substituted pyrroles.

As a final note, a theme mentioned early on in this thesis was that systems such as NMP and *m*FT can be considered as simple analogues to larger, more complex molecules with biological relevance. Therefore, it would be interesting to consider spectroscopic studies, such as those presented herein, on fused-ring systems such as indole or *N*-methylindole. Now that the fields of substituted benzenes and *N*-substituted pyrroles are well established and the spectroscopic activity is now well understood, it may be possible to glean something from the (inevitably more complex) spectra of fused-ring systems, in light of the information presented in this thesis and in the surrounding literature. Indeed, indole may be a solid at room-temperature, but as it has a low melting point, it would not be too difficult to modify a standard pulsed valve to heat it up and produce a significant vapour, and retain the sample in the gas-phase, before seeding in a rare-gas for a supersonic jet expansion. Additionally, it appears that *N*-methylindole is a liquid at room temperature so this may be more facile for the spectroscopist, although it may still require some heating to get a sufficient number density seeded in a free-jet expansion.

15. References

1 M. N. Frey, T. F. Koetzle, M. S. Lehmann and W. C. Hamilton, *J. Chem. Phys.*, 1973, **58**, 2547–2556.

2 F. S. Ihlefeldt, F. B. Pettersen, A. von Bonin, M. Zawadzka and C. H. Görbitz, *Angew. Chemie Int. Ed.*, 2014, **53**, 13600–13604.

3 C. H. Görbitz, K. W. Törnroos and G. M. Day, *Acta Crystallogr. Sect. B Struct. Sci.*, 2012, **68**, 549–557.

4 J. D'Orazio, S. Jarrett, A. Amaro-Ortiz and T. Scott, *Int. J. Mol. Sci.*, 2013, **14**, 12222–12248.

5 H. Ikehata and T. Ono, *J. Radiat. Res.*, 2011, **52**, 115–125.

6 N. D. N. Rodrigues, M. Staniforth and V. G. Stavros, *Proc. R. Soc. A Math. Phys. Eng. Sci.*, 2016, **472**, 20160677.

7 L. A. Baker, M. D. Horbury, S. E. Greenough, P. M. Coulter, T. N. V. Karsili, G. M. Roberts, A. J. Orr-Ewing, M. N. R. Ashfold and V. G. Stavros, *J. Phys. Chem. Lett.*, 2015, **6**, 1363–1368.

8 N. D. N. Rodrigues, N. C. Cole-Filipiak, M. D. Horbury, M. Staniforth, T. N. V. Karsili, Y. Peperstraete and V. G. Stavros, *J. Photochem. Photobiol. A Chem.*, 2018, **353**, 376–384.

9 A. L. Whittock, T. T. Abiola and V. G. Stavros, *J. Phys. Chem. A*, 2022, **126**, 2299–2308.

10 T. G. Smijs and S. Pavel, *Nanotechnol. Sci. Appl.*, 2011, **4**, 95–112.

11 M. D. Newman, M. Stotland and J. I. Ellis, *J. Am. Acad. Dermatol.*, 2009, **61**, 685–692.

12 I. Pugliesi, N. M. Tonge and M. C. R. Cockett, *J. Chem. Phys.*, 2008, **129**, 104303.

13 S. H. Wollman, *J. Chem. Phys.*, 1946, **14**, 123–130.

14 R. Vasudev and J. C. D. Brand, *J. Mol. Spectrosc.*, 1979, **75**, 288–296.

15 A. Boatwright, N. A. Besley, S. Curtis, R. R. Wright and A. J. Stace, *J. Chem. Phys.*, 2005, **123**, 021102.

16 P. Butler, D. B. Moss, H. Yin, T. W. Schmidt and S. H. Kable, *J. Chem. Phys.*, 2007, **127**, 094303.

17 J. R. Gascooke, U. N. Alexander and W. D. Lawrance, *J. Chem. Phys.*, 2011, **134**, 184301.

18 A. Uskola, F. J. Basterretxea and F. Castaño, *Mol. Phys.*, 2002, **99**, 133–141.

19 S.-H. Lee, C.-Y. Wu, S.-K. Yang and Y.-P. Lee, *J. Chem. Phys.*, 2006, **125**, 144301.

20 J. I. Murakami, K. Kaya and M. Ito, *J. Chem. Phys.*, 1979, **72**, 3263–3270.

21 T. Cvitaš and J. M. Hollas, *Mol. Phys.*, 1970, **18**, 101–111.

22 J. L. Durant, D. M. Rider, S. L. Anderson, F. D. Proch and R. N. Zare, *J. Chem. Phys.*, 1983, **80**, 1817–1825.

23 T. G. Wright, S. I. Panov and T. A. Miller, *J. Chem. Phys.*, 1995, **102**, 4793–4803.

24 A. De La Cruz, J. Campos and M. Ortiz, *J. Mol. Spectrosc.*, 1996, **180**, 305–310.

25 G. Lembach and B. Brutschy, *Chem. Phys. Lett.*, 1997, **273**, 421–428.

26 A. Andrejeva, W. D. Tuttle, J. P. Harris and T. G. Wright, *J. Chem. Phys.*, 2015, **143**, 0–22.

27 P. T. Whiteside, A. K. King, J. A. Davies, K. L. Reid, M. Towrie and P. Matousek, *J. Chem. Phys.*, 2005, **123**, 204317.

28 P. T. Whiteside, A. K. King and K. L. Reid, *J. Chem. Phys.*, 2005, **123**, 204316.

29 J. R. Gascooke, E. A. Virgo and W. D. Lawrance, *J. Chem. Phys.*, 2015, **142**, 0–13.

30 C. G. Eisenhardt and H. Baumgärtel, *Berichte der Bunsen-gesellschaft für Phys. Chemie*, 1998, **102**, 1803–1807.

31 M. Schauer, K. Law and E. R. Bernstein, *J. Chem. Phys.*, 1984, **81**, 49–56.

32 J. T. Meek, S. R. Long and J. P. Reilly, *J. Phys. Chem.*, 1982, **86**, 2809–2811.

33 P. J. Breen, J. A. Warren, E. R. Bernstein and J. I. Seeman, *J. Chem. Phys.*, 1987, **87**, 1917–1926.

34 A. L. L. East, H. Liu, E. C. Lim, P. Jensen, I. Déchène, M. Z. Zgierski, W. Siebrand and P. R. Bunker, *J. Chem. Phys.*, 2000, **112**, 167–175.

35 D. R. Borst and D. W. Pratt, *J. Chem. Phys.*, 2000, **113**, 3658–3669.

36 J. R. Gascooke, D. Appadoo and W. D. Lawrance, *J. Chem. Phys.*, 2021, **155**, 124306.

37 J. R. Gascooke and W. D. Lawrance, *J. Chem. Phys.*, 2013, **138**, 134302.

38 A. M. Gardner, A. M. Green, V. M. Tamé-Reyes, K. L. Reid, J. A. Davies, V. H. K. Parkes and T. G. Wright, *J. Chem. Phys.*, 2014, **140**, 114308.

39 C. G. Hickman, J. R. Gascooke and W. D. Lawrance, *J. Chem. Phys.*, 1996, **104**, 4887–4901.

40 C. D. Cooper, *J. Chem. Phys.*, 1954, **22**, 503–510.

41 R. A. Coveleskie and C. S. Parmenter, *J. Mol. Spectrosc.*, 1981, **86**, 86–114.

42 A. E. W. Knight and S. H. Kable, *J. Chem. Phys.*, 1988, **89**, 7139–7160.

43 D. Rieger, G. Reiser, K. Mueller-Dethlefs and E. W. Schlag, *J. Phys. Chem.*, 1992, **96**, 12–14.

44 G. Reiser, D. Rieger, T. G. Wright, K. Müller-Dethlefs and E. W. Schlag, *J. Phys. Chem.*, 1993, **97**, 4335–4343.

45 E. Sekreta, K. S. Viswanathan and J. P. Reilly, *J. Chem. Phys.*, 1989, **90**, 5349–5359.

46 D. J. Kemp, A. M. Gardner, W. D. Tuttle, J. Midgley, K. L. Reid and T. G. Wright, *J. Chem. Phys.*, 2018, **149**, 0–20.

47 C. Jouvet, C. Dedonder-Lardeux, S. Martrenchard-Barra and D. Solgadi, *Chem. Phys. Lett.*, 1992, **198**, 419–423.

48 W. D. Tuttle, A. M. Gardner, K. B. O’Regan, W. Malewicz and T. G. Wright, *J. Chem. Phys.*, 2017, **146**, 0–16.

49 J. A. Davies and K. L. Reid, *Phys. Rev. Lett.*, 2012, **109**, 1–5.

50 A. M. Gardner, L. E. Whalley, D. J. Kemp, W. D. Tuttle and T. G. Wright, *J. Chem. Phys.*, 2019, **151**, 154302.

51 C. J. Hammond, V. L. Ayles, D. E. Bergeron, K. L. Reid and T. G. Wright, *J. Chem. Phys.*, 2006, **125**, 124308.

52 J. A. Davies and K. L. Reid, *J. Chem. Phys.*, 2011, **135**, 124305.

53 T. Cvitaš and J. M. Hollas, *Mol. Phys.*, 1971, **20**, 645–654.

54 J. R. Gascooke, L. D. Stewart, P. G. Sibley and W. D. Lawrance, *J. Chem. Phys.*, 2018, **149**, 0–14.

55 A. M. Gardner, W. D. Tuttle, P. Groner and T. G. Wright, *J. Chem. Phys.*, 2017, **146**, 124308.

56 K. Walter, K. Scherm and U. Boesl, *Chem. Phys. Lett.*, 1989, **161**, 473–478.

57 A. Held, H. L. Selzle and E. W. Schlag, *J. Phys. Chem. A*, 1998, **102**, 9625–

9630.

58 F. Gunzer and J. Grotemeyer, *Phys. Chem. Chem. Phys.*, 2002, **4**, 5966–5972.

59 F. Gunzer and J. Grotemeyer, *Int. J. Mass Spectrom.*, 2003, **228**, 921–931.

60 B. Zhang, U. Aigner, H. L. Selzle and E. W. Schlag, *Chem. Phys. Lett.*, 2003, **380**, 337–341.

61 K. Watanabe, *J. Chem. Phys.*, 1954, **22**, 1564–1570.

62 J. H. S. Green, *Spectrochim. Acta Part A Mol. Spectrosc.*, 1970, **26**, 1523–1533.

63 J. M. Hollas, H. Musa and T. Ridley, *J. Mol. Spectrosc.*, 1983, **98**, 125–137.

64 A. R. Davies, D. J. Kemp and T. G. Wright, *AIP Adv.*, 2020, **10**, 125206.

65 P. A. Graham and S. H. Kable, *J. Chem. Phys.*, 1995, **103**, 6426–6439.

66 Y. Tsuchiya, K. Takazawa, M. Fujii and M. Ito, *Chem. Phys. Lett.*, 1991, **183**, 107–112.

67 H. D. Rudolph and A. Trinkaus, *Zeitschrift fur Naturforsch. - Sect. A J. Phys. Sci.*, 1968, **23**, 68–76.

68 K. T. Lu, F. Weinhold and J. C. Weisshaar, *J. Chem. Phys.*, 1995, **102**, 6787–6805.

69 K. Okuyama, N. Mikami and M. Ito, *J. Phys. Chem.*, 1985, **89**, 5617–5625.

70 K. Takazawa, M. Fujii, T. Ebata and M. Ito, *Chem. Phys. Lett.*, 1992, **189**, 592–597.

71 K. Takazawa, M. Fujii and M. Ito, *J. Chem. Phys.*, 1993, **99**, 3205–3217.

72 M. Ito, K. Takazawa and M. Fujii, *J. Mol. Struct.*, 1993, **292**, 9–16.

73 T. Suzuki, M. Hiroi and M. Ito, *J. Phys. Chem.*, 1988, **92**, 3774–3778.

74 P. J. Timbers, C. S. Parmenter and D. B. Moss, *J. Chem. Phys.*, 1994, **100**, 1028–1034.

75 L. D. Stewart, J. R. Gascooke and W. D. Lawrance, *J. Chem. Phys.*, 2019, **150**, 0–15.

76 D. J. Kemp, E. F. Fryer, A. R. Davies and T. G. Wright, *J. Chem. Phys.*, 2019, **151**, 084311.

77 S. H. Feldgus, M. J. Schroeder, R. A. Walker, W. K. Woo and J. C. Weisshaar, *Int. J. Mass Spectrom. Ion Process.*, 1996, **159**, 231–244.

78 T. Ichimura, A. Kawana, T. Suzuki, T. Ebata and N. Mikami, *J. Photochem. Photobiol. A Chem.*, 1994, **80**, 145–150.

79 D. J. Kemp, L. G. Warner and T. G. Wright, *J. Chem. Phys.*, 2020, **152**, 064303.

80 A. R. Davies, D. J. Kemp, L. G. Warner, E. F. Fryer, A. Rees and T. G. Wright, *J. Chem. Phys.*, 2020, **152**, 214303.

81 C. D. Cooper, A. D. Williamson, J. C. Miller and R. N. Compton, *J. Chem. Phys.*, 1980, **73**, 1527–1537.

82 M. N. R. Ashfold, S. G. Clement, J. D. Howe and C. M. Western, *J. Chem. Soc. Faraday Trans.*, 1993, **89**, 1153.

83 A. E. W. Knight, C. S. Parmenter and M. W. Schuyler, *J. Am. Chem. Soc.*, 1975, **97**, 2005–2013.

84 A. E. W. Knight, C. S. Parmenter and M. W. Schuyler, *J. Am. Chem. Soc.*, 1975, **97**, 1993–2005.

85 J. Li, C.-K. Lin, X. Y. Li, C. Y. Zhu and S. H. Lin, *Phys. Chem. Chem. Phys.*, 2010, **12**, 14967.

86 T. Suzuki and M. Ito, *J. Chem. Phys.*, 1989, **91**, 4564–4570.

87 W. Arnold, H. Dreizler and H. D. Rudolph, *Zeitschrift für Naturforsch. A*, 1968, **23**, 301–306.

88 S. Huber, J. Makarewicz and A. Bauder, *Mol. Phys.*, 1998, **95**, 1021–1043.

89 J. Makarewicz, S. Huber, B. Brupbacher-Gatehouse and A. Bauder, *J. Mol. Struct.*, 2002, **612**, 117–123.

90 N. Kurai, H. Takeuchi and S. Konaka, *J. Mol. Struct.*, 1994, **318**, 143–149.

91 H. Takeuchi, K. Inoue, J. Enmi, T. Hamada, T. Shibuya and S. Konaka, *J. Mol. Struct.*, 2001, **567–568**, 107–111.

92 D. W. Scott, *J. Mol. Spectrosc.*, 1971, **37**, 77–91.

93 T. J. Dines, L. D. MacGregor and C. H. Rochester, *J. Colloid Interface Sci.*, 2002, **245**, 221–229.

94 K. B. Bec, R. Wieczorek, B. Lydzba-Kopczyzska and J. P. Hawranek, *Acta Phys. Pol. A*, 2013, **124**, 115–121.

95 G. Milazzo, *Gazz. Chim. Ital.*, 1944, **74**, 152.

96 R. McDiarmid and X. Xing, *J. Chem. Phys.*, 1996, **105**, 867–873.

97 A. D. Baker, D. Betteridge, N. R. Kemp, R. E. Kirby and R. E. Kirby, *Anal. Chem.*, 1971, **43**, 375–381.

98 J. G. Philis, *Chem. Phys. Lett.*, 2002, **353**, 84–88.

99 J. G. Philis, *J. Mol. Struct.*, 2003, **653**, 567–570.

100 N. Biswas, S. Wategaonkar and J. G. Philis, *Chem. Phys.*, 2003, **293**, 99–109.

101 N. Kanamaru, *J. Mol. Struct. THEOCHEM*, 2004, **686**, 15–23.

102 A. G. Sage, M. G. D. Nix and M. N. R. Ashfold, *Chem. Phys.*, 2008, **347**, 300–308.

103 G. Piani, L. Rubio-Lago, M. A. Colliery, T. N. Kitsopoulos and M. Becucci, *J. Phys. Chem. A*, 2009, **113**, 14554–14558.

104 C. Tseng, Y. T. Lee and C. Ni, *J. Phys. Chem. A*, 2009, **113**, 3881–3885.

105 L. Blancafort, V. Ovejas, R. Montero, M. Fernández-Fernández and A. Longarte, *J. Phys. Chem. Lett.*, 2016, **7**, 1231–1237.

106 G. Wu, S. P. Neville, O. Schalk, T. Sekikawa, M. N. R. Ashfold, G. A. Worth and A. Stolow, *J. Chem. Phys.*, 2016, **144**, 014309.

107 T. Geng, O. Schalk, S. P. Neville, T. Hansson and R. D. Thomas, *J. Chem. Phys.*, 2017, **146**, 144307.

108 M. J. Paterson and D. Townsend, *Int. Rev. Phys. Chem.*, 2020, **39**, 517–567.

109 I. Frank and K. Damianos, *J. Chem. Phys.*, 2007, **126**, 125105.

110 K. C. Woo and S. K. Kim, *Phys. Chem. Chem. Phys.*, 2019, **21**, 14387–14393.

111 Y. Fu, X. Cheng, J. Zhao, T. Kong, C. Cui and X. Zhang, *Polym. J.*, 2012, **44**, 1048–1055.

112 S. Chavda, K. Mulder, T. Brown, H. Mackay, B. Babu, L. Westrate, A. Ferguson, S. Lin, K. Kiakos, J. Ramos, M. Munde, W. Wilson, J. Hartley and M. Lee, *Med. Chem. (Los. Angeles).*, 2010, **6**, 150–158.

113 V. Bhardwaj, D. Gumber, V. Abbot, S. Dhiman and P. Sharma, *RSC Adv.*, 2015, **5**, 15233–15266.

114 G. Fabregat, E. Córdova-Mateo, E. Armelin, O. Bertran and C. Alemán, *J. Phys. Chem. C*, 2011, **115**, 14933–14941.

115 G. Fabregat, J. Casanovas, E. Redondo, E. Armelin and C. Alemán, *Phys. Chem. Chem. Phys.*, 2014, **16**, 7850–7861.

116 R. Dobay, G. Harsányi and C. Visy, *Anal. Chim. Acta*, 1999, **385**, 187–194.

117 F. Elibal, S. Gumustekin, H. Ozkazanc and E. Ozkazanc, *J. Mol. Struct.*, 2021, **1242**, 130712.

118 A. R. Davies, D. J. Kemp and T. G. Wright, *Chem. Phys. Lett.*, 2021, **763**, 138227.

119 A. R. Davies, D. J. Kemp and T. G. Wright, *J. Mol. Spectrosc.*, 2021, **376**, 111410.

120 A. R. Davies, D. J. Kemp and T. G. Wright, *J. Chem. Phys.*, 2021, **154**, 224305.

121 A. R. Davies, D. J. Kemp and T. G. Wright, *J. Chem. Phys.*, 2021, **155**, 117101.

122 G. Herzberg, *Infrared and Raman Spectra of Polyatomic Molecules*, D. Van Nostrand Company, Inc, New York, 1st edn., 1945.

123 G. Herzberg, *Electronic Spectra of Polyatomic Molecules*, D. Van Nostrand Company, Inc, Princeton, 1st edn., 1966.

124 P. R. Bunker and P. Jensen, *Molecular Symmetry and Spectroscopy*, NRC Press (Canada), Ottawa, 2nd edn., 1998.

125 P. R. Bunker and P. Jensen, *Fundamentals of Molecular Symmetry*, Institute of Physics Publishing, Bristol, 1st edn., 2005.

126 P. Atkins and R. Friedman, *Molecular Quantum Mechanics*, Oxford University Press Inc., New York, 4th edn., 2005.

127 J. M. Hollas, *Modern Spectroscopy*, John Wiley & Sons, Chichester, 4th edn., 1988.

128 J. M. Hollas, *High Resolution Spectroscopy*, John Wiley & Sons, Chichester, 2nd edn., 1998.

129 M. Born and R. Oppenheimer, *Ann. Phys.*, 1927, **389**, 457–484.

130 L. R. Brock and M. A. Duncan, *J. Chem. Phys.*, 1995, **103**, 9200–9211.

131 L. R. Brock and M. A. Duncan, *Chem. Phys. Lett.*, 1995, **247**, 18–23.

132 C. Jouvet, C. Lardeux-Dedonder, S. Martrenchard and D. Solgadi, *J. Chem. Phys.*, 1991, **94**, 1759–1764.

133 A. M. Knight, A. Stangassinger and M. A. Duncan, *Chem. Phys. Lett.*, 1997, **273**, 265–271.

134 K. F. Willey, P. Y. Cheng, C. S. Yeh, D. L. Robbins and M. A. Duncan, *J. Chem. Phys.*, 1991, **95**, 6249–6256.

135 R. J. Plowright, M. J. Watkins, A. M. Gardner, T. G. Wright, W. H. Breckenridge, F. Wallimann and S. Leutwyler, *J. Chem. Phys.*, 2008, **129**, 154315.

136 R. J. Plowright, V. L. Ayles, M. J. Watkins, A. M. Gardner, R. R. Wright, T.

G. Wright and W. H. Breckenridge, *J. Chem. Phys.*, 2007, **127**, 204308.

137 P. M. Morse, *Phys. Rev.*, 1929, **34**, 57–64.

138 G. Herzberg, *Spectra of Diatomic Molecules*, Krieger, Malabar, 2nd edn., 1989.

139 E. B. Wilson, *Phys. Rev.*, 1934, **45**, 706–714.

140 E. Fermi, *Zeitschrift für Phys.*, 1931, **71**, 250.

141 B. T. Darling and D. M. Dennison, *Phys. Rev.*, 1940, **57**, 128–139.

142 D. J. Nesbitt and R. W. Field, *J. Phys. Chem.*, 1996, **100**, 12735–12756.

143 D. B. Moss, C. S. Parmenter and G. E. Ewing, *J. Chem. Phys.*, 1987, **86**, 51–61.

144 C. S. Parmenter and B. M. Stone, *J. Chem. Phys.*, 1986, **84**, 4710–4711.

145 Q. Ju, C. S. Parmenter, T. A. Stone and Z.-Q. Zhao, *Isr. J. Chem.*, 1997, **37**, 379–385.

146 F. Duschinsky, *Acta Physicochim. URSS*, 1937, **7**, 551–556.

147 R. A. Walker, E. Richard, K. T. Lu, E. L. Sibert and J. C. Weisshaar, *J. Chem. Phys.*, 1995, **102**, 8718–8724.

148 J. R. Gascooke and W. D. Lawrance, *J. Phys. Chem. A*, 2022, **126**, 2160–2169.

149 H. C. Longuet-Higgins, *Mol. Phys.*, 1963, **6**, 445–460.

150 L. H. Spangler, *Annu. Rev. Phys. Chem.*, 1997, **48**, 481–510.

151 W. D. Tuttle, University of Nottingham, 2018.

152 D. G. Lister, J. N. MacDonald and N. L. Owen, *Internal Rotation and Inversion*, Adademic Press Inc. (London) Ltd., London, 1st edn., 1978.

153 J. E. Wollrab, *Rotational Spectra and Molecular Structure*, Academic Press Inc. (London) Ltd., London, 1st edn., 1967.

154 J. D. Lewis and J. Laane, *J. Mol. Spectrosc.*, 1977, **65**, 147–154.

155 J. D. Lewis, T. B. Malloy, T. H. Chao and J. Laane, *J. Mol. Struct.*, 1972, **12**, 427–449.

156 E. A. Virgo, J. R. Gascooke and W. D. Lawrance, *J. Chem. Phys.*, 2014, **140**, 154310.

157 D. J. Kemp, University of Nottingham, 2020.

158 D. J. Kemp, W. D. Tuttle, F. M. S. Jones, A. M. Gardner, A. Andrejeva, J. C. A. Wakefield and T. G. Wright, *J. Mol. Spectrosc.*, 2018, **346**, 46–59.

159 H. W. Wilson, *Spectrochim. Acta Part A Mol. Spectrosc.*, 1974, **30**, 2141–2152.

160 G. Varsányi, *Assignments of the Vibrational Spectra of Seven Hundred Benzene Derivatives*, Wiley, New York, 1st edn., 1974.

161 G. Varsányi, *Vibrational Spectra of Benzene Derivatives*, Academic Press New York and London, New York, 1st edn., 1969.

162 R. S. Mulliken, *Phys. Rev.*, 1930, **36**, 611–629.

163 W. D. Tuttle, A. M. Gardner, A. Andrejeva, D. J. Kemp, J. C. A. Wakefield and T. G. Wright, *J. Mol. Spectrosc.*, 2018, **344**, 46–60.

164 A. Andrejeva, A. M. Gardner, W. D. Tuttle and T. G. Wright, *J. Mol. Spectrosc.*, 2016, **321**, 28–49.

165 A. Ellis, M. Fehler and T. Wright, *Electronic and Photoelectron Spectroscopy - Fundamentals and Case Sudies*, Cambridge University Press, Cambridge, 1st edn., 2005.

166 J. R. Gascooke and W. D. Lawrance, *Eur. Phys. J. D*, 2017, **71**, 287.

167 I. Fischer, A. Strobel, J. Staecker, G. Niedner-Schatteburg, K. Müller-Dethlefs and V. E. Bondybey, *J. Chem. Phys.*, 1992, **96**, 7171–7174.

168 A. Strobel, I. Fischer, J. Staecker, G. Niedner-Schatteburg, K. Müller-Dethlefs and V. E. Bondybey, *J. Chem. Phys.*, 1992, **97**, 2332–2337.

169 I. Fischer, A. Lochschmidt, A. Strobel, G. Niedner-Schatteburg, K. Müller-Dethlefs and V. E. Bondybey, *Chem. Phys. Lett.*, 1993, **202**, 542–548.

170 G. Reiser, W. Habenicht and K. Müller-Dethlefs, *J. Chem. Phys.*, 1993, **98**, 8462–8468.

171 F. Merkt and T. P. Softley, *Phys. Rev. A*, 1992, **46**, 302–314.

172 F. Merkt and T. P. Softley, *J. Chem. Phys.*, 1992, **96**, 4149–4156.

173 R. G. Tonkyn, R. Wiedmann, E. R. Grant and M. G. White, *J. Chem. Phys.*, 1991, **95**, 7033–7040.

174 J. Yang, J. Li and Y. Mo, *J. Chem. Phys.*, 2006, **125**, 174313.

175 F. Schlicht, M. Entfellner and U. Boesl, *J. Phys. Chem. A*, 2010, **114**, 11125–11132.

176 V. Distelrath and U. Boesl, *Faraday Discuss.*, 2000, **115**, 161–174.

177 Y. Zhao, I. Yourshaw, G. Reiser, C. C. Arnold and D. M. Neumark, *J. Chem. Phys.*, 1994, **101**, 6538–6551.

178 T. Lenzer, I. Yourshaw, M. R. Furlanetto, G. Reiser and D. M. Neumark, *J. Chem. Phys.*, 1999, **110**, 9578–9586.

179 B. Krassig and V. Schmidt, *J. Phys. B At. Mol. Opt. Phys.*, 1992, **25**, L327–L333.

180 M. Génévriez, D. Wehrli, J. A. Agner and F. Merkt, *Int. J. Mass Spectrom.*, 2019, **435**, 209–216.

181 K. M. Ervin, J. Ho and W. C. Lineberger, *J. Phys. Chem.*, 1988, **92**, 5405–5412.

182 J. L. Gardner and J. A. R. Samson, *J. Chem. Phys.*, 1975, **62**, 1447–1452.

183 D. W. Turner, *Philos. Trans. R. Soc. London. Ser. A, Math. Phys. Sci.*, 1970, **268**, 7–31.

184 L.-S. Wang, J. E. Reutt, Y. T. Lee and D. A. Shirley, *J. Electron Spectros. Relat. Phenomena*, 1988, **47**, 167–186.

185 V. L. Ayles, C. J. Hammond, D. E. Bergeron, O. J. Richards and T. G. Wright, *J. Chem. Phys.*, 2007, **126**, 244304.

186 S. Georgiev, T. Chakraborty and H. J. Neusser, *J. Phys. Chem. A*, 2004, **108**, 3304–3307.

187 W. A. Chupka, *J. Chem. Phys.*, 1993, **98**, 4520–4530.

188 X. Zhang, J. M. Smith and J. L. Knee, *J. Chem. Phys.*, 1992, **97**, 2843–2860.

189 A. M. Gardner, A. M. Green, V. M. Tamé-Reyes, K. L. Reid, J. A. Davies, V. H. K. Parkes and T. G. Wright, *J. Chem. Phys.*, 2014, **140**, 0–22.

190 A. M. Gardner, A. M. Green, V. M. Tamé-Reyes, V. H. K. Wilton and T. G. Wright, *J. Chem. Phys.*, 2013, **138**, 134303.

191 J. P. Harris, A. Andrejeva, W. D. Tuttle, I. Pugliesi, C. Schriever and T. G. Wright, *J. Chem. Phys.*, 2014, **141**, 244315.

192 T. Yanai, D. P. Tew and N. C. Handy, *Chem. Phys. Lett.*, 2004, **393**, 51–57.

193 M. J. Frisch, G. W. Trucks, H. B. Schlegel, G. E. Scuseria, M. A. Robb, J. R. Cheeseman, G. Scalmani, V. Barone, G. A. Petersson, H. Nakatsuji, X. Li, M. Caricato, A. V. Marenich, J. Bloino, B. G. Janesko, R. Gomperts, B. Mennucci, H. P. Hratchian, J. V. Ortiz, A. F. Izmaylov, J. L. Sonnenberg, D. Williams-Young, F. Ding, F. Lipparini, F. Egidi, J. Goings, B. Peng, A. Petrone, T. Henderson, D. Ranasinghe, V. G. Zakrzewski, J. Gao, N. Rega, G. Zheng, W. Liang, M. Hada, M. Ehara, K. Toyota, R. Fukuda, J. Hasegawa, M.

Ishida, T. Nakajima, Y. Honda, O. Kitao, H. Nakai, T. Vreven, K. Throssell, J. A. J. Montgomery, J. E. Peralta, F. Ogliaro, M. J. Bearpark, J. J. Heyd, E. N. Brothers, K. N. Kudin, V. N. Staroverov, T. A. Keith, R. Kobayashi, J. Normand, K. Raghavachari, A. P. Rendell, J. C. Burant, S. S. Iyengar, J. Tomasi, M. Cossi, J. M. Millam, M. Klene, C. Adamo, R. Cammi, J. W. Ochterski, R. L. Martin, K. Morokuma, O. Farkas, J. B. Foresman and D. J. Fox, *Gaussian 16, Revision A.03*, Gaussian Inc., Wallingford, CT, 2016.

194 H. J. Werner, P. J. Knowles, G. Knizia, F. R. Manby and M. Schütz, *Wiley Interdiscip. Rev. Comput. Mol. Sci.*, 2012, **2**, 242–253.

195 K. A. Peterson, D. Figgen, E. Goll, H. Stoll and M. Dolg, *J. Chem. Phys.*, 2003, **119**, 11113–11123.

196 B. P. Pritchard, D. Altarawy, B. Didier, T. D. Gibson and T. L. Windus, *J. Chem. Inf. Model.*, 2019, **59**, 4814–4820.

197 R. W. Wood, *London, Edinburgh, Dublin Philos. Mag. J. Sci.*, 1902, **4**, 396–402.

198 H. A. Rowland, *London, Edinburgh, Dublin Philos. Mag. J. Sci.*, 1893, **35**, 397–419.

199 U. Fano, *J. Opt. Soc. Am.*, 1941, **31**, 213.

200 Lord Rayleigh, *Proc. R. Soc. London Ser. A*, 1907, **79**, 399–416.

201 Lord Rayleigh, *London, Edinburgh, Dublin Philos. Mag. J. Sci.*, 1907, **14**, 60–65.

202 A. Hessel and A. A. Oliner, *Appl. Opt.*, 1965, **4**, 1275.

203 C. Palmer and E. Loewen, *Diffraction Grating Handbook*, Newport Corporation, Rochester, 6th edn., 2005.

204 *Sirah pulsed dye laser service manual*, Sirah Laser und Plasmatechnik GmBH.

205 D. Kessel, *Photochem. Photobiol.*, 1991, **54**, 481–483.

206 F. Liu and X. Zhang, *Biosens. Bioelectron.*, 2015, **68**, 719–725.

207 A. M. Gardner and T. G. Wright, *J. Chem. Phys.*, 2011, **135**, 114305.

208 P. Sinha, S. E. Boesch, C. Gu, R. A. Wheeler and A. K. Wilson, *J. Phys. Chem. A*, 2004, **108**, 9213–9217.

Appendix 1. Mode diagrams for *N*-fluoropyrrole and *meta*-difluorobenzene

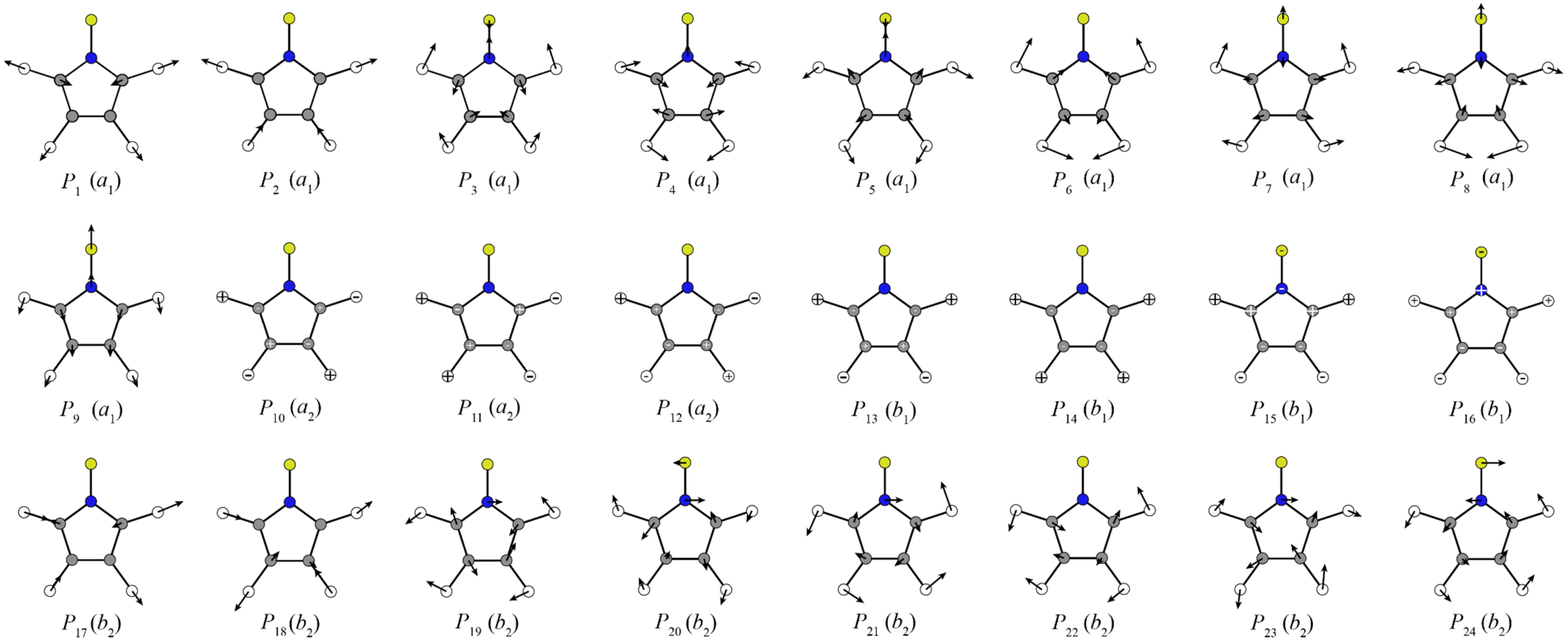

$P_1\ (a_1)$ $P_2\ (a_1)$ $P_3\ (a_1)$ $P_4\ (a_1)$ $P_5\ (a_1)$ $P_6\ (a_1)$ $P_7\ (a_1)$ $P_8\ (a_1)$

$P_9\ (a_1)$ $P_{10}\ (a_2)$ $P_{11}\ (a_2)$ $P_{12}\ (a_2)$ $P_{13}\ (b_1)$ $P_{14}\ (b_1)$ $P_{15}\ (b_1)$ $P_{16}\ (b_1)$

$P_{17}\ (b_2)$ $P_{18}\ (b_2)$ $P_{19}\ (b_2)$ $P_{20}\ (b_2)$ $P_{21}\ (b_2)$ $P_{22}\ (b_2)$ $P_{23}\ (b_2)$ $P_{24}\ (b_2)$

Figure A1.1. Mode diagrams depicting the vibrational modes of *N*-fluoropyrrole and their symmetries, which are the basis of the P_i labelling scheme. Fluorine is yellow, nitrogen is blue, carbon is grey, and hydrogen is white. The lengths of the arrows and sizes of the ‘+’ and ‘-’ symbols approximately indicate the magnitude of the vibrational motion. See Section 11.

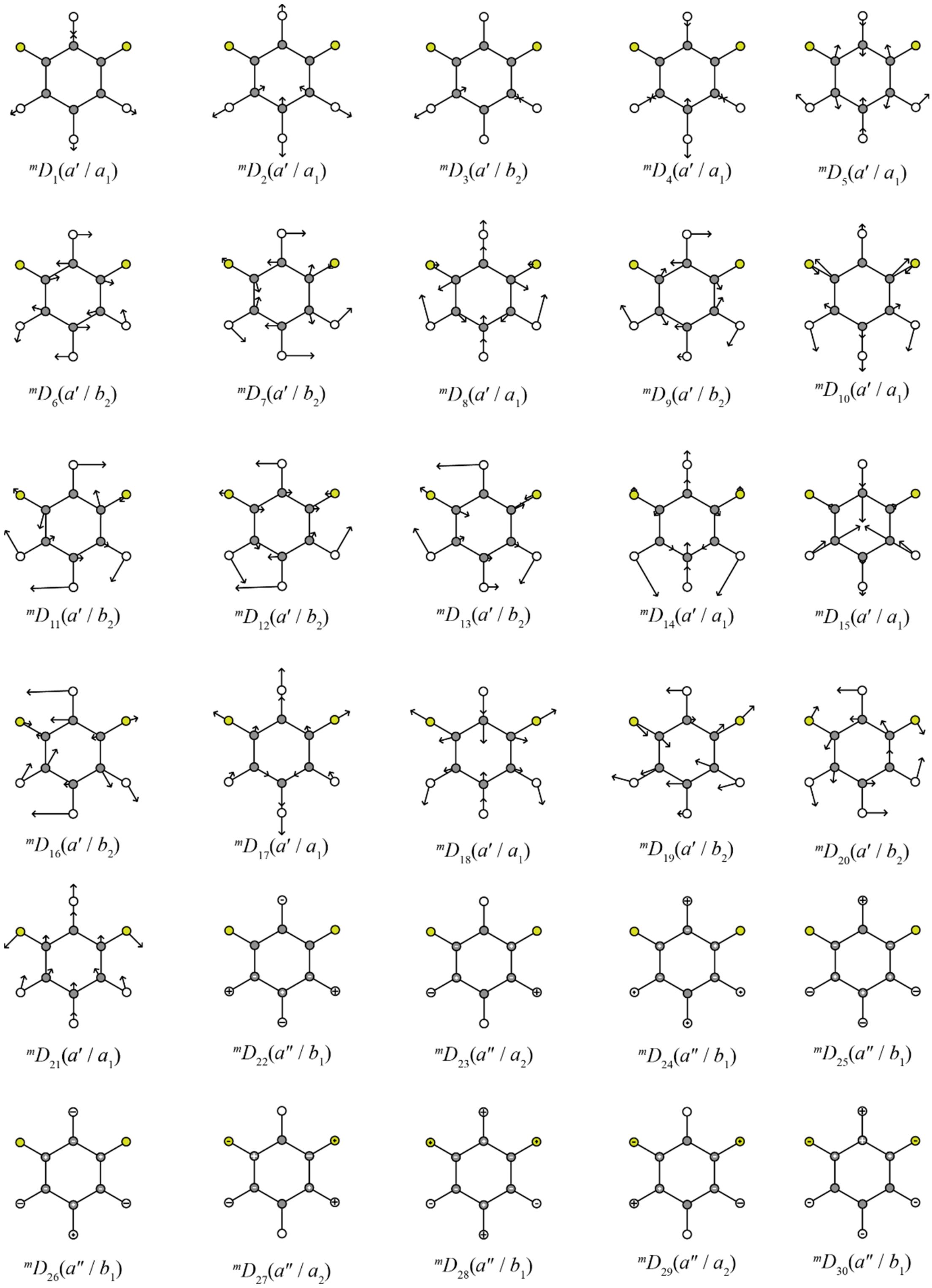

Figure A1.2. Mode diagrams depicting the vibrational modes of *meta*-difluorobenzene, alongside their symmetries, that form the basis of the $^{m}D_{i}$ labelling scheme. Note that symmetries of the a_1 and b_2 modes in C_{2v} decompose to a' in C_s symmetry, and the b_1 and a_2 modes decompose to a''. Fluorine is yellow, nitrogen is blue, carbon is grey, and hydrogen is white. The lengths of the arrows and sizes of the '+' and '-' symbols approximately indicate the magnitude of the vibrational motion. Adapted from Ref. 158.

Appendix 2. Pertinent character tables

Presented below are the character tables for the symmetry classes which have been considered in this thesis.

Table A2.1. Character table for the C_s point group, alongside the linear functions, rotations and quadratic functions.

C_s	E	σ_h		
A'	1	1	x, y, R_z	x^2, y^2, z^2, xy
A''	1	-1	z, R_x, R_y	yz, xz

Table A2.2. Character table for the C_{2v} point group, alongside the linear functions, rotations and quadratic functions.

C_{2v}	E	C_2	$\sigma_v(xz)$	$\sigma_v(yz)$		
A_1	1	1	1	1	z	x^2, y^2, z^2
A_2	1	1	-1	-1	R_z	xy
B_1	1	-1	1	-1	x, R_y	xz
B_2	1	-1	-1	1	y, R_x	yz

Table A2.3. Character table for the C_{3v} point group, alongside the linear functions, rotations and quadratic functions. Note that this character table is isomorphic to the character table of the G_6 MSG.

C_{3v}	E	$2C_3$	$3\sigma_v$		
A_1	1	1	1	z	$x^2 + y^2, z^2$
A_2	1	1	-1	R_z	-
E	2	-1	0	x, y, R_x, R_y	$x^2 - y^2, xy, xz, yz$

Table A2.4. Character table for the D_{3h} point group, alongside the linear functions, rotations and quadratic functions. Note that this character table is isomorphic to that of the G_{12} MSG.

$\mathbf{D_{3h}}$	E	$2C_3$	$3C_2$	σ_h	$2S_3$	$3\sigma_v$		
A_1'	1	1	1	1	1	1		$x^2 + y^2, z^2$
A_2'	1	1	-1	1	1	-1	R_z	
E'	2	-1	0	2	-1	0	x, y	$x^2 - y^2, xy$
A_1''	1	1	1	-1	-1	-1		
A_2''	1	1	-1	-1	-1	1	z	
E''	2	-1	0	-2	1	0	R_x, R_y	xz, yz

Table A2.5. Character table for the G_6 molecular symmetry group, alongside the translational and rotational operations. Note that this character table is isomorphic to the character table of the C_{3v} point group; the translational (T_a, T_b and T_c) and rotational (J_a, J_b and J_c) functions are given with respect to the principal inertial axes rather than Cartesian axes and are not the same as those in the C_{3v} character table.

$\mathbf{G_6}$	E	(123)	(23)*	
A_1	1	1	1	T_a, T_b, J_c
A_2	1	1	-1	T_c, J_a, J_b
E	2	-1	0	

Table A2.6. Character table for the G_{12} molecular symmetry group, alongside the translational and rotational operations. Note that this character table is isomorphic to that of the D_{3h} point group; the translational (T_a, T_b and T_c) and rotational (J_a, J_b and J_c) functions are given with respect to the principal inertial axes rather than Cartesian axes and are not the same as those in the D_{3h} character table.

$\mathbf{G_{12}}$	E	(123)	(23)*	(ab)(cd)	(123)(ab)(cd)	(23)(ab)(cd)*	
A_1'	1	1	1	1	1	1	T_a
A_1''	1	1	1	-1	-1	-1	T_b, J_c
A_2'	1	1	-1	1	1	-1	J_a
A_2''	1	1	-1	-1	-1	1	T_c, J_b
E'	2	-1	0	2	-1	0	
E''	2	-1	0	-2	1	0	

Appendix 3. The $^{m}D_i$ labels and vibrations for *meta*-disubstituted benzenes and the P_i labels and vibrations for *N*-substituted pyrroles

Table A3.1. The $^{m}D_i$ labels, separated by C_s symmetry (G_6 symmetry label in parentheses) and the corresponding calculated harmonic vibrational wavenumbers (in cm^{-1}) for the S_0 states of *m*FT and *m*DFB – the basis for the $^{m}D_i$ vibrational labels. See Ref. 158 for more details and discussion.

$^{m}D_i$	C_{2v}	*m*DFB[a]	*m*FT[a]
	a' (a_1)[b]		
D_1	a_1	3122	3108
D_2	a_1	3116	3089
D_3	b_2	3112	3087
D_4	a_1	3090	3072
D_5	a_1	1597	1578
D_6	b_2	1592	1602
D_7	b_2	1475	1479
D_8	a_1	1439	1419
D_9	b_2	1304	1302
D_{10}	a_1	1255	1240
D_{11}	b_2	1252	1271
D_{12}	b_2	1145	1148
D_{13}	b_2	1102	1127
D_{14}	a_1	1058	1071
D_{15}	a_1	994	989
D_{16}	b_2	941	913
D_{17}	a_1	726	719
D_{18}	a_1	514	519
D_{19}	b_2	502	505
D_{20}	b_2	467	435
D_{21}	a_1	320	285

[a] Harmonic vibrational wavenumbers calculated at the B3LYP/aug-cc-pVTZ level, scaled by 0.97[208]. These values have been obtained from Ref. 158.

[b] The a_1 and b_2 symmetry modes decompose to a' symmetry in the C_s point group and to a_1 in the G_6 MSG.

[c] The a_2 and b_1 symmetry modes decompose to a'' symmetry in the C_s point group and to a_2 in the G_6 MSG.

Table A3.1 (continued). The $^{m}D_i$ labels, separated by C_s symmetry (G_6 in parentheses) and the corresponding calculated harmonic vibrational wavenumbers (in cm^{-1}) for the S_0 states of *m*FT and *m*DFB – the basis for the $^{m}D_i$ vibrational labels. See Ref. 158 for more details and discussion.

$^{m}D_i$	C_{2v}	*m*DFB[a]	*m*FT[a]
	a'' (a_2)[c]		
D_{22}	b_1	963	968
D_{23}	a_2	871	886
D_{24}	b_1	856	860
D_{25}	b_1	767	774
D_{26}	b_1	671	683
D_{27}	a_2	597	557
D_{28}	b_1	455	443
D_{29}	a_2	239	235
D_{30}	b_1	222	198

[a] Harmonic vibrational wavenumbers calculated at the B3LYP/aug-cc-pVTZ level, scaled by 0.97[208]. These values have been obtained from Ref. 158.

[b] The a_1 and b_2 symmetry modes decompose to a' symmetry in the C_s point group and to a_1 in the G_6 MSG.

[c] The a_2 and b_1 symmetry modes decompose to a'' symmetry in the C_s point group and to a_2 in the G_6 MSG.

Table A3.2. The P_i labels, sorted by C_{2v} symmetry (with the G_{12} symmetry label in parentheses), and the corresponding harmonic vibrational wavenumbers (in cm^{-1}) for the S_0 states of NFP and NMP. See Section 11 for more details and discussion.

P_i	NFP[a]	NMP[a]
	a_1 (a_1')	
P_1	3187	3160
P_2	3155	3141
P_3	1446	1492
P_4	1367	1375
P_5	1254	1278
P_6	1048	1075
P_7	1033	1045
P_8	948	956
P_9	632	652
	a_2 (a_2')	
P_{10}	858	863
P_{11}	629	675
P_{12}	608	610
	b_1 (a_2'')	
P_{13}	796	814
P_{14}	681	712
P_{15}	527	603
P_{16}	141	186
	b_2 (a_1'')	
P_{17}	3184	3152
P_{18}	3143	3132
P_{19}	1493	1505
P_{20}	1373	1350
P_{21}	1239	1262
P_{22}	1046	1073
P_{23}	845	864
P_{24}	388	347

[a] Harmonic vibrational wavenumbers calculated at the B3LYP/aug-cc-pVTZ level, scaled by 0.97[208], see Section 11.

Appendix 4. Supplementary material

The following pages contain the supplementary material for the following papers, in the same order as the list below, included as part of this thesis. This material is included here for the convenience of the reader.

1. **Vibrations of pyrrole, *N*-substituted pyrroles and their cations**, *J. Molec. Spectrosc.*, DOI: 10.1016/j.jms.2020.111410. The supplementary material presented below gives the geometric parameter values for pyrrole, *N*-fluoropyrrole, *N*-aminopyrrole and *N*-methylpyrrole and their corresponding cations. (*n.b.*, a title has been added to this for clarity, which does not appear in the document found *via* the above DOI.)

2. **Electronic, vibrational and torsional couplings in N-methylpyrrole: ground, first excited and cation states**, *J. Chem. Phys.*, DOI: 10.1063/5.0050654. The supplementary material presents a correlation table between the vibrational labels used by Biswas *et al.*[100] and the P_i labels (Section 11). Furthermore, we present expansions of the LIF spectrum of the $\tilde{A}^1A_2 \leftarrow \tilde{X}^1A_1$ transition of NMP around the 16^1, 15^1 and 23^1 vibrational bands, showing their band shapes are consistent with the intensity stealing arguments presented therein. We also present geometric data for the CH_3 and pyrrolyl radicals (see Figure 15 of Section 12 and the surrounding discussion). Finally, we show the one-colour and two-colour mass spectra when exciting *via* the 16^1 and 15^1 levels in S_1.

3. **Spectroscopy of *N*-Methylpyrrole-RG (RG = Ar, Kr) complexes: first excited and cation states**, *Chem. Phys. Lett.*, DOI: 10.1016/j.cplett.2022.139800. Included in this supplementary material is a schematic description of the various isomers of NMP-RG that were considered as a part of this work and also the Cartesian coordinates of the optimised geometries of the complexes investigated.

Supplementary Information

Vibrations of pyrrole, N-substituted pyrroles and their cations

Alexander R. Davies, David J. Kemp, and Timothy G. Wright

Pyrrole and Pyrrole$^+$

Parameter	Pyr (C_{2v})	Pyr$^+$ (C_{2v})
Bond lengths / Å		
N-H_1	1.003	1.010
C_1-H_2	1.076	1.079
C_2-H_3	1.076	1.077
N-C1	1.371	1.358
C_1-C_2	1.373	1.429
C_2-C_2	1.422	1.368
Bond angles / °		
H_1-N-C_1	125.1	125.5
C_1-N-C_1	109.8	109.1
N-C_1-H_2	121.3	121.8
N-C_1-C_2	107.7	108.3
C_1-C_2-C_2	107.4	107.2
C_1-C_2-H_3	125.8	124.8

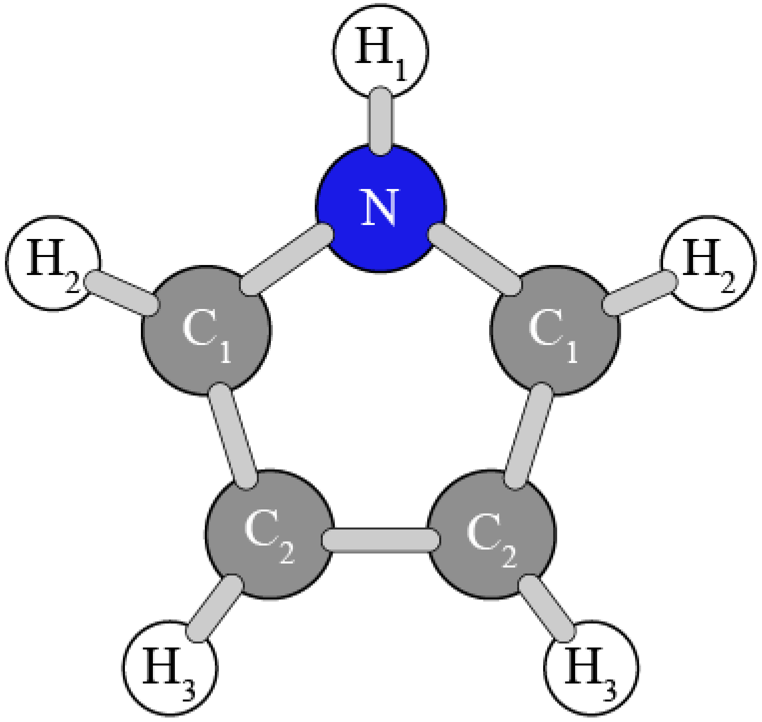

N-Fluoropyrrole and *N*-Fluoropyrrole$^+$

Parameter	NFP (C_{2v})	NFP$^+$ (C_{2v})
Bond lengths / Å		
N-F	1.367	1.342
C_1-H_1	1.074	1.079
C_2-H_2	1.076	1.077
N-C_1	1.359	1.351
C_1-C_2	1.380	1.436
C_2-C_2	1.418	1.366
Bond angles / °		
F-N-C_1	123.2	123.8
C_1-N-C_1	113.7	112.3
N-C_1-H_1	121.6	121.8
N-C_1-C_2	105.1	106.0
C_1-C_2-C_2	108.1	107.8
C_1-C_2-H_2	125.0	124.1

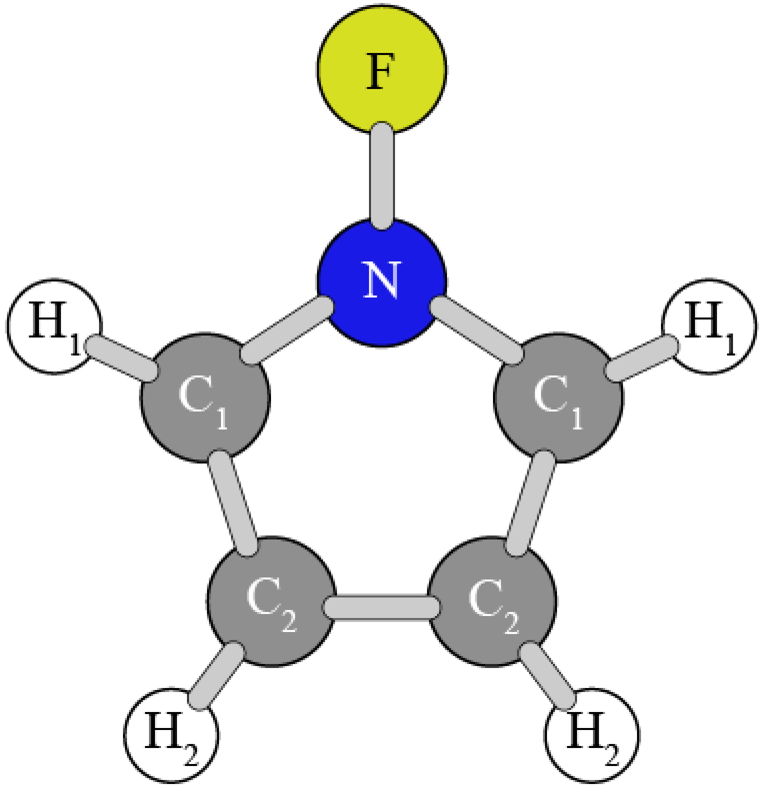

N-Aminopyrrole and *N*-Aminopyrrole$^+$

Parameter	**NAP (C_s)**	**NAP$^+$ (C_{2v})**
Bond lengths / Å		
N_1-N_2	1.401	1.316
N_2-H_A	1.014	1.010
N_2-H_B	1.014	-
N_1-C_1	1.369	1.400
C_1-H_1	1.075	1.076
C_1-C_2	1.374	1.352
C_2-H_2	1.076	1.077
C_2-C_2	-	1.465
C_2-C_3	1.421	-
C_3-H_3	1.076	-
C_3-C_4	1.374	-
C_4-H_4	1.076	-
N_1-C_4	1.375	-
Bond angles / °		
H_A-N_2-H_A	-	121.1
H_A-N_2-H_B	108.7	-
H_A-N_2-N_1	109.5	118.7
H_B-N_2-N_1	109.5	-
N_2-N_1-C_1	122.8	124.6
N_2-N_1-C_4	127.4	-
N_1-C_1-H_1	120.1	120.9
C_1-N_1-C_1	-	110.8
C_1-N_1-C_4	109.8	-
N_1-C_4-H_4	120.9	-
N_1-C_1-C_2	107.7	106.5
N_1-C_4-C_3	107.5	-
C_4-C_3-H_3	125.7	-
C_1-C_2-H_2	125.7	126.0
C_1-C_2-C_2	-	108.1
C_1-C_2-C_3	107.4	-
C_4-C_3-C_2	107.5	-
Dihedral angle / °		
H_A-N_2-N_1-C_1	120.5	7.840

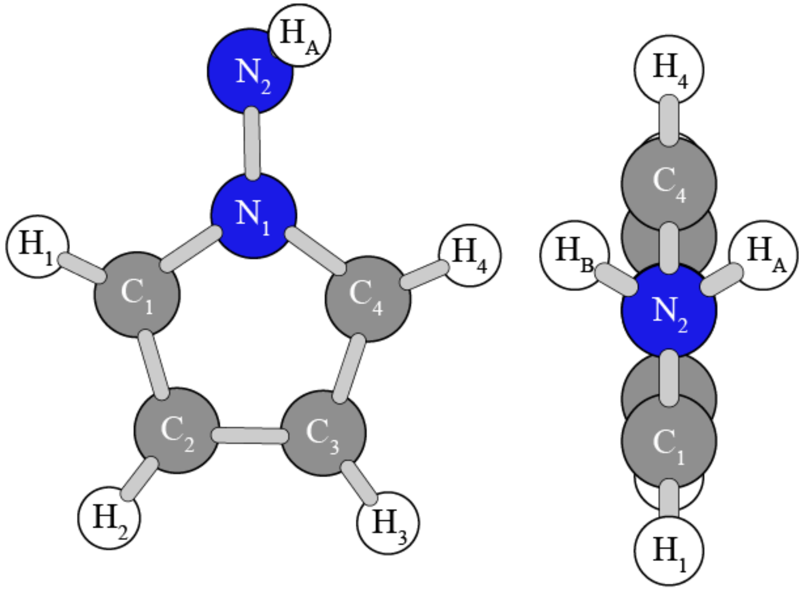

N-Aminopyrrole - C_s
NH_2 Pyramidal

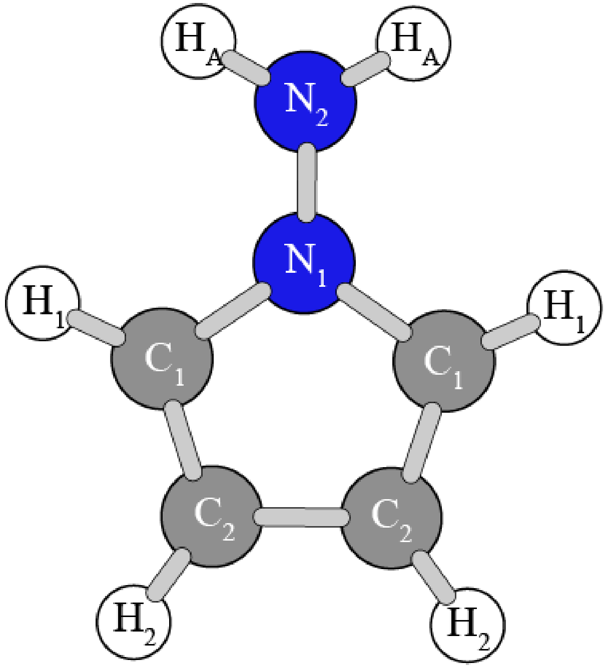

N-Aminopyrrole$^+$ - C_{2v}
NH_2 Planar

'-' means this parameter is not applicable to the molecule.

N-Methylpyrrole and *N*-Methylpyrrole⁺

Parameter	NMP (C_s)	NMP⁺ (C_s)
Bond lengths / Å		
C_{Me}-H_A	1.088	1.085
C_{Me}-H_B	1.092	1.087
C_{Me}-H_C	1.088	1.087
N-C_{Me}	1.448	1.471
N-C_1	1.372	1.350
C_1-H_1	1.076	1.079
C_1-C_2	1.375	1.436
C_2-H_2	1.077	1.077
C_2-C_2	1.419	-
C_2-C_3	-	1.365
C_3-H_3	-	1.077
C_3-C_4	-	1.426
C_4-H_4	-	1.079
N-C_4	-	1.367
Bond angles / °		
H_A-C_{Me}-H_B	108.8	109.4
H_A-C_{Me}-H_C	108.4	109.4
H_B-C_{Me}-H_C	108.8	110.1
H_A-C_{Me}-N	109.7	108.6
H_B-C_{Me}-N	111.6	109.6
H_C-C_{Me}-N	109.7	109.6
C_{Me}-N-C_1	125.5	126.6
C_{Me}-N-C_4	-	125.6
C_1-N-C_1	108.9	-
C_1-N-C_4	-	107.8
N-C_1-H_1	120.8	121.5
N-C_1-C_2	108.4	109.2
C_1-C_2-H_2	125.8	124.7
C_1-C_2-C_2	107.2	-
C_1-C_2-C_3	-	106.9
C_2-C_3-C_4	-	106.8
C_2-C_3-H_3	-	128.3
C_3-C_4-N	-	109.2
C_3-C_4-H_4	-	129.6
Dihedral angles / °		
H_A-C_{Me}-N-C_1	33.43	0.008
H_B-C_{Me}-N-C_1	87.12	119.5

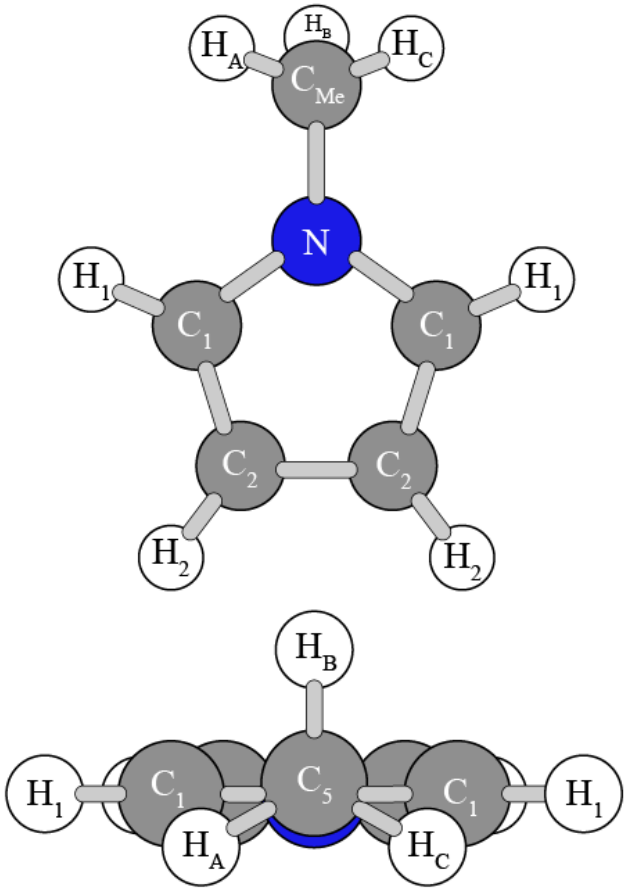

N-Methylpyrrole - C_s
CH_3 Staggered

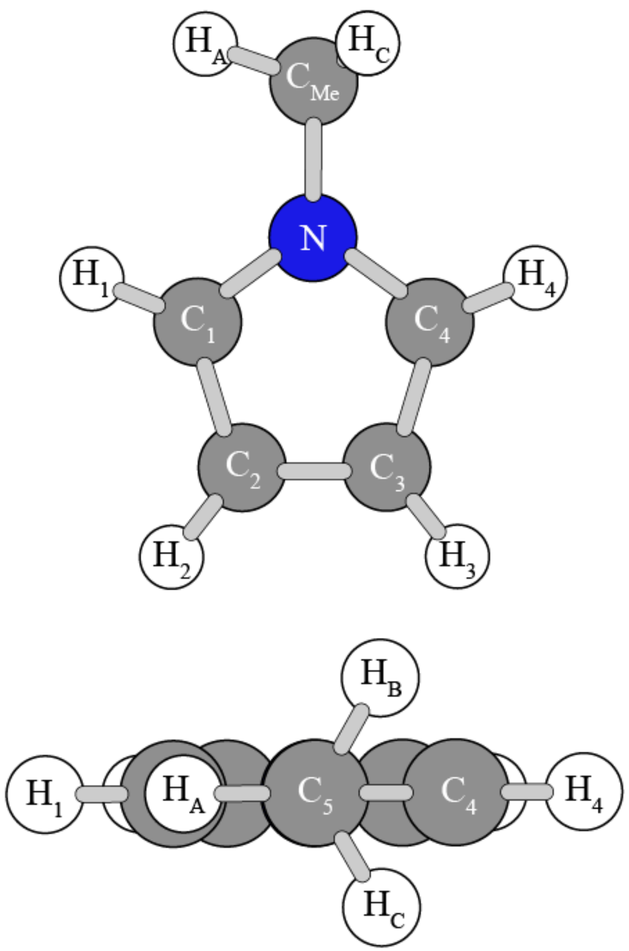

N-Methylpyrrole⁺ - C_s
CH_3 Eclipsed

'-' means this parameter is not applicable to the molecule.

Supplementary Information

Electronic, vibrational and torsional couplings in *N*-methylpyrrole: ground, first excited and cation states

Alexander R. Davies, David J. Kemp, and Timothy G. Wright[a]

School of Chemistry, University of Nottingham, University Park, Nottingham NG7 2RD, UK

[a]Email: Tim.Wright@nottingham.ac.uk

Table SI: Correlation between the labels used by Biswas et al.[1] and the P_i labels[2] used in the present work.

Biswas	P_i
$\boldsymbol{a_1}$	
1	**1**
2	**2**
4	**3**
6	**4**
7	**5**
8	**6**
9	**7**
10	**8**
11	**9**
$\boldsymbol{a_2}$	
12	**10**
13	**11**
14	**12**
$\boldsymbol{b_1}$	
19	**13**
20	**14**
21	**15**
22	**16**
$\boldsymbol{b_2}$	
23	**17**
24	**18**
26	**19**
28	**20**
29	**21**
31	**22**
32	**23**
33	**24**
Me	
25	Me_1
16	Me_2
3	Me_3
27	Me_4
17	Me_5
5	Me_6
18	Me_7
30	Me_8
15	Me_9

---

[1] N. Biswas, S. Wategaonkar, and J. G. Philis, Chem. Phys. **293**, 99 (2003).

[2] A. R. Davies, D. J. Kemp and T. G. Wright, J. Molec. Spec. **376**, 111410 (2021).

Figure S1: Expanded views of the 16^1, 15^1 and 23^1 LIF bands and principal inertial axes for NMP.

These band contours demonstrate that the 16^1 and 15^1 bands are type *b*, consistent with being induced via vibronic intensity stealing from a $^1B_2 \leftarrow S_0$ electronic transition, while the 23^1 band is type *c*, consistent with being induced via vibronic intensity stealing from a $^1B_1 \leftarrow S_0$ electronic transition. The *x*-axis wavenumber scale is merely given as an indication of scale.

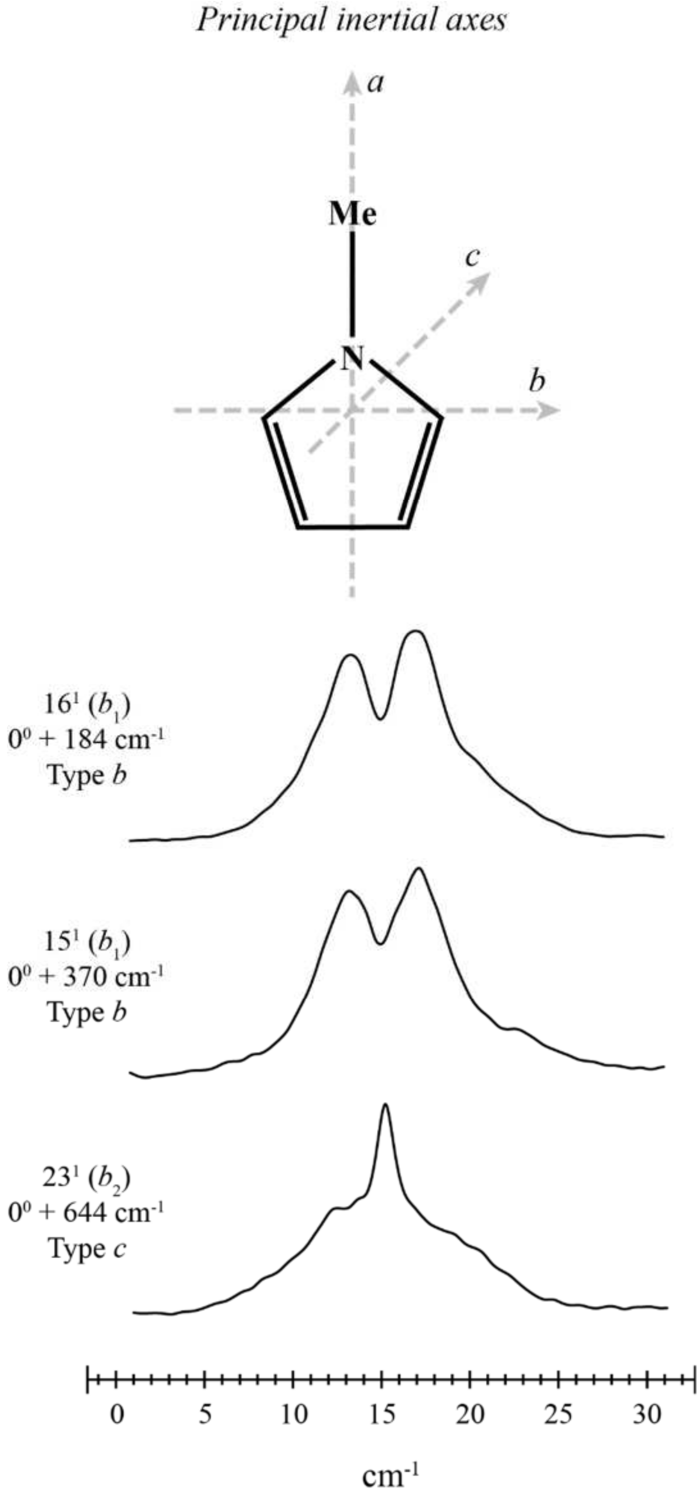

Figure S2: Optimized geometries (CAM-B3LYP/aug-cc-pVTZ) of pyrrolyl ($\tilde{X}^2A_2$) and CH_3 ($\tilde{X}^2A_2''$).

These correspond to the lowest-energy dissociation asymptote of *N*-methyl pyrrole into pyrrolyl + CH_3, and the energies are employed in Figure 15 of the main article.

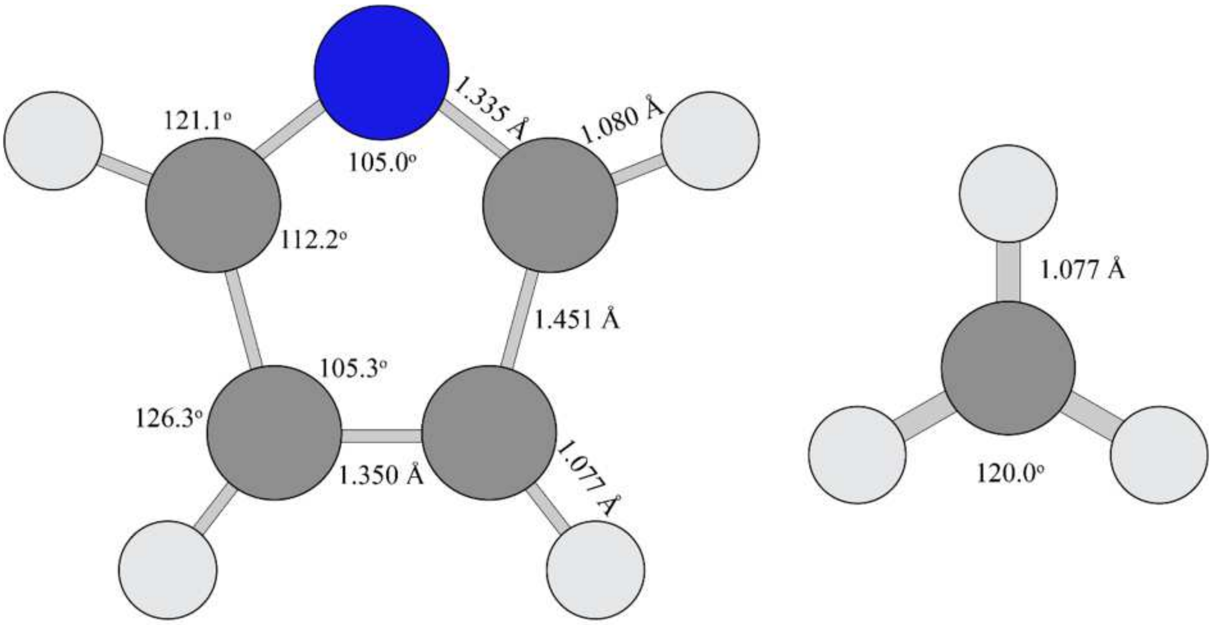

$\tilde{X}^2A_2$ - Pyrrolyl
C_{2v}

$\tilde{X}^2A_2''$ - Methyl
D_{3h}

Figure S3: Mass spectra in a (1+1) and (1+1′) REMPI experiment recorded when exciting via 16^1, with the excitation wavenumber set above the first step in the PIE curve (see Figure 7 of main text) at ~23,100 cm^{-1}

Suggestions of assignments for a number of the bands are given. The NMP$^+$ parent-ion signal is off-scale to allow the other masses to be seen. It is deduced that the lower masses come from multiphoton fragmentation. To higher time-of-flight are the ions of various clusters.

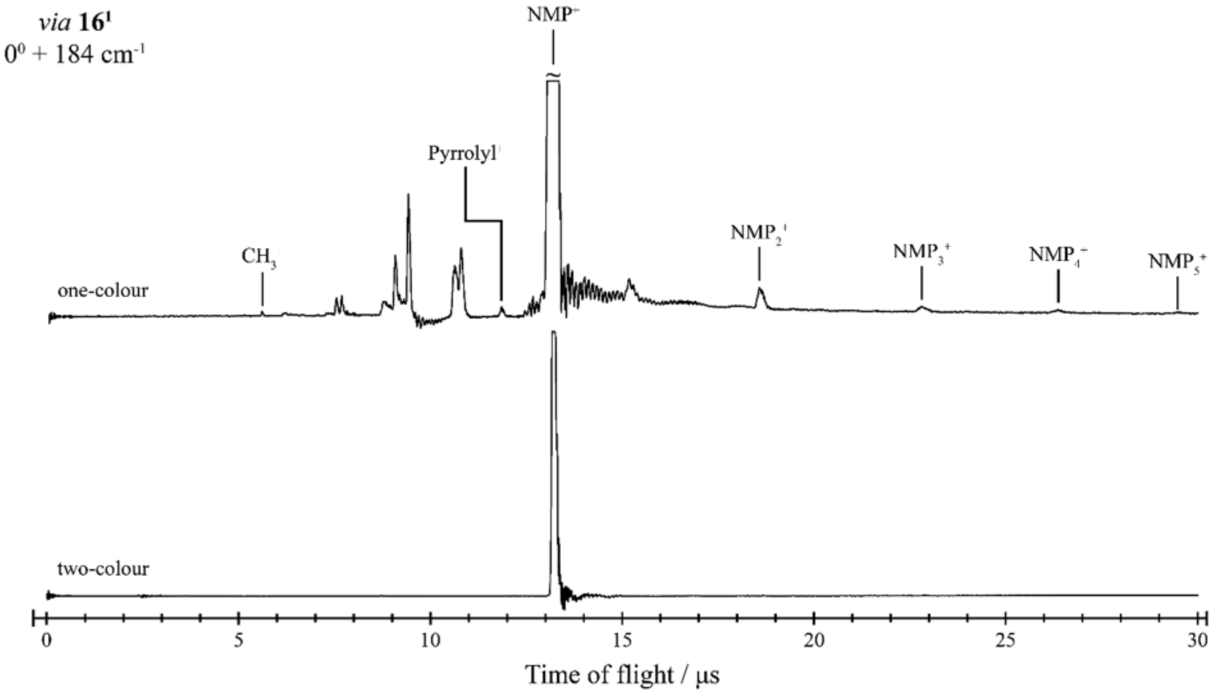

Figure S4: Mass spectra in a (1+1) and (1+1′) REMPI experiment recorded when exciting via 15^1, with the excitation wavenumber set above the first step in the PIE curve (see Figure 7 of main text) at ~22,900 cm^{-1}

Suggestions of assignments for a number of the bands are given. The NMP$^+$ parent-ion signal is off-scale to allow the other masses to be seen. It is deduced that the lower masses come from multiphoton fragmentation. To higher time-of-flight are the ions of various clusters. A new ion appears here: NMP$^+$-Ar, arising as there is a serendipitous resonance involving NMP-Ar at this wavenumber. Spectra have been recorded for this species, and will be reported in due course.

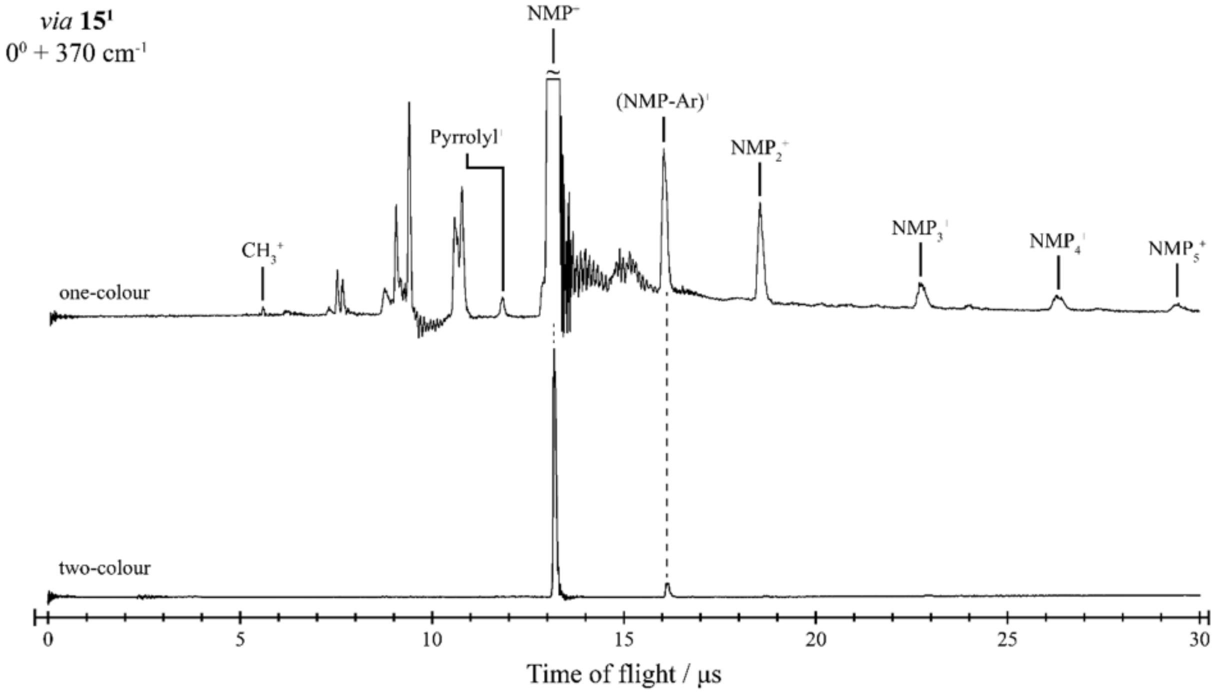

Electronic Supplementary Information

Spectroscopy of *N*-methylpyrrole-RG (RG = Ar, Kr) complexes: first excited and cation states.

Alexander R. Davies, Jessica T. L. Haynes and Timothy G. Wright

Figure S1. Schematic depictions of the conformations investigated. Blue: nitrogen; grey: carbon; white: hydrogen and green: Ar/Kr.

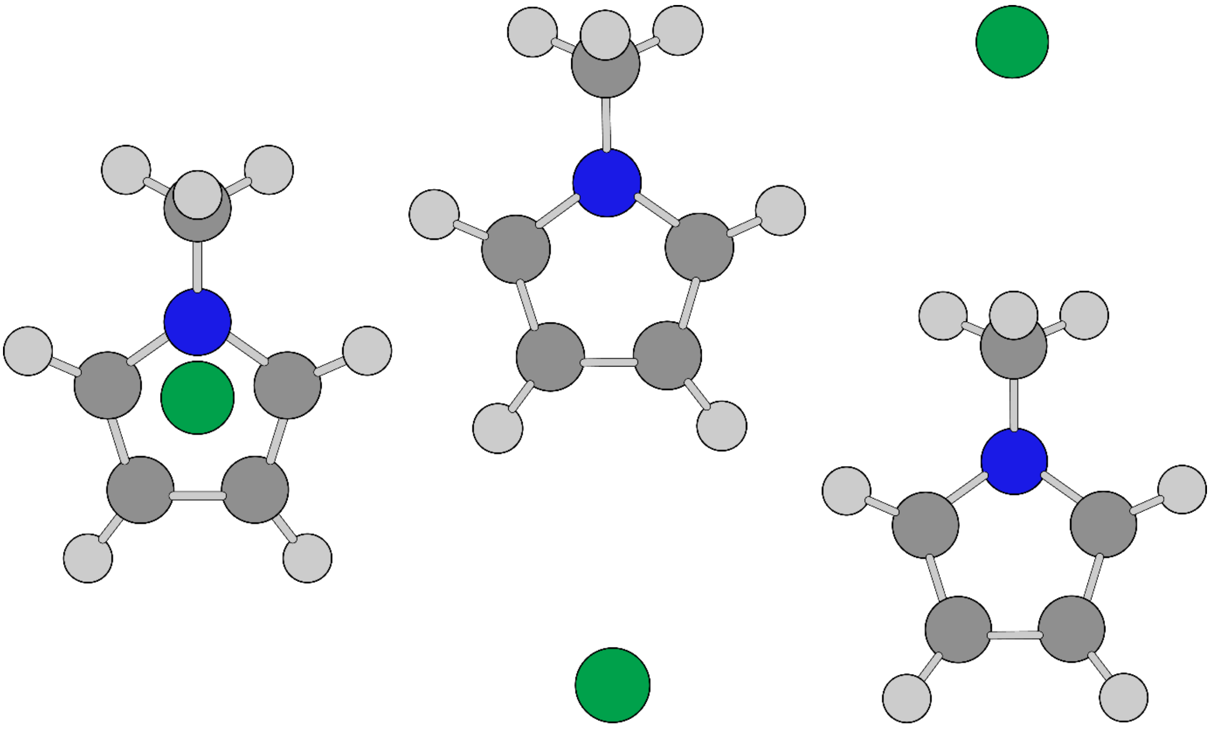

Isomer A Isomer B Isomer C

Geometries of the complexes investigated – given as Cartesian coordinates, (x, y, z) in Ångstrom. These geometries had all real frequencies, unless otherwise stated.

a. NMP-Ar

i. S_0 state [(R/TD/U)-CAM-B3LYP/aug-cc-pVTZ]

1. Ar above the pyrrolyl ring:

C	1.09836200	-0.07540000	-1.11048600
C	1.31338000	-1.36545500	-0.70759600
C	1.31337500	-1.36545700	0.70763400
C	1.09835500	-0.07540300	1.11052600
N	0.97394300	0.70856500	0.00002000
H	1.02875900	0.35083400	-2.09603700
H	1.46415100	-2.21101500	-1.35576000
H	1.46414300	-2.21101900	1.35579700
H	1.02874600	0.35082800	2.09607700
C	0.65183100	2.11538600	0.00002100
H	1.07799400	2.58795300	0.88168400
H	1.07796100	2.58794500	-0.88166100
H	-0.42646600	2.27848100	0.00004100
Ar	-2.57692800	-0.22755500	-0.00004900

2. Ar aligned with the methyl rotor:

C	1.87516900	-1.11055400	-0.01513500
C	3.18196200	-0.70764400	0.03607800
C	3.18193300	0.70769600	0.03607700
C	1.87512400	1.11055300	-0.01513800
N	1.08217300	-0.00001700	-0.05210500
H	1.44365200	-2.09610400	-0.03330700
H	4.04054200	-1.35577300	0.06007600
H	4.04048700	1.35586100	0.06007400
H	1.44356600	2.09608600	-0.03331200
C	-0.36075500	-0.00004600	-0.02306900
H	-0.73707700	0.88145800	-0.53647100
H	-0.73704200	-0.88156400	-0.53647500
H	-0.74096500	-0.00005600	0.99901800
Ar	-4.15827600	0.00000900	0.01512500

3. Ar at the base of the pyrrolyl ring:

C	-1.41296300	-1.11056500	-0.01932800
C	-0.10519900	-0.70764900	-0.01104500
C	-0.10519900	0.70764900	-0.01104500
C	-1.41296300	1.11056500	-0.01932800
N	-2.20671700	0.00000000	-0.03026500
H	-1.84483000	-2.09612200	-0.02335900
H	0.75381500	-1.35558900	-0.01524000
H	0.75381500	1.35558900	-0.01524000
H	-1.84483000	2.09612200	-0.02335900
C	-3.64791700	0.00000000	0.04642200
H	-4.04065300	0.88162000	-0.45437100
H	-4.04065300	-0.88162000	-0.45437100
H	-3.99378000	0.00000000	1.08065100
Ar	3.87831000	0.00000000	0.01128300

ii. S_1 state

1. Ar above the ring – note this is a rigid optimisation, where the NMP moiety was fixed at its S_1 state optimised geometry and only the Ar was allowed to relax – see text for details:

C	-1.68538300	-0.08824300	-1.09071100
C	-2.02843200	-1.39986100	-0.67955600
C	-2.06182400	-1.38796900	0.67896000
C	-1.73628200	-0.05910900	1.08823800
N	-1.51699500	0.69284100	0.00356100
H	-1.55765100	0.31205000	-2.08061600
H	-2.21899200	-2.22217700	-1.34473400
H	-2.28483100	-2.19706100	1.35030400
H	-1.65855300	0.35282900	2.07861200
C	-1.15538800	2.11155600	-0.01777000
H	-1.10373300	2.46896600	1.00753000
H	-0.18367400	2.22436800	-0.49616300
H	-1.91853600	2.66549600	-0.56199100
Ar	4.08604400	-0.19514500	0.00817600

2. Ar aligned with the methyl rotor:

C	1.85884500	1.09227400	0.00031000
C	3.22026700	0.66183000	0.00047000
C	3.20274900	-0.69716300	0.00035300
C	1.84043000	-1.08791100	0.00014500
N	1.05942600	0.01876200	0.00012100
H	1.45584500	2.08946200	0.00032700
H	4.06942000	1.32069500	0.00063100
H	4.03607000	-1.37587500	0.00039900
H	1.40658900	-2.07201200	0.00000100
C	-0.40438700	0.02008700	-0.00000500
H	-0.76147000	-0.48544200	0.89584800
H	-0.74762500	1.05176800	-0.00056400
H	-0.76129700	-0.48632900	-0.89542400
Ar	-4.13449700	-0.00601700	-0.00053900

3. Ar at the base of the pyrrolyl ring:

C	1.46770300	1.09141600	-0.00005600
C	0.10155000	0.67560800	-0.00012600
C	0.10438200	-0.68342400	-0.00015900
C	1.46261200	-1.08895800	-0.00011300
N	2.25541300	0.00925000	-0.00005000
H	1.88155700	2.08403300	-0.00001400
H	-0.74077300	1.34300500	-0.00014800
H	-0.73655500	-1.35250600	-0.00021500
H	1.88592400	-2.07752800	-0.00012300
C	3.71888600	-0.00535100	0.00002900
H	4.07096800	-0.51522900	-0.89551800
H	4.07391900	1.02243600	-0.00007700
H	4.07087700	-0.51502000	0.89573200
Ar	-3.96803400	0.00057300	0.00018100

iii. D_0^+ state

1. Ar above the pyrrolyl ring:

C	1.64588100	0.24342000	-0.87139900
C	1.94060100	-1.12731900	-0.58437700
C	1.33294200	-1.42248000	0.59420900
C	0.67114000	-0.23945800	1.02387000
N	0.88390600	0.74698700	0.11368400
H	1.94702400	0.84537400	-1.71453200
H	2.53628400	-1.77167000	-1.20800200
H	1.33261700	-2.35775800	1.12695600
H	0.07869100	-0.06514700	1.90841200
C	0.35408200	2.10964200	0.19768200
H	0.67210400	2.56675100	1.13030500
H	0.74319100	2.68590700	-0.63492000
H	-0.73072400	2.08310000	0.14460500
Ar	-2.69080000	-0.36657200	-0.20602900

2. Ar aligned with the methyl rotor:

C	-1.79470500	1.09269100	-0.00024700
C	-3.16886100	0.69037400	-0.00040700
C	-3.18169300	-0.66808900	-0.00038600
C	-1.82487600	-1.09237500	-0.00021200
N	-1.01470100	-0.00028700	-0.00013100
H	-1.37327500	2.08585400	-0.00021200
H	-4.00709600	1.36591900	-0.00051900
H	-4.03392000	-1.32560000	-0.00047700
H	-1.41604000	-2.09093800	-0.00014400
C	0.45024900	-0.02802200	0.00002300
H	0.80668700	-0.53824900	-0.89018700
H	0.81796300	0.99233500	0.00026500
H	0.80648400	-0.53858800	0.89011900
Ar	4.03452300	0.00465500	0.00052400

3. Ar at the base of the pyrrolyl ring:

C	1.37161900	1.09144400	0.00002100
C	0.00355000	0.66966900	0.00001000
C	0.00984200	-0.68886100	0.00001100
C	1.37213100	-1.09413700	0.00001900
N	2.16722200	0.00944200	0.00002200
H	1.77900900	2.09045500	0.00002200
H	-0.84586200	1.33100100	0.00000400
H	-0.83479100	-1.35599700	0.00000600
H	1.79504200	-2.08682300	0.00002000
C	3.63188100	0.00220800	0.00002600
H	3.99485100	-0.50325600	-0.89045400
H	3.98448300	1.02805800	0.00003700
H	3.99484400	-0.50327100	0.89050000
Ar	-3.74290400	0.00287800	-0.00004600

b. NMP-Kr [(R/TD/U)-CAM-B3LYP/aug-cc-pVTZ(-PP); ECP10MDF used for Kr)

i. S_0 state

1. Kr above the pyrrolyl ring:

C	1.74379300	-0.11844500	-1.11048700
C	1.86048800	-1.42111900	-0.70758000
C	1.86048300	-1.42112000	0.70760800
C	1.74377800	-0.11844800	1.11051700
N	1.67912700	0.67269800	0.00001500
H	1.70691000	0.31185600	-2.09603400
H	1.94670900	-2.27566500	-1.35576400
H	1.94669900	-2.27566700	1.35579100
H	1.70688100	0.31185100	2.09606400
C	1.46650100	2.10021900	0.00001600
H	1.92784100	2.53846500	0.88169300
H	1.92785600	2.53846800	-0.88165300
H	0.40400600	2.34600500	0.00000700
Kr	-2.09364000	-0.06474200	-0.00001800

2. Kr aligned with the methyl rotor:

C	2.90220100	-1.11056300	-0.01515700
C	4.20889200	-0.70765200	0.03839400
C	4.20887500	0.70769600	0.03821000
C	2.90215900	1.11056400	-0.01504100
N	2.10927500	-0.00001300	-0.05343100
H	2.47070100	-2.09611000	-0.03408400
H	5.06742400	-1.35578700	0.06391600
H	5.06739000	1.35586000	0.06359900
H	2.47062300	2.09609600	-0.03389100
C	0.66630800	-0.00004100	-0.02712600
H	0.29082100	0.88144900	-0.54118200
H	0.29085000	-0.88149200	-0.54127100
H	0.28403100	-0.00009900	0.99421300
Kr	-3.33437100	0.00000400	0.00797300

3. Kr at the base of the pyrrolyl ring:

C	-0.01679800	2.38540500	1.11056700
C	-0.01679800	1.07760900	0.70764200
C	-0.01679800	1.07760900	-0.70764200
C	-0.01679800	2.38540500	-1.11056700
N	-0.02268900	3.17920000	0.00000000
H	-0.01808000	2.81727800	2.09612900
H	-0.02641600	0.21869200	1.35568500
H	-0.02641600	0.21869200	-1.35568500
H	-0.01808000	2.81727800	-2.09612900
C	0.06312100	4.61988800	0.00000000
H	-0.43517600	5.01578100	-0.88162200
H	-0.43517600	5.01578100	0.88162200
H	1.09952200	4.95918000	0.00000000
Kr	0.00119600	-3.12757200	0.00000000

ii. S_1 state

1. Kr above the ring:

C	-2.62521100	-0.06574600	-1.08854000
C	-3.00734300	-1.36859400	-0.68154200
C	-3.00758200	-1.36993200	0.67753200
C	-2.62377000	-0.05856700	1.09176500
N	-2.40847500	0.69808500	0.00867100
H	-2.50023400	0.33740300	-2.07755600
H	-3.23928400	-2.17736600	-1.35008900
H	-3.23950900	-2.17868300	1.34617100
H	-2.50179100	0.33786400	2.08389800
C	-1.99735500	2.10257600	-0.00738300
H	-1.80712000	2.41795100	1.01557300
H	-1.08405700	2.19816400	-0.59281800
H	-2.79504100	2.70563000	-0.43786600
Kr	3.15538700	-0.11016600	0.00002800

2. Kr aligned with the methyl rotor:

C	2.86375400	1.09219700	0.00038100
C	4.22546700	0.66245700	0.00050100
C	4.20866800	-0.69650100	0.00057500
C	2.84638500	-1.08802400	0.00042600
N	2.06499100	0.01819100	0.00032000
H	2.46010500	2.08908600	0.00031100
H	5.07429600	1.32170600	0.00055300
H	5.04235000	-1.37473900	0.00069400
H	2.41301900	-2.07230300	0.00041200
C	0.60105400	0.01882500	0.00014700
H	0.24398300	-0.48733700	0.89558700
H	0.25711200	1.05025000	0.00015700
H	0.24419200	-0.48725200	-0.89542300
Kr	-3.29616500	-0.00279100	-0.00046400

3. Kr at the base of the pyrrolyl ring (*n.b.* this geometry has two imaginary frequencies which are 7.54*i* and 0.74*i* cm^{-1}):

C	2.50840800	1.09138400	0.00008800
C	1.14239900	0.67539000	0.00010900
C	1.14539600	-0.68364100	0.00009500
C	2.50352800	-1.08902100	0.00010900
N	3.29633000	0.00933000	0.00008100
H	2.92208100	2.08410800	0.00007600
H	0.29989900	1.34260000	0.00011400
H	0.30440700	-1.35269100	0.00009100
H	2.92694300	-2.07757900	0.00010600
C	4.75972000	-0.00509300	0.00005100
H	5.11191100	-0.51477000	-0.89553000
H	5.11464900	1.02269600	0.00006900
H	5.11194300	-0.51481000	0.89559700
Kr	-3.25619000	0.00030600	-0.00010600

iii. D_0^+ state:

1. Kr above the pyrrolyl ring:

C	2.34361100	0.15336300	-0.87418700
C	2.51631800	-1.23674200	-0.58235700
C	1.88298000	-1.47352900	0.59584100
C	1.32671100	-0.23540100	1.02057200
N	1.62720000	0.72530800	0.10794900
H	2.69767300	0.72379400	-1.71864300
H	3.05410600	-1.93302300	-1.20273900
H	1.79934000	-2.40340400	1.13143900
H	0.75112000	-0.00668800	1.90370500
C	1.21897200	2.12934300	0.18667700
H	1.58378200	2.56321200	1.11327900
H	1.64897400	2.66413600	-0.65344500
H	0.13546300	2.19630200	0.14296000
Kr	-2.18867800	-0.13621300	-0.09865200

2. Kr aligned with the methyl rotor:

C	2.78074600	1.09274100	0.00034200
C	4.15485900	0.69013900	0.00054700
C	4.16739800	-0.66831000	0.00049700
C	2.81046100	-1.09227400	0.00035500
N	2.00053100	-0.00002800	0.00025400
H	2.35948700	2.08597100	0.00029600
H	4.99322800	1.36551200	0.00067000
H	5.01946600	-1.32601900	0.00058200
H	2.40134700	-2.09071700	0.00029700
C	0.53558000	-0.02749400	0.00009600
H	0.17878500	-0.53766200	0.89017600
H	0.16769700	0.99279100	-0.00010900
H	0.17899100	-0.53793800	-0.88990800
Kr	-3.22213900	0.00220700	-0.00041100

3. Kr at the base of the pyrrolyl ring:

C	2.28750900	1.09145800	-0.00003700
C	0.91951100	0.66953900	0.00000000
C	0.92591900	-0.68899000	-0.00002400
C	2.28813800	-1.09416500	-0.00002300
N	3.08324200	0.00953900	0.00000500
H	2.69485900	2.09048100	-0.00002900
H	0.06942600	1.33005500	0.00001900
H	0.08071400	-1.35543800	-0.00002200
H	2.71122000	-2.08677200	-0.00001500
C	4.54781500	0.00239900	0.00004200
H	4.91091500	-0.50303000	-0.89041300
H	4.90037900	1.02826700	0.00005100
H	4.91087800	-0.50303300	0.89051200
Kr	-2.99095700	0.00142400	0.00000300